Influence of Residual Stresses on Fatigue Response of Welded Tubular K-Joints

THÈSE N^{O} 5056 (2011)

PRÉSENTÉE LE 27 MAI 2011
À LA FACULTÉ ENVIRONNEMENT NATUREL, ARCHITECTURAL ET CONSTRUIT
LABORATOIRE DE LA CONSTRUCTION MÉTALLIQUE
PROGRAMME DOCTORAL EN STRUCTURES

ÉCOLE POLYTECHNIQUE FÉDÉRALE DE LAUSANNE

POUR L'OBTENTION DU GRADE DE DOCTEUR ÈS SCIENCES

PAR

Claire ACEVEDO

acceptée sur proposition du jury:

Prof. J.-F. Molinari, président du jury
Prof. A. Nussbaumer, Dr J.-M. Drezet, directeurs de thèse
Dr M. Duflot, rapporteur
Prof. M. Fontana, rapporteur
Prof. G. Marquis, rapporteur

ÉCOLE POLYTECHNIQUE
FÉDÉRALE DE LAUSANNE

Suisse
2011

The most exciting phrase to hear in science, the one that heralds new discoveries, is not "Eureka!" (I found it!) but "That's funny...".
Isaac Asimov

If we knew what it was we were doing, it would not be called research, would it?
Albert Einstein

Abstract

Seeking light and transparent bridge designs, engineers and architects have found an efficient and artistic way to fulfill their requirements: steel tubular bridges. In these modern tubular truss bridges, welded K-joints have been shown to be critically susceptible to fatigue failure induced by repeated traffic loads. Despite the research devoted to the study of fatigue during the last 35 years, especially in the offshore oil industry, estimating their fatigue resistance of tubular truss bridges is difficult and solutions are approximate. This is due to the complexity of the parameters influencing bridge fatigue strength, including: 1) complex loadings, 2) applied stress concentrations in joints, 3) welding imperfections, 4) welding residual stresses, and 5) size effects. Some design rules and studies are available to estimate these effects; however, residual stresses in tubular K-joints remain unknown as well as their influence on fatigue crack propagation. Residual stresses are well known to have detrimental influence on fatigue crack propagation in other metallic structures, and further study is a necessary for improving the understanding of K-joint fatigue behaviour.

To address this problem, the main objective of this research is to assess, experimentally and numerically, welding residual stresses and their influence on the fatigue response of K-joints.

In this thesis, experimental measurements of the residual stress fields were investigated through neutron-diffraction, hole-drilling and X-ray methods. Results have shown that, principal residual stresses are oriented transversely, i.e. perpendicularly to the weld direction, both at and near the surface. Residual stresses can reach the S355 steel yield strength at the weld toe. This orientation is particularly detrimental for fatigue because it is also the orientation of the principal applied stresses, and as a consequence high residual and applied stresses superimpose. Moreover, it is proved that a restraining effect occurs in the gap region in-between the braces remaining the critical residual stresses high in the gap region.

Two large scale tubular truss beams were subjected to high-cycle fatigue in order to assess the effect of residual stresses on fatigue response of welded tubular K-joints. These tests revealed that tensile residual stresses do not affect the fatigue crack growth in details loaded in tension (hot-spot 1), whereas they play a significant role in details loaded in compression (hot-spot 1c). Tensile residual stresses enable crack opening, making the fatigue cycle partly or entirely effective to crack propagation. Based on these tests and previous tests from the ICOM test database, it is recommended to design all (tension or compression) K-joints using a strength curve $\mathrm{S_{rhs}} - \mathrm{N_f}$ category 100 (for $\mathrm{T} = 16$ mm).

A thermo-mechanical finite element model was also developed to numerically reproduce the residual stress creation (using ABAQUS and MORFEO codes). Once the numerical results were validated by comparison with experimental results, the finite element model was used to model other K-joint geometries. A geometrical parametric study was performed to identify the most influential parameters affecting the residual stress distribution (technological size effect). It is found that a raise of the wall chord thickness T (proportional scaling) or of the wall thickness ratio $\tau = \frac{\mathrm{t}}{\mathrm{T}}$ (non-proportional scaling) strongly increases the magnitude of tensile transverse residual stresses. Based on this parametric study, residual stress distributions with depth for transverse, longitudinal and radial directions are proposed.

Finally, an extended finite element method (X-FEM) model was used to propagate a fatigue crack under residual and applied stresses. An analytical model based on the effective stress intensity factor range $\Delta\mathrm{K_{eff}}$ (fracture mechanics) and combined with the proposed distribution for residual stresses was also established to predict fatigue crack propagation in joints loaded in tension and in compression.

Keywords: *residual stresses, fatigue, tubular structures, K-joints, welding, finite element, crack propagation, fracture mechanics, neutron diffraction, hole-drilling, steel bridge.*

Résumé

A la recherche de structures toujours plus légères et transparentes, les ingénieurs et les architectes ont trouvé une manière efficace et élégante de satisfaire leurs exigences: les ponts tubulaires métalliques. Dans ces ponts modernes à treillis tubulaires, les joints soudés en K sont les points délicats qui doivent être dimensionnés à la fatigue sous l'action répétée des charges de trafic. Malgré les recherches vouées à l'étude de la fatigue durant les 35 dernières années, en particulier par l'industrie offshore, la prédiction de leur résistance en fatigue reste un problème délicat dont les solutions sont souvent approximatives. Ce constat s'explique par la complexité des paramètres influençant la résistance en fatigue de ce genre d'ouvrage : 1) les chargements complexes, 2) les concentrations de contraintes au niveau des joints, 3) les imperfections laissées par le soudage, 4) les contraintes résiduelles de soudage ainsi que 5) les effets d'échelle. Des règles de conception ont été établies et des études effectuées dans le but d'estimer ces effets, à l'exception des contraintes résiduelles de soudage. Celles-ci restent inconnues dans ce type de joints, ainsi que leur influence sur la propagation de fissure en fatigue. L'étude de ces contraintes résiduelles, bien connues dans d'autres structures métalliques pour avoir une influence néfaste sur la propagation des fissures en fatigue, est un point clé de l'amélioration de la compréhension du comportement en fatigue des joints en K.

Dans ce contexte, l'objectif de cette recherche est d'évaluer expérimentalement et numériquement le champ de contraintes résiduelles dues au soudage et de déterminer leur influence sur la résistance en fatigue des joints tubulaires soudés en K.

D'une part, les contraintes résiduelles ont été évaluées au moyen de trois méthodes utilisant la diffraction de neutrons, le trou incrémental et les rayons X. Les résultats obtenus ont permis de montrer que, proche de la surface, les contraintes résiduelles principales sont orientées transversalement, c'est à dire perpendiculairement au cordon de soudure. Elles atteignent la limite élastique de l'acier S355 des tubes au pied du cordon de soudure. Cette orientation est extrêmement défavorable en fatigue car elles vont se combiner avec les contraintes appliquées dont la direction principale est identique. L'effet de bridage créé dans la zone d'espacement inter-diagonales a également été mis en évidence. Il force les contraintes résiduelles transversales à garder des valeurs élevées dans toute cette zone.

D'autre part, des essais de fatigue à grand nombre de cycles ont été également réalisés sur deux poutres tubulaires (grande échelle) afin d'évaluer l'influence des contraintes résiduelles sur la réponse en fatigue des joints en K. Ces essais ont révélé que les contraintes résiduelles de traction n'influencent pas la propagation des fissures dans les joints tendus alors que dans les joints comprimés, elles jouent un rôle primordial puisqu'elles permettent à la fissure de s'ouvrir en rendant le cycle de fatigue partiellement ou entièrement efficace à la propagation. Sur la base de ces essais, combinés à d'autres effectués à l'ICOM, il est recommandé d'utiliser une courbe $\mathrm{S_{rhs} - N_f}$ de catégorie 100 (pour une épaisseur $\mathrm{T} = 16$ mm) pour dimensionner les joints de ponts en K à la fatigue.

Un modèle aux éléments finis thermo-mécanique a été développé afin de recréer numériquement la formation des contraintes résiduelles lors du soudage (logiciels ABAQUS et MORFEO). Une fois les valeurs numériques validées par comparaison avec les valeurs expérimentales, les modèles numériques ont pu être étendus à d'autres géométries au travers d'une étude paramétrique. Ainsi, les paramètres géométriques, ayant la plus forte influence sur la distribution des contraintes résiduelles, ont pu être mis en exergue. Il s'agit principalement de l'épaisseur de la paroi de la membrure T ou du rapport des épaisseurs $\tau = \frac{\mathrm{t}}{\mathrm{T}}$ dont les augmentations accroissent significativement l'intensité des contraintes résiduelles transversales de traction. En se basant sur cette étude paramétrique, les équations de distribution des contraintes résiduelles transversale, longitudinale et radiale à travers l'épaisseur ont été proposées.

Finalement, la propagation de fissures sous charges appliquées et contraintes résiduelles a été simulée au moyen de la méthode des éléments finis étendus (X-FEM) ainsi que par un modèle analytique. Ce dernier est basé sur le cumul des facteurs K (mécanique de la rupture) et sur les distributions de contraintes résiduelles proposées précédemment afin de prédire la propagation de la fissure dans les joints comprimés comme dans les joints tendus.

Mots-clés: *contraintes résiduelles, fatigue, structures tubulaires, joints en K, soudage, éléments finis, propagation de fissure, mécanique de la rupture, diffraction de neutrons, trou incrémental, ponts métalliques.*

Acknowledgements

I would like to thank Prof. Alain Nussbaumer (ICOM Lab.), director of this thesis and Dr. Jean-Marie Drezet (LSMX Lab.), co-director, for guiding me through the winding path of the PhD. I am particularly grateful to Prof. Nussbaumer for his valuable advice and interesting discussions throughout my research, and to Dr. Drezet for the useful advice and great enthusiasm he showed in working with me on the numerical model. I would also like to thank Prof. Jean-Paul Lebet, the ICOM director, and Prof. Manfred Hirt, the former ICOM director, they both gave me the opportunity to work in a high-quality research environment.

This research would not have been possible without the funding of the Swiss National Science Foundation (SNF), the donation of the tube specimens by Vallourec & Mannesmann Tubes and the fabrication of the large scale truss beams by Zwahlen and Mayr S.A., Switzerland.

I would also like to thank the members of the defence jury: Prof. Marquis (Aalto University School of Science and Technology, Helsinhki, Finland), Prof. Fontana (ETHZ), Dr. Duflot (CENAERO, Gosselies, Belgium) as well as Prof. Molinari (EPFL) who chaired the jury.

One of the challenges of my PhD was to deal with interdisciplinary questions. Collaboration was the best way to face these questions. A first successful collaboration was possible thanks to Dr. Alexander Evans (from the Paul Scherrer Institute, Switzerland and then from the Institut Laue Langevin, France). He provided valuable stimulating assistance and a friendly support for neutron-diffraction experiments. In a second collaboration, special acknowledgments are due to Dr. Laurent D'Alvise, Dr. Marc Duflot and Dr. Jean-Pierre Lefebvre from the CENAERO research center (Belgium) for their energy, availability, and willingness to build an efficient scientific collaboration. Finally, I would like to sincerely thank Dr. Andreas Rossoll (LMM Lab., EPFL) for his time, interest, and advice on the X-FEM models.

I wish to express my gratitude to the competent team of the structural laboratory: Sylvain Demierre, Gérald Rouge, Patrice Gallay, Roland Gysler and Gilles Guignet for their assistance for the experimental work. It was a pleasure to work in their delightful company. I would also like to thank the students who helped me with the experimental tests: Damien Roth, Manuel Schmocker, Sylvain Chaubert, Clémens Schagerl and Valentin Gavillet.

My time at ICOM has been memorable thanks to my colleagues. A great thanks to Claudio, our discussions have been a real breath of fresh air and a great thanks to all the ICOM team, especially to Maria, Dimitrios, Gary, Gustavo, Nariman, Farshid, Luis, Danijel, Rahel, Michel, Senta, Matthias, Scott... for the good times we spent at work and out of work.

I am also greatly indebted to colleagues and friends from I-BETON, MCS, EESD and IMAC laboratories, and especially to Damien, Roberto and Thibault for our passionate discussions seeking to improve the world of civil engineering. Also to Mylène, Talayeh, James, Clotaire, Guillaume, Aga and Sarah for the good memories of the ski season.

Finally, my gratitude goes to my family for their love, understanding, and encouragement. Last but not least, I would like to thank my husband, my soulmate and the future father of our baby, for his love, his unconditional support, and his eternal confidence in me. Manuel, you brought me the solid foundation and the balance I needed to build my thesis project.

Contents

Abstract i

Résumé ii

Acknowledgements v

Contents vii

Notations xiii

- Indices . . . xvi
- Abbreviations . . . xvi
- Symbols . . . xvi

Glossary of Terms xvii

1 Introduction 1

- 1.1 Motivation and background . . . 1
  - 1.1.1 Context . . . 1
  - 1.1.2 Problem statement . . . 1
- 1.2 Thesis objectives . . . 4
- 1.3 Scope of the thesis . . . 4
- 1.4 Organisation of this thesis . . . 5
- 1.5 Main challenges . . . 6

I State of the art 7

2 Description of physical phenomena occurring during the welding process 9

- 2.1 Fusion welding process . . . 9
- 2.2 Physical phenomena in welds . . . 10
  - 2.2.1 Arc and weld pool . . . 10
  - 2.2.2 Thermal transfer . . . 11
  - 2.2.3 Phase transformation in mild steels . . . 12
  - 2.2.4 Mechanical effects . . . 15
- 2.3 Couplings between thermal field, microstructure evolution and mechanical field . . . 18
- 2.4 Summary and conclusions . . . 19

3 Fatigue life assessment 21

- 3.1 Introduction . . . 21
- 3.2 Fatigue assessment methods . . . 22

3.3 **Focus on fracture mechanics** . . . 23
3.3.1 Characterization of the stress field in the vicinity of the crack tip . . . 23
3.3.2 Fatigue crack propagation . . . 26
3.4 **Main factors affecting fatigue** . . . 27
3.4.1 Load cases . . . 27
3.4.2 Stress concentration . . . 27
3.4.3 Imperfections and local weld geometry . . . 27
3.4.4 Residual stresses . . . 27
3.5 **Other aspects to consider in fatigue strength** . . . 30
3.5.1 Size effect . . . 30
3.5.2 Constant versus variable amplitude loading . . . 31
3.5.3 Influence of the stress ratio R . . . 31
3.6 **Summary and conclusions** . . . 32

II Experimental investigations **33**

4 K-joint manufacturing and welding processes, characterization of the steel S355J2H **35**
4.1 **Introduction** . . . 35
4.2 **Tubes manufacturing process** . . . 35
4.3 **Fabrication and welding process** . . . 37
4.4 **Material properties of the S355J2H steel** . . . 40
4.4.1 Designations . . . 40
4.4.2 Chemical composition . . . 41
4.4.3 Mechanical properties . . . 43
4.4.4 Thermal properties . . . 44
4.5 **Parameters inducing cold cracking effects** . . . 45
4.6 **Hardness testing** . . . 47
4.6.1 Procedure . . . 47
4.6.2 Results and discussion . . . 47
4.7 **Summary and conclusions** . . . 51

5 Residual stress measurements **53**
5.1 **Comparison of different techniques** . . . 53
5.2 **Hole Drilling Method** . . . 55
5.2.1 Stress calculation using hole-Drilling method . . . 55
5.2.2 Experimental description . . . 57
5.2.3 Results and discussion . . . 61
5.2.4 Conclusions . . . 63
5.3 **Neutron Diffraction** . . . 64
5.3.1 Objectives . . . 64
5.3.2 Physical principle . . . 64
5.3.3 Specificities of the **POLDI** at the Paul Scherrer Institute (PSI) and of the **SALSA** at the Institute Laue-Langevin (ILL) . . . 66
5.3.4 Experimental description . . . 71
5.3.5 Results and discussion . . . 78
5.3.6 Conclusions . . . 84
5.4 **X-ray** . . . 85
5.4.1 Experimental description . . . 85
5.4.2 Results and discussion . . . 85

5.5 Comparison between residual stresses obtained using hole-drilling, neutron diffraction and X-ray methods . . . 86
5.6 Summary and conclusions . . . 88

6 Fatigue experimental investigations **89**
6.1 Introduction: strategy and objectives . . . 89
6.2 Experimental program . . . 92
  6.2.1 Fatigue test principle . . . 92
  6.2.2 Description of specimens and test series . . . 92
  6.2.3 Test setup . . . 95
  6.2.4 Test procedure . . . 98
  6.2.5 Measurement equipment . . . 99
6.3 Measurement results and interpretations . . . 105
  6.3.1 From strain and deflection measurements . . . 105
  6.3.2 Test results . . . 119
6.4 Discussion . . . 130
  6.4.1 Crack development under fully-tensile loading . . . 130
  6.4.2 Crack development under fully-compressive loading . . . 130
  6.4.3 Crack development under partly-tensile or partly-compressive loading . 132
  6.4.4 Crack depth evolution . . . 133
  6.4.5 Fatigue strength estimation . . . 135
  6.4.6 Size effect correction . . . 135
6.5 Summary and conclusions . . . 136

III Numerical models and simulations **137**

7 Numerical analysis for welding induced residual stress estimation **139**
7.1 Introduction . . . 139
  7.1.1 Objectives . . . 139
  7.1.2 Analysis type . . . 139
  7.1.3 Finite element codes . . . 140
7.2 Recommendations and simplifying assumptions . . . 140
  7.2.1 Recommendations and methodology to simplify the problem . . . 140
  7.2.2 Simplifying assumptions . . . 143
7.3 Geometry of K-joints . . . 143
  7.3.1 The adopted system of units . . . 145
  7.3.2 Parametric equations of the chord-brace, weld-brace and weld-chord intersections . . . 145
  7.3.3 The weld shape . . . 147
  7.3.4 Dimensions of the modeled K-joints . . . 148
  7.3.5 Symmetry of the problem . . . 149
7.4 Material behaviour model . . . 149
  7.4.1 Thermal analysis . . . 149
  7.4.2 Mechanical analysis . . . 150
7.5 Loading . . . 152
  7.5.1 Thermal analysis . . . 152
  7.5.2 Mechanical analysis . . . 156
7.6 Mesh . . . 156
  7.6.1 Finite element type . . . 156

7.6.2 The generated mesh . . . 157
7.7 Convergence study . . . 157
7.7.1 Convergence h study . . . 159
7.7.2 Convergence p study . . . 160
7.7.3 Computation times . . . 165
7.8 Model validation and results . . . 165
7.8.1 Cross-section of the fusion zone . . . 165
7.8.2 Comparison with residual stresses obtained from neutron diffraction measurements . . . 166
7.8.3 Dissymmetry of the 3D residual stress field . . . 173
7.8.4 Similarities of residual stress distribution between joints with a chord wall thickness of 20 mm and 30 mm . . . 174
7.9 Summary and conclusions . . . 176
8 Geometrical parametric study **177**
8.1 Introduction . . . 177
8.1.1 Objectives . . . 177
8.1.2 Scope of parameters study . . . 177
8.2 Results of parametric study . . . 180
8.2.1 Residual stress distribution as a function of z absolute value and z/T relative value . . . 180
8.2.2 Influence of the proportional scaling on residual stress distribution . . . 183
8.2.3 Influence of the wall thickness ratio τ on residual stress distribution . . . 183
8.2.4 Influence of the diameters ratio β on residual stress distribution . . . 184
8.2.5 Influence of the chord slenderness γ on residual stress distribution . . . 184
8.2.6 Influence of the normalized gap parameter $\frac{\mathrm{g}}{\mathrm{D}}$ on residual stress distribution 184
8.3 Proposed functions for residual stress distribution . . . 190
8.4 Summary of proportional and non proportional scaling influence on residual stress distribution . . . 191
8.5 Summary and conclusions . . . 196
9 Estimation of fatigue crack propagation in a field of residual and applied stresses **197**
9.1 Introduction . . . 197
9.1.1 Objectives . . . 197
9.1.2 A short introduction on eXtended Finite Element Method X-FEM . . . 197
9.2 The extended finite element model . . . 198
9.2.1 Presentation of the model . . . 198
9.2.2 Results and discussion . . . 200
9.2.3 Future improvements of the numerical crack propagation model . . . 203
9.3 The analytical fatigue model based on fracture mechanics . . . 204
9.3.1 Proposed distribution for transverse residual stresses and $\mathrm{K}_{\mathrm{res}}$ . . . 204
9.3.2 Comparison of stress intensity factors . . . 204
9.4 Summary and conclusions . . . 206
10 Conclusion **207**
10.1 Summary and main conclusions . . . 207
10.2 Major contributions . . . 211
10.3 Future research . . . 211
References **215**

A Plans of tubular truss beams tested under fatigue 223

B Hole-Drilling Theory 259

C Strong and weak forms for transient non-linear heat conduction 265

D Residual stress field from ABAQUS parametric study 273

Notations

a	1. depth of a crack at the deepest point in the crack plan; 2. flow tensor
a_f	final crack depth
a_i	initial crack depth
a_th	threshold crack depth
c	half of the crack length
d	1. outside brace diameter; 2. depth of a crack at the deepest point in the depth direction
$\mathbf{d}$, $\mathbf{d}^e$	global and element temperature matrices
e	eccentricity between the intersection of brace and chord axes
$\mathbf{f}^e$	element flux matrix
f_y	yield stress
f_u	ultimate yield stress
g	gap distance
h	convective film coefficient
k	thermal conductivity (isotrope case)
n	hardening exponent
p	accumulated plastic strain
q	heat flux
$\bar{q}$	prescribed heat flux
q_{conv}	convective heat flux
q_{conv}	radiative heat flux
s	volumetric heat source
t	1. brace wall thickness; 2. time
u	1. displacement; 2. specific internal energy
w	weight functions

$\mathbf{B}^e$	element shape function derivative matrix
C	material constant
C	1. elasticity matrix; 2. specific heat
$\mathbf{C}^e$	element capacitance matrix
C_{eq}	equivalent specific heat (combining the specific heat and the latent heat of fusion/solidification)
D	1. outside chord diameter; 2. thermal conductivity matrix
E	modulus of elasticity or Young's modulus

F	force
H	hardening modulus
K	stress intensity factor
$\mathbf{K}^e$	element conductance matrix
K_{eff}	stress intensity factor effective
K_{th}	stress intensity factor threshold
L	latent heat
L_{ch}	chord length between two nodes
$\mathbf{L}^e$	gather matrix
N	number of load cycles
N_1	number of cycles at 15% change in strain near point of crack initiation
N_2	number of cycles at detection of a crack
N_3	number of cycles at through thickness cracking
N_4	number of cycles at complete loss of joint strength
$\mathbf{N}^e$	shape function matrix
Q	1. load force; 2. heat generation
$Q_{\min}$	minimum load
$Q_{\max}$	maximum load
R	load ratio
T	1. chord wall thickness; 2. temperature
$\bar{T}$	prescribed temperature
$S_{\mathrm{R,hs}}$	hot-spot stress range
U	internal energy
W_1	first parameter defining the weld size
W_2	second parameter defining the weld size
W_3	third parameter defining the weld size
α	1. chord length slenderness ($\frac{2L_{ch}}{D}$); 2. thermal expansion coefficient
β	diameters ratio ($\frac{d}{D}$)
γ	chord slenderness ($\frac{D}{2T}$)
ϵ	1. strain; 2. surface emissivity
ϵ_{ax}	axial strain
ϵ^{el}	elastic strain
ϵ_{hs}	hot-spot strain
ϵ_{ipb}	in-plane bending component of strain
ϵ_{nom}	nominal strain
ϵ_{opb}	out-of-plane bending component of strain
ϵ^{pl}	plastic strain
ϵ_{res}	residual strain
ϵ^{th}	thermal strain

θ	brace angle
λ	wave length
ν	Poisson's ratio
ρ	1. weld notch root radius; 2. material density
σ	stress
σ_{ax}	axial stress
σ_{equ}	equivalent stress (Von-Mises stress in this document)
σ_{hs}	hot-spot stress
σ_{ipb}	in-plane bending component of stress
σ_{nom}	nominal stress
σ_{opb}	out-of-plane bending component of stress
σ_{res}	residual stress
σ_{SB}	Stefan-Boltzmann constant (radiation law)
τ	1. wall thickness ratio ($\frac{t}{T}$); 2. shear stress
ζ	normalized gap parameter ($\frac{g}{D}$)

Indices

adm	admissible
app	applied
ax	axial
b	bending
br	brace
ch	chord
eff	effective
i	initial
hs	hot-spot
ipb	in-plane bending
opb	out-of-plane bending
res	residual
$\mathbb{X}_E$	due to actions
$\mathbb{X}_{\text{eff}}$	effective
$\mathbb{X}_{\text{eq}}$	equivalent
$\mathbb{X}_{\text{f}}$	failure, at failure, related to failure
$\mathbb{X}_{\text{i}}$	initial
$\mathbb{X}_{\text{inert}}$	in or for inert conditions
$\mathbb{X}_i$	i-th value, case or time period
$\mathbb{X}_{\text{n}}$	normal, normalized, national
$\mathbb{X}_{\text{test}}$	in laboratory testing, in laboratory conditions
$\sigma^{(i)}$	i-th value, case or time period (avoids σ_1 and σ_2, which are the principal stresses)
$\mathbb{X}^{(1)}$	related to a single crack
$\mathbb{X}^{(k)}$	related to k cracks

Abbreviations

$^\circ C$	celsius degree
J	Joule
K	kelvin
ACPD	alternating current potential drop
BM	base material
CE	carbon equivalent according to the IIW
CET	carbon equivalent content according to the EN 1011:2000
CHS	circular hollow section
FE	finite element
FZ	fusion zone
HAZ	heat-affected zone
HV	Vickers hardness
LEFM	linear elastic fracture mechanics
ILL	Institut Laue-Langevin
MAG	metal active gas
ND	neutron diffraction
POLDI	multiple Pulse-OverLap-DIffractometer (PSI)
PSI	Paul Scherrer Institute
RHS	rectangular hollow section
SALSA	Strain Analyser for Large and Small scale engineering Applications (ILL)
SCF	stress concentration factor
SIF	stress intensity factor

Symbols

Δ	range, difference
$\boldsymbol{\epsilon}$	strain matrix
Γ_T, Γ_q	essential (temperature) and natural (heat flux) boundary (thermal an.)
Γ_u, Γ_t	essential (displacement) and natural (traction) boundary (mechanical an.)
$\tilde{\nabla}$	gradient vector
$\boldsymbol{\nabla}$	gradient matrix
∇^2	laplacian operator
Ω	domain of the problem
$\boldsymbol{\sigma}$	stress matrix

Glossary of Terms

As-welded The condition of the weld metal after welding without any treatment.

Conduction The passage of electricity throught wires: heat throught metal.

Convection The movement in a gas or liquid caused by warm gas or liquid rising and cold gas or liquid sinking.

Crack In the present document, the crack refers to the fatigue crack and presents the following dimensions.

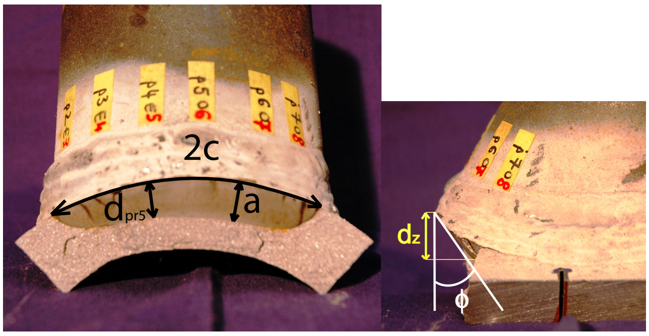

Figure 1: Nomenclature to describe a crack: $2c$ is the crack length , a is the crack depth at the deepest point, d is the crack depth measured at probe location (probe 5 in this figure), d_z is the projection of d on the vertical axis, Φ is the starting angle.

Defect A flaw that is unacceptable.

Deformation Any change of form or shape produced in a body by stress or force.

Fatigue 'The process of initiation and propagation of cracks through a structural part due to action of a fluctuating stress' (definition from the Eurocode 3 Part 1-9).

Flaw General term describing a condition or change that indicates an abnormal condition or imperfection in a material.

Gap The distance between the brace outer walls at the chord crown toe.

Geometrical parameters Non-dimensional parameters characterizing the joint geometry: slenderness, brace-to-chord ratios, etc. (see figure 2).

Geometrical size effect It refers to the through-thickness stress gradient that arises at geometrical discontinuities (e.g. notches) and/or due to bending and torsional loads, which can be addressed by stress analysis. Due to the presence of a steeper stress gradient in smaller specimen, a grain at the surface of a small specimen will experience a lower strain than the same grain at the surface of a thick specimen, for the same stress at the surface and the same nominal stress at mid-depth [Orjasäter 1995].

Hardness Property or extent of being hard. Measured by extent of failure of indentor point of any one of a number of standard testing instruments to penetrate the product.

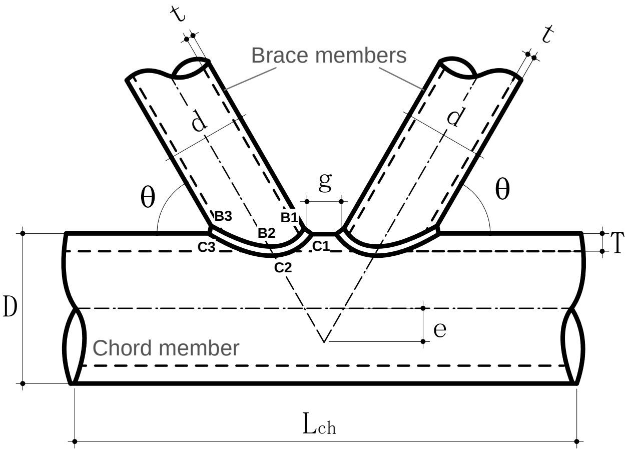

D: outside chord diameter
T: chord wall thickness
d: outside brace diameter
t: brace wall thickness
e: eccentricity (positive in fig. above)
g: gap distance
L_{ch}: chord length between two nodes

$\alpha = \frac{2L_{ch}}{D}$: chord length slenderness
$\beta = \frac{d}{D}$: diameters ratio
$\gamma = \frac{D}{2T}$: chord slenderness
$\tau = \frac{t}{T}$: wall thickness ratio
θ: brace angle
$\zeta = \frac{g}{D}$: normalized gap parameter

B1: brace crown toe
B2: brace saddle
B3: brace crown heel
C1: chord crown toe
C2: chord saddle
C3: chord crown heel

Figure 2: Definition of dimensions and geometrical parameters for K-joint.

Hot spot A point in a structure where a fatigue crack may initiate (figure 3) due to the combined effect of stress fluctuation, residual stresses, welding imperfections, etc.

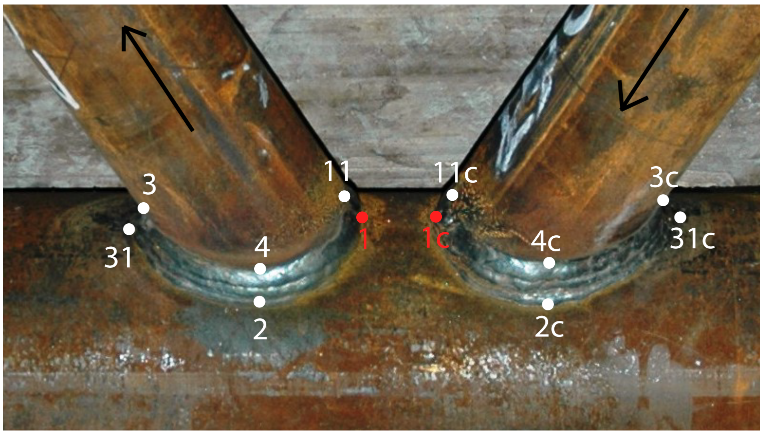

Figure 3: Hot spot number and locations.

K-joint K-shape joint composed of two brace branches welded onto a chord member.

Mode I Loading condition that displaces the crack faces in a direction normal to the crack plane (opening mode).

Residual stress 'Residual stress is a permanent state of stress in a structure that is in equilibrium and is independent of any applied action" (definition from the Eurocode 3 Part 1-9).

Statistical size effect It refers to the increased probability of having a significant initial flaw or change in the material properties with an increase in stressed volume.

Stress range Difference between the maximum and minimum stress in a stress cycle, the most important parameter in fatigue.

Technological or metallurgical size effect It implies that an increased plate size may result in a coarser grain structure, lower yield strength, higher residual stresses, increased risk of hydrogen cracking during fabrication and a lower notch toughness.

Thermal residual stress Residual stresses induced by the gradient of temperature in the welded area due to the heat input.

Transformation residual stress Residual stresses induced by the metallurgical transformations which imply the change of physical material properties.

Transient analysis An analysis that accounts for the time-dependence of input parameters.

Radiation Energy in the form of heat (or light) that is sent out as waves.

Chapter 1

Introduction

1.1 Motivation and background

1.1.1 Context

Over the last decades, welded tubular truss bridges have become a great success, mainly in Europe. The new trend towards this innovative kind of bridge is mainly due to major breakthroughs in modern manufacturing techniques (Wardenier, 2001):

- Roll piercing process to manufacture seamless circular hollow sections (CHS)
- Tridimensional computer guided cutting to fit brace end edges to the outer shape of the chord (and include weld preparation in one step)
- Semi-automatic or automatic welding process to facilitate the production of high quality weld.

These techniques are becoming ever more economically competitive because they are more easily-accessible. In addition, tubular truss bridges are particularly appreciated and demanded by architects because they are 'transparent' and aesthetically attractive, and by engineers for the advantageous resistance of tubular sections to compression, torsion and bending. As a matter of fact, tubular bridges have seen an increasing popularity during the last twenty years.

In this type of bridge, hollow section tube members are most often welded together in K-joints to form truss beams, or in KK-joints to form tridimensional structures (see Fig. 1.1). In order to facilitate welding between horizontal chords and brace members, overlapping of brace members is often avoided by creating a gap region. These K-joints and in particular their gap region are the weak points of welded tubular bridges because they combine high applied stress concentration, local stress concentration (weld and imperfection), high tensile residual stresses and welding imperfections. Despite this fact, K-joints are often chosen in order to minimize the number of joints in bridges. They are economical for span length ranging from 30 to 80 meters.

This modern kind of steel bridges is too new to get enough feedback concerning the long term behavior. Consequently, one has to predict its resistance over time based on laboratory tests, field measurements and numerical simulations.

1.1.2 Problem statement

Welded joints have been shown to be critically susceptible to fatigue failure. Fatigue is one of the most common cause of failure in most welded structures, such as in offshore structures, power

(a) Lully viaduct (canton of Fribourg, Switzerland) composed of two tubular space trusses with KK-joints (typical span 42.75 m, total length 970 m)

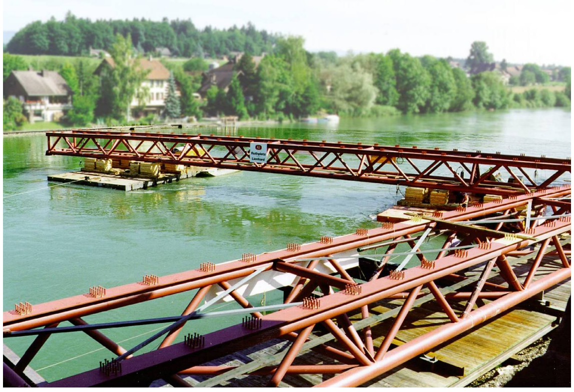

(b) Aarwangen bridge (canton of Bern, Switzerland) composed of two planar tubular trusses with K-joints (2 × 48 m spans)

Figure 1.1: Examples of two tubular bridges built in Switzerland.

plants, ship structures, etc. In high-cycle fatigue, cracks grow gradually and steadily over time under cyclic loads, with stresses below the yield stress and cause failure during the service life of the structure. Indeed, metallic bridges should not only be designed for static loads, a particular caution should be taken with regard to the effects of millions of repeated cycles due to traffic loads. Section dimensions must be controlled by fatigue design and not only by static design.

The fatigue issues in tubular structures

To address this problem for tubular joints, research has been carried out during the last 35 years on their fatigue behavior and was mainly driven by the offshore industry investigations previously done (Zhao et al., 2000). Specific research on tubular bridge fatigue started later, in the 1990's. It quickly showed that design specifications used for offshore structures are not appropriate for tubular truss bridges, mainly because of the geometric parameter values of their tubes (thick tubes with small diameters, chord slenderness $\gamma = \frac{\mathrm{D}}{2\mathrm{T}} < 12$, and typically diameters lower than 600 mm) and the presence of a constructional gap inducing an eccentricity (Schumacher, 2003). Specific approaches for tubular joints in bridges are thus required.

The main parameters influencing the fatigue strength of a tubular structure are the absolute as well as the relative size of its members (size effect), the loading case, the initial crack-like imperfections and the welding residual stress fields (see Fig. 1.2).

Concerning the size effect, it is currently dealt with in analogy to welded plated elements in tension, that is using a size correction formula in which only the main plate thickness appears. The use of this formula for tubes in various structural applications has shown the limitations of

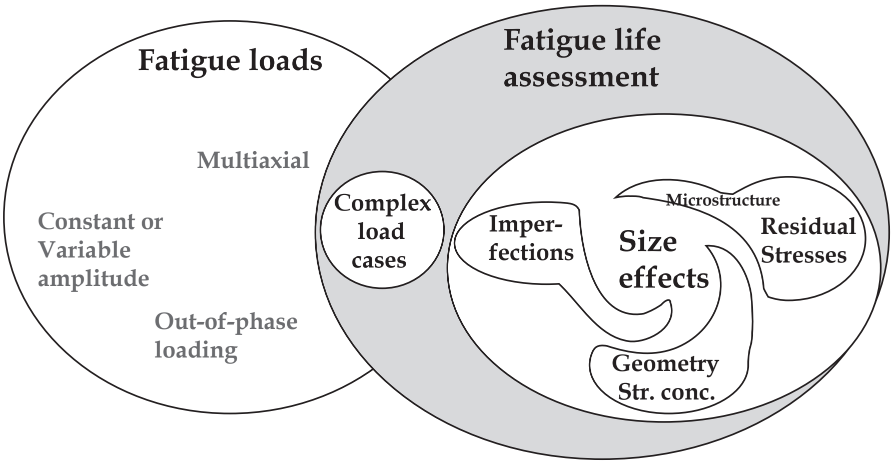

Figure 1.2: Overview of phenomena overlapping in the fatigue strength estimation.

this approach, in particular due to differences in the loading cases and can be very penalizing for thick-walled tubular joints (Schumacher and Nussbaumer, 2006).

In tubular joints, the complexity of the stress field has led to the use of the hot-spot stress concept to characterize the driving stress value at potential fatigue crack locations. Hot-spot stress comprises the effects of joint geometry and the type of load (stress concentration effect). It is a useful tool even though the computation of the stresses using the hot-spot concept does not completely capture the size effect without a correction.

Due to the existence of initial imperfections in welded joints, it has been shown (Gurney, 1979) that stable crack growth dominates the total fatigue life (domains where the failure criteria is a detectable crack or the failure of the specimen). Since welding imperfections of approximately 0.1 mm depth are present in the vicinity of the weld toe (Barsoum and Samuelsson, 2006; Smith and Smith, 1982), they imply high local plastic strains. These imperfections act as a crack initiator meaning that there is almost no crack initiation phase in the fatigue life. Thus, the crack may start to propagate with the first high enough load fatigue cycle.

Some design rules and studies are available to approximately estimate the size effect (Borges et al., 2006; Gurney, 1989; van Wingerde et al., 1997), the applied stress concentration factor and thus the hot-spot stress due to traffic loads (Rom, 1993; API, 2000a; Marshall, 1992; Zhao and Packer, 2000) and the welding imperfection sizes. However, three-dimensional residual stresses in tubular joints remain largely unknown. They have never been determined in K-joints, nor their influence on fatigue crack propagation.

The main gap to fill: residual stress and fatigue life estimation

Residual stresses are internal self-balanced stresses introduced in structures or components by thermally induced deformation during different manufacturing processes, in particular welding in the case of welded joints. Since tensile residual stresses tend to open cracks, they have been shown to have a detrimental influence on fatigue in the case of plated components (Frickle, 2005; Maddox, 1991). In tubular K-joints, the welding process should also lead to high tensile residual stresses within the joint.

It is recognized in the codes, such as IIW recommendations (Hobbacher, 2007) or Eurocode 3 (EN 1993-1-1:2005), that welding high tensile residual stresses lead to the lower bound of the fatigue strength. Their effects are thus already included in the fatigue resistance. However, the fatigue strength curves proposed in these codes for use with hot-spot (geometric) stress method are not applicable to circular hollow section CHS welded joints. To design K-joints against fatigue, one has to use the 'Construction with Hollow Steel Sections' (CIDECT) design guide. The CIDECT detail categories are not consistent with the other codes and it was proved (Schumacher, 2003) that CIDECT recommendations overestimate the stress concentration factors SCF and as a consequence give overestimated fatigue strength curves (in terms of hot-spot stress range) for joints typical to bridges ($\gamma < 12$).

The consequence of failure in a joint in compression is considered in the Eurocodes and CIDECT guide through different strength factor values γ_{Mf} (EN 1993-1-9:2005; Zhao et al., 2000). The definition of fatigue failure, i.e. crack size considered, is implicitly taken as a crack detectable by visual examination. The fact that a visible crack is indeed propagating, or not, is not taken into account.

The CIDECT design guide, for tubular welded joints under fatigue loadings (Zhao et al., 2000), quotes: 'it is presumed that only braces which have some parts of their load range in tension will be liable to cause fatigue failure'. Considering that details loaded in compression are safe means neglecting the influence of tensile residual stresses on crack propagation.

To summarize, the codes currently used to design tubular joints against fatigue are not consistent altogether. In CIDECT, the tubular joints have their own hot-spot fatigue resistance curves; they are different and higher than the curves given for all other welded joints (for plated elements). This is tied to the fact that SCFs are also overestimated when using CIDECT formulas. The failure criterion is not clearly defined in the codes. There are disparities in the way of considering joints loaded in compression and the consequence of failures.

Therefore, in order to get a thorough understanding of the overall phenomenon, this study aims to evaluate experimentally and numerically the welding residual stress field as well as their effect on the fatigue response of K-joints.

1.2 Thesis objectives

To achieve this major aim, the work has been divided into the following objectives:

- quantify the residual stress field at the most critical fatigue locations (hot-spots 1 or 1c) in welded tubular K-joints using neutron-diffraction, hole-drilling, and X-ray methods.
- qualify and quantify the effect of tensile residual stresses on the fatigue crack propagation of welded tubular K-joints through large-scale laboratory tests.
- develop a finite element model for predicting three-dimensional residual stresses in welded K-joints.
- determine, using thermo-mechanical FEM models, the influence of joint size (both absolute and non-proportional) on residual stress distribution and propose distributions for residual stresses based on these findings.
- assess crack propagation under residual and applied stresses, using an extended finite element method model as well as a linear elastic fracture mechanics LEFM analytical model that uses the proposed residual stress distribution.

1.3 Scope of the thesis

This thesis concentrates on welded K-joints, in dimensions used in planar truss beams for bridge construction (road bridges). They are made of a non-alloyed structural steel (mild steel) S355J2H according to EN 10025. They are welded without stiffeners with a metal active gas (MAG) arc welding process.

These bridges and their joints are subjected to high-cycle fatigue. In this work, only the stable crack growth (propagation stage II) which is dominating the total fatigue life is considered. Fatigue experimental investigations are conducted under constant amplitude fatigue loading, in standard laboratory conditions.

The studied residual stresses are induced by the welding. In the area of interest, the tube manufacturing residual stresses are supposed to be removed by the welding. Residual stresses presented herein refer to macroscopic residual stresses significantly affecting the fatigue crack behavior.

1.4 Organisation of this thesis

The organisation of the ten chapters is presented in Fig. 4.2. Each box corresponds to a chapter (except for chapters 2 and 3).

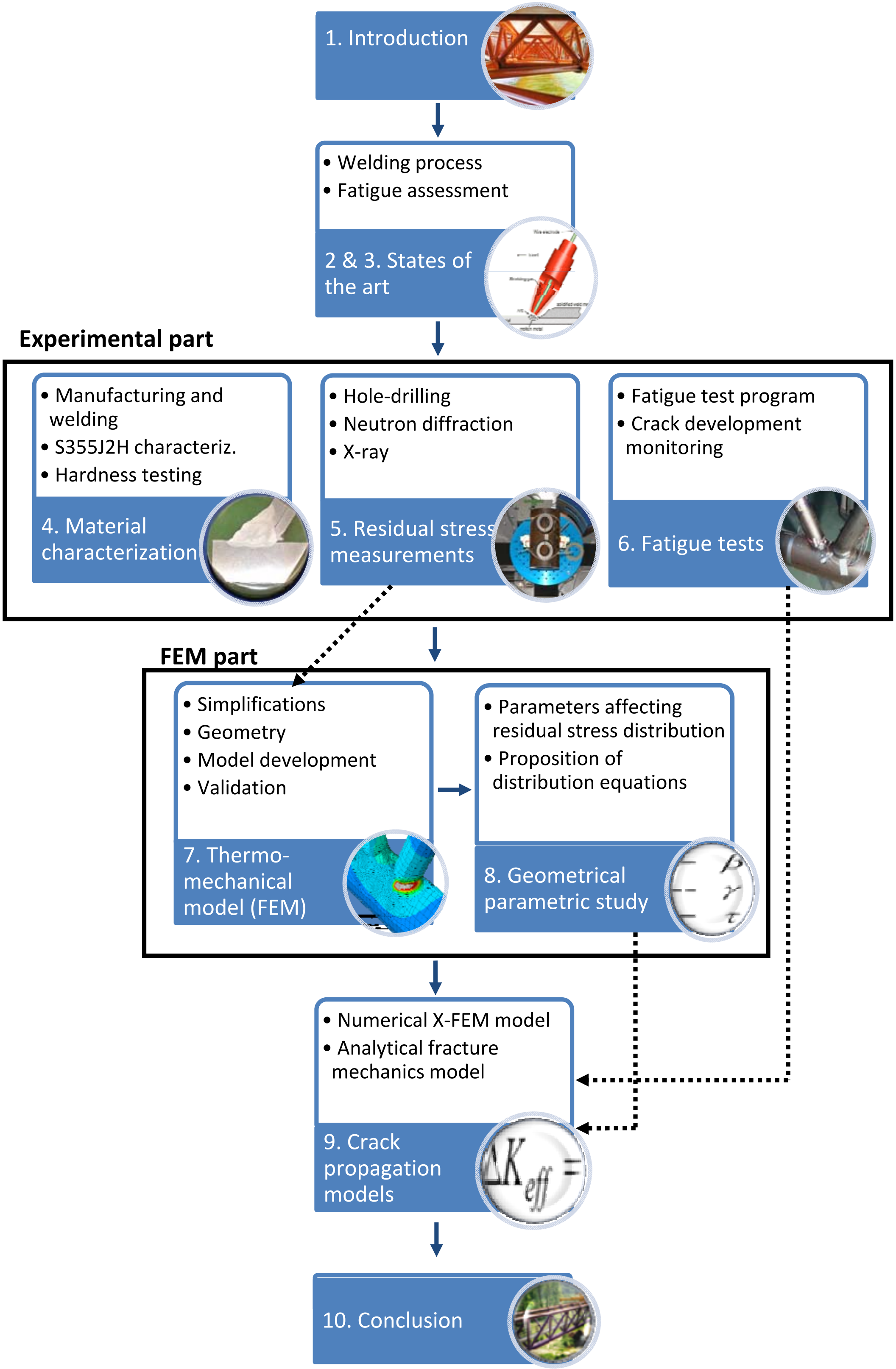
1. Introduction
• Welding process
• Fatigue assessment
2 & 3. States of the art
Experimental part
• Manufacturing and welding
• S355J2H characteriz.
• Hardness testing
4. Material characterization
• Hole-drilling
• Neutron diffraction
• X-ray
5. Residual stress measurements
• Fatigue test program
• Crack development monitoring
6. Fatigue tests
FEM part
• Simplifications
• Geometry
• Model development
• Validation
7. Thermo-mechanical model (FEM)
• Parameters affecting residual stress distribution
• Proposition of distribution equations
8. Geometrical parametric study
• Numerical X-FEM model
• Analytical fracture mechanics model
9. Crack propagation models
10. Conclusion

Figure 1.3: Organisation diagram

1.5 Main challenges

- Design a hole-drilling device for tubular joints geometry in order to measure two-dimensional residual stresses at the surface.
- Measure non-destructively, in thick specimens, three-dimensional residual stresses by neutron diffraction.
- Conduct fatigue tests on large tubular truss specimens and monitor accurately crack depth evolution.
- Numerical residual stress model: identify the aspects of the problem that can be simplified (parameters of lesser influence on the residual stress formation) and develop an accurate model.
- Combine the proposed residual stress distribution with a LEFM analytical model for accurate crack propagation prediction in joints loaded either in tension or in compression.

Part I

State of the art

Chapter 2

Description of physical phenomena occurring during the welding process

This chapter gives an overview of welding and the various processes involved: arc and weld pool processes, thermal transfer, metallurgical aspect and mechanical impacts. It also provides a short explanation on the residual stress formation. This chapter contains the information required to understand welding and how some physical processes are coupled altogether in order to give the basis for the numerical model.

2.1 Fusion welding process

Fusion welding, consisting of heating two adjacent metallic parts in order to melt them together, can be performed using different sources of energy with or without adding a filler material. These sources of energy can be a gas flame (oxyfuel gas welding), an electric arc (arc welding), an electric current (resistance welding), an energy beam (electron beam welding, laser welding). Other sources do not involve melting of materials (solid-state friction: ultrasonic welding, explosion welding, friction welding, etc.) (Champroux and Lê, 1986).

For steel construction, the most common type of welding process is the arc welding because of its ability to provide high quality welds for a wide range of steels and thicknesses, using simple equipments easily adaptable for on-site welding. In this process, a power supply is used to create an electric arc between an electrode and the base material which are previously placed in a gas atmosphere.

Depending on the electrode type, three kinds of arc welding processes are distinguished:

- Using a consumable stick electrode: the **Shielded Metal Arc Welding (SMAW)** or the manual metal arc welding (MMA) are performed manually.
- Using a non-consumable tungsten electrode: the **Gas Tungsten Arc Welding (GTAW)** requires an inert gas protection from atmospheric contamination. A filler metal is not necessary.
- Using a continuous-fed consumable electrode: since it is a semi-automatic or automatic process, this method offers a better productivity than the previous ones.

  The required electrode can be:

  - a solid electrode used in combination with gas metal: **Gas Metal Arc Welding GMAW** (Armao et al., 1995) (see Fig. 2.1).

- ◇ a flux-cored (tubular) electrode used with or without gas protection: **Flux-Cored Arc Welding FCAW** (Macquet, 1999).
- ◇ an electrode (solid or tubular) with a protection ensured by submerging the molten weld under a blanket of granular fusible flux: **Submerged arc welding SAW**.

Concerning gas protection for GMAW and FCAW processes, the gas can be either an inert gas (**Metal Inert Gas MIG**) or an active gas (**Metal Active Gas MAG**). The MAG process is devoted to join non-alloy or low-alloy steels whereas the MIG process is mainly used with stainless steels and nickel alloys.

For Metal Active Gas protection, the gas induces chemical reactions in the molten pool.

Among these arc welding processes, one concentrates on the MAG process combined with a flux-cored electrode, which is adopted for tubular joints welding. The semi-automatic MAG has been chosen by steel fabricators for its high-speed capability and the flux-cored electrode because it associates metallurgical benefits from the solid electrode (high quality welds) with the highest technological and economical faculties. The active gas employed is composed of 82% Argon and 18% CO_2.

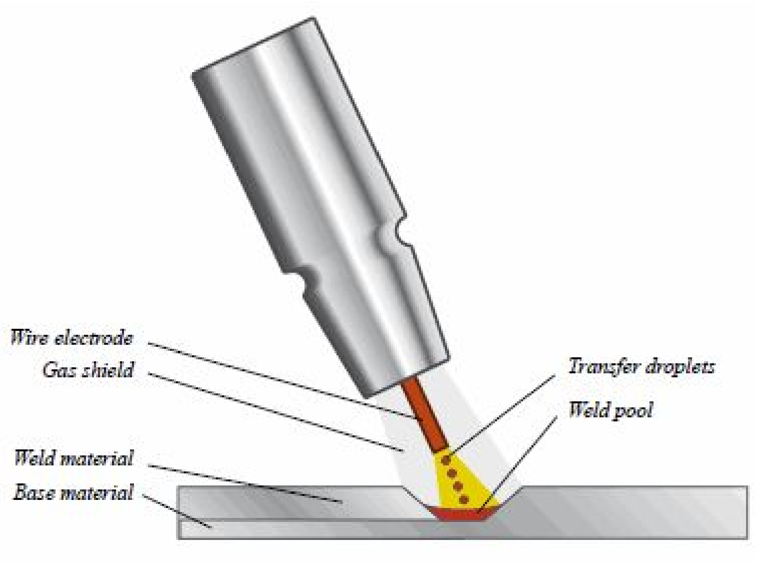

Figure 2.1: The semi-automatic MAG welding process.

2.2 Physical phenomena in welds

Complex physical processes occur during welding: arc and weld pool processes, thermal transfer, metallurgical processes and mechanical processes. They are briefly presented in the following sections.

2.2.1 Arc and weld pool

The electric current passing through the gas of the welding arc is transformed into heat. Only a part of the thermal energy produced by the arc is absorbed by the metal to create a molten pool. The rest of the energy is lost by heat conduction in the solid metal surrounding the weld pool or by radiation and convection (Kou, 2003).

The dynamics of heat transfer in the weld pool is driven by liquid convection (see Fig. 2.2). For arc-welding processes, the convection driven forces are mainly surface-tension forces (due to the Marangoni effect), electromagnetic forces (or Lorentz forces) and buoyancy forces (DebRoy and David, 1995; Zacharia et al., 1995).

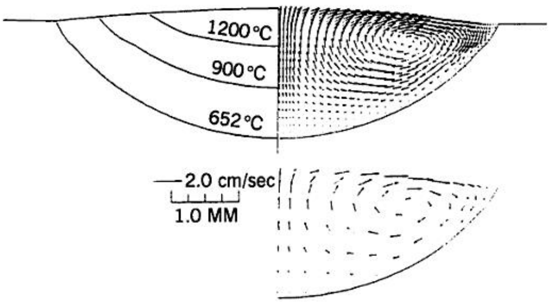

Figure 2.2: Convection flow in the weld pool (Kou, 2003).

The Marangoni effect is due to the variation of surface tension with temperature and solute concentrations; the liquid flows from the region of lower surface tension to the region of higher surface tension (Zacharia et al., 1995). The electromagnetic forces are created by the electric current passing in the weld pool (DebRoy and David, 1995; Woods and Milner, 1971). Buoyancy forces are explained by the variation with temperature of the metal density in the liquid state.

It has been demonstrated that convective flow has a strong influence on the profile of the fusion line (size, shape and penetration of the weld pool) and hence on the residual stress distribution. The accurate evaluation of the weld fusion profile is essential. The fluid convection in the liquid pool can be successfully computed with finite elements (Drezet and Mokadem, 2006). However, to avoid modeling the complex arc and weld pool phenomena, approximate heat source models are often preferred (Goldak heat-source (Goldak et al., 1984), Gauss heat-source, etc.)

2.2.2 Thermal transfer

The temperature distribution evolves along the heat source path as a function of the lateral distance from the weld axis and as a function of time as shown in Fig. 2.3.

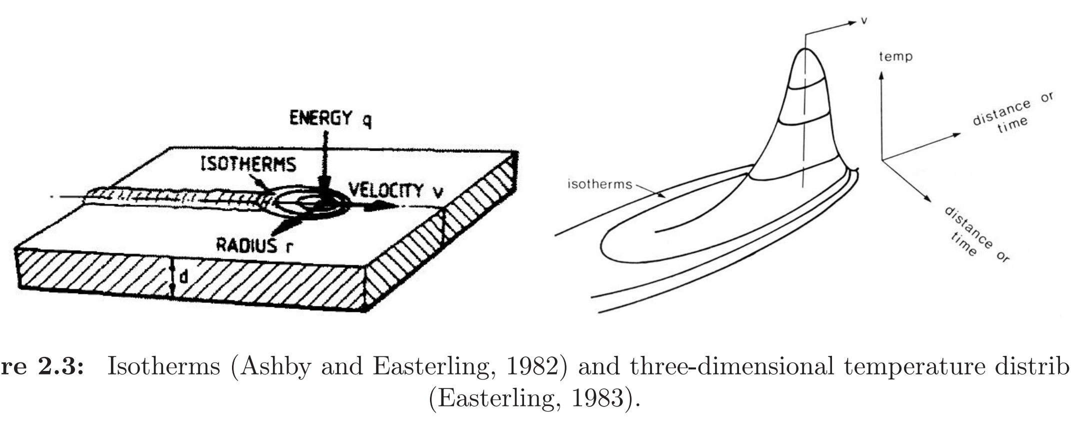

Figure 2.3: Isotherms (Ashby and Easterling, 1982) and three-dimensional temperature distribution (Easterling, 1983).

Along the heat source path, the welding thermal cycle (temperature-time curve) becomes constant after a short distance from the starting point (Saint-Germain, 2006).

The temperature-evolution of a welding thermal cycle is characterised by a rapid heating up to a peak temperature and a longer cooling time as shown in Fig. 2.4.

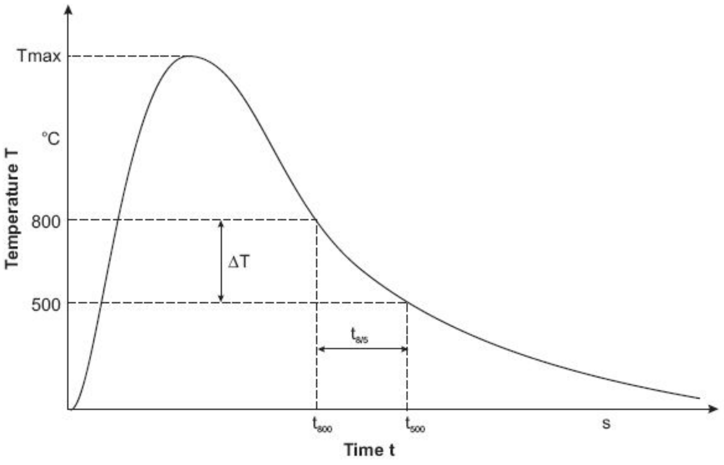

Figure 2.4: The thermal cycle with the cooling time $t_{8/5}$ definition (ISF and Joining Institute, 2004).

The thermal cycle is defined by the initial temperature, the maximum temperature T_{max} and the time of cooling $t_{8/5}$, i.e. time spent between 800 °C to 500 °C ($t_{8/5}$). During this time, the main phase transformation (from ferrite-pearlite to austenite) occurs.

The temperature evolution changes with the position in the weld pool or in the region surrounding the weld pool as depicted in Fig. 2.5. The temperature gradients influence the weld pool shape, the cooling rate of the material and hence the microstructure. Therefore, the heat input and the welding speed should be determined accurately.

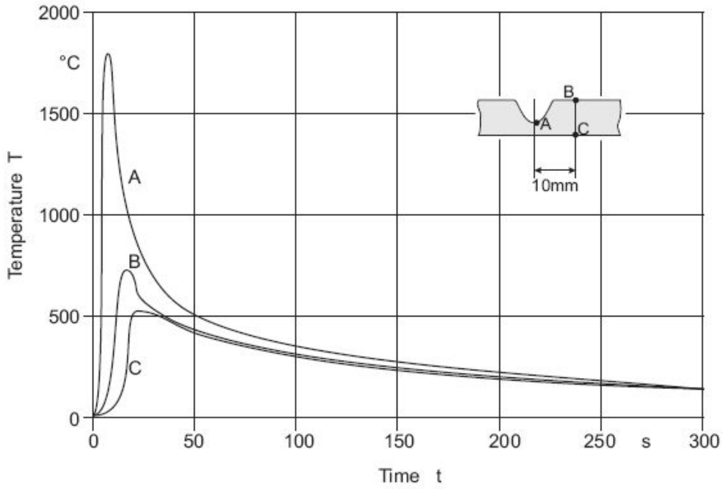

Figure 2.5: The thermal cycles at different locations in the weld vicinity (ISF and Joining Institute, 2004).

2.2.3 Phase transformation in mild steels

Phase transformation depends on the welding thermal cycle presented above: the maximum temperature reached (depending on the distance to the weld axis), the cooling time, and the steel composition, all play a role.

Solid phase transformation during heating: from ferrite-pearlite to austenite

Figure 2.6 from Easterling (1983) shows the different metallurgical zones formed as a function of the local peak temperature in a low carbon steel containing 0.15% of C. Next to the metallurgical zones, the metastable phase diagram iron-cementite (Fe-Fe_3C) is drawn. It gives the transformations as a function of temperature (α stands for ferrite, γ stands for austenite, δ stands for the delta iron and Fe_3C stands for cementite).

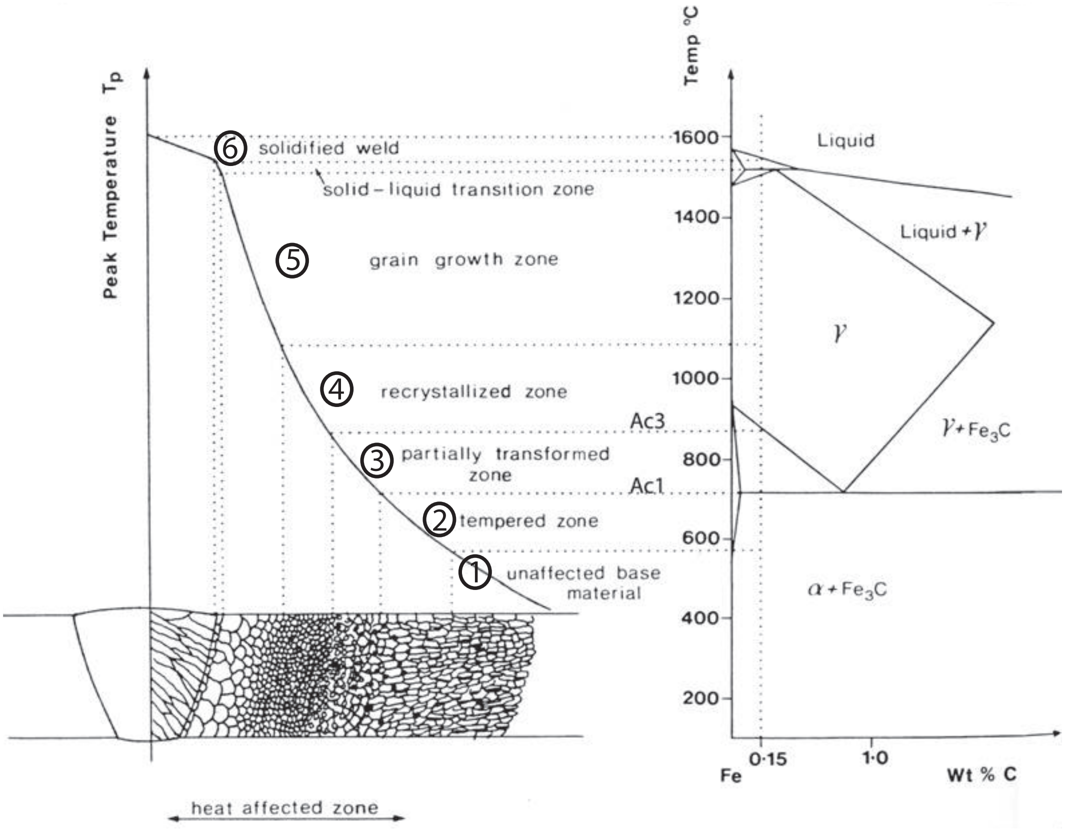
Peak Temperature Tp
Temp °C
⑥ solidified weld
solid – liquid transition zone
⑤ grain growth zone
④ recrystallized zone
③ partially transformed zone
② tempered zone
① unaffected base material
Ac3
Ac1
1600
1400
1200
1000
800
600
400
200
Liquid
Liquid + γ
γ
γ + Fe3C
α + Fe3C
Fe
0·15
1·0
Wt % C
heat affected zone

Figure 2.6: On the left, metallurgical zones formed in the FZ and the HAZ as a function of the maximum reached temperature. On the right, the phase diagram iron-cementite (Easterling, 1983).

Therefore, three main zones can be distinguished:

- The Base Metal BM (**1**) is the area where the temperature does not reach 600 °C. Its microstructure is not affected by the welding. It is composed of ferrite and pearlite. Note that the pearlite is a mix of ferrite and cementite. The ferrite lattice structure is body-centered cubic.
- The Heat-Affected Zone HAZ is adjacent to the BM. This zone was not melted but was transformed into austenite γ at high temperature. It is important to note that the austenitic structure is face-centered cubic. Depending on the distance to the weld axis which influences the austenite grain size, the HAZ can be subdivided into four zones:
  - The Sub-Critical HAZ (SCHAZ) (**2**) with a max. temperature comprised between 600 °C and Ac_1. Ac_1 is the arrest point of temperature during heating corresponding to the beginning of the austenitisation. In this area, the metal is just tempered.
  - The Inter-Critical HAZ (ICHAZ) (**3**) with $Ac_1 < T_p < Ac_3$ where Ac_3 is the arrest point of temperature during heating corresponding to the entire austenitisation. Therefore, in this zone, there is only a partial austenitisation.

  - ◇ The Fine Grained HAZ (FGHAZ) (**4**) with $Ac_3 < T_p < 1100$ °C. The microstructure is entirely composed of austenite grains, meaning that it is recrystallised.
  - ◇ The Coarse Grained HAZ (CGHAZ) (**5**) with $T_p > 1100$ °C implying a growth of the austenite grain size.

- ◆ The Fusion Zone FZ (**6**) is the melted zone where the peak temperature was greater than the liquidus temperature. After cooling, this zone corresponds to the weld area.

Solid phase transformation during cooling

The austenite formed in the HAZ and in the FZ after solidification is then transformed during cooling. This transformation can be explained with a Continuous Cooling Transformation (CCT) diagram or a Time-Temperature Transformation for continuous cooling conditions (continuous TTT).

The CCT diagram, as shown in Fig. 2.7, represents the transformation of steel during cooling and gives accurate informations on phase changes as well as the temperature of these transformations under welding conditions (Radaj, 2003).

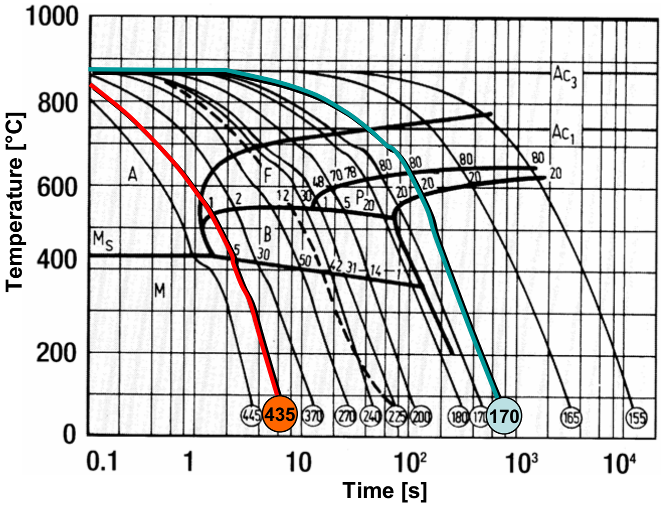

Chemical composition in mass%:

C	Si	Mn	P	S	Al	N
0.17	0.51	1.39	0.025	0.024	0.069	0.005

Austenitization: **900°C for 5 min**

Figure 2.7: The CCT diagram of a S355N steel close to the one we use (Ponge, 2005) (A: austenite, F: ferrite, P: pearlite, B: bainite, M: martensite). Vickers hardness is given in the bottom of the figure for each microstructure.

Note that the diagram should be read along the cooling curves with different cooling rates. Depending on the cooling rates, different transformations occur (Lambert-Perlade, 2001):

- ◆ for rapid cooling rates, the austenite is directly transformed into martensite.
- ◆ for intermediate cooling rates, the transformation is bainitic. For the slowest rate of the intermediate cooling rate, martensite-austenite constituents are often formed. They are well known to decrease the toughness (Bayraktar and Kaplan, 2004; Kaplan and Lambert-Perlade, 2001).
- ◆ for slow cooling rates, ferrite first nucleates at the grain boundary. The non-transformed austenite is enriched by carbon and decomposes to form pearlite.

Three main factors affect the transformation during cooling: the steel composition, the size of the austenite grains and the external stresses (Francis et al., 2007). The bigger the austenite grains form during heating, the more bainite and martensite form during cooling. External stresses also influence the transformations.

Multipass welding

For multiple weld passes, the regions surrounding the weld experience successive thermal cycles. The resulting microstructures are complex. The microstructure formed in the HAZ depends on the sequence of thermal cycles, as depicted in Fig. 2.8.

In general, the highest temperature peak removes the effect of the previous ones but not the effect of the following ones. The influence of multipass welding is presented in Fig. 2.8.

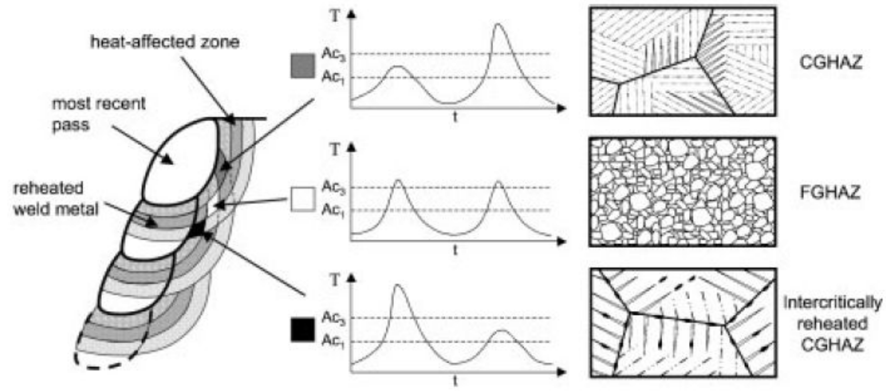

Figure 2.8: Effect of multipass welding on the thermal cycle (Francis et al., 2007). CGHAZ stands for Coarse Grained HAZ. FGHAZ stands for Fine Grained HAZ (also called supercritically reheated coarse grained) and is reheated between Ac_3 and 1100 °C. The Intercritically Reheated Coarse Grained HAZ ICCGHAZ is reheated between Ac_1 and Ac_3.

The CGHAZ and the Intercritically Reheated Coarse Grained HAZ ICCGHAZ are known to be the most brittle areas (Haze and Aihara, 1986; Kenney et al., 1997). During intercritical reheating (between Ac_1 and Ac_3), the Coarse Grained HAZ undergoes partial austenitizing inducing the formation of martensite-austenite constituents along the austenitic grain boundaries. It explains why the material toughness is decreased in the ICCGHAZ.

2.2.4 Mechanical effects

From the mechanical point of view, non-uniform thermally induced deformations might lead to plastic strains and residual stresses or distortions.

Residual stresses induced by welding have three main origins (Lu et al., 1991):

- the gradient of temperature in the welded area due to the heat input. These stresses are called **thermal residual stresses**.
- the mechanical effect: they are linked to clamping (restraining, misfits, etc.). They are also related to the drop of mechanical properties, such as the Young's modulus and the yield stress, at high temperatures.
- the metallurgical transformations which imply the change of physical material properties. These stresses are called **transformation residual stresses**.

These stresses are associated with strains and displacements, called distortions (Masubuchi, 1980). Masubuchi (1980) describes several types of distortions which are shown in Fig. 2.9.

The transverse shrinkage is a shrinkage oriented in the direction perpendicular to the weld whereas the longitudinal shrinkage is oriented parallel to the weld.

The angular change is a consequence of a non-uniform transverse shrinkage in the thickness direction.

The rotational distortion is induced by a transverse shrinkage which is delayed between the beginning and the extremity of the workpiece (due to the torch movement).

The longitudinal bending distortion is induced by a non-uniform longitudinal shrinkage in the transverse direction.

The buckling distortion is created by compressive stresses which cause instability.

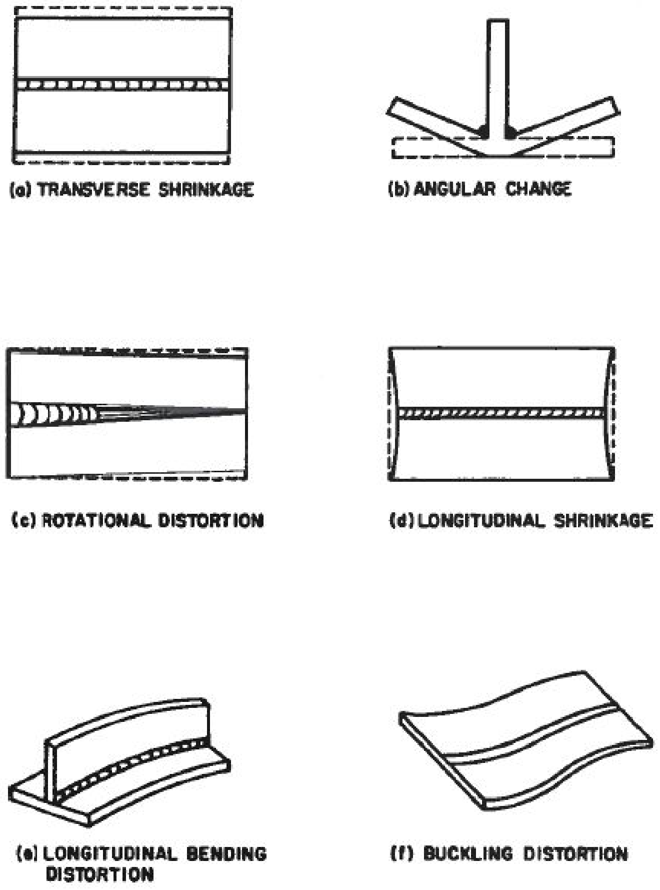
(a) TRANSVERSE SHRINKAGE
(b) ANGULAR CHANGE
(c) ROTATIONAL DISTORTION
(d) LONGITUDINAL SHRINKAGE
(e) LONGITUDINAL BENDING DISTORTION
(f) BUCKLING DISTORTION

Figure 2.9: Types of distortion induced by welding (Masubuchi, 1980).

Formation of welding residual stresses

Residual stresses are self-balancing stresses which can be introduced into materials and components during various manufacturing processes. Each process that causes deformation, can create residual stresses field. That is the case of the welding process where deformations are due to the application of a localised heat input.

These stresses remain in a component in absence of external loads. When a structure is loaded, the residual stresses arising during fabrication superimpose onto the applied stress. Combination of both type of stresses constitutes the internal stresses.

Residual stresses may be so high that even under compressive applied cyclic loadings, they can generate tensile internal stresses, meaning they are able to suppress crack closure leading to crack propagation rates similar to those under applied tension.

They vary at the level of different scales, that is the reason why Masing (1925) distinguished three kinds of residual stresses (see also Fig. 2.10):

- The residual stresses of type I (macroscopic) vary over macroscopic areas (scale of the specimen).
- The residual stresses of type II (microscopic, intergranular) vary over the grain size. They occur because of differences in crystallographic orientation as well as mechanical and physical properties of grains between them (yield strength, Young's modulus, coefficient of thermal expansion, Poisson's ratio, phase change, etc.).

- The residual stresses of type III (microscopic, atomic) vary over several atomic planes inside a grain. They are due to the presence of dislocations which unbalance forces between atoms.

The residual stresses of type II and III are not well known and their influence on crack propagation in metallic components is usually neglected. That is the reason why, this research focuses on residual stresses of type I. Their distribution is defined using continuum mechanics (ignoring polycristalline and multiphase aspects) and can be calculated using finite elements.

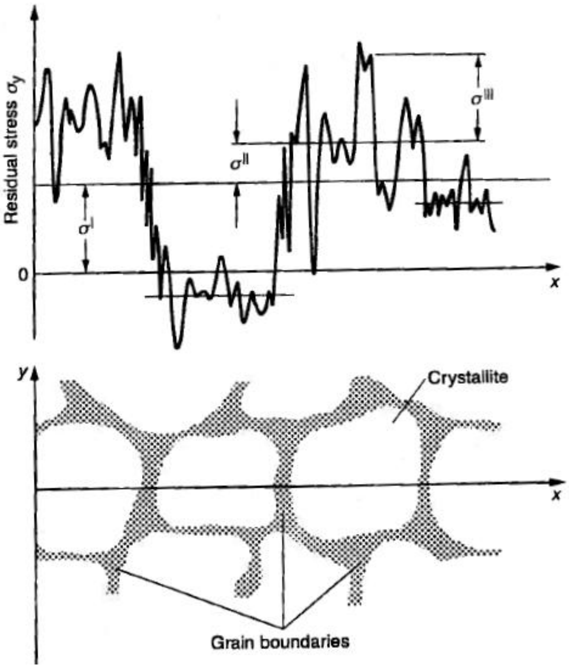

Figure 2.10: The first (I), second (II) and third kind (III) of residual stresses in relation with the grain size (Macherauch et al., 1973; Radaj, 2003).

In the next paragraph, the formation of thermal residual stresses is explained. These stresses will superimpose onto transformation and mechanical residual stresses.

Thermal residual stresses are caused by inhomogeneous volume changes as a result of thermal expansion (important gradient of temperature) which are high enough to induce plastic deformations. If only elastic thermal stresses are generated, they disappear when the temperature field returns to its initial value.

The formation of thermal residual stresses can be described as follows (Radaj, 2003):

- During welding, the weld area is heated up strongly giving rise to a local fusion zone whereas the region surrounding the weld stay cold.
- The heated area expands, it pushes on the surrounding solidified material which resists, therefore creating stresses. Part of these stresses exceeds the yield strength of the material which is lower at high temperatures. This weld region is plastically compressed.
- When cooling-down the temperature differences are removed but residual stresses remain. During cooling the weld area contracts, it pulls on the surrounding solidified material which resists, inducing tensile residual stresses in the weld area and compressive residual stresses in the surrounding region. These stresses are thermal residual stresses.

Note that phase transformations has the opposite effect. The transformation of austenite into ferrite implies a volume increase, even stronger for martensite formation. Thus, it results in compressive stresses in the weld area and tensile stresses in the surrounding region.

To summarize, in the last region cooled down, tensile thermal residual stresses occur whereas compressive transformation residual stresses are created. Depending on the material one or the other can be dominant. The fraction of martensite formed in our steel is studied in chapter 4 in order to assess the importance of transformation residual stresses.

2.3 Couplings between thermal field, microstructure evolution and mechanical field

Often the arc and weld pool physics are not considered in the model and replaced simply by an imposed heat source. Therefore, the fully coupled model is composed of three main states: the thermal state, the metallurgical state and the mechanical state which interact altogether.

These couplings or interactions are summarised in Fig. 2.11. Solid arrows indicate the major interactions.

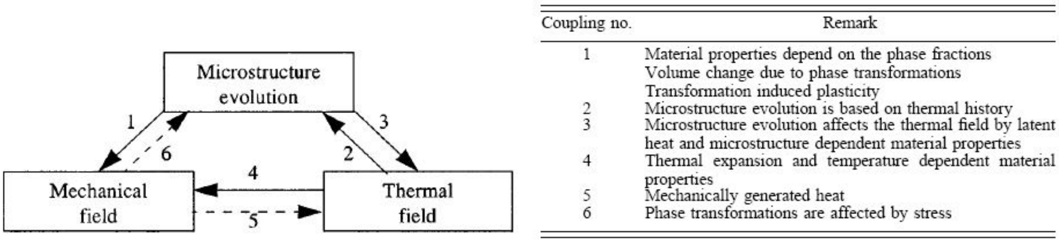
Microstructure evolution
Mechanical field
Thermal field
1
2
3
4
5
6

Coupling no.	Remark
1	Material properties depend on the phase fractions Volume change due to phase transformations Transformation induced plasticity
2	Microstructure evolution is based on thermal history
3	Microstructure evolution affects the thermal field by latent heat and microstructure dependent material properties
4	Thermal expansion and temperature dependent material properties
5	Mechanically generated heat
6	Phase transformations are affected by stress

Figure 2.11: Couplings between thermal, metallurgical and mechanical fields (Börjesson and Lindgren, 2001).

Thermo-metallurgical couplings (2,3)

The welding thermal cycle influences phase transformations (**2**). Conversely, if the microstructure changes, the thermal and material properties will be modified. Moreover, phase transformations are endo- or exothermic and thus impact heat transfer (latent heat) (**3**).

Thermo-mechanical couplings (4,(5))

The temperature affects the material properties and the thermal expansion (**4**). Deformations can induce heat generation (**5**) but this is often neglected (i.e. adiabatic assumption).

Metallo-mechanical couplings (1,(6))

The microstructure evolution influences the material properties, as well as the volume change, and induces deformation plasticity (**1**). On the other hand, deformation also has some effect on phase transformation (**6**), but this effect is often ignored.

Note that, by considering one single microstructure (no phase transformation), it is possible to conduct a thermo-mechanical analysis (two-step analysis) as presented in Fig. 2.12.

To use this model for numerical analysis, it has first to be proved that phase transformation, and especially martensite formation, can be neglected without significantly affecting the residual stress estimation.

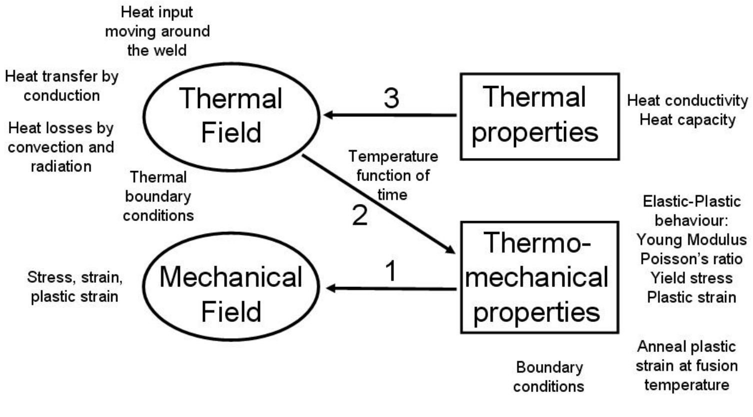
Heat input moving around the weld
Heat transfer by conduction
Heat losses by convection and radiation
Thermal Field
Thermal boundary conditions
3
Thermal properties
Heat conductivity
Heat capacity
Temperature function of time
2
Elastic-Plastic behaviour:
Young Modulus
Poisson's ratio
Yield stress
Plastic strain
Stress, strain, plastic strain
Mechanical Field
1
Thermo-mechanical properties
Boundary conditions
Anneal plastic strain at fusion temperature

Figure 2.12: The thermo-mechanical analysis adapted from Lindgren (2001a).

2.4 Summary and conclusions

In this chapter, the main physical phenomena occurring during the welding are reviewed, as well as their interactions. Understanding these concepts and the aspects of the phenomena that can be simplified, enables to build the welding numerical model.

- To state the problem, it is worth noting that the welding studied in this document uses a Flux-Cored Arc Welding FCAW, more precisely a Metal Active Gas process MAG to produce the joints.
- The main physical processes occurring during welding are: arc and weld pool processes, thermal transfer, metallurgical aspects and mechanical impacts. Often the arc and weld pool processes may be simply replaced in the model by an imposed heat source such as the Goldak or Gauss heat-sources for instance.

  It results that a thermo-mechano-metallurgical model can be used to reproduce the thermal, mechanical and metallurgical states as well as their couplings.

  Moreover, if it can be proved that phase transformation (especially martensite formation) can be neglected without significantly affecting the residual stress estimation, a simplified thermo-mechanical model can be utilized.

  Therefore, one of the first investigation of this research, will be to determine the microstructure formed in our steel by the MAG welding.
- This work concentrates on residual stresses of the type I (macroscopic residual stresses) since they are known to most influence crack propagation in metallic components. Their distribution can be estimated using continuum mechanics in a finite element model.

Chapter 3

Fatigue life assessment

This chapter introduces basic knowledge concerning fatigue phenomenon and main factors affecting fatigue resistance. It focuses on the main significant aspects related to bridge tubular K-joints.

3.1 Introduction

The phenomenon of fatigue may be described as the material resistance decrease under variable or repeated loads (cyclic loading).

The difficulty related to this phenomenon is that, for high-cycle fatigue, failure always occurs with stress values lower than the ultimate limit strength or even below the yield strength of the material, stress values that the structure would be able to withstand if the loads were static. As explained by Gurney (1979), "the fatigue failure of metals may therefore be defined as the formation of a crack or cracks as a result of the repeated application of loads each of which is insufficient, by itself, to cause normal static failure". The American Society for Testing and Materials (ASTM, 1995) defines fatigue as "the process of progressive localized permanent structural change occurring in a material subjected to conditions which produce fluctuating stresses and strains at some point or points and which may culminate in cracks or complete fracture after a sufficient number of fluctuations". These two definitions underline the fact that fatigue is a process, implying a series of loads which are fluctuating.

Different types of materials suffer fatigue failures: metals and alloys, composite and polymers. However, it represents one of the most common cause of failure for metallic structures (Hirt et al., 2006) with corrosion and wear. Fatigue affects several metallic fields depending of their loading forms (Gurney, 1979):

- **time-varying live loads**: bridges (traffic loads), cranes (lifting loads), ships (waves), automotive components, aircraft structures, engine frames.
- **temperature fluctuations**: turbines or boilers (heating and cooling) .
- **pressure fluctuations**: pressure vessels in power plants for instance, pipework .
- **vibrations**: rotative machinery, pipework.
- **atmospheric conditions**: offshore structures (waves: cyclic loading in a corrosive environment).

This thesis focuses on bridge structures and hence live load fluctuations. Depending on the number of cycles (live load fluctuations) to final failure, different fatigue domains and assessment approaches may be specified:

- **High-cycle fatigue** (about 10^3 to 10^8 cycles) is associated with low-stress fatigue (elastic cyclic behaviour) and a large number of cycles. It is commonly described by a 'stress-life' method such as the S-N approach (or Wöhler diagram).
- **Low-cycle fatigue** (typically less than 10^3) is associated with high-stress fatigue, meaning that the stresses are high enough to cause plastic deformation, and a small number of cycles. It is commonly described by a 'strain-life' method.

Two others domains are recently attracted more attention and are: Very High Cycle Fatigue (VHCF) defined by more than 10^9 cycles and the Ultra Low Cycle Fatigue (ULCF) defined by less than 100 cycles.

The behaviour of a bridge structure during the service life (elastic stresses) is governed by high-cycle fatigue. Even though the applied stresses are elastic, fatigue is a result of cyclic plastic strain. Indeed, the fatigue failure starts from one or several microcracks in a region which undergoes localized microplastic strains (crack initiation). They grow and coalesce under fluctuating stresses due to these plastic strains. Propagation of microcracks is called short crack (stage I) followed by the propagation of usually one macrocrack (stage II), called long crack. When the crack becomes larger, the remaining cross section is no longer able to withstand the applied stresses and the final fracture occurs usually in ductile failure. The final failure may also occur by brittle fracture if the fracture toughness K_c is reached.

Therefore, four main stages are distinguished:

- **Initiation** is often described by a 'strain-life' approach such as the Coffin-Manson relationship (Basquin, 1910; Coffin, 1954; Manson, 1953).
- **Propagation stage I** is characterized by a crack growth controlled by the maximum shear stress, implying a zig-zag crack path (Forsyth, 1962; Suresh, 1998).
- **Propagation stage II** implies a crack growth along two slips, resulting in a planar mode I crack path (see Fig. 3.1) perpendicular to the load direction (Forsyth, 1962; Suresh, 1998). The Linear Elastic Fracture Mechanics LEFM with the Paris law is used to evaluate the crack propagation (Lampman et al., 1996; Paris et al., 1968; Wangh and Blom, 1991).
- **Final failure** is also defined as the unstable crack growth (ductile or brittle failure). The final failure is usually fast. The Forman law, which is an extension of the Paris law including the stress ratio $R=\sigma_{\min}/\sigma_{\max}$, evaluates both the propagation stage II and the failure stages.

The 'stress-life' approach S-N curve includes both the crack initiation and the crack propagation.

Usually, it is assumed that the total fatigue life is composed by the initiation, propagation stage I and propagation stage II.

For welded joints, it has been shown (Borges, 2008; Fisher et al., 1970; Gurney, 1979; Maddox, 2000) that crack propagation stage II dominates the total fatigue life (where the failure criteria can either be a detectable crack or the failure of the specimen). Especially because crack-like discontinuities are so large (approximately 0.1 mm), crack initiation and propagation stage I can be neglected, the main part of the fatigue life is consumed by propagation stage II also known as stable crack growth (see section 3.4.3).

3.2 Fatigue assessment methods

There are severals methods developed to evaluate the fatigue resistance of welded CHS joints and presented in the CIDECT design guide (Zhao et al., 2000), the IIW recommendations (Hobbacher, 2007) and the Eurocode 3 part 1-9 (EN 1993-1-9:2005). In this report, three of them are used.

The first two methods are based on statistical analyses of experimental results. They give strength curves to be used in practice. The third method is an analytical theory dedicated to the crack propagation stage and requiring to know several parameters.

- **Classification method**

This is the traditional fatigue analysis method. Based on a large amount of experimental data, it gives fatigue strength curves or $S_{r,nom} - N$ curves for standard classified details. In this method, the nominal stress range (stresses away from the joint) is expressed as a function of the number of stress cycles. Details are classified into different detail categories with a given S-N curve for each category.

For tubular joints, the curves are defined by two values: the detail category corresponding to the nominal stress range under which a joint fail after 2 million cycles and a Cut-off limit, at 10^8 millions cycles, below which the nominal stress range is not considered to contribute to fatigue damage.

The nominal stress is the stress calculated in the cross-section, combining axial and bending stresses. It takes into account the global geometry but not the detail stress concentrations, the notch effect, the residual stresses, etc. Since the $S_{r,nom} - N$ curves are based on experimental data, they include these phenomena.

They are used in most structural codes EN1993, AISC, SIA, etc.

- **Hot-spot stress method (or geometric stress method)**

  The hot-spot approach was first developed for welded tubular joints in the offshore oil industry (American Petroleum Institute, American Welding Society). This fatigue analysis method provides also S-N curves based on experimental data despite the fact that stresses are hot-spot stresses (Maddox, 1997; Niemi, 2006).

  The hot-spot stress, defined for hollow section joints, is the stress located at the weld toe or end, where potential crack initiation sites ('hot-spot') are expected. Contrary to the nominal stress, it includes the effect of the joint geometry (stress concentration) and type of load, but not the local non-linear stress peak due to the weld shape and weld toe radius-eventually defect- (notch effect). This effect is included in the $S_{r,hs} - N$ curves.

  Therefore, the $S_{r,hs} - N$ curve presents the advantage of simplifying the different $S_{r,nom} - N$ curves given for each detail category by including the global detail geometry into the hot-spot stress calculation (Hobbacher, 2007). For CHS and RHS joints, the adopted $S_{r,hs} - N$ curve is equivalent to a detail class 114 in CIDECT for a basic wall thickness of 16 mm. Thickness correction factors are provided for joints with wall thicknesses other than 16 mm (Gurney, 1979; Marshall, 1992; van Wingerde, 1992).

- **Fracture mechanics method**

  Linear Elastic Fracture Mechanics (LEFM) has proven to be a useful analytical tool to estimate the behavior of cracks in solids in order to evaluate the critical loads that cause crack growth. This method is based on the principle of superposition.

  It is assumed in LEFM that an initial crack is present in the material (which is often true with crack-like imperfections induced by welding) implying that no initiation stage is considered.

  In fracture mechanics, a crack can be loaded in three modes as shown in Fig. 3.1.

  In this study, fracture under mode I (the opening mode) is assumed, which is the most common loading mode and usually most relevant when a crack grows perpendicularly to the principal tensile stress direction.

3.3 Focus on fracture mechanics

3.3.1 Characterization of the stress field in the vicinity of the crack tip

For isotropic linear elastic materials, the concept of the stress intensity factor K describes, with a single parameter K, the local stress and strain 2D fields in the vicinity of the crack tip.

The stress state described by LEFM for linear elastic materials presents a crack-tip singularity, meaning that stresses tend to infinity when the r distance (see Fig. 3.2) tends to zero.

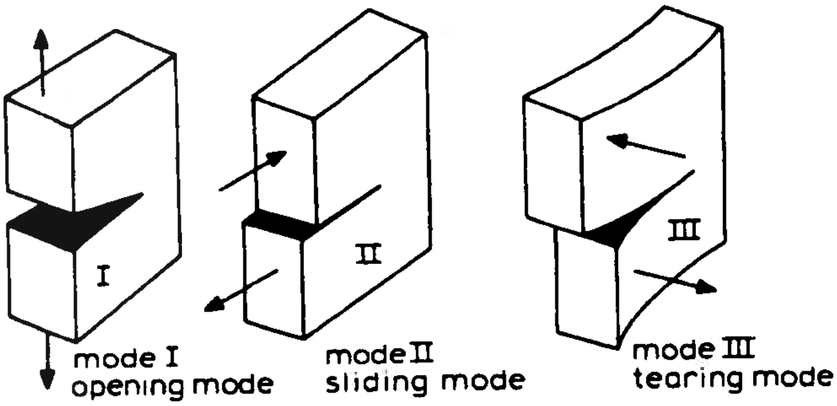

Figure 3.1: Modes of crack loading (Broek, 1986).

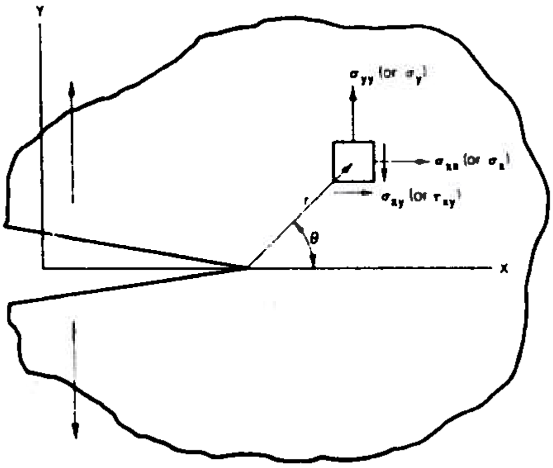
Y
X
σ_{yy} (or σ_y)
σ_{xx} (or σ_x)
σ_{xy} (or τ_{xy})
r
θ

Figure 3.2: Crack in a body (Broek, 1986).

In the case of a sharp crack, stresses at the crack tip can be expressed by the first order terms of asymptotic solutions (Westergaard, 1939). Indeed, when r is small, the first order terms are much greater than the others (singularity $\frac{1}{\sqrt{\mathrm{r}}}$). This appears in the expression of the stress tensor at the crack tip:

$$\sigma_{ij}(r,\theta) = \frac{K_I}{\sqrt{2\pi r}} f_{ij}^{I}(\theta) + \frac{K_{II}}{\sqrt{2\pi r}} f_{ij}^{II}(\theta) + \frac{K_{III}}{\sqrt{2\pi r}} f_{ij}^{III}(\theta) \tag{3.1}$$

where σ_{ij} are stresses on an element dxdy, r is crack tip distance, θ is the angle from the crack plane, K is the stress intensity factor and $\mathrm{f_{ij}}$ are angular functions (Irwin, 1957).

The displacement field at the crack tip is also known. It can be expressed by parabolic functions $\sqrt{\mathrm{r}}$ ($\mathrm{g_i}$ are angular functions):

$$u_i(r,\theta) = \frac{K_I\sqrt{r}}{2\pi} g_i^{I}(\theta) + \frac{K_{II}\sqrt{r}}{2\pi} g_i^{II}(\theta) + \frac{K_{III}\sqrt{r}}{2\pi} g_i^{III}(\theta) \tag{3.2}$$

Note that, for fracture under mode I, the angle θ is zero and the previous equation (3.1) can be simplified in equation (3.3):

$$\sigma_y = \frac{K_I}{\sqrt{2\pi r}} \tag{3.3}$$

Because of this singularity in $\frac{1}{\sqrt{r}}$, different areas around the crack tip can be distinguished depending on the distance r to the crack tip. Figure 3.3 summarizes these regions (Pommier et al., 2009):

- for a large r value: the first order terms are not greater than the others therefore the terms of higher orders have to be included in the stress calculation.
- for a small r value: the first order terms are greater and the stress intensity factors K_I, K_{II} and K_{III} are enough to describe the stress field (K-dominated zone). In this zone, LEFM gives a good approximation of the stress field (in 2D).
- for a tiny r value: there is an area, called the plastic zone, where stresses are so high that the elastic linear theory is not valid. In this zone, the material has a non-linear behaviour. Non-linear fracture mechanics NLFM can be used to describe stresses in this zone.
- in the crack tip vicinity: in this microscopic zone, called process zone, the material damages locally.

In general, LEFM can be used if the process and plastic zones near the crack tip is much smaller than other dimensions of the specimen. It is called small-scale yielding.

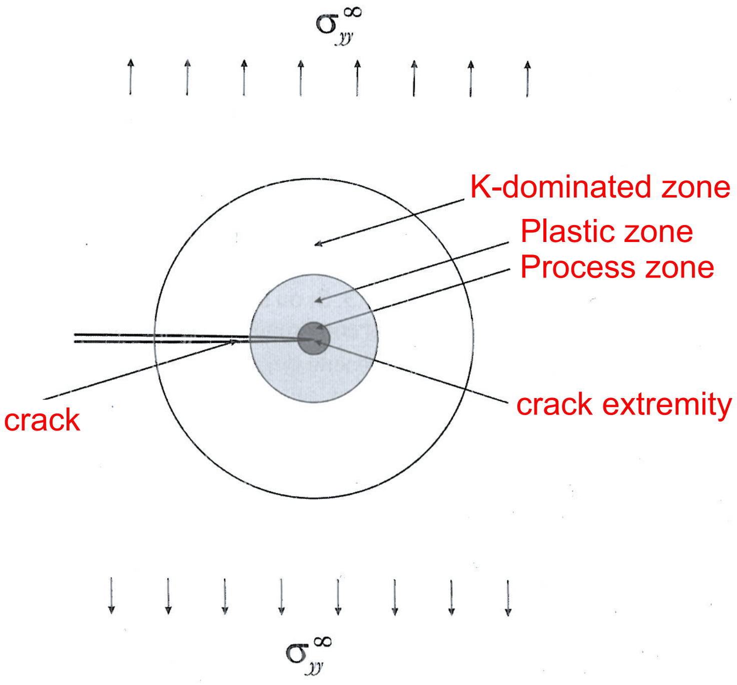

Figure 3.3: Three regions around the crack tip, adapted from Pommier et al. (2009).

The stress intensity factor in a plate with infinite dimensions is defined by Griffith's equation (Griffith, 1920) and generalized to finite dimensions by adding a stress intensity factor corrector Y:

$$K = Y\sigma\sqrt{\pi a} \tag{3.4}$$

where Y is the correction factor for various effects (shape of the crack, presence of free surface, thickness of the plate and non-uniformity of stress distribution), σ is the stress; and a is the crack size.

3.3.2 Fatigue crack propagation

In combination with the LEFM, the well-known Paris law is used in order to predict the stable crack growth under fatigue loadings (Paris and Erdogan, 1963):

$$\frac{da}{dN} = C\Delta K_{app}^{m} \qquad \Delta K_{app} = K_{app,max} - K_{app,min} \tag{3.5}$$

where $\frac{\mathrm{da}}{\mathrm{dN}}$ is the propagation rate (N is the number of cycles), C and m are constants of the material and $\Delta \mathrm{K}_{\mathrm{app}}$ is the applied stress intensity factor range ($\mathrm{K}_{\mathrm{app,max}}$ is related to the applied maximum load and $\mathrm{K}_{\mathrm{app,min}}$ to the applied minimum load).

Equation (3.5) can be adapted to account for the threshold stress intensity factor range, $\Delta \mathrm{K}_{\mathrm{th}}$, under which no propagation can occur.

$$\frac{da}{dN} = C(\Delta K_{app} - \Delta K_{th})^{m} \tag{3.6}$$

To consider the residual stress field and the crack tip plasticity into the LEFM fatigue approach, the principle of superposition can be used to calculate the effective stress intensity factor, $\mathrm{K}_{\mathrm{eff}}$, and its range $\Delta \mathrm{K}_{\mathrm{eff}}$.

As shown by Elber (1970), a fatigue crack can remain close at the crack tip for a portion of the tensile load cycle, meaning that only a part of the cycle is effective in propagating the crack. Indeed, behind the crack tip, tensile deformations are left along crack faces from all previous plastic zones. These deformations come with a shortening of the crack opening displacement, explaining why the crack tip may be closed for a tensile load greater than zero. Hence, K_{op}, defined as the applied stress intensity factor level above which the crack tip opens upon loading, is related to the crack tip plasticity K_{pl}. In the absence of residual stress, $\mathrm{K}_{\mathrm{op}} = -\mathrm{K}_{\mathrm{pl}}$.

However, residual stresses influence also the crack tip opening or closure. Tensile residual stresses, induced by the welding process, tend to open crack faces whereas compressive residual stresses, induced by post-treatment methods, tend to close the crack. The influence of the residual stress distribution can be considered with K_{op}: $\mathrm{K}_{\mathrm{op}} = -(\mathrm{K}_{\mathrm{res}} + \mathrm{K}_{\mathrm{pl}})$.

The concept of $\mathrm{K}_{\mathrm{eff}}$ is based on the following expression:

$$K_{eff} = K_{app} + K_{res} + K_{pl} = K_{app} - K_{op} \tag{3.7}$$

Bremen (1989) proposed the following relation for $\mathrm{K}_{\mathrm{eff}}$, resulting in Equ. (3.8).

$$\Delta K_{eff} = MAX(K_{app,max} - K_{op}, 0) - MAX(K_{app,min} - K_{op}, 0) \tag{3.8}$$

Then the crack closure method is adopted by replacing $\Delta \mathrm{K}_{\mathrm{app}}$ in Equ. (3.6) by the effective $\Delta \mathrm{K}_{\mathrm{eff}}$.

$$\frac{da}{dN} = C(\Delta K_{eff} - \Delta K_{th})^{m} \tag{3.9}$$

The principle of superposition in Equ. (3.7) is based on the assumption that the stress distribution is not affected by the presence of a crack. Based on this assumption, one can calculate $\mathrm{K}_{\mathrm{res}}$ by making use of the weight functions, such as used in Albrecht and Yamada (1977) and $\mathrm{K}_{\mathrm{app}}$ by direct calculation. In case of tubular joints, Bowness and Lee (1999) solution may be used.

Contrary to other fatigue design approaches for tubular joints, such as the classification method (Eurocode 3 part 1-9) or the hot-spot stress method (Hobbacher, 2007), LEFM allows to estimate the crack size and the crack growth rate at any time during the service life of a structure.

3.4 Main factors affecting fatigue

In this section, the most significant factors influencing the fatigue strength of bridge K-joints under isothermal conditions are summarized. Fatigue cracking in these welded joints is caused by the combination of four main parameters, which are shortly described.

3.4.1 Load cases

Traffic loadings result in cyclic stress variations in the structure and its joints. A tubular truss joint is subjected to both normal and bending stress ranges. As shown by Borges (2008), each basic load case (balanced axial brace, un-balanced in-plane bending brace, balanced in-plane bending brace, axial chord, in-plane bending chord) has a different effect on the fatigue behaviour. Borges has identified the balanced axial brace, axial chord and in-plane bending chord to be the most significant. Combining the behaviour of these basic loads is possible (superposition principle) but they are not detrimental in the same site at the same time.

Variable amplitude loading is treated in section 3.5.2.

3.4.2 Stress concentration

Welds are located at geometrical discontinuities where stress deviation occurs, implying stress concentration and thus stress ranges higher than the nominal ones. In complex geometries, stress concentration and fatigue crack location depends on many parameters. Schumacher (Schumacher et al., 2003) for example has given for welded tubular K-joints with $\gamma = \frac{\mathrm{D}}{2\mathrm{T}} < 12$, stress concentration locations and factors as a function of the load case and the geometrical dimensions. Schumacher et al. (2003) proposed useful stress concentration factor (SCF) tables allowing to calculate hot-stresses in K-joints for a large range of dimensions and loads.

3.4.3 Imperfections and local weld geometry

The local weld geometry (toe angle, toe radius, welding imperfections) plays an important role in fatigue strength by creating local stress concentration effects (notch effects). Several authors have measured the welding imperfections induced by the welding process in the vicinity of the weld toe. Barsoum (Barsoum and Samuelsson, 2006) and Smith (Smith and Smith, 1982) have reported their results on non-load carrying fillet welded gusset plate (cruciform joint) made of carbon steel and welded respectively with MAG or laser/MAG process and manual metal arc. Smith described a single continuous 'defect' at the weld toe (average depth of 45 μm, average root radius of 2.6 μm) with some of these imperfections presenting a depth above 0.1 mm. Barsoum showed that fatigue crack mostly grow from imperfections of 0.1 to 0.2 mm in depth. Imperfections imply high plastic strains and act as a crack initiator meaning that there is almost no crack initiation phase in the fatigue life, thus the crack may start to propagate with the first load fatigue cycle. This has been shown (Borges and Nussbaumer, 2008; Schumacher et al., 2003) to occur in tubular joints. It has to be noticed that, as these imperfection values are within the tolerance range prescribed by Code ISO 5817 on welded joints ($\mathrm{h} \leq 0.05.\mathrm{t} \leq 0.5\mathrm{mm}$ for weld quality B), they are called imperfections and not defects.

3.4.4 Residual stresses

Usually residual stresses have a small effect on fatigue crack initiation but they are coupled with phase transformation deformations and changes in the surface roughness which affect crack initiation and growth (McClung, 2007).

With welding imperfections acting like microcracks, residual stresses can have a significant influence on crack propagation, especially when the $\Delta\mathrm{K}_{\mathrm{eff}}$ is close to the grow/no-grow threshold $\Delta\mathrm{K}_{\mathrm{th}}$. It can make the difference between a fatigue microcrack beginning to grow or not (McClung, 2007). Indeed, residual stresses can raise the effective stress intensity factor range above the threshold K value.

Moreover, tensile residual stresses suppress crack closure thus increasing the rate of crack propagation. Therefore, they are able to propagate a crack under compressive applied stresses. That is the reason why tensile residual stress field is often associated with shorter fatigue life. Therefore, the residual stress distribution is essential to estimate accurately the crack development under fatigue loads.

There are several phenomena, summarized by Krebs and Kassner (2007), which tends to modify the magnitude and distribution of residual stresses:

- after welding, phase transformation around the welds can reduce tensile residual stresses, especially in high strength steels (Nitschke-Pagel, 1994). Moreover, the heat input of the welding process can modify material properties and especially the yield limit.
- applied external loads can either increase or decrease residual stresses:
    - **the cyclic yield limit**, usually lower than the static yield limit, can be exceeded by the combined effect of applied and residual stresses. Therefore, residual stresses are reduced so that the maximum combined stress is equal to the cyclic yield limit.
    - **the degree of stress multiaxiality**, the yield limit value depends on the shape and dimensions of the structure (including plate thickness) and on the joint loadings. For small-scale specimen ($T < 20$ mm), the yield limit is reduced but for large-scale specimen ($T \geq 20$ mm), the larger thickness increases the multi-axial effect, increasing the yield limit and thus possibilities for residual stress reduction are decreased. Note that the thickness effect is related to the plane strain-plane stress state.
    - **the notch effect**, due to the weld profile and welding imperfections, can also influence the residual stress magnitude. High notch effect (notch concentration factor $K_t > 2.5$) has the same effect as larger thicknesses because it increases the multiaxiality condition.

To summarize, for large-scale specimens, residual stresses are not or slightly decreased by external loads.

To improve failure predictions, the American and European defect assessment procedures for pressure vessel and piping components, have made progress in weld residual stress estimations during the last decade. Their developments were reported in API 579 Appendix E (API, 2000b) and in BS 7910:1999 of the SINTAP project (SINTAP, 1999). The objectives were to complete the earlier investigation of residual stress data.

A large amount of residual stress measurements were conducted by researchers at Cambridge University on tubular joints (Payne and Porter Goff, 1986). Their main finding was that the mean longitudinal stresses (stresses parallel to the weld direction) never exceeded the material yield stress by more than 20 N/mm^2 and that mean transverse residual stresses (stresses perpendicular to the weld direction) never exceeded 0.65 f_y. Longitudinal residual stresses are usually greater than transverse ones.

Bouchard (Bouchard, 2007) compared the residual stress profiles for pipe girth weld given by SINTAP, API, ASME, etc.

Several other residual stress distributions are proposed in the literature to model the residual stress due to welding in tubular joints. In Stacey et al. (2000), measured longitudinal and transverse residual stresses are presented for a number of details (applicable to pipes or pressure vessels tubular structures including: T-butt joints, pipe-to-endplate joints, tubular T-, and Y-joints). Transverse and longitudinal residual stress distributions based on measurements conducted in T-joints, Y-joints and pipe-to-endplate joints are presented in Fig. 3.4. It confirms that longitudinal residual stresses are larger than transverse residual stresses on the first millimeters below the weld toe.

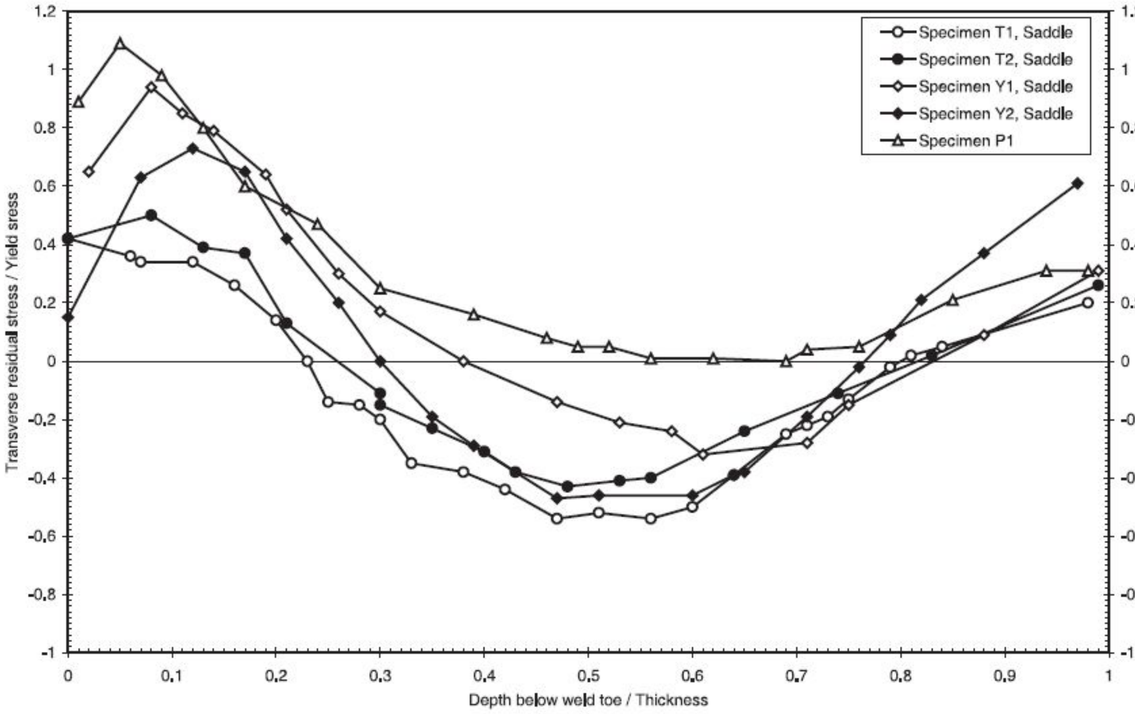

(a) Transverse residual stress distributions

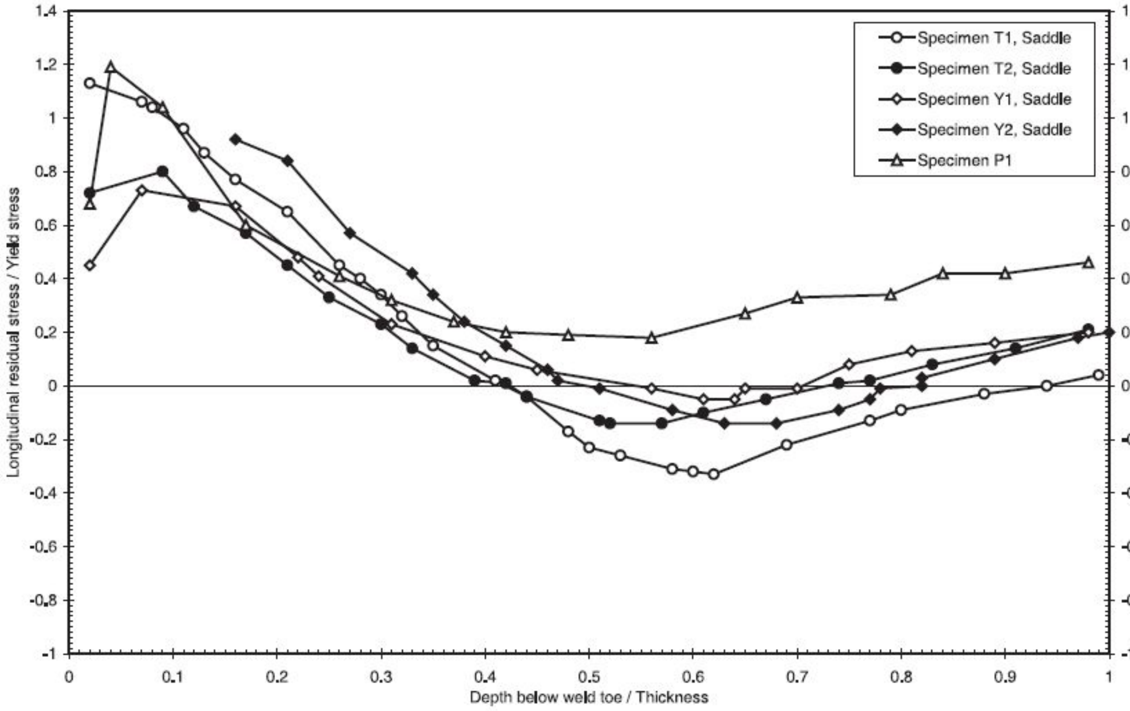

(b) Longitudinal residual stress distributions

Figure 3.4: Residual stress distributions in tubular joints (Stacey et al., 2000).

The pipes and pressure vessels tubes concerned by this study are thin cylinders with diameters ranging between 600 and 1000 mm, whereas tubes in bridges are often thick cylinders, called hollow sections, with diameters lower than 600 mm.

Leggatt (2008) also defined a residual stress distribution for butt welds in pipes.

However, to the best of our knowledge, no data is available concerning residual stress investigations in K-joints used in bridge construction.

3.5 Other aspects to consider in fatigue strength

3.5.1 Size effect

When trying to interpret the size effect in fatigue, the following three basic theoretical arguments are currently accepted (Dijkstra and Van Straalen, 1997; Marshall, 1992; Örjasäter, 1995; van Wingerde et al., 1997). They are summarized here based on Marshall (1992):

- **the statistical size effect** can be simply explained by the fact that the higher the volume of the element, the greater the probability of having an initial defect and or a variation of material properties in this volume is important. Since an initial imperfection of 0.1 mm is considered in our joints, the statistical size effect is not taken into account in this study.
- **the metallurgical or technological size effect**: the increase in thickness of a plate can induce a larger grain size, a decrease of the yield strength, a decrease of the local toughness and especially an increase of residual stresses. The magnitude and the distribution of residual stresses may be changed.
- **the geometrical size effect**: for two plates of different thicknesses with an SCF, loaded at the surface by the same stress and at mid-thickness by the same nominal stress, the thinner plate has a stronger stress variation through its thickness than the thicker plate. Therefore, a surface imperfection such as a notch for instance undergoes a lower stress in the thin plate than in the thick plate (Örjasäter, 1995). The notch concentration factor K_t, characteristic of this effect, depends on the local geometry (effect described above) but also on the detail geometry inducing more or less stress deviation. The geometrical effect is often most significant in welded structures. For fatigue of tubular joints, the geometrical effect size implies that a large-scale joint has a shorter life than a small-scale joint, if they both have the same geometry proportionally scaled and the same stress range.

It is important to state here that in literature three terms are commonly employed to describe the effect under consideration (Schumacher, 2003): scale effect, thickness effect and size effect. 'Scale effect' tends to imply that the joints have been proportionally scaled, 'thickness effect', the most widely used term in welded structures, makes reference to wall thickness of the failed member, which is largely seen as the variable with the most significant influence on this phenomenon. Lastly, 'size effect' is a more general term, which also encompasses differences in fatigue performance between non-proportionally scaled joints, where the size of the weld or attachment may also affect fatigue behaviour of the joint.

For tubular structures, a thickness effect correction is included in the CIDECT design guide to calculate hot-spot stresses (Zhao et al., 2000). The International Institute of Welding (IIW) recommendations (Hobbacher, 2005), for connections between plates only go further, and vary the exponent from 0.1 to 0.3, depending on the weld type, weld profile and mode of loading. However, for bridge joints, the thickness effect correction is not sufficient. Bridge application is an example of non-proportional scaling, where not only the changing wall thickness of the fatigue critical member, but also the relative size of the attachment, the load ratio and the different potential crack sites may affect fatigue behaviour between joints of different sizes. To overcome the weaknesses of the hot-spot stress method for estimating the size effect in welded joints, alternative methods have been proposed such as the one from Poutiainen and Marquis (Poutiainen and Marquis, 2004). They proposed a new modified structural stress to better capture the stress state for thick plates or load-carrying welds.

Borges (Borges, 2008) developed a model which properly predicts proportional and non-proportional scaling effects of tubular K-joints based on a large experimental database.

3.5.2 Constant versus variable amplitude loading

Variable amplitude loadings can modify residual stresses in a different way (Krebs and Kassner, 2007) than constant amplitude loadings. If applied and residual stresses exceed the yield limit, the residual stress level is reduced in the first cycles for constant amplitude loading whereas for variable amplitude loading, it is reduced each time high load amplitudes are encountered. Therefore, the residual stress level is rapidly stable under constant amplitude whereas it can be constantly changing under variable amplitude.

Concerning fatigue strength under variable amplitude loading, Dubois (Dubois, 1994) showed that the concept of equivalent stress range is valid but that it would be necessary to also take into account the equivalent value for the maximum stress.

3.5.3 Influence of the stress ratio R

According to the IIW recommendations (Hobbacher, 2007), the fatigue strength is dependent on the stress range but not on the stress ratio R and the mean stress. This consideration is shown not to be true for small-scale specimens but it is verified for large-scale specimens Gurney (1977); Krebs and Kassner (2007); Lieurade (1987).

3.6 Summary and conclusions

The main concepts of the fatigue phenomenon are described in this chapter.

It focuses on several aspects of the fatigue behaviour which are specific to the study of bridge tubular K-joints.

- Bridge structures are subjected to high-cycle fatigue (low-stress, large number of cycles). The difficulty related to high-cycle fatigue is that the failure always occurs with stress values below the yield strength of the material, stress values that the structure would be able to withstand if the loads were static. Therefore, these joints have to be designed for cyclic loadings as well as for static loadings during the service life.
- The most common approaches to describe high-cycle fatigue are the stress-life method (S-N cuves) or the linear elastic fracture mechanics LEFM approach. LEFM presents the major advantages to characterize the stress field in the crack tip vicinity with a single parameter, the stress intensity factor K and to estimate when and how the crack will propagate.

  Moreover, using the concept of the effective stress intensity factor K_{eff}, the residual stresses as well as the crack closure effect can be taken into account.

  LEFM is only valid for stable crack growth (propagation stage II) implying the presence of an initial crack-like 'defect' (which is the case in welded tubular joints).
- Four main factors significantly affect the fatigue strength of bridge joints:
  - load cases applied to the joints which are often multi-axial and complex.
  - stress concentrations at the weld location due to geometrical discontinuities. Stress concentration factors are available from the Schumacher et al. (2003) work as a function of load cases and geometrical dimensions.
  - welding imperfections of approximately 0.1 mm at the weld toe create notch stress concentrations.
  - tensile residual stresses due to welding superimpose to applied stresses. They are able to suppress crack closure and therefore to propagate a crack under compressive applied stresses. For large-scale specimens, such as tubular joints, they are not or slightly reduced by external loadings. For K-joints, no residual stress data is available in the literature.
- The crack propagation model used to evaluate fatigue life has to take into account this stress field complexity, which is strongly influenced by size effects. Two size effect types are underlined in this study:
  - the metallurgical or technological size effect which increases residual stresses when the specimen thickness increases.
  - the geometrical size effect which implies that a large-scale joint has a shorter life than a small-scale joint, if they both have the same geometry and the same stress range.

Part II

Experimental investigations

Chapter 4

K-joint manufacturing and welding processes, characterization of the steel S355J2H

In this chapter, the tubes manufacturing process and hence the fabrication and welding processes of tubular K-joints are presented, including an overview of phenomena inducing cold cracking. Material characterizations of the steel S355J2H are provided. Some of these properties, such as thermal and mechanical temperature dependent properties, are required as input values for numerical simulations presented in chapter 7.

4.1 Introduction

Two experimental investigations were carried out. On one hand, on welded Circular Hollow Section (CHS) K-joints in order to measure residual stresses. On the other hand, on large-scale truss beams composed of nine welded K-joints in order to assess their fatigue behavior. Most of the tested isolated K-joints were cut from CHS truss beams. Investigated specimens were manufactured and welded under the same conditions as real bridges by a steel manufacturer. This chapter is an introduction to the experimental part. It aims to give information on the fabrication and welding processes used to produce the K-joints that were tested.

4.2 Tubes manufacturing process

The tubes that we used are Circular Hollow Section CHS, belonging to the family of Structural Hollow Section SHS. They were manufactured using a production process of seamless (i.e., without welds) tubes. The multiple sequence process used for our tubes is composed of three following phases as described in Fig. 4.1:

- **The piercing phase**: the billets, previously heated to approximately 1300 °C in a rotary furnace, are pierced with an internal mandrel afterwards.
- **The elongation and finish-rolling phase**: the circular hollow section is rolled between two semi-circular rolls and an internal mandrel in order to give the tube its external dimension (Mannesmann process).
- **The final preparation and control phase**.

Residual stresses induced by the manufacturing process will not be considered in this research because they are washed by the welding in the area of interest (weld toe region).

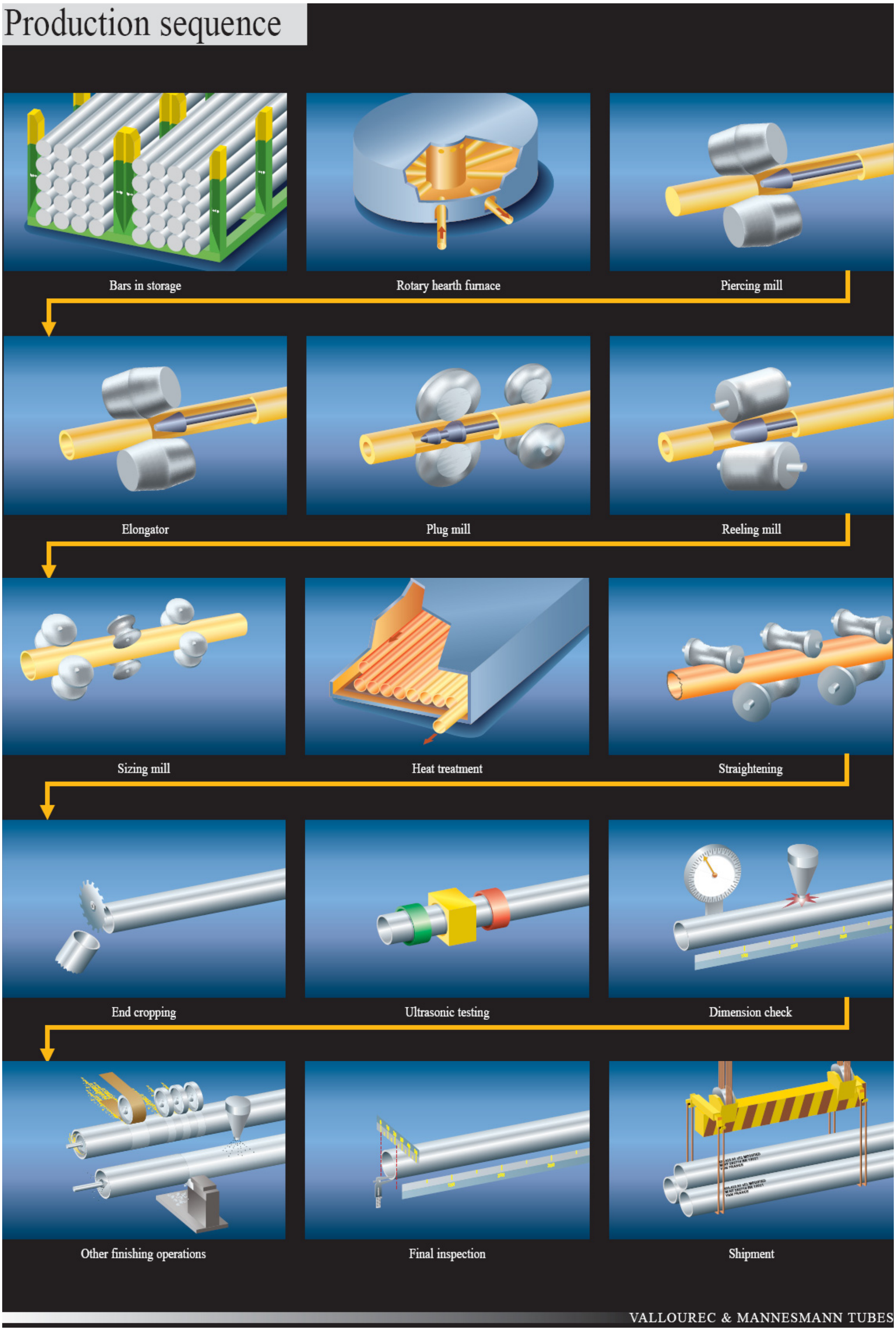
Production sequence
Bars in storage
Rotary hearth furnace
Piercing mill
Elongator
Plug mill
Reeling mill
Sizing mill
Heat treatment
Straightening
End cropping
Ultrasonic testing
Dimension check
Other finishing operations
Final inspection
Shipment
VALLOUREC & MANNESMANN TUBES

Figure 4.1: Production sequence in the tube works of V&M Tubes, Aulnoye, France (Vallourec & Mannesmann Tubes, 2003).

4.3 Fabrication and welding process

An isolated K-joint is composed of two brace branches welded onto a chord member, as shown schematically in Fig. 4.2. It is often preferred to other type of joints, such as N-joints for instance, because fewer K-joints are required to build a truss. Our K-joints are gap joints without any overlapping of braces for ease of fabrication. This implies, however, a noding eccentricity and associated bending moments.

A large-scale tubular truss beam of approximately 9 meter long and 2 meter high is depicted in Fig. 4.3. K-joints samples and tubular truss beams are presented in detail in sections 6 and 5 devoted to fatigue tests and residual stress measurements.

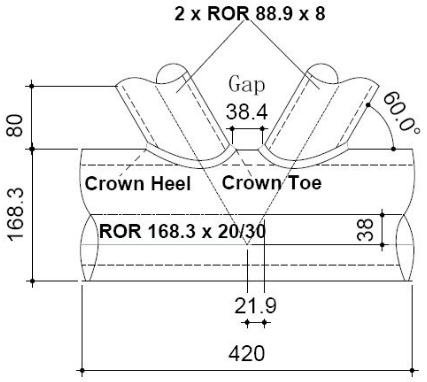

Figure 4.2: Schematic of the K shape welded joint (a ROR section is Circular hollow section designation in Switzerland).

Tridimensional computer guided cutting is used to give to the brace extremity edge the shape of the outer contour of the chord. Beveled edges with angles between 25 °C and 60 °C are also made in order to prepare the edge for full penetration of the weld.

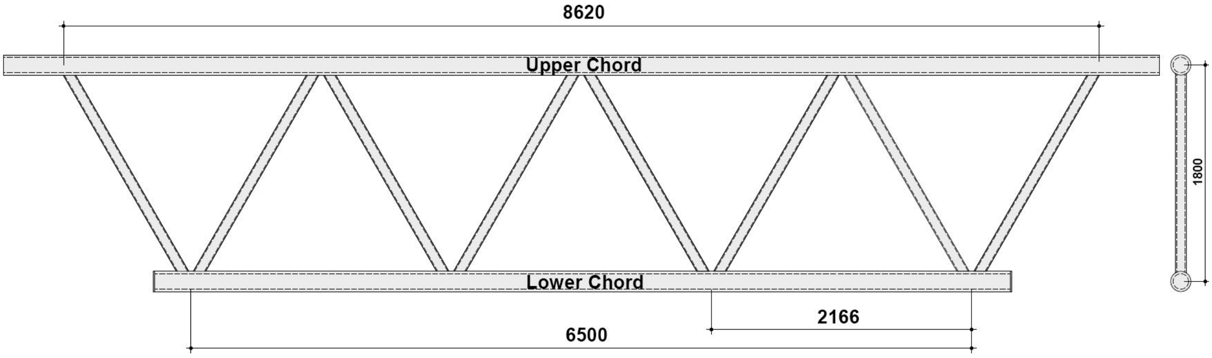

Figure 4.3: Tubular truss beam specimen (dimensions in mm).

Backing rings, placed inside the brace members, enable to facilitate the brace-to-chord welding procedure. Backing rings connected to the chord using initial welding points allow brace members to maintain a fixed position and provide a support surface to guarantee a full penetration weld (see Fig. 4.4). Note that the presence of these backing rings does not affect fatigue resistance as shown by Schumacher (2003).

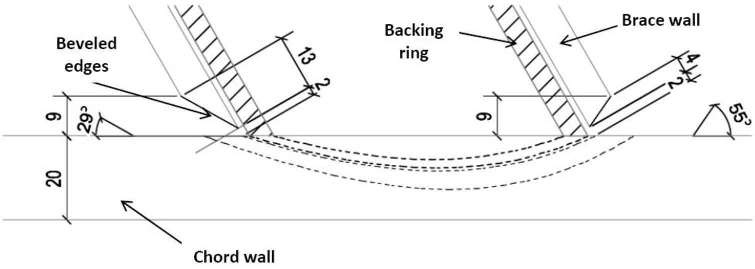

(a) Backing ring in the cross-section of a brace-chord joint.

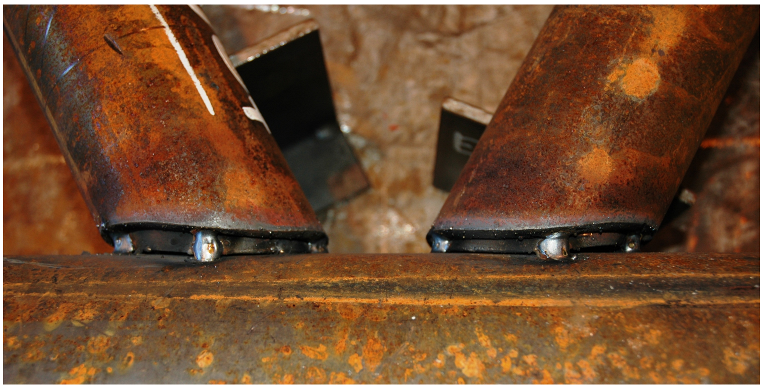

(b) Backing rings fixed onto the chord member by four welding points, and brace extremity positioned over them before welding.

Figure 4.4: Backing rings.

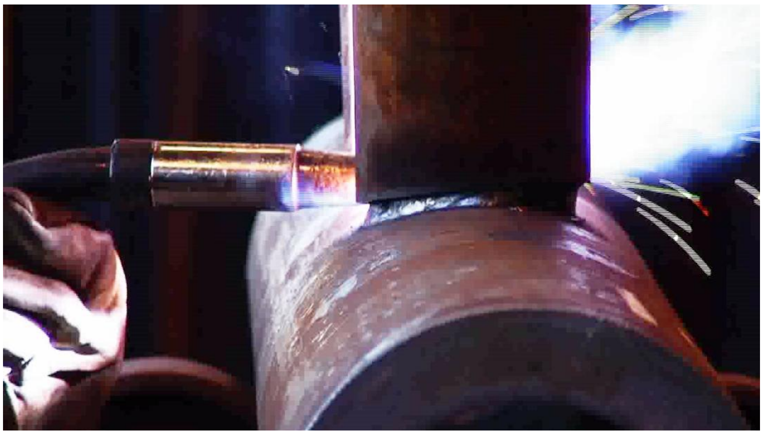

Figure 4.5: Photograph of the welding torch moving from the crown heel to the crown toe position.

The full penetration weld was made by using the flux cored arc welding (FCAW) process MAG 136. A flux-cored electrode Filarc PZ 6113 1.4 mm in diameter was employed according to AWS A5.20-95:E71 T-1 with a gas protection composed of 82% Argon and 18% CO_2. This filarc wire is especially well-known in ship construction because it is easy to employ in any position and it offers high tolerance for poor joint preparations.

The sequence of weld passes used to weld our K-joints is described as follows:

- Chord and brace members are locally pre-heated by flame to 70-90 °C in order to release humidity and to reduce the risk of high hardness and cold cracking (see section 4.5).

- Brace members are welded first on the lower chord from one extremity to the other, and then identically on the upper chord. The K-joints welded are gap joints without any overlapping of braces.
- The welding torch is moved by the welder from the crown heel to the crown toe with a travel speed of 5.5 mm/s (see Fig. 4.5). The welding procedure specifications (WPS) are summarized in Table 4.1.
- For each pass, the welding path is the same and its sequence is illustrated in Fig. 4.6. Once the welds 1 and 2, respectively 3 and 4 are finished and cooled down, the ends of the weld are rounded (grinding) and the surface of the weld is roughly cleaned with a hammer. We also show in Fig. 4.6 the start and stop positions, which do not respect the sequence recommended by Zhao and Packer (2000). In order to prevent the occuring welding defects in the zone where peak stresses are expected, start and stop positions have to be shifted away from the chord crown heel and chord crown toe positions.
- Seven weld passes are needed with our brace dimensions (Fig. 4.2) in order to ensure full penetration of our K-joints. For each of these passes, the welding sequence is repeated in the order shown in Fig. 4.7. The photographs shown in Fig. 4.8 have been taken after two and six passes respectively.
- No post-weld heat treatment is carried out.

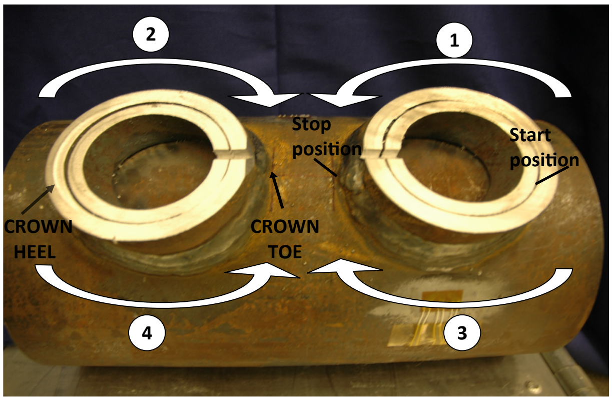

Figure 4.6: Welding path from the crown heel to the crown toe and its sequence.

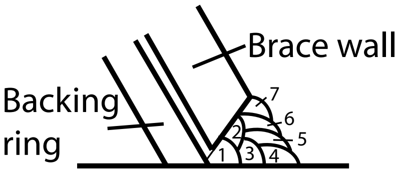

Figure 4.7: The order of the seven weld passes to form the full weld.

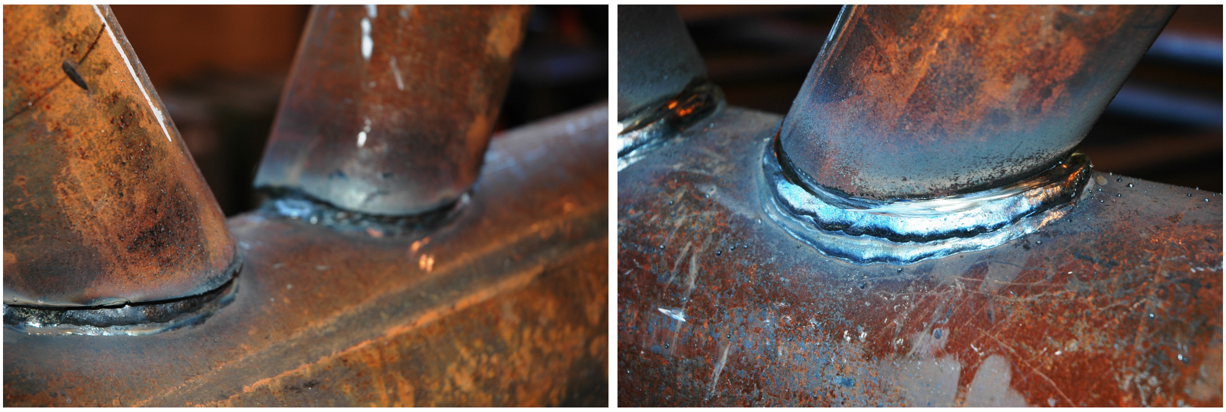

(a) The weld geometry after two passes. **(b)** The weld geometry after six passes.

Figure 4.8: Photographs showing different steps in the welding sequence.

Table 4.1: Welding procedure characteristics.

Electrical wire type	Filarc 1.4 mm
Welding Current (A)	270
Arc Voltage (V)	30
Arc Travel Speed (mm/s)	5.5
Interpass Temperature (°C)	≤ 250
Degree of efficiency	0.75
Range of Thicknesses (mm)	8-30
Number of Passes	7

4.4 Material properties of the S355J2H steel

In steel bridge construction, usually the hot finished steel of grade S355 is chosen. Compared to grade S235, S355 steel has a greater tensile yield stress ($f_y \geqslant 355 N/mm^2$ for a nominal thickness $t \leqslant 16$ mm, $f_y \geqslant 345 N/mm^2$ for a nominal thickness 16 mm $< t \leqslant 40$ mm). Therefore the structural elements may have smaller dimensions and hence smaller weld thicknesses.

The steel grade chosen for our specimens made of hollow sections is S355J2H according to EN 10210-1 (Hot finished structural hollow sections of non-alloyed and fine grain steels). Note that hollow sections may also be cold formed structural hollow sections of non-alloyed and fine grain structural steels (EN 10219-1). The designation S355J2H is used for a structural steel (S) with a minimum yield stress value of 355 N/mm^2 for a nominal thickness $t \leqslant 16$ mm and a minimum toughness of 27 Joules at - 20 °C (J2). The rules for designation can be found in EN 10027-1. In our case, a tubular hollow section (H) is required.

4.4.1 Designations

The different designations of the type of steel are given in Table 4.2.

Table 4.2: Equivalence between European national standards for steel S355J2H.

Code	**Europe EN 10210-1**	**Italy UNI 7806**	**Germany DIN 17121 DIN 17124**	**France NF A 35-501 NF A 49-501**	**Great Britain BS 4360**
Designation	S355J2H	Fe 510 D	St 52-3 N	E 36-4	50 D

There is no exact equivalence between European and American standards. However, the steel grade S355J2H in EN 10210 is quite similar to the steel grade C in ASTM A500 (Cold-formed welded and seamless carbon steel structural tubing in rounds and shapes) and to the steel grade II in ASTM A618/A618M (Hot-formed welded and seamless high-strength low-alloyed structural tubing). Main mechanical values are compared in Table 4.3.

Table 4.3: Mechanical properties of steel grades specified in EN 10210 and ASTM A500, ASTM A618/A618M.

Code Designation	**Europe** **EN 10210-1** S355J2H	**USA** **ASTM A500** C	**USA** **ASTM A618/A618M** II
Min yield stress (N/mm^2) for t $\leqslant$ 16 mm	355	317	345
Min tensile strength (N/mm^2) for t $\leqslant$ 3 mm	510	427	485
Min elongation (%)	22	21	22

4.4.2 Chemical composition

The chemical composition of the Base Metal BM and the Fusion Zone FZ, according to the EN 10210-1:2006 and EN 10210-2:2006, are presented in Tables 4.4 and 4.5. The one for the electrical wire Filarc is given in Table 4.6 according to Welding Industries (1999). In Table 4.4, the effective average values were also calculated for the base metal based on measured data given by the producer Vallourec & Mannesmann tubes.

Table 4.4: Steel S355J2H Base Metal composition (% of weight): nominal and measured values.

Elements (Base Material)	**Nominal Max. Mass % (EN 10210)**	**Effective Average Mass % (VM analysis)**
Carbon C	$\leq$ 0.18	0.17
Silicon Si	$\leq$ 0.55	0.26
Manganese Mn	$\leq$ 1.60	1.36
Phosphorus P	$\leq$ 0.030	0.01
Sulfur S	$\leq$ 0.030	0.004
Chromium Cr	$\leq$ 0.10	0.05
Molybdenum Mo	$\leq$ 0.08	0.005
Nickel Ni	$\leq$ 0.3	0.04
Copper Cu	$\leq$ 0.40	0.06
Aluminum Al	$\leq$ 0.100	0.03
Vanadium V	no spec.	0.043
Titanium Ti	$\leq$ 0.050	0.001
Nitrogen N	no spec.	0.007
Boron B	$\leq$ 0.0008	0.0002
Niobium/Columbium Nb/Cb	no spec.	0.002

Table 4.5: Weld composition (% of weight), only nominal values are available.

Elements (Weld-Fusion Zone)	**Nominal Max. Mass %**	**Nominal Min. Mass %**
Carbon C	0.18	0.08
Silicon Si	0.9	0.33
Manganese Mn	1.75	1.58
Phosphorus P	0.03	0.02
Sulfur S	0.03	0.01

Table 4.6: Filarc wire(% of weight), only nominal values are available.

Elements (Filarc PZ 6113)	**Nominal Max. Mass %**	**Nominal Min. Mass %**
Carbon C	0.07	0.04
Silicon Si	0.6	0.3
Manganese Mn	1.1	0.7
Nickel Ni	0.9	0.6
Phosphorus P	0.025	
Sulfur S	0.025	

Based on its composition, we can analyse the S355J2H. This is a non-alloyed structural steel (presence of smaller quantities of Mn, Mo, Ni, etc. compared to the element quantity required to be considered as alloyed steels according to the ISO specification 4948/1). It is a standard steel used for structural purposes, also called mild steel because the carbon proportion is comprised between 0.15 and 0.30 %. Since it contains more than 1.2 % of manganese (but less than 1.8 %), it is referred to as carbon-manganese C-Mn steel.

Current structural steels have a carbon content ranging from 0.05 % to 0.25%. Increasing the carbon content is the cheapest way to increase strength. However, a carbon content above 0.25% and a rapid cooling to room temperature often results in formation of martensite (see CCT diagram in Fig. 2.7). The higher the carbon content, the more brittle and harder is the martensite in steel.

Manganese is beneficial to the production process since it combines with impurities linked to oxygen and sulfur. However, a low sulfur content ($S < 0.01$ %) in presence of manganese may increase the risk of martensite formation (Steinhauer, 1998). Silicon has the same faculty as manganese to combine with oxygen.

Impurities such as phosphorus and sulphur are present in this steel in admissible quantities. Other residual elements such as chromium, molybdenum, nickel, copper and aluminum are unavoidable as well, and are also present in acceptable small quantities.

Due to the manufacturing process of this steel, the microstructure of the base material is mainly composed of ferrite and pearlite. These two main microstructures are shown in Fig. 4.9.

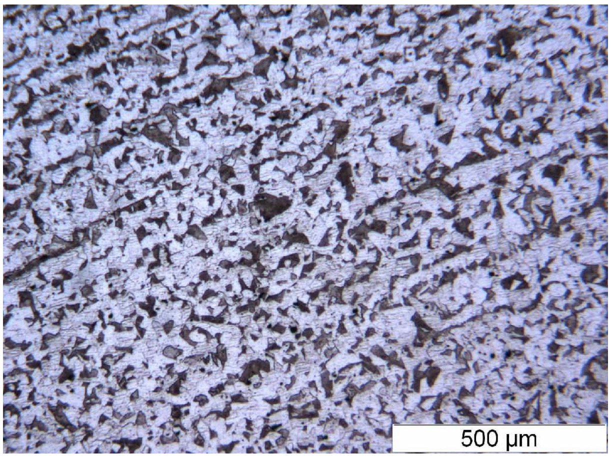

Figure 4.9: Microstructure of S355J2H in the as-delivered state as revealed by optical microscopy, showing ferrite (light grey areas) and pearlite (black areas).

4.4.3 Mechanical properties

The mechanical properties of the ferritic grade S355J2H C-Mn steel are presented in Table 4.7. As with the chemical composition, the normative values are given by the EN 10210-1 and the effective values are obtained from measurements. These values are given at a temperature of 20°C.

Table 4.7: S355 mechanical properties

Mech. Properties	**Nominal values (EN 10210)**	**Eff. aver. values (VM analysis)**
Young modulus E (N/mm^2)	210000	
Poisson ratio ν	0.3	
Yield stress (N/mm^2)		
for $t \leq 16$ mm	Min 355	
for 16 mm $< t \leq 40$ mm	Min 345	385
Tensile strength (N/mm^2)	Min 470 - Max 630	553
Elongation (%)	Min 22	25
Impact energy at - 20 °C (J)	Min 27	27

Several mechanical properties used in the mechanical analysis to simulate the residual stress formation are also given. The elastic properties such as the Young's modulus E, the Poisson's ratio ν and the thermal expansion α are defined in Table 4.8 as a function of temperature according to the EN 1993-1-2:2005(E) for the Young's modulus, according to Michaleris (2011) for the Poisson's ratio and the thermal expansion.

Table 4.8: Young's modulus, Poisson's ratio and the thermal expansion of the mild steel.

T(°C)	**20**	**100**	**200**	**300**	**400**	**500**	**600**	**700**	**800**	**900**	**1000**	**1465**	**1544**
E (10^3 $.N/mm^2$)	210	210	189	168	147	126	65.1	27.3	18.9	14.2	13	10	1
ν	0.296	0.311	0.33	0.349	0.367	0.386	0.405	0.423	0.442	0.461	0.48	0.48	0.48
α ($10^{-6}/°C$)	11.7	11.7	11.8	12.2	12.9	13.2	13.6	13.8	-	-	-	15.0	-

Concerning the plastic properties, they are defined by the yield stress and the stress value for a plastic strain of 10% as a function of temperature (Table 4.9). These data are taken from Michaleris (2011).

Table 4.9: Stress evolution as a function of plastic strain and temperature.

T(°C)	**20**	**100**	**200**	**300**	**400**	**500**	**600**	**700**	**800**	**900**	**1000**	**1465**	**1544**
f_y(N/mm^2) for (0% plastic strain)	345	332	308	276	235	186	128	69	64	46	11		
σ(N/mm^2) for 10% plastic strain	423	410	386	342	290	231	163	96	84	61	21		
σ(N/mm^2) for 100% plastic strain												1	0.1

All these properties are summarized in Fig. 4.10.

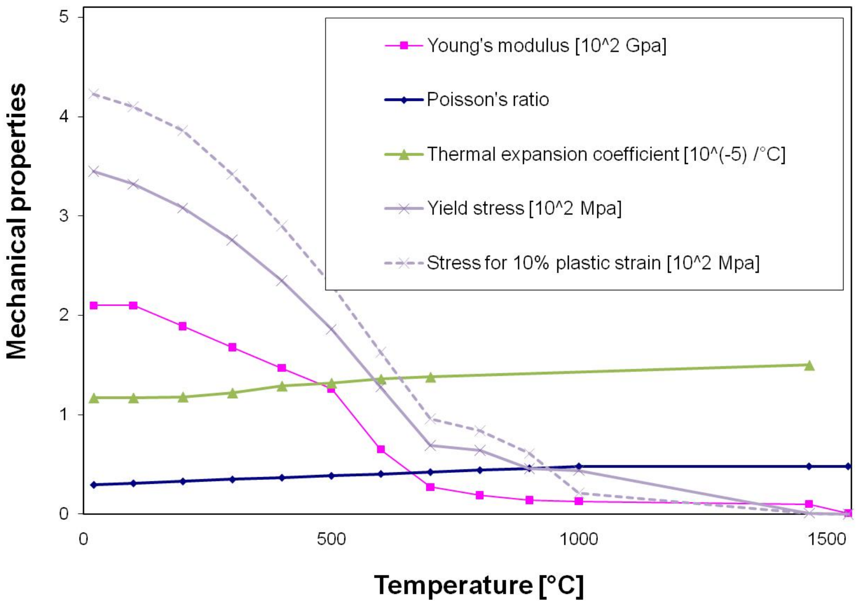

Figure 4.10: Temperature-dependent mechanical properties for steel S355.

4.4.4 Thermal properties

Main thermo-physical properties of carbon steels are presented in this section. The thermal conductivity k and specific heat C values are presented in Tables 4.10 and 4.11 according to the EN 1993-1-2:2005(E). The density value does only weakly depend on temperature, hence the value 7850 kg/m^3 was fixed. The latent heat L between solidus and liquidus (from 1465 to 1544 °C^{-1}) is considered using a value of 247000 J/(kg) (Raymond and Chipman, 1967). These data will be used further to simulate the thermal behavior of the material.

Table 4.10: Thermal conductivity of carbon steels including S355.

T(°C)	**20**	**100**	**200**	**300**	**400**	**500**	**600**	**700**	**800**	**900**	**1200**
k (W.m^{-1}. °C^{-1})	53.3	50.7	47.3	44	40.7	37.4	34	30.7	27.3	27.3	27.3

Table 4.11: Specific heat (heat required to raise the temperature of a body) of carbon steels including S355.

T(°C)	**20**	**100**	**200**	**300**	**400**	**500**	**600**	**650**	**700**	**735**	**750**	**800**	**900**	**1200**
C (J.kg^{-1}. °C^{-1})	440	488	530	565	606	667	760	814	1008	5000	1483	803	650	650

All these properties are summarized in Fig. 4.11.

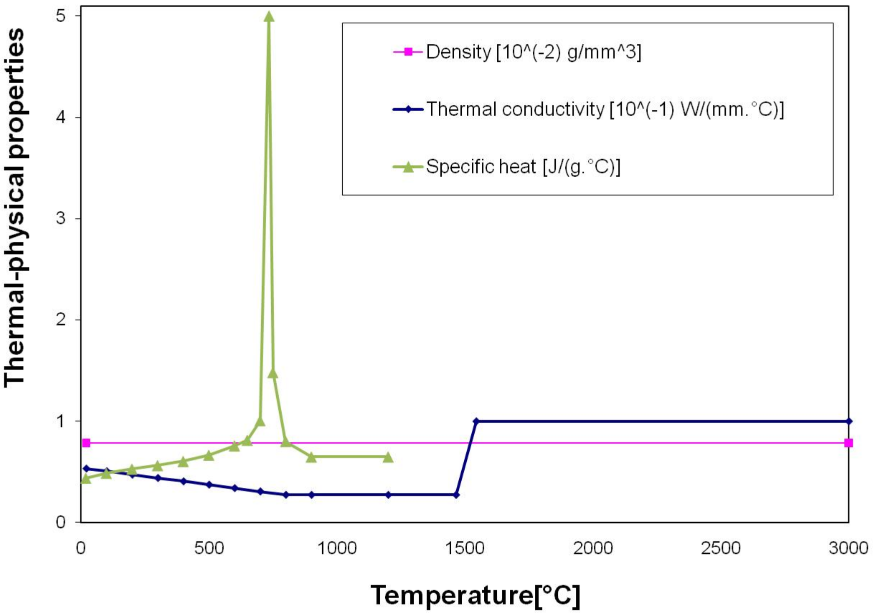

Figure 4.11: Temperature-dependent thermal properties for steel S355.

Note that the EN 1993-1-2:2005(E) gives a high peak of specific heat (5000 J.kg^{-1}. °C^{-1}) at 735 °C. The specific heat increase at that temperature is mainly due to phase transformation of ferrite-pearlite to austenite. This peak is theoretically non defined (indefinite pole) at that temperature but for consistency, it would be more appropriate to take the peak value of 1100 J.kg^{-1}. °C^{-1} given by experimental investigations (Miettinen, 1997). Both peak solutions have been tested and lead to the same results regarding the residual stress simulations.

4.5 Parameters inducing cold cracking effects

Cold cracking occurs in steels at low temperature (below 200 °C) during cool-down of the weld. Fundamentals of cold crack formation are described in EN ISO 17642-1:2004. It is associated with the formation of martensite. Due to welding, the microstructure in a zone of base metal close to the fusion zone is altered by temperature variations. In this zone, called the heat affected zone HAZ, martensite-austenite constituent may be formed. It is precisely in the HAZ that micro-cracks are formed because martensite is brittle. Indeed, when the HAZ undergoes high deformations under external fatigue loadings, a significant number of dislocations is formed. Due to the presence of martensite and its high hardness, the motion of these dislocations is reduced. Their accumulation in the HAZ may create micro-cracks.

Note that another phenomenon induced by the welding process is the hot tearing or solidification cracking, occurring at high temperatures (solidification temperature). More informations can be found in the work of Drezet and Rappaz (Drezet et al., 2008). In our case, cracking only appears at low temperatures.

The risk of cold cracking is related to the following factors:

- **Brittle microstructure (martensite) in the HAZ**: martensite is formed by quenching (rapid cooling) of austenite. The quantity of martensite depends on the rate of cooling and on the steel composition (see section 2.2.3). The martensite formation in the HAZ of welded joints is usually not expected if the quantity of carbon stays below 0.22 - 0.25% (ISF and Joining Institute, 2004) because the critical cooling rate becomes high and difficult to reach for low-carbon steels.

The cooling rate is related to the initial temperature of the component, to its thickness and to the heat input during welding. A low initial temperature, a large component thickness or a low heat input favor martensite formation.

Hardenability, which is a measure for the ease of martensite formation, is linked to the chemical composition of the steel, notably to larger quantities of carbon and other alloying elements.

The carbon equivalent content is a useful tool to assess the hardenability and the susceptibility of steels to cold cracking.

There is two formulas for carbon equivalent content, the carbon equivalent content CE defined by the IIW (IIW, 1967) (Equation (4.1)) and the carbon equivalent content CET specified in EN 1011:2000 (Equation (4.2)).

$$\mathrm{CE_{IIW}} = \mathrm{C} + \frac{\mathrm{Mn}}{6} + \frac{\mathrm{Cr+Mo+V}}{5} + \frac{\mathrm{Ni+Cu}}{15} \text{ in mass \%} \tag{4.1}$$

$$\mathrm{CET} = \mathrm{C} + \frac{\mathrm{Mn+Mo}}{10} + \frac{\mathrm{Cr+Cu}}{20} + \frac{\mathrm{Ni}}{40} \text{ in mass \%} \tag{4.2}$$

Based on the chemical composition presented in Table 4.4, a CE of 0.42 % and a CET of 0.31 % have been calculated.

According to AWS, for a CE above 0.4%, there is a risk of cold cracking in the HAZ. No limits are given directly for the CET but it is a prerequisite to calculate the preheating temperature (see results in the next paragraph). Note that the CE has only been calculated for the base material; one has also to verify this value for the filler material and to compare both values in order to verify if carbon migration is avoided. Since the effective chemical composition of the filler material is unknown, this verification is not done.

To evaluate the susceptibility of a steel to cold cracking, one can also directly perform hardness testing. Results for this kind of test are presented in section 4.6. To avoid cold cracking, hardness should not exceed values of 350-400 HV, which is our case (section 4.6).

- **Amount of (diffusible) hydrogen in the weld zone**: hydrogen is considered as a damaging impurity in steels that may create serious defects and has a high diffusion coefficient (interstitial). During the welding procedure, hydrogen mainly comes from humidity, which is present in the flux (SAW) or in the electrode (or from oil and dust on the metal surface). Therefore, arc welding with gas protection, the one used in our case, introduces less hydrogen than processes with a protection by a blanket of granular fusible flux (SAW).

  Atmosphere humidity surrounding the arc is partially absorbed in the molten zone. During solidification, part of the hydrogen diffuses to the the HAZ and to the BM and creates voids, which are crack initiation site.

  The hydrogen content in the weld metal is one of the major factors determining the minimum pre-heat temperature and the soaking conditions (post-weld heating treatment) needed to avoid cracking.

  This pre-heat temperature has been calculated using the formula specified in EN 1011:2000 and described by Liedtke et al. (2009). A temperature of 61 °C for the chord wall thickness of 20 mm and of 90 °C for the chord wall thickness of 30 mm have been calculated for the S355J2H steel. This calculation has been done using an estimated hydrogen content HD of 5 ml/100g for the filler Filarc PZ 6113, a carbon equivalent CET of 0.31% and a heat input $Q = k \times \frac{U \times I}{v} = 0.8 \times \frac{28.6(V) \times 270(A)}{5.5(mm/s)}$ of 1.2kJ/mm.

- **Restraint induced stresses**: crack position and orientation depend on the combination of hydrogen and tensile stress concentrations at the weld joint.

As a conclusion, more investigations will be conducted (see section 4.6) to evaluate the susceptibility of S355J2H steel to cold cracking and to estimate the martensite formation. Nevertheless some additional actions can help to reduce the risk of cold cracking:

- **pre- and post-heating**: pre-heating up to 60-90 °C is required for the K-joints under study. However, the pre-heating carried out on the samples used in this study is made by flame and therefore seems to be too localized to provide a uniform temperature distribution in the component. This procedure can be improved. Moreover, once welding is completed, action can be taken to slow down the cooling to ambient temperature, such as wrapping the weld area in special heat-resistant blankets.
- **similar quantity of carbon in the base material and the filer material**: since carbon concentration is related to the formation of martensite, one has to verify that carbon migration can not occur due to difference in carbon content.
- **starting and stopping sequence as recommended by Zhao and Packer (2000)**: in order to reduce the risk of the occurrence of defects in the most loaded area.
- **careful storage in the products (flux, electrode) used for welding** in order to control the amount of humidity present in these products.
- **surface preparation for welding**: to remove oil and dust from the surface which may provide additional hydrogen.

4.6 Hardness testing

4.6.1 Procedure

Hardness measurements were carried out on a cross-section sample cut at the weld area joining brace and chord walls (see Fig. 4.12a).

The cross-section corresponds to the longitudinal symmetry plane. This section was first polished using abrasive paper and diamond powder (μm mirror polishing). Then, it was etched with Nital (2% HNO3 for 100 ml of ethanol) during 10 s. This metallography procedure allows one to distinguish three main areas: the BM, the FZ and the HAZ (Fig. 5.1). Phase tranformations occuring in steel material during welding and involving changes in the microstructure are described in chapter 2.

Vickers hardness testing (according to EN ISO specification 6507-1) was conducted on this cross-section, in the different zones presented above, in order to draw a map of hardness. In our tests, a 1 kg-force was used with an applied time of 16 seconds. The hardness (HV) may be linked to the tensile strength of the material as $\mathrm{f_u} \approx 3.15$ HV (Steinhauer, 1998). A minimum distance between indentations of 2.5 d (around 0.3 to 0.6 mm), where d is the indention diameter, have been respected to ensure that a measurement is not affected by a previous one.

Hardness was measured at 55 points in the cross-section. Then, these values were used to draw a map of hardness. Figure 4.13 shows this map and the data points superimposed with the metallographic image.

4.6.2 Results and discussion

The maximum hardness value measured is 232 HV and is found in the HAZ, at the weld toe in between braces. It is precisely in this region that the fatigue crack initiates and propagates because of applied stress concentration, high tensile residual stresses and welding imperfections.

Two other regions of high hardness values are situated in the HAZ on the brace member side. It is also interesting to note that hardness values are not uniform along the HAZ profile (from 180 to 232 HV). Lowest hardness values ($\approx$ 150 HV) are generally situated in the BM surrounding the HAZ.

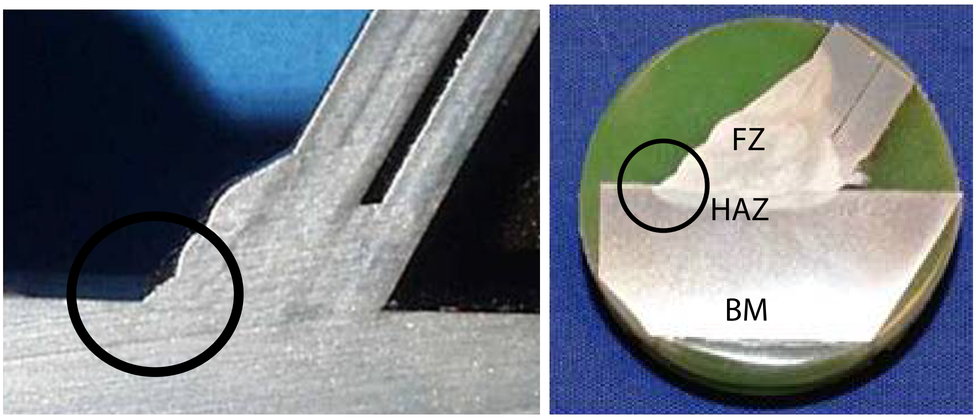

(a) Region where the test sample was cut **(b)** Test sample section

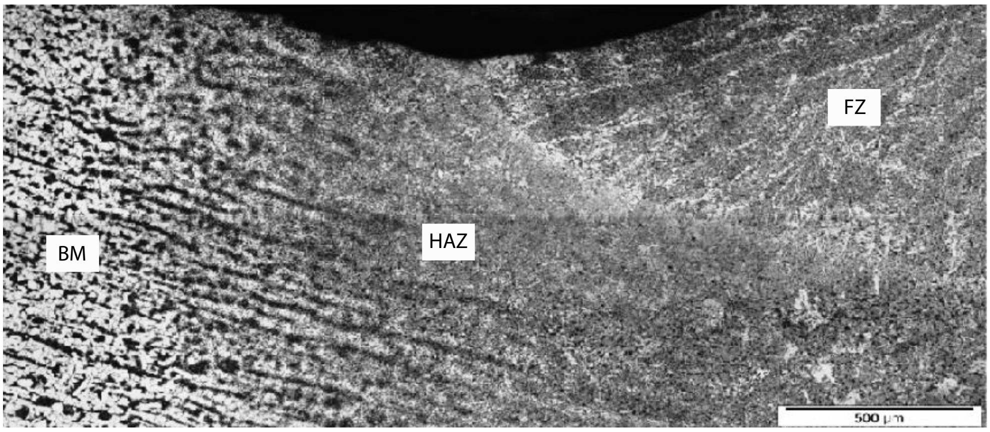

(c) Metallography at the weld toe of the sample

Figure 4.12: Sample used for hardness testing.

To summarize, hardness values are in a range between 150 and 200 HV in the BM, between 170 and 210 HV in the FZ and between 180 and 232 HV in the HAZ. The Vickers hardness values are given in Table 4.12 for different microstructures that can be found in the HAZ of a low-alloyed steel. The S355J2H is a non-alloyed steel, however its composition is close to the one of a low-alloyed steel, therefore it is believed that table 4.12 can be used for this steel. Moreover, the CCT diagram and the hardness-cooling time-microstructure diagram of a S355N steel are presented in Fig. 4.14.

Based on these informations, we can deduce that the microstructure in the HAZ (180 to 232 HV) is mainly composed of ferrite (50 to 80%), bainite (0 to 30%), pearlite (0 to 20%) and martensite (0 to 20%).

The optical micrograph, shown in Fig. 4.15, seems to confirm the presence of acicular ferrite (large light areas) and bainite (aligned planes along a certain direction). However, it is difficult to identify martensite and pearlite, and to quantify the fraction of each microstructure. The martensite has certainly been reheated and is difficult to distinguish from bainite. From the micrograph, it seems that there is more bainite and/or martensite than ferrite.

The presence of martensite in this zone may be linked to the fact that this part of the HAZ corresponds to the Coarse Grained HAZ (CGHAZ), heated with temperature above 1100 °C, or to the Intercritically Reheated Coarse Grained HAZ (ICCGHAZ), reheated by a successive weld pass between Ac_1 and Ac_3. It was shown in section 2.2.3 that the CGHAZ and the ICCGHAZ are the most brittle area because they have formed martensite-austenite constituents.

Therefore, the fraction of martensite formed in our steel is low or the martensite is reheated in a less hard form, explaining the obtained hardness values. However it makes the weld toe HAZ

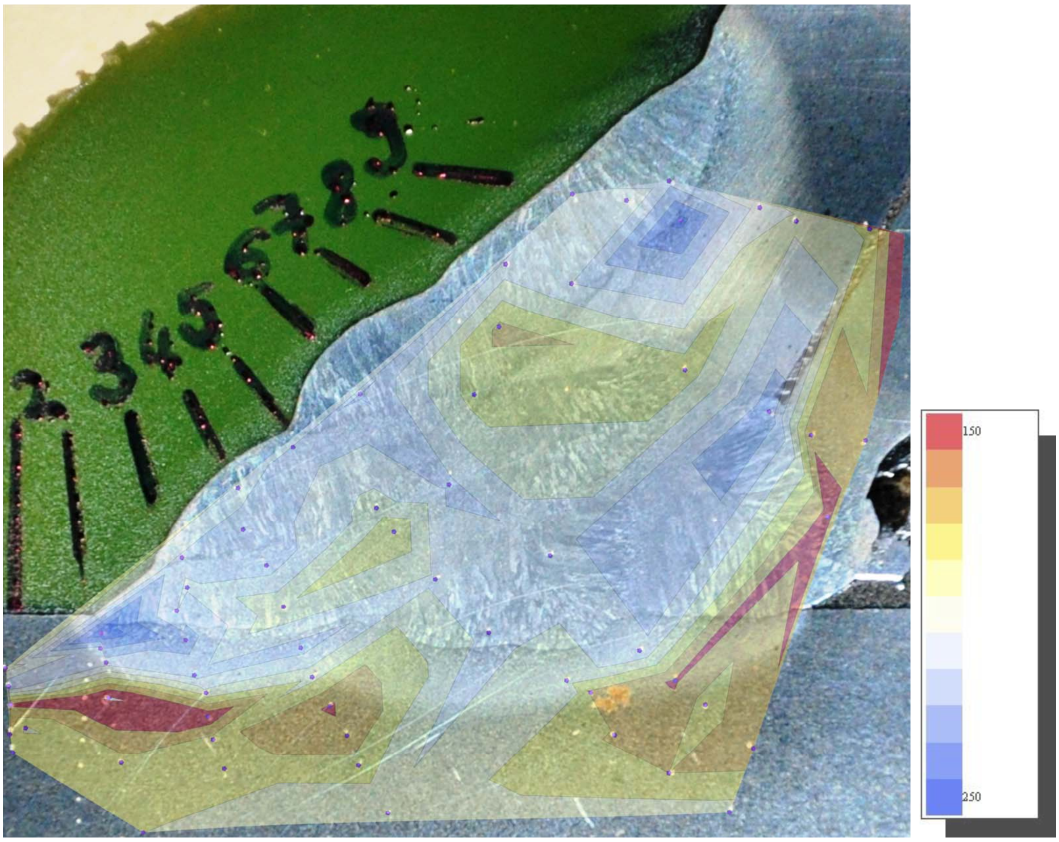

Figure 4.13: Map of hardness measurements (measurement points are represented by blue dots).

more brittle and more likely than other areas to initiate a crack.

Considering hardness values, they never exceed 350 to 400 HV, thus cold cracking is avoided.

Moreover, considering that martensite formation is low, the transformation residual stresses (see section 2.2.4), i.e. inducing compressive stresses in the weld area can be also considered as low. They may be neglected for the residual stress analysis leading to the use of a thermo-mechanical model.

Table 4.12: Microstructures and the corresponding Vickers hardness ranges of a low-alloyed steel (ISF and Joining Institute, 2004)

Microstuctures	Average Vickers Hardness (approximately)
Ferrite	84
Austenite	263
Perlite (granular)	211
Perlite (lamellar)	316
Cementite	632 - 684
Martensite	421 - 948

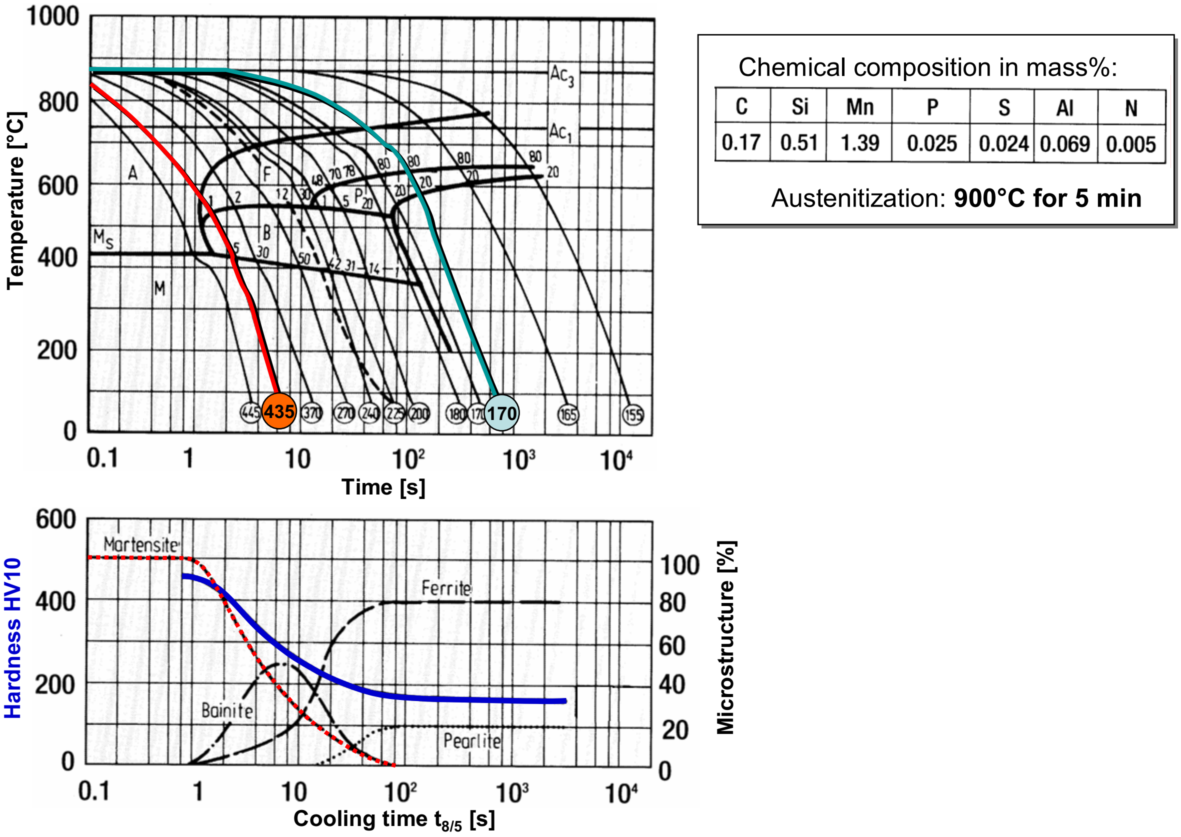

Chemical composition in mass%:

C	Si	Mn	P	S	Al	N
0.17	0.51	1.39	0.025	0.024	0.069	0.005

Austenitization: **900°C for 5 min**

Figure 4.14: Continuous-cooling-transformation CCT and hardness-cooling time-microstructure diagram of S355N (Ponge, 2005).

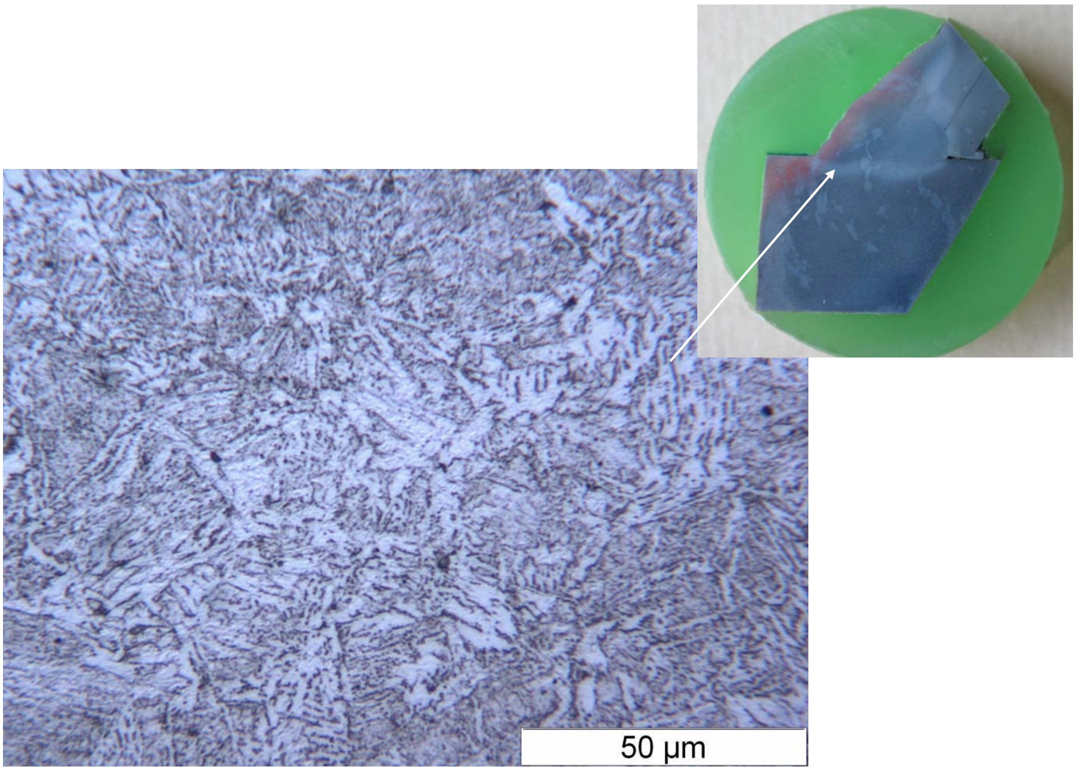

Figure 4.15: Microstructure of S355J2H observed in the HAZ.

4.7 Summary and conclusions

- **Manufacturing process**: tubes are fabricated using piercing and rolling without welding seams (Mannesmann process). Residual stresses induced by the manufacturing process will not be considered in this research because they are washed by the welding in the area of interest (weld toe region).
- **Welding process**: tubular K-joints studied in this work are composed of two braces welded onto a continuous chord member. Seven weld passes are carried out from the crown heel to the crown toe ensuring a full penetration. Start and stop positions of the weld path are located at the crown heel and crown toe positions respectively. They coincide with the zone where the stresses are maximum and the welding defect occur. These welding features will be used to reproduce numerically the process. For future welding, as an improvement, start and stop positions should be moved away from the critical zone.
- **Steel S355J2H**: this standard steel for tubular bridge construction is a non-alloyed structural steel (mild steel) mainly composed of carbon and manganese (C-Mn steel). Chemical composition, mechanical and thermal properties are given in section 4.4. Thermal and mechanical data will be used for numerical analysis of residual stresses.
- **Cold cracking and martensite formation**: the calculation of the carbon equivalent content and the hardness testing have shown that S355J2H is not particularly susceptible to cold cracking. However, it is proved that the area of highest hardness is located in the HAZ of the weld toe. **It is shown that the fraction of martensite formed in this area is low or has been reheated and retransformed in a less hard form, however it makes the HAZ more brittle and more likely than other areas to initiate a crack.**

  Therefore, it is a detrimental factor that adds to other factors (local stress concentrations, high tensile residual stresses and to welding imperfections) to explain why the fatigue crack initiation and propagation starts from the HAZ.

  Considering that martensite formation is low, the transformation residual stresses inducing compressive stresses in the HAZ, can also be considered as low. They may be neglected for the residual stress analysis leading to the use of a thermo-mechanical model.

Chapter 5

Residual stress measurements

Large tensile residual stresses, produced by welding, may considerably influence the fatigue behaviour of the specimen. That is the reason why residual stress effects have to be taken into account in fatigue design. It is important to have high quality measurement methods in order to obtain accurate residual stress data (magnitude and distribution). This chapter is devoted to residual strain measurements using hole-drilling, neutron diffraction and X-ray techniques.

5.1 Comparison of different techniques

This section presents the most common methods used to measure residual stresses with their characteristics and limitations. Nowadays, the destructive and non-destructive methods used to measure residual strains are more and more reliable. Various conventional methods cited by the CETIM (Bouchelier and Lu, 1987; Lu, 1996) as well as more recent methods (Withers et al., 2008) are summarized in Table 5.1. This list is not exhaustive. As a reminder, residual stresses of type I are macroscopic, residual stresses of type II are microscopic with the size of the grain, residual stresses of type III are microscopic with the size of the several lattice planes.

Table 5.1: Comparison of different method characteristics (data for usual use).

Methods	Type of residual stresses	Minimum analysis zone	Minimum depth analysis	Usual precision	Inspection depth	Method explanations
Non-destructive methods						
X-ray	type I, II, III	0.5 mm^2	$\sim$ 10-100 μm	± 20 MPa	1-50 μm	Measure the space change between crystalline planes, popular method, portable equipment, two-dimensional residual stresses at the surface, measurements of good accuracy.
Synchrotron diffraction		$\sim$ 0.1 mm^3			35 mm	Modern technology (3rd generation): high intensity X-ray method used for analyzing thinnest area and offering a faster acquisition time. The low angle scatter (2-20°) does not allow to measure strains in directions 3-6.
Neutron diffraction	type I, II	4 mm^3	1 mm	± 30 MPa	2-50 mm	Measure the space change between crystalline planes, equipment particularly expensive, three-dimensional residual stresses though the depth, the sample size is limited, difficulty to rotate the sample around the point of measurement, measurements of good accuracy.
Ultrasonic	type I, II, III	0.1-30 mm^2	$\sim$ 15-300 μm	± 20 MPa	1-10 mm	Results not always satisfactory because many parameters can influence the results (hardness, microstructure, composition, etc).
Magnetic	type I, II, III	1-100 mm^2	100 μm	± 20 MPa	0.1-10 mm	Quick and not expensive method, two-dimensional residual stresses. Microstructure and stress state changes have a significant influence on results, therefore it is requested to perform calibration tests to correct the measurement weakness.
Locally destructive methods						
Hole-drilling	type I	0.5 mm^2	20 μm	± 20 MPa	0.02-15 mm	Simple, inexpensive and quick method, popular method, portable equipment convenient in practice, two-dimensional residual stresses at the surface, difficulty to obtain accurate and reliable data (diameter errors, eccentricity, surface roughness, etc). For the hole-drilling, measurements are not reliable for stresses exceeding 60% of the yield strength.
Contour method					1-50 cm	After sectioning a specimen without introducing additional stresses, the contour profile of the two half-pieces enable to estimate the residual stresses initially present. Sensitivity of the method to the movement of the workpiece during the cutting phase. Interesting to choose a measurement surface that will be studied in details by neutron diffraction for example.
X-ray (in depth meas.)	type I, II, III	0.5 mm^2	$\sim$ 10-100 μm	± 20 MPa	10 mm	See X-ray explanations above. Local material removed by electrochemically polishing therefore subsurface residual stresses can be measured.
Destructive methods						
Layer removal		$\sim$ 1 mm^2	$\sim$ 10-100 μm		all the thickness	Measurement of surface strains or displacement after a layer is removed, the remeoval of transverse and longitudinal layers give the transverse and longitudinal residual stress components.
Sectioning	type I	100 mm^2	1-2 mm	± 10 MPa	all the thickness	Prismatic specimen machined into thin layers on one side, distortions resulting from the rebalancing are measured on the opposite side. The dimensional residual stresses are measured in the plane of the layer and must be constant in the layer plane.

5.2 Hole Drilling Method

The hole drilling method is a widely used method for measuring residual stresses for the reasons given above.

The principle of the Hole-Drilling method was first proposed by Mathar in 1934 (Mathar, 1934). From 1950 until now, the accuracy of the procedure has been greatly improved, and in 1981, it has been standardised in ASTM Standard Test Method E837. In this document, we have referred to the last updated version ASTM E837-08 (ASTM, 2008).

This method is based on the stress relaxation induced by the drilling of a small hole: generally 1-5 mm in diameter and a depth approximately equal to its diameter. As illustrated in Fig. 5.1a, strain gauge rosettes, glued around the hole before drilling, measure the relieved surface strains. Thus, from these relieved strains, it is possible to calculate the residual stress field present in the material before the hole was drilled.

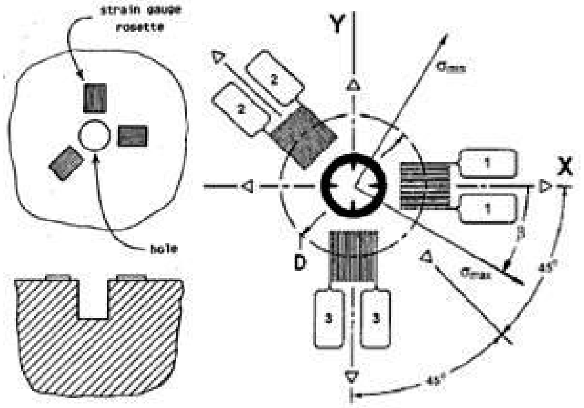

(a) Hole-drilling principle (Lu, 1996)

(b) Strain gauge rosette (ASTM, 2008)

Figure 5.1: Sample used for hardness testing.

This method is often defined as a semi-destructive method because the material is locally removed and the residual stresses are relaxed in a limited area. As a consequence, the residual field can only be estimated near the surface.

5.2.1 Stress calculation using hole-Drilling method

In this method, surface strains are measured by means of rosette composed of three electrical-resistance strain gauges with a special direction each. As shown in Fig. 5.1b, the direction of gauge 1 is the reference direction (the x-axis), gauge 2 is 45° or 135° clockwise of the reference and gauge 3 is 90° clockwise of the reference. Three strain-gauges are needed in order to evaluate the values of the three originally in-plane stresses σ_x, σ_y and τ_{xy}, or to evaluate the principal stresses σ_{min}, σ_{max} and β, the angle between the x-axis and the direction of σ_{max}.

This method is based on several assumptions:

- **The material is homogeneous isotropic linear-elastic.** However, if the residual stresses induced are closed to the yield strength of the material, local yielding could occur due to stress concentrations around the hole. To provide accurate results, the residual stresses should not exceed 60% of the material yield stress, which could be the case of large weld-induced residual stress. If residual stresses reach the yield stress limit, a measurement error is estimated to 10 to 30% (and greater).

- **The evaluation of residual stresses is available only near the surface.** Until a depth approximately equal to the hole diameter.

- **The stress state at any depth is a plane stress state in xy plane.**

- **Stresses are uniform throughout the hole depth.** However, it is possible to measure non-uniform stresses with the incremental hole-drilling method. The hole is drilled by depth steps or increments. For each increment the stresses are assumed to be uniform, but they can vary from one step to the next. Non-uniform stress measurements can only be made with "thick" samples (sample with a thickness greater than the hole drilled diameter).

- **No additional stresses are induced by the drilling** (no local yielding, no overheating).

- **The area of application is a flat uniform surface**. However, Cherouat et al. (2002) have studied the effect of curvature on stresses obtained the hole-drilling and shown the errors are really small. For hole drilling on a spherical surface with a radius greater than 35 mm, the error on the calibration coefficient is smaller than 5 %: the sphere surface can be considered like a planar surface.

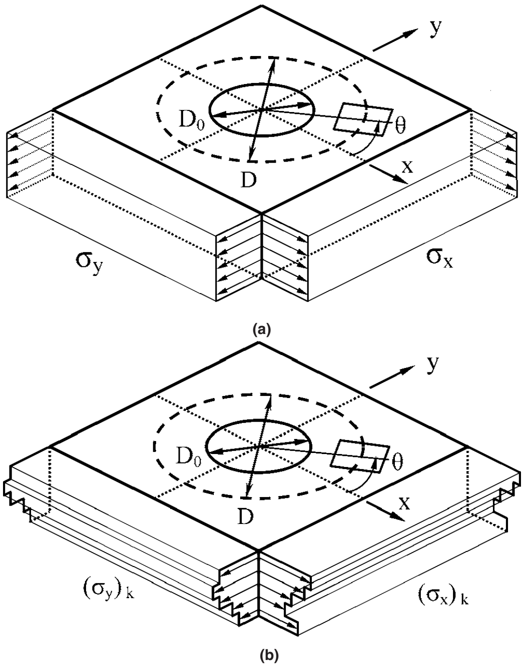

Figure 5.2: Uniform and non-uniform stress distribution measured respectively by the hole-drilling and the incremental hole-drilling methods (Hutchings et al., 2005).

Two different applications of this method can be distinguished:

- **The through-hole application:** for the case of a hole drilled through the complete thickness of a ***thin*** plate in which the residual stresses are ***uniform*** in the depth direction, an exact solution can be calculated from the theory of elasticity.

- **The blind-hole application:** it is the most used application because practical specimens are not often thin and flat. However, the hole geometry is too complex for a direct calculation of the residual stress state, there is no closed-form solution for this case. That is the reason why the blind-hole analysis is based on the through-hole analysis extended by the introduction of empirical coefficients, $\bar{a}$ and $\bar{b}$, experimentally or numerically determinated.

The through-hole analysis theory is developed in annex C.

From the theory, the relationship (5.1) between the residual stresses present in the material before the hole was drilled, and the relaxed surface strains ε by the hole-drilling is as follows:

$$\varepsilon = \frac{1+\nu}{E}.\bar{a}.\frac{\sigma_{max}+\sigma_{min}}{2} + \frac{1}{E}.\bar{b}.\frac{\sigma_{max}-\sigma_{min}}{2}\cos 2\beta \tag{5.1}$$

The calibration constants $\bar{a}$ and $\bar{b}$ are based on finite element calculations and are dependent on type of hole geometry (through-hole or blind hole), on rosette geometry, on hole diameter and on depth, but not on the material. The ASTM E837-08 (ASTM, 2008) provides these calibration coefficients for three types of Vishay Micro-Measurement Rosettes (Vishay Measurements, 1996).

5.2.2 Experimental description

Test samples

The samples were joints of the tubular truss beams. They were either as-welded or previously tested under fatigue loading but not cracked. These joints are described in details in chapter 4.

Strain-gauge rosettes

Our first choice was to use HBM rosettes type RY61R (rectangular) and RY61S (circular) specially designed for hole-drilling measurements. They include a drawn target in order to insure proper centering of the hole. These rosettes present a gauge circle with a diameter D of 5.1 mm and require a small drill-hole D_0, of 1.6 mm.

However, the calibration constants $\bar{a}$ and $\bar{b}$ were not available for HBM rosettes. Since the ASTM (2008) provides these informations for the Vishay rosettes, we have used Vishay rosettes type CEA-06-062UM-120 and EA-06-062RE-120 in a second time. As shown in Fig. 5.3 , the CEA rosette is rectangular and corresponds to the ASTM 1/16 in. Type B rosette whereas the EA is circular and corresponds to the the ASTM Type A rosette. The first one is particularly useful for making measurements in the vicinity of the weld toe. The diameter of the gauge circle is D = 5.13 mm and the drilled hole is approximately D_0 = 1.7 mm. The Vishay gauges are quite similar to the HBM gauges. They have to be glued to smooth surfaces which have initially been sandpapered.

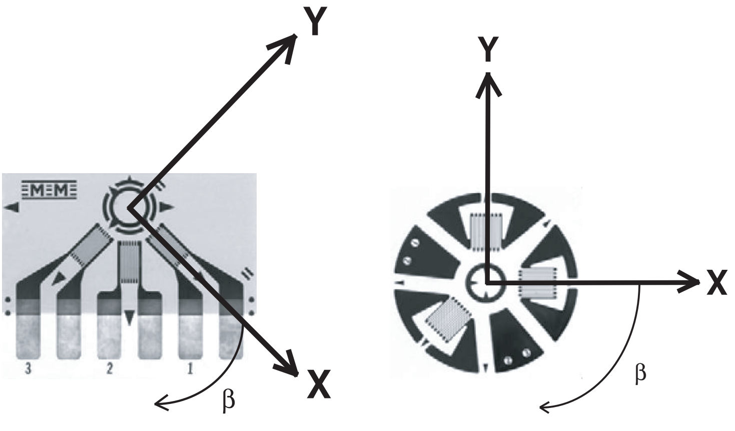

(a) Gauge CEA-06-062UM-120 **(b)** Gauge EA-06-062RE-120

Figure 5.3: Vishay rosettes specially designed for hole-drilling.

Hole-Drilling Instrumentation

According to ASTM E837-08 (ASTM, 2008), the hole-drilling method is designed for flat surface areas, such as plates. Even though, one can find in the literature residual stress measurements on curved surfaces (range of curvature radius from 300 to 500 mm) made by hole drilling (Cherouat et al., 2002; Stacey et al., 2000).

It was not possible to order a suitable drilling instrumentation to make measurement on our tubular components because of their curved surface and because of the narrow gap (approximately of 38 mm) at the weld joint area. As a consequence, we have developed our own drilling system shown in Fig. 5.4, convenient for the chord diameter of 168.3 mm and allowing measurement in the edge of the weld in spite of the small distance between the braces.

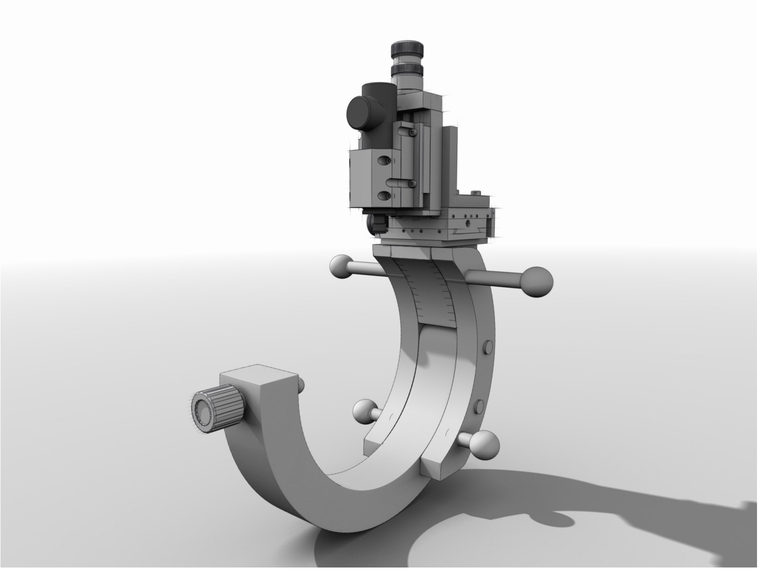

Figure 5.4: Hole-drilling device developed at ICOM.

The drilling system is composed of:

- A half-ring clamping support system that ensures the stability of the device and facilitates attachment on curved surfaces.
- An optical microscope which allows alignment of the drill bit on the rosette target, in order to keep eccentricity of the hole within tolerances (± 0.004 D, in our case ± 0.02 mm).
- Screws set on the device to adjust position in directions X, Y and Z.
- An electric turbine which replaces the microscope once this drill-position has been found. The drilling speed of 80000 rpm is sufficient to prevent machining-induced residual stresses in the hole-area because carbon steel is not as sensible as stainless steel or nickel alloys.

Special titanium carbide end mills (ATC-200-062T), with a 1.6 mm diameter are used with this turbine because they are suitable for Vishay strain-gauge rosettes.

Figure 5.5 show the hole-drilling device installed on the sample.

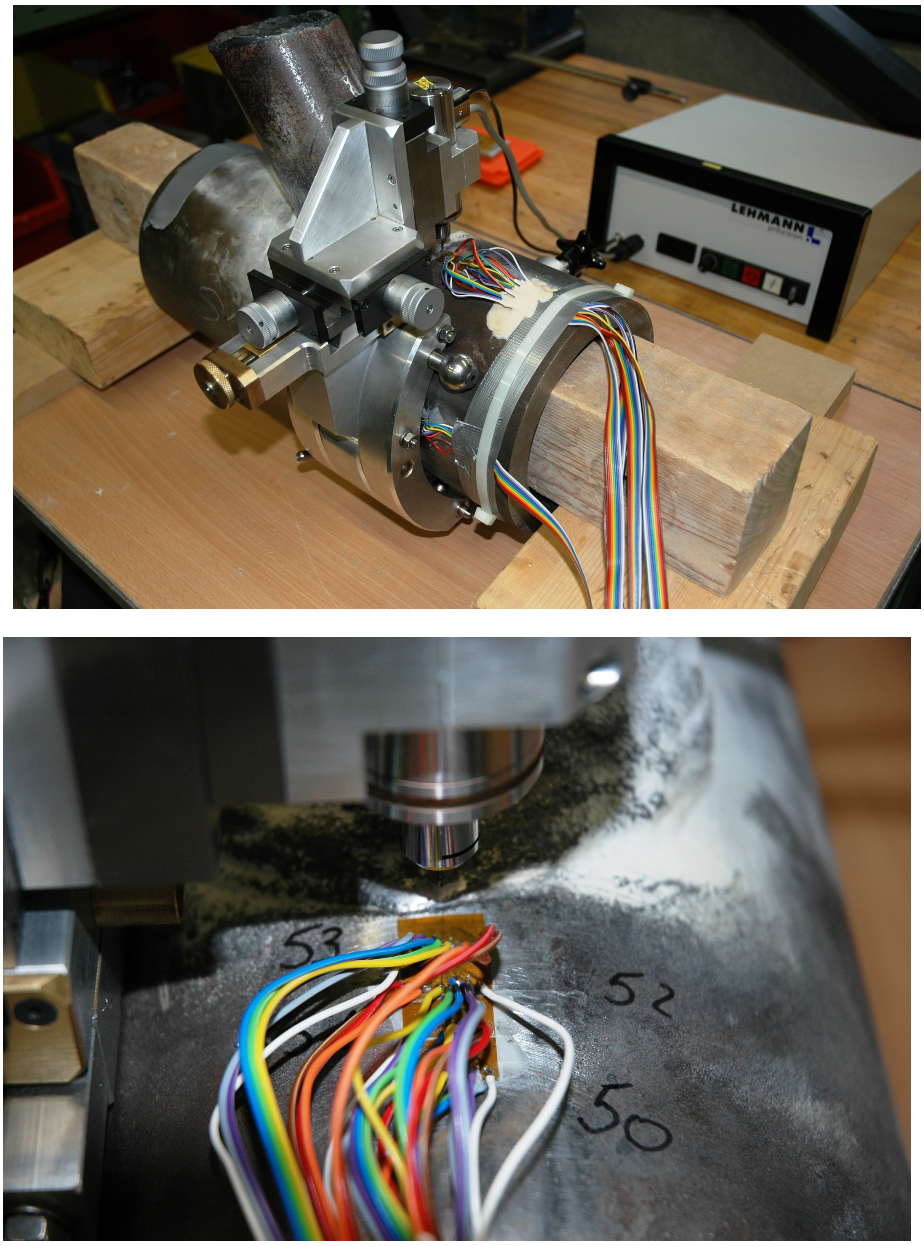

Figure 5.5: Hole-drilling device installed and ready to drill the hole.

Calibration experiments

In order to appreciate the accuracy of the calibration constants $\bar{a}$ and $\bar{b}$ for blind-hole analysis and the reproducibility of the results, calibration tests was performed. One test was conducted on HBM rosettes and another one on Vishay rosette. A brace piece of the truss-beam was chosen for this test in order to keep the same material. The brace has a Circular Hollow Section of 88.9 × 8 mm.

This specimen, equipped with two rosette types (rectangular and circular), was loaded under a tension force increasing from 0 to 140 kN, inducing uniform tensile stress σ_c smaller than one third of the yield stress. The set-up is presented in Fig. 5.6. The rosettes were glued in such a way that directions 3 and 1 (see Fig. 5.1b) concord with the tensile stress direction and its perpendicular direction.

The calibration procedure (Vishay Measurements, 1996) consists in measuring the rosette strains, once before drilling the hole (under the tension force) and finally after drilling a 2 mm deep hole (under the same tensile force). The hole was drilled without loading, and the strains recorded during this operation were removed.

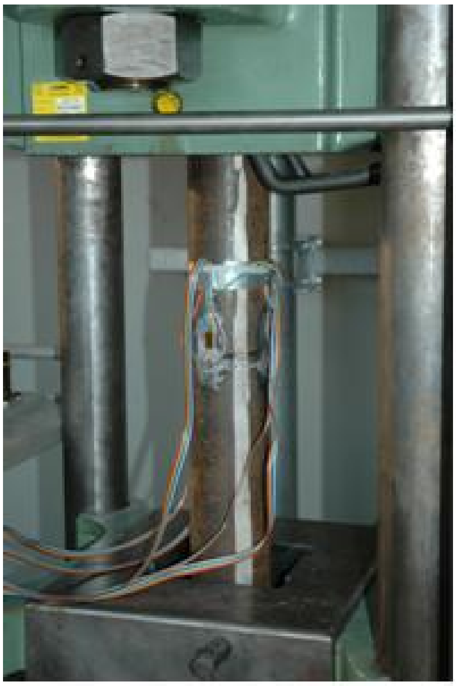

Figure 5.6: Calibration testing set-up.

We can calculate the relieved stresses using ASTM coefficients and compare results with stresses. In Fig. 5.7a and 5.7b, the points correspond to calculated stress values (circular points for circular rosettes and square points for rectangular rosettes) from measurements and the line represent theoretical stress values.

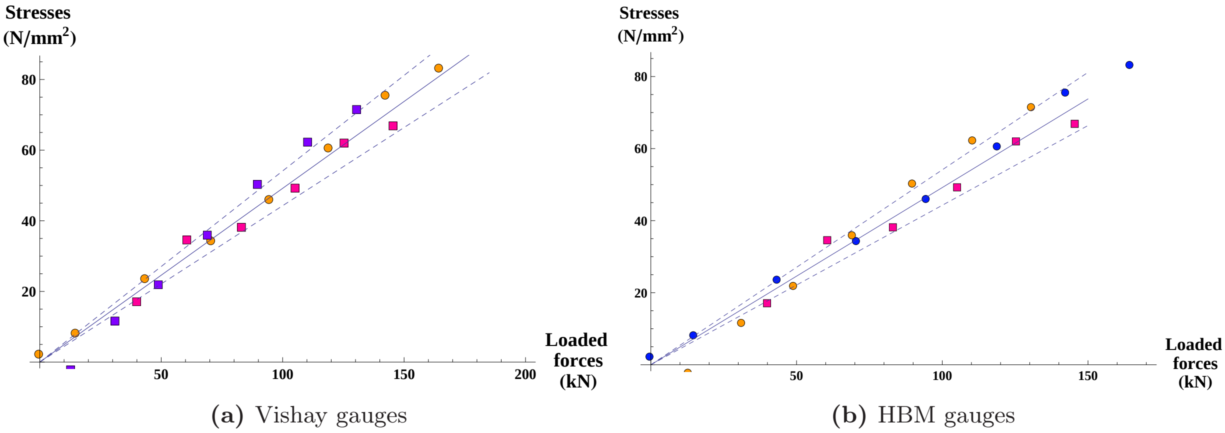

(a) Vishay gauges (b) HBM gauges

Figure 5.7: Vishay rosettes specially designed for hole-drilling.

The plots show that calculated stresses are approximately within ± 10% (dashed lines) of the ideally expected stresses. For the hole drilling method, this can be acceptable.

5.2.3 Results and discussion

Measurements in the crown heel area of the joint

The first measurements were conducted in the crown heel area of a non-cracked joint as seen in Fig. 5.8.

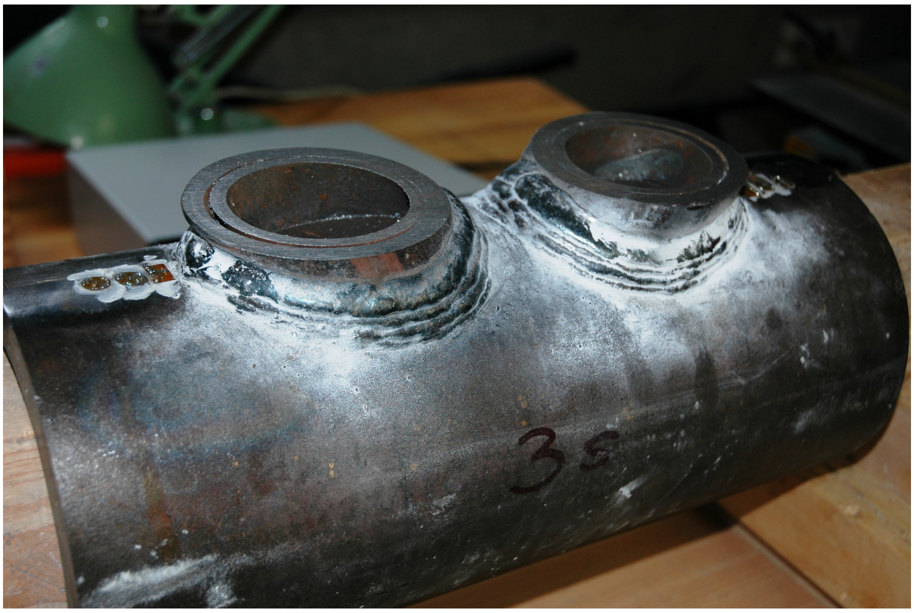

Figure 5.8: Hole-drilling rosettes glued in the crown heel area for residual strain measurements.

Residual stresses are measured, due to relaxation from a 2 mm deep hole, with an increasing distance from the weld toe. Three points of measurement are drilled on each side of the attached brace and residual stresses are calculated by means of uniform stress method. In Fig. 5.9, transverse residual stresses (hoop stresses) are represented by circular symbols and longitudinal residual stresses (axial stresses) by cross symbols. An envelope for these data is then plotted, corresponding to the fitted distribution of the mean values data set ± the standard deviation.

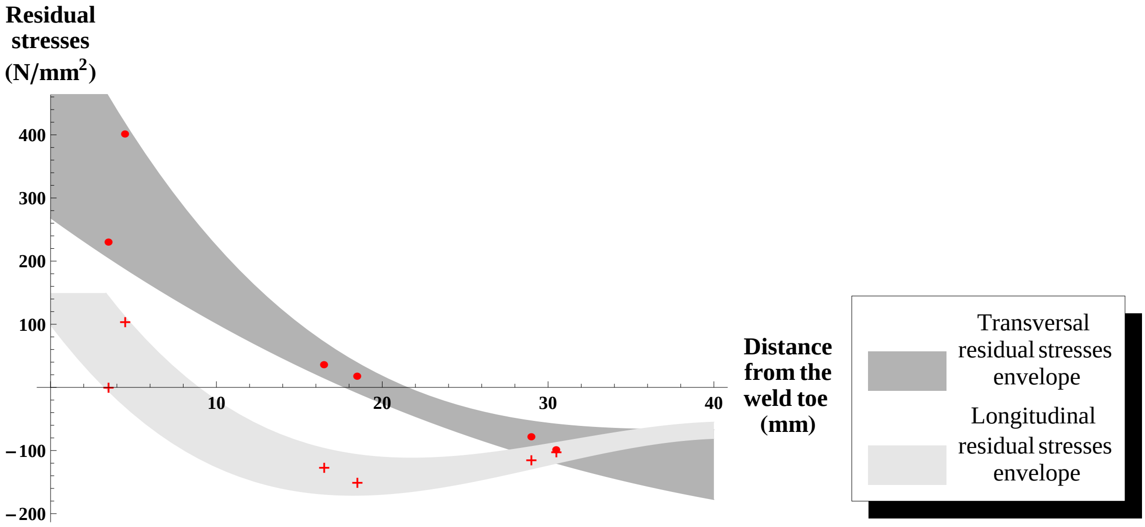

Figure 5.9: Transverse and longitudinal measured residual stresses in function of the distance.

In Fig. 5.10, the residual stress distribution of butt welds in pipes reported in Leggatt (2008) is plotted along with the previous envelopes on our welded K-joint. Leggatt, in (Leggatt, 2008), has shown the similarity between residual stresses calculated with the theory of the elastic behaviour of thin cylinders and those measured by the hole drilling method on a circumferential butt weld of a 600 mm diameter pipe.

According to Leggatt's curves, longitudinal residual stresses are greater than transversal ones in the vicinity of thin cylinders butt welds. However. Fig. 5.10 shows that this is not the case for thick cylinders such as bridge tubular K-joints: transverse residual stresses are greater than longitudinal ones. Moreover, the magnitude of transversal residual stresses is high in K-joints, it could exceed 60% of the yield stress value ($0.6 \times 385 \simeq 231$ N/mm^2). Note that above this value, the validity of the hole-drilling method is not guaranteed.

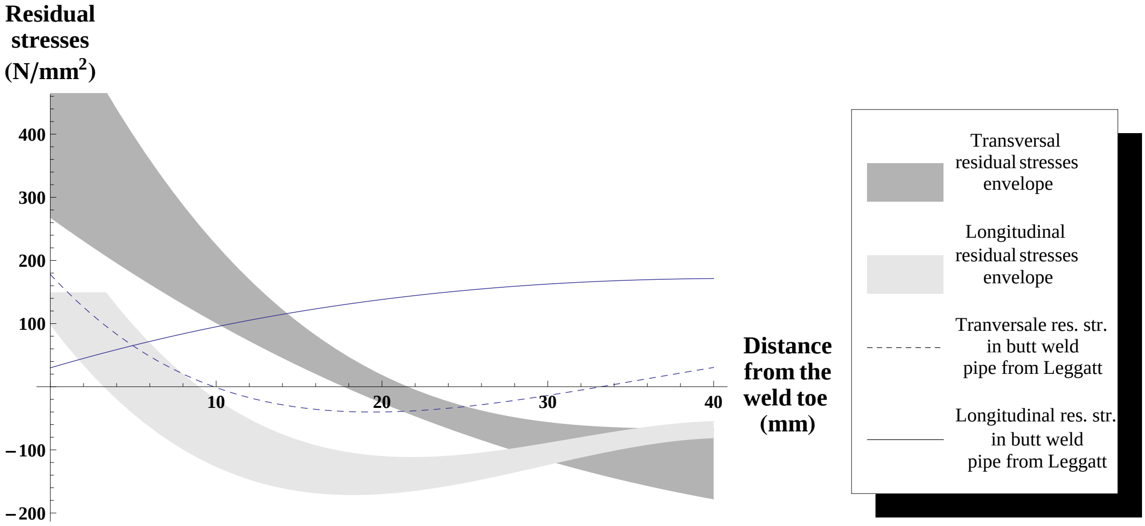

Figure 5.10: Comparison between Leggatt (2008) and measured residual stresses.

Measurements in the crown toe area of the joint (gap region)

Residual strains were mainly measured in the gap region, where fatigue cracks are usually expected. Measurements have be done on joints with different thicknesses (T=20mm or 30mm). Joints were either as-welded and fatigue-tested, however not particular differences have been noticed between both types concerning the residual stress magnitude. Figure. 5.11 gives the residual stress

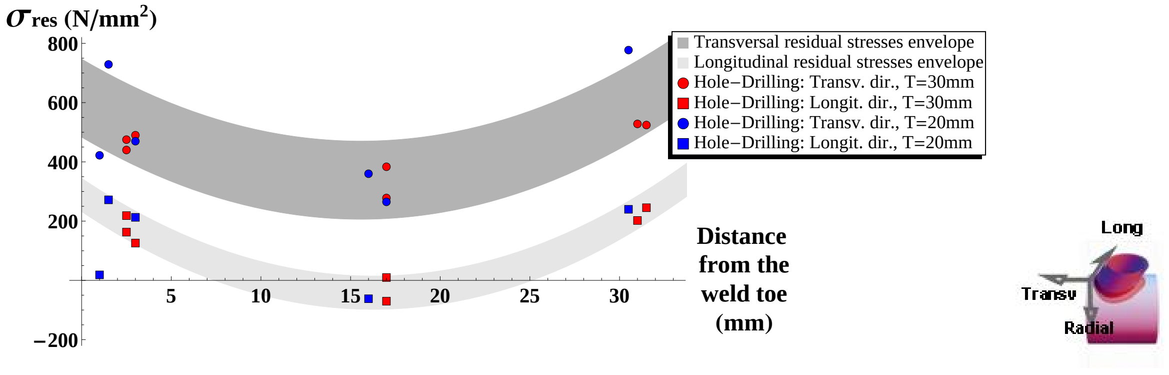

Figure 5.11: Transversal and longitudinal residual stress data points measured by hole-drilling at 2mm depth.

It is confirmed that transversal residual stresses perpendicular to the weld (dark grey envelope) are greater than longitudinal residual stresses parallel to the weld (light grey envelope). It has to be highlighted that the orientation of the greater residual stresses is also the orientation of the applied fatigue load principal stresses, implying that they will superimpose. Moreover, it can also be seen that transversal residual stress value reaches the yield stress value of the material and that there is a strong restraining effect between the braces keeping transversal residual stresses at a high value. Therefore, the particular geometry of the K-joint (with a gap area) is responsible for high residual stresses in the gap region, which is critical for fatigue.

5.2.4 Conclusions

It has been shown that the drilling system developed for tubes has given the general trends for surface transverse and longitudinal residual stresses. The first residual stress evaluations on bridge tubular joints, presented herein, have led to drastically different residual stress fields than those found in the literature on pipe and pressure vessel tubes.

At the surface, the greater residual stresses are critically oriented perpendicularly to the weld direction, which is also the orientation of the externally applied stresses. It has been shown that transversal residual stress value reaches the yield stress of the material and that there is a strong restraining effect between the braces keeping transversal residual stresses at a high value.

5.3 Neutron Diffraction

5.3.1 Objectives

In order to model crack propagation in welded tubular bridges using a three dimensional finite element model, we need to evaluate the residual stress field along the crack path and in its surroundings. The main objective of these residual stress measurements is to evaluate intensity as well as variability of the triaxial residual stresses.

Triaxial local residual stresses of tubes have only been obtained by a few researchers, Mochizuki (Mochizuki et al., 2000) being one among them. He was able to determine local residual stress distribution using neutron diffraction measurements, but he did it only in butt joints between tubes. To the best of our knowledge, the triaxial residual stress state and its distribution in depth has never been determined on tubular K-joints.

To measure the local residual stresses without releasing them, neutron diffraction is the only non-destructive technique that allows to evaluate the triaxial residual stress field deep inside polycrystalline materials. Indeed, neutrons can penetrate to great depths, up to 3 to 6 cm from the surface for steel materials using neutron diffraction instruments presented in this document, whereas other techniques cannot. This stems from the fact that uncharged neutron particles only interact weakly with most engineering materials, giving rise to large penetration depths. Even high-energy synchrotron X-rays are more limited to the near-surface (penetration generally less than 1 cm) (Hutchings et al., 2005). The hole-drilling semi-destructive method is often restricted to the first millimeters.

Moreover neutrons are not only particles, they behave also as waves allowing to evaluate atomic spacings and residual strains.

Therefore, neutron diffraction (ND) is a powerful tool to provide through-thickness residual stresses. Its popularity has been ever growing since it was standardized by an ISO published in 2001 (ISO/TTA 3:2001 (Webster, 2001)). By reorienting the sample, it allows the measurement of strain values in three directions.

5.3.2 Physical principle

Neutron diffraction is used to provide information on atomic structure of crystalline materials. Crystallographic planes which are parallel have the same Miller indice hkl, and the same lattice spacing d_{hkl}. In order to simplify notation, d_{hkl} is replaced by d hereafter.

Under stress, the atomic lattice deforms, consequently the lattice acts as a strain gauge. The lattice spacing of these planes d changes. Thus, if the lattice spacing under stress-free conditions d_0 is known, then the strain can be calculated:

$$\varepsilon = \frac{d - d_0}{d_0} \tag{5.2}$$

The d spacing can be obtained by using Bragg's law.

Bragg's law

In 1912, Bragg showed, based on his experiments, that if a crystal matter is bombarded with a beam which has approximately the same wavelength as the lattice spacing of the material, then a phenomenon of diffraction occurs. When scattering neutron waves encounter atomic nuclei, these waves are diffracted in another direction with an angle 2θ. Since neutrons are reflected in the same direction by parallel atomic planes, neutron waves can interfere.

Due to differences in the distance the scattering wave has to travel in order to hit an atom, the waves don't have the same phase. It means that the re-emitted waves interfere with each other, either constructively or destructively (see figure 5.12). If the interference is constructive, the waves add together in order to produce a peak of intensity, observable by the neutron detector. In other words, sharp peak intensity can only be found at a specific 2θ angles (for a fixed wavelength).

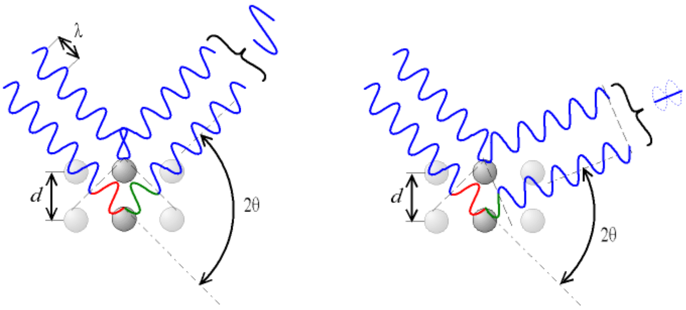

Figure 5.12: Constructive and destructive interference waves.

As a consequence, it is possible to express the Bragg's law (equation (5.3)) as the supplementary path traveled by the deepest wave: 2d $\sin\theta$. The interference is constructive if the difference of phase between the two paths is a multiple of 2π, thus if the supplementary path is a multiple of the wavelength (see figure 5.13).

$$n\,\lambda = 2d\ \sin\theta \tag{5.3}$$

λ is the wavelength
n is an integer
d is the spacing between the planes of the atomic lattice
θ is the angle between the incident and scattering beams

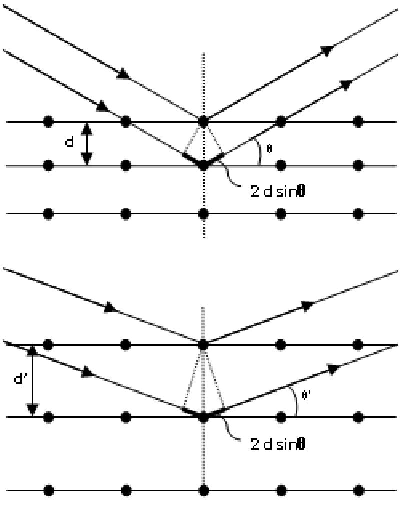

Figure 5.13: d.sinθ path.

Hence, for a constructive interference corresponding to a certain difference of phase, an increase of the d spacing implies a decrease of θ.

Elastic strain can be obtained by measuring the lattice spacing change $\Delta\mathrm{d} = \mathrm{d} - \mathrm{d}_0$ (PSI method, see equation (5.2)) or the scattering angle change $\Delta\theta = \theta - \theta_0$ (ILL method). The relation between Δd and $\Delta\theta$ is given by the total derivative of the d-spacing Bragg law equation $\mathrm{d} = \frac{\mathrm{n}\lambda}{2\mathrm{sin}\theta}$:

$$\begin{aligned} dd &= \frac{\partial d}{\partial \theta}.d\theta + \frac{\partial d}{\partial \lambda}.d\lambda && (5.4) \\ &= \frac{-n\lambda}{2\sin\theta}.\frac{\cos\theta}{\sin\theta}.d\theta + \frac{n}{2\sin\theta}.d\lambda && (5.5) \end{aligned}$$

then

$$\frac{dd}{d} = -\cot\theta.d\theta + \frac{d\lambda}{\lambda} \qquad (5.6)$$

Therefore, for a fixed wavelength and knowing d_0 or θ_0 (under stress free conditions), strain can be calculated as follows:

$$\varepsilon = \frac{d - d_0}{d_0} = -\cot\theta.(\theta - \theta_0) \qquad (5.7)$$

The orientation of principal residual stresses at the surface were known from previous hole-drilling measurements (Acevedo and Nussbaumer, 2009a). These three directions (x,y,z) were assumed to be the principal ones for the in-depth strain measurements. Residual stresses can then be calculated thanks to the generalised Hooke's law (21432:2005, 2006):

$$\begin{aligned} \sigma_x &= \frac{E}{1+\nu}.(\varepsilon_x + \frac{\nu}{1-2\nu}.(\varepsilon_x + \varepsilon_y + \varepsilon_z)) && (5.8) \\ \sigma_y &= \frac{E}{1+\nu}.(\varepsilon_y + \frac{\nu}{1-2\nu}.(\varepsilon_x + \varepsilon_y + \varepsilon_z)) && (5.9) \\ \sigma_z &= \frac{E}{1+\nu}.(\varepsilon_z + \frac{\nu}{1-2\nu}.(\varepsilon_x + \varepsilon_y + \varepsilon_z)) && (5.10) \end{aligned}$$

where
E, standing for E_{hkl}, is the Young modulus
ν, standing for ν_{hkl}, is the Poisson ratio

5.3.3 Specificities of the POLDI at the Paul Scherrer Institute (PSI) and of the SALSA at the Institute Laue-Langevin (ILL)

The nuclei of atoms are composed of protons and neutrons. Outside the nucleus, free neutrons are unstable, so free neutrons cannot be found in nature. To produce them, one needs to extract them from the atomic nuclei bound with an important transfer of energy.

To produce a neutron source, neutrons can be extracted by nuclear fission or by spallation reaction.

Paul Scherrer Institute

The Paul Scherrer Institute (PSI) is a the largest center of public research in Switzerland, principally developed for natural and engineering sciences. The center offers research facilities to carry out experiment with a neutron source produced by spallation reaction (SINQ).

The Spallation Neutron Source (SINQ)

Neutron spallation, used by SINQ, is the process by which neutrons are ejected from a heavy metal bombarded with a proton beam (figure 5.14). High energy protons, coming from the proton accelerator, are oriented on a heavy metal target, for example a lead bar. The protons collide with the lead nuclei and transfer a large amount of energy. This released energy evaporates neutrons in all directions. At the PSI, each proton releases approximately ten neutrons.

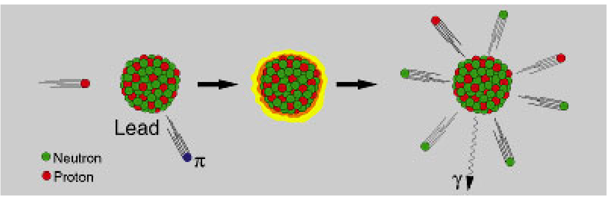
Lead
Neutron
Proton
π
γ

Figure 5.14: The process of the spallation reaction (Spallation Neutron Source SINQ, 2009).

These high energy neutrons are then slowed down in a moderator material (tank filled with water) and oriented by guides to create a beam. Neutrons follow a long flight path (14 m for the POLDI instrument) before encountering the sample and finally be counted in banks of detectors.

Time-of-flight diffractometer: the multiple Pulse-OverLap-DIffractometer POLDI

POLDI uses the time-of-flight (TOF) method to measure the lattice spacing. This is achieved by measuring the time passed from the emission of a neutron from a rotating chopper to the time at which it is detected (chopper to detector). During diffraction, the neutron does not transfer energy to the sample. Then, it is possible to measure the neutron energy only based on the time-of-flight. The pulse, neutron beam segments, are created using a rotating chopper, shown in figure 5.15, letting pass only several neutrons through a slit during a short period of time. This technique allows to know the departure time of the neutron segment (time of emission).

Figure 5.15: The rotating chopper disc with its 32 slits (Spallation Neutron Source SINQ, 2009).

Each beam segment continues, reaches the sample and is diffracted with a 2θ angle to be collected by the detector, as depicted in figure 5.16.

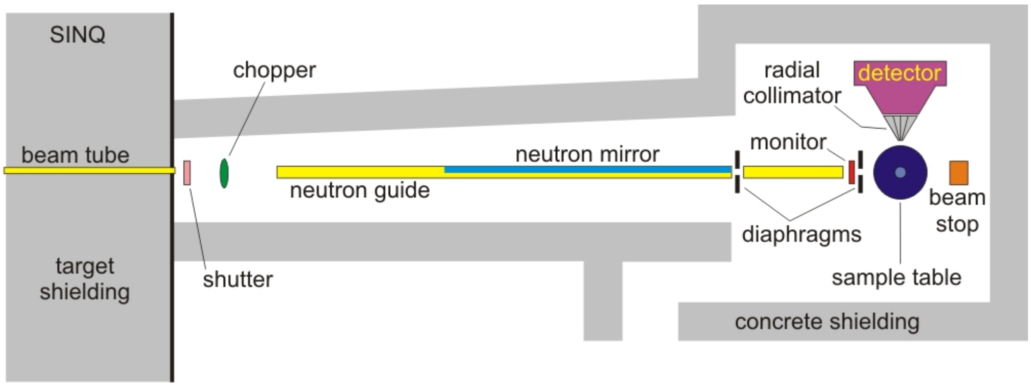
SINQ
chopper
radial collimator
detector
beam tube
monitor
neutron mirror
neutron guide
beam stop
diaphragms
target shielding
shutter
sample table
concrete shielding

Figure 5.16: POLDI instrument overview (Spallation Neutron Source SINQ, 2009).

The conventional TOF diffractometer uses separate pulses with a fixed diffraction angle and a beam with a large range of wavelengths, this wavelength is calculated from the time-of-flight. The TOF is determined by the arrival time relative to the opening of the chopper slit. Therefore, to obtain precisely this wavelength, pulse has to be send separately with a certain time between each emission in order to avoid pulse overlap: the fastest neutron from a subsequent pulse can never catch the slowest neutron from the preceding pulse. Knowing the wavelength and the fixed diffraction angle, the lattice spacing can be easily calculated using equation (5.3).

In contrast, POLDI utilises pulse-overlap, meaning that several pulses may arrive simultaneously (Stuhr et al., 2006). The main advantage of the POLDI is the short time interval between neutron pulses linked with the increase of the neutron flux onto the sample. Since the detector not only measures the time-of-flight but also the scattering angle 2θ which is not fixed in that case, pulses can be identified by these two parameters. Indeed, for a family of similar atomic planes (constant d), the scattering angle 2θ is proportional to the wavelength, and hence to the time-of-flight. Then, knowing θ and the proportionality coefficient, the lattice spacing can be calculated as shown hereafter.

Since the intensity of the neutron beam can easily be measured in function of the arrival time and of the scattering angle, one can draw the time versus 2θ plot, as depicted in figure 5.17.

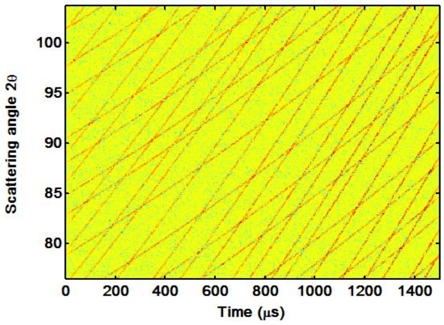

Figure 5.17: Lines of diffracted neutrons in function of arrival time and scattering angle: time-2θ plot for a powdered Germanium sample ((Stuhr et al., 2006), (Spallation Neutron Source SINQ, 2009)).

The lines represented in this figure are called the Bragg lines. Each Bragg line corresponds to an atomic plane, if the slope of the lines ($\frac{2\theta}{t}$ or $\frac{2\theta}{\lambda}$) are the same, they represent the same atomic plane family. Therefore, figure 5.17 presents two atomic plane families. From the slope of the Bragg line, the time of flight can be calculated and it is possible to determine from which slit of the chopper the neutron beam come. Finally, one can evaluate the wavelengths and the lattice spacings d.

The short time interval implies that a high intensity, combined with a high resolution, can be achieved. The resolution is linked with the length of the pulse (neutron quantity) and thus with the chopper speed whereas intensity is linked with the chopper duty cycle. Both can be adjusted simultaneously.

Institute Laue-Langevin

The Institute Laue-Langevin (ILL), located in Grenoble (France), uses a 58 MW high-flux nuclear reactor to produce free neutrons. The reactor is only devoted to research and not to energy production. The ILL is financed by international funds and offers international researchers possibilities to use their facilities and the most intense neutron source in the world: $1,5.\ 10^{15}$ neutrons.s^{-1}.cm^{-2} (Laue-Langevin, 2007). Its consortium is composed of primary contributors: France, Germany and United-Kingdom as well as secondary contributing countries (Switzerland, Spain, Italy, Russia, Austria and Czech Republic).

The Nuclear Neutron Source

The ILL research reactor is simpler and smaller than a power reactor, however it needs a special designed fuel core. To cool the core and to slow down the neutrons, the core is placed in a heavy water swimming pool.

Two types of sources deliver neutrons: graphite hot source for hot neutrons ($\lambda < 0.3$Å) and liquid deuterium cold source for cold neutrons (0.3 Å $< \lambda <$ 20 Å), which is the range of wavelength used in SALSA instrument for this project.

At ILL, each nuclear fission emits between 2 and 3 neutrons. Theses neutrons are then guided to different instruments such as SALSA by super-mirror neutron guides ensuring low neutron background noise.

Powder diffractometer: the Strain Analyser for Large and Small scale engineering Applications SALSA

SALSA instrument is a monochromatic strain diffractometer. It uses a double-focusing monochromator to select a single wavelength of neutrons from a continuous flux of thermal neutrons (slow neutrons) of 5. 10^7 neutrons.s^{-1}.cm^{-2} (Pirling et al., 2006).

As shown in figure 5.18, the sample is fixed on the hexapod, a platform lying on six servo-hydraulic jacks allowing the achievement of accurate translational and rotational movements. The neutron beam is oriented onto the sample position by a double-focusing monochromator in combination with slits/collimators. The neutron beam passes through a first collimator, is diffracted by the sample onto a second collimator before reaching the detector. The gauge volume is then defined by the slits of these two collimators. Since the slits are automatically controlled, the gauge volume can be monitored during scans. However, slits can only be used if the sample-slit distance does not exceed 50 mm, that is the reason why they were not used. Therefore, our measurements were done with a gauge volume of 2mm x 2mm x2 mm imposed by the collimators' geometry.

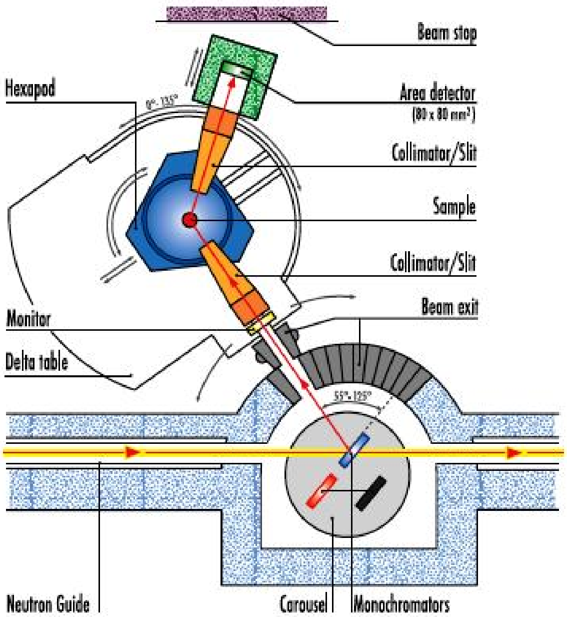

Figure 5.18: View of the SALSA instrument: neutron guide, monochromator and detector (Hughes et al., 2006).

Main features of PSI's and ILL's diffractometers

The Table 5.2, extracted from Fitzpatrick and Lodini (2003), summarizes the main features of the two neutron sources used in our experimental investigations.

Table 5.2: Main features of PSI and ILL.

	PSI (CH)	ILL (F)
Source	SINQ	HFR-ILL
Type	neutron spallation pulses of n.	nuclear fission continuous n. flux
Power	1000 kW	58 MW
Thermal flux (10^{14}n/s/cm^2)	2	15
Neutron production	10 n/ proton	2-3n/ fission

In Table 5.3, the main features of POLDI and SALSA are summarized. In PSI, the lattice spacing is obtained through the wavelength whereas at ILL it is obtained through the scattering angle.

Table 5.3: Main features of POLDI and SALSA.

	POLDI (PSI)	SALSA (ILL)
Beam pulse features	$2\theta - \lambda$	$\lambda_{\text{fixed}} - 2\theta$
Wavelength (λ)	1.1 - 5 Å	1.64 Å (α-Fe) (1.3-3 Å in general)
Scattering angle 2θ	$90 \pm 15°$	$90 \pm 5°$
Flux at sample pos. (10^6n/s/cm^2)	6	50
Resolution (10^{-3})	1-2	2
Meas. time (in the surface area), gauge v. $2 \times 2 \times 2$ mm^3)	30 min	5 min

For both instruments, a wavelength around 1.6 Å is chosen because it ensures a scattering angle of approximately 90° for all common materials usually tested. It enables to obtain a cubic gauge volume. Ferritic steel (α-Fe) with a d of 1.17 Å requires a wavelength of $\sim$ 1.64 Å to diffract the wave with a 90° angle.

That is the reason why at ILL this wavelength is fixed at 1.64 Å. An increase of the scattering angle is directly linked with a decrease of the lattice spacing. At POLDI, the scattering angle is 90 ± 5 so that mostly neutrons with λ around 1.6 Å contribute to the final diffraction peaks.

5.3.4 Experimental description

Test samples

The samples investigated were welded joints fabricated and welded in the same conditions as real bridges by a steel bridge fabricator. The first sample AW-30 was as-welded (untested) whereas the others (FAT-20 and FAT-30) were cut from Circular Hollow Section (CHS) truss beams, 9 meters long and 2 meters high (see Section 6.2). These truss beams were previously tested under fatigue, however, the joints cut from them were only non-cracked joints. Altogether, neutron-diffraction measurements were performed on three joints. These joints are identified and illustrated in Fig. 5.19 and in Table 5.4.

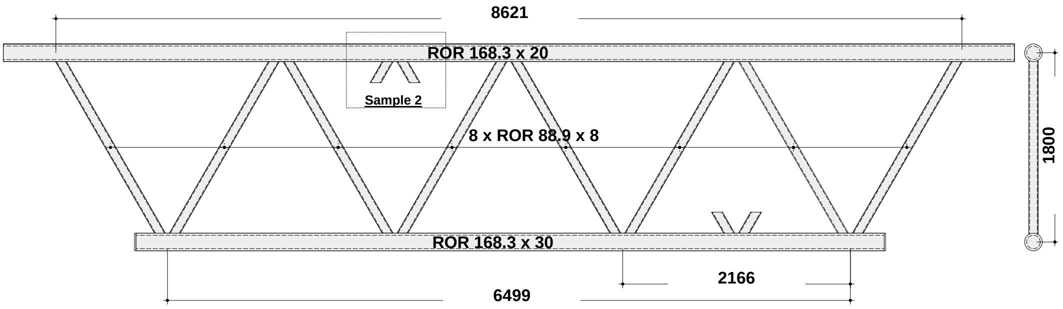

(a) Beam S6 with joint sample called FAT-20

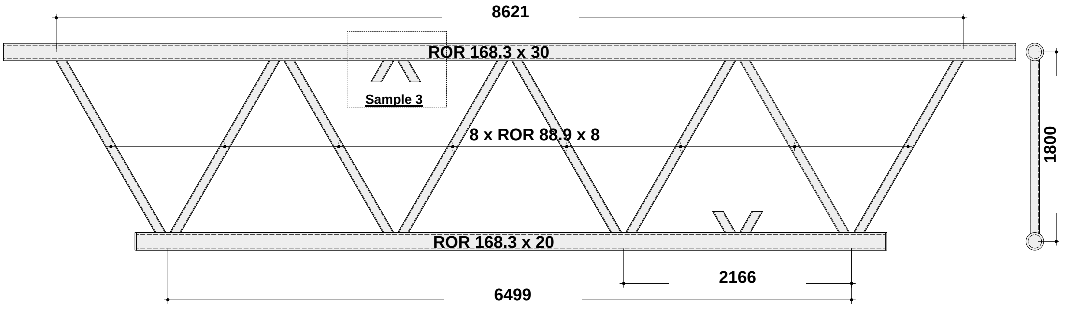

(b) Beam S7 with joint sample called FAT-30

Figure 5.19: Truss beams with fatigue-tested joints devoted to neutron diffraction measurements.

Table 5.4: Test samples characteristics.

Sample n °	ND Institute	Loading History	Chord dim. [mm]	Brace dim. [mm]
AW-30	PSI	As-welded	168.3 × 30	88.9 × 8
FAT-20	ILL	Fatigue-tested	168.3 × 20	88.9 × 8
FAT-30	PSI	Fatigue-tested	168.3 × 30	88.9 × 8

Each sample is composed of part of the chord with two braces branches welded onto it, forming a K-joint, schematically shown in Fig. 5.20.

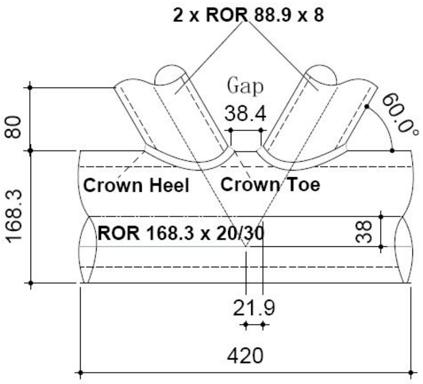

Figure 5.20: Schematic of the K shape welded joint (dimensions in mm).

Truss CHS members are made of grade S355J2H carbon-manganese steel (see Section 4.4).

Microstructure

Due to the welding process, the microstructure in a zone of Base Metal (BM) close to the weld, or Fusion Zone (FZ), is altered by heat transfer. In this Heat Affected Zone (HAZ), martensite-austenite constituents are formed. It is precisely in the HAZ that the crack initiates because of contribution of stress concentration, metallurgical discontinuities and high number of dislocations in the HAZ microstructure. Then, crack propagates in the BM. As shown in Fig. 5.21, apart from the first millimeter, the crack profile path is essentially within the BM.

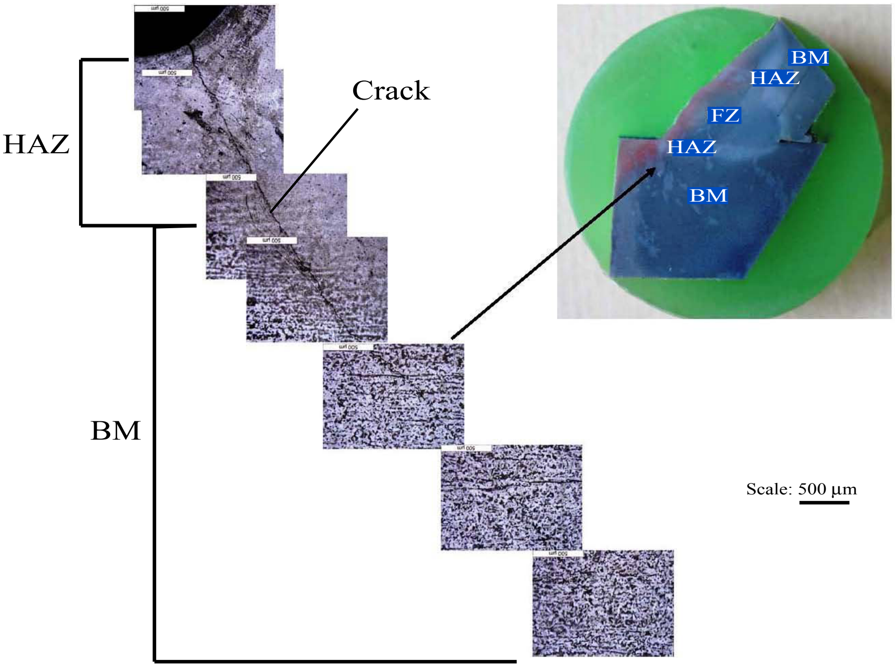

Figure 5.21: A typical example of the crack path in one of the joints investigated. The crack surface is in reality curved in two directions.

The micrograph presented in Fig. 5.22 reveals taht the microstructure of the studied BM is mainly composed of ferrite and pearlite grains. The pearlite consists of alternating layers of ferrite (alpha iron) and cementite (Fe_3C). Globally, ferrite represents the major fraction of volume, even in the HAZ.

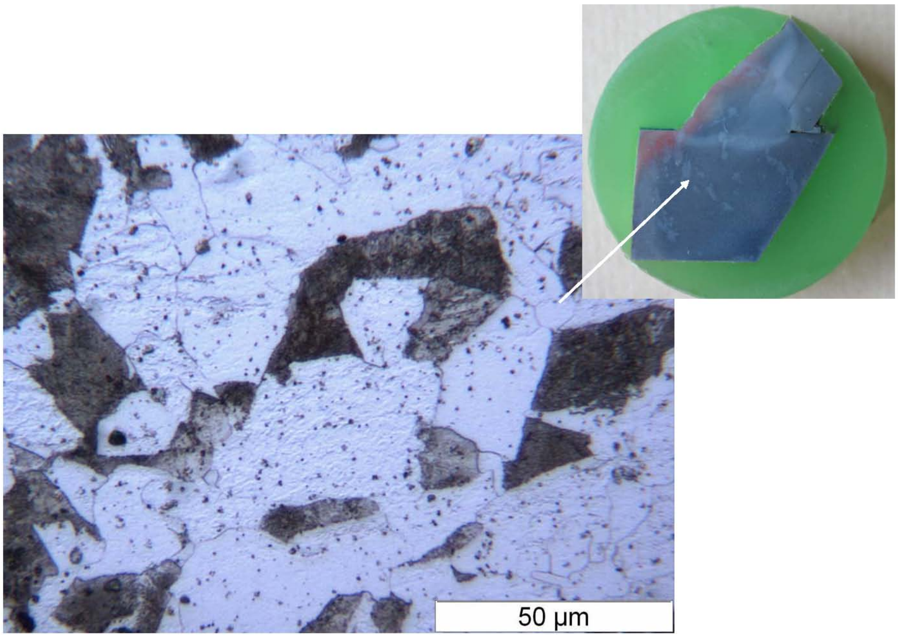

Figure 5.22: Microstructure of S355J2H in the as-delivered state as revealed by optical microscopy. It shows a ferritic and pearlitic microstructure. Large light grey areas are ferrite (alpha iron) crystals and large black areas are colonies of pearlite (composed of ferrite and cementite- Fe_3C).

Experimental method

Stress-free reference samples

As explained in Section 5.3.2, neutron diffraction method allows one to measure the lattice spacing or the scattering angle and thus to calculate the elastic strain ε (equation (5.7)).

In this equation, one needs to know also the stress-free reference d_0 or θ_0. In order to relax residual stresses, small cubes were cut by electro-discharge machining (EDM) for PSI samples and with a diamond blade for ILL sample. These sectioning methods were chosen to minimise the chance of inducing new residual stresses.

By EDM, two sets of stress-free samples were machined to measure the d_0 spacing in the Heat Affected Zone (HAZ) and also in the Base Metal (BM). For the first set in the HAZ, two cubes of dimension 1mm x 1mm x 1mm were cut out and for the second set in the BM, four cubes of dimension 2mm x 2mm x 2mm were taken at different depths from the surface (centers of cubes are at 1.5mm, 4mm, 7mm and 10 mm depth) as depicted in Fig. 5.32. With the diamond blade, straight cuts were made at 3 mm from the surface to form a stick (section 3mm x 8mm) containing a part of the BM and a part of the HAZ. Results of measurement conducted on stress-free samples are presented in Section 5.3.4.

Three measurement directions

In order to measure strain in a certain direction, the sample was oriented so that the bisector between the incident and the diffracted neutron beam coincided with that direction.

For the tested sample, it was planned to measure transverse strain (perpendicular to the weld direction), longitudinal strain (parallel to the weld direction) and radial strain (in the radial direction of the tube) in the weld toe vicinity. By reorienting the sample, strain values were obtained in these three directions (see Fig. 5.24). The mean scattering angle is approximately of $2\theta = 90^\circ$as explained in Section 5.3.3.

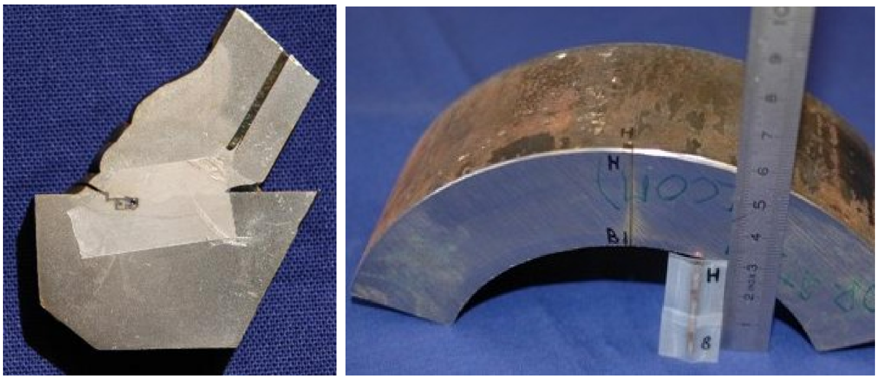

(a) cubes HAZ (PSI) **(b)** cubes BM (PSI)

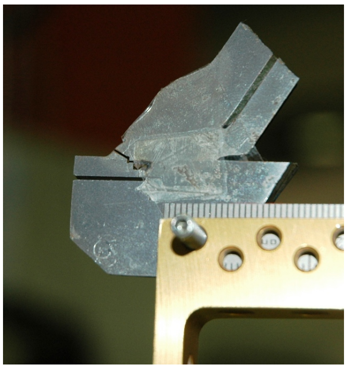

(c) sample with a stick cut by a diamond blade (ILL)

Figure 5.23: Joint parts after removal of stress-free reference samples.

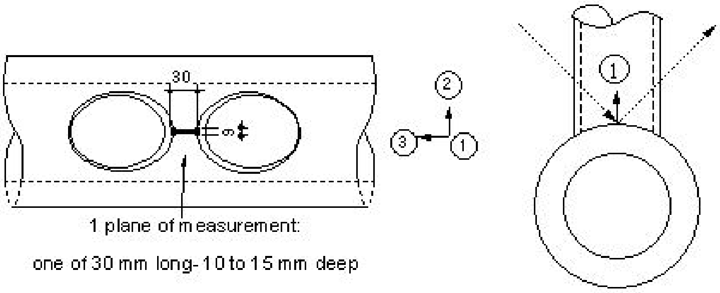
30
9
2
3
1
1 plane of measurement:
one of 30 mm long- 10 to 15 mm deep
1

(a) The plane of measurement **(b)** radial direction (dir. 1)

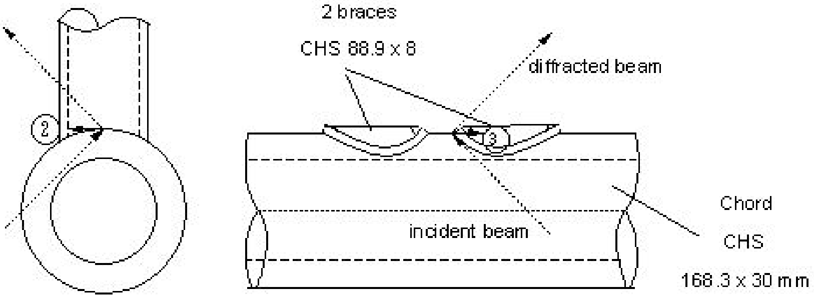
2
2 braces
CHS 88.9 x 8
diffracted beam
3
incident beam
Chord
CHS
168.3 x 30 mm

(c) longitudinal direction (dir. 2) **(d)** transverse direction (dir. 3)

Figure 5.24: Beam paths and directions of lattice spacing measurements.

In order to obtain the spatial resolution required to measure the residual strain variation through tube thickness, the choice of the gauge volume (region of intersection of the incident and diffracted beams) had to be determined carefully.

The gauge volumes used are summarized in Table 5.5. They have been chosen to measure with sufficient statistics within a short period of time. As it will be seen further in this document, the gauge volume of the sample AW-30 was not appropriate to provide triaxial strains, therefore it was increased for the second sample tested at PSI (sample 3, FAT-30).

Table 5.5: Gauge volumes chosen for each test sample.

Sample n °	ND Institute	Gauge volume [mm^3]
AW-30	PSI	$2 \times 2 \times 2.5$
FAT-20	ILL	$2 \times 2 \times 2$
FAT-30	PSI	$3.8 \times 3.8 \times 3.8$

Since the residual strain obtained is the mean value of the distribution over the sampling gauge volume (mm^3), the highest strain value located at a stress concentration will always be underestimated.

Diffraction

In a polycrystal, the diffraction peak gives the average of the strains in the different types of grains present in the gauge volume. However, the response of diffraction peaks for each crystallographic lattice plane may differ from the global response. Since measuring multiple reflections is not always feasible, the lattice plane reflection which fits best the global macrostrains has to selected.

During the experiments, residual strains were measured with the (211) Bragg reflection, presenting the advantage of achieving a 90° diffraction angle for a wavelength of 1.6 Å. However, to relate this measured strains to the macrostresses of interest, it must be assumed that the (211) atomic plane is weakly affected by intergranular strains, or in other words its response is linear and independent of the regime (elastic or plastic) (Hutchings et al., 2005) (Pang et al., 1998). The VAMAS standard (Webster, 2001) recommends suitable lattice planes for several crystal structures. For the body-centered cubic of ferrite, the lattice planes (110) and (211) are recommended (see Fig. 5.25). Therefore, the (211) reflection is a good choice for reliable and efficient measurement of strain in S355J2H steel.

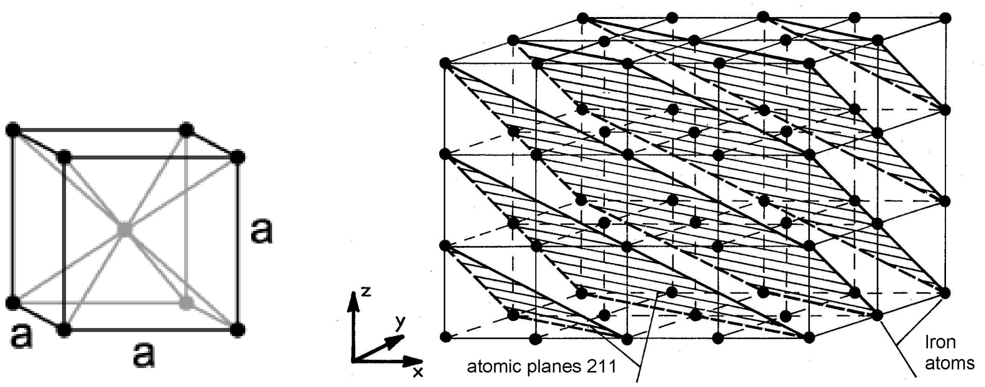

(a) BCC structure

(b) atomic plane 211

Figure 5.25: Crystal elementary structure and (211) atomic planes.

The Young's modulus E and the Poisson's ratio ν in the (211) atomic plane ($E_{211} = 220000 N/mm^2$ and $\nu_{211} = 0.28$ (Wimpory and ohms, 2010)) have been shown to be close to those of the bulk S355J2H steel ($E = 210000 N/mm^2$ and $\nu = 0.3$). These values are valid in transverse, longitudinal and radial directions. The S355J2H bulk moduli values were used for stress calculation.

Data analysis and results

Reflections

From the diffraction spectrum, representing the intensity versus the lattice spacing d_{211} or versus the scattering angle, diffraction peaks were observed. As explained in Section 5.3.4, the (211) peak was used for strain calculation. An example of reflection is shown in Fig. 5.26 for one PSI's series with the fitted-curve giving the neutron momentum transfer $Q = 2\pi/d$.

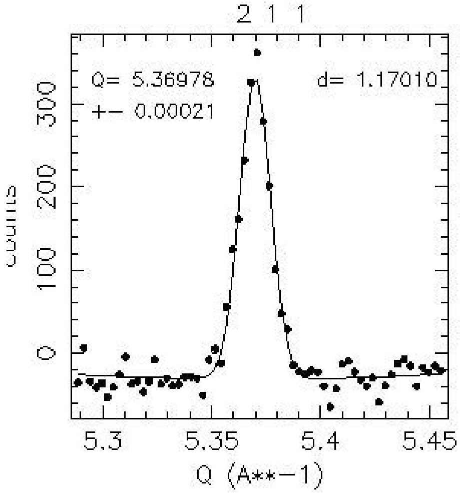

Figure 5.26: 211 Bragg reflection extracted from the diffraction spectrum (POLDI, PSI).

The error calculated from the fitted-curve is given with respect to d (or Q as shown in Fig. 5.26) at PSI and with respect to θ at ILL. Thus, the error related to strain is then deduced ($error_d/d$ respectively $error_\theta/(\tan\theta_0)$).

Stress-free lattice spacing

The average values of d_0 and $2\theta_0$ measured respectively at PSI and at ILL for the HAZ metal and for Base Metal sets of samples are summarized in Table 5.6.

Table 5.6: Measured stress free d_0 and $2\theta_0$ for BM and HAZ.

	Base Material BM average of 4 cubes	Heat Affected Zone HAZ average of 2 cubes
d_0 ($\mathring{A}$) - PSI	1.1707 ± 0.00009	1.1706 ± 0.00014
$2\theta_0$ (°) - ILL	89.493 ± 0.005	89.483 ± 0.007

The absolute values of d_0 or $2\theta_0$ resulting from both instruments are not comparable due to calibration variation.

d_0 can be deduced from measurements on both instruments and the difference between the BM and HAZ in both cases was less than 100 $\mu\epsilon$. Therefore the d_0 measured in the BM was used throughout. The POLDI and SALSA used their own respective d_0 due to differences in calibration.

It has to be noted that these reference values, expected to be different in the BM and HAZ, are very close. Since the sample did not seem to be textured (in a material textured by plastification, the atomic plans are not distributed randomly but they present a preferred orientation), it is assumed that the d_0 spacing is the same in the three principal directions and the value of $d_0 = 1.1707$ Å or $2\theta_0 = 89.493°$ was kept for strain calculation since the Base Metal is the main part of the sample.

Strain measurements

The lattice spacing d_{211} in the K-shape joint sample was measured at different locations positioned along a line between the two welds as illustrated in Fig. 5.27. At each location a depth scan has been made comprising points at several depths, i.e. distances from the surface.

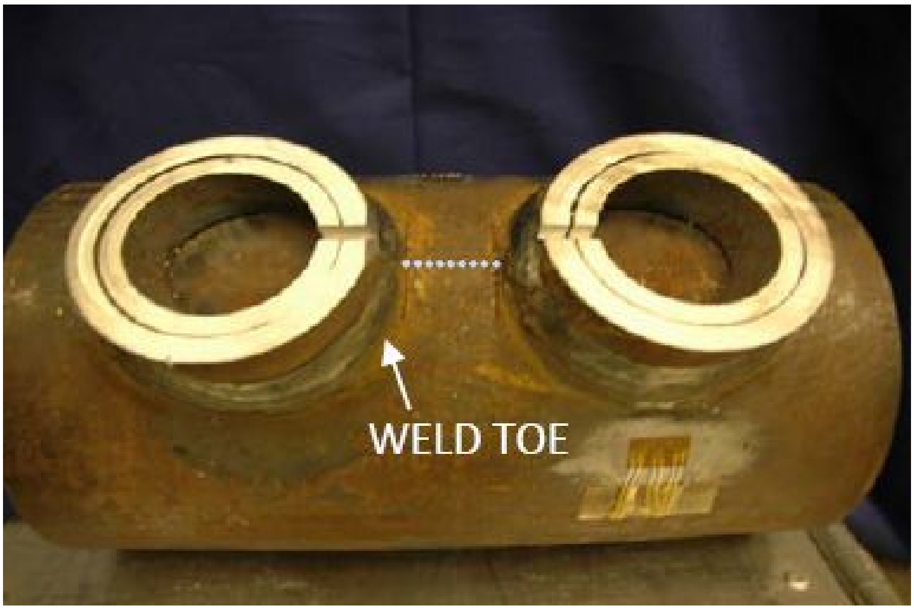

Figure 5.27: Measurement line positions on sample surface.

Beam path length limit

For the first series AW-30, strain was obtained only in the radial direction. Two shortcomings were encountered for the longitudinal and transverse directions (dir. 2 and 3). First, the path length of the beam through the 30 mm thick tube exceeded the maximum feasible limit of POLDI for neutrons in steel (≈ 30 mm), most of neutrons have been diffracted by the steel they penetrate before reaching the gauge volume for the configuration shown in Fig. 5.24. Moreover, when the sample was reoriented in order that the incident-diffracted beam plane be parallel to the directions 2-3 plane, the neutron beam collided with the welds resulting in a path length also exceeding the limit. Therefore, it was not possible to measure the longitudinal nor the transverse residual strains of this sample. That is the reason why, in the second and third series FAT-20 and FAT-30, windows were cut in the tube, away from the region of the weld without affecting the stresses in the zone of interest, in order to avoid the penetration of both walls (Fig. 5.28). Note also that the maximum feasible limit for neutrons in steel is greater at ILL, it corresponds approximately to a path length limit of 60 mm. This is due to a drastically lower background and a much higher flux.

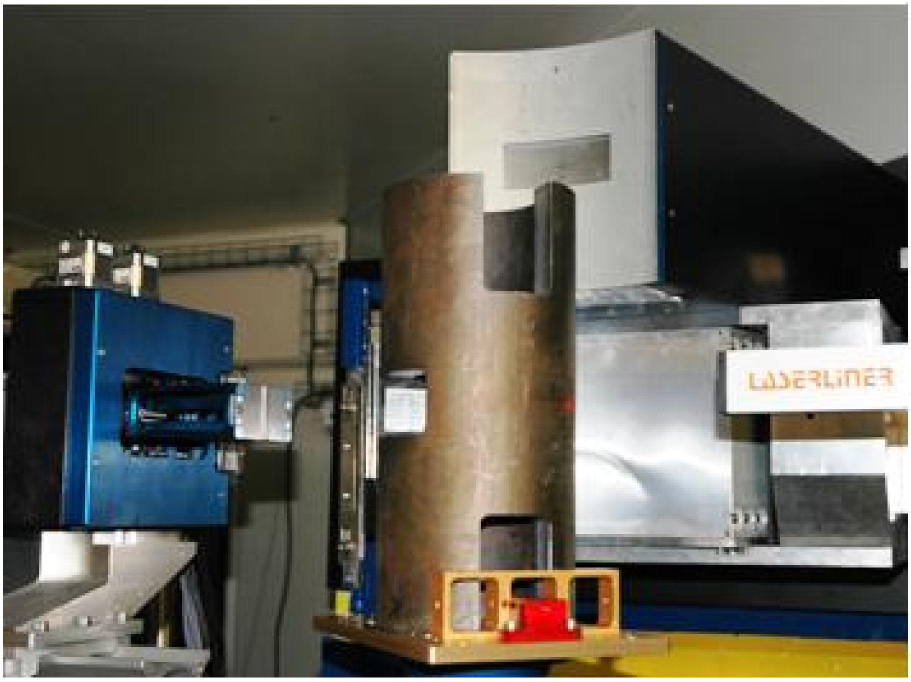

Figure 5.28: Windows cut in the samples to shorten the neutron beam path through the tube.

5.3.5 Results and discussion

Strains were calculated using formula (5.7) and the stress-free lattice values given in Table 5.6.

As shown in Table 5.4, two parameters differ in the samples characteristics: the chord wall thicknesses (20 or 30 mm) and the loading history (as-welded or fatigue-tested). Hence, by comparing results for samples AW-30 and FAT-30, a possible shakedown effect of fatigue cycles can be evaluated. Moreover, the results between samples FAT-20 and FAT-30 should give informations on size effects influence.

Shakedown effect

In high-cycle fatigue under constant amplitude, the first stress cycles can induce elastic shakedown, meaning that local plastic deformation may cause a redistribution and a relaxation of residual stresses. The modification of the residual stress level is particularly linked with the yield behaviour and the geometrical conditions such as the chord wall thickness (Krebs and Kassner, 2007). On the one hand, for a sufficiently ductile material, if the combination of residual and applied stresses exceeds the cyclic yield limit (lower than the static yield limit), it implies a decrease of residual stresses. On the other hand, high wall thickness (over 20 mm) increases the multi-axial condition and hence limits the reduction of residual stresses.

In order to identify a possible peak stress relaxation and redistribution during the first fatigue cycles, strains at different positions underneath the weld toe from the as-welded (AW-30 series) and fatigue-tested (FAT-30) samples are compared in Fig. 5.29. The fatigue tested sample was part of a truss specimen subjected to 110000 cycles with a maximum applied stress around -17N/mm^2 and a minimum applied stress around -1N/mm^2 in the brace side of the chord. These fatigue experiments are described in more detail in (Acevedo and Nussbaumer, 2009b).

Since only radial strains were obtained from the first series, comparisons are based on this strain direction. It can be seen on Fig. 5.29 that indeed some relaxation of the radial strain field occurs within the first 4 mm, resulting in a redistribution of strain magnitude along the depth in the chord wall thickness. However, this conclusion cannot be extended to transverse and longitudinal strains even if this shakedown effect is often encountered for high-cycle fatigue with high stress range (Bremen, 1987; Stacey et al., 2000).

The magnitude of any relaxation in these directions remains to be confirmed.

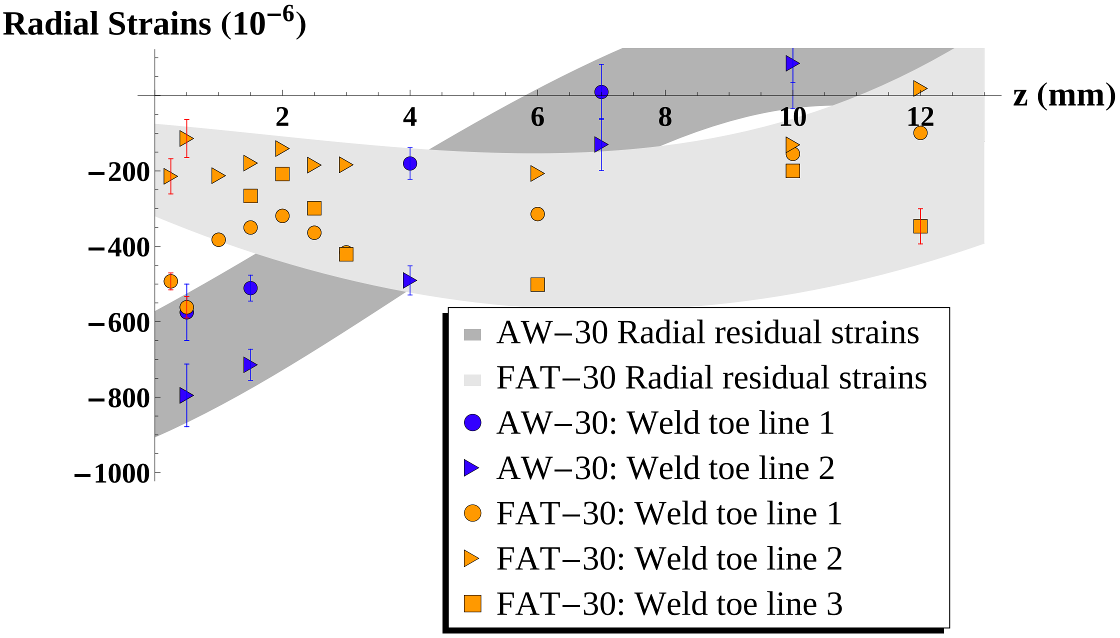

Figure 5.29: Shakedown effect study. Measurement points and envelopes of radial residual strains in function of depth, for the as-welded sample (AW-30) and the fatigue-tested sample (FAT-30), both with chord wall thicknesses of 30 mm. Measurement points are taken along vertical lines underneath the weld toe.

Size effect

A study concerning the influence of the sample thickness on the residual stress distribution has also been conducted to identify if the residual stress distribution function is best related to z/T or to z (where z is the depth below the surface of chord wall and T the chord wall thickness). Comparison between neutron diffraction transverse strains in the weld toe vicinity, for a chord wall thickness of 20 mm (FAT-20 series) and of 30 mm (FAT-30 series) is presented in Fig. 5.30.

It seems that the transverse strain distribution is better related to z than to z/T. Since the transverse strain distributions versus depth z are quite similar for a 20 mm or a 30 mm thick wall, it was decided to consider it as a non-proportional size-effect. The reason is that the welding process, the wire size and the heat input were the same for all samples. It is true however that distributions do not perfectly superpose and the trend is not so clear for longitudinal and radial strains. This must be confirmed by further measurements.

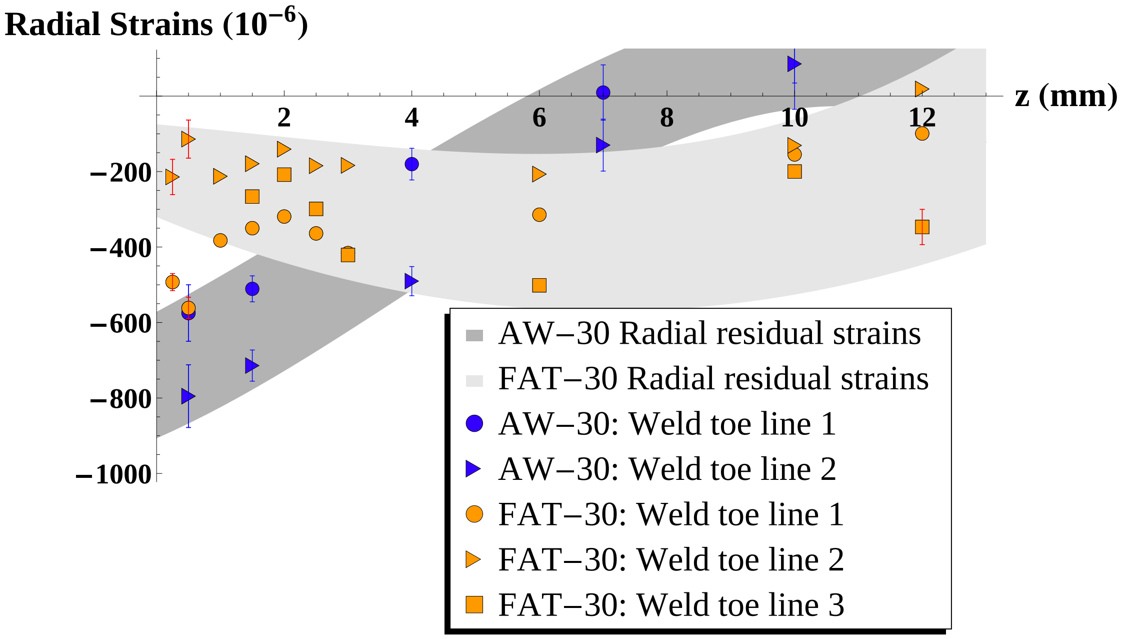

(a) Representation in function of depth z

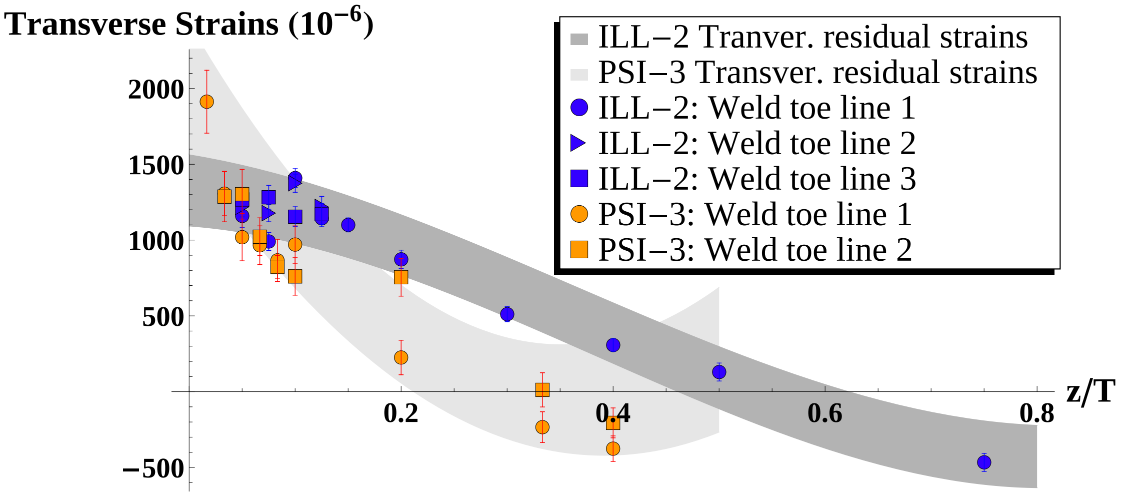

(b) Representation in function of depth over thickness z/T

Figure 5.30: Size effect study. Measurement points and envelopes of transverse residual strains for the fatigue-tested samples (FAT-20 and FAT-30) expressed in function of z or z/T. Measurement points are taken along vertical lines underneath the weld toe.

Residual stresses maps

Based on the previous considerations, the second and third series of measurements are used to estimate the residual stress distribution. Since more data points are available from the measurements at ILL, these results allows the construction of residual stress 2D maps. Residual stress values deduced from the second series of measurements are superimposed on these maps, as depicted in Fig. 5.32b, 5.32c, 5.32d. The transverse direction is perpendicular to the weld, the longitudinal direction is parallel to the weld and the radial direction is the depth direction. Points of measurement were taken along the longitudinal tube axis, along a line in the gap between the two welds and depth scans were made (see plane of measurement in Fig. 5.32a). A thousand points were used to draw these maps.

Figure 5.31 gives another representation of the residual stress distribution along a vertical line underneath the weld toe. Discrepancies between samples FAT-20 and FAT-30 appear in the surface area (from 1 to 3 mm depth) and for a depth below 10 mm and may be attributed to the effect of the wall thickness. Although the results indicate that increasing the wall chord thickness tends to decrease the transverse residual stress magnitude at the surface, care is due since the statistical error on the POLDI data is relatively high.

Figures 5.32b and 5.32c show that tensile transverse residual stresses are close to or even reach the effective yield stress value of 385 N/mm^2 (Table 4.7) in the area around the weld toe (350 to 420 N/mm^2 for a depth between 2 and 3 mm) and are greater than longitudinal ones, which is not the case for tubular butt welds (Stacey et al., 2000). Moreover, this particular orientation of the largest tensile residual stresses is also the orientation of the externally applied stresses. As a consequence, they will superimpose in a detrimental way. In addition, the magnitude of the transverse residual stress remains high in the gap region due to a restraining effect between the braces. This effect induces tensile residual stresses over most of the wall thickness and in the whole gap region. Note that these residual stress maps are not self-equilibrated in section since only a localised region is observed. In conclusion, the geometry of the welded K-joint is responsible for the high applied stresses and for high residual stresses due to welding in the same region, which is critical for fatigue.

For these data, neutron diffraction proved to be a powerful method allowing for the estimation of residual stresses in 3D for many points deep below the surface in a complex geometry (welded tubular K-joints). Results are obtained with a good accuracy for such depths.

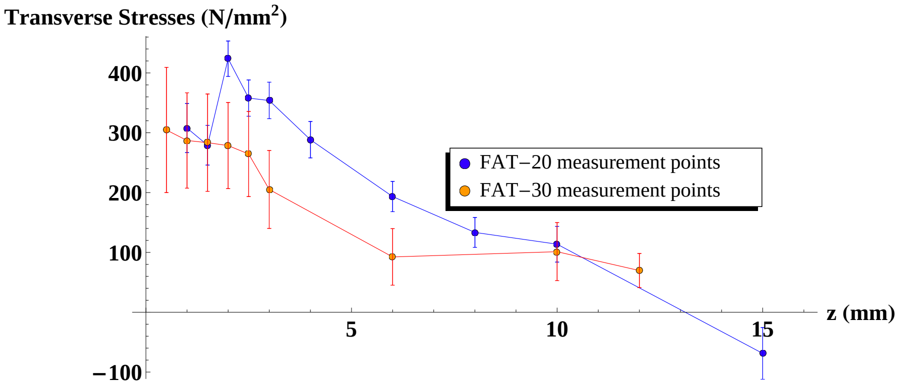

(a) Transverse residual stresses

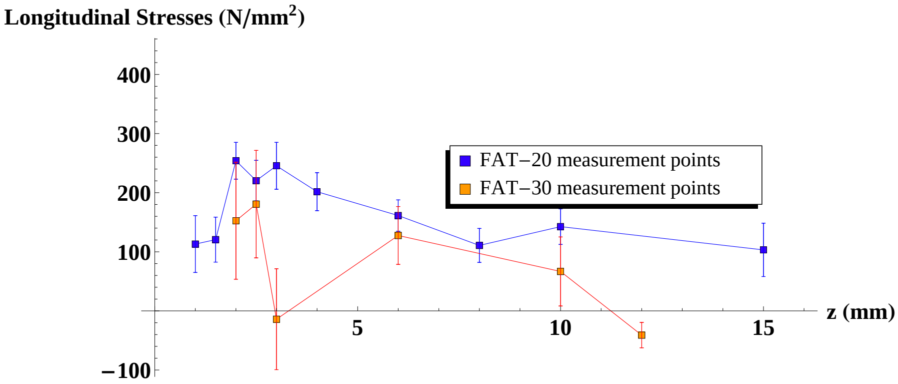

(b) Longitudinal residual stresses

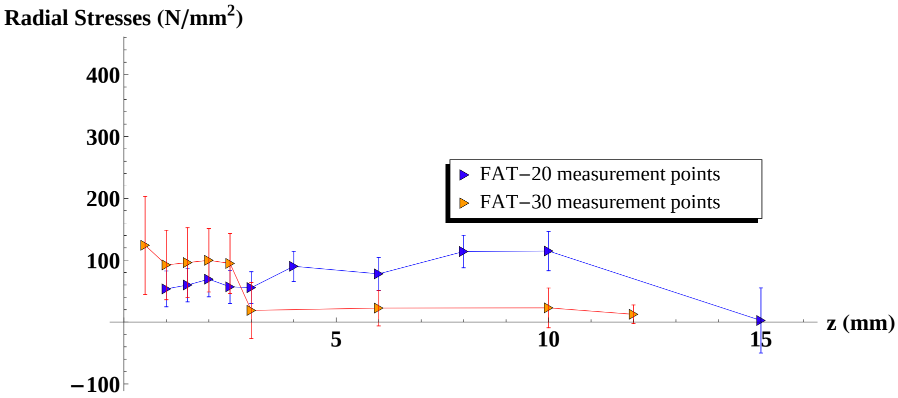

(c) Radial residual stresses

Figure 5.31: Calculated data points and error bars of residual stresses versus depth along a vertical line underneath the weld toe (fatigue-tested samples FAT-20 and FAT-30). Transverse, longitudinal and radial directions are respectively the principal direction I, II and III in the surface of the chord.

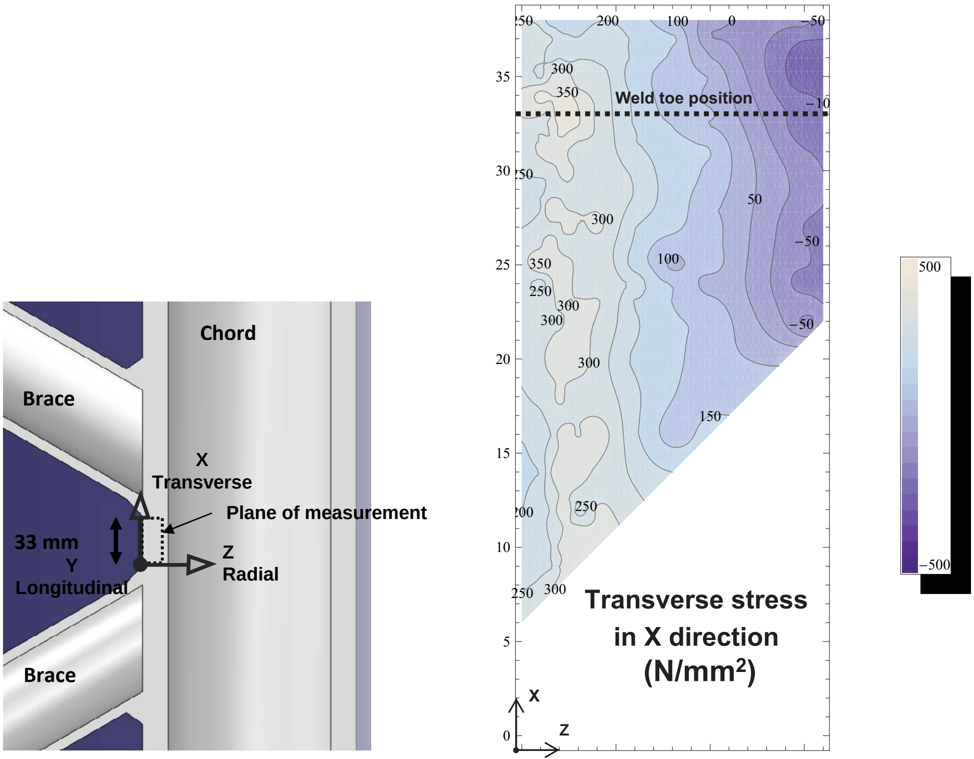

(a) Plane of measurement (b) Stresses in the transverse direction

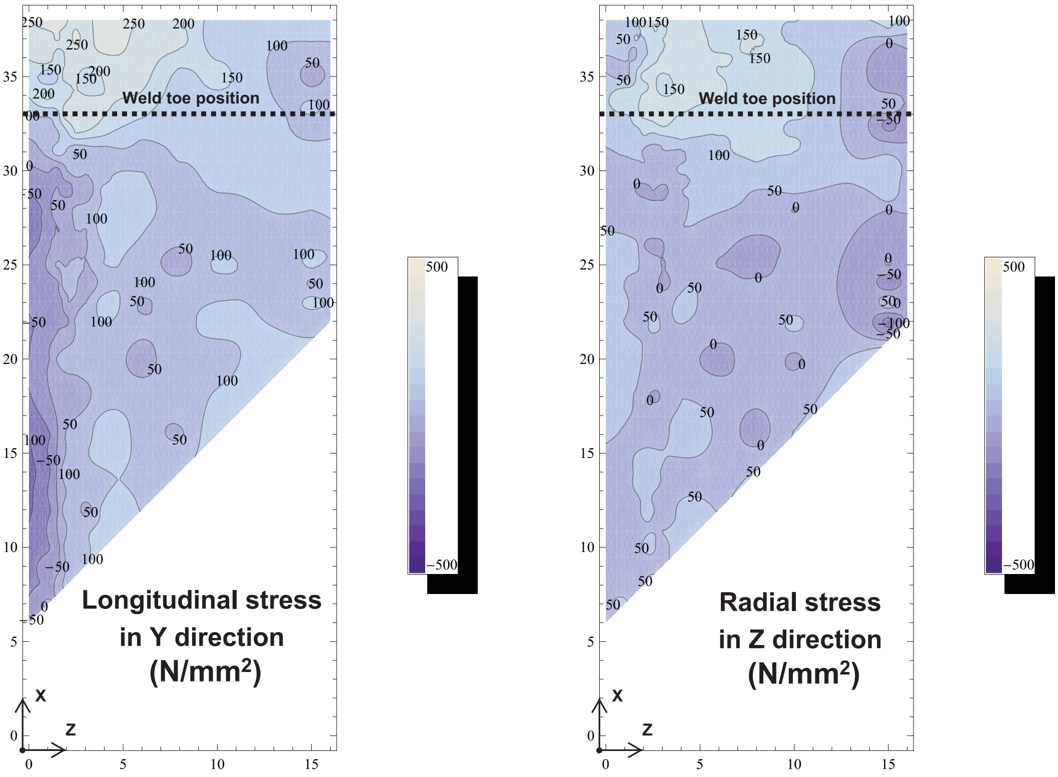

(c) Stresses in the longitudinal direction (d) Stresses in the radial direction

Figure 5.32: Calculated residual stress maps from measurements in the third series (FAT-30).

5.3.6 Conclusions

The residual strain (and thus stress) field in a welded bridge joint made of C-Mn steel has been evaluated using the POLDI time-of-flight diffractometer at the Paul Scherrer Institute and the SALSA diffractometer at the Institute Laue-Langevin.

Neutron diffraction proved to be a powerful and reliable method to collect large quantities of data from the surface to 15 mm depth in a complex geometry (welded tubular K-joints). Thanks to this technique, triaxial measurements of residual strain field were possible. Results have shown that transversal residual stress magnitude is close to or equal to the yield strength of the steel S355J2H and is greater than in the longitudinal direction. This distribution is drastically different from those of the more common tubular butt welded joints. This particular orientation of the greatest residual stresses is critical because it is also the orientation of the externally applied stresses. Moreover, these measurements have led to another unexpected result; residual stress magnitudes remain high in the gap region due to a restraining effect between braces. Therefore, the fatigue cracks observed in complex K-joint geometry may be explained by combining the transverse residual stresses with the applied stresses. The geometry of the K-joint is responsible for the high applied stresses and for high residual stresses due to welding in the same region which is critical for fatigue. Therefore, in this region, taking into account the transverse residual stresses is key in estimating the fatigue strength of K-joint.

Neutron diffraction indicated a probable shake-down effect. It also revealed the existence of a non-proportional size effect. However these last points have to be confirmed respectively by new neutron diffraction investigations and by numerical parametric studies.

5.4 X-ray

The principle of the X-ray method is closed to the one of the neutron diffraction method: estimate the lattice spacing d. The Bragg's law is also available for X-ray beams and therefore the equation (5.7) is used to calculate the residual strains. For X-ray, the measured value is the scattering angle θ.

The main difference between X-ray and neutron diffraction is that X-ray beam does not penetrate really deep (up to 0.025 mm). Therefore, only two-dimensional residual strains can be measured using X-ray.

X-ray measurements were performed at IFS (Braunschweig University, Germany) on the 30 mm thick as-welded sample previously tested at PSI (AW-30).

5.4.1 Experimental description

X-ray measurements were performed at IFS (Braunschweig University, Germany) on the 30 mm thick as-welded sample previously tested at PSI (AW-30).

The residual stress measurement was accomplished by a middle point free 8 axis ω / ψ diffractometer. By using Cr-K$_\alpha$ beam the interference line from 211 ferrite lattice plane under seven ψ angle (0°, 13°, 18°, 27°, 33°, 39°and 45°) and 2θ between 150°and 162°. The diameter of the measurement spot was 1 to 2 mm. For evaluation of the measured interference lines the center of gravity method was applied. The residual stresses were then determined by means of sin2ψ method and following parameters:

- Elasticity constant: 1/2 S_2 = -6,08 x 10-6 mm^2/N
- Modulus of elasticity: 206000 N/mm^2
- Poisson ratio : 0.28

The data points were positioned at different locations in a line between the two welds as illustrated in Fig. 5.27. Unlike neutron-diffraction data points, these ones are only situated at the surface. Transverse and longitudinal strains are obtained.

Measurements were conducted once the sample AW-30 and once on this sample after milling the brace up to the top of the welds (see Fig. 5.33).

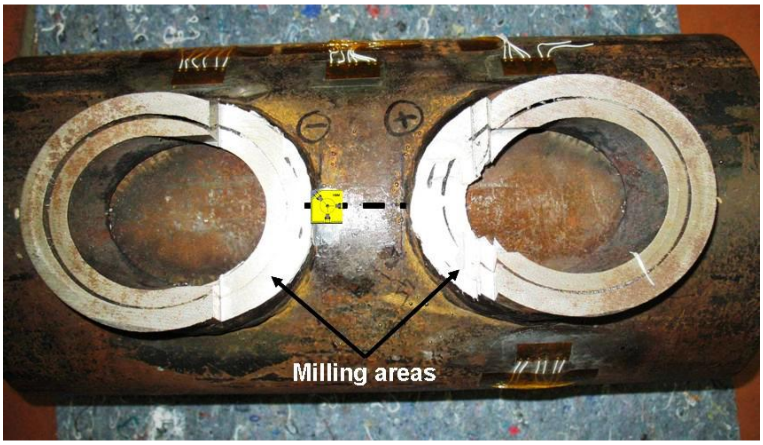

Figure 5.33: As-welded sample AW-30 after milling part of the braces.

5.4.2 Results and discussion

Results are shown in Fig. 5.34. It is seen that the milling do not particularly influence the residual stress distribution.

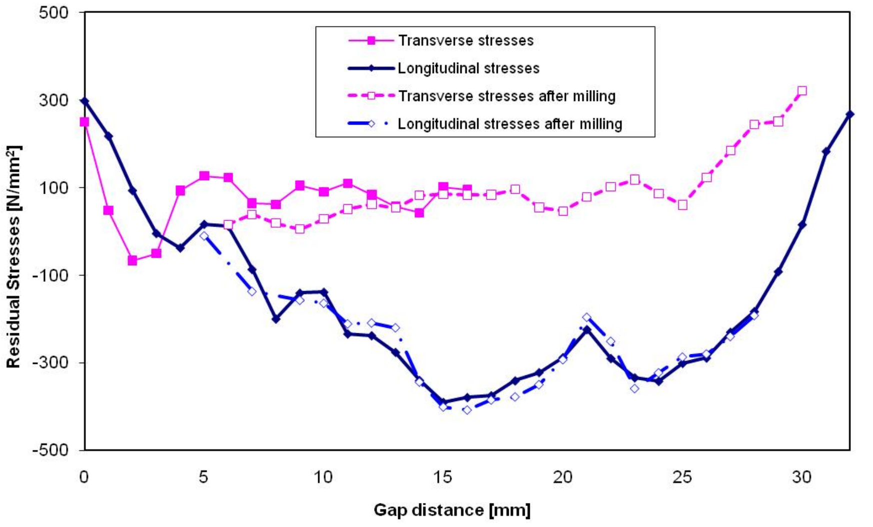

Figure 5.34: Tranverse and longitudinal residual stresses obtained using X-ray. Measurements were performed at the surface along the axial line in the gap on the as-welded sample AW-30.

Transverse residual stresses are still higher than longitudinal ones except in the weld toe region of one brace side. However, this effect in not confirmed on the other side, results are not symmetrical. The magnitude of residual stresses is drastically different from the one found by hole-drilling but quite in good agreement with the one obtained by neutron diffraction on the same sample (AW-30).

Results are discussed in more detail in the next section 5.5 by comparing measurements obtained using the three different methods.

5.5 Comparison between residual stresses obtained using hole-drilling, neutron diffraction and X-ray methods

In Figure 5.35, transverse and longitudinal stresses along the axial line in the gap are compared. Neutron diffraction points drawn in this figure were measured at a depth of 2 mm, as well as hole-drilling data points unlike x-ray results which were obtained at the surface (depth less than 0.025 mm).

Results are not in very good agreement between the three techniques. This discrepancy is partially explained as follows.

First of all, hole-drilling values seem to be higher than others especially in the weld vicinity region where residual stress reaches the value of the yield stress. However, it is well known that if residual stresses exceed 60% of the material yield stress, the accuracy of the hole-drilling measurement will decrease, explaining why values deduced from hole-drilling are even greater than 400 N/mm^2.

Concerning neutron-diffraction investigations, although few values are available for the 3rd series at PSI (FAT-30), one can argue that data points are shifted by approximately 200 N/mm^2 compared to the 2nd series (FAT-20), highlighting the fact that the residual stress magnitudes are decreased, especially on the first millimeters, when the wall chord thickness is increased (see Fig. 5.30 and 5.31). This trend seems to be confirmed by X-ray measurements which show some similarity with neutron diffraction values for sample with a 30 mm chord thickness. Note that measurements were not carried out at the same depth for X-ray method (depth less than 0.025 mm) and neutron diffraction method (2 mm depth).

Based on these results, neutron diffraction measurements seem to be more reliable because their accuracy is well-known and is not decreased for stress values close to the yield stress of the material.

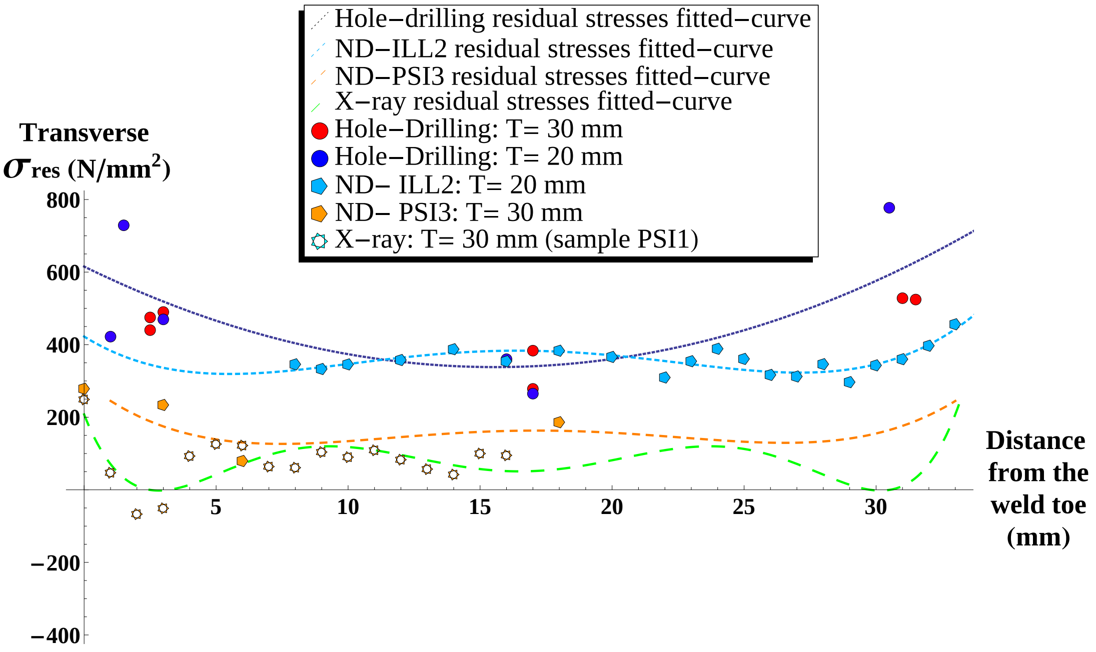

(a) Transverse direction

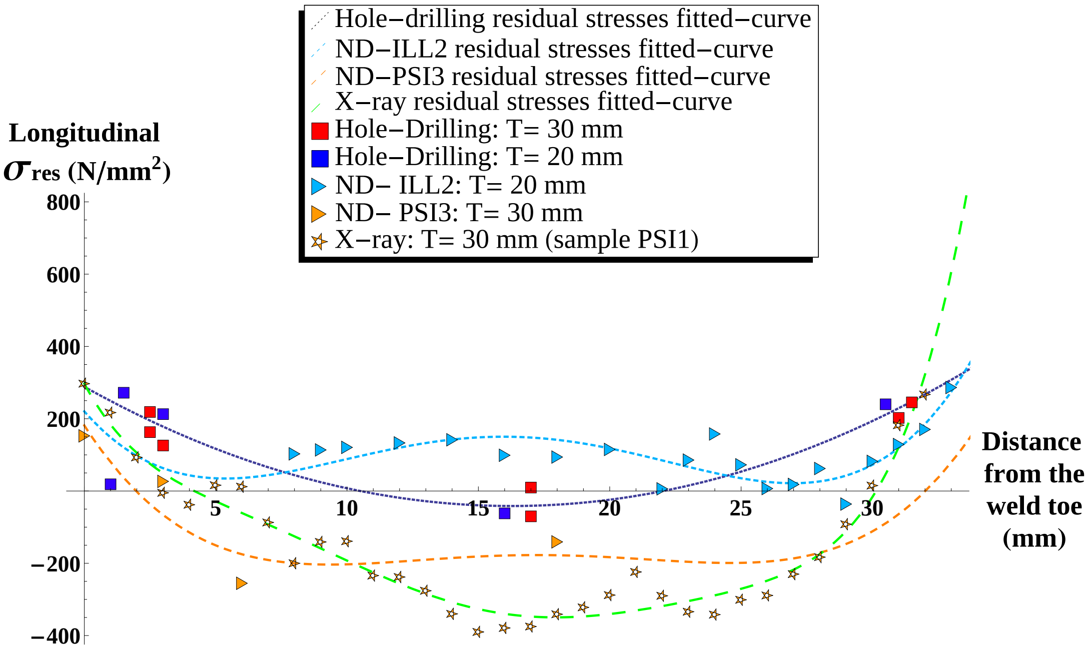

(b) Longitudinal direction

Figure 5.35: Comparison of residual stress distribution (hole-drilling, neutron diffraction and X-ray) along the axial line in the gap knowing that weld toes are situated at 0 and ∼ 33mm.

5.6 Summary and conclusions

Results show that residual stress magnitude reaches the yield strength of the S355J2H steel at the weld toe. At and near the surface, the greater residual stresses were critically oriented perpendicularly to the weld direction, which is also the orientation of the externally applied stresses. This finding has led to a drastically different residual stress orientation than found in the literature for pipe and pressure vessels tubes where residual stresses parallel to the weld direction are dominant. In addition, the restraining effect in-between the braces composing the joints created high perpendicular residual stresses in the gap region. The geometry of the K-joint creates both high applied stresses as well as, high residual stresses (from welding) which is critical for fatigue.

Neutron diffraction is a more powerful and reliable method than hole-drilling and X-ray methods to measure residual stresses but more demanding and costly.

Chapter 6

Fatigue experimental investigations

This chapter describes the two fatigue tests that were carried out on large-scale tubular truss beams (S6 and S7) to investigate the fatigue behavior of welded joints composing tubular structures. These tests were designed to qualify and quantify the influence of residual stresses on the fatigue behaviour, the size effect due to the chord wall thickness and the crack development under different cyclic applied load cases. These results should improve the knowledge on fatigue life estimation for welded K-joints and help designers to focus on the most significant parameters influencing fatigue life during the design process of new bridges or during the evaluation process of an existing bridge.

6.1 Introduction: strategy and objectives

The first goal of this study was to investigate the effects of tensile residual stresses on the fatigue behavior of K-joints. Since the shape of these joints is quite particular, the residual stress distribution may be more or less detrimental. The chosen strategy to separate the residual stress effect from the total internal stress effect was to focus on the behavior of joints loaded in compression where cracks can only grow under high tensile residual stresses. The idea was to study crack development in a joint composed of a chord loaded in compression, one brace loaded in tension and the other one loaded in compression. Then, the crack may initiate and propagate from the weld toe on the tensile or compressive brace side. If the crack propagates on the compressive side, it will give evidence of tensile residual stress effect and allows one to set this effect apart from external loads effect.

The second objective was to study the influence of a geometrical dimension or parameter having a strong size effect. This size effect is quite critical in tubular joint design because it tends to lower fatigue strength in thicker specimens (Zhao et al., 2000). The term of size effect is applicable to joints that have been proportionally scaled (with the same geometrical parameters) or non-proportionally scaled. The choice of this geometrical dimension was driven by the idea of finding a parameter which could influence both the geometrical size effect and technological size effect. By technological size effect, we do not mean the difference in steel quality between elements of different thicknesses but the difference in the residual stress distribution between thinner and thicker tube wall induced by the same welding process. The chord wall thickness T seems to produce this double effect. However, it is not straightforward to identify this effect.

On the first hand, by increasing the T thickness of a specimen keeping the same nominal and surface stresses, the stress concentration decreases less steeply underneath the surface of a thicker specimen. Hence, at the crack-like imperfection depth, the stress concentration value is higher in the thicker specimen. This is the geometrical size effect. On the other hand, increasing T obviously implies a decrease of nominal stresses. It has been previously shown (ARSEM, 1985; Schumacher et al., 2003) in offshore and bridge structures that it also causes a drop of stress concentration at the connection between chord and braces ($\gamma = \frac{D}{2T}$ and $\tau = \frac{t}{T}$ are the most significant parameters on stress concentration). Globally, by increasing T, one can lower stress concentration value at the imperfection depth in a non-proportional way and benefits of a longer fatigue life. This non-proportionality is linked with the geometrical size effect.

Furthermore, in welded structures made of plates and tubes, the residual distribution proposed is, most of the time, expressed as a function of b/T where b is the depth below the surface and T is the plate or tube wall thickness (Bouchard, 2007; Stacey et al., 2000; standard institute BSI, 2000). Indeed, an increased wall thickness T may result in a different position with the peak of residual stresses and then a different combination with applied stresses. We call it a technological size effect. For this reason, the upper and lower chord thicknesses were chosen to be different in each specimen S6 and S7.

To evaluate fatigue life under different load cases, fatigue tests were performed on large scale truss beams. They were preferred to isolated K-joints because they allowed us to combine, in a single specimen, joints loaded under different multi-axial applied stress fields either in tension or in compression. The size of the specimens represented approximately half to 2/3 of the size of real truss bridges. Hence, joints were manufactured and welded in the same conditions as bridge joints (see Section 4) ensuring to induce similar welding imperfections and residual stress distribution. As shown in Table 6.2, most of the joints geometrical parameters are within the range of currently built joints in order to collect reliable results which can be compared to real bridge data.

Except for the chord wall thickness which was altered, the dimensions of test specimens S3 and S5 (Table 6.2) previously tested in our laboratory were kept identical in order to benefit from previously obtained test results. Therefore, new data values may be compared with previous ones.

The test objectives and means to achieve them are synthesized in Table 6.1.

Table 6.1: Main objectives and means of fatigue investigation.

Objectives	**Means**
Quantify the effect of tensile residual stresses on the fatigue crack development (initiation, propagation: crack shape, propagation rate, stress intensity factor)	Monitor the fatigue crack growth of a joint located on the upper chord (chord loaded in compression). Compare the crack development at the weld toes in tension and compression.
Study the effect of tensile residual stresses on the fatigue crack development with another residual stress distribution	For the same joints located on the upper chord of specimens S6 and S7 but with different T dimensions, compare the crack development at the same weld toe position.
Qualify the influence of T on fatigue strength	For the same joints in specimens S6 and S7, compare the number of cycles corresponding to a fixed crack depth value as well as the crack shape.
Qualify the fatigue behavior in joints loaded under different load cases	Measure strains, deduce stresses and compare crack dimensions of geometrically identical joints, under different load conditions in the same chord.
Compare the fatigue behavior of joints tested with a large database of test results and with design curves	Calculate the hot-spot stress, plot the $S_{R,hs} - N$ points of test results (specimens S6 and S7, database specimens S1 to S5) in combination with the design curves (IIW design curves).

Table 6.2: Nominal dimensions (mm) and geometrical parameters for specimens series tested under fatigue loading (S1 to S7) and for real bridges.

		Nominal dimensions (mm)					Geometrical parameters						
Series joints/ bridge	**Number of spec.**	**Eccentr. e**	**Gap g**	**Chord** $D_{sup} \times T_{sup}$	**Chord** $D_{inf} \times T_{inf}$	**Brace d × t**	α $(\frac{2L_{ch}}{D})$	β $(\frac{d}{D})$	$\gamma_{sup}/\gamma_{inf}$ $(\frac{D}{2T})$	τ_{sup}/τ_{inf} $(\frac{t}{T})$	ζ $(\frac{g}{D})$	$\frac{e}{D}$	θ **(°)**
S1 *	4	20-28	20-29	I-beam	273 × 20	139.7 × 12.5	15.4	0.51	/6.83	/0.63	0.1	0.1	60
S2 *	4	50-55	54-60	I-beam	273 × 20	139.7 × 12.5	15.4	0.51	/6.83	/0.63	0.2	0.2	60
S3 *	4	28-39	31-44	I-beam	168.3 × 12.5	88.9 × 8	25.0	0.53	/6.73	/0.64	0.2-0.3	0.2	60
S4 *	4	*Geometrically identical to S1 and S2, but all joints were post-weld treated*											
S5 †	2	22	19.9	168.3 × 20	168.3 × 20	88.9 × 8	25.0	0.53	4.21/4.21	0.4/0.4	0.12	0.13	60
S6	1	32-39	32-39	168.3 × 20	168.3 × 30	88.9 × 8	25.0	0.53	4.21/2.81	0.4/0.27	0.23	0.23	60
S7	1	34-38	34-38	168.3 × 30	168.3 × 20	88.9 × 8	25.0	0.53	2.81/4.21	0.27/0.4	0.23	0.23	60
Antrenas FR-1994					arch 1200 × 32	508 × 16		0.42	/18.75	/0.5			
Aarwangen CH-1997				406 × 36-50	406 × 36-50	194 × 20-28	12.4	0.48	4.1-5.6	0.4-0.78			45
Lully CH-1997				508 × 25-50	508 × 25-50	267 × 11-25	14.0	0.53	5.1-10.2	0.22-1			60
Nesenbachtal GE-1999				324 × 16-80	324 × 16-80	194 × 10-60	19.5	0.60	2-10.1	0.63-0.75			46
Dättwil CH-2001				508 × 50	508 × 50	267 × 11-25	14.4-14.8	0.53	5.1	0.22-0.5			60
Korntal-M. GE-2002				457 × 45-65	457 × 45-65	267 × 28-45	16	0.58	3.5-5.1	0.62-0.69			60
St-Kilian GE-2006				I-beam	610 × 50-60	298.5 × 55-60	∼12.5	0.49	/5.1-6.1	1-1.1			∼60
Usual bridge values except for arches				300-700 × 10-80	300-700 × 10-80	100-300 × 10-60	10 - 20	0.4 - 0.6	3 - 12	0.2 - 1.1		0.2	40 -60

* Schumacher (2003).
† Borges (2008).

6.2 Experimental program

6.2.1 Fatigue test principle

Figures 6.1a and 6.1b depicts the test principle. The specimen is a planar tubular truss beam composed of welded joints. The test static system consisted of a simple beam standing on concrete blocks located under the extremities of its upper chord. A cyclic concentrated load was applied at the center of the upper chord with a load range of $\Delta Q = Q_{max} - Q_{min}$ and a load ratio $R = \frac{Q_{min}}{Q_{max}}$. The fatigue test was carried out under constant amplitude loading (ΔQ= constant).

The cyclic fatigue load Q was applied until the first crack propagated through the full thickness (corresponding to N_3, the number of cycles to through thickness cracking).

6.2.2 Description of specimens and test series

Two large scale tubular truss beams (8.6 m long and 1.8 m high) were tested under fatigue loading. Figure 6.1 depicts the main dimensions and the Circular Hollow Sections (CHS) chosen for the truss girders. The execution drawings from the steel manufacturer are given in annex A Fig. A.1 and A.2. The specimens fabrication and welding process as well as the material properties are described in Section 4.

Investigated parameter: T dimension

As shown in Table 6.2, the two specimens S6 and S7 were geometrically identical to each other except for the thickness T of their upper and lower chord (respectively 20 mm and 30 mm for S6, 30 mm and 20 mm for S7). The 20 mm chord wall was chosen to be identical to specimen S5. The 30 mm chord wall was selected to be, on one side greater than 20 mm, and on the other hand small enough to remain the critical hot-spot location in the chord (hot-spot 1, see Fig. 3) and not in the brace (hot-spot 11). The hot-spot 1 is the most common crack location encountered in K-joints.

Eccentricity between brace and chord axes

Each specimen was composed of two continuous chords with braces welded onto them. It has to be mentioned that in order to facilitate the welding process, braces did not overlap: a gap distance g was introduced between braces and chord weld toe. Hence, a positive eccentricity e was accepted between brace and chord axes.

A nominal gap value of g = 38.4 mm, corresponding to an eccentricity e = 38 mm was required for all specimens. The effective gap values, reported in Table 6.3, were measured on each specimen and the effective eccentricities were deduced. Since the gap distance is not the distance between the weld toes but between the brace outer walls at the chord crown toe (see Fig. in 6.3), it was difficult to measure it with a precision better than ± 5 mm.

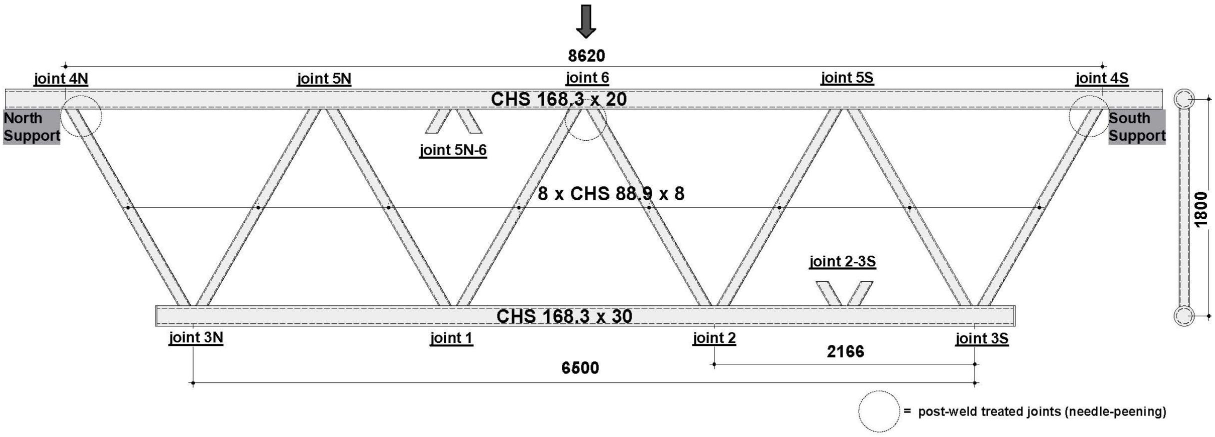
8620
joint 4N
joint 5N
joint 6
joint 5S
joint 4S
CHS 168.3 x 20
North Support
South Support
joint 5N-6
8 x CHS 88.9 x 8
1800
joint 2-3S
CHS 168.3 x 30
joint 3N
joint 1
joint 2
joint 3S
2166
6500
= post-weld treated joints (needle-peening)

(a) General configuration of the beam specimen S6 (dimensions in mm)

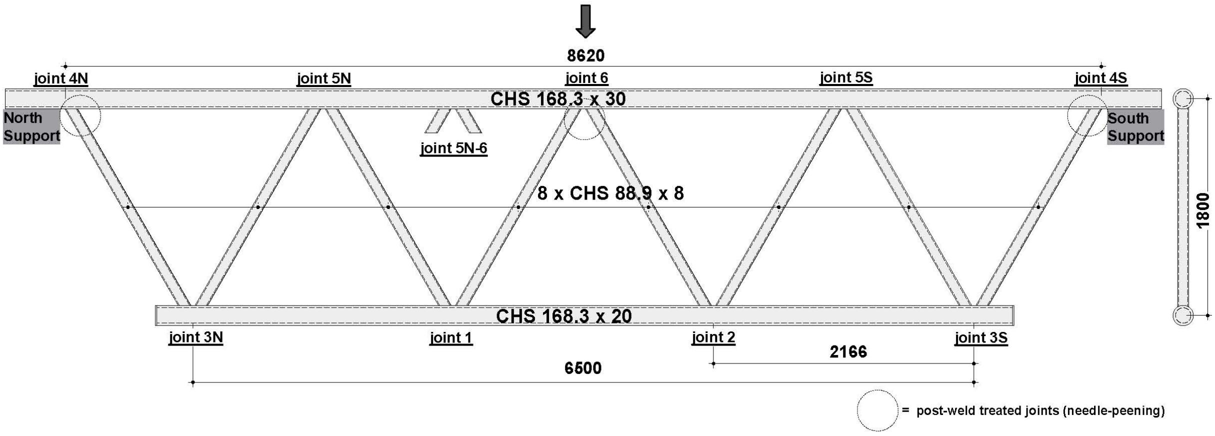
8620
joint 4N
joint 5N
joint 6
joint 5S
joint 4S
CHS 168.3 x 30
North Support
South Support
joint 5N-6
8 x CHS 88.9 x 8
1800
CHS 168.3 x 20
joint 3N
joint 1
joint 2
joint 3S
2166
6500
= post-weld treated joints (needle-peening)

(b) General configuration of the beam specimen S7 (dimensions in mm)

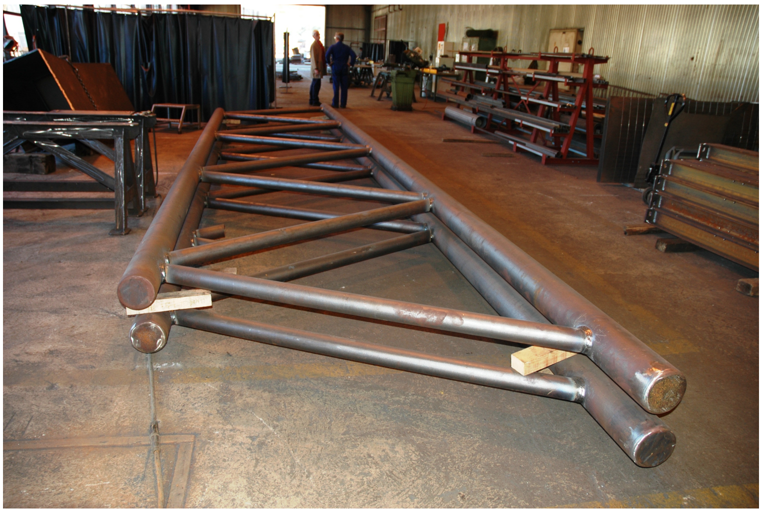

(c) Photo of the two truss beams at the steel factory

Figure 6.1: Overview of truss beam specimens S6 and S7 with main dimensions (in mm) and joint identification.

As-welded and post-weld treated joints

The joints located at the support positions and at the actuator position were to remain during these tests; they were post-weld treated by needle-peening in order to prevent early cracking and dangerous collapse during the tests (see Fig. 6.2). This technique aimed at introducing

Table 6.3: Measured gap values and deducted eccentricity values.

Joint	Gap g [mm]	Eccentricity e * [mm]	g/D	e/D	Notation
S6-3S	47	45	0.28	0.27	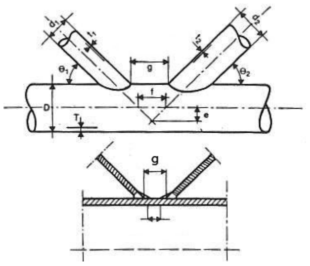 d1 t1 d2 t2 g θ1 θ2 f D e T g
S6-3N	48	46	0.29	0.28	
S6-1	45	44	0.27	0.26	
S6-2	47	45	0.28	0.27	
S6-5S	46	45	0.27	0.26	
S6-5N	49	47	0.29	0.28	
S7-3S	49	47	0.29	0.28	
S7-3N	43	42	0.26	0.25	
S7-1	43	42	0.26	0.25	
S7-2	44	43	0.26	0.25	
S7-5S	43	42	0.26	0.25	
S7-5N	49	47	0.29	0.28	

* e calculated based on $e = \frac{1}{2}(\frac{g \sin\theta + d}{\cos\theta} - D)$.

compressive residual stresses in the surface layer of the weld toe vicinity in order to increase the fatigue resistance of the treated joints. The rest of the joints were left as-welded, meaning that a total of six joints J3N, J3S, J1, J2 (on the chord loaded in tension) and J5N, J5S (on the chord loaded in compression) were likely to crack under fatigue loadings within a reasonable amount of testing time.

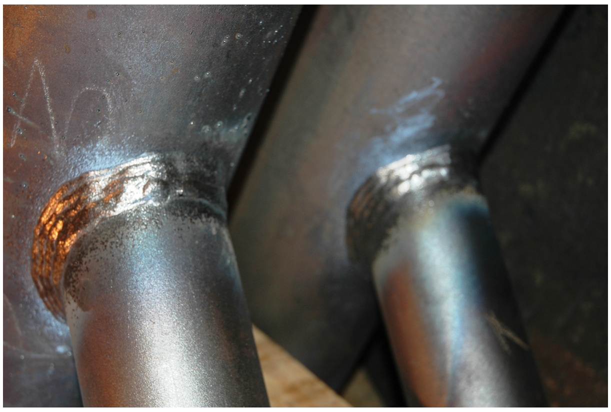

Figure 6.2: Joints J4S at support position after needle peening.

Non-destructive controls after the welding process

Before delivering the specimens, non-destructive controls such as magnetic particle testing and ultrasonic testing were carried out by the steel manufacturer conforming to EN 10204-3.1 in order to verify that no imperfections above the tolerance (weld quality B according to ISO 5817) were present.

Geometrical parameters of tubular bridges and test series

Four series S1, S2, S3 and S5 using similar specimens with different chord and brace CHS profiles (Table 6.2) were tested at ICOM's laboratory by Schumacher et al. (2003) and Borges (2008). However, series S1 to S4 were devoted to joints welded on the chord loaded in tension. In these series, tubular joints were bolted onto an I-beam upper chord.

Due to the fact that specimen's dimensions were in the domain of $\frac{1}{2}$ to $\frac{2}{3}$ of the real size of the bridge investigated, manufacturing and welding processes were carried out in the same way by the steel manufacturer. Although non-dimensional joint parameters β, γ, τ and θ of the test series are similar to those of real tubular truss bridges, the α parameter of test series S3 to S7 is almost the double of the real bridges parameters or, in other words, the slenderness of our specimens is greater than those of currently existing bridges. This difference, which may influence the bending to axial stress ratio, will be discussed further on in section 6.3.1.

Intermediate joints for residual stress measurements purpose

One can note the presence of intermediate joints which were not connected to the rest of the truss (see Fig. 6.3). These joints, called J2-3S and J5N-6 in Fig. 6.1a and 6.1b, were used to investigate residual stress distribution on non-cracked joints. Indeed, one can ensure that these joints were welded in the same conditions as the others and underwent the same fatigue loadings without any crack propagation since their braces were unloaded. Their residual stresses will be compared in Section 5 with those of an as-welded (untested) joint.

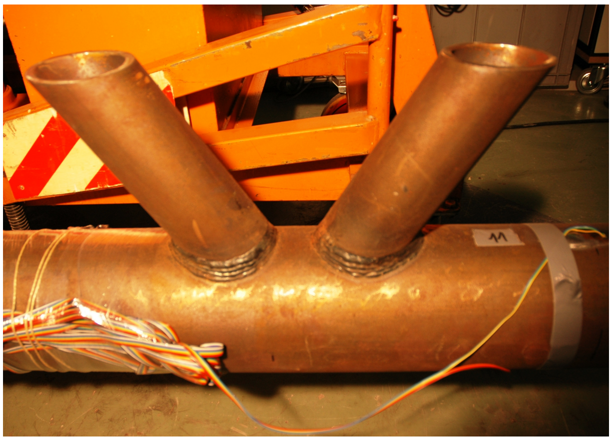

Figure 6.3: Particular joint with part of braces welded on the lower chord (specimen S6, joint 2-3S).

6.2.3 Test setup

The test setup is illustrated in Fig. 6.4. It was similar to the one used by Borges (2008).

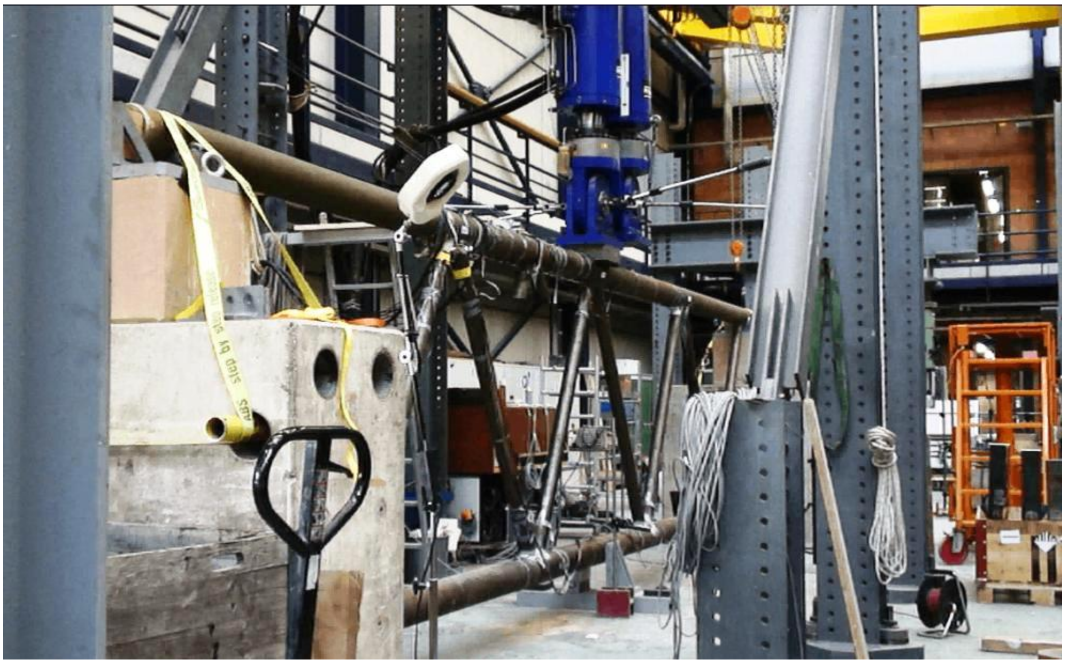

Figure 6.4: Photo of specimen S6 during the fatigue test.

A servo-hydraulic actuator Hydrel, shown in Fig. 6.5, was used to simulate fatigue loadings. It has a static load capacity of ± 1200 kN and a maximum stroke of 250 mm. The concentrated load was introduced by means of steel block which fit the outer chord surface. The same blocks were used under each end of the top chord, allowing the chord to move slightly in the longitudinal direction on its supports. The chord was also clamped vertically on its support.

The Hydrel actuator was controlled through an electronic steering device with a function generator: any amplitude force history can be introduced. For fatigue tests, the load control was required. The force value was constantly registered, compared with the imposed value and adjusted to fit the imposed load whatever the deflection could be. In addition, deflection limit-a relative vertical displacement of 0.5 mm - was entered to the actuator device in order to prevent dangerous collapse. During the experiments, this limit was reached once the first joint of each specimen developed a through-thickness crack.

Fatigue loads were applied with a constant load range of $\Delta Q = 549$ kN and a load ratio $R = \frac{Q_{min}}{Q_{max}} = 0.1$ (minimum load $Q_{min} = 61$ kN, maximum load $Q_{max} = 610$ kN). This load range was chosen to be identical to previously tested series S5. Chord nominal stress range and load ratio R are the same as for series S3 ($\Delta Q = 396$ kN but with T = 12.5 mm), series S5 and joints with a thickness T of 20 mm in series S6 and S7. Initially, the load range value was chosen high enough to ensure that some fatigue cracks occur in the specimen and that the through thickness cracking is reached for a number of cycles smaller than one million.

It was known from the $S_{R,hs}$-N curve for CHS joints (Zhao et al., 2000) that the constant amplitude fatigue limit -corresponding to the hot-spot stress range limit value under which no fatigue damage occurs- is comprised between 77 and 65 N/mm^2 for a chord wall thickness between 20 and 30 mm respectively. According to the fatigue strength curve obtained by Schumacher et al. (2003) for K-joints with different computation of SCF, the constant amplitude fatigue limit values were approximately of 58 N/mm^2 (20 mm chord wall) and 50 N/mm^2 (30 mm chord wall). The load range value was based on this later limit value while complying with the fact that bridges in-service are submitted to applied maximum nominal stress lower than the yield strength of the material. Therefore, the hot-spot stress range applied in tension and compression joints at location hot-spot 1 (see Fig. 3) were ranging from 85 to 285 N/mm^2 (absolute values).

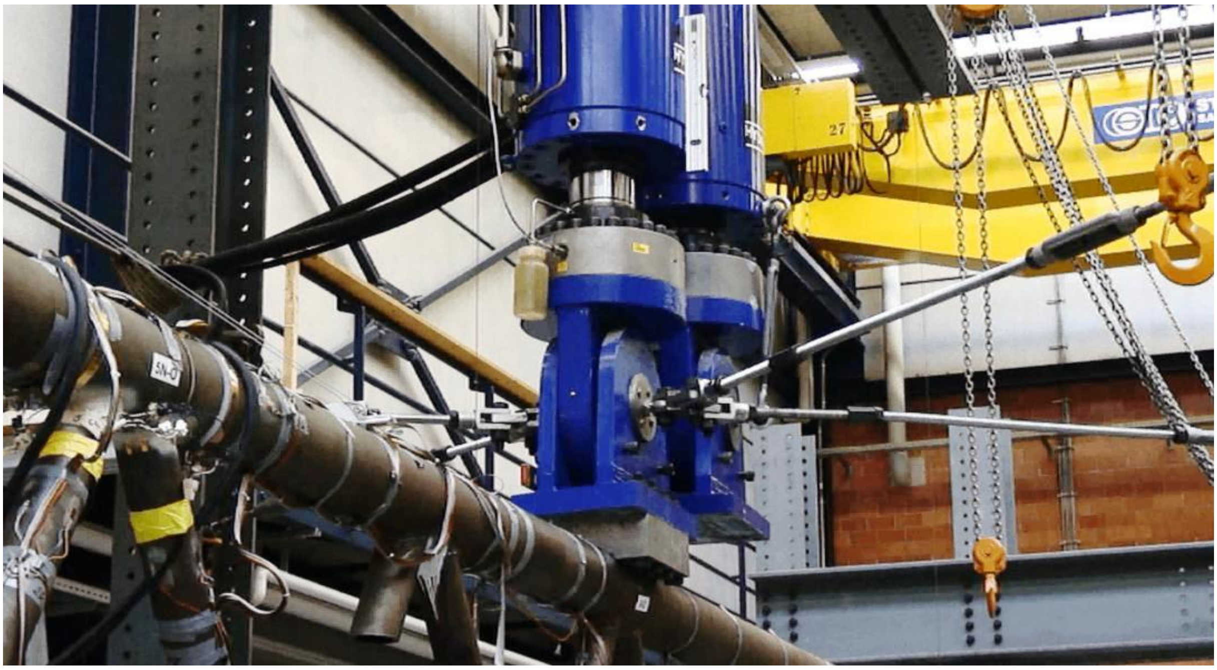

Figure 6.5: Actuator Hydrel 1200 kN for fatigue solicitation.

A load ratio of 0.1 was preferred to a null value due to the fact that imposing experimentally Q_{min}= 0 is never really feasible. The Q_{min} value should be slightly above 0 to avoid movements of supports.

The frequency of the sinusoidal fatigue load was selected to be 0.7 hz. It is well known that under environmental conditions (water, temperature,etc.), cyclic frequency has a strong influence on crack growth rate (Schijve and Broek, 1961; Shih and Wei, 1974). Since fatigue tests were performed in laboratory air under constant temperature and humidity, it is believed that the frequency value has no significant influence on crack propagation. The same observation can be made regarding the tubular bridges since the steel is protected from the environment by layers of paint. The frequency value was taken for practical reasons (reasonable fatigue test time, resonance frequencies avoidance, up to 0.7 hz the period was not long enough to let the actuator reach Q_{max} value).

As shown in Fig. 6.6, the lower chord of the truss was supported laterally by rigid plates covered with "Teflon" layers in order to avoid disturbing lateral displacements due to fabrication tolerances and possible lateral instability.

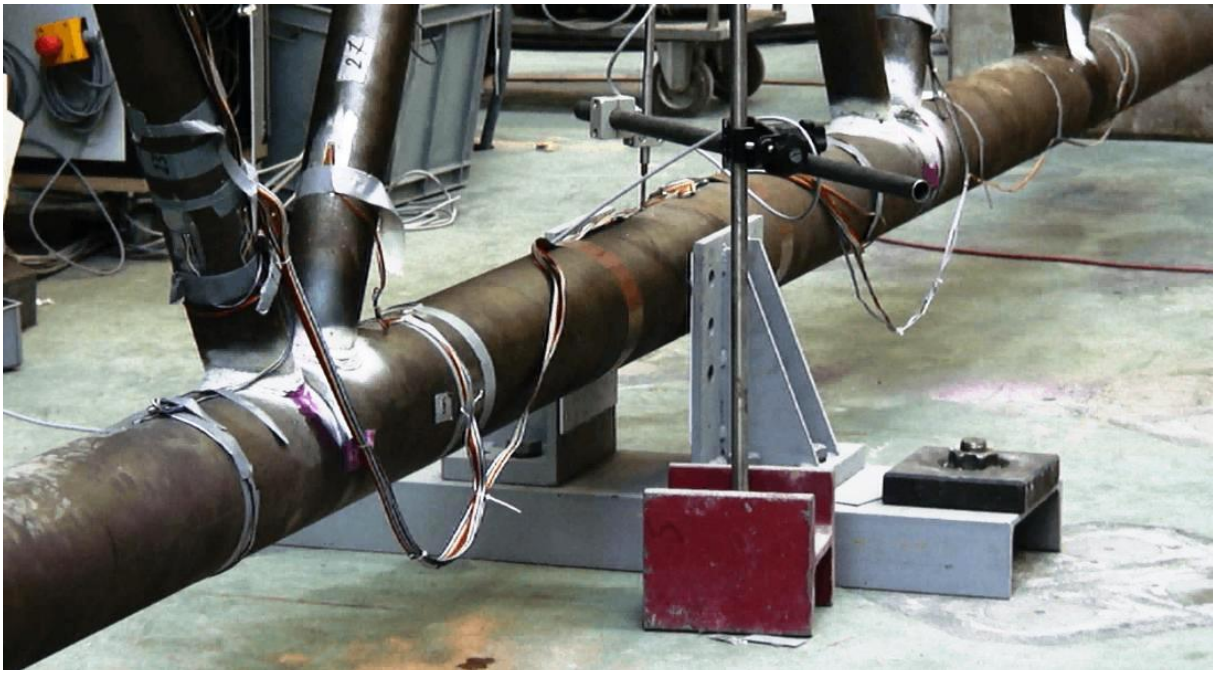

Figure 6.6: Lower chord supported laterally by plates covered with Teflon.

6.2.4 Test procedure

Tests were divided into two alternatively repeated steps: a static test and a fatigue test. The procedure is summarized hereafter in Table 6.4

Table 6.4: Test procedure applied for the first and second tests on specimens S6 and S7 respectively.

Initial static test	**Static procedure:** - Load Q increased up to Q = 180 kN (30% Q_{max}) and then back to zero (load increments of 20 kN between 0 and Q_{min}=61 kN, and of 60 kN between Q_{min} and 180 kN) → load cell actuator measurements → strain gauge measurements → deflection measurements under the bottom chord of the truss (Linear Variable Displacement Transducer LVDT) - Load Q increased up to Q_{max}=610 kN and back to zero (load increments of 60 kN achieved in 5 sec, wait 10 sec at each stage) → same static measurements than above **First fatigue cycles applied (around 100)** **Static procedure**
Fatigue test	**Fatigue procedure:** - Load cycles applied (between Q_{min}=61 kN and Q_{max}=610 kN, R=Q_{min}/Q_{max}=0.1 and f=0.7 hz) → measurement of crack depth versus number of cycles using Alternating Current Potential Drop (joint S6-5N for the first test, joints S7-5N and S7-1 for the second test)
Static test + **Non destructive examinations** (at N=49000 cycles for S6, N=46000 cycles for S7)	**Static procedure** - Crack detection → dye penetrant/magnetic inspections (beam unloaded) or alcohol based liquid sprayed during cyclic loading.
Fatigue test	**Fatigue procedure**
Static test + non -destr. examinations (at N=90000 cycles for S6, N=85000 cycles for S7)	**Static procedure** → ink marking
Fatigue test	**Fatigue procedure**
Static test + non -destr. examinations (at N=140000 cycles for S6)	**Static procedure** → beach marking
Fatigue test	**Fatigue procedure**
Static test + non -destr. examinations (at N=180000, 200000 and 230000 cycles for S6)	**Static procedure** → visual control of crack propagation

During the initial static test, strain measurements at different load increments confirmed the linearity of the specimen responses.

Thereafter, the one hundred cycles applied to the specimen were aimed to observe some residual stress redistribution and relaxation (shakedown effect). However, strain measurement registered after the second loading step did not show any noticeable difference.

6.2.5 Measurement equipment

The two specimens were equipped with several monitoring techniques:

- ***Uni-axial strain gauges and displacement transducer (static test meas.)***

  As shown in Fig. A.4 and A.5, forty six uni-axial strain gauges (120 Ω) with a grid length of 10 mm were glued on truss members in order to measure the nominal strain member distribution under static loadings. It comprises axial strain (ax), in-plane bending strain (ipb) and out-of-plane bending strain (opb). The last ones being most of the time negligible. With one pair of gauges glued on the outer surface of tubes in the plane of the truss, it is possible to deduct the axial strains and in-plane bending strains. One or two supplementary gauges positioned out-of the truss plane let us know the out-of-plane strains. Positioning two groups of gauges along a truss member between two nodes provides the linear variation of the in-plane bending strains along the member. Then, strains can be linearly extrapolated to the joint of interest. Half of the truss was significantly instrumented by strain gauges whereas, on the other half, only few gauges were disposed to control the strain symmetry between both sides. Moreover, additional gauges were placed around the intermediate joint (Fig. 6.3) in order to verify that no stress deviation occur.

  The gauges were placed as close as possible to the joint, at fixed distances from it (1.9D on the chord and 2.2d on the brace members). These distances have been investigated by Schumacher (2003) in order to ensure that they were positioned far enough from the joint to avoid the stress perturbation due to geometry change. It was shown that, even though these distances were smaller than the recommended 3D and 3d (van Wingerde, 1992), they are still in the region not perturbed by the joint.

  Deflection measurements were conducted using a standard LVDT (Linear Variable Displacement Transducer) situated under the mid-length of the bottom chord. During static tests, deflection was registered a HBM's MGCplus data acquisition system at the same time than applied load (actuator load cell) and strains.

- ***Penetrant and magnetic non-destructive examinations (static test meas.)***

  Magnetic inspection consists of putting some liquid containing ferrous particles at the surface of a specimen and subjecting it to a magnetic field. The magnetic field is created using an AC Tiede TWN 220N device creating an alternating current with a frequency of 50-60 Hz. The applied magnetic field strength is 15-20 A/cm. The presence of a crack or a crack-like imperfection at the surface allows the magnetic flux to leak. Therefore, the particles are concentrated in the area of leakage, underlining the position of the crack. In the dye penetrant technique, a penetrant is applied to the surface of the specimen. The penetrant penetrates in the cracks and surface imperfections. Therefore, after removing the excess of penetrant from the surface, a developer is able to reveal the penetrant remaining at the surface imperfections. Alcohol based liquid was also sprayed during cyclic loading. In presence of a crack, the alcohol can be detected because it goes in and out when crack opens and closes.

  These techniques were used to detect the first crack during fatigue testing (see Fig. 6.7).

- ***Ink and beach marking (fatigue test meas.)***

  Ink and beach marking (see Fig. 6.8) allowed us to mark the crack shape after a given number of cycles. Both types of marks were investigated once the cracks were opened. Ink marking is obtained by spraying alcoholic ink into a crack, then by imposing some cycles in order to help the penetration of the ink and finally by letting the ink dry in the crack opened position. In series S6 and S7, joints 3N, 3S, 1 and 2 were ink-marked after 90000 cycles. Beach mark is the mechanical way to mark the crack front by changing some fatigue

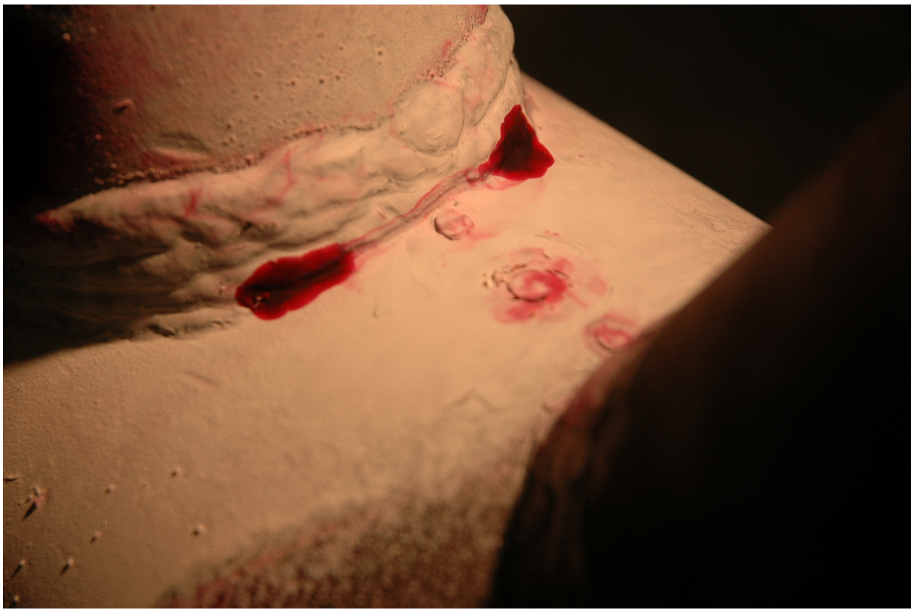

Figure 6.7: A crack revealed (in red) by the dye penetrant technique.

loading characteristics. In our case, following Husset et al. (1985) recommendations, the maximum load was kept identical with a load amplitude divided by two, meaning that maximum and minimum fatigue loads were Q_{max}=610 kN and Q_{min}=335 kN. This loading cycle was applied during 10000 cycles, and taken into account in the fatigue cycle counting as 1250 cycles ($(1/2)^3$x10000cycles). Since a second ink marking can wash the mark made by the first one, beach-marking is often used as a second marking method. Indeed, joints 3N, 3S, 1 and 2 of the specimen S6 have been beach-marked after 140000 cycles. Since the fatigue test for specimen S7 ended before reaching 140000 cycles, no beach-marking was made for this specimen.

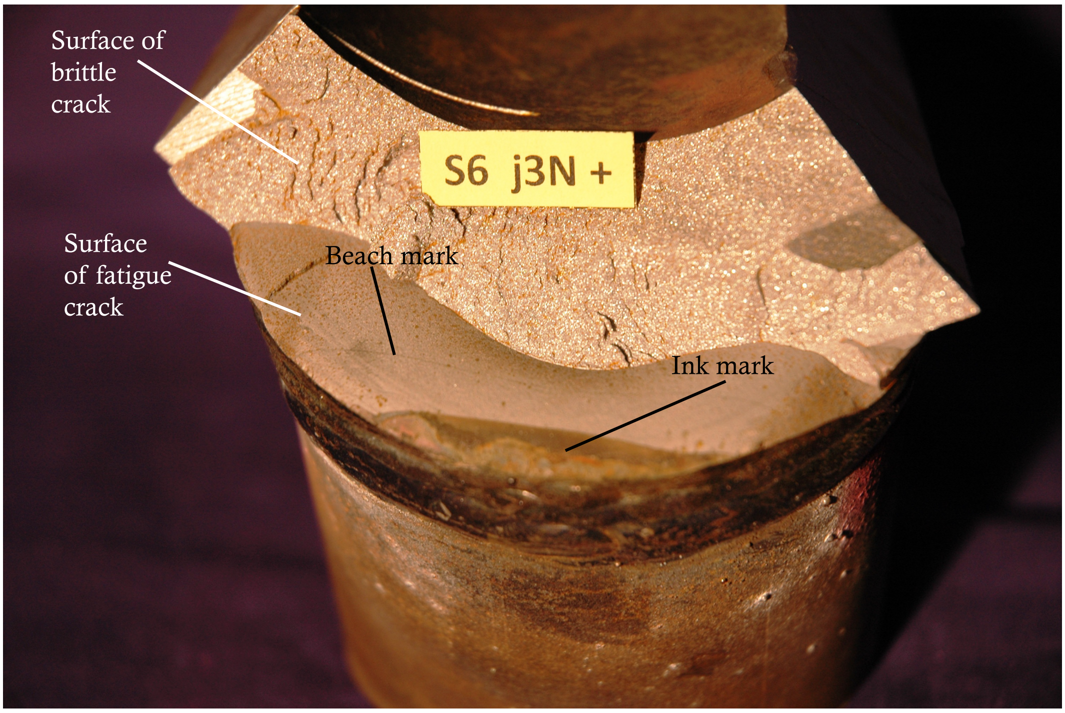

Figure 6.8: Ink mark and beach mark visible on a crack opened after testing.

◆ ***Crack opening (after testing)***

After testing, cracks were opened. The crack opening procedure consists in freezing the joint sample in liquid nitrogen in order to break it in a brittle manner under dynamic loading using an actuator. The surface texture being different between the fatigue crack and the brittle crack, it is easy to measure the final fatigue crack dimensions. As shown in Fig. 6.8, the bright granular area is typical of brittle fracture whereas the smooth area is the fatigue crack region (friction of the bottom and top of the crack).

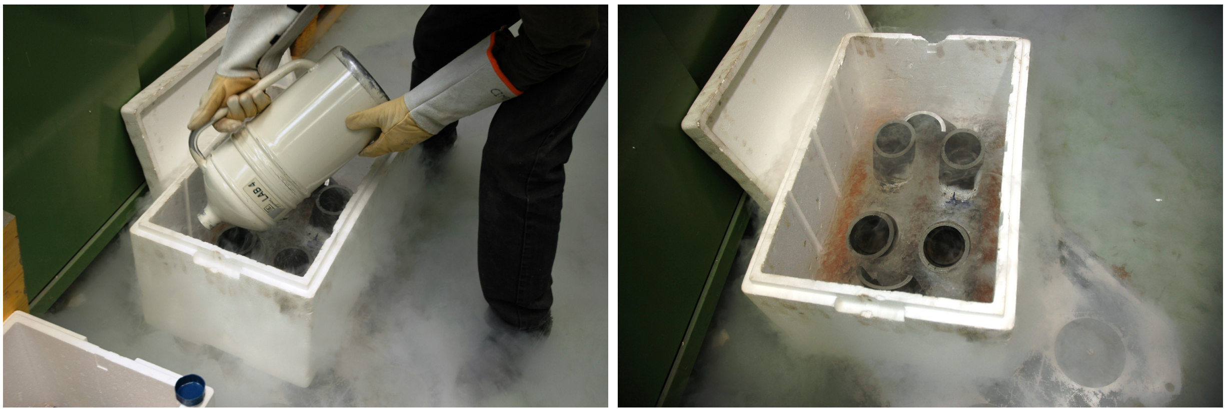

(a) Liquid nitrogen poured on cut joint samples **(b)** Liquid nitrogen boiling

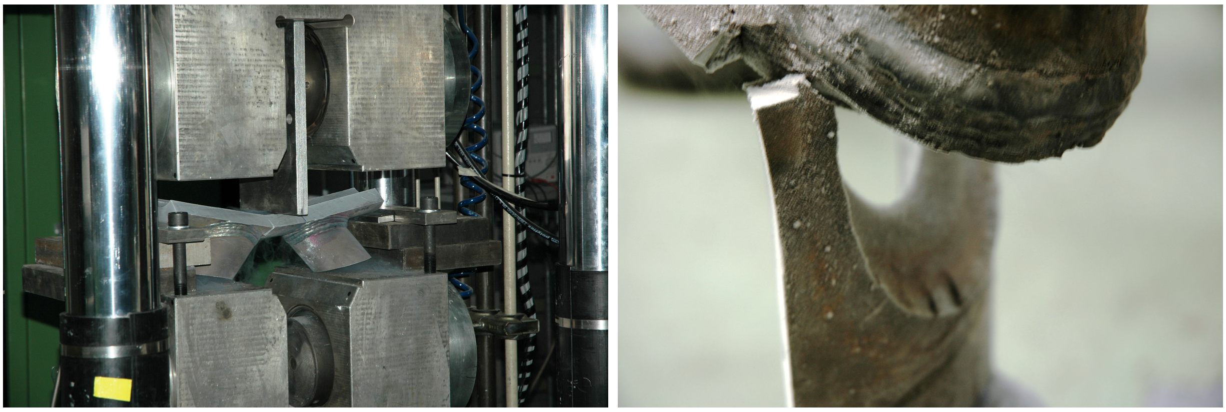

(c) The freezed sample broken under the actuator **(d)** Crack opened

Figure 6.9: Crack opening using liquid nitrogen.

◆ ***Alternating Current Potential Drop (fatigue test meas.)***

Alternating Current Potential Drop (ACPD) is a well-known method to follow the crack depth evolution during a fatigue test (Dover and Holdbrook, 1980; Dover and Monahan, 1994). This non destructive technique is based on the property of alternating current to flow on a thin layer close to the surface (skin effect) of electrical conductive materials (Chiew et al., 2004; Matelect, 2006). Note that this skin effect is not possible with the Direct Current Potential Drop DCPD. Therefore, with ACPD, when the skin current encounters a crack, it goes down and up along crack faces (see Fig. 6.10). The main difficulty of this technique is to place the probes at the location where crack will initiate. For K-joints, this difficulty is minimized because crack always initiate at hot-spot position on the weld toe.

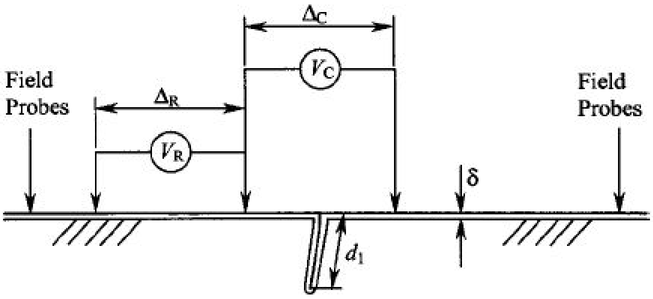

Figure 6.10: ACPD technique: δ is the skin current thickness, $\mathrm{d_1}$ is the crack depth at probe 1 location, $\mathrm{V_R}$ and Δ_R are respectively the reference potential drop and the reference probe distance, $\mathrm{V_c}$ and Δ_c are respectively the potential drop and the probe distance across the crack (Chiew et al., 2004).

The potential drop between two probes is proportional to the distance covered by the current between these probes:

$$V_R \propto \Delta_R \tag{6.1}$$
$$V_c \propto \Delta_c + 2d \tag{6.2}$$

The main dimensions and parameters describing a crack are defined in Fig. 6.11 and as follows:

- ◇ d is defined as the measured depth of a crack (at probe location) in the crack plane.
- ◇ a is the depth of a crack at the deepest point in the crack plane.
- ◇ 2c is the length of a crack.
- ◇ $\mathrm{d_z}$, $\mathrm{a_z}$ are respectively d and a distances projected to the vertical axis z (or chord radial axis).
- ◇ Φ is the crack angle with the vertical axis at the beginning of the crack growth.

Note that d is not the deepest point along the weld toe, it is the value measured at the probe position.

As a consequence, it is possible to calculate the crack depth in the crack plane of any surface crack occurring between the probes based on ACPD measurements as follows:

$$d = \frac{\Delta_R}{2}\left(\frac{V_c}{V_R} - \frac{\Delta_c}{\Delta_R}\right) \tag{6.3}$$

This relation is only directly applicable to an infinite long crack. Considering a semi-elliptical crack in tubular joint, a modification factor should be applied to take into account the two-dimensional shape of the crack. A factor with values ranging from 1.05 to 1.1 has been shown to be sufficient for crack depth estimation in low aspect ratio fatigue crack, $\frac{\mathrm{d}}{\mathrm{2c}} \approx 0.1$ (Dover and Monahan, 1994).

In our experiments, the probe distances Δ_c and Δ_R are the same values. Probes were positioned with a distance of the order of 4 mm across the demarcation line between the weld and the chord surface, and close to detected imperfections. Due to the geometry of the joint, this line is not perfectly drawn and the probe distance can vary. That is the reason why, independent measures were taken for each probe. The reference potential drop values V_R are the first V_c values obtained on the joint before any cracking occurred.

From the previous equation, the crack depth variation for a given number of cycles can be calculated as:

$$\Delta d = d_{N+\Delta N} - d_N = \frac{\Delta_R}{2}\left(\frac{V_{c,N+\Delta N}}{V_R} - \frac{V_{c,N}}{V_R}\right) \tag{6.4}$$

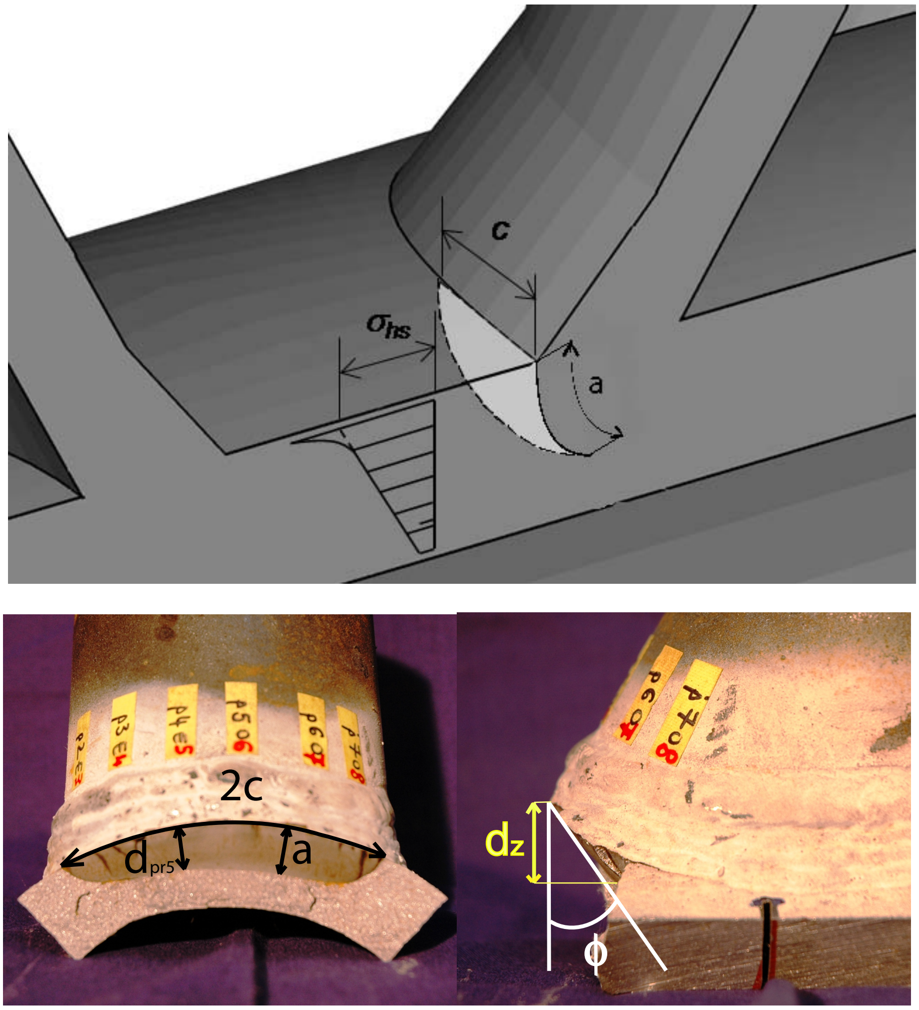

Figure 6.11: Nomenclature to describe a crack: 2c is the crack length , a is the crack depth at the deepest point, d is the crack depth measured at probe location (probe 5 in this figure), d_z is the projection of d on the vertical axis, Φ is the starting angle. d is defined as the measured depth of a crack (at probe location) in the crack plane.

Then, the crack propagation rate can be estimated as $\Delta d/\Delta N$ and the experimental stress intensity factor ΔK is deducted from the Paris law:

$$\Delta K = \left(\frac{1}{C}\frac{\Delta d}{\Delta N}\right)^{\frac{1}{m}} \tag{6.5}$$

where $C = 2 \times 10^{-13}(\mathrm{mm/cycle})(\mathrm{N/mm}^{3/2})^{\mathrm{m}}$ and $m = 3$ according to Gurney (1979) for ferrite steels. These constant values have been previously shown by Borges (2008) to give good results.

The ACPD equipment prototype used during the test is illustrated in Fig. 6.13b. It produces a current with a frequency of 5 Hz and an intensity of 75 A. HBM's UPM 100 Multipoint Measuring Unit was used to continuously record the potential drop and capture the crack evolution during cyclic loading. Usually ACPD equipments are used with high frequency (1 to 10 kHz) in order to ensure that a thin skin current is produced. The skin thickness or the skin depth δ is calculated as follows (Saguy and Rittel, 2005):

$$\delta = \frac{1}{\sqrt{\pi \ \mu_r \ \mu_0 \ \sigma f}} \tag{6.6}$$

where
μ_r is the relative magnetic permeability
μ_0 is the magnetic permeability of free space
σ is the metal conductivity
f is the current frequency.

In our case, at a frequency of 5 Hz, the studied S355 steel has a skin depth of 4 mm approximately ($\mu_0 = 4\ \pi 10^{-7}$ H/m, $\mu_\mathrm{r} = 500$, $\sigma = 5.810^6$ S/m (Blitz, 1997)). For a frequency of 5 kHz, this skin depth value would be of 0.1 mm. The 4 mm depth is so large compared to the chord wall thickness or to the crack depth (ratio < 10) that the problem is considered as a **thick skin** case. However, previous equations are only valid for thin skin cases, therefore the equations should be adapted according to Saguy and Rittel (2005). The global solution proposed by Saguy and Rittel (2005) to predict crack depth for all cases from thin to thick skin problems was applied. The resulting crack depth was increased by 20% compared to the crack depth obtained for the thin skin case (see equ. (6.3)).

The ACPD crack depths were compared to the final values determined once the cracks were open using liquid nitrogen. Some discrepancies were observed between results (80% difference) that can be resolved by a proper calibration. These discrepancies in the results could be due to the perturbations of the potential gradient around the crack area. For thick-skin problems, this perturbation occurs at distances of the order of crack depth (Lugg et al., 1988). Since the probe distance is small, the measurements were done in this perturbated area except when the crack was really small. Furthermore, the crack is inclined which may have produced an asymmetry into the surface voltage. These phenomena are depicted in Fig. 6.12.

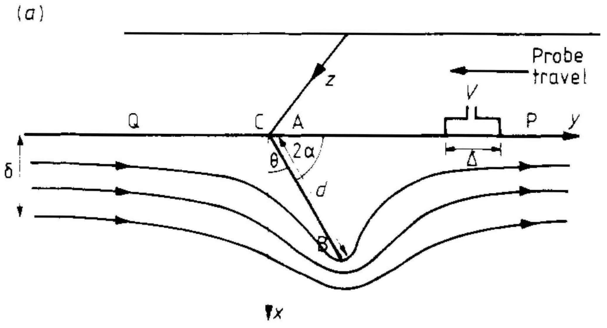

Figure 6.12: Thin skin case: perturbation area of the potential drop due to the presence of an inclined crack (Lugg et al., 1988).

The open-crack and ACPD results were used in a regression analysis to generate a calibration curve. The real crack depth d^* (from crack opening) is expressed in function of d, the ACPD crack depth. d^* is not exactly the crack depth. It is the crack propagation depth since the ACPD is calibrated on joints containing imperfections. The depth of imperfection, not included in d^*, is approximately 0.1 mm.

$$d^* = 1.85\ d \tag{6.7}$$

All results presented below have been corrected with the calibration coefficient (symbolised with *).

Joint 5N (see Fig. 6.13) of specimen S6 was equipped with 8 probes, joints 2 and 5N of specimen S7 with respectively 3 and 5 probes.

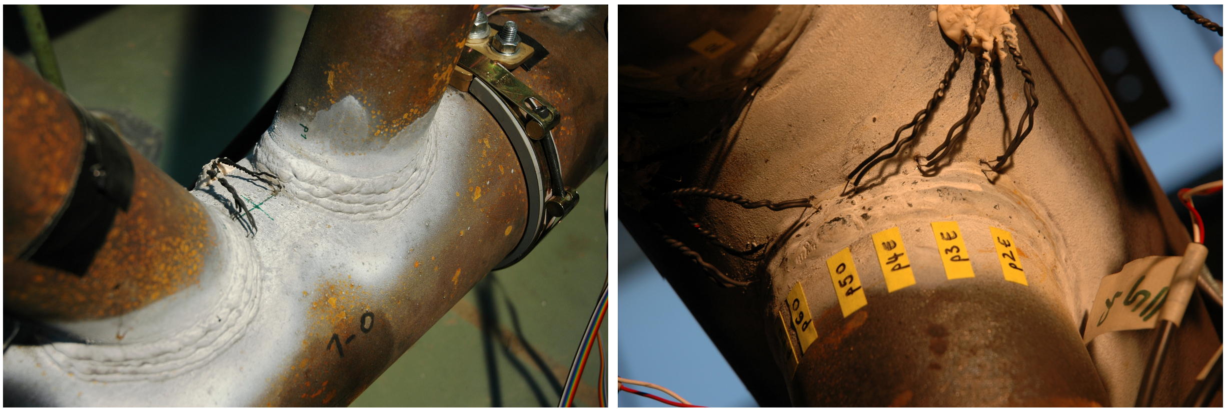

(a) Voltage probes and field probe in joint S7-1 **(b)** Voltage probe positions for joint S6-5N

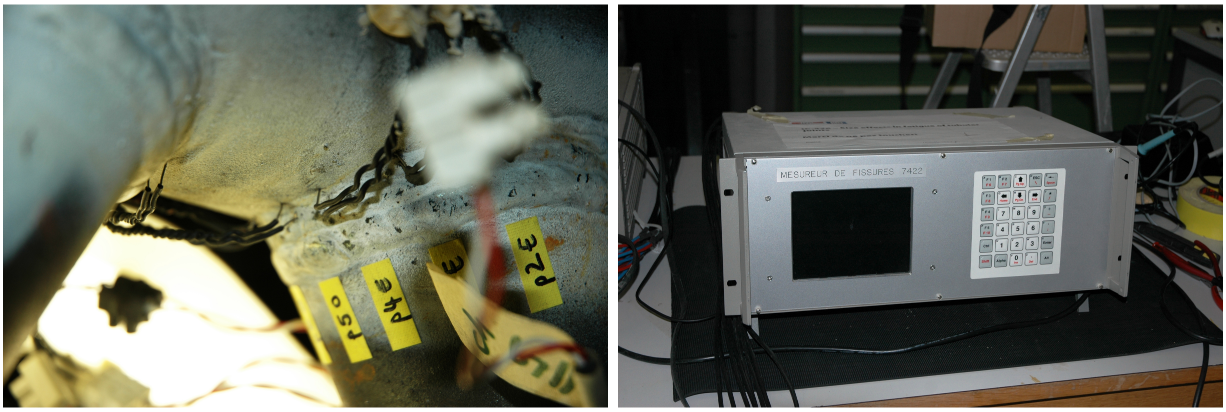

(c) Zoom on voltage probes (joint S6-5N) **(d)** Crack measurement acquisition box

Figure 6.13: Alternating Current Potential Drop equipment.

6.3 Measurement results and interpretations

6.3.1 From strain and deflection measurements

First static verifications

The first static test measurements, mostly done during initial static tests, let us verify the **linearity** of strain and deflection response at different load increment under consecutive loading/unloading tests. The difference in strain values between loading and unloading steps were usually within 5% except for some rare values. These results seemed to be acceptable to validate the response linearity.

Strain values between gauges were compared for the applied load range $\Delta Q = Q_{max} - Q_{min}$. Subtraction of measurement values (under Q_{max} and Q_{min}) corrects repeated errors in strain measurements obtained when some gauges were not automatically reset to zero. The first aim of this comparison was to verify the assumption of **symmetry** made to minimize the gauge number. Strain measurement results acquired under Q_{min}, Q_{max} and ΔQ are given in Tables A.1, A.2, A.3 for S6 and in Tables A.4, A.5, A.6 for S7.

Strain values registered by symmetrical gauges, for instance gauges 5 and 9, should be approximately identical (see Fig. A.4). Results were quite surprising: symmetrical gauges positioned on the lower chord side were in good agreement (difference less than 2 %) whereas on the upper chord side an average difference of 12% was systematically found (gauges 35-36-37-38 vers gauges 43-44-45-46). This effect occured for both specimens S6 and S7.

Therefore, additional gauges were glued on the upper chord of specimen S7 in order to investigate this problem. It was shown that this asymmetrical effect, arising only for in-plane and out-of-plane bending, increase from the actuator position to the support position. After looking for different possible explanations such as asymmetry in support positions, initial distortion of the upper chord, loss of joint rigidity due to cracking, discrepancies in gap distances, differences between brace and chord angle, discrepancies in chord wall thicknesses, etc. None of these assumptions were satisfactory. Finally, it was found that the problem comes from a misalignment between support positions and the actuator loading position, meaning that the concentrated load was not applied perfectly vertically, increasing bending stresses close to the upper chord supports.

Since the main part of the test was done when this effect was identified, it was too late to correct it. For future similar tests, one should pay attention to this alignment which may change non negligibly the bending stresses.

Strain values were also studied to quantify the out-of-plane bending. For instance, gauges 6 and 8 gave information on the axial (ax) and **out-of-plane bending (opb) strains**. From gauges 6, 8, 36, 38, 44, 46 (chord meas.) and 18, 21, 24, 26 (brace meas.), it was seen that strain due to out-of-plane bending represent in average 5% of axial strain in chord and brace members under ΔQ load for both specimens.

Therefore, we have verified that out-of-plane bending strains were small which was to be expected for a planar truss loaded in its plane. For the rest of this study, opb strains will be neglected and only axial and in-plane bending strains are relevant.

Strain and deflection evolution during tests

Tables A.1 A.2 A.3 A.4 A.5 A.6 show also strains and deflection measurements registered during static tests periodically carried out at different number of cycles.

It is clear from deflection measurements (LVDT or stroke's actuator) that the truss deflection was identical all along the tests (average value of 9.2-9.3 mm for both specimens under $\Delta Q =$ 550 kN) even when through-cracking was achieved. Therefore, the global truss rigidity was not influenced by the number of cycles until through-crack occurred.

The presence of cracks did not influence much the strain values except in the braces loaded in tension of joints 1 and 2. Indeed, in these joints with deep cracks, there is a redistribution of strains from the brace crown toe to the brace crown heel (from gauges 25 to 23, and 31 to 32).

Strain extrapolated at the weld toe

As explained above, measured strains were mainly composed of axial (ax) and in-plane bending (ipb) strains. Axial strains are constant along members between two joints whereas in-plane bending strain may vary linearly over length of members. Therefore, knowing strain values of two groups of gauges along a truss member between two nodes (outside the joint perturbation area) enables to extrapolate in-plane bending strains at the weld toe (critical point). Thus, ε_{ax} and ε_{ipb} were determined for each joint at the weld crown toe situated on the tension brace (hot-spot 1) or on the compression brace (hot-spot 1c).

Strains $\varepsilon_{\mathrm{ax-br}}$, $\varepsilon_{\mathrm{ipb-br}}$ were based on measurements on brace members (br) and $\varepsilon_{\mathrm{ax-ch}}$, $\varepsilon_{\mathrm{ipb-ch}}$ on measurements on chord members (ch). The total idealized nominal strain ($\varepsilon_{\mathrm{nom}}$), inducing cracking at the weld toe, was calculated through a summation of all these strains ($\varepsilon_{\mathrm{ax-br}}, \varepsilon_{\mathrm{ipb-br}}, \varepsilon_{\mathrm{ax-ch}}, \varepsilon_{\mathrm{ipb-ch}}$) at hot-spots.

Strain results, for S6 and S7 joints, are reported in Table 6.5. They were deducted from average strain measurements given in Tables A.3 A.6 under $\Delta Q = 550$ kN.

Table 6.5: Strains extrapolated at crown toes (hs1 or hs1c) for as-welded joints, $\Delta Q = 550$ kN.

Joint	**Tension brace**			**Compression brace**			**Chord side T. brace**			**Chord side C. brace**		
	$\Delta\varepsilon_{ax-br}$ [10^{-6}]	$\Delta\varepsilon_{ipb-br}$ [10^{-6}]	$\Delta\varepsilon_{nom-br}$ [10^{-6}]	$\Delta\varepsilon_{ax-br}$ [10^{-6}]	$\Delta\varepsilon_{ipb-br}$ [10^{-6}]	$\Delta\varepsilon_{nom-br}$ [10^{-6}]	$\Delta\varepsilon_{ax-ch}$ [10^{-6}]	$\Delta\varepsilon_{ipb-ch}$ [10^{-6}]	$\Delta\varepsilon_{nom-ch}$ [10^{-6}]	$\Delta\varepsilon_{ax-ch}$ [10^{-6}]	$\Delta\varepsilon_{ipb-ch}$ [10^{-6}]	$\Delta\varepsilon_{nom-ch}$ [10^{-6}]
S6-3S	767 [*]	256 [*]	1023	-767 [*]	-256[*]	-1024	0 [*]	0 [*]	0	123	-104 [*]	19
S6-3N	767 [†]	256 [†]	1023	-767	-256	-1024	0 [‡]	0 [‡]	0	130	-104	26
S6-1	733	151	883	-710	10	-700	114	-14	100	245	-131	114
S6-2	720	151 [*]	871	-710 [*]	10 [*]	-700	123	-14 [*]	108	244	-133	111
S6-5S	720	260 [*]	980	-775 [*]	-281 [*]	-1056	-269	11 [*]	-258	-67 [*]	-140 [*]	-207
S6-5N	733	260	993	-775	-281	-1056	-273	11	-262	-67	-140 [‡]	-207
S7-3S	769 [*]	290 [*]	1059	-769 [*]	-290 [*]	-1059	0 [*]	0 [*]	0	187 [*]	-108 [*]	79
S7-3N	769 [†]	290 [†]	1059	-769	-290	-1059	0 [†]	0 [†]	0	187	-108	79
S7-1	729	192	921	-707	-39	-746	147	-2	144	344	-138	206
S7-2	731	192 [*]	923	-707 [*]	-39 [*]	-746	147 [*]	-2 [*]	144	343	-138 [*]	204
S7-5S	731	256 [*]	987	-768 [*]	-300 [*]	-1068	-193	14 [*]	-179	-72 [*]	-118 [*]	-190
S7-5N	731	256	987	-768	-300	-1068	-197	14	-183	-72	-118 [‡]	-190

[*] strains not measured: symmetry was assumed between the right and left sides of the truss (even though an error of 5 to 20 % is known to be present in joint S6-5S and S7-5S).

[†] not measured strains: symmetry was assumed between the right and left sides of the joint .

[‡] not measured strains:calculated using beam FE Model.

Stress calculation in trusses made out of tubes

Based on extrapolated strain measurements given above, axis stresses can be calculated using the 2D Hooke's law:

$$\sigma_x = \frac{E}{1-\nu^2}(\varepsilon_x + \nu\varepsilon_y) \tag{6.8}$$

Assuming that strain in the axis direction x is dominating compared to strains in the other direction ($\varepsilon_x >> \varepsilon_y$) and that the Poisson's ratio ν=0.3 for steel, the equation can be reduced to σ_x= 1.1 E ε_x.

A stress-strain ratio between 1.1 and 1.2 has been confirmed numerically by van Wingerde (1992) and experimentally by Frater (1993). Investigations conducted by van Wingerde et al. (1997) on a large database of joint hot-spot strain results have concluded that a ratio of 1.17 is more appropriate, which is in total agreement with Schumacher (2003)'s results. Therefore, this value was adopted for stress calculation:

$$\sigma_x = 1.17E\varepsilon_x \tag{6.9}$$

Stresses, calculated from strain measurements are given in Tables A.1 A.2 A.3 A.4 A.5 A.6. Table 6.6 reports extrapolated stresses at weld crown toe positions, determined from strains presented in Table 6.5.

Stress values for both specimens are close, within ±10N/mm^2 on average considering the fact that their chord wall thicknesses are different.

In-plane bending moments present in members are also reported in Table 6.6 using the nominal-to-axial stress ratio defined in equation (6.10).

$$\frac{\sigma_{ax} + \sigma_{ipb}}{\sigma_{ax}} = \frac{\sigma_{nom}}{\sigma_{ax}} \tag{6.10}$$

Examining results presented in Table 6.6, these ratios vary between 1 and 1.4 in braces, between 0.9 and 1 on the tension brace side of the chord and between 0.2 and 3.1 on the compression brace side of the chord. It means that in braces, in-planebending stresses always increase the axial stress effect at crown toe positions (ratios>1) whereas in the tension brace side of chord, they show the opposite trend: they partially counteract for the axial stress effect. In the compression brace side of the chord, both trends can be found. Due to the fact that axial stresses are low in chords, the total nominal-to-axial stress ratios can be significantly high even for small bending stress values.

Comparing these results with previous tests results S3 (see Table 6.6), it is shown that they are globally similar.

Table 6.6: Stresses calculated at crown toes (hs1 or hs1c) for as-welded joints, $\Delta Q = 550$ kN for S6 and S7 series, $\Delta Q = 396$ kN for S3 series.

Joint	**Tension brace**				**Compression brace**				**Chord side T. brace**				**Chord side C. brace**			
	$\Delta\sigma_{ax-br}$ [N/mm^2]	$\Delta\sigma_{ipb-br}$ [N/mm^2]	$\Delta\sigma_{nom-br}$ [N/mm^2]	$\frac{\Delta\sigma_{nom}}{\Delta\sigma_{ax}}$ $-_{\text{br}}$	$\Delta\sigma_{ax-br}$ [N/mm^2]	$\Delta\sigma_{ipb-br}$ [N/mm^2]	$\Delta\sigma_{nom-br}$ [N/mm^2]	$\frac{\Delta\sigma_{nom}}{\Delta\sigma_{ax}}$ $-_{\text{br}}$	$\Delta\sigma_{ax-ch}$ [N/mm^2]	$\Delta\sigma_{ipb-ch}$ [N/mm^2]	$\Delta\sigma_{nom-ch}$ [N/mm^2]	$\frac{\Delta\sigma_{nom}}{\Delta\sigma_{ax}}$ $-_{\text{ch}}$	$\Delta\sigma_{ax-ch}$ [N/mm^2]	$\Delta\sigma_{ipb-ch}$ [N/mm^2]	$\Delta\sigma_{nom-ch}$ [N/mm^2]	$\frac{\Delta\sigma_{nom}}{\Delta\sigma_{ax}}$ $-_{\text{ch}}$
S6-3S	188 [*]	63 [*]	251	1.33	-188 [*]	-63 [*]	-251	1.33	0 [*]	0 [*]	0	-	30	-26 [*]	5	0.15
S6-3N	188 (222)[†]	63 (90) [†]	251	1.33	-188	-63	-251	1.33	0 [‡]	0 [‡]	0	-	32	-26	6	0.20
S6-1	180	37	217	1.21	-174	2	-172	0.99	28	-3	25	0.88	60	-32	28	0.47
S6-2	177	37 [*]	214	1.21	-174 [*]	2 [*]	-172	0.99	30	-3 [*]	27	0.89	60	-33	27	0.45
S6-5S	177	64 [*]	241	1.36	-190 [*]	-69 [*]	-259	1.36	-66	3 [*]	-63	0.96	-16 [*]	-34 [*]	-51	3.09
S6-5N	180	64	244	1.35	-190	-69	-259	1.36	-67	3	-64	0.96	-16	-34 [‡]	-51	3.09
S7-3S	189 [*]	71 [*]	260	1.38	-189 [*]	-71 [*]	-260	1.38	0 [*]	0 [*]	0	-	46 [*]	-27 [*]	19	0.42
S7-3N	189 (230) [†]	71 (138) [†]	260	1.38	-189	-71	-260	1.38	0 [‡]	0 [‡]	0	-	46	-27	19	0.42
S7-1	179	47	226	1.26	-174	-10	-183	1.06	36	-0.5	36	0.99	85	-34	51	0.60
S7-2	180	47 [*]	227	1.26	-174 [*]	-10 [*]	-183	1.06	36 [*]	-0.5 [*]	36	0.99	84	-34 [*]	50	0.60
S7-5S	180	63 [*]	243	1.35	-189 [*]	-74 [*]	-262	1.39	-47	3 [*]	-44	0.93	-18 [*]	-29 [*]	-47	2.65
S7-5N	180	63	243	1.35	-189	-74	-262	1.39	-48	3	-45	0.93	-18	-29 [‡]	-47	2.65
S3-1/2				~ 1.4				~ 1.2				~ 1.0				NA

[*] symmetry was assumed between the right and left sides of the truss (even though an error of 5 to 20 % is known to be present in joint S6-5S and S7-5S).

[†] symmetry was assumed between the right and left sides of the joint (or in brackets values obtained using force equilibrium).

[‡] calculated using beam FE Model.

Structural analysis

In order to compare the nominal member stresses obtained experimentally with the ones provided by structural analysis, an appropriate finite element method model has to be chosen. Current specifications proposes models composed of simple bar elements and idealized joints.

One has to remind that, for truss beam under static loading, simplified truss analysis is used to determine forces assuming that:

- member ends are pinned or hinge connected.
- member axes possess one coincident intersection point in a joint.

In other words, no bending moment is taken into account in that kind of model.

Such assumptions are acceptable for static analysis, because at ULS, yielding occur and bending moments will be redistributed.

However, for fatigue considerations in-service, the effect of in-plane bending moments, even small, have to be considered in the stress range evaluation. Concerning our joints, in-plane bending moments are induced by both connection stiffness and eccentricity between brace and chord axes intersection (see Table 6.3).

Walbridge (2005) has compared four structural models (see Fig. 6.14) considering the effects of in-plane bending moments.

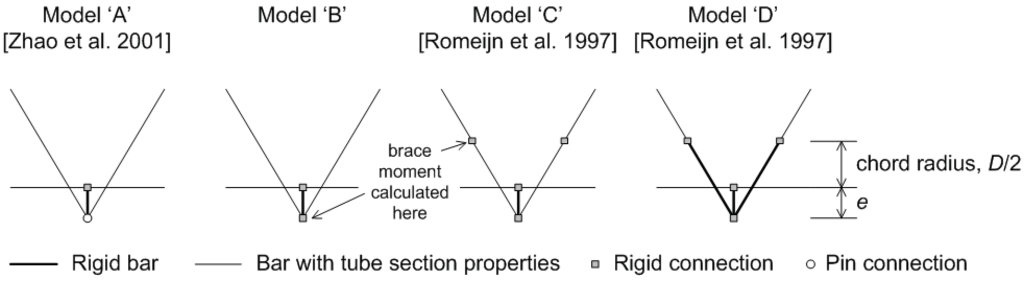

Figure 6.14: Joint models proposed in literature considering the eccentricity effect with different connection types (Walbridge, 2005).

Model 'A' is recommended by the CIDECT design guide (Zhao et al., 2000) and the EN 1993-1-9: 2005. In this simplified model, brace ends are assumed pinned. To consider bending moment effects, axial member forces are multiplied by a magnification factor. For CHS non-overlapping K-joints, this factor has a value of 1.5 in chord members and 1.3 in brace members. The magnification factor takes into account the in-plane moments due to the stiffness of the connection. The in-plane moments linked with the eccentricity between brace end and the continuous chord is modeled physically. Therefore, specimen's nominal-to-axial stress ratios can not be compared directly with these magnification factors.

Model 'B' is similar to Model 'A', except that braces are rigidly connected.

Model 'C' (Romeijn et al., 1997) is identical to Model 'B' but it proposes to calculate the brace moments at the intersection of brace with the outside of the chord wall, which is the real connection position.

In Model 'D' (Romeijn et al., 1997), the fictitious part of the brace members inside the chord are modeled as infinitely stiff. This model is also reported by Dijkstra et al. (1996) in TNO fatigue report on which fatigue design guidelines are based. Correction factors are provided in order to take into account the local flexibility of the joint (a factor of 1.25 for bending chord stresses, a calculated factor of 0.91 for axial brace stresses on the lower chord, 0.93 for axial brace stresses on the upper chord, 0.4 for bending brace stresses on the lower chord, 0.22 for bending brace stresses on the upper chord).

Factors in models 'A' (CIDECT) and 'D' (TNO) are mostly devoted to offshore structures ($\gamma \geq 12$).

According to Walbridge (2005), the model presenting results the closest to the measured values is the **Model 'C'**. He has shown that Model 'C' over-estimates the measured hot-spot stress range by 9.9 N/mm^2 on average (error of 10% approximately). For this reason, Model 'C' was chosen for the structural analysis.

The structural truss model type 'C' (Fig. 6.15) assumes that the truss is simply supported, loaded by its dead weight and a concentrated force Q = 550 kN at mid-span. Eccentricity at nodes between braces and the continuous chord is set constant and equal to 38 mm. The nodes at the extremities of the upper chord are not positioned exactly on supports, a 4 cm eccentricity had to be introduced. Axial force and bending moment diagrams obtained are shown in Fig. A.6, A.7, A.8 and A.9.

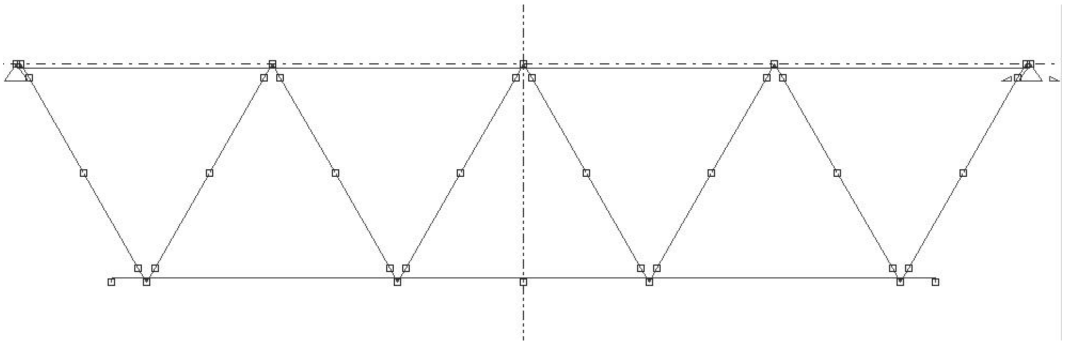

Figure 6.15: Truss model used to compare model stresses (joint model 'C') and measured stresses.

Resulting stresses are given in the Table 6.8 at the intersection between brace and chord outer walls. It can be seen that for most of the stresses, they were estimated lower (Model 'C') than they were in reality.

Then, the nominal stress ranges $\Delta\sigma_{\mathrm{nom}}$ at the specimen gauge positions were compared with nominal stress ranges calculated using Model 'C', Model 'A' with CIDECT magnification factors and Model 'D' with TNO correction factors.

Since stress values were quite similar for both specimens, investigations were conducted only on specimen S7. Table 6.7 summarizes the percent error calculations by taking the stresses deduced from strain measurements as reference value.

Table 6.7: Percent errors between stresses deducted from measurements and stresses calculated using Model 'C', Model 'A', Model 'D'.

	Percent errors [%]			
	Lower chord	**Brace**	**Upper chord**	**Total**
Model 'C'	13	10	5	9
Model 'A' (with CIDECT factors)	-25 *	-21 *	-50 *	-32 *
Model 'D' (with TNO factors)	14	17	5	12

* Negative value indicates overestimation.

Whatever is not shown in this table is that Model 'C' systematically under-estimates the stress values, whereas CIDECT Model 'A' systematically over-estimates these values. Concerning TNO Model 'D', it under-estimates globally stress values in chord and brace members. Nevertheless, the study reaches the same conclusion as Walbridge (2005), the model producing the best estimations compared to experimental values is Model 'C'.

Table 6.8: Structural stresses obtained at crown toes (hs1 or hs1c) using Model 'C', under dead weight and $\Delta Q = 550$ kN.

Joint	**Tension brace**				**Compression brace**				**Chord side T. brace**				**Chord side C. brace**			
	$\Delta\sigma_{ax-br}$ [N/mm^2]	$\Delta\sigma_{ipb-br}$ [N/mm^2]	$\Delta\sigma_{nom-br}$ [N/mm^2]	$\frac{\Delta\sigma_{nom}}{\Delta\sigma_{ax}}$	$\Delta\sigma_{ax-br}$ [N/mm^2]	$\Delta\sigma_{ipb-br}$ [N/mm^2]	$\Delta\sigma_{nom-br}$ [N/mm^2]	$\frac{\Delta\sigma_{nom}}{\Delta\sigma_{ax}}$	$\Delta\sigma_{ax-ch}$ [N/mm^2]	$\Delta\sigma_{ipb-ch}$ [N/mm^2]	$\Delta\sigma_{nom-ch}$ [N/mm^2]	$\frac{\Delta\sigma_{nom}}{\Delta\sigma_{ax}}$	$\Delta\sigma_{ax-ch}$ [N/mm^2]	$\Delta\sigma_{ipb-ch}$ [N/mm^2]	$\Delta\sigma_{nom-ch}$ [N/mm^2]	$\frac{\Delta\sigma_{nom}}{\Delta\sigma_{ax}}$
S6-3S	170	53	223	1.31	-171	-48	-219	1.28	0	0	0	-	27	-23	4	0.15
S6-3N	170	53	223	1.31	-171	-48	-219	1.28	0	0	0	-	27	-23	4	0.15
S6-1	158	28	186	1.18	-154	-14	-168	1.09	27	-2	25	0.93	51	-29	22	0.43
S6-2	158	28	186	1.18	-154	-14	-168	1.09	27	-2	25	0.93	51	-29	22	0.43
S6-5S	158	37	195	1.23	-170.5	-44.5	-215	1.26	-54	-5	-59	1.09	-19	-34	-53	2.79
S6-5N	158	37	195	1.23	-170.5	-44.5	-215	1.26	-54	-5	-59	1.09	-19	-34	-53	2.79
S7-3S	170	53	223	1.31	-171	-50	-221		0	0	0	-	37	-28	9	0.24
S7-3N	170	53	223	1.31	-171	-50	-221		0	0	0	-	37	-28	9	0.24
S7-1	157	30	187	1.19	-153	-14	-167		37	3	40	1.08	71	-30	41	0.58
S7-2	157	30	187	1.19	-153	-14	-167		37	3	40	1.08	71	-30	41	0.58
S7-5S	157	38	195	1.24	-171	-45	-216		-39	-5	-44	1.13	-13	-30	-43	3.3
S7-5N	157	38	195	1.24	-171	-45	-216		-39	-5	-44	1.13	-13	-30	-43	3.3

Proportion of bending in the truss members

Taking Model 'C' as the structural model to study the truss behavior, a parametric study was conducted in order to determine the influence of the chosen geometrical parameters (α, β, γ and τ) on bending. Parameters were varied one by one, keeping the other parameters constants. Their ranges were specified in order to fit with values commonly used for bridges. The study focuses on evaluating the total nominal-to-axial ratio on the tension side of brace in chord for joints 1 and 3N and on the compression side for joint 5N. Results are presented in Table A.13.

From this study, it is shown:

- Parameter γ (studied range $4.2<\gamma<15$) does not influence the proportion of bending in studied braces.
- Parameters β and τ (studied range $0.48<\beta<0.61$, $0.25<\tau<0.63$) have a low influence on the nominal-to-axial ratios. This influence is slightly more pronounced for joint 3N brace.
- Parameter α (studied range $10<\alpha<25$) affects in a non-negligeable way the bending part. Since the α parameter of test series S3 to S7 is 25 whereas it is approximately 14 in bridges, one has to verify if tests are representative of real bridge behavior. It is shown that a variation of α from 10 to 25 can imply a change in the nominal-to-axial ratio up to 20%. It stems out from the fact that a low α parameter can be illustrated as moving the joints closer. Therefore it is related to a decrease of truss member slenderness and an increase of in-plane moment values in braces. On the whole, the bending moments are underestimated in tests on specimens S3 to S7 (of approx. 15%) compared to bridge geometry.
- Eccentricity between brace and chord axes (studied 0, 38 and 100 mm): obviously the more eccentricity the more bending moments. Increasing the eccentricity increases linearly the nominal-to-axial ratios by ∼10% from 0 to 100 mm and by ∼6% from 0 to 38 mm.
- The proportion of bending is more significant in tension braces for joints 3N than for joints 1. This proportion does not change drastically between the tension and compression braces of joints, except for joint 1 where the compression brace undergo less bending than the tension brace (see Table 6.6).

The nominal-to-axial stress ratios can be indirectly compared with magnification factors MFs proposed in Model 'A'(MF = 1.3 in brace members for CHS gap K-joints). Since MFs accounts only for the in-plane moments due to connection stiffness, one has to set the nominal-to-axial stress ratio due to the stiffness effect apart from the one due to the eccentricity effect. From the previous parametric study, the ratios have to be reduced by 6%. Resulting values are between 1.08 and 1.3 from the above studied braces. Therefore, these results are safely covered by the 1.3 magnification factor proposed by CIDECT.

Hot-spot stress calculation

At the weld toes, where fatigue cracks are expected, geometrical discontinuities cause stress deviations and stress concentrations. The stress concentration locations and factors depend on both joint geometry and load type, however they do not include local effects such as the weld shape and radius (notch effects).

By simply multiplying nominal stresses by the corresponding stress concentration factors SCFs, stresses at the weld toe called hot-spot stresses can be calculated.

The following equation (6.11) (Zhao et al., 2000) has been proposed for the calculation of hot-spot stress range in tubular joints at a particular hot-spot location i. Since stresses are elastic, the total hot-spot stress range $\Delta\sigma_{hs,i}$ or $S_{R,hs,i}$ is the superposition of individual hot-spot stress ranges under each load case (axial brace force: ax-br, moment in brace: ipb-br, axial chord force: ax-ch, moment in chord: ipb-ch) at the joint location i:

$$\Delta\sigma_{hs,i} = \Delta\sigma_{ax-br} \,.\, SCF_{i,ax-br} + \Delta\sigma_{ipb-br} \,.\, SCF_{i,ipb-br} + \Delta\sigma_{ax-ch} \,.\, SCF_{i,ax-ch} + \Delta\sigma_{ipb-ch} \,.\, SCF_{i,ipb-ch} \tag{6.11}$$

The total hot-spot stress range can also be expressed as follows:

$$\begin{aligned}
\Delta\sigma_{hs,i} &= \Delta\sigma_{tot\ nom}.(\frac{\Delta\sigma_{nom-br}}{\Delta\sigma_{tot\ nom}}.\frac{\Delta\sigma_{ax-br}}{\Delta\sigma_{nom-br}}.SCF_{i,ax-br} + \frac{\Delta\sigma_{nom-br}}{\Delta\sigma_{tot\ nom}}.\frac{\Delta\sigma_{ipb-br}}{\Delta\sigma_{nom-br}}.SCF_{i,ipb-br} \\
&+ \frac{\Delta\sigma_{nom-ch}}{\Delta\sigma_{tot\ nom}}.\frac{\Delta\sigma_{ax-ch}}{\Delta\sigma_{nom-ch}}.SCF_{i,ax-ch} + \frac{\Delta\sigma_{nom-ch}}{\Delta\sigma_{tot\ nom}}.\frac{\Delta\sigma_{ipb-ch}}{\Delta\sigma_{nom-ch}}.SCF_{i,ipb-ch}) \\
&= \Delta\sigma_{tot\ nom}.SCF_{tot,i} \qquad (6.12)
\end{aligned}$$

The SCF tables were determined by Schumacher et al. (2003) for similar K-joints presenting the following features:

- SCFs were given for a large range of geometric parameters 0.5 $<\beta<$ 0.7, 4 $<\gamma<$ 30, 0.3 $<\tau<$ 0.7 and brace angles θ (45°or 60°) corresponding well to our specimens geometry. The K-joints were characterized by a low γ value ($\gamma < 12$) - in opposite to CIDECT and IIW guidelines - and the presence of a gap (or an eccentricity). The gap and weld sizes followed the tube diameters and thicknesses. The chord length ratio parameter α was not taken into account. Despite the influence of this parameter on the stress concentration is often neglected, Shao et al. (2008) has shown that, for low γ values ($\gamma < 12$), α has a significant effect on the SCF values of tubular T-joints under axial loads. This effect is not considered in our case but in future research, it is an interesting point to develop.
- SCFs were given for five load cases: balanced axial brace (ax-br), un-balanced in-plane bending brace (ipb1-br), balanced in-plane bending brace (ipb2-br), axial chord (ax-ch) and in-plane bending chord (ipb-ch). In our case, the balanced in-plane bending brace is not considered because it almost never occurs. Therefore, ipb1-br is renamed ipb-br.
- The study only covers K-shape joints and not joints situated at the chord extremity such as joints J4N, J4S, J3N and J3S. The SCF factors were only based on experimental results obtained in joints J1 and J2.
- SCFs were examined for six joint locations (hot-spots) 1, 11, 2, 3, 31, 4, which seem to be the most critical locations in joints with $\gamma < 12$. Location 1 (hot-spot 1) is situated at the chord crown toe on the tension side.
- The factors were obtained on the tension brace side of joints loaded in tension, such as joints J1 and J2 in our case.

Linear interpolation (and occasionally extrapolation) was used to capture the SCF at hot-spot 1 corresponding to the non-dimensional parameters of our joints (β, γ and τ) for brace angles θ of 60°.

Table A.14 reports for each joint the SCF values under each load case at the joint location hs1. Tables A.15 and A.16 recap the partitioning of stresses deducted from nominal stress values (Table 6.6) and the total SCF resulting by applying equation (6.12). Note that the stress range partition is determined for both tension side (tension brace and chord side tension brace: hot-spot **1**) and compression side (compression brace and chord side compression brace: hot-spot **1c**). SCF values calculated from Schumacher's tables (Schumacher et al., 2003) were then corrected to account for the stress-strain ratio of 1.17: $\mathrm{SCF}_{1,\mathrm{cor}} = \mathrm{SCF}_1/1.17$ (see equation (6.9)) which was not included.

It has to be underlined that the SCFs applied to calculate hot-spot stresses in joints loaded in compression (hot-spot 1c) were obtained from study on joints loaded in tension. It might give not as accurate values for this kind of joints as for the tension ones.

The hot-spot stresses were finally calculated by applying either equation (6.11) or equation (6.12) as demonstrated in Tables 6.9 and 6.10. These values were also synthesised graphically in Fig. 6.16 and 6.17. Note that, in these figures, the given values are calculated at the hot-spot locations

1 and 1c. The stresses in the drawings are not in equilibrium because shear stresses are not presented in these figures.

Note that the load ratio R = 0.1 corresponds to an applied stress ratio **R** $=\sigma_{\min}/\sigma_{\max}=$ **0.1 in joints loaded in tension** (Table 6.9) and an applied stress ratio **R** $=\sigma_{\min}/\sigma_{\max}=$ **10 in joints loaded in compression** (Table 6.10). These loadings are closed to zero-tension loading for R = 0.1 and zero-compression loading for R = 10.

Among these applied loadings, locations in joints can undergo a **fully-tensile loading** (brace and chord in tension), a **part-tensile/-compressive loading** (brace or chord in tension) or a **fully-compressive loading** (brace and chord in compression).

Table 6.9: Hot-spot stresses calculations for each joint at location hs1 for the crown toe on the tension side (tension brace and chord side tension brace). The joints highlighted in gray are fully-tensile loaded.

Joint	$\Delta\sigma_{ax}$ $_{-br}$ [N/mm^2]	SCF_{ax} $_{-br,cor}$	$\Delta\sigma_{ipb}$ $_{-br}$ [N/mm^2]	SCF_{ipb} $_{-br,cor}$	$\Delta\sigma_{ax}$ $_{-ch}$ [N/mm^2]	SCF_{ax} $_{-ch,cor}$	$\Delta\sigma_{ipb}$ $_{-ch}$ [N/mm^2]	SCF_{ipb} $_{-ch,cor}$	$\Delta\sigma_{tot}$ $_{nom}$ [N/mm^2]	SCF $_{tot,1,cor}$	$\Delta\sigma_{hs,1}$ [N/mm^2]
S6-3S	188	0.60	63	0.41	0	1.03	0	1.07	251	**0.55**	**139**
S6-3N	188	0.60	63	0.41	0	1.03	0	1.07	251	**0.55**	**139**
S6-1	180	0.60	37	0.41	28	1.03	-3	1.07	242	**0.61**	**148**
S6-2	177	0.60	37	0.41	30	1.03	-3	1.07	241	**0.62**	**148**
S6-5S	177	0.95	64	0.63	-66	1.11	3	1.18	177	**0.78**	**139**
S6-5N	180	0.95	64	0.63	-67	1.11	3	1.18	180	**0.78**	**141**
S7-3S	189	0.95	71	0.63	0	1.11	0	1.18	260	**0.87**	**225**
S7-3N	189	0.95	71	0.63	0	1.11	0	1.18	260	**0.87**	**225**
S7-1	179	0.95	47	0.63	36	1.11	-0.5	1.18	262	**0.92**	**240**
S7-2	180	0.95	47	0.63	36	1.11	-0.5	1.18	262	**0.92**	**240**
S7-5S	180	0.60	63	0.41	-47	1.03	3	1.07	199	**0.45**	**89**
S7-5N	180	0.60	63	0.41	-48	1.03	3	1.07	198	**0.44**	**88**

Table 6.10: Hot-spot stresses calculations for each joint at location hs1c for the crown toe on the compression side (compression brace and chord side compression brace). The joints highlighted in gray are fully-compressive loaded.

Joint	$\Delta\sigma_{ax}$ $_{-br}$ [N/mm^2]	SCF_{ax} $_{-br,cor}$	$\Delta\sigma_{ipb}$ $_{-br}$ [N/mm^2]	SCF_{ipb} $_{-br,cor}$	$\Delta\sigma_{ax}$ $_{-ch}$ [N/mm^2]	SCF_{ax} $_{-ch,cor}$	$\Delta\sigma_{ipb}$ $_{-ch}$ [N/mm^2]	SCF_{ipb} $_{-ch,cor}$	$\Delta\sigma_{tot}$ $_{nom}$ [N/mm^2]	SCF $_{tot,1c,cor}$	$\Delta\sigma_{hs,1c}$ [N/mm^2]
S6-3S	-188	0.60	-63	0.41	30	1.03	-26	1.07	-247	**0.55**	**-135**
S6-3N	-188	0.60	-63	0.41	32	1.03	-26	1.07	-245	**0.54**	**-133**
S6-1	-174	0.60	2	0.41	60	1.03	-32	1.07	-144	**0.53**	**-76**
S6-2	-174	0.60	2	0.41	60	1.03	-30	1.07	-145	**0.53**	**-77**
S6-5S	-190	0.95	-69	0.63	-16	1.11	-34	1.18	-310	**0.91**	**-284**
S6-5N	-190	0.95	-69	0.63	-16	1.11	-34	1.18	-310	**0.91**	**-284**
S7-3S	-189	0.95	-71	0.63	46	1.11	-27	1.18	-241	**0.85**	**-205**
S7-3N	-189	0.95	-71	0.63	46	1.11	-27	1.18	-241	**0.85**	**-205**
S7-1	-174	0.95	-10	0.63	85	1.11	-34	1.18	-133	**0.88**	**-117**
S7-2	-174	0.95	-10	0.63	84	1.11	-34	1.18	-133	**0.89**	**-118**
S7-5S	-189	0.60	-74	0.41	-18	1.03	-29	1.07	-309	**0.62**	**-192**
S7-5N	-189	0.60	-74	0.41	-18	1.03	-29	1.07	-309	**0.62**	**-192**

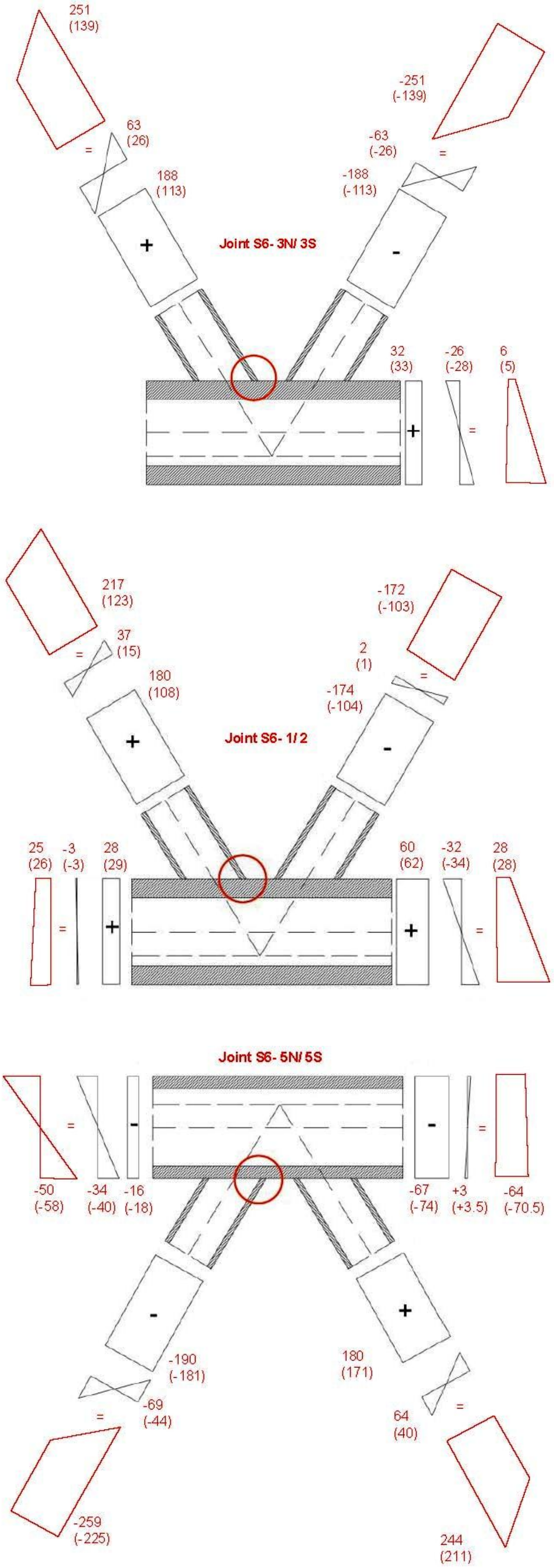
251
(139)
-251
(-139)
63
(26)
-63
(-26)
188
(113)
-188
(-113)
=
+
-
Joint S6- 3N/ 3S
32
(33)
-26
(-28)
6
(5)
217
(123)
-172
(-103)
37
(15)
2
(1)
180
(108)
-174
(-104)
Joint S6- 1/ 2
25
(26)
-3
(-3)
28
(29)
60
(62)
-32
(-34)
28
(28)
Joint S6- 5N/ 5S
-50
(-58)
-34
(-40)
-16
(-18)
-67
(-74)
+3
(+3.5)
-64
(-70.5)
-190
(-181)
180
(171)
-69
(-44)
64
(40)
-259
(-225)
244
(211)

Figure 6.16: Idealized nominal stresses and hot-spot stresses in brackets deduced from strain measurements in each member of specimen S6 joints (values given in N/mm^2). The circle is surrounding the critical location hs1 for joints with a chord loaded in tension and hs1c for joints with a chord loaded in compression.

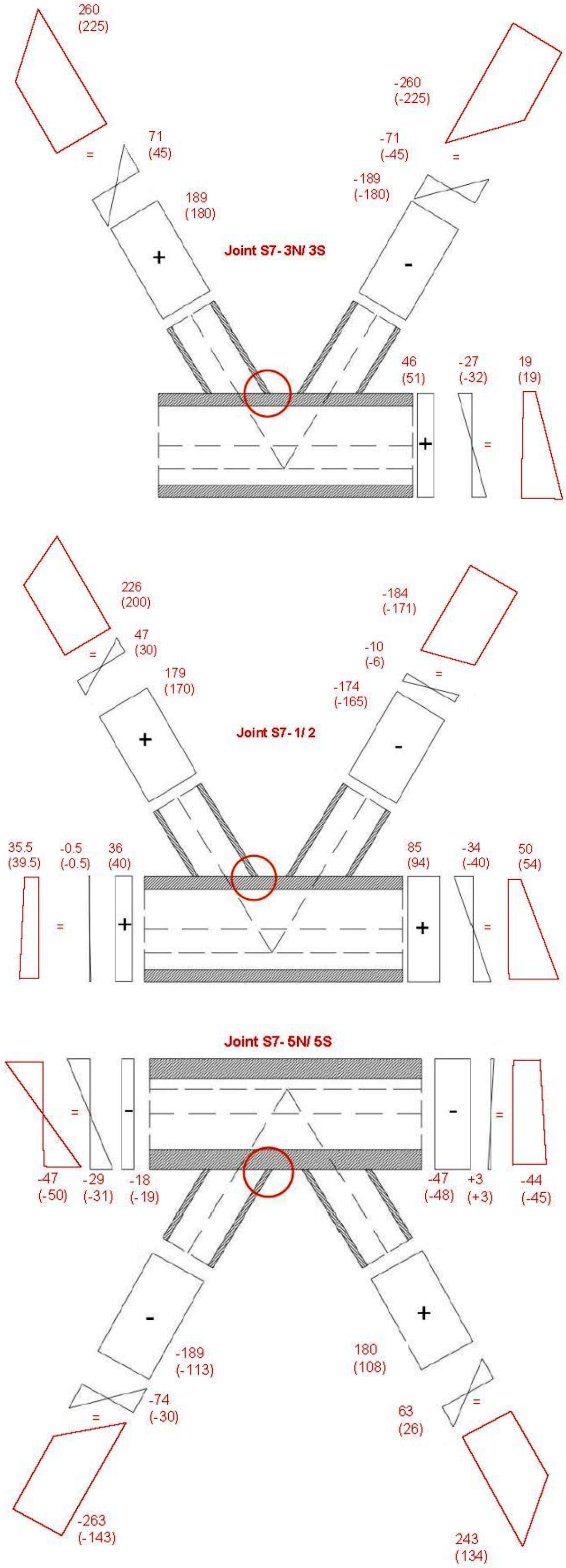
260
(225)
-260
(-225)
71
(45)
-71
(-45)
189
(180)
-189
(-180)
Joint S7-3N/3S
+
-
46
(51)
-27
(-32)
19
(19)
226
(200)
-184
(-171)
47
(30)
-10
(-6)
179
(170)
-174
(-165)
Joint S7-1/2
+
-
35.5
(39.5)
-0.5
(-0.5)
36
(40)
85
(94)
-34
(-40)
50
(54)
Joint S7-5N/5S
-47
(-50)
-29
(-31)
-18
(-19)
-47
(-48)
+3
(+3)
-44
(-45)
-189
(-113)
180
(108)
-74
(-30)
63
(26)
-263
(-143)
243
(134)

Figure 6.17: Idealized nominal stresses and hot-spot stresses in brackets deduced from strain measurements in each member of specimen S7 joints (values given in N/mm^2). The circle is surrounding the critical location hs1 for joints with a chord loaded in tension and hs1c for joints with a chord loaded in compression.

It can be seen that the calculated hot-spot stresses are lower than the nominal stresses and this trend seems to be linked to the chord wall thickness. We can argue that when the stress deviation occurs between a thin brace wall and a thick chord wall, there is an effect of 'low pressure stress area' with the stresses values dropping in the area of the weld toe. This trend was also confirmed by results of test series S5 as well as by finite element analyses for joint S7-1, giving a $\Delta\sigma_{\mathrm{hs,1}} = 220\mathrm{N/mm^2}$ and a $\Delta\sigma_{\mathrm{hs,1c}} = -126\mathrm{N/mm^2}$ compared to respective total idealized nominal stresses of $\Delta\sigma_{\mathrm{totnom}} = 262\mathrm{N/mm^2}$ and a $\Delta\sigma_{\mathrm{totnom}} = -133\mathrm{N/mm^2}$. Figure 6.18 depicts this phenomenon for axial brace loading, the predominant part of the total $\Delta\sigma_{\mathrm{hs,1}}$.

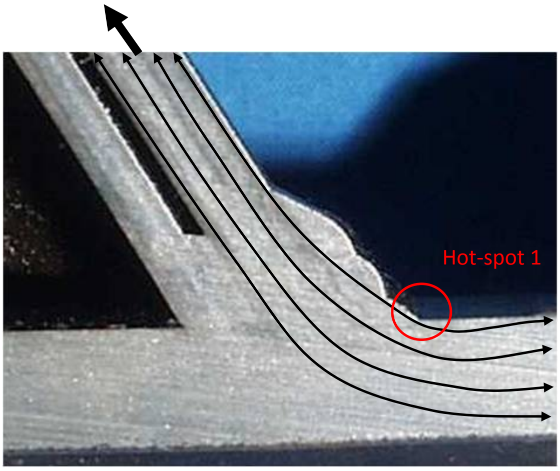

Figure 6.18: Stress deviation occurring under the weld crown toe (hs 1) for balanced axial brace (ax-br).

Nominal and hot-spot stress ranges were compared in Table 6.11 between test series S6 and S7 and the other test results previously obtained in our laboratory (see Table 6.2). Joints S5-2 j5N- and S6 j5N-, as well as joints S5-2 j1+ and S7 j1+ have exactly the same geometric dimensions except for their gap or eccentricity values.

Table 6.11: Nominal and hot-spot stress ranges comparison between joints tested at ICOM laboratory (+ stands for the crown toe on the tension side, - stands for the crown toe on the compression side). Values for specimens S1 to S5 were adapted to take into account a stress-strain ratio of 1.17 (see equation (6.9)) and to correspond to extrapolated $\Delta\sigma_{nom-br}$ and $\Delta\sigma_{nom-ch}$ at location hs1 or hs1c.

Joint	β	γ	τ	e/D	Brace	Chord	**Location1**	
					$\Delta\sigma_{nom-br}$	$\Delta\sigma_{nom-ch}$	$\Delta\sigma_{hs,1}$	$SCF_{tot,1,cor}$
	[-]	[-]	[-]	[-]	[N/mm^2]	[N/mm^2]	[N/mm^2]	[-]
S1-1+	0.51	6.83	0.63	± 0.1	91.2	12.8	114 *	1.10
S2-1+	0.51	6.83	0.63	0.18-0.2	84-86	14-17	139	1.37
S3-1+	0.53	6.73	0.64	0.2-0.23	85-90	42-47	187-196	1.44-1.47
S4-1+	0.51	6.83	0.63	0.19	89.2	17.7	148.4	1.39
S5(-2)-1+	0.53	4.21	0.4	0.13	**190**	**50**	**211** †	**0.89**
S5(-2)-5N-	0.53	4.21	0.4	0.13			**-248** †	
S6-1+	0.53	2.81	0.27	0.21	217	25	148 ‡	0.61
S6-5N-	0.53	4.21	0.4	0.23	**-259**	**-50**	**-284** ‡	**0.91**
S7-1+	0.53	4.21	0.4	0.20	**226**	**35.5**	**240** ‡	**0.92**
S7-5N-	0.53	2.81	0.27	0.23	-263	-47	-192 ‡	0.62

* calculated using FEM (Schumacher et al., 2003), ΔQ = 594 kN for S1, S2 and S4, ΔQ = 396 kN for S3.
† calculated using BEM (Borges, 2008), ΔQ = 550 kN.
‡ calculated using SCF tables determined by Schumacher et al. (2003), ΔQ = 550 kN.

The hot-spot stress range values for S5-2 joints were obtained by Borges (2008) using Boundary Elements with welds modeled as realistically as possible, whereas for series S1 to S4 Schumacher et al. (2003) has chosen Finite Elements with the weld profile minimum values defined in the AWS guidelines (AWS, 2000). In the Fig. 6.19, the chord weld length $L_{w,ch}$ is given all along the weld according to the AWS guidelines (series S1 to S4 and SCF tables), to the joint S5-2 j2 measurements and to a realistic weld profile (series S5).

Since the gap size and the weld geometry play a significant role in the SCF evaluation, one can expect some discrepancy in SCF values between series S5 and S6-S7. However, the few results from series S5 are in reasonably good agreement with S7 results. The difference of hot-stress values (10-15%) between series S5 and S6-S7 can be explained by the difference of nominal stresses. This observation is significant, it means that the weld shape should be modeled using the weld profile proposed by Borges (2008).

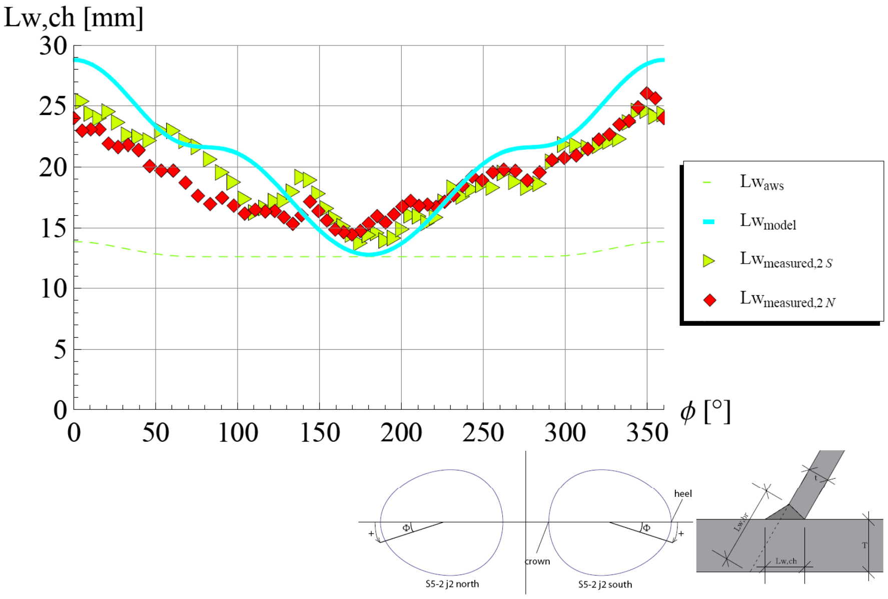

Figure 6.19: Chord weld lengths $L_{w,ch}$ (figure from Borges (2008): comparison between the AWS profile (minimum values) chosen for SCF tables (Schumacher et al., 2003), the S5-2 j2 measurement values and a realistic weld profile chosen to calculate host-spot stresses for S5 series.

6.3.2 Test results

Crack location

Tables A.19 and A.20 present photographs of the cracks that occurred in joints of specimens S6 and S7.

It can be seen that for both specimens, cracks propagated in all as-welded joints (joints 1, 2, 3N, 3S, 5N and 5S). Cracks grew in the chord wall and along the weld toe whatever the sign of applied stresses, positive or negative. In total, twelve cracks per specimen were counted.

All these cracks occurred at the weld toe in-between the braces, at locations hs1 for the tensile brace side or hs1c for the compressive brace side. According to Fig. 6.16 and 6.17, hot-spots where crack initiated were always locations of highest applied stresses and hot-spot stresses (considering hot-spot locations 1 and 1c). In addition, other aspects such as local weld geometry, local imperfections, high hardness values (see 4.6) and high tensile residual stresses tend to make these positions even more critical.

Cracks initiate in the HAZ because of contribution of stress concentration, metallurgical discontinuities, physical discontinuities and high numbers of dislocations in the HAZ microstructure.

Then, the crack propagates in the BM. Apart from the first 2 millimeters, the crack profile path is essentially within the BM (see Fig. 5.21 for joint S5-1 or -2 at hs1).

Crack initiation and development

The main part of the crack depth development was followed using the Alternating Current Potential Drop equipment presented in section 6.2.5. Figures 6.20a, 6.21a and 6.21b summarize the voltage probe positions along the weld toe on both specimens. For the first test on specimen S6, probes were only situated in joint S6-5N, on the tension brace side (2 probes) as well as on the compression brace side (6 probes). For specimen S7, two joints were equipped: S7-5N with 2 probes on the tension brace side and 3 probes on the compression brace side, and S7-1 with 2 probes on the tension brace side and 1 probe on the compression brace side. Figures 6.20b and 6.21c present the calibrated crack depth in function of the number of cycles. The same results are presented numerically in Tables A.21 and A.22. Based on these results, it can be said that probes P1 and P5 are the most representatives of the crack growth occurring at hs1 (part-tensile loading) and hs1c (fully-compressive loading) in joint S6-J5N. Similarly, probes P1 and P2 are the most significant for hs1c (part-compressive loading) and hs1 (fully-tensile loading) in joint S7-J2 and probes P4 and P6 are the most significant for hs1 (part-tensile loading) and hs1c (fully-compressive loading) in joint S7-J5N.

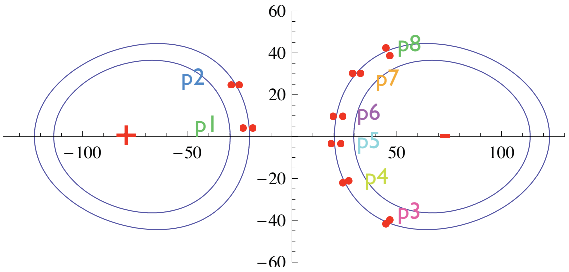

(a) ACPD probe positions for joint S6-J5N, the curved line represent the bottom and top positions of the weld

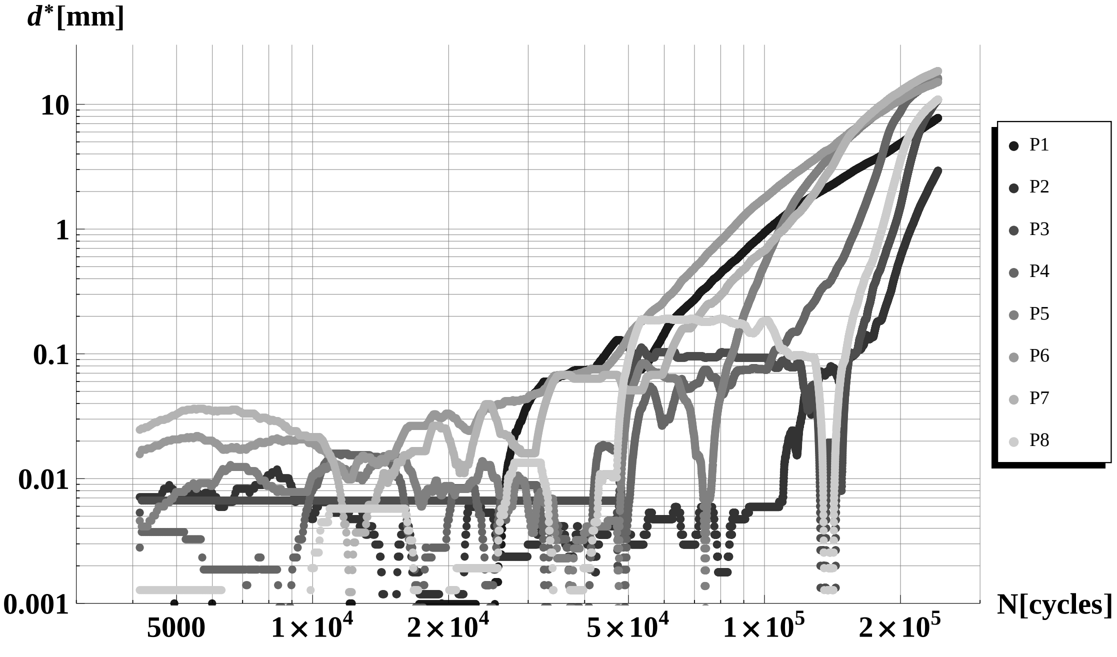

(b) measurements in Joint S6-J5N

Figure 6.20: ACPD probe positions for specimen S6 and resulting crack depth measurements versus number of cycles.

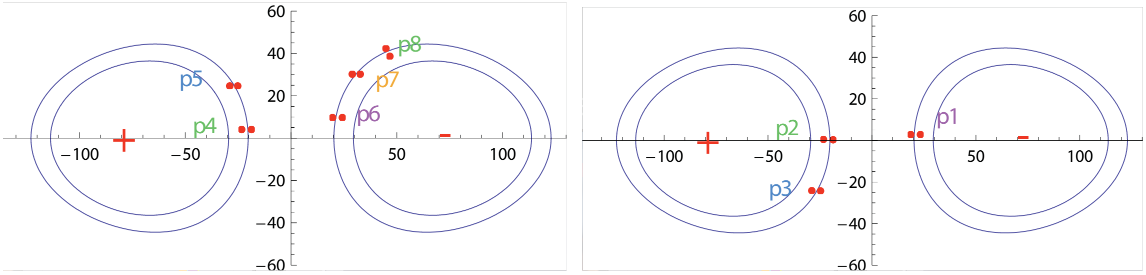

(a) Joint S7-J5N **(b)** Joint S7-J1

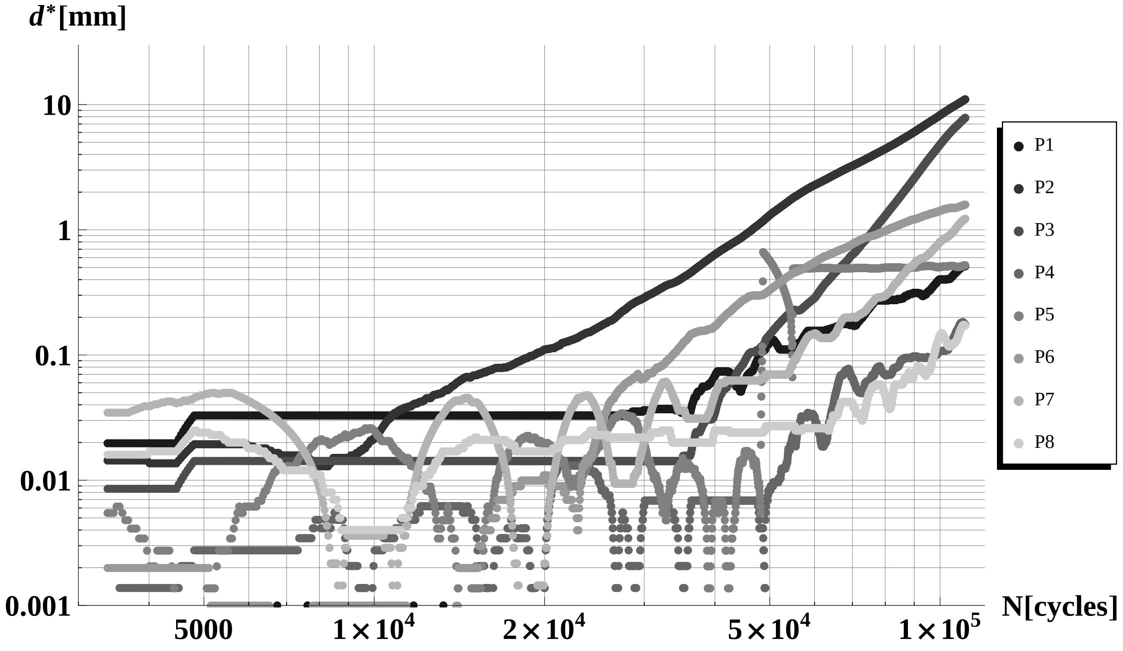

(c) measurements in Joint S7-J5N and S7-J1

Figure 6.21: ACPD probe positions for specimen S7 and resulting crack depth measurements versus number of cycles.

Defining the transition from the initiation stage to the crack propagation stage is not straightforward. For practical reasons, the limit for the crack propagation stage was characterized by the detection of the crack. For usual non destructive techniques, it was often 0.5 to 1 mm. This definition is completely dependent of the instrument resolution and is not satisfactory.

From the fracture mechanics viewpoint, the crack propagation stage begin when the stress intensity factor range is greater than the threshold value: $\Delta \mathrm{K}_{\mathrm{exp}} > \Delta \mathrm{K}_{\mathrm{th}}$. The threshold value was estimated by Zheng (1987) as follows:

$$\Delta K_{th} = 320(1 - R) \tag{6.13}$$

With a stress ratio of 0.1, one obtains $\Delta \mathrm{K}_{\mathrm{th}} = 288 \mathrm{N/mm}^{3/2}$. This value was previously used by Borges and Nussbaumer (2008). This value corresponds to a propagation rate of approximately 5×10^{-6} mm/cycle using equation (6.5). This rate value is so small that the registered data are of the same order of magnitude than the background noise, without any physical sense. To compensate for this effect, the number of cycles at the beginning of the propagation stage is determined using both $\Delta \mathrm{K}_{\mathrm{th}}$ and a significant increase of d* registered.

According to ACPD measurements (see Fig. 6.22, 6.23, 6.20 and 6.21), the crack growth starts between 12000 and 16000 cycles for joint S6-5N (probe 5, hs1c) and between 8000 and 10000 cycles for joint S7-1 (probe 2, hs1). Therefore, the initiation life represents 7% on average of the number of cycles to through-thickness cracking N_3. It confirms the asumption that the initiation stage is small compared to the total fatigue life.

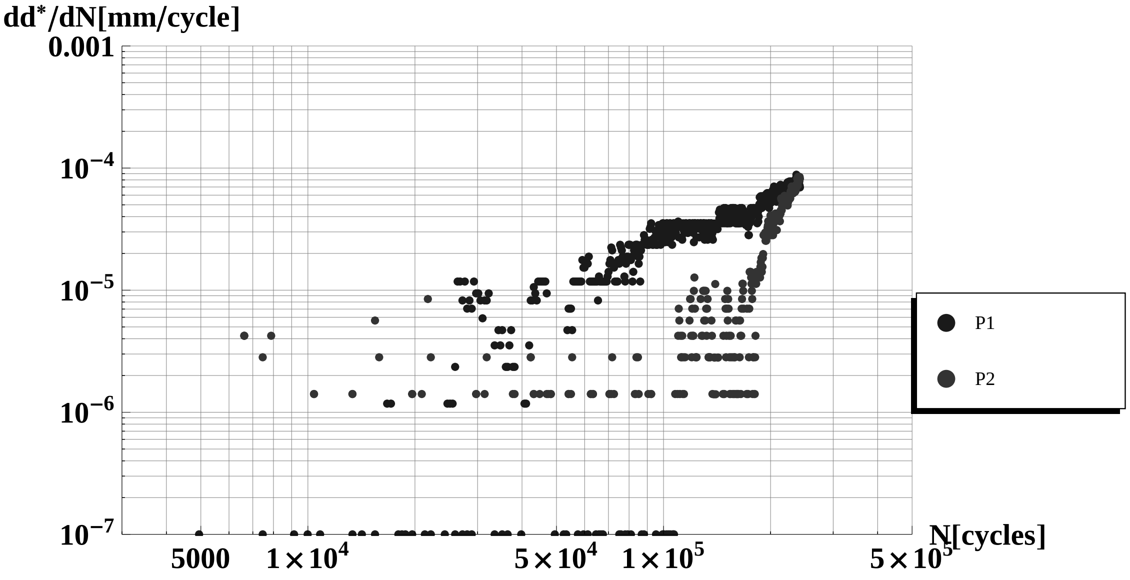

(a) Joint S6-J5N, tensile brace side

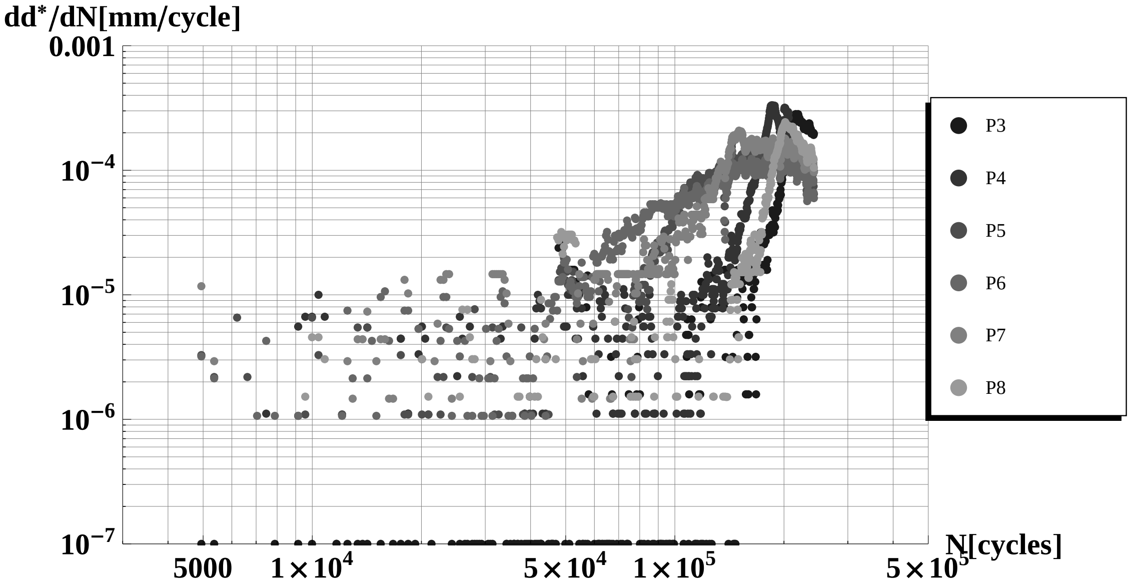

(b) Joint S6-J5N, compressive brace side

Figure 6.22: Crack propagation rates measured in joint S6-J5N using ACPD in function of the number of cycles (log-log scale).

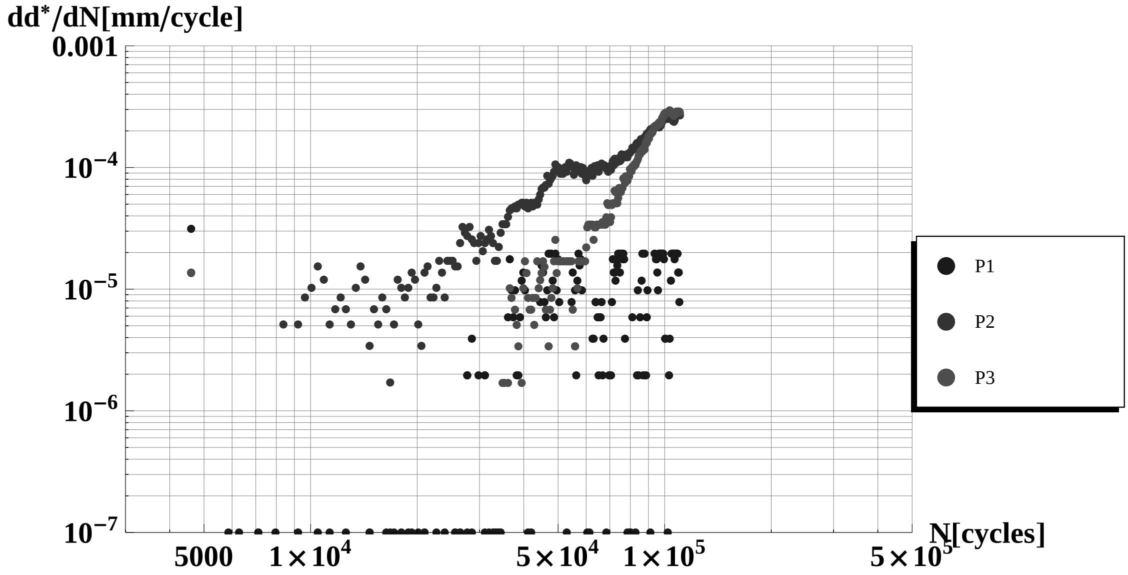

(a) Joint S7-J5N

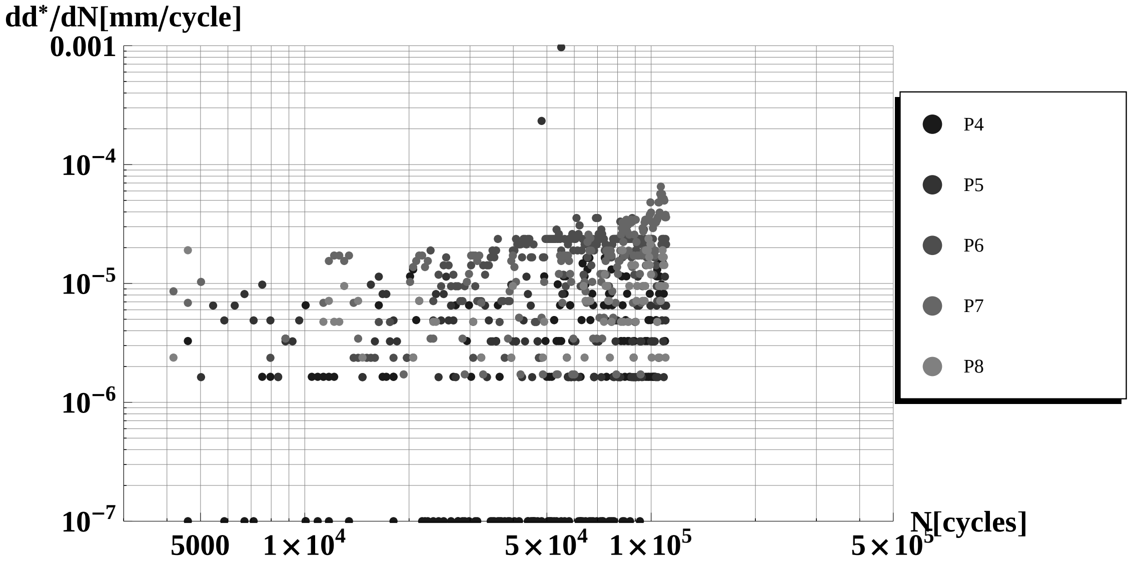

(b) Joint S7-J1

Figure 6.23: Crack propagation rates measured in joint S7-J5N and S7-1 using ACPD in function of the number of cycles (log-log scale).

Through thickness cracking (defined at N_3 cycles)

The first test on specimen S6 was stopped after 242000 cycles, when a through crack occurred in joint S6-3S+. For the second test, the through crack appeared sooner in joint S7-3S+ after only 111000 cycles (see Fig. 6.24). At 50000 cycles, the first cracks in joints S7-3S+ and S7-3N+ were detected with dye penetrant whereas in specimen S6, no crack was detected for the same number of cycles (see Table A.18).

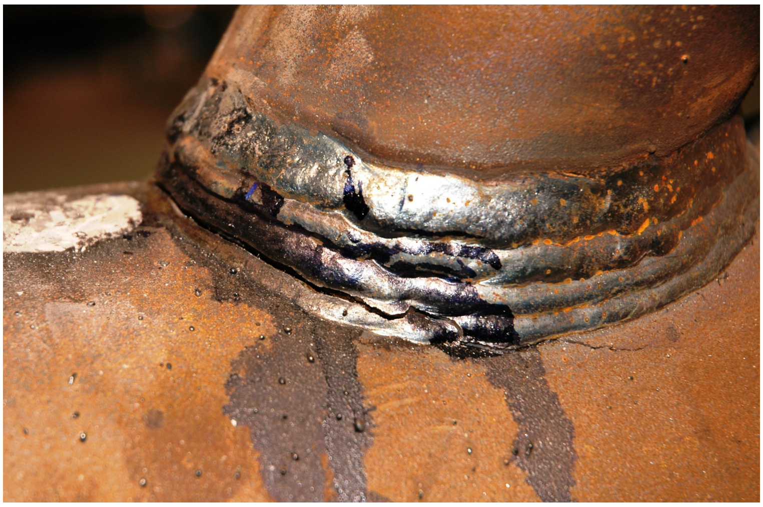

Figure 6.24: The critical crack obtained in joint S7-3S.

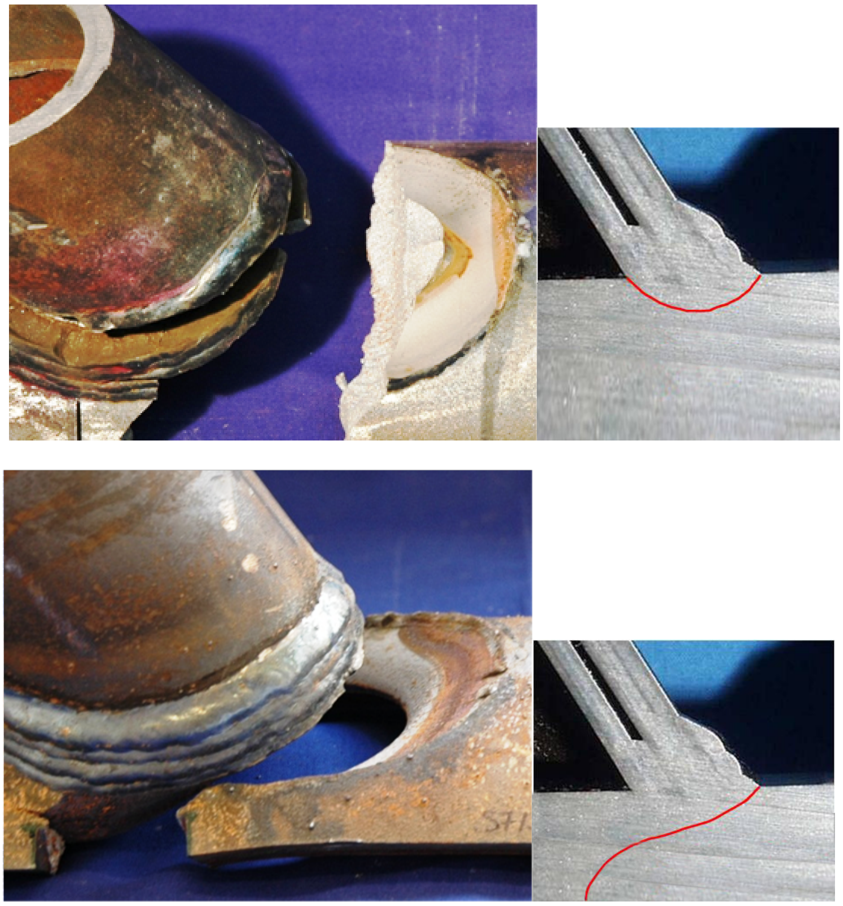

Figure 6.25: Critical crack shape of joints S6-3S (T = 30 mm) on the top and S7-3S (T = 20 mm) on the bottom.

The classification from bigger to smaller final crack in term of crack depth a is given in Tables A.19 and A.20. The bigger cracks obtained at the end of the fatigue tests were located at hs1 on the chord loaded in tension (S6-3S+, S6-3N+, S6-2+, S6-1+ / S7-3S+, S7-3N+, S7-2+, S7-1+). Cracks second in size were obtained at hs1c on the chord loaded in compression (S6-5N-, S6-5S-/S7-5N-, S7-5S-). Concerning the smallest cracks, the ranking of their size is different in specimens S6 and S7 and difficult to evaluate.

Therefore both critical cracks were situated in the joint at the extremity of the lower chord. However, the shape of their crack surface was completely different as shown in Fig. 6.25. Note that both joints are geometrically the same except for their wall chord thickness.

The crack that started from the brace weld toe of joint S6-3S loaded in tension propagated following a curved path from the weld toe to the backing ring crown toe, passing underneath the brace wall and weld, whereas in joint S7-3S the crack went directly through the 20 mm thickness of the chord after 111000 cycles.

$S_{\mathrm{rhs}} - N$ ***curves***

The fatigue test results, including all series S1 to S7, are reported in Fig. 6.26a in the form of logarithmical $S_{\mathrm{rhs}} - N$ curves (or $\Delta\sigma_{\mathrm{R,hs}} - N$ curves). For all points, the hot-spot stress range $\Delta\sigma_{\mathrm{R,hs}}$ was taken at hot-spot 1 or hot-spot 1c. The data set comprises joints with thicknesses T ranging from 6 to 40 mm, represented in Fig. 6.26 with symbol sizes proportional to the thickness of the joint chord. The hot-spot stress range values given in Tables 6.9 and 6.10 were corrected, using the size effect correction determined by van Wingerde et al. (1997), in order to represent the fatigue strength of an equivalent 16 mm thick joint. Therefore, results can be compared between joints with different wall chord thicknesses. The number of cycles used in the plot refers to $N_{3,T/2}$, the number of cycles to half-thickness cracking of the chord wall. Since cracks at hs1c usually do not attain the through-thickness, the choice of the half-thickness crack as 'failure' criterion was very important to compare results obtained in compression with others obtained in tension. At half-thickness, it was found from previous tests that the majority of the fatigue life (60% to 80% of the number of cycles to through-thickness cracking) had usually been consumed. The number of cycles $N_{3,T/2}$ were, for most of the joints, interpolated and, for others, extrapolated based on the surface crack length 2c. This extrapolation was done for joints in which cracks almost reached the half-thickness criterion in order to have a uniform comparison basis.

Following the IIW recommendations (Hobbacher, 2007), a statistical analysis of results on fully-tensile loaded details was carried out. The mean S-N curve was set up through a linear regression analysis with a constant slope of $m = 3$ up to the constant amplitude fatigue limit, $N = 5 \cdot 10^6$ cycles. Then, the characteristic curve was determined at 2.2 standard deviation (for 22 data points) below the mean value of log N, thus given the reference value of fatigue strength $S_{\mathrm{rhs}(2\cdot10^6),95\%}$ defined as the 95% percentile with a confidence level of 75% for a two-sided interval. As shown in Fig. 6.26a, the obtained reference value at $N_{3,T/2}$, also called the detail category, was 80.

The same analysis was carried out with $S_{\mathrm{rhs}} - N_4$ data where N_4 is the number of cycles at which there is a complete loss of the joint strength. The N_4 value was obtained by multiplying the number of cycles to through-thickness cracking, N_3, by 1.49 according to van Wingerde et al. (1997). The resulting detail category was 103 which is inferior to the CIDECT and IIW $S_{\mathrm{R,hs}} - N$ design curves category 114 for tubular joints with $T = 16$ mm (Zhao et al., 2000). A direct comparison is however difficult since the IIW recommendations does not strictly apply to our geometrical parameters (i.e. the SCF and hot-spot stress ranges cannot be computed using the IIW formulas). The SCF's computed by the IIW overestimate the real SCF's for our geometrical parameters ($\gamma < 12$) according to Schumacher and Nussbaumer (2006), and thus the IIW S-N curve 114 overestimates the fatigue life. The category 100, depicted in Fig. 6.26b, is more reliable for the fatigue design of tubular joints with a $\gamma < 12$. It is worth noting that Schumacher and Nussbaumer (2006) found a detail category 86, lower than 100 for S1 & S2 test results, however the hot-spot stress range values were not corrected for an equivalent 16 mm thick joint and only

8 data points were available at that time.

In Fig. 6.26a, the detail categories 80 and 100 are drawn, as well as the absolute hot-spot stress range values at hs1 or hs1c under fully-tensile, fully compressive, part-tensile and part-compressive loading. However, it is important to note that the data points for details in compression (square symbols) are drawn for fully effective hot-spot stress range values. It implies that tensile residual stresses are high enough to make the stress range entirely tensile up to half the thickness of the chord wall. If the stress range is only partly tensile, the effective hot-spot stress range to crack propagation would belong to the light gray area reported in Fig. 6.26a for details in compression. It is known from previous neutron diffraction measurements (see Figures 5.31), that residual stresses are high enough on the first millimeters (at least 5mm) to keep the stress range fully effective.

Size-effect study

As explained before, the experimental hot-spot stress range has to be corrected in order to take into account the well-known size effect. Once corrected, the results can be compared with the design curve, the $\mathrm{S_{R,hs}} - \mathrm{N}$ curve for T = 16 mm (Detail category 114).

There are two types of structural (geometrical) size effect: the proportional and the non-proportional size effect. In the proportional size effect, all the dimensions are proportionally scaled meaning that the non-dimensional parameters β, γ and τ are kept identical, which is not the case for the non-proportional size effect. In case of proportional scaling, the thickness correction factor expression is inspired from Gurney's correction factor for plates:

$$\frac{\Delta\sigma_{hs,T}}{\Delta\sigma_{hs,T_{ref}}} = (\frac{T_{ref}}{T})^n \tag{6.14}$$

where $\Delta\sigma_{\mathrm{hs,T}}$ is the hot-spot stress range for a tube thickness T, $\Delta\sigma_{\mathrm{hs,T_{ref}}}$ is the hot-spot stress range for a reference tube thickness $\mathrm{T_{ref}}$ and n is the size effect exponent.

Hereafter are summarised the main thickness correction factor available for plate and tubular joints:

- Gurney 's rule (Gurney, 1981) developed for plates:

  $$(\frac{22}{T})^{0.25}$$

  Note that Gurney based its factor on nominal stresses, and not on hot-spot stresses.

- The factor proposed by van Wingerde et al. (1997) for tubular joints and adopted by CIDECT and IIW recommendations:

  $$(\frac{16}{T})^n$$

  with n ranging between 0.24 and 0.402 ($n = 0.06 \times \log N_4$ for $10^4 < N_4 < 5x10^6$ and $n = 0.402$ for $5x10^6 < N_4 < 10^8$). Based on the fact that this factor is deduced from a database mainly composed of member thicknesses of 6 to 16 mm, it is known from (Schumacher et al., 2003) that this correction factor overestimates the size effect for wall thicknesses greater than 16 mm.

- The factor recommended by Eurocode 3, part 1-9 for plates:

  $$(\frac{25}{T})^{0.2}$$

  is almost similar to the Gurney's rule.

- The factor proposed by Borges and Nussbaumer (Nussbaumer et al., 2010):

  $$(\frac{16}{T})^{0.16}$$

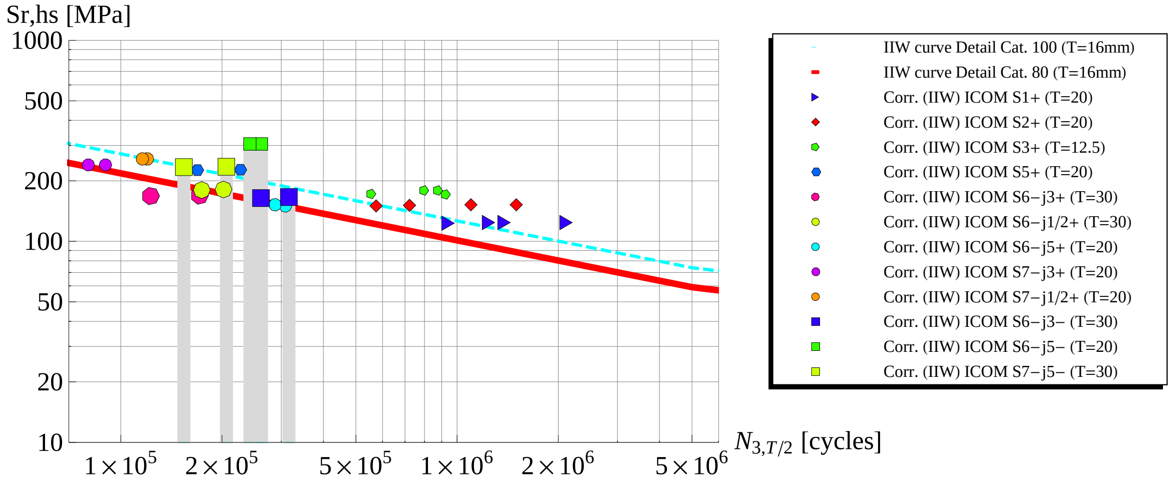

(a) $S_{rhs} - N$ curve at half-thickness cracking. The gray areas represent the possible values of the effective hot-spot stress range values to crack propagation at hs1c.

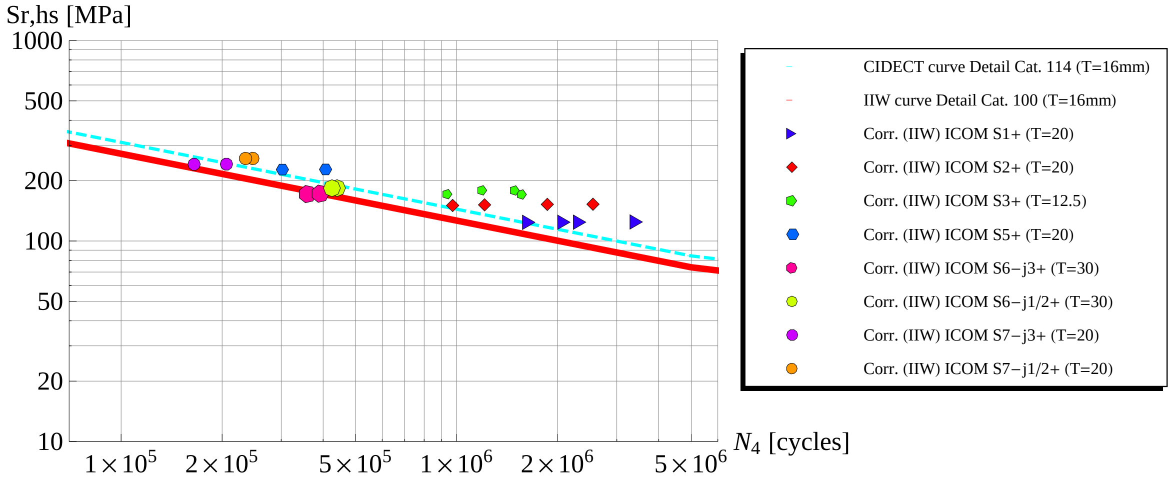

(b) $S_{rhs} - N$ curve for a complete loss of the joint strength cracking

Figure 6.26: Fatigue test results (hot-spot stress range values corrected to the equivalent 16 mm thickness) for series S1 to S7 and corresponding detail categories 80 and 100.

. This value is closed to the one proposed by MacDonald and Maddox (2003) for pipeline girth butt-joints:

$$(\frac{16}{T})^{0.15}$$

.

To be consistent, a reference tube thickness of 16 mm is kept all along this study. The $S_{rhs} - N_4$ curves are drawn for different size effect exponent presented above. The curves are compared in order to determine the most appropriate thickness correction factor.

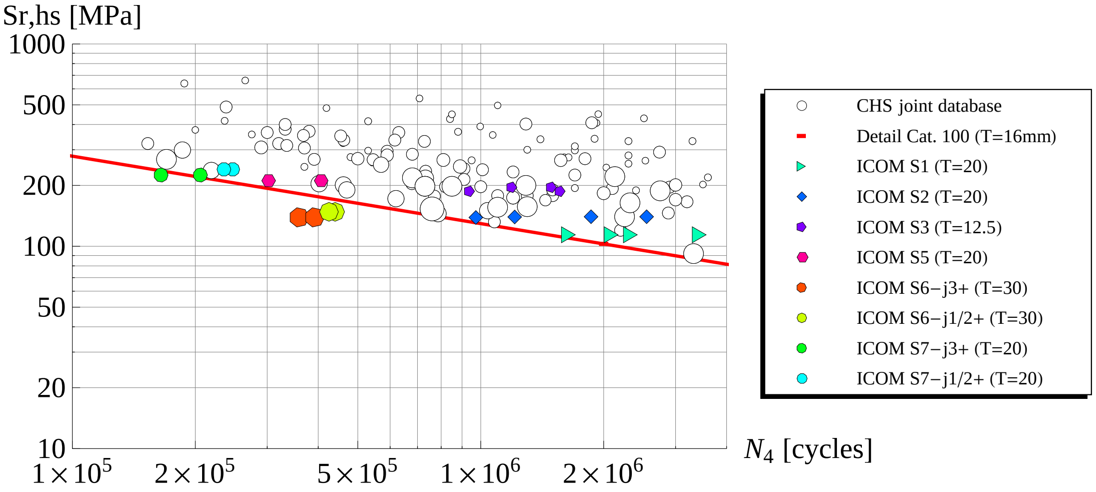

Figure 6.27: Fatigue test results (hot-spot stress range values not corrected for thickness effect) for series S1 to S7 and detail category 100.

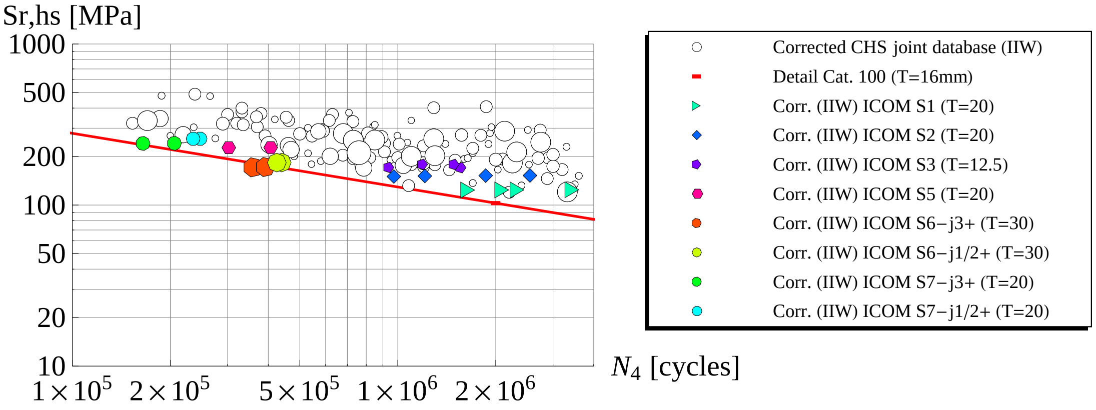

Figure 6.28: Fatigue test results (hot-spot stress range values corrected according to CIDECT and IIW to the equivalent 16 mm thickness) for series S1 to S7 and detail category 100.

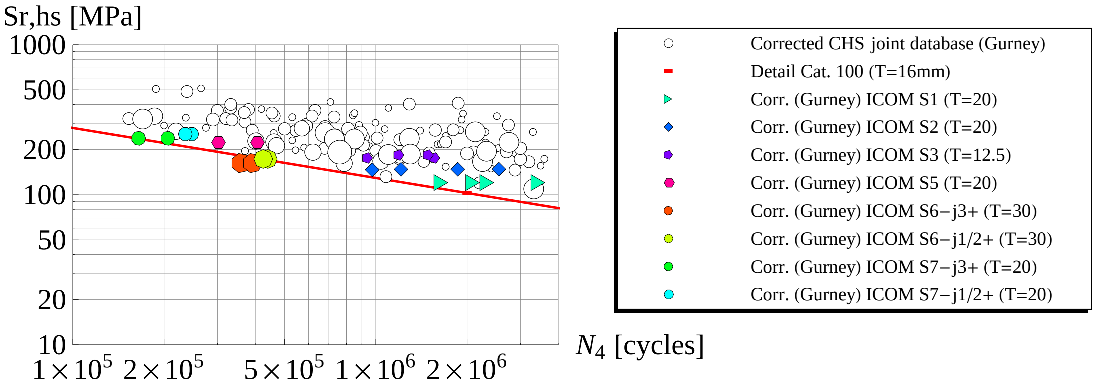

Figure 6.29: Fatigue test results (hot-spot stress range values corrected according to Gurney and EC3: n=0.25 to the equivalent 16 mm thickness) for series S1 to S7 and detail category 100.

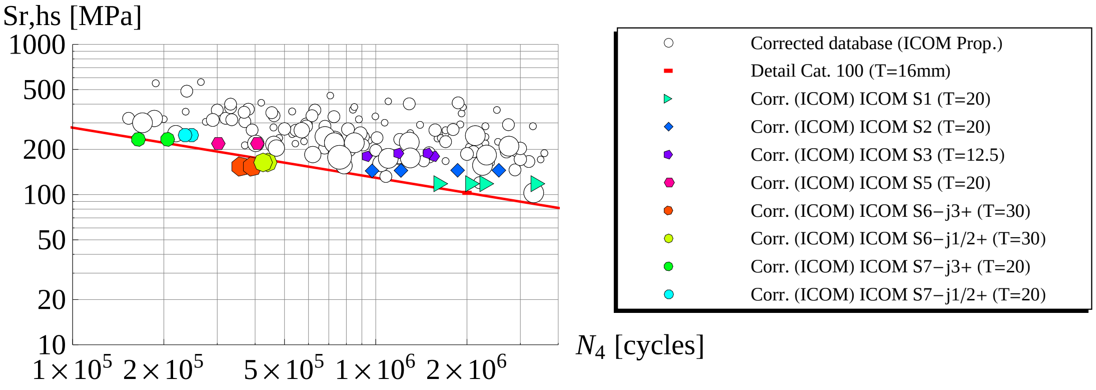

Figure 6.30: Fatigue test results (hot-spot stress range values corrected according to Borges and Nussbaumer : n=0.16 to the equivalent 16 mm thickness) for series S1 to S7 and detail category 100.

The standard deviation between the ICOM data points and detail category 100 has been calculated. It results that the three corrections give almost the same standard deviation of 0.37: 0.378 for the CIDECT and IIW factor, 0.369 for the Gurney and EC3 factor and 0.367 for Borges and Nussbaumer factor, the last one providing slightly better results. Therefore, it is difficult to conclude which one is the most appropriate thickness correction factor. More data is required to draw a clear conclusion.

It also can be seen that all corrected results fall above the design curve except joints S6-3N and S6-3S. It seems that size effect is not perfectly corrected by these thickness corrections. Indeed, our joints are scaled non-proportionally. The variations of parameters β, γ and τ have also to be taken into account in the correction. Borges (2008) developed a relationship for non-proportional analysis. However, it was not validated for low values of γ and τ ($\gamma < 4.2$, $\tau < 0.4$).

6.4 Discussion

6.4.1 Crack development under fully-tensile loading

The difference in the number of cycles to through-thickness cracking (N_3) in joints S6-3S and S7-3S indicates a difference in the crack propagation rate (Tables A.17 and A.18). It can be easily explained by the variation between the $\Delta\sigma_{hs,1}$ of joints S6-3S and S7-3S (Table 6.9). Since the well-known Paris law (Paris and Erdogan, 1963) is used to estimate the crack propagation rate for a stable crack growth in fatigue, the propagation rate is a function of the hot-spot stress range to the power of m. Roughly, for a same final crack length, the propagation rate of joint S7-3S should be 3 to 4 times higher than the one of joint S6-3S. Knowing that in reality $a_f = 25$ mm in joint S6-3S and $a_f = 35$ mm in joint S7-3S, then the multiplier is adjusted by a factor 2 to 3. This estimation is in good agreement with the resulting propagation rate. Therefore, the change in the crack propagation rate between joints S6-3S and S7-3S can be entirely explained by the variation of the applied stress range. Figure 6.26 confirms the previous explanation by showing that results for both joints are approximately aligned on the same detail category 80.

The angled path followed by the crack varies between joints S6-3S and S7-3S (see Fig. 6.25). This indicates that the direction of principal stresses is more affected by the brace loads in joint S6-3S than in joint S7-3S. Indeed, the applied stress values in the 30 mm wall chord (S6-3S) underneath the brace in compression are smaller than in the 20 mm wall chord (S7-3S). Therefore, for approximately the same brace stresses, the proportion of brace stresses is higher in joint S6-3S explaining why crack turns around the brace wall toe and do not cut across the chord wall. In joint S7-3S, crack turns toward the brace at mid-chord thickness, however chord stresses are high enough to change their direction and drive the crack path through the chord wall. Despite the fact that the applied stress range in joints 1 and 2 is higher, they are less critical than in joints 3S and 3N, stressing again the importance of the brace stress proportion.

Therefore, cracks occurring at hs1 under fully-tensile loading are driven by applied stresses. Their propagation rate is influenced by the applied stress range magnitude and their crack path seems to be strongly dependent on the applied stress range distribution and especially the proportion of brace stresses. In other words, the residual stress field does not affect the crack growth in details loaded in tension.

6.4.2 Crack development under fully-compressive loading

The previous conclusions are not applicable to cracks at hs1c (fully-compressive loading). For instance, it is seen in Fig. 6.31 representing the crack depth development followed using the ACPD measurements, that the crack propagation rate at hs1c is similar in joints S6-5N and S7-5N, whereas hot-spot stress magnitudes are different. In addition, the crack angle seems to be maintained through the thickness independently of applied stress distribution. Hence at hs1c the crack path is mainly influenced by the tensile residual stresses.

To understand how a crack can develop under fully-compressive fatigue loading, the experimental stress intensity factor ranges were deducted and plotted from ACPD measurements as a function of the calibrated crack depth (equation (6.5)). Figure 6.32 gives evidence that, under compressive and tensile applied stresses, the ΔK is still positive explaining why cracks propagate even under compressive loads. The positive ΔK in compression can only result from high tensile residual stresses, making the local stresses partly or entirely tensile. Thus, at least a part of the fatigue cycle is relevant (or effective) to crack propagation: $0 \leq \Delta K_{eff} \leq \Delta K_{app}$. Figure 6.32 indicates that a main part of the fatigue cycle is effective and does not seem to decrease with depth up to 15 mm. It is shown from these measurements and from previous residual stress investigations (see Fig. 5.31), that the particular geometry of K-joints induce tensile residual stresses which remain high in the gap region through, at least, half of the chord wall thickness.

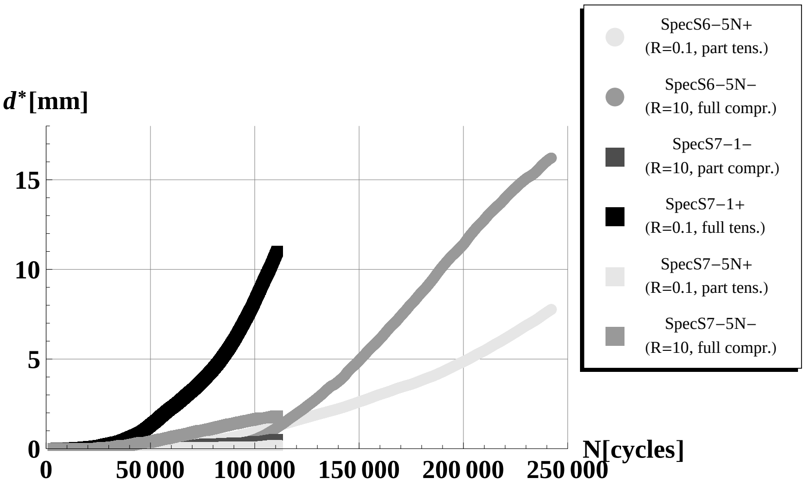

Figure 6.31: Fatigue crack development in the monitored joints.

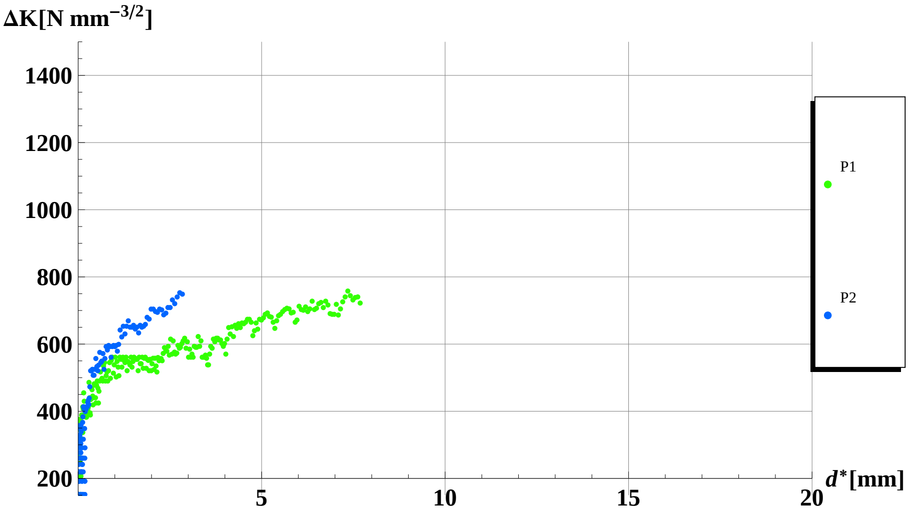

(a) Joint S6-J5N, tension brace side

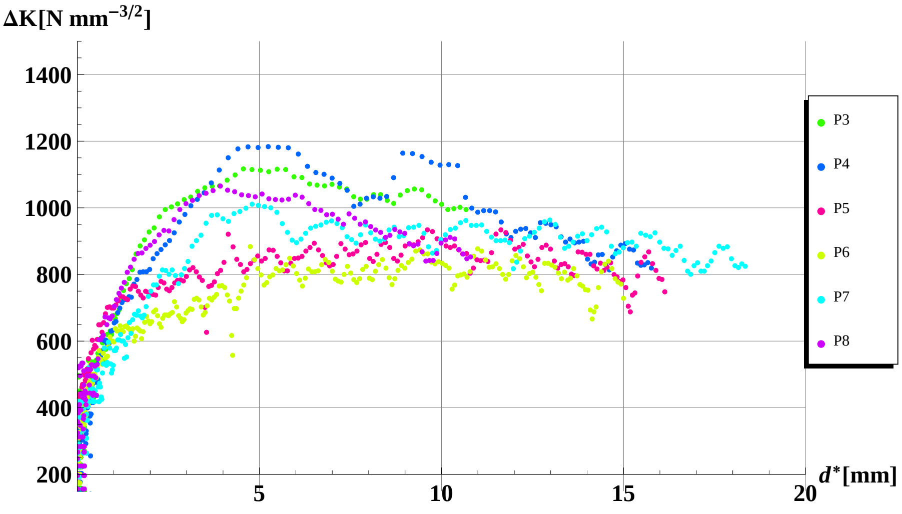

(b) Joint S6-J5N, compression brace side

Figure 6.32: Stress intensity factor range in joint S6-J5N versus the measured crack depth in the crack plane (log-log scale).

Tensile residual stresses play a significant role in crack propagation since they enable cracks to propagate at locations where applied compressive stresses are high.

6.4.3 Crack development under partly-tensile or partly-compressive loading

Crack propagation at hs1c on the chord loaded in tension (part-compressive loading) or hs1 on the chord loaded in compression (part-tensile loading) is more complex to explain. For instance, in comparing the crack in detail S6-5N+ (part-tensile loading) and the crack in detail S6-3S+ (full-tensile loading), cracks initiate and propagate with totally different rates despite the fact that both details have almost the same hot-spot stress range (see Table A.17). It appears that, for the same hot-spot stress range, cracks grew slowly in details submitted to part-tensile loading.

The cracks in details S7-3N- and S7-3S- (part-compressive loading) were also compared to cracks in details S7-5N- and S7-5S- (fully-compressive loading) presenting similar hot-spot stress range (see Table A.18). Since cracks occurred under compressive loading, it is clear that the crack development depends on the tensile residual stress field. It is seen that the critical crack occurred in fully-compressive loaded details even though cracks grew quite similarly in other details. It is worth noting that crack sizes are too small to draw a definite conclusion.

An explanation may be proposed for this phenomenon. For part-tensile loading, the crack initiated in the surface at hs1 under tensile loading and grew in the depth of the wall chord thickness under more and more compressive loading. For part-compressive loading, the stress field on the crack path is reversed. In other words, the part-tensile or part- compressive loading is the transition between a tensile loading type and a compressive loading type, thus between two different fatigue crack behaviors. The maximum crack opening is shifted under tensile and compressive loading involving a disturbance that probably slows down the crack propagation.

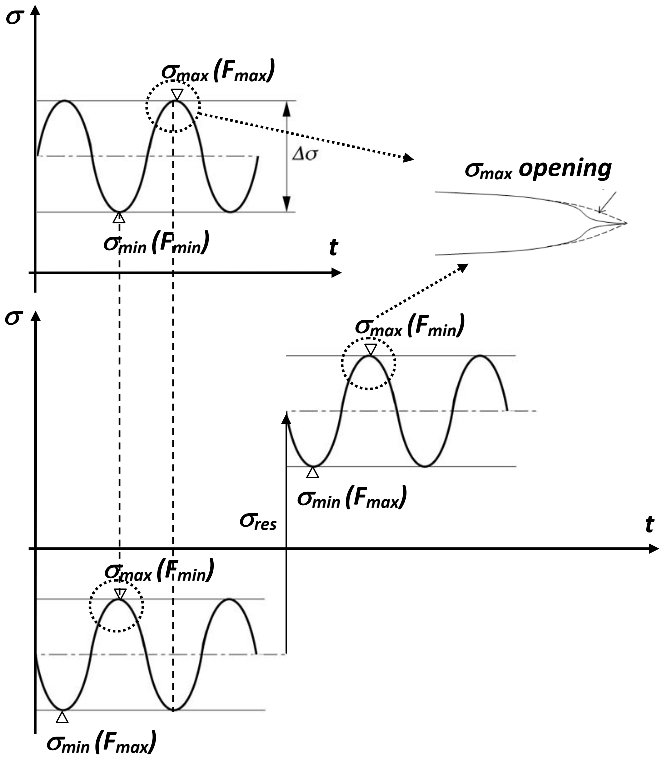

Figure 6.33: The stress cycle under fully tensile loading (top figure) and under fully compressive loading with high tensile residual stresses (bottom figure). The part of the cycle, during which the crack is wide open, is phase shifted between both loading types.

6.4.4 Crack depth evolution

The evolution of the crack growth is shown in Fig. 6.34. Given the crack propagation rate as a function of the calibrated crack depth. It shows different trends under tensile and compressive loadings.

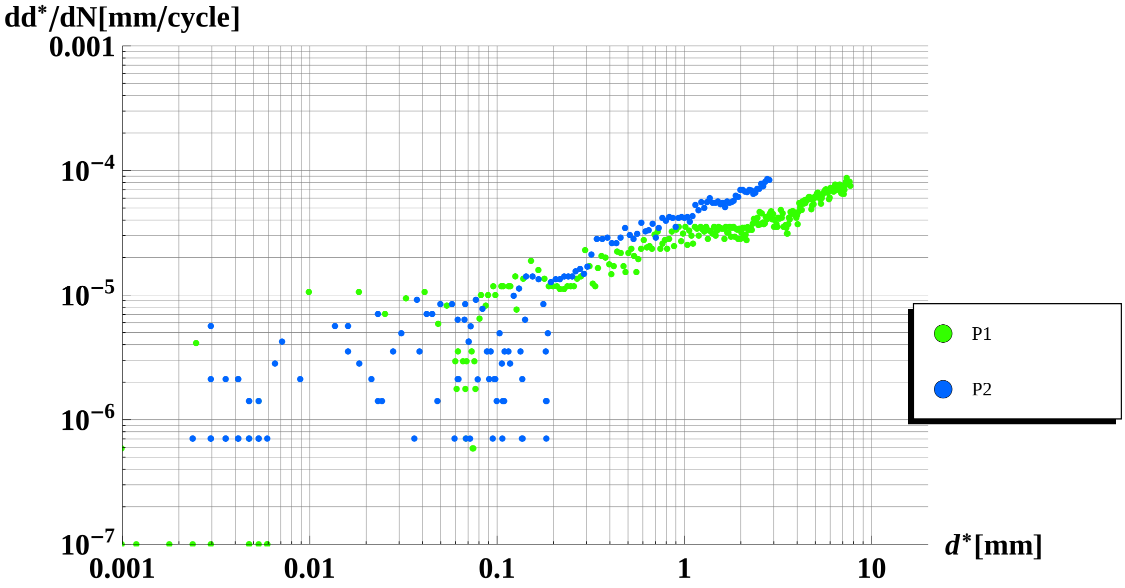

(a) Joint S6-J5N, tension brace side

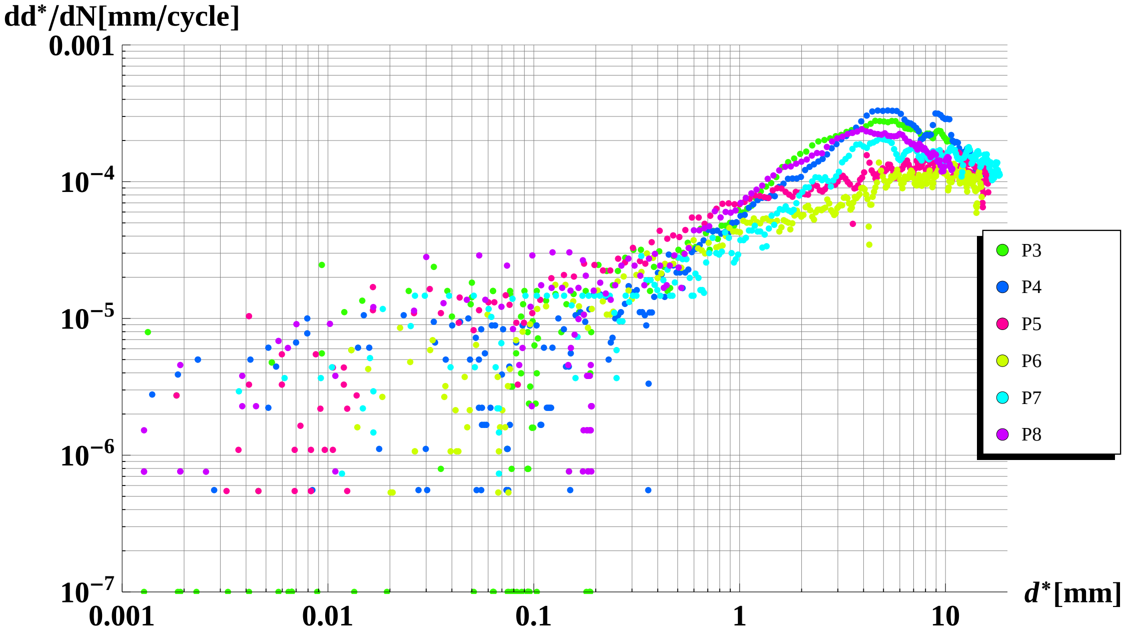

(b) Joint S6-J5N, compression brace side

Figure 6.34: Measured crack propagation rates in joint S6-J5N versus the measured crack depth in the crack plane (log-log scale).

Crack initiation and growth in joint S6-J5N first occurred from hot-spot 1c (S6-J5N-probe5 at 12000-16000 cycles, compression brace side). Then, a crack started to develop from hot-spot 1 (S6-J5N-probe1 at 25000-30000 cycles, tension brace side). The propagation rate increases on the tensile brace side whereas it decreases on the compressive brace side. This difference in the crack propagation rate evolution is also demonstrated in Fig. 6.31: an exponential increase is pointed at hs1 (S6-J5N-probe1, S7-J1-probe2) and a decrease a few millimeters away from hs1c (S6-J5N-probe5, S7-J5N-probe6).

In Fig. 6.34, the inflexion point of the curve corresponds to a crack depth of the order of 5 mm in the crack plane (or 4 mm in the vertical plane). At that point, tensile residual stresses probably become smaller. Therefore, cracks on the sides of tension and compression braces continued to grow with different rates.

Concerning joint S7-5N (probes 4 to 8), the rates of propagation seem to reach approximately the same values until 1 mm -crack depth value when the test was stopped-. As shown previously, the crack path is driven by the tensile stress distribution at hs1c, and this distribution should be quite similar in both joints at least on the first millimeter.

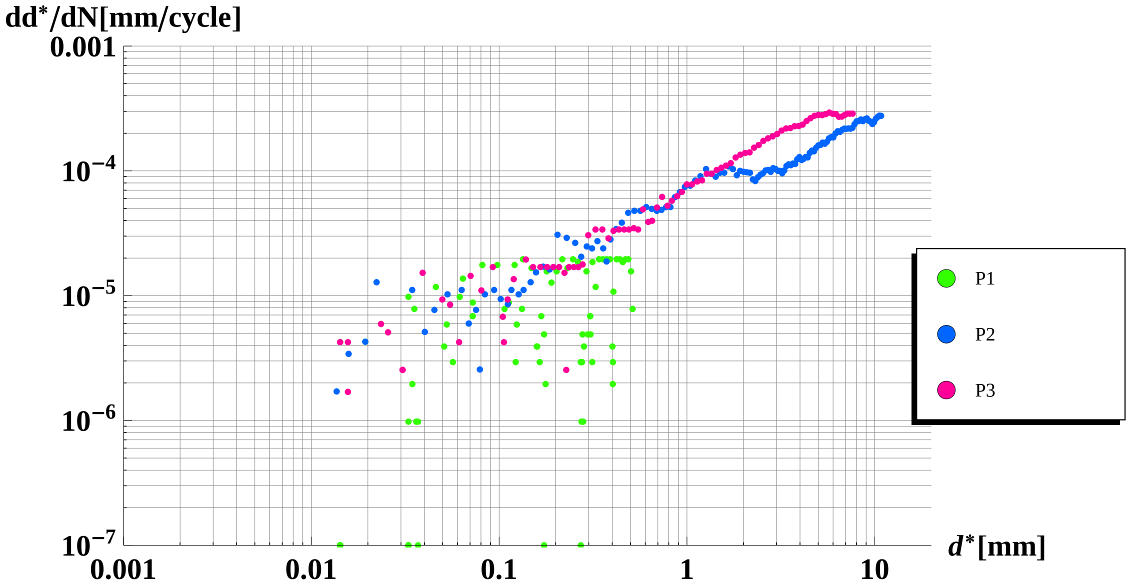

(a) Joint S7-J1

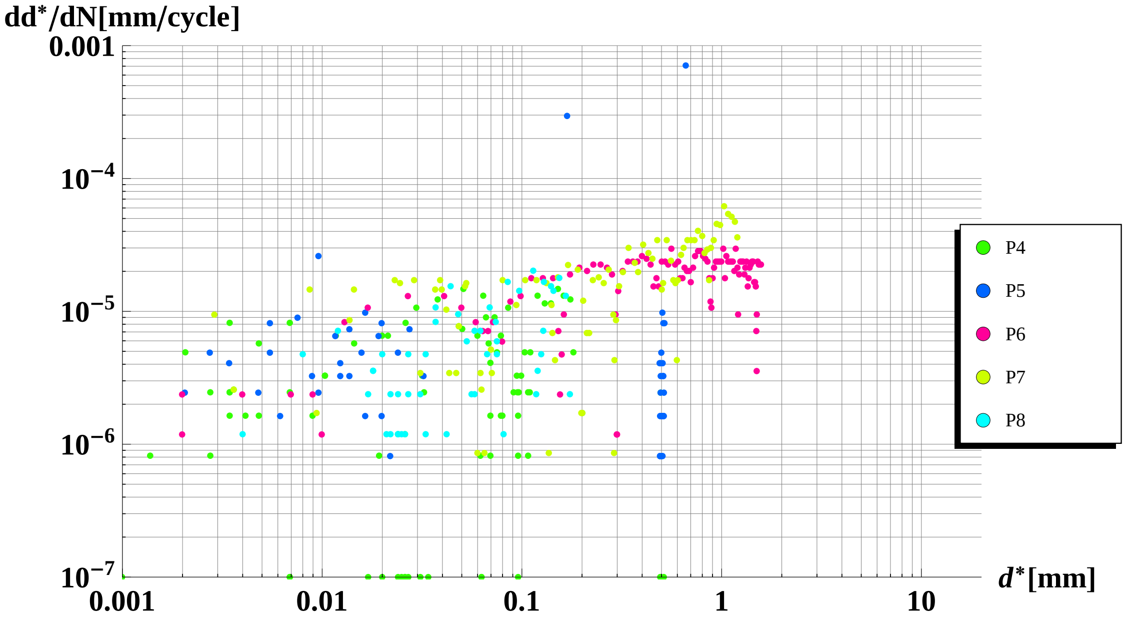

(b) Joint S7-J5N

Figure 6.35: Measured crack propagation rates in joints S7-J1 and S7-J5N versus the measured crack depth in the crack plane (log-log scale).

Figure 6.35 also confirmed that at hs1 of joint S7-1 (probes 1 and 2), crack initiates and propagates faster than at hs1c of joint S7-5N (probe 6).

6.4.5 Fatigue strength estimation

In Figure 6.26, an unexpected result is clearly seen: the details loaded under fully- or part-compressive loading in the tests do not have a different behavior than details loaded under tension. In other words, this figure proves that details in compression are not safer than others. Whatsmore, they may be even more critical since their effective hot-spot stress range values to fatigue crack propagation are smaller or equal to the ones presented in Fig. 6.26 (gray areas). To determine the exact value of the effective hot-spot stress range, the residual stress distribution should be accounted for at each potential hot-spot location.

To simplify the fatigue life estimation for details loaded in compression, it is proposed to assume conservatively that the applied stress range is entirely tensile. Then, details with $\gamma < 12$ loaded in both tension or compression can be designed with detail category 100, taking the absolute applied stress range as S_{rhs} value. The fact that details in compression did not reach the through-thickness failure criterion is discussed below. The detail category 100 estimates more accurately the effect of size on the fatigue strength of welded tubular joints. It is more consistent with the hot-spot fatigue classes proposed in the IIW and Eurocode 3, part 1-9 annex B for welded joints. In order to keep the same predicted resistance (known to be reliable) and compensate for the overestimated SCF, the SCF values given in CIDECT and IIW have to be reduced. A reduction factor of 100/114 applied to IIW formulas for SCF could be an elegant solution to update the IIW and CIDECT recommendations.

To make the distinction between the consequences of fatigue cracks in details loaded in tension and compression, a partial resistance factor γ_{Mf}=1 is chosen for details in compression (damage tolerant design, low consequence of failure according to in Eurocode 3, part 1-9) and γ_{Mf}=1.15 for details in tension (damage tolerant design, high consequence of failure).

6.4.6 Size effect correction

The thickness correction factor given by the CIDECT-IIW, by GURNEY-EC3 and by Borges and Nussbaumer are compared based on the ICOM test data. However, they provides almost the same corrections. The Borges and Nussbaumer's factor gives slightly better results than the others. More data is required to clearly identify the most appropriate thickness correction factor.

Moreover, it is important to note that in Fig. 6.26, some corrected values fall well above the design curve, especially the ones related to joints with 30 mm chord wall thickness. The size effect is not perfectly corrected with the correction factor used in this study proposed by van Wingerde et al. (1997). Also, the tests with non-proportional sizing, i.e. series S5, are not corrected as well as the other series.

It seems that the size effect correction is still not well solves.

6.5 Summary and conclusions

Two fatigue tests were performed on large-scale specimens, typical to bridge construction. The crack development was followed in the welded tubular K-joints in order to determine the influence of the welding residual stresses on the fatigue behaviour. The experimental investigations on the tubular truss specimens were carried out with a load ratio $R = 0.1$. Therefore, details in tension were tested almost under zero-tension loading ($R = 0.1$) and details in compression under almost zero-compression loading ($R = 10$). The following conclusions can be drawn from the present study:

- Cracks occurring at hs1 under fully-tensile loading are driven by applied stresses, especially the proportion of brace stresses, influencing the crack shape, the propagation rate and the stress intensity factor. The residual stress field does not affect the fatigue crack growth in details loaded in tension.
- Cracks occurring at hs1c under fully-compressive loading are due to the presence of high tensile residual stresses making the fatigue cycle partly or entirely effective to crack propagation. Based on Alternating Current Potential Drop measurements (ACPD), it is shown that the stress intensity factor range remains highly positive within the range of measurement depths (up to 15mm). Therefore, in the tested K-joints, tensile residual stresses play a significant role in fatigue crack propagation since they enable cracks to propagate up to at least half of the chord wall thickness under applied compressive stresses.
- Cracks occurring at hs1 under part-tensile loading or at hs1c under part-compressive loading are more complex to analyse since they show a transition behaviour between tensile and compressive loadings. Despite this fact, their fatigue strength is not significantly better than the details under fully-tensile loadings.
- It is seen from the test results that, if through thickness cracking is considered as the fatigue failure criterion, details loaded in compression are not critical. The critical cracks were located at hs1 for each test, in joints combining the highest hot-spot stress range with the highest proportion of brace stresses. However, if the failure criterion is the half-thickness crack, details loaded under compression also reach that criterion at about the same number of cycles and thus are not safer than the others.
- The failure criterion is not coherent in the codes. Therefore, we recommend to design all (tension or compression) CHS K-joints with $\gamma < 12$ using a strength curve $S_{rhs} - Nf$ category 100 for $T = 16$ mm . On the loading side, the hot-spot stress range should be determined with the correct SCF ((as close as possible to the 'real' effective value)) and taken as the total applied hs stress range in absolute value. However, a distinction between the failure consequence of fatigue cracks in details loaded in tension and compression is made through the partial strength factor value (according to Eurocode3, part 1-9): $\gamma_{Mf}=1$ for detail in compression and $\gamma_{Mf}=1.15$ for detail in tension.
- It is important to note that the size effect correction used in this study (IIW correction) does not perfectly correct the size effects (proportional and non-proportional). The Borges and Nussbaumer's factor gives slightly better results than the others, however not justifying the additional complexity in the correction factor at this time.

Part III

Numerical models and simulations

Chapter 7

Numerical analysis for welding induced residual stress estimation

This chapter describes the numerical analysis used to estimate welding induced residual stresses. The main idea is to combine the welding simulations presented hereafter with crack propagation analyses presented in the next chapter. This two steps approach aims to evaluate fatigue crack propagation under residual and applied stress fields. The numerical analysis can be used to design the geometry of K-joints loaded under fatigue stresses in order to optimize the fatigue life of these joints. Thermo-mechanical simulations introduced in this chapter are focused on the fusion welding process (arc welding MAG process defined in chapter 2) generally used to fabricate tubular bridge joints. These simulations provide the 3D residual stress distribution along the weld. The calculated residual stresses are compared with measured residual stresses in order to evaluate the accuracy of the numerical models.

7.1 Introduction

7.1.1 Objectives

The main objectives are the following:

- Determine which aspects of the problem can be simplified and develop the welding model.
- Simulate the three-dimensional residual stress distribution (orientation and magnitude) in the region surrounding the weld.
- Compare these residual stresses with measured residual stresses (chapter 5) in order to estimate the ability of the numerical simulation to predict these stresses.
- Identify the position of highest residual stresses.
- Verify previous considerations taken from fatigue test results, in particular similarities of residual stress distribution for joints with T = 20 mm and T = 30 mm.

7.1.2 Analysis type

In general, to simulate the welding process, the thermal, metallurgical and mechanical states of the structure have to be described, as well as the interactions between them. In the case of mild steel, it is assumed that phase transformations have a small effect on residual stresses generation (see section 7.2.1), therefore the problem is reduced to a thermo-mechanical analysis (Fig. 2.12).

A one way coupled or uncoupled thermo-mechanical analysis is performed. The response of the joint to welding is evaluated in two steps. First, a 3D thermal problem is solved and the temperature field history generated by welding is determined. The heat transfer is transient because the temperature varies with time. Then, the mechanical problem is solved using the temperature field as input data. The effects of the mechanical work on the thermal analysis are ignored. Since the thermal and mechanical properties are temperature-dependent, the problem is non linear. The main advantage of the uncoupled analysis, compared to a fully coupled analysis (solving at the same time temperature and displacement fields) is its flexibility, its efficiency and thus it is less computational time consuming.

7.1.3 Finite element codes

Two codes are chosen to perform thermo-mechanical analyses: ABAQUS® (ABAQUS, 2009) and MORFEO® (MORFEO, 2009) from Cenaero research center. ABAQUS presents large analysis capabilities (nonlinear, transient, dynamic, etc.) whereas MORFEO is rather dedicated to welding and manufacturing (Manufacturing ORiented Finite Element tOol MORFEO).

The main advantage of ABAQUS is that it is a general code allowing to solve efficiently different kinds of problems, even highly nonlinear problems. A lot of features and element types are implemented in this code. However, for thermo-mechanical problems, some tools are missing especially concerning the weld connection between components or the heat flux: the heat source (double ellipsoid, double elliptic cone, cylindric, spheric, etc.) and the heat flux trajectory have to be developed by the user through a user subroutine. In MORFEO, these tools are available. Since this code is focused on the welding process, the computation time is minimized by using dedicated solvers.

Both ABAQUS and MORFEO's models do not take into account the phase transformation evolution (for a thermo-metallurgical-mechanical analysis). This aspect is in development in MORFEO.

7.2 Recommendations and simplifying assumptions

7.2.1 Recommendations and methodology to simplify the problem

Welding is a highly nonlinear problem. As shown in Fig. 2.11, one has to take into account the thermal process, the metallurgical process, the mechanical process as well as the interactions between them in order to model the development of the welding residual stresses. This means that heat source should be modeled, the multipass welding thermal cycle should be evaluated at each point of the material, the induced phase transformations have to be known, the mechanical characteristics of each material (base material and weld material) for each microstructure (ferrite, pearlite, austenite...) at each temperature, between 20 C to 1500 C, and for each weld pass have to be estimated, etc.

Our first objective is to determine the aspects of this problem that can be simplified for our steel grade and for our welding process in order to obtain an accurate estimation of the residual stresses in a reasonable computational time.

Different simplified numerical procedures have been developed.

P. Dong proposed such a simplified analysis method in the Welding Research Council Bulletin Dong and Hong (2002) in order to improve quality for fracture mechanics based fitness-for-service assessments. This bulletin provides recommended procedures and indicates which phenomena are of low importance in determining the final residual stress state. A particular interest is showed in pressure vessel and piping components made of carbon steel or stainless steel.

L.-E. Lindgren proposed also several recommendations in Lindgren (2001a,b,c) in order to define the finite element modeling of welding in general.

Heat flow modeling - Arc and weld pool phenomena procedure

The first step consists in modeling the heat flow mechanisms between the welding molten pool and the base material (BM) in the neighbourhood of the weld.

To simply the problem of molten pool dynamics modeling, it has been shown that the ***weld fusion profile*** can be directly used as an input parameter. This weld fusion profile is defined as the geometry and size of the weld pool penetration, and can be evaluated with cross-sectional macrographs for example.

An ***equivalent heat source*** is approximated in order to reproduce the weld fusion profile by ***heat conduction based thermal analysis***. This analysis can either employ a finite element method, such as ABAQUS transient heat transfer procedure and MORFEO non-linear transient thermal problem, or an analytical method, such as Rosenthal analytical solution (Drezet et al., 2006). The last method has the advantage to be independent of finite element models and to require less time but has also its inherent drawbacks (constant thermal properties, no latent heat, etc.).

Thermal analysis procedure

The choice of a 2D/axisymmetric or 3D residual stress model is not without consequence in a thermal analysis.

Most of the residual stresses prediction are based on 2D cross-section models due to the fact that these two-dimensional models are less demanding than three-dimensional models. However, it has to be underlined that, if a heat input parameter is analysed with a 2D thermal model, it will provide a non negligible ***overheating***. The resulting molten zone of the model will be significantly larger than those defined by the weld fusion profile. This overheating will have a strong impact on the residual stress distribution: longitudinal residual stresses in particular are largely overestimated. This phenomenon can be explained by the fact that the heat loss and the conduction transport in the third direction are not taken into account.

Note that an alternative solution would be to use a 3D analytical heat flow solution method to calculate the equivalent heat source, presented as a ***3D temperature history solution*** in the base metal, and transform it in a 2D model by taking a unit weld length in the third direction.

In this analytical method, other localized effects should be added such as the important variations of residual stresses at the start/stop positions.

Remarks:

- It is important to compare the size and shape of the weld fusion profile evaluated with the thermal analysis to the measured weld fusion profile, taken as an input parameter, in order to prevent overheating. The peak temperature should also be compared with thermocouple temperature measurements if available. Indeed, in the IIW Round-Robin investigation (RSDP 1996), it has been shown that there were large discrepancies among various researchers predictions and that most of those results induced overheating.
- Sensitivity analysis devoted to the influence of the number of passes on the residual stress approximation implies that a ***three-pass*** model is sufficient to describe the residual stress distributions of a multiple-pass weld according to Dong and Hong (2002). Lindgren (2001a) did not propose a number of weld passes but underlines the fact that merging weld passes into one equivalent pass by keeping the total heat input gives the most accurate results.

Phase Transformation - Metallurgical analysis procedure

Another aspect of the analysis is the metallurgical analysis which is coupled with the thermal and mechanical analyses. This aspect of the problem is one of the most complex parts. In his recommendations (Dong and Hong, 2002), P.Dong has analysed the influence of phase transformations on the final residual stress distribution and he concludes that predictions with or without considering these transformations is quite similar for low or mild carbon steel. He explains this observation by the following reasons:

- Martensitic transformation is relatively localized around the HAZ area and consequently induced residual stress variations are so small that they are difficult to measure experimentally.
- Such transformations create local compression residual stress (of approximately 5 % of the total residual stresses), then if we neglect them, we have a conservative estimation of fracture aspects.
- These local variations in residual stress distribution do not really have an impact on the stress intensity factors.

Obviously, this simplification to consider phase transformation effects as negligible is not true for several type of steels (casting steel, steel plate hot rolling, etc.), and also not true for low temperature transformation. In fact, for steel where the transformation is martensitic (the austenite is transformed into martensite during cooling), a volumetric change and a yield strength change are associated with the transformations decreasing drastically the tensile residual stress intensity, sometimes up to negative values (Dean and Hidekazu, 2006; Francis et al., 2007). That is the reason why finite element codes such as SYSWELD, developed a model that is able to take phase transformations into consideration.

To be convinced that the fraction of martensite formed in S355J2H steel is low, one can see in section 4.6 the hardness testing conducted in the HAZ and the FZ.

Welding related material behaviour - Mechanical analysis procedure

Once the temperature history has been obtained from the heat flow modeling, stress calculations based on thermo-mechanical analysis can be done. Welding-related material behaviours are modeled in this part:

- Metal deposition and melting/remelting strain annihilation.
- Stress-plastic strain behaviour.
- Temperature-dependent mechanical properties.

Metal deposition and melting/remelting strain annealing

One of the most important point to consider, in order to obtain a realistic plastic strain field, is the melting/remelting effects. Indeed, in the metal area heated above the melting temperature, the material comes back to its zero plastic strain (i.e. fully annealed state). If this plastic strain annihilation is not taken into account, it will lead to an accumulation of plastic strain at each weld pass, inducing unrealistic residual stresses. There is some finite element codes, like ABAQUS, that are able to eliminate this melting plastic strain. Using the *ANNEAL TEMPERATURE option, plastic strains accumulated in the fusion zone are canceled when the temperature is greater than the solidus temperature.

The birth and death technique can also be used. The birth element represents the material deposition with a zero plastic strain. All elements are defined from the beginning in the model but they are activated only when a new pass is added, meaning that they are absent from the calculation until their birth. Nevertheless, these special elements are not able to simulate remelting between two passes. Remelting, in multi-pass weld, requires to formulate a unified weld constitutive model using a plastic strain annealing procedure.

Another technique using the 'quiet elements' can also be used (Lindgren, 2001a). In this technique, all the weld elements are included in the model from the beginning but their material properties, such as the Young's modulus, take low values. Therefore, they do not affect the rest of the model until a new pass is created and they take their real material values. The accumulated plastic strain should also be annealed before the element recovers its real characteristics.

Stress-plastic strain behaviour

Dong and Hong (2002) proposed a stress-plastic strain curve that represents a realistic strain hardening behaviour. This curve does not limit the strain field to 2% plastic strain, as suggested in the IIW Round-Robin Koppenhoefer and Gordon (2000) in order to prevent a plastic strain accumulation amplified by overheating effects.

Lindgren shows that the choice between a kinematic and isotropic hardening depends on the studied welding process. However, a good choice seems to combine both hardening types.

This issue does not usually lead to the same answers from different authors.

Temperature-dependent mechanical properties

Mechanical properties (Young's Modulus, Poisson's Ratio, stress-strain curves) as well as thermo-physical properties change with temperature, especially between the room temperature and 700 °C. These properties can be found in different codes and metal handbooks. For temperatures beyond 700 °C, stress-strain curves are difficult to obtain by experimentation. However, the yield strength evolution between 700 °C and 1500 °C does not have a significant impact on residual stress estimations because the yield strength is considerably low at these temperatures, that is the reason why the yield strength at 1500 °C is assumed to be approximately 1/100 of those at room temperature.

Lindgren shows also that a cut-off temperature is often used in analyses. Above this temperature, no changes in mechanical properties are taken into account. He recommends that this temperature value is comprised between the austenization temperature and the melting temperature, the closer to the melting temperature the better.

Lindgren underlines that the most important mechanical properties are the Young's modulus, the thermal dilatation coefficient and the parameters defining the plastic behaviour.

It is appropriate to combine kinematic and isotropic hardening in order to get accurate residual stresses in the weld metal, but very few data are available.

7.2.2 Simplifying assumptions

Modeling of stress build-up during welding is a complex problem that can often be simplified because some aspects of the problem do not significantly affect the residual stress estimation. Based on previous recommendations, the simplifying assumptions of this model are the following:

- An uncoupled thermo-mechanical finite element formulation is chosen to solve the problem. The metallurgical aspects are neglected for this type of mild steel, except the heat release due to phase transformations which is taken into account in the thermal cycle.
- Multi-pass welding is simulated as a single pass with an equivalent spherical heat source. This heat source is composed of a volumetric flux moving on the weld path at the given welding speed. The characteristics of the heat source are determined so that the computed size of the weld pool matches the one measured on a macrograph. Metal deposition is not considered, the finite elements representing the weld are present in the model from the beginning.
- The thermal analysis is formulated in terms of heat conduction, heat losses by radiation and convection and heat input simulating the welding source. Latent heat of fusion is also included. Since fluid flow is not considered, an artificial increase of thermal conductivity is introduced above the melting temperature of the steel.
- The mechanical analysis is based on an elastic-plastic material behaviour with a linear isotropic work hardening ignoring rate-dependent (creep) effects at high temperatures.

7.3 Geometry of K-joints

The K-joint geometry is defined parametrically in order to easily transform the model for parametric study purposes. First, the chord and inclined braces tubes are modeled, the intersection of their outer surfaces defining the chord-brace intersection curves.

In a second time, the chord tube is translated upwards (by $Y_1 = W1 \times \sin\theta$ see Fig. 7.2), its outer surface cutting the brace outer surfaces to create the weld-brace intersection curves.

In a third time, fictitious braces with a diameter slightly greater than the brace diameters $(d + 2 \times W2)$ are centered on the brace axis translated by ± W3. Their intersection with the outer surface of the chord are the weld-chord intersection curves.

Weld-brace and weld-chord intersection curves, delimiting the weld position are depicted in Fig. 7.1.

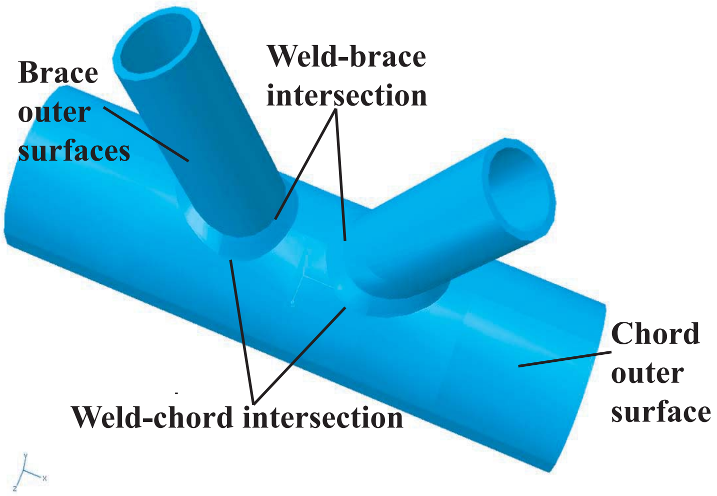
Brace outer surfaces
Weld-brace intersection
Chord outer surface
Weld-chord intersection

Figure 7.1: Definition of weld-brace and weld-chord intersections.

Distances W1, W2 and W3 (Fig. 7.2) were proposed by Borges (2008) based on the comparison with measured weld width.

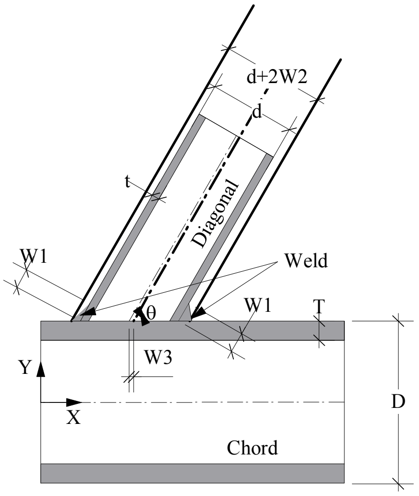
d+2W2
d
t
Diagonal
W1
Weld
W1
T
θ
W3
Y
X
D
Chord

Figure 7.2: Weld geometry defined by Borges (2008).

7.3.1 The adopted system of units

The unit system used is given in Table 7.1. Note that as lengths are expressed in mm, all stresses have MPa units.

Table 7.1: Unit system used in the model.

Length	mm
Force	N ($=\frac{kg\times m}{s^2}$)
Mass	kg
Time	s
Stress	MPa or N/mm^2
Energy	J (= N × m)
Density	kg/mm^3
Conductivity	W/(mm.°C)
Specific heat	J/(kg.°C)
Latent heat	J/(kg.°C)
Volumetric heat source	W/mm^3

7.3.2 Parametric equations of the chord-brace, weld-brace and weld-chord intersections

Chord-brace intersection

In Fig. 7.3, the global coordinate system (X,Y,Z) as well as the local coordinate system (x,y,z) are defined.

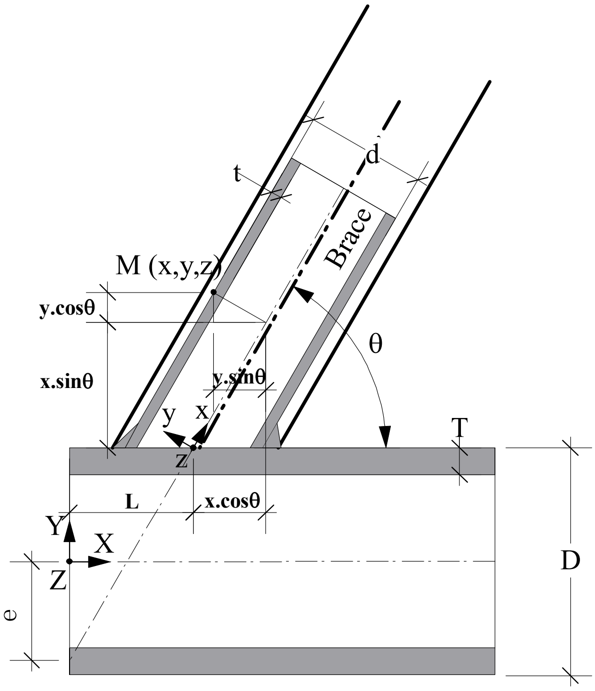

Figure 7.3: Coordinate systems and denominations.

Points on the chord outer surface follow the equation $Y^2 + Z^2 = (D/2)^2$ in the (X,Y,Z) system and points on the brace outer surface follow the equation $y^2 + z^2 = (d/2)^2$ in the (x,y,z) system.

The parametric equations for the cylinder describing the brace outer surface is:

$$\begin{cases} x = & x_1 \\ y = & \dfrac{d}{2}\cos\phi \\ z = & \dfrac{d}{2}\sin\phi \end{cases} \tag{7.1}$$

where ϕ is the local polar angle varying from 0 to 2π. As x_1 vary, the point on the brace surface moves parallel to the x axis.

It is possible to express the local coordinate system in the global coordinate system as follows (projection of the M point in local coordinate system):

$$\begin{cases} X = & (x\cos\theta - y\sin\theta) + L \\ Y = & \dfrac{D}{2} + x\sin\theta + y\cos\theta \\ Z = & z \end{cases} \tag{7.2}$$

where $L = \frac{e + D/2}{\tan\theta}$.

Therefore, equ. (7.1) can be given in the global coordinate system:

$$\begin{cases} X = & x_1\cos\theta - \dfrac{d}{2}\cos\phi\sin\theta + L \\ Y = & \dfrac{D}{2} + x_1\sin\theta + \dfrac{d}{2}\cos\phi\cos\theta \\ Z = & \dfrac{d}{2}\sin\phi \end{cases} \tag{7.3}$$

The intersection curve between the brace and the chord should verify the chord equation: $Y^2 + Z^2 = (D/2)^2$. Therefore, by introducing the equ. (7.3) in $Y^2 + Z^2 = (D/2)^2$, one can find the unknown value of x_1 and write the parametric equations of the chord-brace intersection.

Note that there are two chord-brace intersections: the brace cut in the chord surface in the area of positive Y coordinate, and also in the area of negative Y coordinate. Only the first solution corresponds to our geometry. Therefore the second solution is indicated in brackets in the following equation:

$$\begin{cases} X = & L - \dfrac{d}{2}\cos\phi\sin\theta - \cot\theta\left(\dfrac{D}{2} + \dfrac{d}{2}\cos\phi\cos\theta - (+)\sqrt{(\dfrac{D}{2})^2 - (\dfrac{d}{2})^2\sin^2\phi}\right) \\ Y = & (-)\sqrt{(\dfrac{D}{2})^2 - (\dfrac{d}{2})^2\sin^2\phi} \\ Z = & \dfrac{d}{2}\sin\phi \end{cases} \tag{7.4}$$

Weld-brace intersection

The parametric equations are similar to equ. (7.4) except that W1 × $\sin\theta$ is added to the Y coordinate owing to translation and hence W1 × $\cos\theta$ is added to the L value:

$$\begin{cases} X = & L + W1\cos\theta - \dfrac{d}{2}\cos\phi\sin\theta - \cot\theta\ (\dfrac{D}{2} + \dfrac{d}{2}\cos\phi\cos\theta \\ - & \sqrt{(\dfrac{D}{2})^2 - (\dfrac{d}{2})^2\sin^2\phi)} \\ Y = & \sqrt{(\dfrac{D}{2})^2 - (\dfrac{d}{2})^2\sin^2\phi} + W1\sin\theta \\ Z = & \dfrac{d}{2}\sin\phi \end{cases} \tag{7.5}$$

Weld-chord intersection

The parametric equations are also similar to equ. (7.4) except that W3 is added to L and W2 is added to $\frac{d}{2}$:

$$\begin{cases} X = & L + W3 - (\dfrac{d}{2} + W2)\cos\phi\sin\theta - \cot\theta\ (\dfrac{D}{2} + (\dfrac{d}{2} + W2)\cos\phi\cos\theta \\ - & \sqrt{(\dfrac{D}{2})^2 - (\dfrac{d}{2} + W2)^2\sin^2\phi)} \\ Y = & \sqrt{(\dfrac{D}{2})^2 - (\dfrac{d}{2} + W2)^2\sin^2\phi} \\ Z = & (\dfrac{d}{2} + W2)\sin\phi \end{cases} \tag{7.6}$$

Surface middle weld curve

Finally using the weld-brace and weld-chord intersection equations, one can easily find the middle curve by calculating the average equations. These equations will be used later to define the heat source trajectory:

$$\begin{cases} X = & L + \dfrac{W3 + W1\cos\theta}{2} - (\dfrac{d}{2} + \dfrac{W2}{2})\cos\phi\sin\theta \\ - & \cot\theta\ (\dfrac{D}{2} + (\dfrac{d}{2} + \dfrac{W2}{2})\cos\phi\cos\theta \\ - & (Y - \dfrac{W1}{2}\sin\theta)) \\ Y = & \sqrt{(\dfrac{D}{2})^2 - (\dfrac{d}{2} + \dfrac{W2}{2})^2\sin^2\phi} + \dfrac{W1}{2}\sin\theta \\ Z = & (\dfrac{d}{2} + \dfrac{W2}{2})\sin\phi \end{cases} \tag{7.7}$$

The W1, W2 and W3 values proposed by Borges (2008)

These values are proportional to the brace wall thickness t:

$$\begin{cases} W1 = & 1.88t \\ W2 = & 1.25t \\ W3 = & 0.627t \end{cases} \tag{7.8}$$

7.3.3 The weld shape

As explained above the weld shape is based on the weld-brace and weld-chord curves which were defined by comparison with measured weld profiles. To simplify the weld definition, the surface of the weld is not modeled convex as in reality (see Fig. 7.4) despite the fact that the angle between the tube surface and the tangent to the weld surface at the chord and brace crown toes are known to influence the fatigue strength (Gurney, 1979; Newman and Gurney, 1959; Sanders et al., 1965). We assume that the weld toe angles are not too different between the model and reality, and hence that the effect of the weld toe angles is small.

Moreover, the radius of the weld toe as well as the width to the height of the weld overfill have also a significant effect on the fatigue behaviour (Takahashi and Ito, 1971; Yamaguchi et al., 1966) but this was not introduced neither.

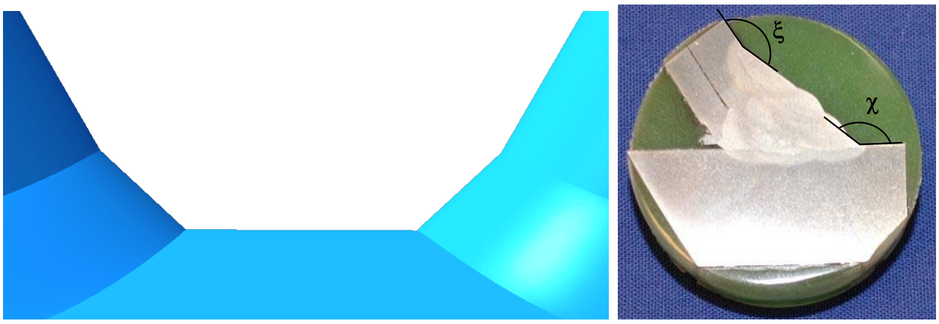

(a) Modeled weld geometry **(b)** Real weld geometry

Figure 7.4: Comparison between the modeled weld profile and the real weld profile.

7.3.4 Dimensions of the modeled K-joints

The K-joints geometry and dimensions correspond to the K-joints tested under fatigue loading and on which residual stress measurements were performed. There are two types of K-joints with similar geometry except for the wall thickness of their chords. The first geometry based on a chord with a wall thickness of 20 mm is called Ref-T20 (geometry 1) and the second with a wall thickness of 30 mm is called Ref-T30 (geometry 2). Their dimensions and geometrical parameters are given in Table 7.2.

The lengths of the chord and brace were found interactively. First, a chord length of 1300 mm and a brace length of 600 mm (450 mm remaining once cut by the chord) were chosen. The first simulations were carried out on this geometry. Based on the area really affected by the welding process, it was possible to reduce the model size to the following dimensions.

Table 7.2: Main dimensions (mm) and geometrical parameters for modeled K-joints.

Mod nb	D	T	d	t	Chord Length	Brace Length	β	γ	τ	e	g	θ	W1	W2	W3
1	168.3	20	88.9	8	600	350	0.53	4.21	0.4	49.3	51	60°	15	10	5
2	168.3	30	88.9	8	600	350	0.53	2.81	0.27	49.3	51	60°	15	10	5

In order to leave sufficient space for welding, Schumacher (2003) chose two criteria to respect, the gap value g must not be greater than 4 t and the real gap value g' (distance between the weld toes) must be greater than 1.6 T. In reality, the criterion generally observed is the first one $g > 4$ t. This the one we applied in our study.

To verify that the modeled K-joint is close to reality, we compare the modeled geometry with the surface of the FAT-20 sample measured by laser scanning at ILL (chord wall of 20 mm, fatigue tested). Figure 7.5 shows that both geometries are fitting well in the region of the weld toes, but the brace surfaces are not properly superimposed. The shifting of the brace positions is not particularly important in comparison with the weld positions. This imprecision is due to the fact that, in the case of this joint, the width of the weld in contact with the chord is smaller than the equivalent width in our model geometry. The weld width distances proposed by Borges (2008) are based on an average of measured weld width.

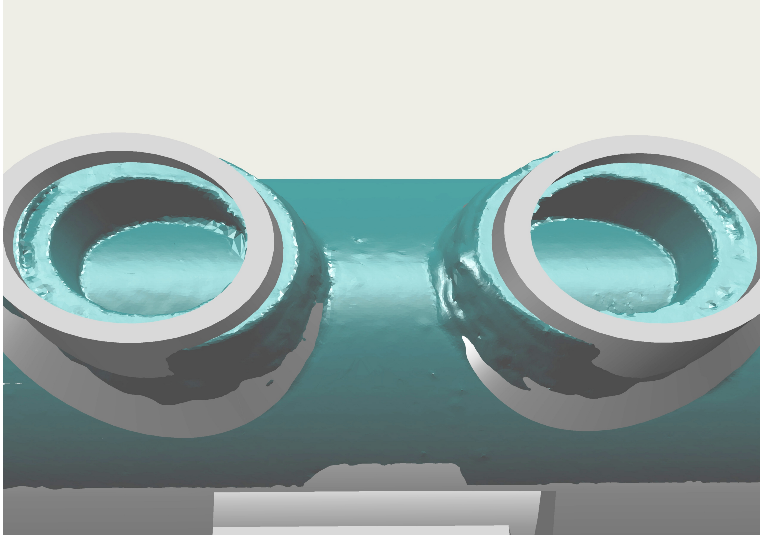

Figure 7.5: Superimposition of the modeled geometry Ref-T20 (in gray) with the surface of the FAT-20 sample (in blue) measured by a laser scanner at ILL.

7.3.5 Symmetry of the problem

The K-joint geometry has two planes of symmetry. However the trajectory of the heat source is not symmetric since the welds are made sequentially (see Fig. 4.6). Therefore, it is not possible to reduce the model size using symmetry.

7.4 Material behaviour model

7.4.1 Thermal analysis

The main objective of this analysis is to calculate the temperature distribution as a function of time during the welding and cooling steps. During welding, the heat is transferred by conduction to the sample. Solving the heat conduction problem consists in solving the energy balance equation in a control volume during an increment of time Δt:

Heat input	+	Heat conducted into the volume	-	Heat conducted out of the volume	=	Change in internal energy within the volume
(Heat source)		(Heat flow in)		(Heat flow out)		

Note that for a steady-state problem (the temperature is not changing with time), there is no change in internal energy within the volume.

This relation can be reduced to the following as demonstrated in annex C:

$$\text{Energy balance} \; : \; \rho \, \frac{\partial u^t}{\partial t} = -\boldsymbol{\nabla}^T \mathbf{q} + s \tag{7.9}$$

where

ρ is the density of the material in kg/mm^3
u^t is the specific internal energy u in J/kg
q is the heat flux, defined as the rate of heat conducted across a surface, in J/(s.mm^2 = W/mm^2)
s is the rate of volumetric heat generation in J/(s.mm^3 = W/mm^3)

The rate of specific internal energies $\frac{\partial \mathrm{u}^t}{\partial \mathrm{t}}$ can be expressed in function of an equivalent specific heat C$_{eq}$ in J/(kg.°C) (see annex C):

$$\frac{\partial u^t}{\partial t} = C_{eq} \frac{\partial T}{\partial t} \tag{7.10}$$

The Fourier's law (constitutive equation) relates the heat flux to the temperature:

$$\mathbf{q} = -\mathbf{D}\boldsymbol{\nabla} T \tag{7.11}$$

where D is the temperature dependent thermal conductivity matrix in J/(s.mm.°C) = W/(mm.°C). In isotropic case, **D** is reduced to one coefficient, the thermal conductivity k.

To solve the second order equation, one boundary condition is required at each point of the boundary. This boundary condition is either based on temperature or on heat flux:

$$\begin{cases} \text{Natural boundary condition} \;\; q_n = & \mathbf{q}^T\mathbf{n} = \bar{q} \;\; \text{on} \;\; \Gamma_\mathrm{q} \;\; \text{(Neumann condition)} \\ \text{Essential boundary condition} \;\; T = & \bar{T} \;\; \text{on} \;\; \Gamma_\mathrm{T} \;\; \text{(Dirichlet condition)} \end{cases} \tag{7.12}$$

In our case, the boundary condition is a prescribed flux $\bar{\mathrm{q}}$ traducing natural convection and radiation to the environment.

The thermal analysis can be summarised as follows:

- **Variables:** essential variable : temperature T, natural variable : heat flux q.
- **Material:** conductivity k= f(T), specific heat C=f(T), density ρ, latent heat at solidus-liquidus temperature (see annex C).
- **Boundary conditions:** $\bar{\mathrm{q}}$, $\bar{\mathrm{T}}$.
- **Heat input:** volumetric heat source s = f(t,M) function of time and position.

The thermal conductivity and specific heat values are given in Tables 4.10 and 4.11.
To take into account that, at a temperature greater than the solidus temperature (T = 1465 °C for our steel), the convective flow accelerates the weld pool temperature homogenization, the conductivity value is increased to three times its value at the solidus temperature (Goldak et al., 1984; Papazoglou and Masubuchi, 1982; Saint-Germain, 2006) and kept constant at T $\geq$ T$_{\mathrm{solidus}}$.
The density value is constant and equal to 7850 kg/m^3. The latent heat L induced by the fusion/solidification between solidus and liquidus is considered, using a value of 247000 J/(kg.°C) (Raymond and Chipman, 1967).

7.4.2 Mechanical analysis

Equilibrium is defined as the static-mechanical relation:

$$\boldsymbol{\nabla}^T\boldsymbol{\sigma} + \mathbf{b} = \mathbf{0} \tag{7.13}$$

where $\boldsymbol{\nabla}^\mathrm{T}\boldsymbol{\sigma}$ is the divergence of the stress field (transpose of the gradient matrix $\boldsymbol{\nabla}$) and **b** is the body force per unit volume. Note that in vector form, the previous equation can be expressed as $\tilde{\nabla}.\ \tilde{\sigma_\mathrm{x}} + \mathrm{b_x} = 0$ for the x axis for instance.

The strain can be decomposed into elastic, plastic and thermal parts:

$$\boldsymbol{\epsilon} = \boldsymbol{\epsilon}^{el} + \boldsymbol{\epsilon}^{pl} + \boldsymbol{\epsilon}^{th} \tag{7.14}$$

Therefore, the generalised Hooke's law (constitutive equation) is expressed as:

$$\boldsymbol{\sigma} = \mathbf{C}\boldsymbol{\epsilon}^{el} = \mathbf{C}(\boldsymbol{\epsilon} - \boldsymbol{\epsilon}^{pl} - \boldsymbol{\epsilon}^{th}) \tag{7.15}$$

where **C** is the elasticity matrix.
And the kinematics equation for small deformations is:

$$\boldsymbol{\epsilon} = \boldsymbol{\nabla}\mathbf{u} \tag{7.16}$$

Therefore, if the elastic and thermal parts are known, the plastic part needs to be defined in order to solve the following expression:

$$\boldsymbol{\nabla}^T(\mathbf{C}(\boldsymbol{\nabla}\mathbf{u} - \boldsymbol{\epsilon}^{pl} - \alpha(\mathbf{T} - T_0))) + \mathbf{b} = \mathbf{0} \tag{7.17}$$

where α is the isotropic temperature-dependent coefficient of thermal expansion and **T** is the temperature obtained from the thermal analysis assuming that T_0=20 °C is the reference.

To define the plastic strain, one requires first a yield criterion which allow to evaluate if the solid behaves elastically or plastically. The yield criterion defines the elastic limit and is expressed as a scalar yield function f(σ). f = 0 corresponds to the plastic surface in the stress space and f < 0 corresponds to the domain of elasticity.
Based on the Von-Mises yield criterion and the Ludwik's law ($\sigma = \sigma_\mathrm{y} + \mathrm{Hp}^\mathrm{n}$), the yield function f is expressed as follows:

$$f(\sigma, p) = \sigma_{equ} - (\sigma_y + Hp^n) \tag{7.18}$$

where
p is the accumulated plastic strain
σ_equ is the equivalent stress, chosen to be the Von-Mises stress in this case
σ_y is the initial yield stress
H is the hardening modulus
n is the hardening exponent or hardening index

Strain hardening implies that the yield stress increases with the accumulated plastic strain p. Moreover, in reality when a cyclic loading is applied, the tensile yield strength is increased whereas the compressive yield strength is decreased. This phenomenon is called the Bauschinger effect and is linked to the kinematic hardening. However, since it is difficult to find data concerning the kinematic hardening for our type of steel, the Bauschinger effect was not taken into account and a simpler isotropic hardening law was used.
In the case of isotropic strain hardening, the yield stress can be expressed as $\sigma_\mathrm{y} + \mathrm{Hp}^\mathrm{n}$. For a linear strain hardening, the hardening exponent n is equal to 1. The linear isotropic strain hardening law is illustrated in Fig. 7.6.

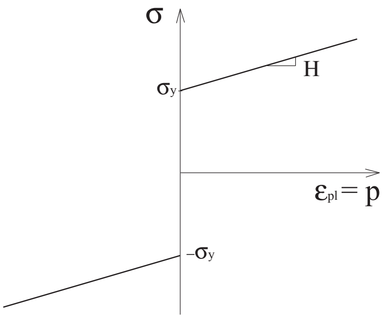

Figure 7.6: The linear isotropic strain hardening law (H is the hardening modulus).

The plastic strain increment is then expressed using the associated flow rule:

$$\dot{\boldsymbol{\epsilon}}^{pl} = \mathbf{a}\dot{\mathbf{p}} \tag{7.19}$$

where the flow tensor **a** is defined as:

$$\mathbf{a} = \frac{df}{d\boldsymbol{\sigma}} \tag{7.20}$$

The mechanical analysis can be summarised as follow:

- **Variables:** essential variable : displacement u, natural variable : stress σ
- **Material:**
  - The Young's modulus E=f(T) and the Poisson's ratio ν=f(T) for the elastic part. They are given in Table 4.8.
  - The yield stress σ_y or $\mathrm{f_y}$=f(T) and the stress evolution as a function of the accumulated plastic strain $\sigma_\mathrm{y} + \mathrm{Hp}$ for the plastic part. In Table 4.9, the stress values are described for 0% of plastic strain (yield stress) and 10% of plastic strain.
  - The thermal expansion coefficient α=f(T) for the thermal part. Data can be found in Table 4.8.
- **Boundary conditions:** Essential boundary condition on displacements $\mathrm{u} = \bar{\mathrm{u}}$. In our case, displacements are set to zero (fixed end-support) at the chord right extremity (coordinate x $>$ 0). No traction or compression is applied.

7.5 Loading

7.5.1 Thermal analysis

As explained above, the thermal problem is often modeled by imposing an initial temperature, heat input conditions as well as heat loss conditions on the boundary. The heat input by the welding process is modeled using an equivalent heat source model able to reproduce the shape of the weld fusion profile and the temperature evolution (thermal cycle).

Initial and boundary conditions

To solve the equation (C.8), an initial condition is required which is often an imposed temperature:

$$T(x, y, z, t_0) = T_{in} \tag{7.21}$$

In our case, the initial temperature is fixed to 20 °C for all nodes of the model.

The boundary condition is either a temperature boundary condition and/or a flux boundary condition: $\mathrm{T} = \bar{\mathrm{T}}$ on Γ_T or $\mathrm{q_n} = \tilde{\mathrm{q}}.\tilde{\mathrm{n}} = \bar{\mathrm{q}}$ on Γ_q.

In our case, we consider the flux boundary condition on all the surfaces.

The heat flux $\bar{\mathrm{q}}$ can be defined as the convective heat flux $\mathrm{q_{conv}}$ and the radiation heat flux $\mathrm{q_{rad}}$.

The relationship for the convective heat flux is implemented in the option *FILM in ABAQUS (Cauchy condition).

$$q_{conv} = -h(T)(T - T_0) \tag{7.22}$$

where
h is the film coefficient (in $\mathrm{W.mm^{-2}.K^{-1}}$)
T_0 is the temperature of the environment (reference sink temperature).
T and T_0 can be expressed in °C or in K.

The heat flux on a surface due to radiation to the environment is described by the well-known Stefan-Boltzmann law. This equation is implemented in the option *RADIATE in ABAQUS.

$$q_{rad} = \sigma_{SB}.\epsilon.(T^4 - T_0^4) \tag{7.23}$$

where
σ_{SB} is the Stefan-Boltzmann constant, equal to $5.67.10^{-8}$ $\mathrm{W.m^{-2}.K^{-4}}$
ϵ is the surface emissivity
T is the temperature of the body (in Kelvin)
T_0 is the temperature of the environment (reference sink temperature in Kelvin)

In our model, we have combined both. In ABAQUS, we have used a *FILM option with a h film coefficient comprising the convective film coefficient $\mathrm{h_{conv}}$ and an equivalent radiation film coefficient $\mathrm{h_{rad}} = \sigma_{SB}.\epsilon.(T^3 + T^2.T_0 + T.T_0^2 + T_0^3)$.

Brown gives the temperature-dependent thermal material constants, including the emissivity and the convective heat transfer coefficient, of a mild steel (Brown and Song, 1992). Concerning the convective heat transfer coefficient $\mathrm{h_{conv}}$, since it does not have a strong influence on the total h film coefficient, it was kept constant and equal to 2.5 $\mathrm{W.mm^{-2}.K^{-1}}$. The emissivity values, varying from 0.2 and 0.65, were taken from Brown and Song (1992).

The total h film coefficient used to solve the equation $\bar{\mathrm{q}} = \mathrm{q_{conv}} + \mathrm{q_{rad}} = -\mathrm{h_{tot}}(\mathrm{T} - \mathrm{T_0})$ are given in Table 7.3. One can note that $\mathrm{h_{tot}}$ becomes important above 1000 °C owing to radiation.

Table 7.3: The convective film coefficient $\mathrm{h_{conv}}$ cumulated to the equivalent radiation film coefficient $\mathrm{h_{rad}}$.

T(°C)	**0**	**75**	**100**	**200**	**300**	**500**	**750**	**1000**	**1590**	**5000**
$\mathrm{h_{tot}}(10^{-6}\mathrm{W.mm^{-2}.K^{-1}})$	3.53	4.76	5.9	8.56	12.2	24.8	51.5	91.9	263	5720

The heat input

The heat generated by the welding process is modeled using a volumetric heat source s. This heat source is determined as a function of the electrical power:

$$s = \frac{Q}{V} = \frac{\eta U I}{V} \tag{7.24}$$

where η is the degree of efficiency, U is the voltage, I is the current of the arc welding and V is the volume of heated material.

For one single pass, a current with I= 270 A and U= 30 V was used. The arc welding efficiency ranges usually between 70% and 90%. This amount corresponds to the part of heat input effectively utilised to create the weld, the rest is lost by convection and radiation.

In order to merge the seven weld passes into one equivalent pass, it is recommended to keep the total heat input (Lindgren, 2001a) of the seven weld passes. Therefore, using an efficiency of 0.732, an equivalent heat generation Q of the order of 41500 W is obtained. The volumetric heat source s takes the value 5.87 W/mm^3.

To approximate the heat source of a MIG or MAG welding process, the double ellipsoid model (Goldak et al., 1984) gives good results. However, it requires to experimentally identify several dimensional parameters describing the ellipsoid geometry.

Therefore, simplified heat source models (Fig. 7.7) are chosen:

- a spherical model in ABAQUS defined by its radius r= 15 mm.
- a truncated circular cone model in MORFEO defined by the radii of its two bases: r$_1$= 15 mm, r$_2$= 9.3 mm, and by its height h= 15 mm.

The heat source dimensions were chosen to fit best the measured weld pool size (see Fig. 7.4b). Once the dimensions are chosen for the sphere, the ones for the truncated circular cone are defined in order to produce the same volume of heated material. The heat generation Q is kept identical for both heat sources.

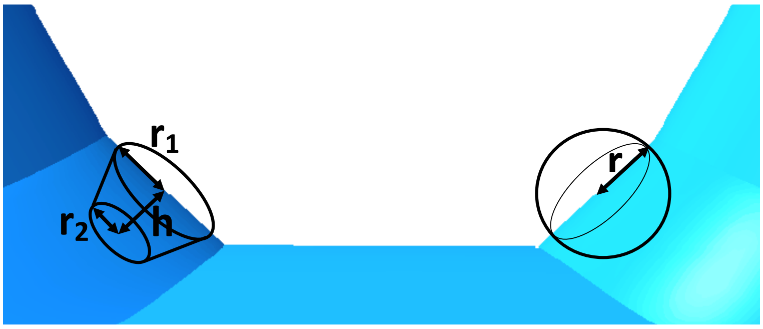

Figure 7.7: Heat-sources: the truncated circular cone model used in MORFEO on the left and the spherical model used in ABAQUS on the right.

The volume of both sources is identical and equal to ~ 7100 mm^3, hence s is given by:

$$s = \frac{Q}{V} = 5.9 \ \ \mathrm{W/mm^3} \tag{7.25}$$

The heat source trajectory

The heat source is moving around the weld from the crown heel to the crown toe according to equation (7.7). Four equivalent heat trajectories are modeled following the surface middle weld curve.

A user subroutine was developed in ABAQUS (*DFLUX) in order to model the heat input moving along with the torch. The movement is based on the local polar angle $\phi = \mathrm{w} \times \mathrm{t}$ where w is the angular velocity and t the time. An angular velocity of $\pi/25 = 0.126$ rad/s was measured during the welding, it corresponds to a welding speed of 5.5 mm/s.

Since the torch position depends on the time, the beginning time of each weld path is adapted to obtain the starting point at the crown heel position (corresponding to the welding procedure) and to leave a cooling time as close as possible to the actual measured time. A negative angle ϕ gives the opposite direction of rotation.

The time steps adopted to model the four weld paths are given in Table 7.4. A welding step lasts 25 s and a cooling step lasts 125 s. The heat input is introduced linearly during the first 2 seconds of the welding steps. The last cooling step is drastically increased in order to be sure that the entire model is cooled down to the room temperature at the end of the simulation. The time given for this last step is fixed in MORFEO but in ABAQUS the step ended only when 20 °C is reached everywhere in the piece.

Figure C.3 shows the heat source traveling around the weld from the crown heel to the crown toe during the weld path 3.

Table 7.4: The welding and cooling time steps.

Step name	**angle ϕ** (rad)	**total time** (s)
		0
Waiting step		
	π	24
Welding step, path 1		
	0	51
Cooling step		
	π	174
Welding step, path 2		
	0	201
Cooling step		
	π	324
Welding step, path 3		
	0	351
Cooling step		
	π	474
Welding step, path 4		
	0	501
Cooling step		
	π	~ 9501

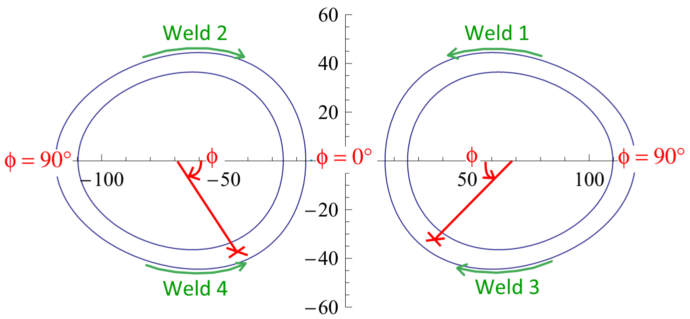

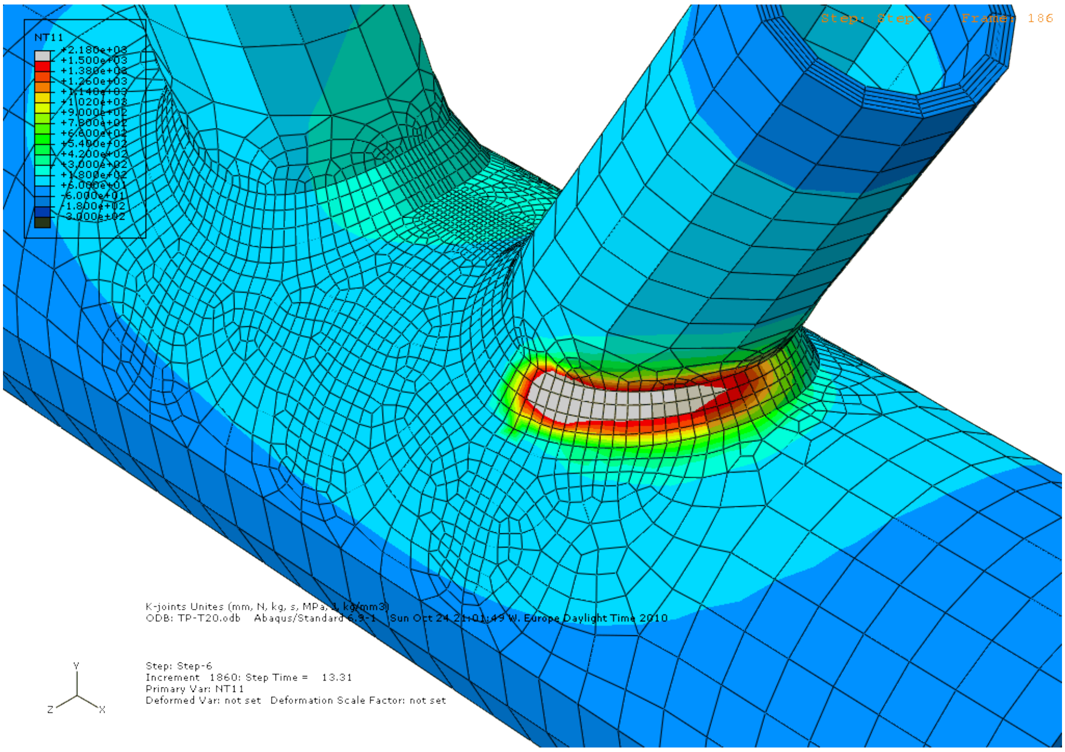
Step: Step-6   Frame: 186
NT11
+2.180e+03
+1.500e+03
+1.380e+03
+1.260e+03
+1.140e+03
+1.020e+03
+9.000e+02
+7.800e+02
+6.600e+02
+5.400e+02
+4.200e+02
+3.000e+02
+1.800e+02
+6.000e+01
-6.000e+01
-1.800e+02
-3.000e+02
K-joints Unites (mm, N, kg, s, MPa, 1 kg/mm3)
ODB: TP-T20.odb   Abaqus/Standard 6.9-1   Sun Oct 24 21:01:49 W. Europe Daylight Time 2010
Y
Z
X
Step: Step-6
Increment 1860: Step Time = 13.31
Primary Var: NT11
Deformed Var: not set   Deformation Scale Factor: not set

Figure 7.8: Temperature distribution during the third welding step (gray area corresponds to the melted zone, T ≥ 1500 °C.

7.5.2 Mechanical analysis

The previous time steps, as well as the mesh, are kept identical for the thermal and mechanical analyses.

Concerning the boundary conditions, the chord is fixed at its extremities by constraining the node displacements in three directions.

The plastic strains accumulated in the fusion zone are annealed in ABAQUS (*ANNEAL TEMPERATURE option) once the temperature has reached the solidus temperature at T = 1465 °C corresponding to the beginning of melting.

7.6 Mesh

7.6.1 Finite element type

In order to model the welding induced residual stresses, 3D continuum (solid) elements were found to be the most appropriate. The element shape chosen was the hexahedron (brick) because it has proved to offer a better convergence and accuracy than tetrahedron (FREY and Jirousek, 2001; Lindgren, 2001a). However, meshing complex geometry with hexahedra is not as simple as with tetrahedra and the aspect ratio (ratio of the longest to shortest side lengths in an element) of hexahedra must be kept small (max 10 to 20) to obtain accurate results. That is the reason why in some particular locations, the wedge or prism shape was also used.

Lindgren (Lindgren, 2001a) proposed to use preferably finite element shape functions of the first order (linear) with hexaedron to model the thermal process. Therefore, this implies the use of an element with 8 nodes (see Fig. 7.9).

Ideally, Lindgren (2001a) recommended to use quadratic (second order) elements for the mechanical analysis and linear elements for the thermal analysis. If the shape functions for temperature are linear, the volumetric thermal strain calculated in the mechanical analysis is linear ($\epsilon^{\text{th}} = \alpha\Delta\text{T}$). And if the shape functions for displacement are quadratic, the strains obtained as the displacement derivatives are also linear. However, this is not possible in our case because the mesh is identical in both analyses. As explained above, linear elements have been chosen. In order to avoid locking between linear and constant strains, linear element with reduced integration (one Gauss point) are used in the mechanical analysis.

To summarise, 8-node brick elements are used in ABAQUS: DC3D8 for diffusive heat transfer elements (thermal analysis) and C3D8R with reduced integration for stress/displacement elements (mechanical analysis). DC3D8 elements have only one degree of freedom: the temperature T whereas C3D8R elements have three degrees of freedom: the displacements u, v, w.

In MORFEO, 8-node brick elements are also used but reduced integration is not available. Therefore, 8-node brick elements are used with 8 Gauss points (exact integration).

These elements seem to be the most efficient to obtain accurate results with an acceptable computational time.

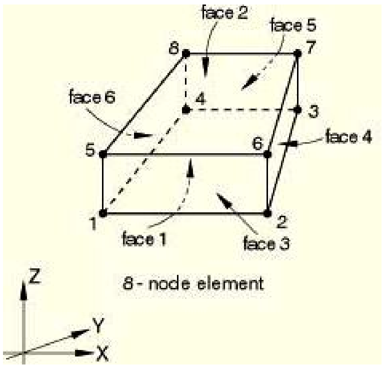

Figure 7.9: A 8-node element defined in ABAQUS with its node ordering and face numbering (ABAQUS, 2009).

7.6.2 The generated mesh

Figure 7.10 depicts the model, it is composed of 30833 nodes and 25544 elements for the Ref-T20 (geometry 1) and 38983 nodes and 33843 elements for the Ref-T30 (geometry 2).

The global coarse mesh has a size of approximately 20 mm. The area all around the weld is refined to reach a size of 5 mm. A strip of 20 mm width in the gap area and underneath the weld is even more refined (Fig. 7.10b) to 2 mm in the surface area and 5 mm in depth.

7.7 Convergence study

Two types of convergence study have been conducted in order to choose an appropriate mesh size and to confirm the choice of the shape functions order:

- a study on the convergence h, by refining the mesh size h (length of the longest side of the element) without changing the shape order.
- a study on the convergence p, by changing the order of interpolation p without changing the mesh size.

As the computational time is too large to carry out the convergence study during the entire welding time, the study was focused on the first 6 seconds of welding. For this case, the welding began at the weld crown toe and moved in the direction of the crown heel. The studied model corresponds to the Ref-T20 geometry. The temperature and residual stress results were compared along a surface line in the gap area and along a line through the wall chord thickness from the weld crown toe.

Since, welding is modeled during only 6 seconds, the results have no real physical meaning for residual stress estimation but they allow us to study the convergence.

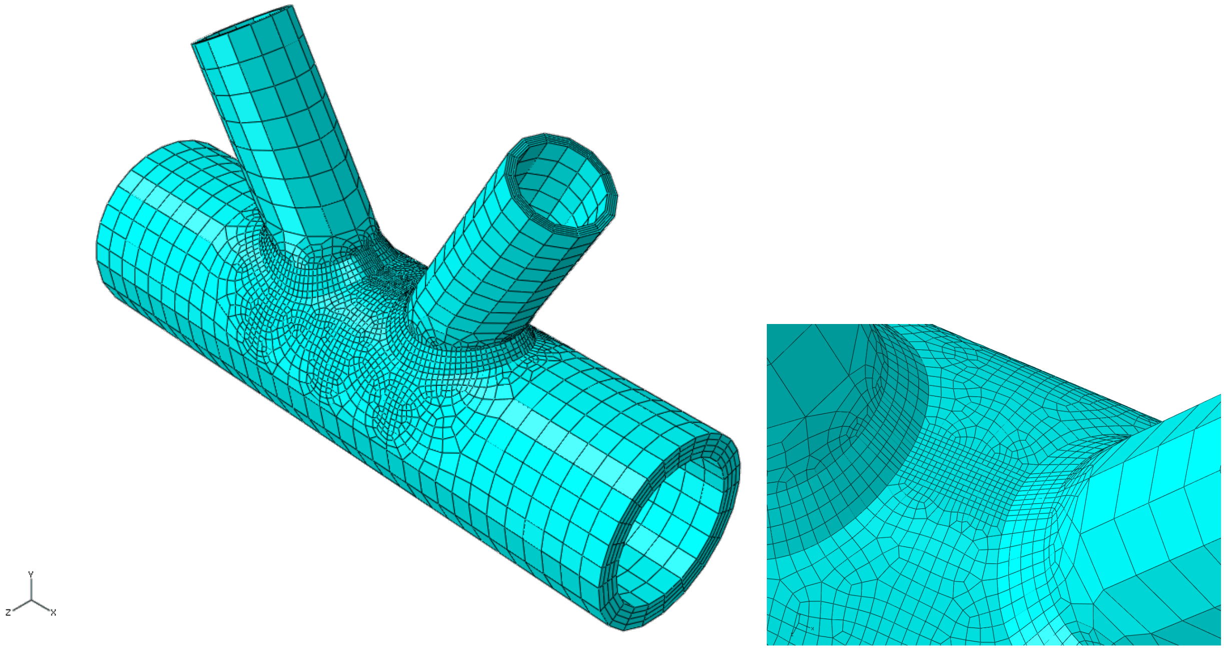

(a) 3D view **(b)** Refinement area

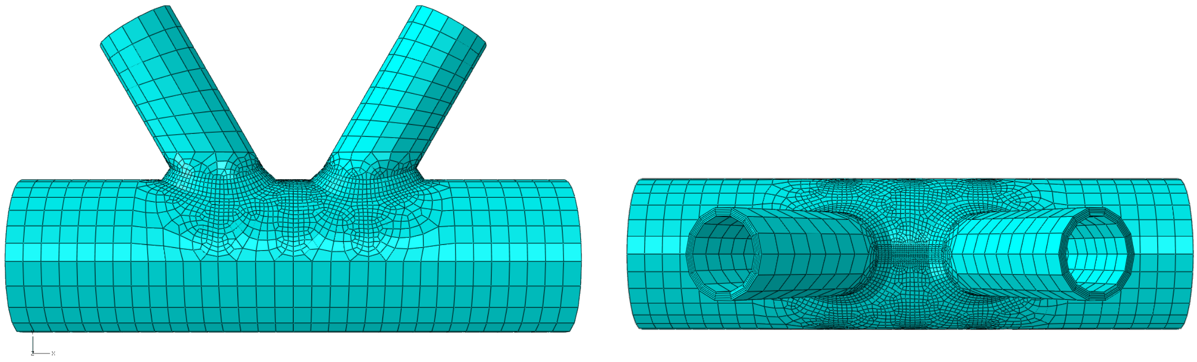

(c) Axial view **(d)** Top view

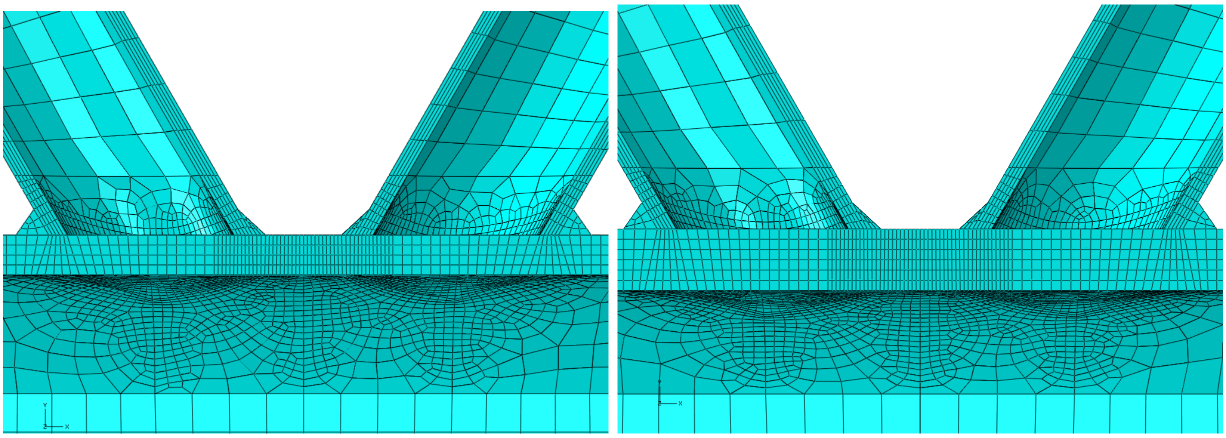

(e) Axial cut in the Ref-T20 geometry **(f)** Axial cut in the Ref-T30 geometry

Figure 7.10: The typical mesh used for geometries Ref-T20 and Ref-T30.

7.7.1 Convergence h study

Table 7.5: The models used to study the convergence h

Model name	**Strip element size (mm)**	**Chord element size (mm)**	**Comput. time (3 cpus)**	**Model**
DC3D8-1to3mm	1 × 2.5	3 × 2.5	47 h	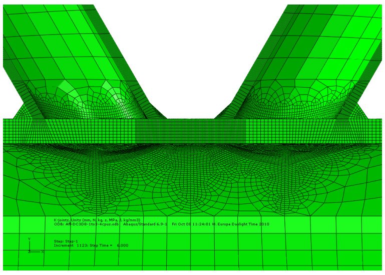
DC3D8-2to5mm	2 × 5	5 × 5	5 h	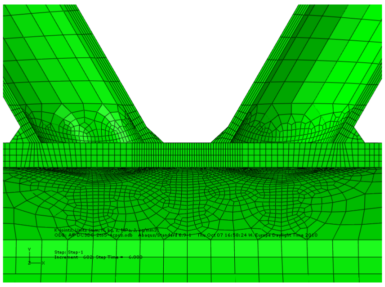
DC3D8-4to5mm	4 × 10	5 × 10	1h50	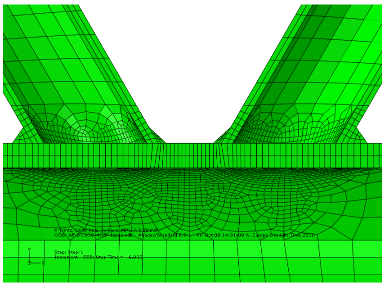
DC3D8-original	-	5 × 5 (1 × 5 underneath the weld)	11 h	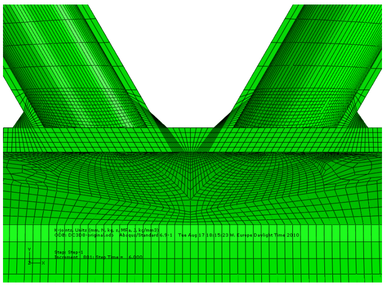

The four models studied in this part are presented in table 7.5.

In the first three models, the element size in the area of interest (area underneath the weld toe) is doubled between one model and the following. The fourth model was the first we elaborated, however too many elements are highly distorted around the weld. In the last model, the element size underneath the weld toe varies from 1×5 to 5×5 mm^2.

The results in terms of temperature are presented in Fig. 7.11 and in terms of residual stresses (Von Mises) in Fig. 7.12. It is important to note that the temperature values are calculated at the nodes (unique nodal values) whereas the stress values are calculated at the element integration point. On the following graphs, values obtained at the Gauss points are interpolated or extracted at the intersections between the path of distribution and the element faces. That is the reason why in the DC3D8-original model, where a vertical line crosses several times the element faces, there is a significant number of data points.

From Fig. 7.11, one can clearly see a convergence trend from the coarser to the finer mesh even though the exact solution is unknown. Results obtained for models DC3D8-2to5mm and DC3D8-1to3mm are close (less than 10% difference). Coarse meshes highly over-estimate the temperature.

From Fig. 7.12, results are more heterogeneous but the convergence trend is still significant. The model DC3D8-4to5mm turns out to be inaccurate. Results from model DC3D8-original do not always stay in between models DC3D8-2to5mm and DC3D8-1to3mm. There is a difference between results of models DC3D8-2to5mm and DC3D8-1to3mm up to 15% along the gap and through the wall chord thickness. The residual stress distribution through the depth is the most meaningfull with regard to the fatigue crack propagation occuring at the weld toe. It can be shown, if the model DC3D8-1to3mm is the closest to the exact solution, that model DC3D8-2to5mm underestimates residual stresses up to 8 mm and overestimates or shifts the distribution curve for greater depths.

Based on that comments and on the fact that the computational time is nine times greater for the model DC3D8-1to3mm than DC3D8-2to5mm, the mesh size of the DC3D8-2to5mm is chosen for the geometry Ref-T20.

7.7.2 Convergence p study

Two additional models are studied for the convergence p. These models use quadratic (shape functions of second order) elements corresponding to 20 node elements.

These models as well as the linear element models, are presented in table 7.6. Figure 7.13 shows that the quadratic elements drastically improved the results for the coarser mesh (model 4to5mm). For the refined model (2to5mm), it shifts the temperature results down to 20 °C maximum. The trend and the temperature magnitude of the model DC3D8-2to5mm are accurate enough to estimate the temperature evolution.

Table 7.6: The models used to study the convergence p

Model name	Strip element size (mm)	Interpolation order	Computation time (3 cpus)
DC3D20-2to5mm	2 × 5	2	65 h
DC3D20-4to5mm	4 × 10	2	15 h
DC3D8-2to5mm	2 × 5	1	5 h
DC3D8-4to5mm	4 × 10	1	1h50

Figure 7.14 proves that quadratic elements also improve the stress results for the coarser mesh, however it provides very few values through the depth. For the 2to5mm model, the stress distribution found with a second order shape function is higher that the one found previously for the finer mesh model (DC3D8-1to3mm). It is difficult to identify which one is closest to the exact value. We just note that the chosen model (DC3D8-2to5mm) tends to underestimate the peak of residual stresses. Based on convergence study p, the model DC3D8-2to5mm still offers a good ratio between result quality and computation time.

To conclude, the model with 8-node elements and a mesh size of 2 mm × 5 mm in the area of interest, gives really accurate results for the thermal analysis, and good results for the mechanical analysis.

From this study, it has to be highlighted that in order to estimate properly residual stresses, the appropriate mesh size predicting accurately the temperature distribution must be identify. A good predictions of temperatures in the thermal analysis is the basis of good results in the following mechanical analysis.

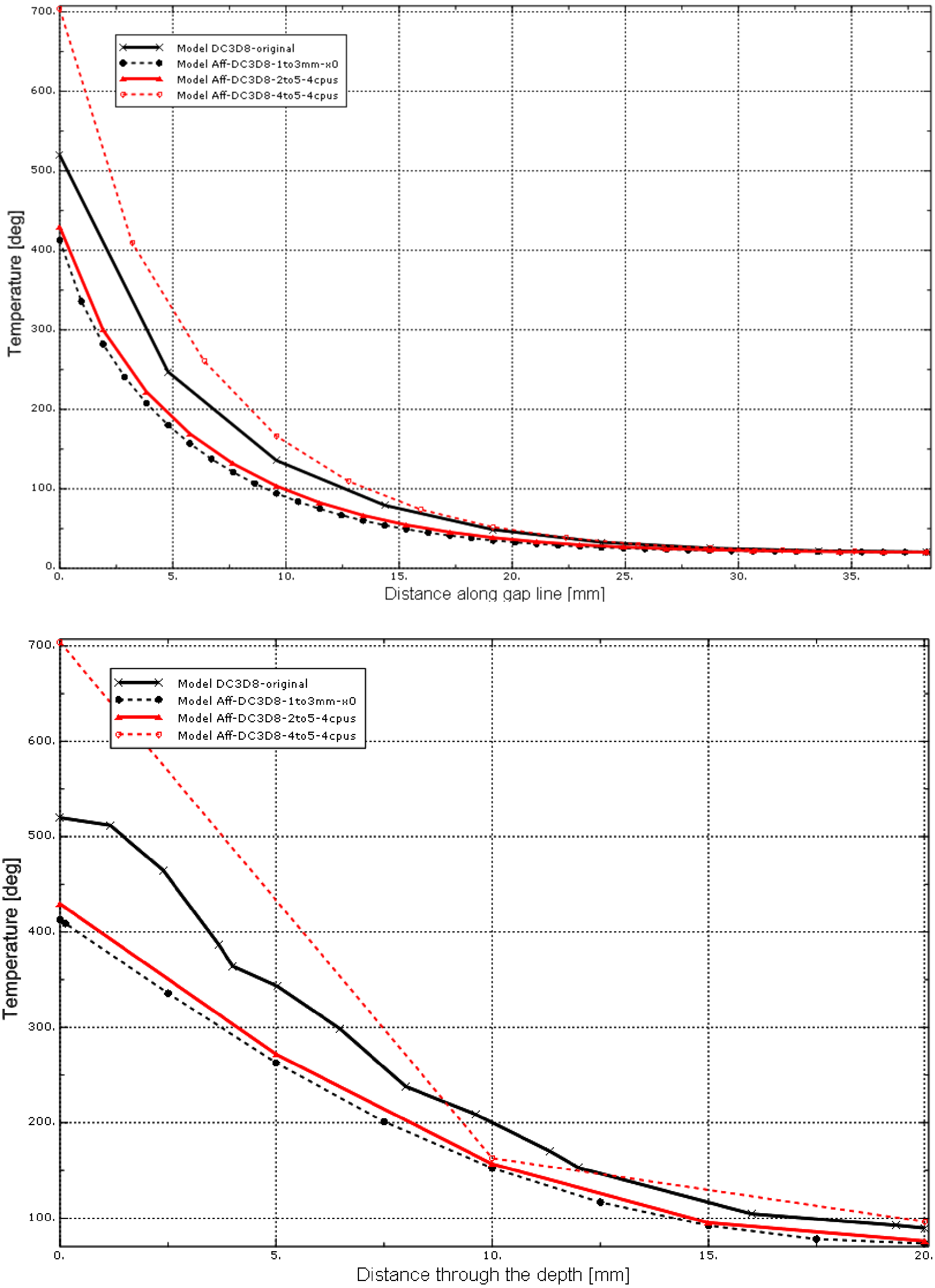

Figure 7.11: Convergence h: comparison of the temperature distribution along the gap line and through the chord wall thickness for the different models after 6s welding.

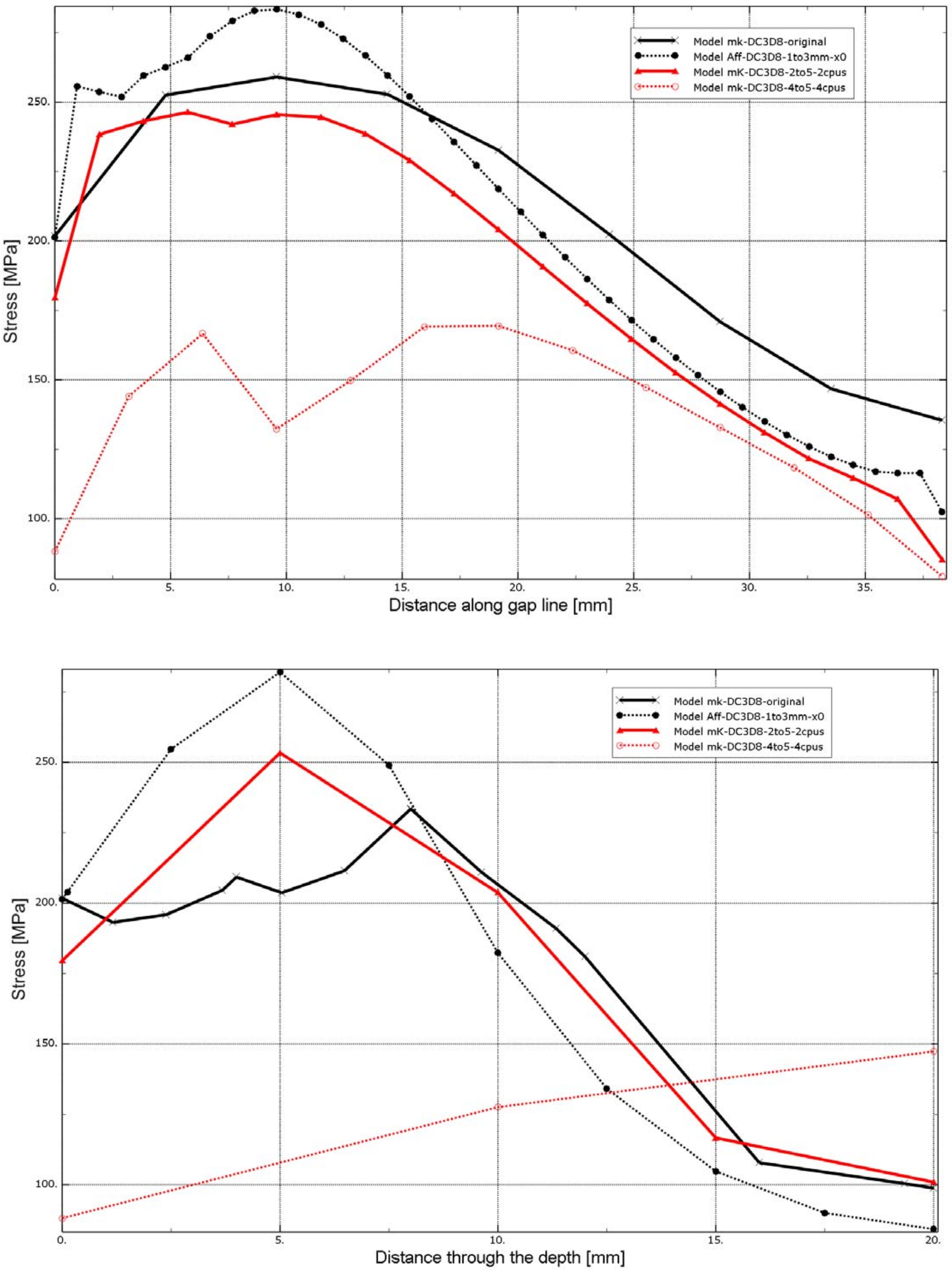

Figure 7.12: Convergence h: comparison of the Von Mises stress distribution along the gap line and through the chord wall thickness for the different models after 6s welding.

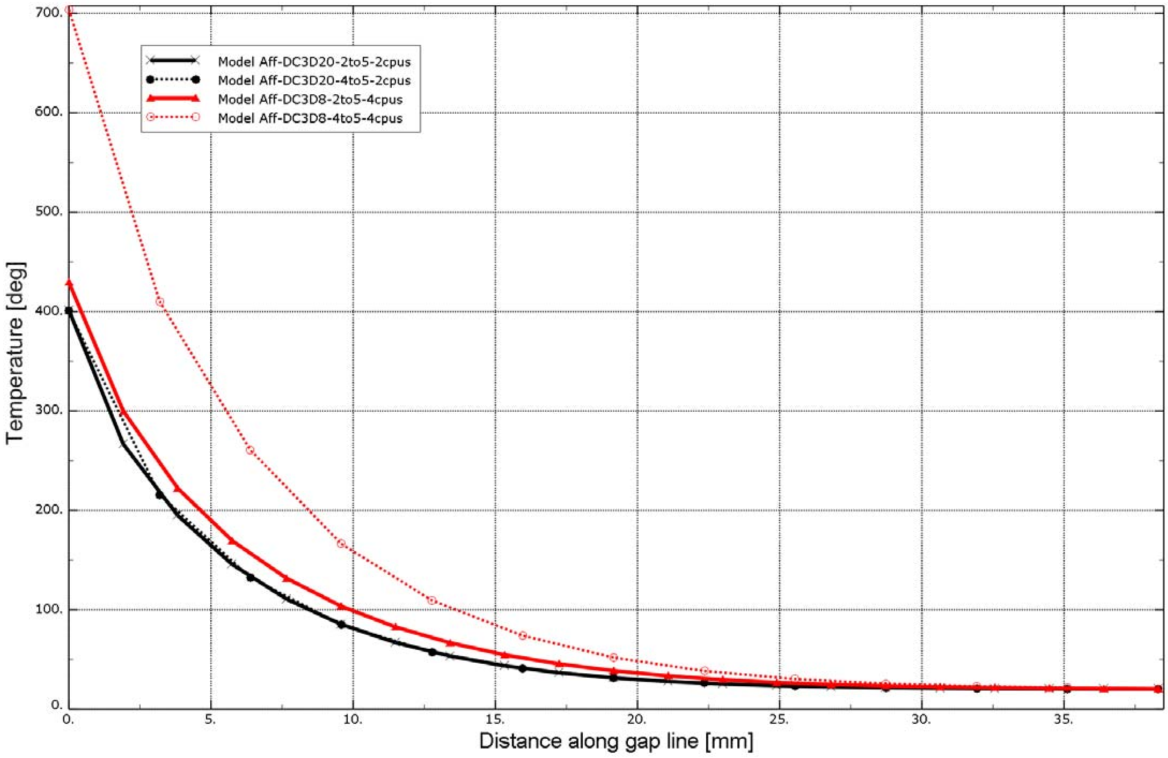

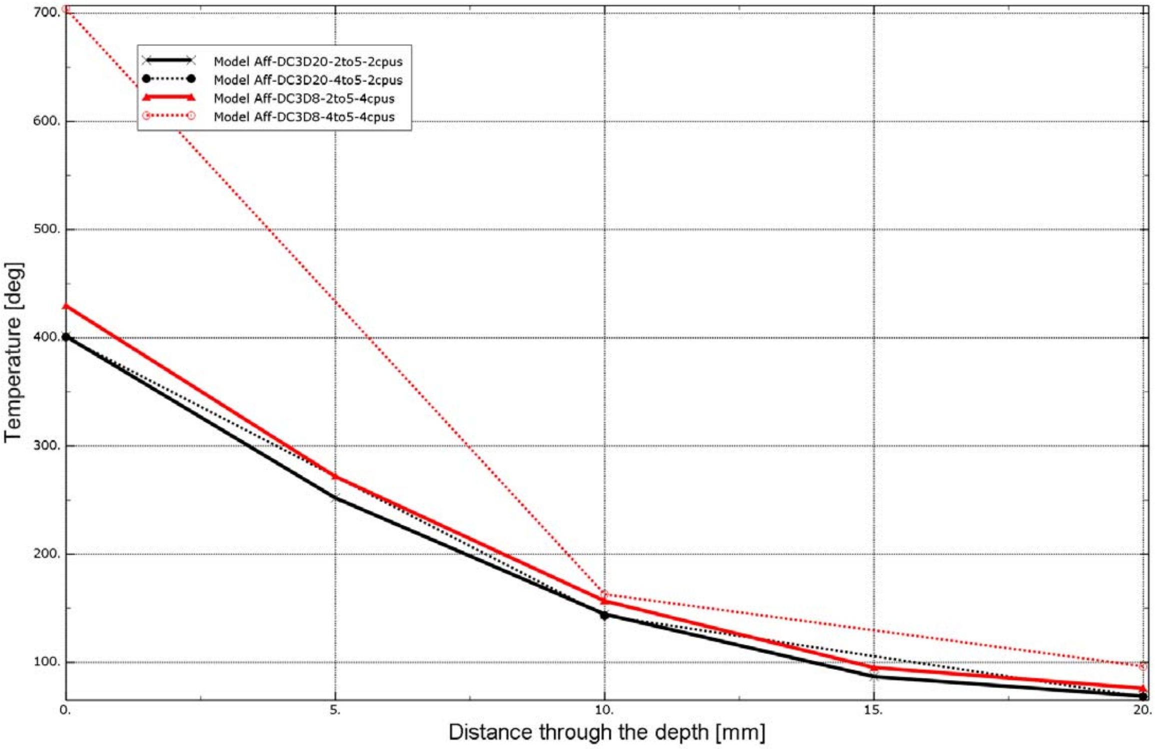

Figure 7.13: Convergence p: comparison of the temperature distribution along the gap line and through the chord wall thickness for the different models after 6s welding.

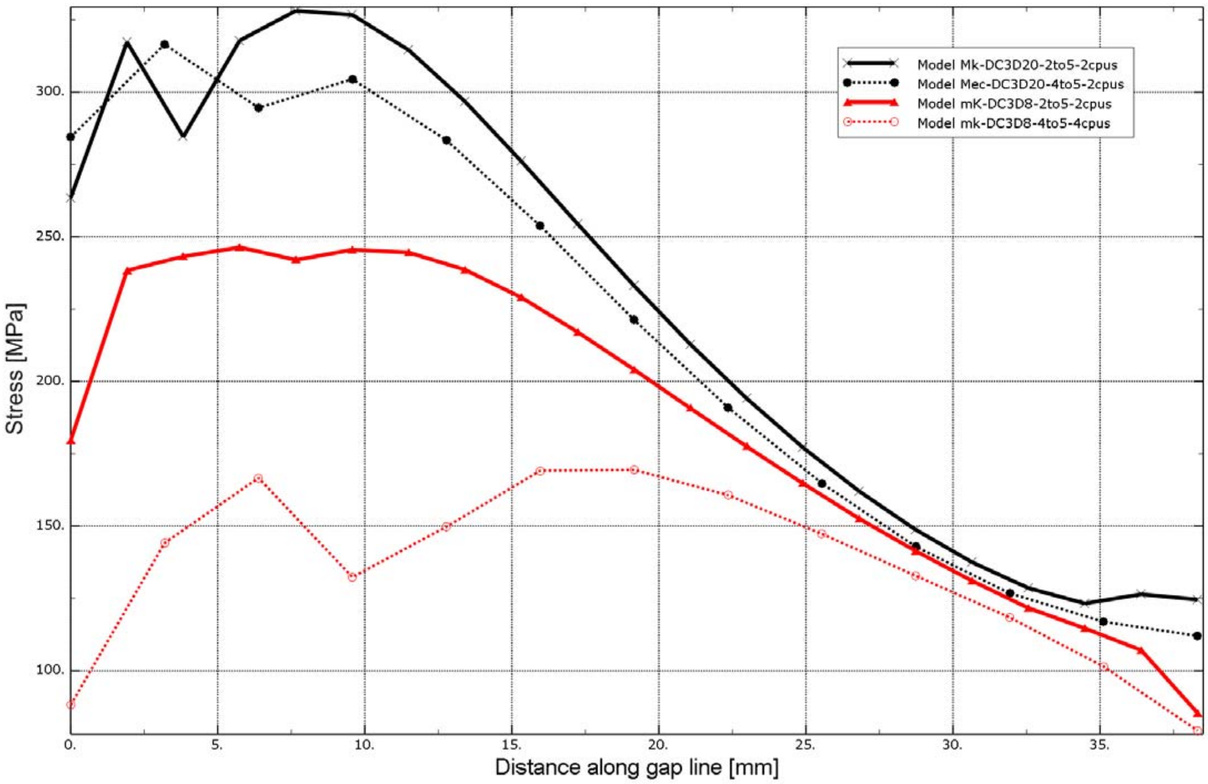

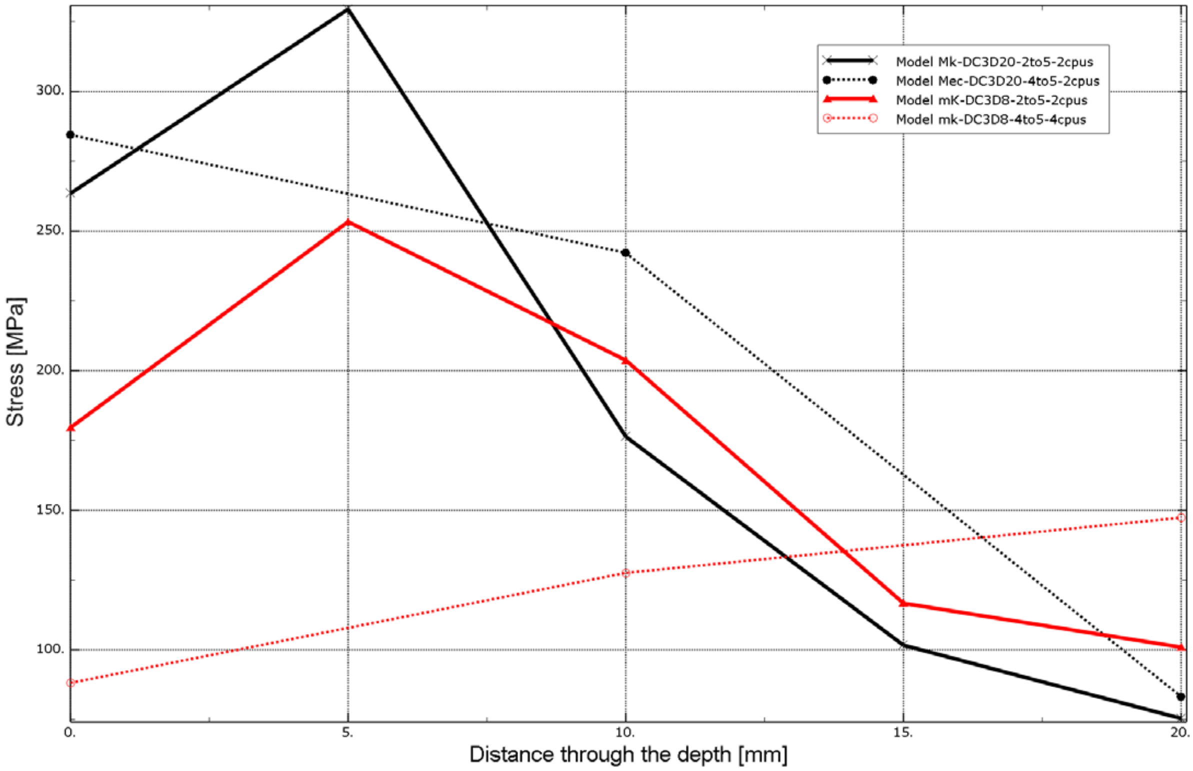

Figure 7.14: Convergence p: comparison of the Von Mises stress distribution along the gap line and through the chord wall thickness for the different models after 6s welding.

7.7.3 Computation times

The computation times to simulate the geometry Ref-T20 are the following:

- ABAQUS: 103 hours (thermal part) + 5 hours (mechanical part) using 4 processors (Altix cluster, Linux/Itanium 2: processor speed 1.6 Ghz, 4 operations per cycle)
- MORFEO: 3.5 hours (thermal and mechanical parts) using 8 processors (Ernest HPC cluster: processor speed 2.66 Ghz, 4 operations per cycle)

Note that this huge difference is mainly explained by the different time steps utilized in each code (adaptive in ABAQUS, fixed in MORFEO: see section C.4).

7.8 Model validation and results

7.8.1 Cross-section of the fusion zone

As specified in the recommendations section (section 7.2.1), an intermediate validation of the model consists to control that the weld fusion profile generated by the thermal analysis is close to the one given by the numerical model. If it is not the case, the mechanical analysis will not give reliable residual stress results.

Figure 7.15 compares the fusion zones obtained from a macrography (Fig. 7.15a) and from the numerical analysis (Fig. 7.15b and 7.15c). It is seen that the fusion zone (in gray in Fig. 7.15b) is not exactly similar between the three figures. The models give a greater area especially in the brace direction. The heat affected zone obtained with the ABAQUS code (in color in Fig. 7.15b) is also slightly greater than the real one: 4 mm width instead of 2 mm in reality. In MORFEO, the HAZ is bounded by the white line (600 °C) and red zone (1500 °C). It seems that the FZ is smaller in this case and the HAZ is located a bit too high in the weld. These differences are due to the heat source definitions (spherical versus truncated circular cone). The spherical model gives a fusion profile which is close to reality. It might be also partly explained by the fact that there is a better energy conservation in ABAQUS as it controls the temperature variation and the time step.

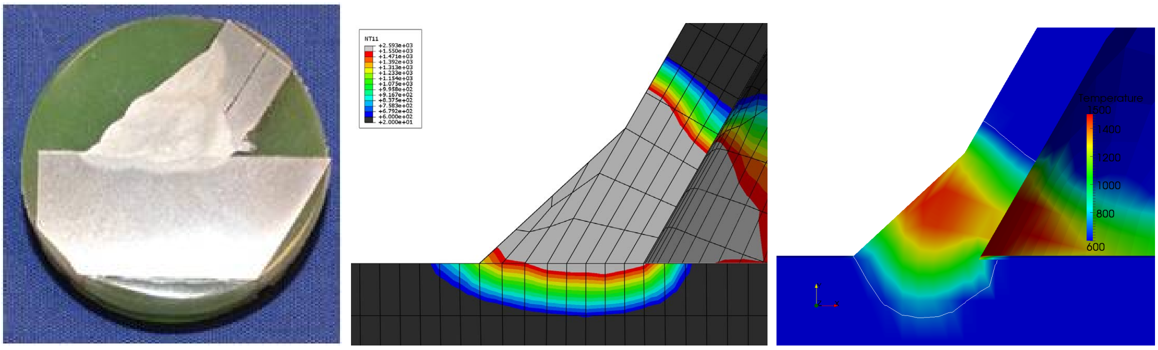

(a) Sample **(b)** ABAQUS model **(c)** MORFEO model

Figure 7.15: Comparison of the FZ and the HAZ between the macrography and the models at the end of the welding step 1. In the ABAQUS model, the FZ is in gray and the HAZ is colored. The HAZ corresponds to temperatures between 600 °C to 1500 °C.

Ideally, temperature measurements during the welding process using thermocouples should be compared with the temperature cycle obtained from the thermal analysis. However, in our case, such measurements were not carried out. The evolution of the temperature, calculated using ABAQUS, at the weld toe is presented in Fig. 7.16.

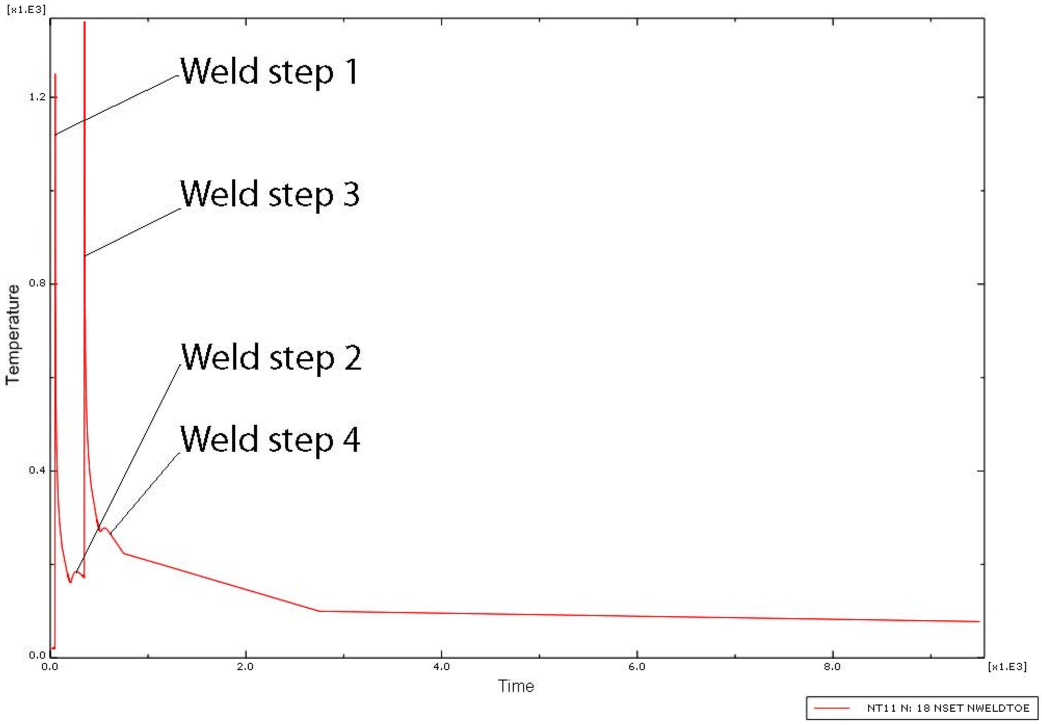

Figure 7.16: Temperature evolution as computed with ABAQUS at node 18 situated in the right weld toe area undergoing the welds 1 and 3.

7.8.2 Comparison with residual stresses obtained from neutron diffraction measurements

Validation of ABAQUS and MORFEO results for Ref-T20 and Ref-T30 geometries

Ref-T20 geometry

Residual strain measurements were conducted on a K-joint sample with a chord wall of 20 mm thickness (FAT-20). Residual stress maps built from these measurements and already presented in section 5.3.5 are compared in Fig. 7.17 to residual stress maps resulting from numerical models.

First of all, the results obtained numerically confirmed once again that transverse residual stresses are greater than longitudinal ones, which are greater than radial ones.

For transverse stresses, both models are able to show a restraining effect in the gap area and a maximum transverse residual stress value underneath the weld toe at depth ranging between 2 and 5 mm. Surprisingly, the weld toe showing highest transverse residual stresses do not appear to be the same in both models.

Concerning longitudinal and radial stresses, the models present quite similar results. The longitudinal data obtained from experiments are more complex than the numerical ones: in the middle of the gap, longitudinal residual stresses are slightly compressive at the surface but quickly become tensile in depth in experimental data.

Globally, numerical results are in an acceptable agreement with experimental results.

The residual stress distribution along a vertical line underneath the weld toe is then studied. Figure 7.18 depicts these distributions in the three axis directions.

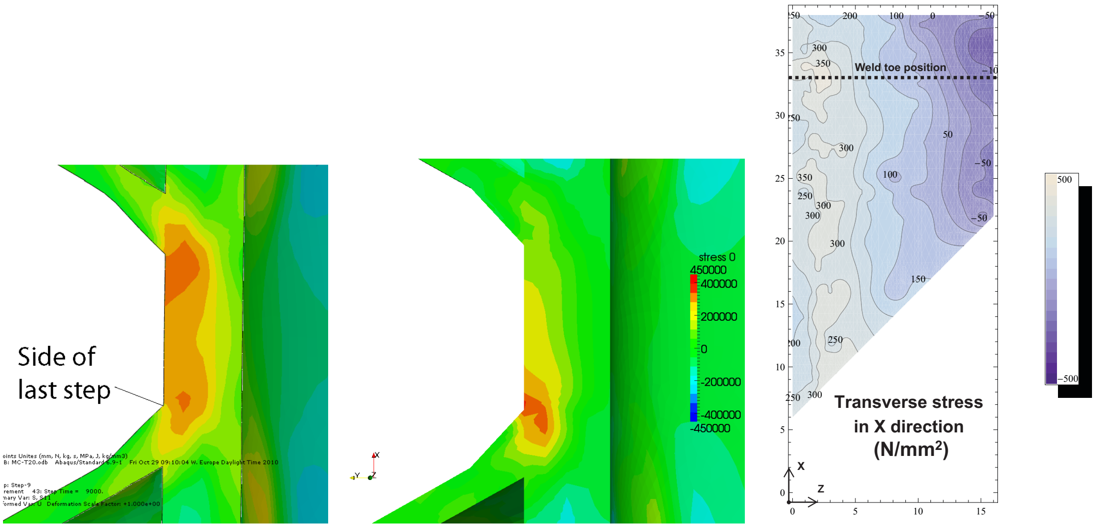

(a) Tr. dir., ABAQUS code **(b)** Transverse dir., MORFEO code **(c)** Transverse dir., Exp. data

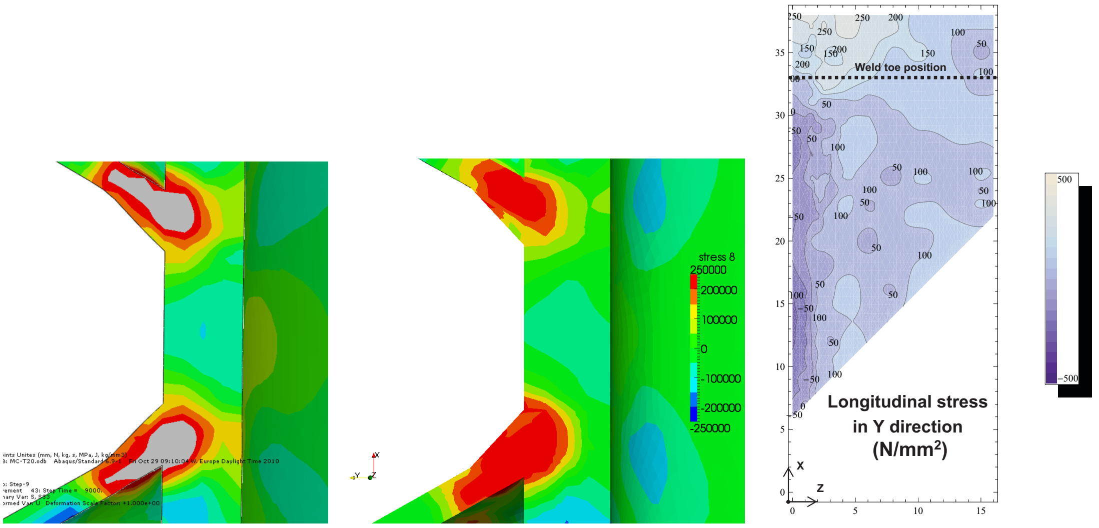

(d) Long. dir., ABAQUS code **(e)** Longitudinal dir., MORFEO code **(f)** Longitudinal dir., Exp. data

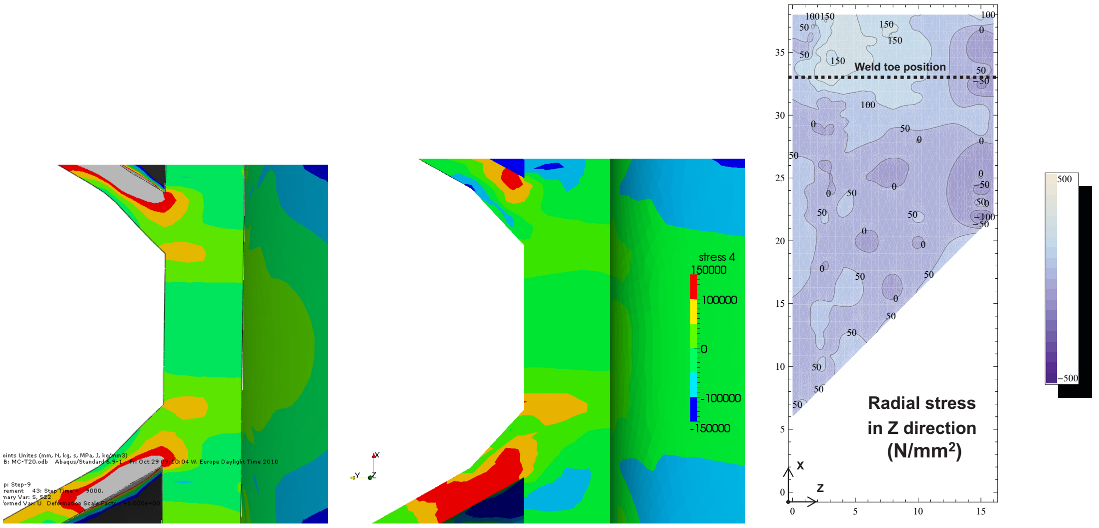

(g) Radial dir., ABAQUS code **(h)** Radial dir., MORFEO code **(i)** Radial dir., Exp. data

Figure 7.17: Residual stress maps representing transverse, longitudinal and radial stress variation in the gap area and through the chord wall thickness. The color scale for numerical results is given in kPa whereas the experimental stress values are given in MPa (N/mm^2).

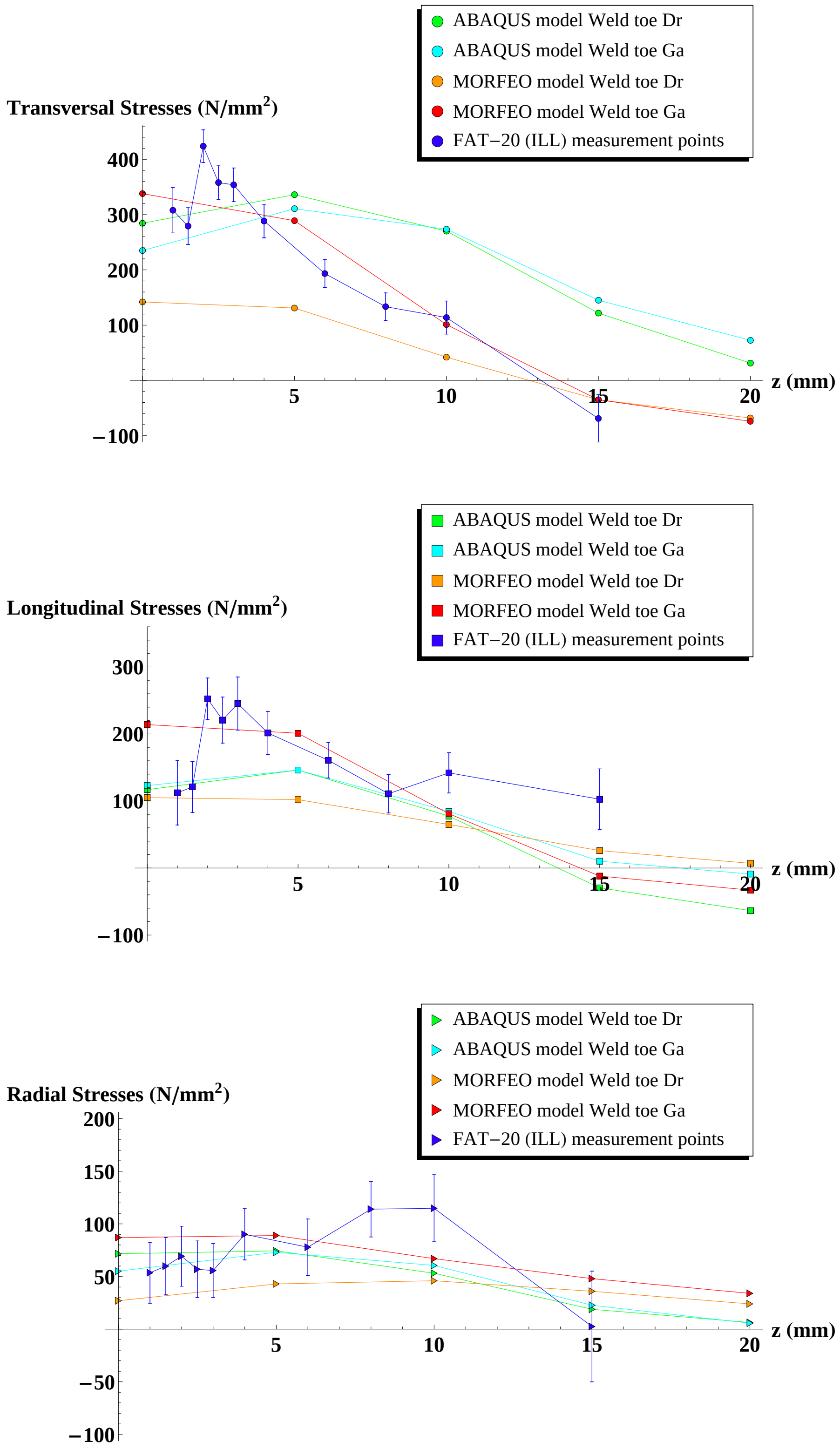

Figure 7.18: Comparison of transverse, longitudinal and radial residual stress distributions as a result of ABAQUS and MORFEO models versus the neutron diffraction measurement results (K-joint with a chord wall thickness of 20 mm).

Figure 7.18 shows that the distributions give the global magnitude of residual stresses but it is not able to capture the peak values. This is mainly due to the lack of data points available to draw the distribution curve. Moreover, the transverse residual stress distribution obtained with ABAQUS is shifted to the right compared with the experimental distribution. This means that transverse residual stresses should be compressive at 13 mm depth but the ABAQUS models present tensile residual stresses through all the depth. This phenomenon may be due to an improper consideration of melting latent heat, however the same latent heat has been introduced in both numerical models.

Concerning the comparison between both codes, MORFEO shows an important discrepancy between the depth distributions underneath the right and the left weld toes. Such a discrepancy does not appear with ABAQUS results. This difference between both result data is difficult to explain; it might be attributed to the different heat source models (sphere versus truncated circular cone) and to the time increment techniques (see section C.4).

Ref-T30 geometry

Neutron-diffraction measurements were also carried out on a 30 mm thick sample (FAT-30). Numerical curves presented hereafter have only been modeled with ABAQUS code.

The curves obtained numerically and presented in Fig. 7.19 give results quite distant from those obtained experimentally. It can be argued that the experimental results are not accurate enough and that too few points were obtained numerically to draw a reliable curve.

Under these conditions, the model can not be clearly validated with the Ref-T30 geometry.

Still the same offset in curves of transverse residual stresses is present as with the Ref-T20 geometry.

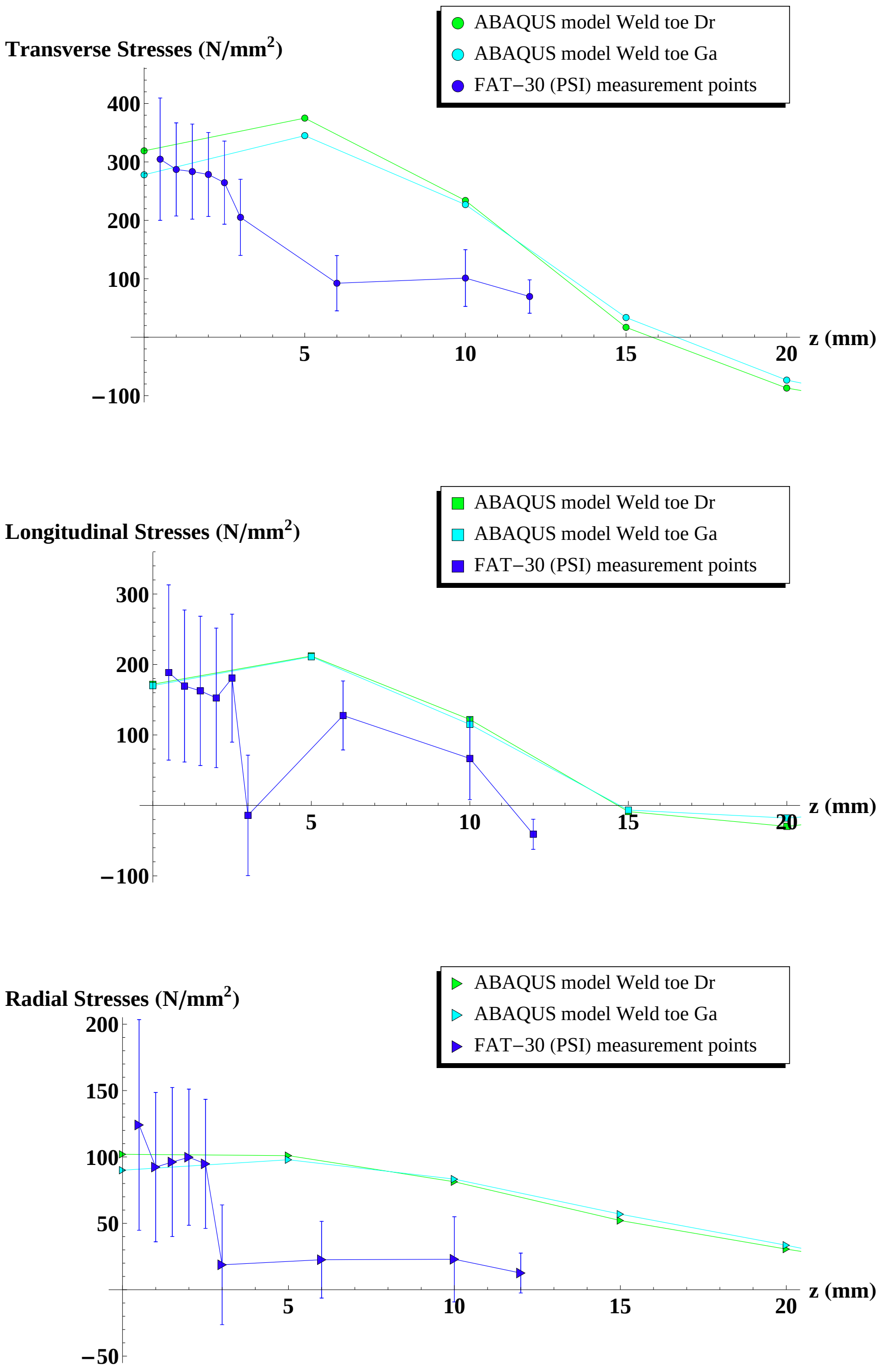

Figure 7.19: Comparison of transverse, longitudinal and radial residual stress distributions from ABAQUS model versus the experimental results (K-joint with a chord wall thickness of 30 mm).

Validation of ABAQUS and MORFEO results with a refined mesh

The results shown previously present an acceptable agreement, however not enough data points are available to compare precisely the computed stresses with the ones measured by neutron diffraction.

That is the reason why, for a clear validation purpose, a refined mesh of Ref-T20 model is proposed hereafter. The mesh size is adapted in the strip gap area in order to increase with the depth as shown in Fig. 7.20. The size of the mesh increases from 1.25 mm at surface to a maximum of 4.5 mm.

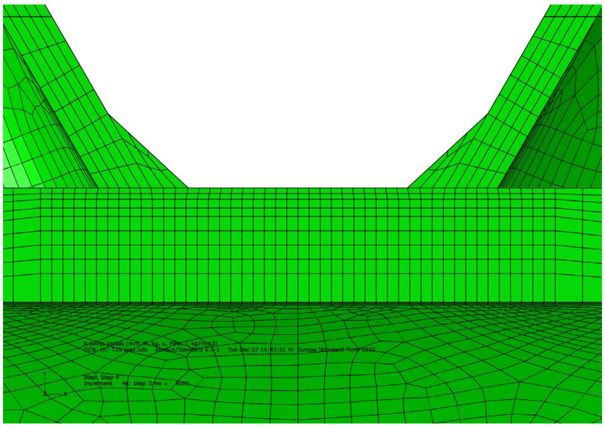

Figure 7.20: Refined mesh: increasing mesh size in the depth direction.

The curves in Fig. 7.21 draw more accurately the residual stress distributions. MORFEO results for transverse stresses fit especially well the experimental data.

For ABAQUS transverse stresses, the numerical curves are still shifted but their shapes are in good agreement with experimental ones, and the maximum values they reach are quite close to the experimental ones.

For longitudinal and radial stresses, ABAQUS curves seem to better follow the experimental data values.

There is still a significant difference between the right and left weld toe distributions obtained from MORFEO. For longitudinal stresses on the left weld toe, MORFEO results particularly overestimate peak stresses.

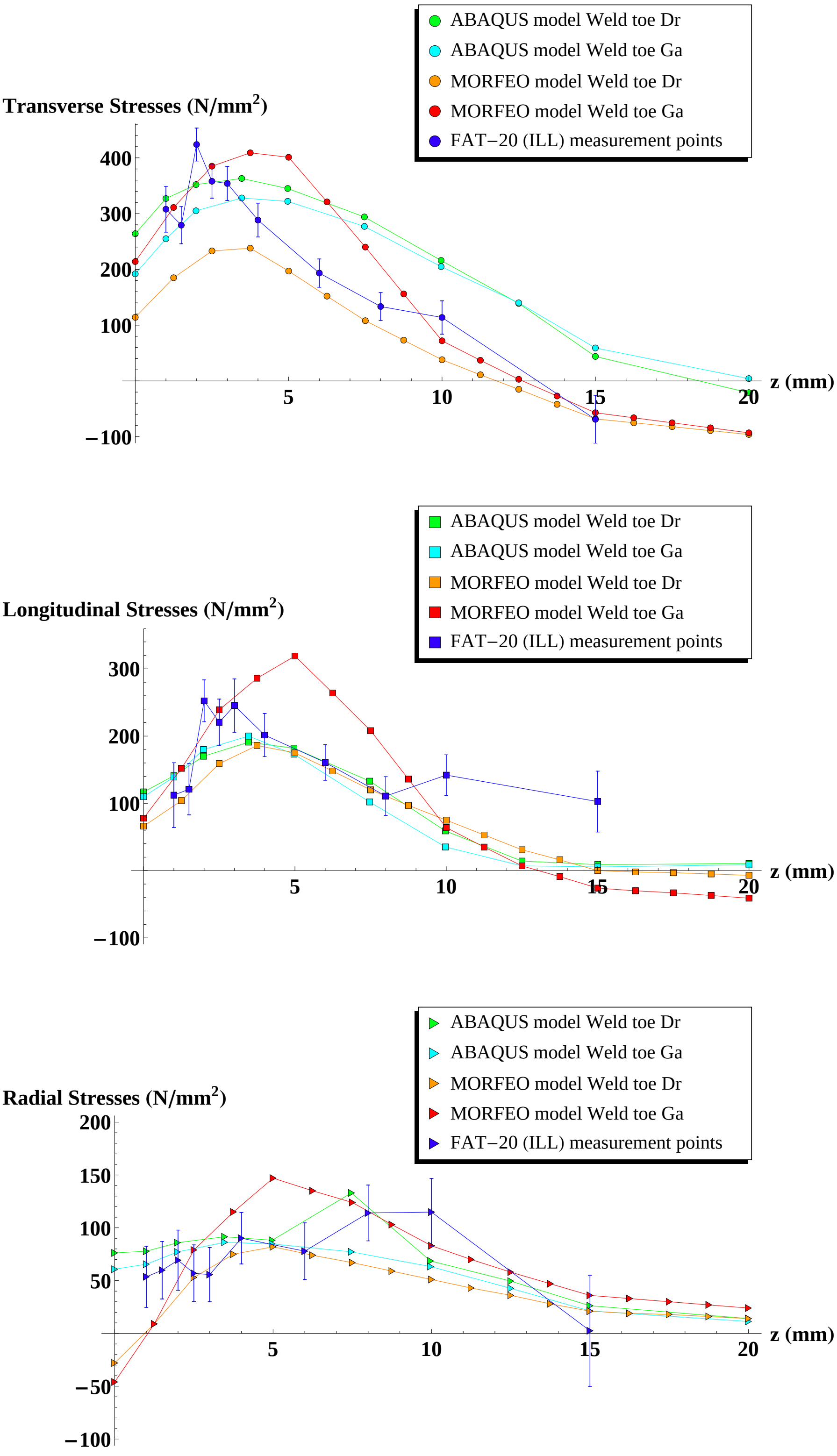

Figure 7.21: Comparison of transverse, longitudinal and radial residual stress distributions (ABAQUS, MORFEO and experimental data) for a refined model of Ref-T20.

7.8.3 Dissymmetry of the 3D residual stress field

Both residual stress fields (ABAQUS and MORFEO) show an axial dissymmetry. As shown in Fig. 7.22 the residual stresses induced by the welding paths 1 and 2 are partially removed by the subsequent welding paths 3 and 4 which leave residual stresses of highest magnitude.

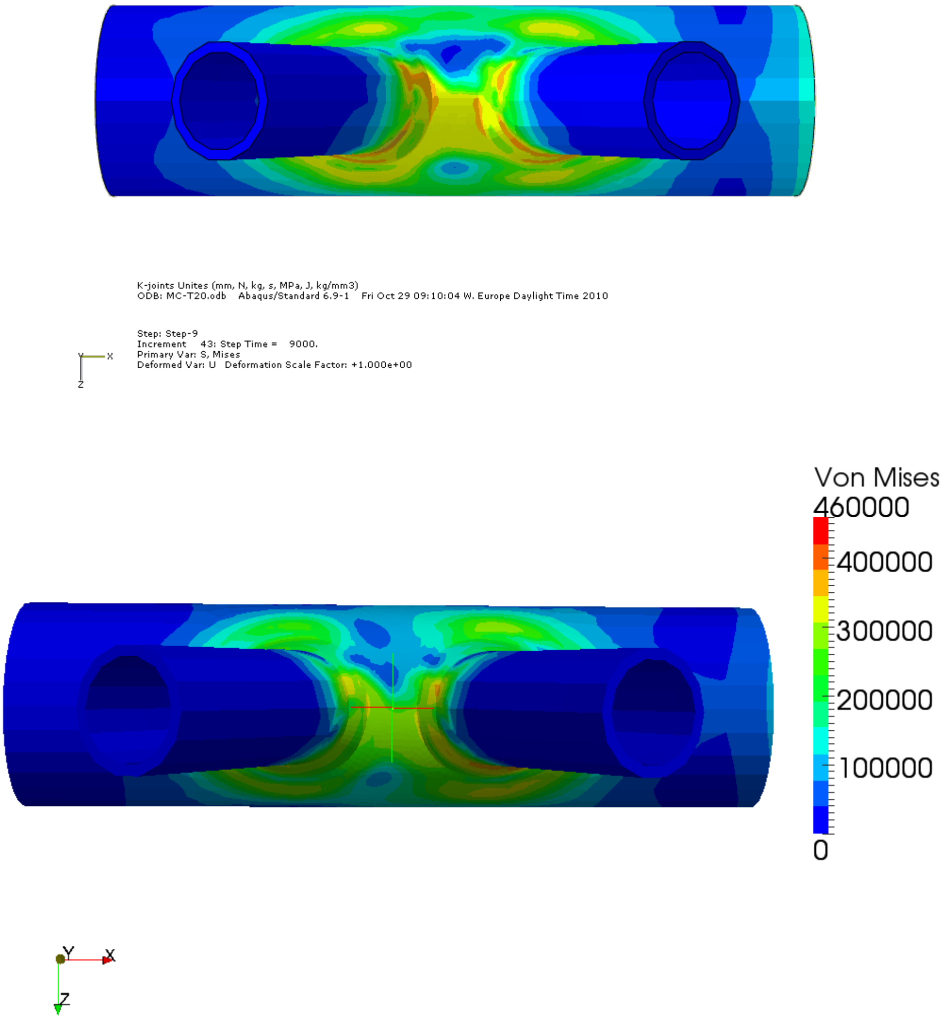
K-joints Unites (mm, N, kg, s, MPa, J, kg/mm3)
ODB: MC-T20.odb Abaqus/Standard 6.9-1 Fri Oct 29 09:10:04 W. Europe Daylight Time 2010
Step: Step-9
Increment 43: Step Time = 9000.
Primary Var: S, Mises
Deformed Var: U Deformation Scale Factor: +1.000e+00
Y
X
Z
Von Mises
460000
400000
300000
200000
100000
0
Y
X
Z

Figure 7.22: Top view showing the three-dimensional field of Von Mises residual stress: ABAQUS stresses on the top and MORFEO stresses on the bottom. For better comparison, the colour scale is the same for the two snapshots and is given in kPa.

By cutting the chord section with a vertical plane passing through the weld toe (Fig. 7.23), it can be seen that the tensile transverse residual stresses are balanced by the compressive stresses on the upper half of the chord section.

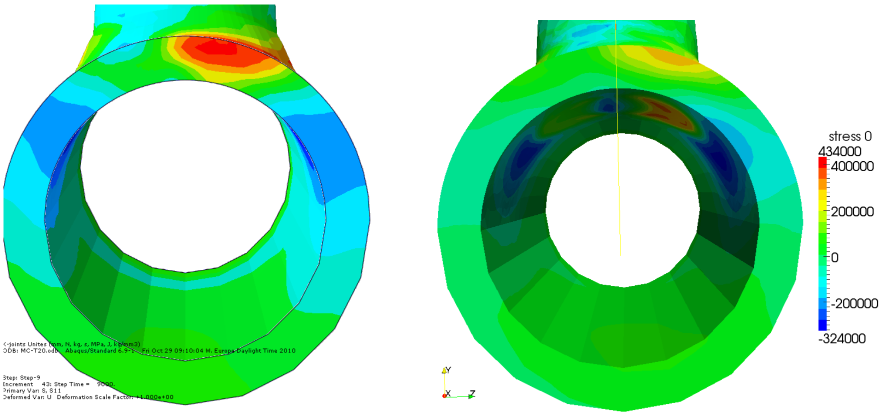
K-joints Unites (mm, N, kg, s, MPa, J, kg/mm3)
ODB: MC-T20.odb Abaqus/Standard 6.9-1 Fri Oct 29 09:10:04 W. Europe Daylight Time 2010
Step: Step-9
Increment 43: Step Time = 9000.
Primary Var: S, S11
Deformed Var: U Deformation Scale Factor: +1.000e+00
Y
X
Z
stress 0
434000
400000
200000
0
-200000
-324000

Figure 7.23: Cut view presenting the transverse residual stress distribution through the cross-section (same colour scale). The color scale for numerical results is given in kPa.

7.8.4 Similarities of residual stress distribution between joints with a chord wall thickness of 20 mm and 30 mm

This study aims to verify previous considerations that tend to demonstrate that the residual distribution is almost the same on the first millimeters even though the chord wall thickness increases. In other words, the residual stress distribution does not depend on the wall thickness.

This seems to be confirmed by the following curves comparing the residual stresses obtained numerically with ABAQUS on the geometries Ref-T20 and Ref-T30.

The curve shapes are quite similar for both geometries even though the slope of transverse stresses is not the same above 5 mm. The distributions are translated vertically to give larger residual stresses for larger thicknesses.

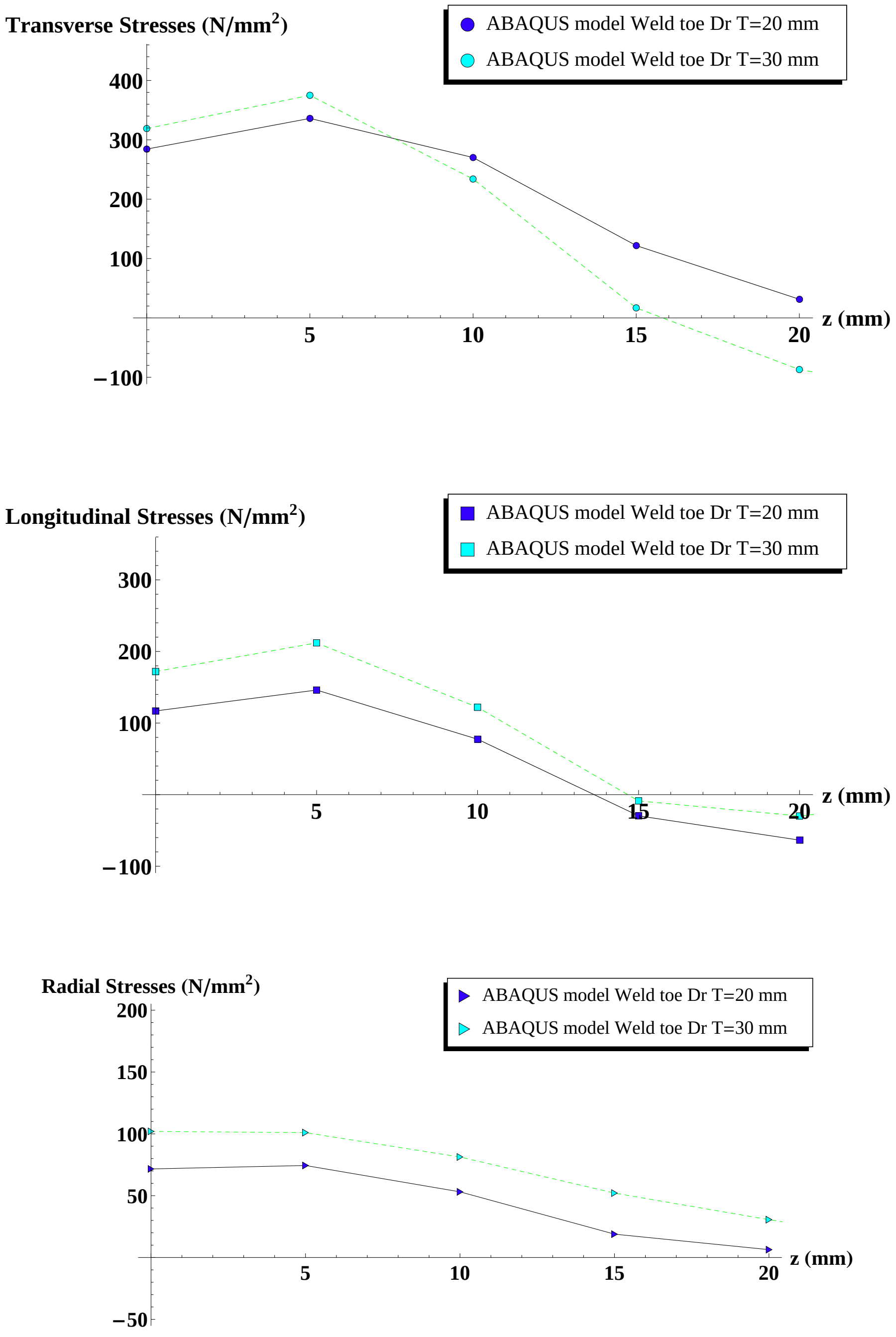

Figure 7.24: Comparison of residual stress distribution obtained numerically using ABAQUS for a wall chord thickness of 20 and 30 mm.

7.9 Summary and conclusions

A three-dimensional finite element analysis is used to accurately predict heating/cooling of welding sequences. The main assumptions and results of the model are presented below.

- The main assumptions used to develop the model are presented in this chapter. The most important simplification is that the multi-pass welding process is modeled as a single equivalent pass with a heat input corresponding to the total heat input of the seven weld passes. An uncoupled thermo-mechanical finite element formulation is chosen to solve the problem without considering phase transformations. The mechanical analysis is based on an elastic-plastic material behaviour with a linear isotropic work hardening. These simplifications are intended to generate a model able to simulate rapidly and efficiently residual stresses and to provide good quality results.
- The numerical results, obtained using the ABAQUS and MORFEO codes, have shown to be globally in good agreement with the experimental results obtained from neutron diffraction measurements. Our simplified model proved its ability to reproduce residual stress distribution in the region surrounding the welds even though the peak values are not always well captured and the distribution is sometimes shifted. Results are shifted in particular with the ABAQUS model giving an overestimation of residual stresses values above 5 mm depth.
- Numerical simulations have clearly given confirmation of the restraining effect occurring in the gap area for transverse residual stresses. It is seen also that the transverse residual stress field is asymmetric, the highest residual stress values occurring in the area where the final welding paths were made (welding paths 3 and 4). It was not possible to determine at which weld toe the highest residual stresses appears because ABAQUS and MORFEO give contradictory results.
- To simulate the welding residual stresses, the thermo-mechanical model must be able to provide accurate temperature distributions. To this end, an appropriate mesh size (convergence study) must be identify and the weld fusion profile generated by the thermal analysis has to be compared with the fusion zone obtained from a macrography for instance.
- Similarities in the stress distributions curves are found for chord wall thicknesses of 20 mm and 30 mm meaning that the thickness does not influence the distribution (non-proportional thickness effect). This effect has to be confirmed with the parametric study, simulating a large range of thicknesses.

Chapter 8

Geometrical parametric study

This chapter is devoted to a parametric study based on the finite element model presented and validated in the previous chapter 7. This study aims at identifying the influence of different parameters and geometries on the residual stress field. The different models are all built using the ABAQUS Code. Afterwards, equations of residual stress distribution through the chord wall thickness are proposed for the region surrounding hot-spots 1 and 1c.

8.1 Introduction

8.1.1 Objectives

This parametric study aims at investigating the dimensional and non-dimensional joint parameters $\beta = \frac{\mathrm{d}}{\mathrm{D}}$, $\gamma = \frac{\mathrm{D}}{2\mathrm{T}}$, $\tau = \frac{\mathrm{t}}{\mathrm{T}}$ and $\frac{\mathrm{g}}{\mathrm{D}}$ affecting at most the residual stress distribution, and hence the fatigue strength of joints under stress ratios $\mathrm{R} < 0.5$.

Borges (Borges, 2008) has made a similar study on the influence of these parameters on stress concentration factors, stress intensity factors and fatigue strength. He concluded that the increase of parameters T and τ induces a strong increase of the SCF and SIF values whereas parameter β has a minor influence. Therefore, an increase of T or τ tends to reduce the fatigue strength while an increase of β increases the fatigue strength. The parameter γ has different influences depending on the applied load case.

Borges did not consider residual stresses in his study. In our parametric study, we investigate if these parameters show similar trends or not on the residual stress field, and if these trends can explain in combination with the applied loads effect, the fatigue behaviour of joints.

8.1.2 Scope of parameters study

The studied K-joint geometries are chosen to correspond to bridge geometries. Parameters are depicted in Fig. 8.1 in order to illustrate the significance of the parameter variation on the geometry. Each parameter is studied one by one, the others being kept constants. The brace angle is kept constant $\theta = 60°$. It is relevant to note from Fig. 8.1 and Table 8.1 that a change of the brace wall thickness t induces a change of the weld size (W1, W2 and W3 dimensions). In our cases, t is varied for the proportional scaling (Fig. 8.1a), for the parameter τ study (Fig. 8.1b) and indirectly for the parameter γ study to keep τ constant (Fig. 8.1d).

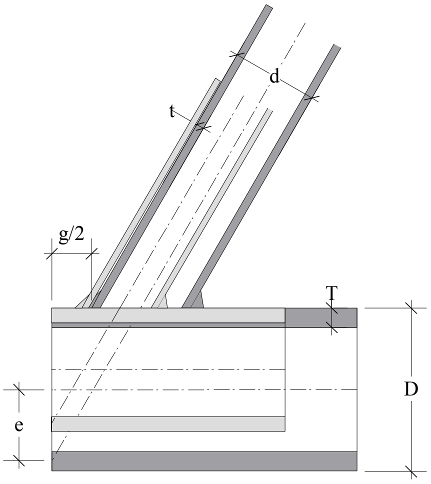

(a) Proportional scaling

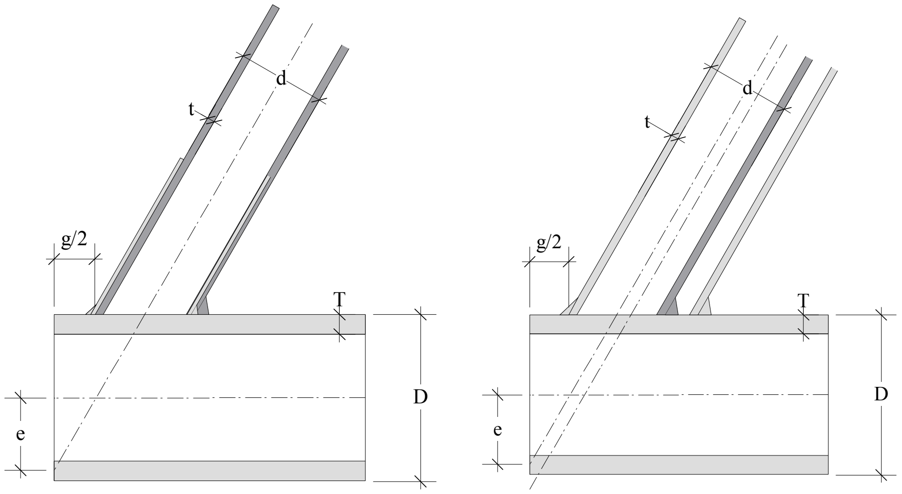

(b) $\tau = \frac{\mathrm{t}}{\mathrm{T}}$, changing t

(c) $\beta = \frac{\mathrm{d}}{\mathrm{D}}$, changing d

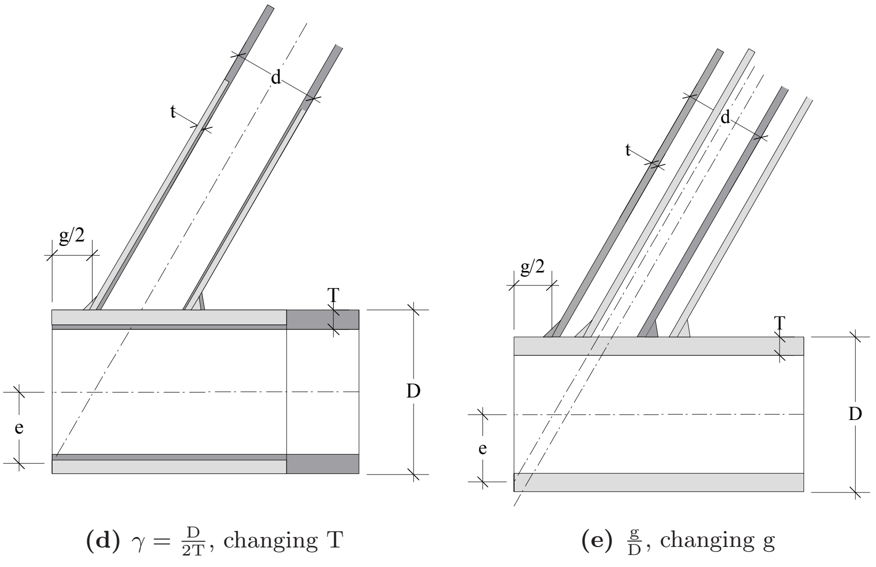

(d) $\gamma = \frac{\mathrm{D}}{2\mathrm{T}}$, changing T

(e) $\frac{\mathrm{g}}{\mathrm{D}}$, changing g

Figure 8.1: Proportional scaling and non-proportional scaling retained for the parametric study.

Table 8.1 presents the list of parameters used for this study. The models follow the definition of the geometry presented in the previous chapter, section 7.3.

Table 8.1: Dimensions and parameters defining the parametric joint models. The reference modeled geometries Ref-T20 and Ref-T30 are presented in gray.

		Dimensions (mm)						Parameters								Coefficients for the equation of the torch trajectory							
		D	T	d	t	Chord Length	Brace Length	β	γ	τ	g' (mm)	g (mm)	g/D	e (mm)	e/D	w1 (mm)	w2 (mm)	w3 (mm)	Q (W)	L +(W3+W1 cosθ)/2 (mm)	d/2+W2/2 (mm)	D/2 (mm)	W1/2 sinθ (mm)
Ref. models	**1**	168.3	20	88.9	8	600	350	0.53	4.21	0.4	38	51	0.30	-49	-0.29	15.0	10.0	5.0	41500	83.3	49.5	84.2	6.5
	2	168.3	30	88.9	8	600	350	0.53	2.81	0.27	38	51	0.30	-49	-0.29	15.0	10.0	5.0	41500	83.3	49.5	84.2	6.5
Proport. Scaling	**3**	84	10	45	4	600	350	0.53	4.2	0.4	19	26	0.31	-25	-0.30	7.5	5.0	2.5	5187	45.3	25.0	42.0	3.3
		168.3	20	88.9	8			0.53	4.21	0.4	38	51	0.30	-49	-0.29	15.0	10.0	5.0	41500	89.7	49.5	84.2	6.5
	4	244.5	30	127	12.5	750	450	0.52	4.08	0.42	59	79	0.32	-74	-0.30	23.5	15.6	7.8	159551	133.0	71.3	122.3	10.2
	5	505	60	268	24	1200	700	0.53	4.2	0.4	116	155	0.31	-150	-0.30	45.1	30.0	15.0	1127785	270.7	149.0	252.5	19.5
Non-proportional scaling	**6**	168.3	20	88.9	4	600	350	0.53	4.21	0.2	38	45	0.26	-49	-0.29	7.5	5.0	2.5	5187	80.0	47.0	84.2	3.3
		168.3	20	88.9	8			0.53	4.21	0.4	38	51	0.30	-60	-0.36	15.0	10.0	5.0	41500	89.7	49.5	84.2	6.5
	7	168.3	20	88.9	12	650	400	0.53	4.21	0.6	38	58	0.34	-72	-0.43	22.6	15.0	7.5	141913	99.3	52.0	84.2	9.8
	8	168.3	20	108	8	650	400	0.64	4.21	0.4	38	51	0.30	-79	-0.47	15.0	10.0	5.0	41500	100.7	59.0	84.2	6.5
		168.3	20	88.9	8			0.53	4.21	0.4	38	51	0.30	-60	-0.36	15.0	10.0	5.0	41500	89.7	49.5	84.2	6.5
	9	168.3	30	88.9	12.5	650	400	0.53	2.81	0.42	38	58	0.35	-73	-0.43	23.5	15.6	7.8	159551	100.5	52.3	84.2	10.2
		168.3	20	88.9	8			0.53	4.21	0.4	38	51	0.30	-60	-0.36	15.0	10.0	5.0	41500	89.7	49.5	84.2	6.5
	10	168.3	10	88.9	4	600	350	0.53	8.42	0.4	38	45	0.26	-49	-0.29	7.5	5.0	2.5	5187	80.0	47.0	84.2	3.3
		168.3	20	88.9	8			0.53	4.21	0.4	38	51	0.30	-60	-0.36	15.0	10.0	5.0	41500	89.7	49.5	84.2	6.5
	11	168.3	20	88.9	8	650	400	0.53	4.21	0.4	78	91	0.54	-95	-0.56	15.0	10.0	5.0	41500	109.7	49.5	84.2	6.5
	12	168.3	20	88.9	8	750	500	0.53	4.21	0.4	155	168	1.00	-162	-0.96	15.0	10.0	5.0	41500	148.2	49.5	84.2	6.5

Welding power Q (W) is calculated for each geometry as a function of the weld geometry. It is assumed that the volumetric heat source s is kept constant, s = 5.87 W/mm^3 for each weld size. Q is obtained using equation (8.1) where the reference volume V corresponds to half the volume of a sphere. The radius of the sphere r is related to the weld dimensions, which is set equal to the W1 dimension (see section 7.3).

$$Q = sV = s\ \frac{1}{2}\ \frac{4}{3}\ \pi\ r^3 = s\ \frac{2}{3}\ \pi\ W1^3 \quad (\text{in } \frac{\text{W}}{\text{mm}^3} \times \text{mm}^3 = \text{W}) \tag{8.1}$$

The calculated Q value is given for each geometry of the parametric study in Table 8.1.

It is important to note that, to be consistent with the convergence study, the type of FE and the mesh size are kept identical for all the models. The mesh size is the one already validated for models Ref-T20 and Ref-T30. It corresponds to the model DC3D8-2to5mm in Table 7.5 (strip elements: 2 mm × 5 mm, chord elements: 5 mm × 5 mm). These fixed dimensions explain why in thin chord walls a few elements are present through the thickness whereas in thick chord walls many more elements enable to draw the residual stress profile. However, for 10 mm thick chord walls an exception is made and the mesh is refined in order to have 4 mesh elements through the thickness so as to draw stress distributions.

8.2 Results of parametric study

The stress distributions presented in this section are given along a vertical line through the wall chord thickness from the hot-spots 1 or 1c. Numerical data are obtained using ABAQUS model, only results from the right weld toe (positive x coordinate) are shown in this section. They give values slightly larger than the left side one, however the difference between both is small.

8.2.1 Residual stress distribution as a function of z absolute value and z/T relative value

In the section devoted to neutron diffraction measurements (section 5.3.5), a study was conducted to identify if the residual stress distribution function is best related to z or to z/T (z is the depth from the surface defined along a vertical axis, T is the chord wall thickness). By comparing measurements for chord wall thicknesses of 20 and 30 mm, it seemed that the transverse strain distribution is better related to z than to z/T. This first consideration needs to be confirmed with the parametric study done on a large range of thicknesses.

Most of the distributions that can be found in the literature (Lee et al., 2005; Stacey et al., 2000) are in contradiction with this result. They are usually expressed as a function of z/T.

In this section, results from the parametric study are expressed as a function of z, as well as a function of z/T in order to define the best expression. The results are presented in Fig. 8.2 and 8.3 respectively for proportional scaling and non-proportional γ parameter because T changes in both studies. They are given along a vertical line through the wall chord thickness from the hot-spots 1 and 1c.

It is seen in both figures that the residual stress distribution is best defined by a function of z/T. This effect was not so clear when comparing distributions for T values of 20 and 30 mm because these thicknesses were too close to see a real difference in distributions.

For the rest of the parametric study, residual stresses are presented as a function of z/T.

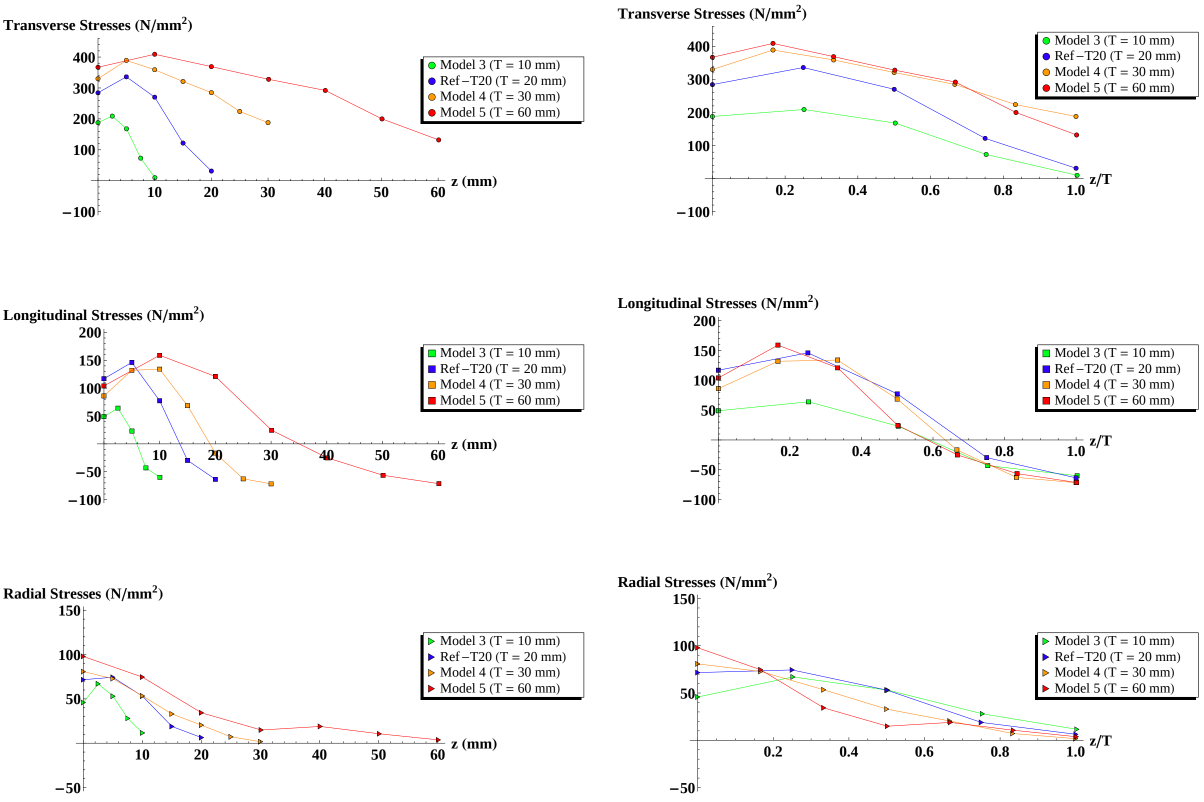

Figure 8.2: Model results for the proportional scaling, drawn as a function of z and of z/T.

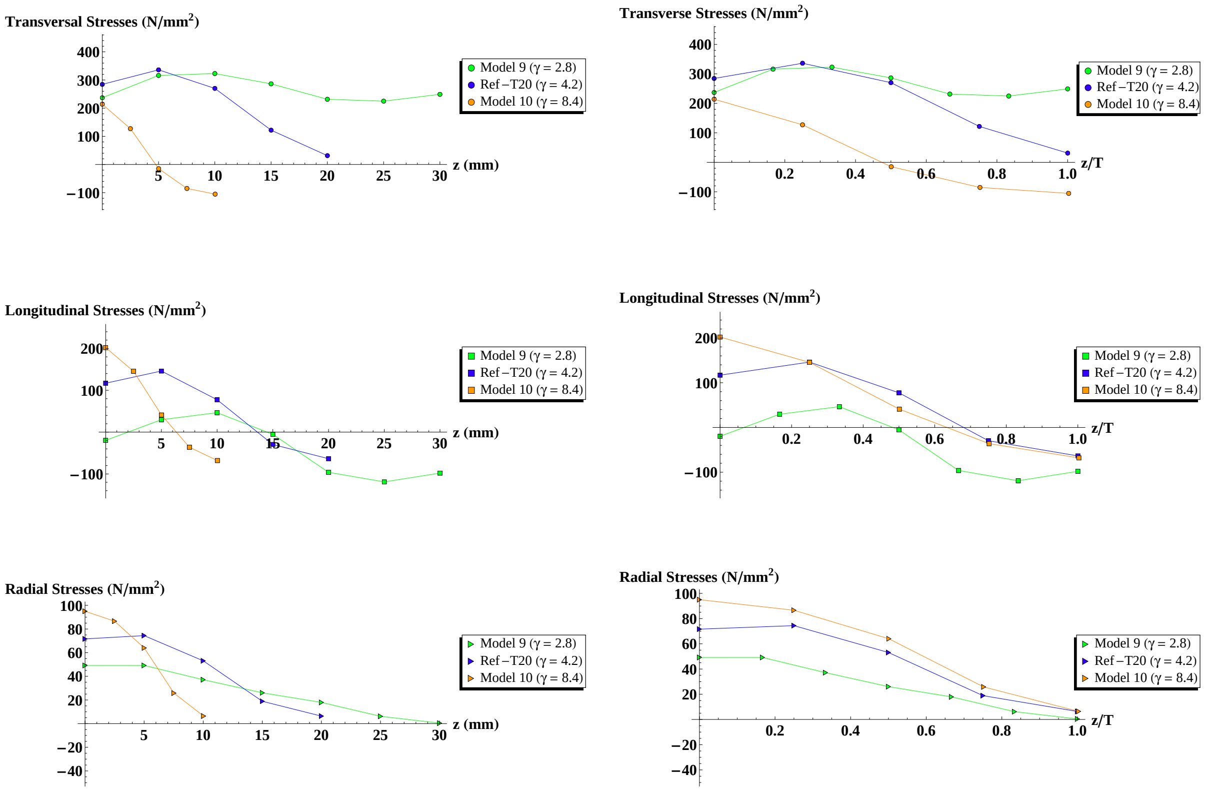

Figure 8.3: Model results for the non-proportional parameter γ, drawn as a function of z and of z/T.

8.2.2 Influence of the proportional scaling on residual stress distribution

In Fig. 8.4, residual stresses obtained for the proportional scaling are presented in terms of distribution through the wall chord thickness. In Fig. D.1, D.3 , D.4 , D.5 (Annex D), the residual stress fields are presented in a radial and an axial cross section, as well as in an axonometric view.

From these figures, the following implications on the stress distributions are drawn:

- a decrease in the K-joint size implies an overall reduction in the magnitude of transverse residual stresses in all the area surrounding the welds (curves shifted down). The zone of tensile transverse residual stresses becomes also much larger in absolute terms. This phenomenon is linked with the increase of the weld size, hence with the increase of the heat input Q.
- the longitudinal stress distribution superimposes except for the smallest scaling (T =10 mm) which undergoes a reduction of stress magnitude close to the surface. Globally a decrease of joint size implies also a decrease of the longitudinal stress magnitude but this effect is concentrated at the weld root (in the chord wall), explaining why this is not visible in Fig. 8.4.
- the general form of the radial stress distribution does change drastically with proportional scaling. A size decrease induces a radial stress decrease in the weld root area (in the brace wall).

In order to determine what are the implications of a proportional scaling on a residual stress distribution, assumed to be fitted by a third order polynomial function $a(z/T)^3 + b(z/T)^2 + c(z/T) + d$, we have to analyse if the proportional scaling influences the shape of the stress distribution curve (then influences each coefficient a, b, c and d) or keep globally the shape of distribution without necessarily keeping the magnitude (then influences globally $a(z/T)^3 + b(z/T)^2 + c(z/T) + d$). To increase the distribution accuracy, the influence would be considered on each coefficient but to limit the number of unknown values to determine, the global influence should be chosen if it is more appropriate.

Concerning transverse stresses, the distribution shape is similar for the four models, however the distribution is better fitted by considering the four coefficients. For longitudinal stresses, the distribution shapes are quite close despite the fact that the smallest scale (T= 10 mm) gives slightly different results. For radial stresses, the distribution changes between the models.

Therefore, it seems that the proportional scaling has a global influence on the longitudinal stress distribution and influences each coefficient a, b, c and d of the transverse and radial stress distribution. This is expressed as follows, where T_0 is a reference chord wall thickness. Note that it was a choice to use reference dimensions and parameters (T_0, τ_0, β_0, γ_0 and $(g/D)_0$) in order to remind for which initial geometry the distributions were proposed. T_0 is equal to 30 mm.

$$\sigma_{res} = (a(z/T)^3 + b(z/T)^2 + c(z/T) + d)(\frac{T}{T_0})^e \quad \text{for longitudinal stresses} \tag{8.2}$$

$$\sigma_{res} = (a(\frac{T}{T_0})^e(z/T)^3 + b(\frac{T}{T_0})^f(z/T)^2 + c(\frac{T}{T_0})^g(z/T) + d(\frac{T}{T_0})^h) \quad \text{for transverse and radial stresses} \tag{8.3}$$

8.2.3 Influence of the wall thickness ratio τ on residual stress distribution

In Fig. 8.5 and D.6, D.7, it is seen that a change of τ influences the shape of the transverse, longitudinal and radial stress distributions as well as their magnitude. An increase of τ raises the transverse stress magnitude and extends this magnitude on a large region in the wall chord. However, for longitudinal stresses, an increase of τ dissipates much more the heat input in a larger size of weld and therefore decreases the stress intensity. Concerning the radial stresses, an increase of τ increases the radial stress magnitude in the weld root area (in the brace wall) and reduces it at the weld toe.

Therefore, the parameter τ seems to influence each coefficient a, b, c and d of the stress distribution:

$$\sigma_{res} = (a(\frac{\tau}{\tau_0})^i (z/T)^3 + b(\frac{\tau}{\tau_0})^j (z/T)^2 + c(\frac{\tau}{\tau_0})^k (z/T) + d(\frac{\tau}{\tau_0})^l) \tag{8.4}$$

where τ_0 is equal to 0.4.

8.2.4 Influence of the diameters ratio β on residual stress distribution

For the study of the β parameter, only two models are available. In Fig. 8.6, and D.8, it is shown that the shape of the distributions for transverse, longitudinal and radial stresses does not seem to change with β but this can be explained by the fact that the two β parameters are rather close. This parameter seems to have a small influence on the residual stress distribution and magnitude, which is mainly due to the fact that the weld size and the heat input do not change.

In that case, it is chosen to take into account the effect of β on each coefficient a, b, c and d. After fitting the curves, it was seen that the equation can be simplified for the radial distribution by considering a global influence:

$$\sigma_{res} = (a(\frac{\beta}{\beta_0})^m (z/T)^3 + b(\frac{\beta}{\beta_0})^n (z/T)^2 + c(\frac{\beta}{\beta_0})^o (z/T) + d(\frac{\beta}{\beta_0})^p) \text{ for transverse and longitudinal str} \tag{8.5}$$

$$\sigma_{res} = (a(z/T)^3 + b(z/T)^2 + c(z/T) + d)(\frac{\beta}{\beta_0})^m \text{ for radial str} \tag{8.6}$$

where β_0 is equal to 0.53.

8.2.5 Influence of the chord slenderness γ on residual stress distribution

Figure 8.8 shows that the distributions do not evolve as a function of γ for longitudinal and radial stresses while it is the case for transverse stresses. From Fig. D.9 and D.10, it is seen that they evolve but only in the weld region without really affecting the chord wall stresses.

The equations of distribution are then expressed as follows:

$$\sigma_{res} = (a(\frac{\gamma}{\gamma_0})^q (z/T)^3 + b(\frac{\gamma}{\gamma_0})^r (z/T)^2 + c(\frac{\gamma}{\gamma_0})^s (z/T) + d(\frac{\gamma}{\gamma_0})^t) \text{ for transverse stresses} \tag{8.7}$$

$$\sigma_{res} = (a(z/T)^3 + b(z/T)^2 + c(z/T) + d)(\frac{\gamma}{\gamma 0})^q \text{ for longitudinal and radial stresses} \tag{8.8}$$

where $\gamma 0$ is equal to 4.21.

8.2.6 Influence of the normalized gap parameter $\frac{\mathrm{g}}{\mathrm{D}}$ on residual stress distribution

Figure 8.8 shows that the shape of the distributions does not change with $\frac{\mathrm{g}}{\mathrm{D}}$ in the weld toe region. Fig. D.11 and D.12 confirm it and also give the proof that the restraining effect in the gap region disappears for large gap dimensions.

$$\sigma_{res} = (a(z/T)^3 + b(z/T)^2 + c(z/T) + d)(\frac{g/D}{(g/D)_0})^u \tag{8.9}$$

where $(\mathrm{g/D})_0$ is equal to 0.3.

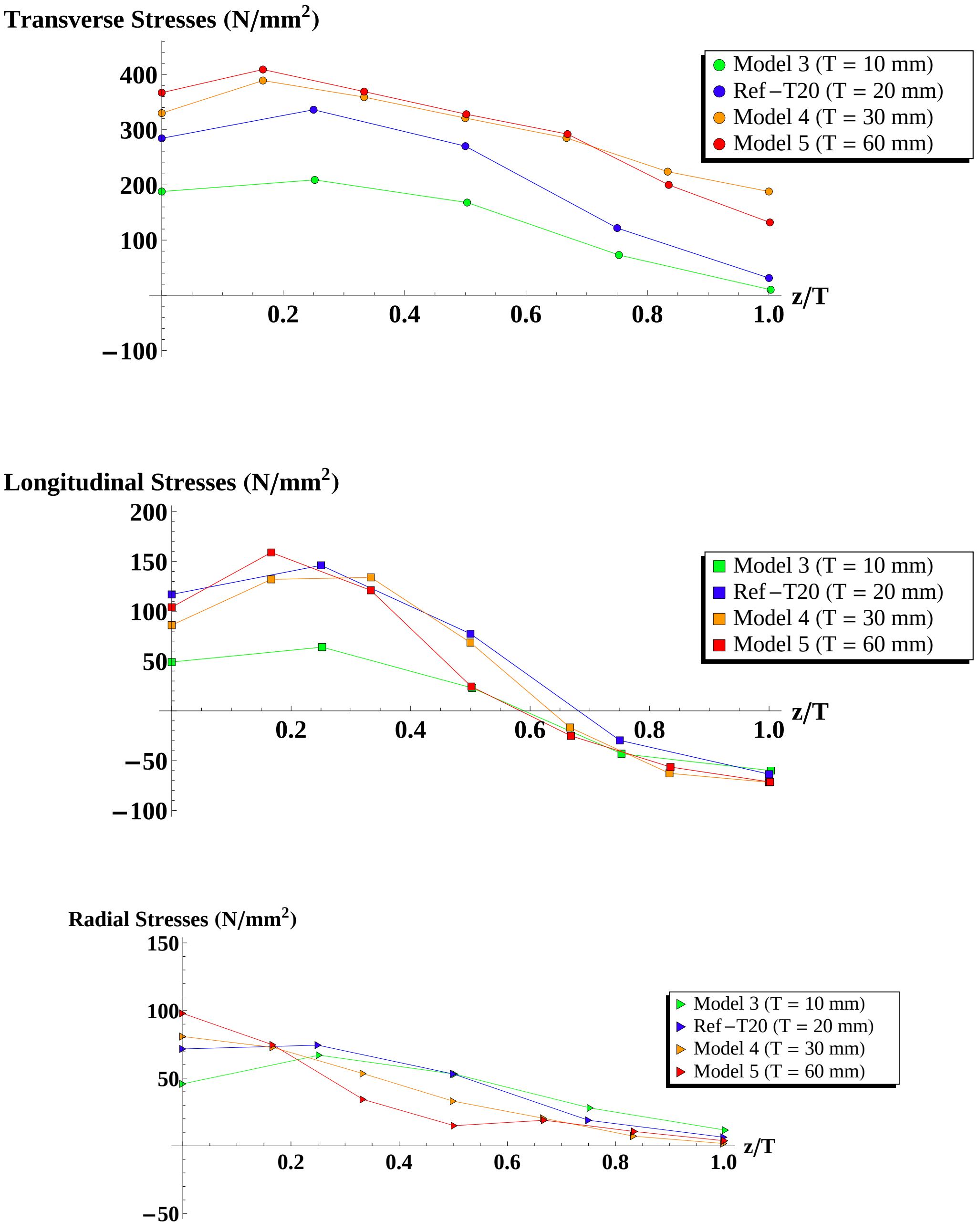

Figure 8.4: Model results for the proportional scaling, drawn as a function of z/T.

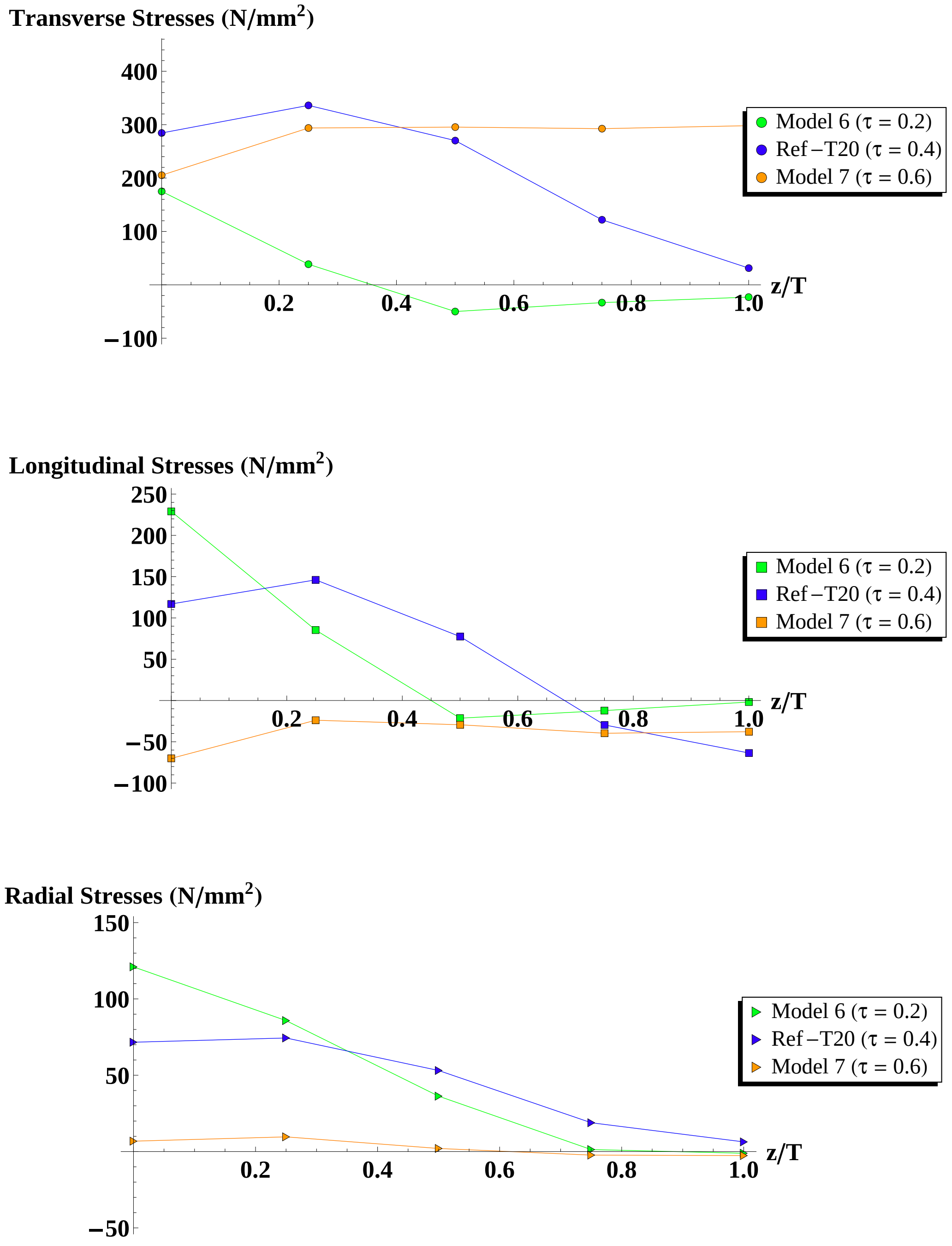

Figure 8.5: Model results for the parameter τ (non prop. scaling), drawn as a function of z/T.

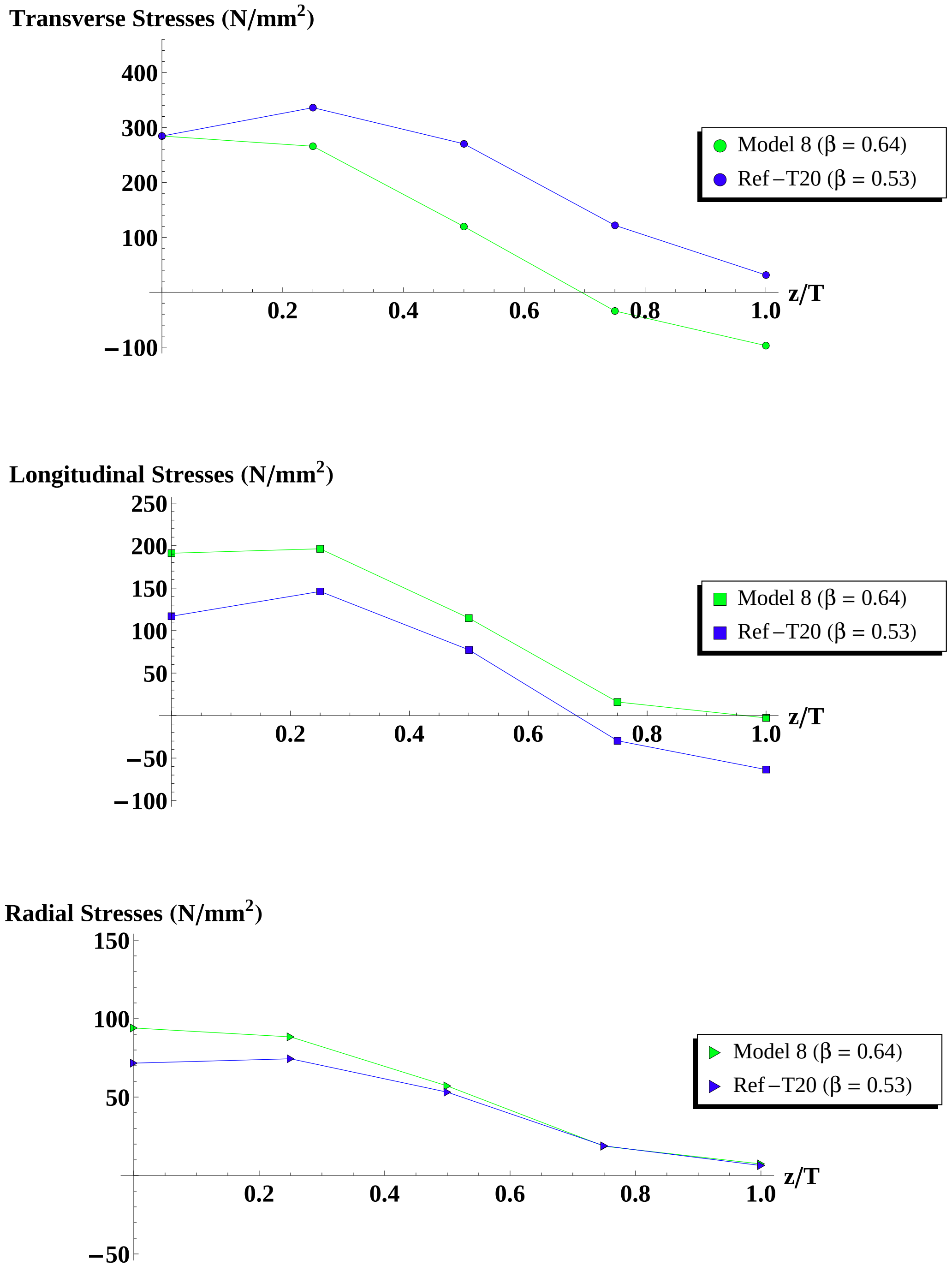

Figure 8.6: Model results for the parameter β (non prop. scaling), drawn as a function of z/T.

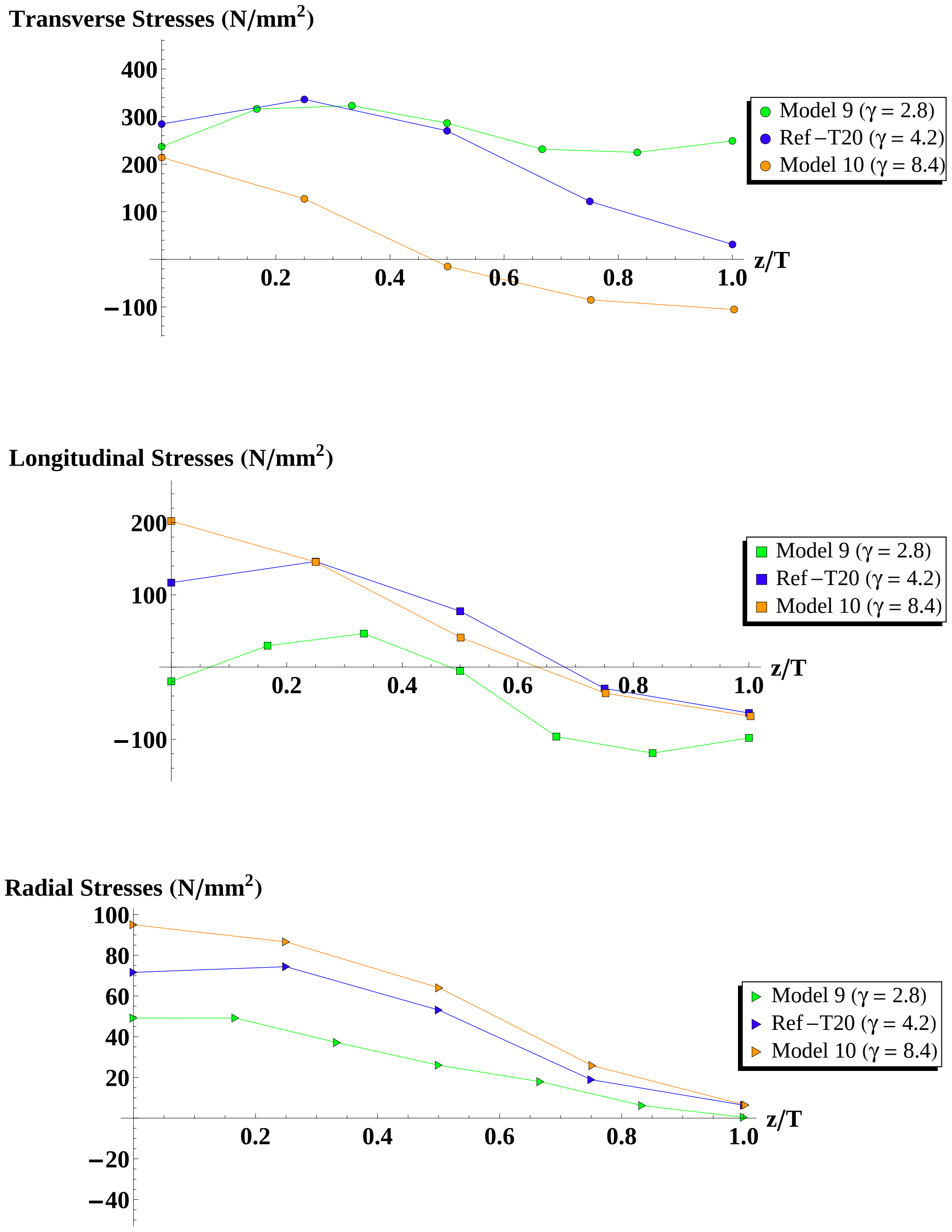

Figure 8.7: Model results for the parameter γ (non prop. scaling), drawn as a function of z/T.

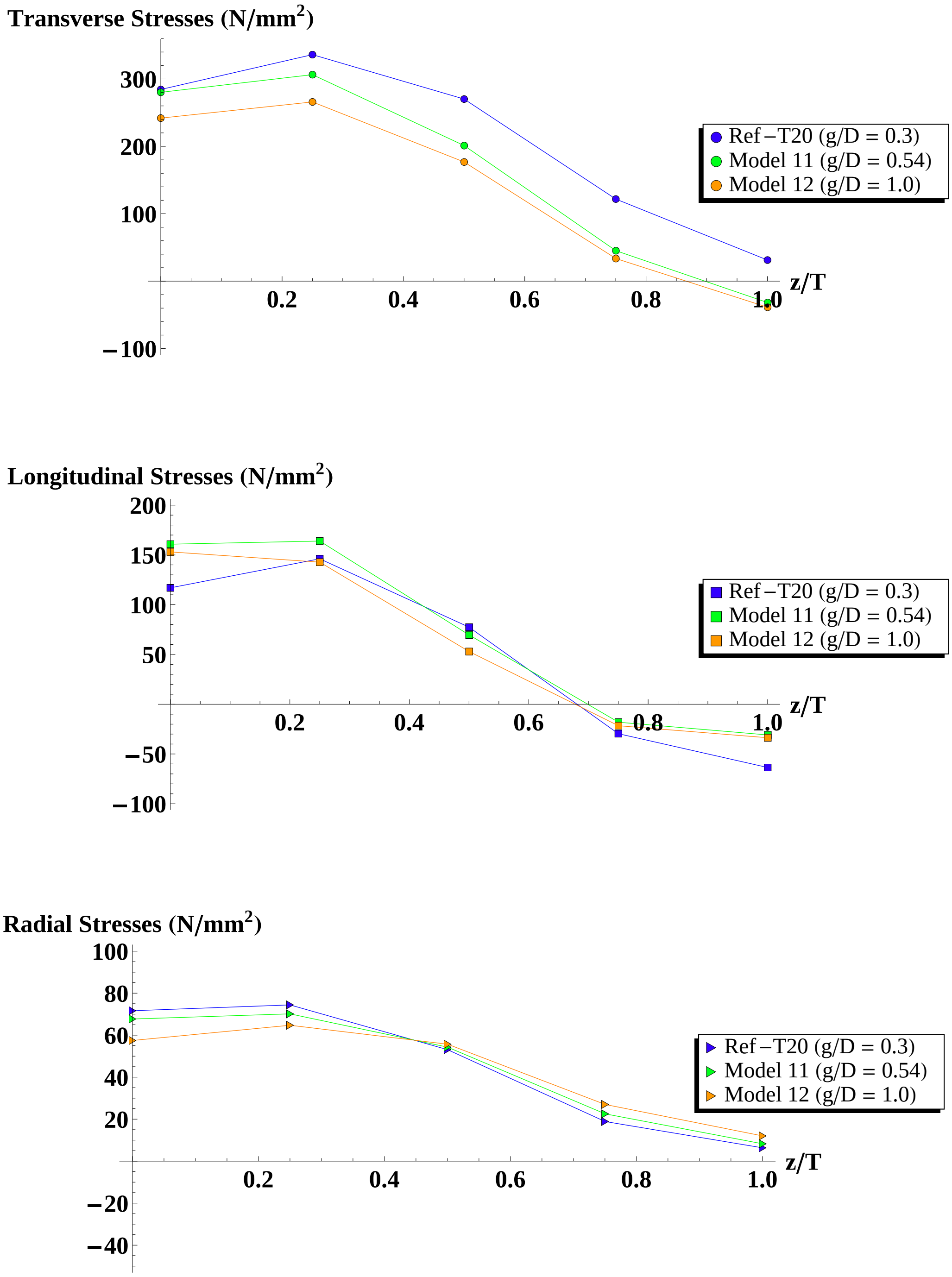

Figure 8.8: Model results for the parameter γ (non prop. scaling), drawn as a function of z/T.

8.3 Proposed functions for residual stress distribution

From the parametric models, the functions of stress distribution are calculated iteratively using a least-square fit, based on previous considerations.

The expressions obtained are given in the following equations (8.11), (8.12) and (8.13) in the form of third order polynomial equations. The linear term of the equations tends to zero and is neglected. Moreover the influence of the gap parameter $\frac{\mathrm{g}}{\mathrm{D}}$ on the radial stresses is also found to be negligible.

The reference geometric parameters for the following equations are:

$$T_0 = 30\ mm;\ \tau_0 = 0.4;\ \beta_0 = 0.53;\ \gamma_0 = 4.21;\ (g/D)_0 = 0.3; \tag{8.10}$$

$\mathrm{T_0}$ = 30 mm is chosen, instead of 20 mm, because it gives a slightly better fit.

- for transverse residual stresses:

$$\boxed{\sigma_{res,transv} = \frac{1}{(\frac{g/D}{(g/D)_0})^{0.15}}[300\frac{(\frac{T}{T_0})^{0.3}(\frac{\tau}{\tau_0})^{0.4}}{(\frac{\beta}{\beta_0})^{0.25}} - 300\frac{(\frac{\beta}{\beta_0})^{4}(\frac{\gamma}{\gamma_0})^{1.6}}{(\frac{T}{T_0})^{0.5}(\frac{\tau}{\tau_0})^{1.5}}\ (z/T)^2 + 60\frac{(\frac{\beta}{\beta_0})^{8}(\frac{\gamma}{\gamma_0})^{2.5}}{(\frac{T}{T_0})^{1.2}(\frac{\tau}{\tau_0})^{3}}\ (z/T)^3]} \tag{8.11}$$

- for longitudinal residual stresses:

$$\boxed{\sigma_{res,long} = (\frac{g/D}{(g/D)_0})^{0.25}(\frac{T}{T_0})^{0.25}(\frac{\gamma}{\gamma_0})^{0.9}[125\frac{(\frac{\beta}{\beta_0})^{3.2}}{(\frac{\tau}{\tau_0})^{0.9}} - 470\frac{(\frac{\beta}{\beta_0})^{2}}{(\frac{\tau}{\tau_0})^{1.65}}\ (z/T)^2 + 270\frac{(\frac{\beta}{\beta_0})^{2.6}}{(\frac{\tau}{\tau_0})^{2.2}}\ (z/T)^3]} \tag{8.12}$$

- for radial residual stresses:

$$\boxed{\sigma_{res,radial} = (\frac{\beta}{\beta_0})^{1.5}(\frac{\gamma}{\gamma_0})^{0.6}[75\frac{(\frac{T}{T_0})^{0.1}}{(\frac{\tau}{\tau_0})^{0.8}} - 230\frac{(\frac{T}{T_0})^{0.3}}{(\frac{\tau}{\tau_0})^{1.4}}\ (z/T)^2 + 160\frac{(\frac{T}{T_0})^{0.3}}{(\frac{\tau}{\tau_0})^{1.6}}\ (z/T)^3]} \tag{8.13}$$

These distribution functions are available for 10 mm < T < 60 mm, 0.2 < τ < 0.6, 0.53 < β < 0.64, 2.8 < γ < 8.4, 0.3 < $\frac{g}{D}$ < 1 and brace angles θ of 60°. They are valid for a diameter D close to 170 mm.

These functions are depicted in Figures 8.9, 8.10 and 8.11, and compared with numerical data points for proportional and non-proportional scaling (parameters τ; β; γ and g/D). From these figures, it is seen that the functions do not perfectly fit the numerical data but they give the main trend (magnitude and shape) of the distributions, thus providing to the designer a global overview of as-welded residual stress field. To improve the quality of these functions and to extend the validity domain, more parametric studies should be performed by changing the diameter D and by increasing the range of parameters, especially for β. It is recommended to perform these new studies with MORFEO-Welding because it requires less computing time and gives better transverse residual stress results. Simulations can be conducted with a refined mesh in a reasonable time.

Moreover, in Fig. 8.12, the functions are also compared with stresses obtained by neutron diffraction (ILL, sample FAT-20). The same conclusions about ABAQUS results as in chapter 7 are found. The estimated residual stresses do not capture the peak value in general, and the transverse curve is shifted to the right. Thus, the estimated transverse residual stress distribution becomes compressive at a deeper point than the measured distribution. On the contrary, the estimated longitudinal residual stress distribution becomes compressive at a shallower point than the measured distribution.

8.4 Summary of proportional and non proportional scaling influence on residual stress distribution

From previous numerical results, it is seen that a variation of parameters causes:

- a variation of transverse residual stresses in the chord wall underneath the weld and in the gap region
- a variation of longitudinal residual stresses in the weld region close to the weld root (on the chord side)
- a variation of radial residual stresses in the upper weld region (on the brace side)

For this reason, residual stresses affecting the weld toe area, where the crack starts to propagate, are mainly transverse residual stresses. Moreover, from previous investigations, it is known that their orientation is also the most detrimental for fatigue cracking.

In the weld toe area, parameters most influencing the magnitude of tensile residual stresses in the proposed functions of distribution are:

- for transverse residual stresses: T (proportional scaling) and τ.
- for longitudinal residual stresses: β and γ. Nevertherless, Fig. 8.5 would have suggested that the parameter τ has also a strong influence.
- for radial residual stresses: β and γ. Once again, τ should also have a strong influence.

The parameter influence on the fatigue strength (Borges, 2008) and on the magnitude of tensile transverse residual stresses are summarized in Table 8.2. It is worth noting that increasing T and τ has the double effect of reducing the fatigue strength under applied load and increasing the tensile transverse stresses at the weld toe implying also a decrease of the fatigue strength (for $R < 0.5$). Therefore, for design purposes, these parameters are determinants in the choice of the geometry to increase the fatigue life of these joints.

Table 8.2: Influence of the different parameters and the T dimension on the fatigue strength and on the magnitude of tensile transverse residual stresses.

Increase in	Fatigue strength (applied stresses)	Tensile Transverse residual stress magnitude
T (prop. scaling)	$\searrow\searrow$	$\nearrow\nearrow$
τ	$\searrow\searrow$	$\nearrow\nearrow$
β	$\nearrow$	$\searrow$
γ	$\leftrightarrow$	$\searrow$
g/D	$\searrow$	$\leftrightarrow$

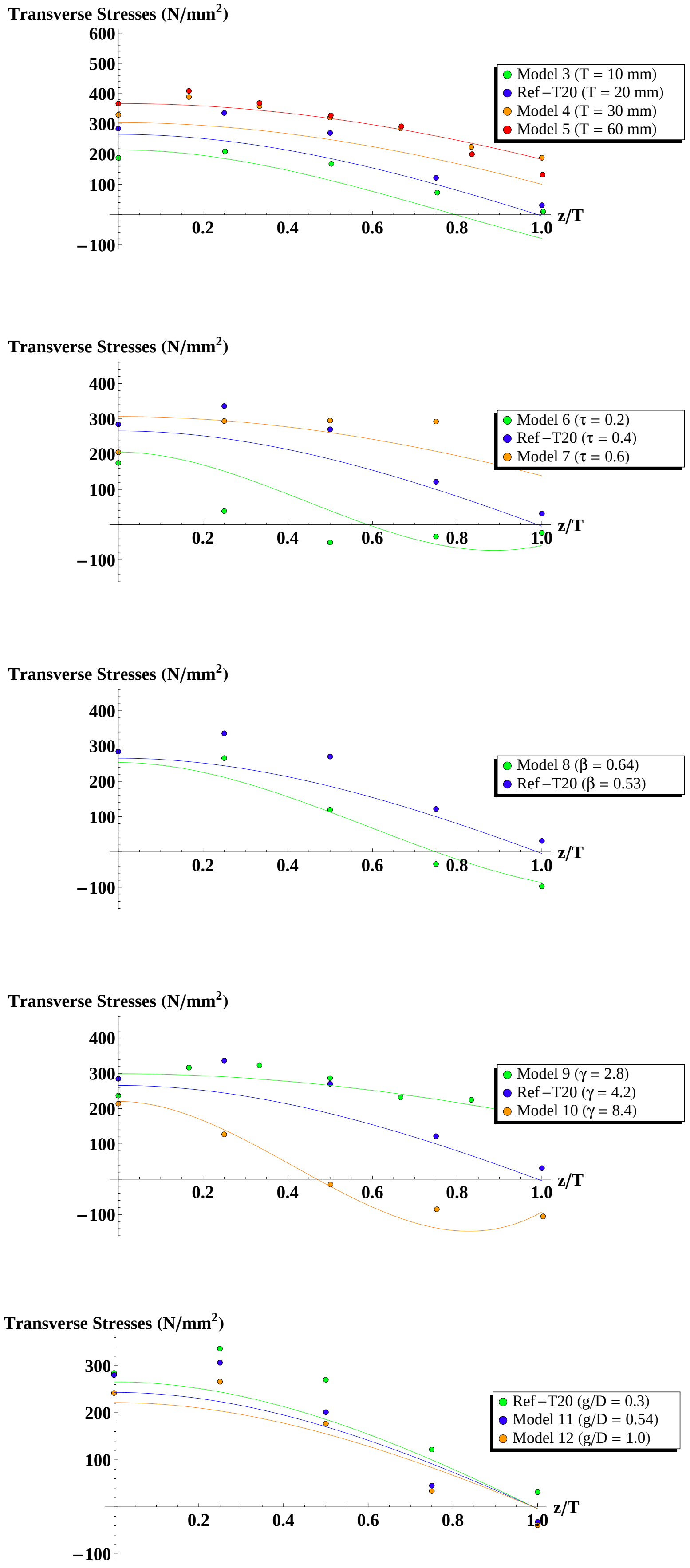

Figure 8.9: The proposed function for transverse residual stresses compared with the numerical data (proportional scaling, parameter τ, parameter β, parameter γ and parameter g/D). The curves represent the functions of distribution, the points represent the FE analysis results.

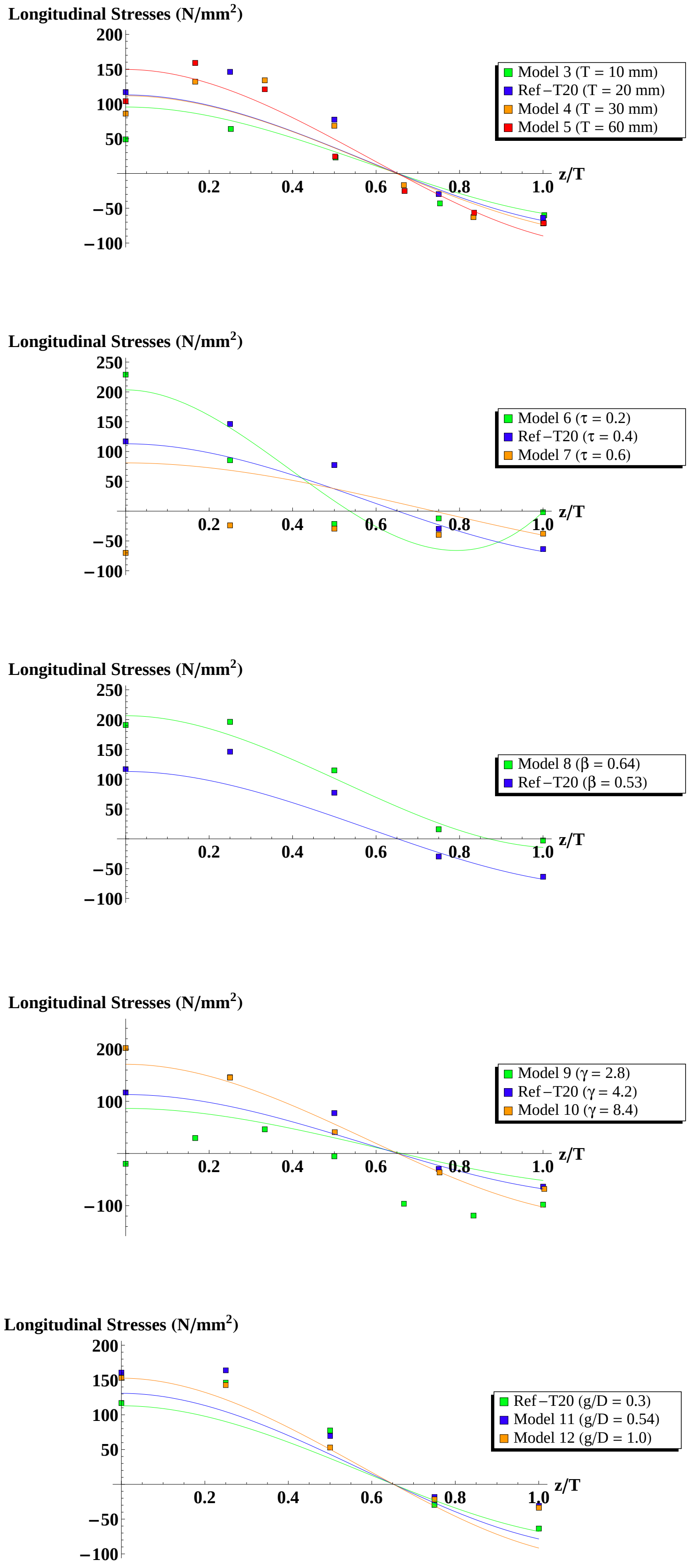

Figure 8.10: The proposed function for longitudinal residual stresses compared with the numerical data (proportional scaling, parameter τ, parameter β, parameter γ and parameter g/D). The curves represent the functions of distribution, the points represent the FE analysis results.

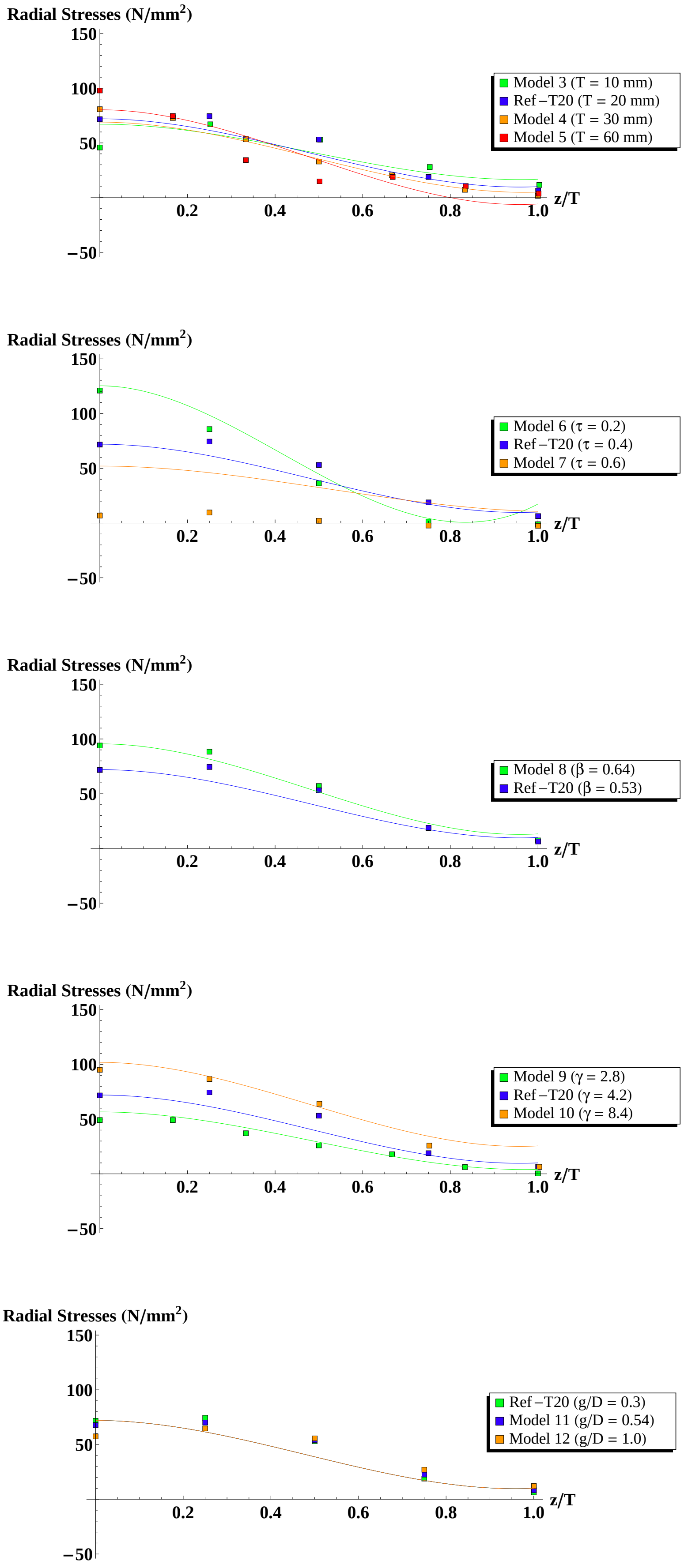

Figure 8.11: The proposed function for radial residual stresses compared with the numerical data (proportional scaling, parameter τ, parameter β, parameter γ and parameter g/D). The curves represent the functions of distribution, the points represent the FE analysis results.

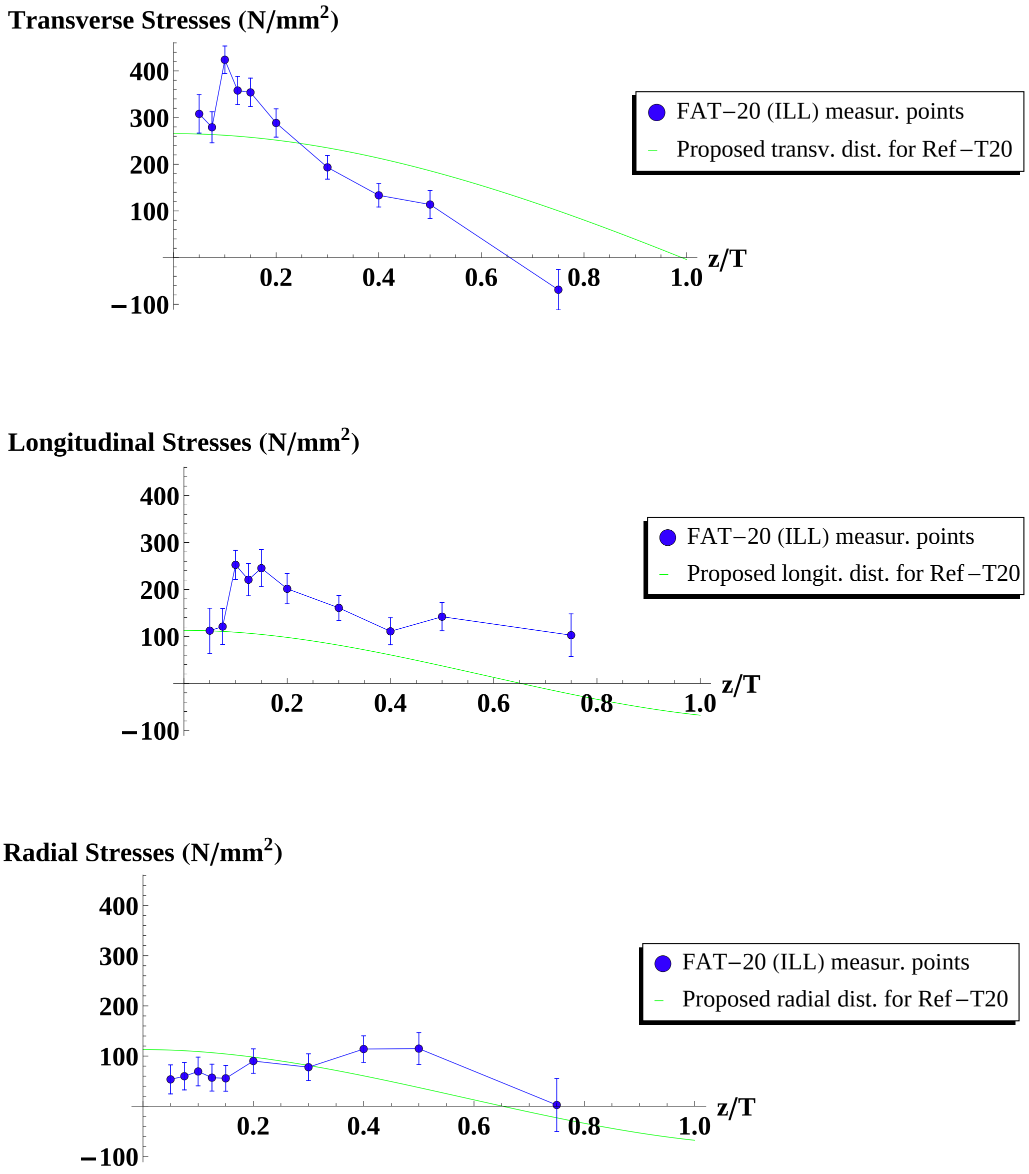

Figure 8.12: The proposed functions of stress distribution compared with the experimental data (neutron diffraction, sample FAT-20).

8.5 Summary and conclusions

A parametric study on proportional and non proportional scaling (parameters $\tau = \frac{\mathrm{t}}{\mathrm{T}}$, $\beta = \frac{\mathrm{d}}{\mathrm{D}}$, $\gamma = \frac{\mathrm{D}}{2\mathrm{T}}$, $\frac{\mathrm{g}}{\mathrm{D}}$) is carried out in this chapter based on the results of ABAQUS numerical models.

- Functions for residual stress distributions are proposed in order to provide the designer with analytical functions showing the main trends of residual stresses. He can design the joints without having to build a complex finite element model.

  The new distributions are suitable for K-shape joints in mild steel welded with a metal active gas arc welding process. They are given along a vertical line that starts from the weld toe (hs1 or hs1c) and penetrates in depth. Their validity domain is the following: 10 mm $<$T$<$ 60 mm, 0.2 $<\tau<$ 0.6, 0.53 $<\beta<$ 0.64, 2.8 $<\gamma<$ 8.4, 0.3 $<\frac{g}{D}<$ 1 and brace angles θ of 60°.

- In this study, it is shown that high residual stresses affecting the weld toe area, where the crack starts to propagate, are mainly transverse residual stresses (high longitudinal and radial residual stresses affect more the weld root region).

  A significant conclusion of this chapter is that the magnitude of tensile transverse residual stresses is strongly increased by a raise of T (proportional scaling) or τ (non-proportional scaling) values. From Borges (2008), the same parameters also strongly reduce the fatigue strength under applied loads. Therefore, these parameters have a combined effect on residual stresses and applied loads influencing both the fatigue strength of K-joints.

Chapter 9

Estimation of fatigue crack propagation in a field of residual and applied stresses

Crack propagation in a joint loaded with both welding induced residual stresses and fatigue stresses is evaluated in two steps. First, a 3D finite element analysis as described in chapter 7 is conducted to determine the residual stress distribution. Afterwards, a 3D extended finite element analysis is performed with two loading types: residual stresses previously simulated with MORFEO-Welding and the fatigue cyclic loadings. Crack propagation simulations are performed with MORFEO-Crack from the Cenaero research center. In addition, the fatigue crack propagation is also estimated with analytic fracture mechanics analysis.

9.1 Introduction

9.1.1 Objectives

The main objectives are the following:

- Assess crack propagation under residual and applied stresses, using an extended finite element model (residual stresses being previously calculated using MORFEO-Welding).
- Assess crack propagation under Linear Elastic Fracture Mechanics (LEFM) conditions combined with the proposed residual stress distribution.
- Compare the stress intensity factors for both evaluations with the ones measured with the Alternating Current Potential Drop method (ACPD).

9.1.2 A short introduction on eXtended Finite Element Method X-FEM

This method is based on the partition of unity method PUM (Babuska and Melenk, 1997) developed to extend the polynomial function space of classical finite element methods by introducing new functions, known a priori to approximate the problem. The X-FEM was introduced in 1999 by Belytschko and co-workers (Belytschko and Black, 1999; Moës et al., 1999).

The additional functions, called enrichment functions, enrich the solution space in order to better approximate the problem of interest. As partition of unity, the $\mathrm{N_i}$ functions have to verify: $\sum_{\mathrm{i}\in\mathrm{N}} \mathrm{N_i}(\mathrm{x}) = 1$.

For crack tip singularity in linear elastic materials, the asymptotic solutions of the problem are known as:

$$u_i(r,\theta) = \frac{K_I\sqrt{r}}{2\pi}g_i^I(\theta) + \frac{K_{II}\sqrt{r}}{2\pi}g_i^{II}(\theta) + \frac{K_{III}\sqrt{r}}{2\pi}g_i^{III}(\theta) \tag{9.1}$$

Therefore, the crack tip enrichment functions can be added to the conventional displacement field.

In addition, Heaviside enrichment functions are also added in order to enrich the discontinuous elements, located around the crack, and allow them to open the crack faces. A discontinuous element is considered as the superposition of two continuous elements with phantom nodes (Hansbo and Hansbo, 2004). This approach allows to use extended finite elements within a FE model without remeshing.

The Heaviside function is the following:

$$H = \begin{cases} 1 & if\ \phi > 0 \\ -1 & if\ \phi < 0 \end{cases} \tag{9.2}$$

where ϕ is a function used to describe the crack. Indeed, to locate the crack position, the level set method is used. The level set $\phi = 0$ represents the crack surface and the level set $\psi = 0$ represents the surface perpendicular to the crack surface and containing the crack front. The intersection between both level sets defines the crack front.

The X-FEM displacement function is given in equation (9.3):

$$\boxed{u(x) = \sum_i N_i(x)(u_i + \underbrace{H(x)a_i}_{\text{Heaviside enrichment}} + \underbrace{\sum_{\alpha=1...4} F_\alpha(x)b_{i,\alpha}}_{\text{Crack tip enrichment}})} \tag{9.3}$$

where N_i and u_i are respectively the conventional shape functions and the conventional DOF (FEM), H_i and a_i are the Heaviside functions and the corresponding enriched DOF, F_α and $b_{i,\alpha}$ are the crack tip functions and the corresponding enriched DOF.

Note that the Heaviside enrichment is applied only to the nodes where elements are cut by the crack and the crack tip enrichment to the nodes surrounding the crack tip.

The main advantages of X-FEM are the following:

- The crack is independent of the mesh, therefore remeshing is not necessary.
- The crack path has not to be defined a priori.
- Because a singular crack tip enrichment is used, the rate of convergence is improved.

9.2 The extended finite element model

Fatigue crack propagation, under the superposition of residual stresses and applied stresses, is simulated with MORFEO-Crack.

9.2.1 Presentation of the model

Geometry and mesh

The geometry is the one of the Ref-T20 joint presented in section 7.3 for the thermo-mechanical model. The mesh has been changed from 8-node hexahedra elements to 4-node tetrahedra elements because tetrahedra have shown to be more robust for crack propagation.

The model simulates crack propagation and not the crack initiation, hence an initial crack is required by the model. The extended finite element method is mesh-independent, however, the initial crack front needs to pass through 5 to 10 elements in order to enable convergence. Therefore the mesh was refined around the initial crack position as shown in Fig. 9.1. The mesh size is decreased linearly from a size of 10 mm at 100 mm from the crack front position to a size of 0.1 mm at 2 mm or less from the crack front position.

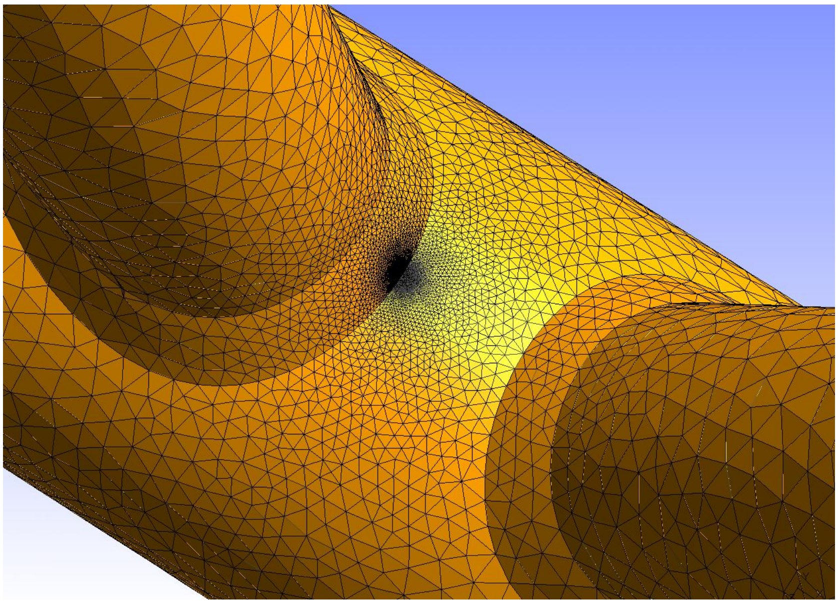

Figure 9.1: Tetrahedra mesh with local refinement around the initial crack site (GMSH code (Geuzaine and Remacle, 2010)).

Initial crack shape and dimensions

The crack position is defined using the level sets. The initial crack is situated at the hot-spot 1. The crack is shaped like a half-ellipse with a minimum radius r_{min}= 0.5 mm in the radial chord direction and a maximum radius r_{max}= 1.25 mm in the direction parallel to weld. Note that the crack depth a is assumed to be 0.5 mm in this model, whereas it was previously explained (see section 3.4.3) that the crack imperfection measured in K-joints usually has a depth of 0.1 mm. This assumption is taken in order to avoid excessive refinement around the crack, which would greatly increase the computing time.

In this application, stress intensity factors corresponding to cracks less than 0.5 mm depth are not computed. Residual stress field values in the surface layer (0-1 mm) are not reliably determined with neutron diffraction measurements and cannot be determined with other methods exactly at the weld toe. Determination of these residual stresses as well as computing crack propagation in this layer is a specific work outside the scope of this thesis.

Projection of the residual stress values at mesh nodes

The residual stress field calculated with MORFEO-Welding is projected from the hexahedral element mesh (thermo-mechanical model) to the new tetrahedral element mesh used by MORFEO-Crack. The Gauss point stress values of the first mesh are interpolated or extrapolated to the nodes of the second mesh.

Applied loads

Currently, MORFEO-Crack allows for the introduction of axial and shear forces but not bending moments. Therefore, stresses due to bending moments are reproduced in the weld toe area by applying shear forces at the brace and chord extremities; hence, the stress field is only correct in the weld toe area, not along members.

The applied loads correspond to the loading of joint S7-J3S, where the critical crack occurred during the test (see Table A.18 in Annex A).

Enrichment area

The displacement field is enriched with Heaviside functions in a narrow band of 0.5 mm width around the crack front and with crack tip functions within a radius of 0.4 mm along the crack tip.

Material behaviour

The material is defined as elastic (linear elastic problem). The steel Young's modulus and the Poisson's ratio are given in the model (see section 4.4.3).

Propagation law

The stress intensity factors K are computed along the crack front using the J-integral method. The crack growth rate is based on the Paris law used in a proportional relationship (only the m constant is needed). A maximum crack depth increment Δa_{max} is chosen by the user for each increment of propagation. This depth is reached for the maximum ΔK along the crack front. In our case, Δa_{max} is set to 0.5 mm.

Then, the crack depth increment Δa of the other points along the crack front are calculated using a proportionality relationship, as shown in Equation (9.4).

$$\frac{\Delta a_{max}}{\Delta K_{max}^{m}} = \frac{\Delta a}{\Delta K^{m}} \tag{9.4}$$

where m is the material constant, equal to 3 in the model.

At each increment step, the new crack is considered instead of the initial crack. Eighty increment steps were simulated with the model.

Note that, it is assumed in the model that the applied minimum load is zero; therefore, $\Delta K = K$. This assumption is not a problem in our case where Q_{min} is close to zero, but in general this is actually a limitation of the model.

Another significant assumption is that only fatigue loadings can be considered by the model; therefore, residual stresses are not taken as static stresses but as cyclic stresses. They vary between 0 and σ_{res}.

9.2.2 Results and discussion

Figure 9.2 shows the crack surface obtained, in the presence of residual stresses and fatigue loading, in joint S7-J3S at the end of the simulation of the propagation, that is after 80 steps of calculations (crack depth of 12 mm).

It is seen that the crack turns as it grows into the chord wall thickness like it was the case during the fatigue test (see Fig. 9.3). However, the crack turns less in the simulation (approximately 30 °from the vertical axis) than in the test (approximately 45 °from the vertical axis). Moreover, at the surface, the crack does not follow the weld toe like it did in the test. The crack deviates from the weld toe to 'enter' (few millimeters) in the weld area (Fig. 9.2c and 9.2d).

Globally, up to a crack depth of 12 mm, the simulated crack path and the experimental crack path are rather similar. For further comparison, the number of crack growth increment should be extended until the through thickness crack is obtained. Then we will check if the numerical method allows for reproducing the particular shape of the experimental crack.

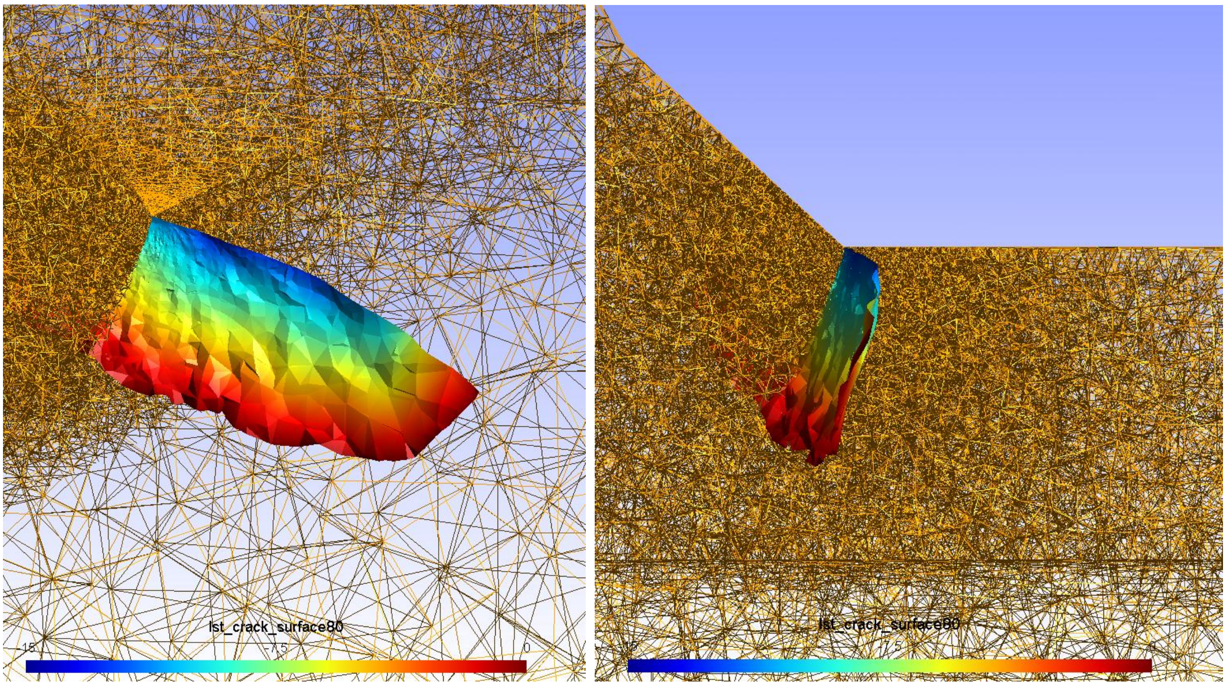
lst_crack_surface80
-15
-7.5
0
lst_crack_surface80

(a) 3D view **(b)** Chord wall section view

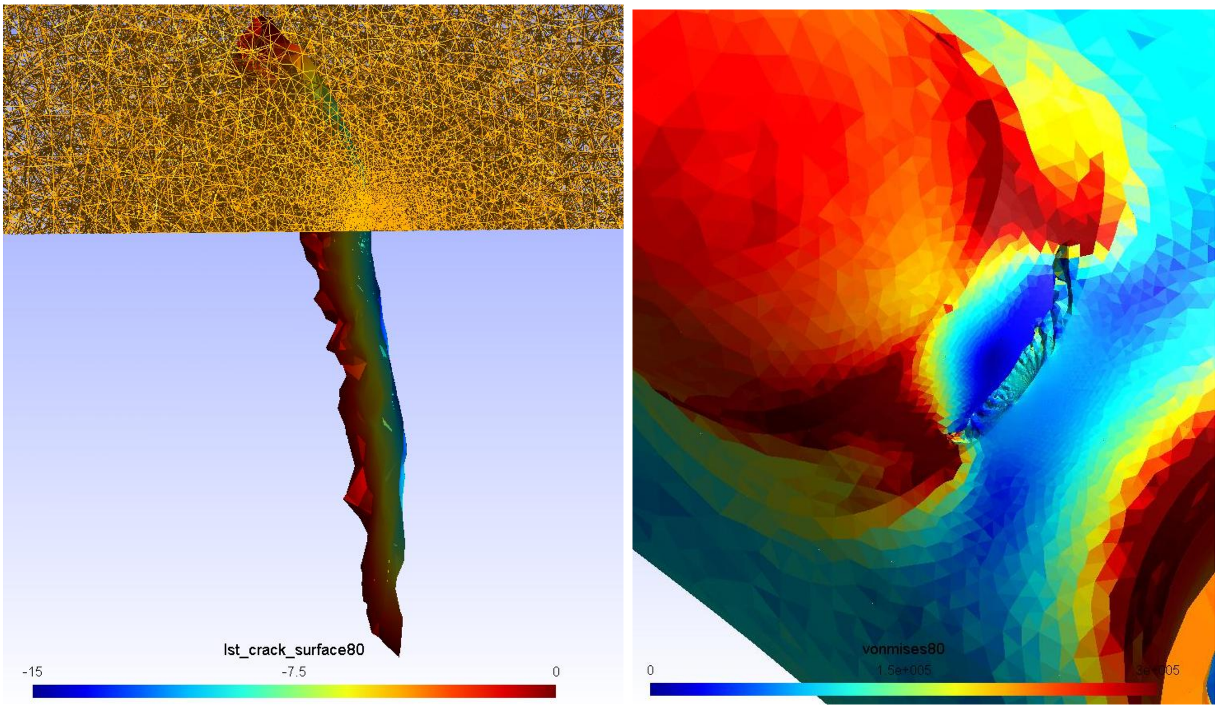
lst_crack_surface80
-15
-7.5
0
vonmises80
0
1.5e+005
3e+005

(c) Top view **(d)** Amplification of the crack opening

Figure 9.2: 3D crack surface obtained with MORFEO-Crack for joint S7-J3S. The truss represents the mesh edges visible for half of the joint.

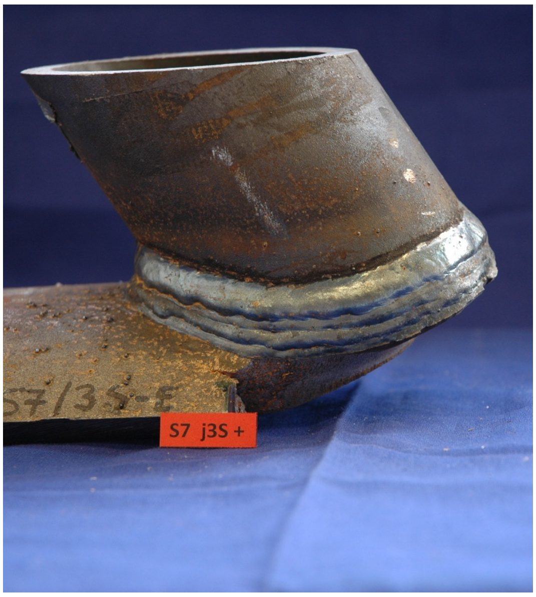

Figure 9.3: View of the real crack surface (fatigue test).

Concerning the stress intensity factor results, Fig. 9.4 depicts their evolution as a function of the vertical depth (from hs1 position). K_{max} (maximum applied SIF), K_{min} (minimum applied SIF) and ΔK_{morfeo} (SIF range propagating the crack) are presented. K_{max}, K_{min} and ΔK_{morfeo} are the results of three different simulations conducted with the maximum applied stresses (K_{max}), the minimum applied stresses (K_{min}) and the combination of the applied stress range ($\Delta K = K_{max} - K_{min}$) with the residual stresses (K_{res}).

The K values are taken in the vertical plane including the hot-spot 1; therefore, these values are not always the highest along the crack front. The K values given in Fig. 9.4 are the equivalent SIFs, calculated with the 3 mode SIFs. It is noticed that they are approximately equal to the mode I SIFs.

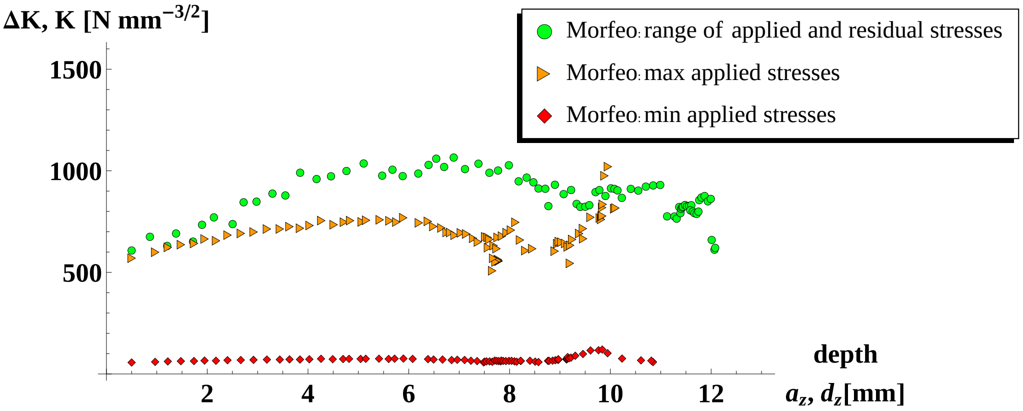

Figure 9.4: Stress intensity factors at max. depth point K_{max} (corresponding to the maximum applied stresses), K_{min} (corresponding to the minimum applied stresses) and ΔK_{morfeo} (corresponding to the applied stresses and residual stresses).

From Fig. 9.4, it seems that the ΔK_{morfeo} corresponds to the addition of the ΔK and K_{res}. However, it is known from the fatigue tests (see section 6.4.1) that, the residual stress field does not affect the fatigue crack growth for cracks occurring at hs1 under fully-tensile loading. Their propagation is only influenced by the applied stress range.

This simulation result could have been expected since residual stresses are considered like applied stresses. Therefore, propagation does not occur under cyclic applied stresses and static residual stresses but under cyclic equivalent stresses, fluctuating between $\sigma_{\mathrm{max}} + \sigma_{\mathrm{res}}$ and zero.

In other words, the crack closure concept is not yet implemented in MORFEO-Crack and shows here that it is required to correctly predict the crack propagation in the presence of static residual stresses and cyclic applied stresses.

The involvement of the residual stress field in the crack propagation can be predicted through the concept the crack closure/opening and the effective stress intensity factor range (section 3.3):

$$\Delta K_{eff} = MAX(K_{app,max} - K_{op}, 0) - MAX(K_{app,min} - K_{op}, 0) \tag{9.5}$$

where the applied SIF level above which the crack tip opens upon loading, $\mathrm{K_{op}}$, is influenced by the presence of residual stresses.

Concerning the simulation of crack propagation under fatigue loading without residual stresses, this model is perfectly well adapted and offers great possibilities. In future works, some improvements need to be done in order to make this model capable of estimating fatigue crack propagation in a field of residual and applied stresses.

9.2.3 Future improvements of the numerical crack propagation model

- Introduce the crack closure method, based on $\mathrm{K_{op}}$, in the model.
- Define residual stresses as a static loading, not a cyclic loading.
- Introduce the possibility to consider an applied minimum load which is not zero.
- Introduce tools to take directly into account bending moments.
- Take into account interaction and coalescence between cracks.

Without these improvements, one cannot estimate and compare the crack propagation rates nor the fatigue lives of joints.

9.3 The analytical fatigue model based on fracture mechanics

In order to propose a model able to predict crack propagation under applied and residual stresses, an analytical model is proposed based on the crack closure and ΔK_{eff} concepts. This model is inspired by the model developed by Walbridge (2005). The crack propagation is only computed at the point of maximum depth. The crack is semi-elliptical and with a shape assumed equal to $a/c = 0.2$. The main limitation of this model is that it requires assumptions on a/c and on the crack path. In this case, the crack path is considered in a vertical plane including the hs1 or hs1c positions.

9.3.1 Proposed distribution for transverse residual stresses and K_{res}

It has been shown in this thesis that residual stresses in the transverse direction are the most significant for crack propagation in K-joints. Therefore, the analytical model uses the proposed distribution for transverse residual stresses (see section 8.3).

The stress intensity factor K_{res} obtained from this distribution is calculated using $K_{res} = Y\sigma_{res}\sqrt{\pi a}$ and presented in Fig. 9.5.

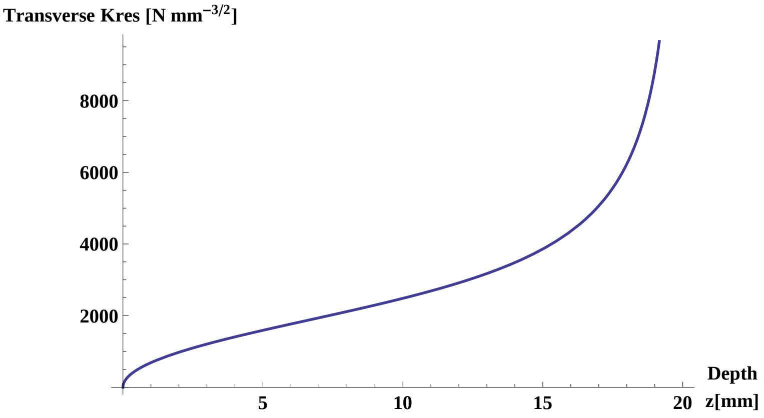

Figure 9.5: Transverse residual stress intensity factor K_{res} based on the proposed distribution (section 8.3).

9.3.2 Comparison of stress intensity factors

Within the fracture mechanics fatigue model presented in section 3.3, the applied SIF range, ΔK_{app}, is calculated using the Bowness and Lee (1999) formulation based on Q_{max} and Q_{min} values. The opening SIF K_{op} is obtained from K_{res} and from K_{pl}. The threshold SIF range, ΔK_{th}, is expressed as follows (Zheng, 1987): $\Delta K_{th} = 320.(1 - R)$ and is equal to 288 $N.mm^{-3/2}$ with $R = 0.1$.

Then the effective SIF range can be deduced from Equation (9.5). Figure 9.6 combines the SIF range obtained from ACPD measurements in joint S6-J5N and from the analytical fracture mechanics model. Fig. 9.6a corresponds to the detail loaded in compression and Fig. 9.6b corresponds to the detail loaded in tension.

It appears that in both cases, under compressive and tensile applied stresses, the effective ΔK_{eff} is positive explaining why cracks propagate on both sides. A positive ΔK_{eff} in a joint loaded under compression is only possible because $K_{op} < K_{app,max} < 0$ whereas in the absence of residual stresses $K_{op} > K_{app,max}$. Indeed, the more positive K_{res} is, the more negative K_{op} is. In a special K-joint geometry with high tensile residual stresses and restraining effects, K_{res} remains high for important crack depths, implying that K_{op} remains highly negative, although, not high enough to keep the entire cycle effective for crack propagation ($\Delta K_{eff} < \Delta K$). Therefore, the crack propagation rate is driven by $\Delta K_{eff} = K_{app,max} - K_{op}$.

To summarize, in joints loaded under compression, tensile residual stress distribution has a strong influence on magnitude and shape of ΔK_{eff}, and finally ΔK_{eff} deduced from LEFM is a convenient tool to estimate if the crack will propagate faster, slower or just stop. On the other hand, in joints loaded under tension, since K_{op} is usually lower than $K_{app,min}$, $\Delta K_{eff} = \Delta K_{app}$ with or without presence of tensile residual stresses.

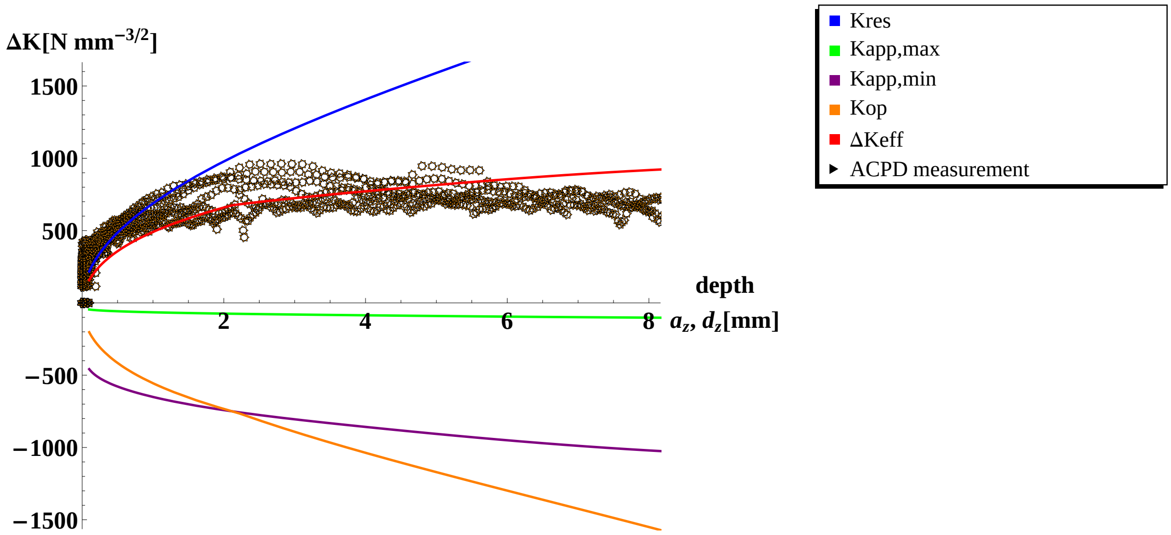

(a) S6-J5N hot-spot 1c

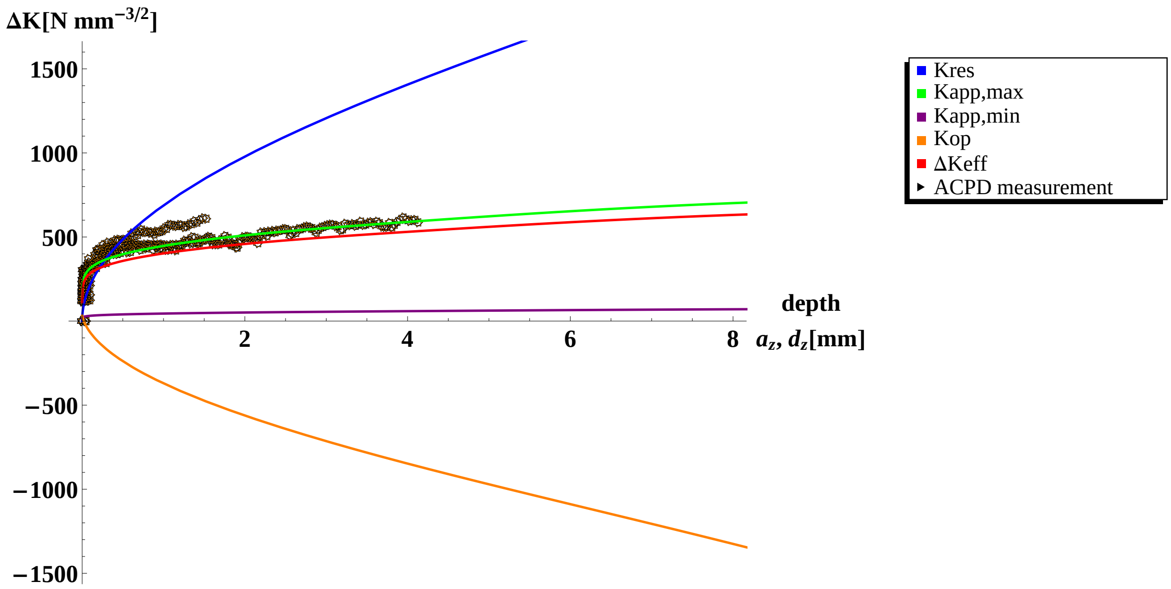

(b) S6-J5N hot-spot 1

Figure 9.6: Comparison of stress intensity factors between fatigue test values and LEFM analytical fatigue model curves: on the compressive brace side and on the tensile brace side.

From Fig. 9.6, the results of the analytical model are in good agreement with the experimentally deduced effective stress intensity factor range. This method is a useful tool to estimate ΔK_{eff}.

The assumption, that the stress distribution is not affected by the presence of a crack, seems to be acceptable. The proposed transverse residual stress distribution has given good results.

However, this model has also some limitations: it can not predict the crack shape development, the changing crack angle (the crack is assumed to be planar), etc.

9.4 Summary and conclusions

This chapter aims to estimate the fatigue crack propagation in a field of residual stresses and applied stresses. Two different approaches, an X-FEM model and an analytical LEFM model, are proposed to reach this objective.

- The X-FEM model:

  It was found that the MORFEO-Crack model has limitations. The model is well adapted for estimating crack propagation under fatigue loading; however, it considers residual stresses as additional applied stresses and this leads to erroneous results. The crack closure needs to be implemented into the X-FEM model to give accurate results in the presence of residual stresses. It would also be useful to take into account crack coalescence. The MORFEO-Crack model needs to be further developed to achieve its full potential.

- The analytical LEFM model:

  This model requires more assumptions about the crack. The results show fairly good correspondence with ACPD measurements for details loaded in tension as well as in compression (fatigue loadings). LEFM gives evidence that the tensile residual stress distribution has a strong influence on magnitude and shape of ΔK_{eff} for joints loaded in compression. High tensile residual stresses in the gap region make ΔK_{eff} positive, keeping most of the cycle effective for crack propagation. On the contrary, in joints loaded in tension, the minimum applied stresses are usually above the level needed to open the crack and thus the presence of tensile residual stresses does not influence the ΔK_{eff} value.

Both methods are interesting and complementary. And even though the X-FE model needs to be further developed to achieve its full potential, it offers the possibility to predict the crack shape development; the analytical LEFM does not.

Chapter 10

Conclusion

Modern steel tubular road bridges are most often composed of welded trusses with K-shaped joints; however, these joints are susceptible to fatigue under traffic loading. Fatigue cracks typically develop in the gap region, at the weld toe in-between the tubes forming the K-joints, even though this is not the only location where the hot-spot stresses reach local maximas. As shown in this work, a detrimental combination of applied stresses, residual stresses and imperfections induced by welding may explain why cracks often initiate in the vicinity of the weld toe even under compressive loads. Currently, three-dimensional residual stresses and their influence on the fatigue response have never been determined in K-joints.

The aim of this thesis is to assess the welding residual stress field and evaluate its influence on the fatigue response of welded tubular K-joints.

The K-joints studied in this thesis are joints typical of steel bridge construction. Their dimensions and their chord slenderness $\gamma = \frac{D}{2T} < 12$ parameter make them behave differently from joints used in the offshore industry. They are made of a non-alloyed structural steel (mild steel) S355J2H according to EN 10025. The K-joints are welded with a metal active gas (MAG) arc welding process.

10.1 Summary and main conclusions

Below is summarized how the five objectives given in section 1.2 were reached, along with key findings. The major conclusion for each objective is given in each title.

1. **Welding induces high tensile residual stresses, critically oriented in bridge K-joints**

   Objective: quantify the residual stress field at the most critical fatigue locations (hot-spots 1 or 1c) in welded tubular K-joints using neutron-diffraction, hole-drilling, and X-ray methods.

   Measurements were conducted on several K-joint samples which were either as-welded or fatigue tested. The neutron-diffraction method allowed for non-destructive measuring of the triaxial residual stresses deep inside the wall chord thickness. The hole-drilling and X-ray methods allowed for semi-destructive determination of the two-dimensional residual stresses at the surface. Neutron diffraction is a more powerful and reliable method to measure residual stresses than hole-drilling or X-ray techniques, but more demanding and costly. To adapt to the complex geometry of the K-joints (curved surface, narrow gap), a hole-drilling device had to be designed, built and calibrated. Large quantities of data measured by neutron-diffraction allowed for detailed residual stress maps in three chosen orthogonal directions.

Conclusions

Results show that **residual stress magnitude reaches the yield strength of the S355J2H steel at the weld toe**. **At and near the surface, the greater residual stresses were critically oriented perpendicularly to the weld direction**, which is also the orientation of the externally applied stresses. This finding has led to a drastically different residual stress orientation than found in the literature for pipe and pressure vessels tubes where residual stresses parallel to the weld direction are dominant. In addition, **the restraining effect in-between the braces composing the joints creating high perpendicular residual stresses in the gap region**. The geometry of the K-joint creates both high applied stresses as well as high residual stresses (from welding), which is critical for fatigue.

2. **Tensile residual stresses lead to similar fatigue crack growth in tubular joints loaded in tension and compression**

Objective: qualify and quantify the effect of tensile residual stresses on the fatigue crack propagation of welded tubular K-joints through large-scale laboratory tests.

The chosen strategy to separate the residual stress effect from the total internal stress effect, was to load joints in compression where cracks can only grow under high tensile residual stresses, and then compare them with joints loaded in tension.

Two large scale tubular truss beams, with details loaded in compression and in tension were subjected to high-cycle fatigue (constant amplitude). Performing fatigue tests on large scale specimens allowed the combination of complex loading with the presence of welding imperfections and the residual stress field that occur in actual bridge structures. The two specimens S6 and S7 were geometrically identical to each other except for the thickness of their upper and lower chord (respectively 20 mm and 30 mm for S6 and 30 mm and 20 mm for S7). This choice was driven by the idea that the chord wall thickness T could influence both the technological size effect (residual stress distribution) and the geometrical size effect. Experimental investigations were carried out with an applied load ratio R = 0.1; therefore, details in tension were tested almost under zero-tension loading (R = 0.1) and details in compression under almost zero-compression loading (R = 10). The fatigue crack development was monitored by the Alternating Current Potential Drop method (ACPD) for details loaded in tension and compression. The crack shape, the propagation rate, and the stress intensity factor were obtained in several details. Based on the fatigue results, and combined with existing data from the ICOM laboratory, the $\Delta\sigma_{\mathrm{R,hs}} - \mathrm{N}$ curves were drawn for an equivalent 16 mm thick joint and compared with the CIDECT $\Delta\sigma_{\mathrm{R,hs}} - \mathrm{N}$ design curve category 114.

Conclusions

Cracks occurring at a hot-spot under full-tensile loading are driven by applied stresses, the residual stress field does not affect the fatigue crack growth in details loaded in tension. Cracks occurring at hs1c under full-compressive loading are caused by the presence of high tensile residual stresses, making a part of the fatigue cycle or the entire cycle effective in propagating the crack. In the K-joints tested, tensile residual stresses enabled cracks to propagate up to (at least) half of the chord wall thickness under applied compressive stresses.

The results indicate that details loaded in compression are not critical when through thickness cracking is considered as the fatigue failure criterion. In joints combining the highest hot-spot stress range with the highest proportion of brace stresses, critical cracks were located at hs1 for each test. **When the failure criterion is the half-thickness crack, details loaded in compression also reach that criterion near the same number of cycles and thus are not safer than details loaded in tension**.

The failure criterion is not coherent in the codes. Therefore, **it is recommended to design all (tension or compression) CHS K-joints with $\gamma < 12$, using a strength curve $\mathrm{S_{rhs}} - \mathrm{Nf}$ category 100 for T = 16 mm**. This makes it compatible with the IIW hot-spot stress categories. On the loading side, the hot-spot stress range should be determined with the correct SCF (from Schumacher (2003)) and taken as the total applied hs stress range in absolute value. Distinction between the failure consequence of fatigue cracks for details loaded in tension and compression can be made through the partial strength factor value (according to Eurocode3, part 1-9): γ_{Mf}=1 for details in compression and γ_{Mf} =1.15 for details in tension.

3. **3D thermo-mechanical FE model can predict the 3D residual stress field**

Objective: develop a finite element model for predicting three-dimensional residual stresses in welded K-joints.

Three-dimensional finite element analysis was used to accurately predict heating/cooling of welding sequences. Some aspects of the problem which do not significantly affect the residual stress estimation were simplified. Since it was previously found that martensitic transformation localized in the HAZ area is small for S355J2H steel, metallurgical aspects were neglected. An uncoupled thermo-mechanical approach was used to first solve the 3D transient temperature field, and then the displacement field, using the temperature field as input. Another important simplification was that the 7-pass welding process was modeled as a single equivalent pass. A heat input that corresponded to the total heat input of the seven weld passes was used. The mechanical analysis was based on an elastic-plastic material model with linear isotropic work hardening. These simplifications are intended to generate a model able to simulate rapidly and efficiently residual stresses while providing quality results. The numerical simulations were performed with the finite element code ABAQUS® and the welding and manufacturing oriented code MORFEO®.

The obtained residual stress distributions are compared with the previous neutron-diffraction measurements to estimate the accuracy of the numerical simulation.

Conclusions

The numerical results were in good global agreement with the experimental results obtained from neutron diffraction. The simplified model **demonstrated the ability to reproduce residual stress distributions in the region surrounding the welds**, even though the peak values were not always well captured and the distribution was sometimes shifted. In general, MORFEO-Welding predicted the transverse residual stress distribution more accurately, whereas the ABAQUS results fit better with the longitudinal stress distribution. These results confirmed the residual stress orientation obtained experimentally. It also demonstrated the strong restraining effect that occurs in the gap area, keeping transverse residual stresses at a high value. Moreover, it was found that the **transverse residual stress field is asymmetric along the axial chord direction**, with the highest residual stress values occurring on the side where the final welding steps were made.

4. **Residual stress distributions with depth at the critical fatigue locations (hot-spots 1 or 1c) are proposed**

   Objective: determine, using thermo-mechanical FEM models, the influence of joint size (both absolute and non-proportional) on residual stress distribution and propose distributions for residual stresses based on these findings.

   A geometrical parametric study was performed using the validated thermo-mechanical FE model in ABAQUS. A range of dimensional and non-dimensional joint parameters $\beta = \frac{\mathrm{d}}{\mathrm{D}}$, $\gamma = \frac{\mathrm{D}}{2\mathrm{T}}$, $\tau = \frac{\mathrm{t}}{\mathrm{T}}$ and $\frac{\mathrm{g}}{\mathrm{D}}$ were investigated. Their influence on residual stress distributions was studied. This effect is a technological size effect. Based on these results, distributions of transverse, longitudinal and radial residual stresses with depth are proposed in the form of third order polynomial equations. The new distributions are suitable for K-shape joints in mild steel, welded with a MAG arc welding process. The residual stress distributions are given along a vertical line that starts from the weld toe (hs1 or hs1c) and penetrates in depth. The validity domain is as follows: 10 mm $<$T$<$ 60 mm, 0.2 $<\tau<$ 0.6, 0.53 $<\beta<$ 0.64, 2.8 $<\gamma<$ 8.4, 0.3 $<\frac{g}{D}<$ 1 and brace angles θ of 60°.

   Conclusions
   It was shown that high residual stresses affecting the weld toe area, where the crack starts to propagate, are mainly transverse residual stresses. High longitudinal and radial residual stresses have more effect in the weld root region.

   Particularly relevant for K-joint design, **the magnitude of tensile transverse residual stresses is strongly increased by a raise of T (in proportional scaling) or/and $\tau = \frac{\mathrm{t}}{\mathrm{T}}$ (in non-proportional scaling)**. In previous studies, the same parameters were also shown to reduce the fatigue strength under applied loads. These parameters have a combined effect on residual stresses and applied loads influencing the fatigue strength of K-joints.

5. **The concept of $\Delta\mathrm{K}_{\mathrm{eff}}$, considering crack closure aspects, is a convenient tool to predict fatigue crack propagation in the field of residual and applied stresses**

   Objective: assess crack propagation under residual and applied stresses, using an extended finite element method model as well as a linear elastic fracture mechanics LEFM analytical model that uses the proposed residual stress distribution.

   An extended finite element method X-FEM model was used to propagate a fatigue crack independent of the mesh. The crack path does not need to be defined a priori. The residual stress field used in this model was previously calculated with MORFEO-Welding, then the crack propagation is simulated under residual and applied stresses with MORFEO-Crack. The stress intensity factors K were calculated along the complete crack front for each crack increment.

   Independently, K was also determined from an analytical fatigue model based on linear elastic fracture mechanics (LEFM). In order to calculate the residual stress intensity factor $\mathrm{K}_{\mathrm{res}}$, the proposed transverse residual stress distribution was used. Effective stress intensity factor ranges, $\Delta\mathrm{K}_{\mathrm{eff}}$, were compared with the ones measured with the Alternating Current Potential Drop ACPD method during fatigue tests.

Conclusions

It was found that the X-FEM model has limitations. While it is well adapted for estimating crack propagation under fatigue applied stresses, it considered residual stresses as additional applied stresses, leading to erroneous results. **The crack closure needs to be implemented in the X-FEM model** to give accurate results in the presence of residual stresses. It would also be useful to take into account crack coalescence.

The analytical LEFM model showed fairly good correspondence with ACPD measurements for details loaded in tension as well as in compression (fatigue loadings). LEFM gave evidence that the tensile residual stress distribution has a strong influence on magnitude and shape of ΔK_{eff} for joints loaded in compression. **High tensile residual stresses in the gap region create a positive ΔK_{eff}, keeping most of the cycle effective for crack propagation**. For joints loaded in tension, the minimum applied stresses are usually above the level needed to open the crack and thus the presence of tensile residual stresses does not influence the ΔK_{eff} value.

Both methods are interesting and complementary. And even though the X-FE model needs to be further developed to achieve its full potential, it offers the possibility to predict the crack shape development; the analytical LEFM does not.

10.2 Major contributions

- The database of 3D residual stress results, obtained by neutron-diffraction in thick specimens using the high-tech and costful equipments of the Paul Scherrer Institute and the Institute Laue-Langevin (spallation reaction and nuclear reaction), is a valuable source of information.
- The design and construction of a hole-drilling device, adapted to the complex geometry of the K-joints (curved surface, narrow gap), enables measuring of two-dimensional residual stresses at the surface.
- The monitoring for crack propagation in details loaded in compression and tension during fatigue tests, gives relevant results explaining why and how cracks can propagate under compression.
- The new recommendation for designing K-joints using a fatigue strength curve $S_{rhs} - N_f$ category 100 for $T = 16$ mm is compatible with the IIW hot-spot stress categories. This recommendation is tied to a hot-spot stress range determined with the correct SCF (as close as possible to the 'real' effective value). The recommended partial strength factor is $\gamma_{Mf}=1$ for details in compression and $\gamma_{Mf}=1.15$ for details in tension.
- The development of a thermo-mechanical model able to accurately reproduce residual stresses with reduced computational complexity and computing time.
- The proposed distributions for residual stresses provide designers with the main trends of residual stresses corresponding to this joint geometry.
- The LEFM fatigue model that proved to be reliable and convenient in estimating fatigue crack propagation in joints loaded in compression or in tension.

10.3 Future research

Based on this work, several possible extensions or improvements are presented below:

- **Concerning the material properties**:
  - Filler material: its chemical composition, as well as its thermal and mechanical properties can help to understand if there are significant differences between the filler and the base material, which can explain a potential carbon migration for instance.

  - ◇ Base material: perform experimental tests to investigate the thermal and mechanical properties of the base material as a function of temperature. It is important to obtain these properties especially between the room temperature and 700 °C because they have a more significant impact on residual stress estimations.

- ◆ **Concerning the fatigue tests**:
  - ◇ The effect of the chord length ratio parameter α: the α parameter of tested specimens is almost the double of the real bridges α. It was shown in this work that this parameter affects the bending moments of the truss members. These bending moments are underestimated in tests (approximately 15%) compared to bridge geometry.

    According to Shao et al. (2008), this parameter also affects the stress concentration factors of joints with low γ values ($\gamma < 12$) under axial loads. These conclusions were drawn for tubular T-joints. This point has to be further investigated before testing other specimens with the same α parameter (section).
  - ◇ Improve the ACPD technique: in order to ensure that a thin skin current is produced and allows for a straightforward calculation of the crack depth, the frequency should be increased from 5Hz to 1 kHz at least. Moreover, some more sophisticated techniques are useful to obtain the crack inclination to the vertical axis (Lugg et al., 1988). These techniques may also be applied in future tests.

- ◆ **Concerning the welding model**:
  - ◇ Multi-pass welding: in this work, an equivalent single pass was used to represent the 7 passes because the multiple passes simulation have conducted to an unaffordable computing time with ABAQUS. However, with MORFEO, the computing time has been strongly reduced and multi-pass welding can be simulated.

    The single pass welding gives good results but they can be improved by taking into account several passes. It is proposed to reduce the 7 passes to 3 passes as recommended by Dong and Hong (2002) (section 7.2.1) according to a sensitivity analysis of the number of passes needed for the model. To obtain a realistic plastic strain field, it is necessary to consider the plastic strain annealing at each weld pass (section 7.2.1). This function is already included in the current model. It is also recommended to use the birth and death technique to activate the new passes created one by one.
  - ◇ Several welding sequence should be studied using this numerical model, and especially the sequence moving the start and stop positions away from the critical zone. Future weldings would be greatly improved based on these results.
  - ◇ Phase transformation for high strength steel: phase transformations can be neglected with S355J2H, however with other types of steel, such as high strength steel, stainless steel, etc., phase transformation effects have to be considered. Therefore, a thermo-mechano-metallurgical model has to be used (section 2.3). This type of model is challenging because the proportion of each microstructure at each temperature of the thermal cycle has to be well known.
  - ◇ Temperature measurements: It would be helpful to compare the thermal cycle and the peak temperature obtained at the end of the thermal analysis with thermocouple temperature measurements conducted during the welding. This comparison, as well as the weld fusion profile comparison, would help to increase the model accuracy.
  - ◇ Heat source: it can be interesting to use other heat sources than those used in this study (spherical or truncated circular cone sources). In particular, the Goldak heat source is known to provide good results for the MAG-MIG-TIG welding process. Since the Goldak source has a double ellipsoid shape, one has to determine several parameters in order to define the source geometry. This parameter identification can be complex but it must be carefully done to correctly simulate the size of the molten zone. Another heat source that can be tested is a circular cone model. Its triangular

    cross would better fit the molten zone section. It can be easily extended from the truncated circular cone source.
  - Weld shape effect: in the model, the convex surface of the weld was not considered despite the fact that angles between the tube surface and the tangent to the weld surface at the chord and brace crown toes as well as are radius of the weld toe are known to influence the fatigue strength (section 7.3.3).

    Their effects should be studied more thoroughly.
- **Concerning the geometrical parametric study**:
  - Extension of the study: extend the study to a larger range of parameters and dimensions in order to enlarge the domain of validity in which the proposed residual stress distributions can be used (section 8.3). It is recommended to perform these new studies with MORFEO-Welding because it requires less computing time and gives better transverse residual stress results. Simulations can be conducted with a refined mesh in a reasonable time. It is also necessary to experimentally control the heat input Q introduced to weld joints with different geometries.
- **Concerning the X-FEM model**:
  - K_{op} and ΔK_{eff}: introduce the crack closure method, based on K_{op}, and the ΔK_{eff} concept to allow the crack propagation estimate in a field of residual and applied stresses.
  - Simulate the coalescence: a double approach can be implemented, based on the work of Peeker (1997), who is able to calculate both the crack initiation and the stable crack growth stages. Crack can initiate, coalesce and propagate with such a model.
  - Static stress: define residual stresses as a static loading, not a cyclic loading.
  - Bending moments: introduce tools to take bending moments directly into account.
  - K_{min}: introduce the possibility to consider an applied minimum load which is not zero.

References

The IIW Formula for Carbon Equivalent. Doc. IX-535-67, International Institute of Welding (IIW), 1967.

Guidelines to the numerical determination of stress concentration factors of tubular joints. E & FN Spon, 1993. ISBN 0-419-18770-7.

21432:2005, D.-C.-I. *Non destructive testing. Standard test method for determining of residual stresses by neutron diffraction. British Standards Institute.* February 2006. ISBN 0 580 47396 1.

ABAQUS. *Analysis user's manual version 6.9.* Dassault Systèmes, 2009.

Acevedo, C. and Nussbaumer, A. Residual stress estimation of welded tubular K-joints under fatigue loads. 12th International Conference on Fracture ICF12 (T12.001), Ottawa, Canada, July 2009a.

Acevedo, C. and Nussbaumer, A. Study on crack propagation in tubular joints under compressive fatigue loadings. International Conference Fatigue Design 2009, Senlis, France, November 2009b. ISBN 978-2-85400-908-8.

Albrecht, P. and Yamada, K. Rapid calculation of stress intensity factors. *Journal of Structural Engineering ASCE*, 103(ST2):377–389, 1977.

API. *Recommended practice for planning, designing and constructing fixed offshore plattforms.* API Recommended Practice 2A (RP2A), 21st Edition, Washington, USA, 2000a.

API. *Recommended Practices for Fitness-for-Service.* API Recommended Practice RP-579, 2000b.

Armao, F., Byall, L., Kotecki, D. and Miller, D. *GMAW welding guide.* Lincoln Electronic, 1995.

ARSEM. *Guides pratiques sur les ouvrages en mer. Vol. 1 Assemblages tubulaires soudes.* Guides pratiques sur les ouvrages en mer. Editions Technip, 1985. ISBN 2-7108-0497-2.

Ashby, M. and Easterling, K. A first report on diagrams for grain growth in welds. *Acta metallurgica*, 30:1966–1978, June 1982.

ASTM. *Standard Definitions of Fatigue, 1995 Annual Book of Standards, E 1150-1987.* 1995.

ASTM. *Standard test method for determining residual stresses by the hole-frilling strain-gage Method, E 837-08.* E837, American society for testing and materials, 2008.

AWS. *Structural Welding Code.* American Welding Society, D 1.1-2000, 2000.

Babuska, I. and Melenk, J. The Partition of Unity Method. *Int. J. Numer. Meths. Eng.*, 40:727–758, 1997.

Barsoum, Z. and Samuelsson, J. Fatigue assessment of cruciform joints welded with different methods. *Steel Research International*, 77(12):882–888, 2006.

Basquin, O. The exponential law of endurance tests. *Proc. ASTM*, 10:625–630, 1910.

Bayraktar, E. and Kaplan, D. Mechanical and metallurgical investigation of martensite austenite constituents in simulated welding conditions. *Journal of Materials Processing Technology*, 153-154:87–92, 2004.

Belytschko, T. and Black, T. Elastic crack growth in finite element with minimal remeshing. *International Journal for Numerical Methods in Engineering*, 45:601–620, 1999.

Blitz, J. *Electrical and magnetic methods of non-destructive testing.* Non-destructive evaluation series. Chapman & Hall, 1997.

Borges, L. and Nussbaumer, A. Advanced numerical modelling of fatigue size effects in welded CHS K-joints. In *12th International Symposium on Tubular Structures (ISTS 12), Shanghai, ISTS 12.* 2008.

Borges, L., Schumacher, A. and Nussbaumer, A. Size effects on the fatigue behaviour of welded CHS bridge joints. In *International Conference on Fatigue and Fracture in the Infrastructure, Philadelphia, USA*. 2006.

Borges, L. C. *Size Effects in the Fatigue Behaviour of Tubular Bridge Joints*. PhD Thesis EPFL 4142, Ecole Polytechnique Federale de Lausanne (EPFL), 2008.

Börjesson, L. and Lindgren, L.-E. Simulation of multipass welding with simultaneous computation of material properties. *Transactions of the ASME*, 123:106–111, January 2001.

Bouchard, P. Validated residual stress profiles for fracture assessments of stainless steel pipe girth welds. *International Journal of Pressure Vessels and Piping*, 84:195–222, 2007.

Bouchelier, C. and Lu, J. *Les contraintes résiduelles dans les constructions soudées*, chapter Mesure des contraintes résiduelles dans les soudures. Méthodes disponibles, exemples d'application. CETIM, 1987.

Bowness, D. and Lee, M. *Weld toe magnification factors for semi-elliptical cracks in T-Butt joints*. Offshore Technology Report-OTO 199 014. UK : Health and Safety Executive (HSE), 1999.

Bremen, U. *Determination des contraintes residuelles au pied des cordons de soudure bruts ou traites, mesures et interpretation des resultats, pub ICOM 188*. ICOM, EPFL, Laboratoire de la construction metallique (ICOM), September 1987.

Bremen, U. *Amélioration du comportement à la fatigue d'assemblages soudés: etude et modélisation de l'effet de contraintes résiduelles*. Ph.D. thesis, Lausanne: EPFL Thesis 787, 1989.

Broek, D. *Elementary engineering fracture mechanics*. Kluwer academic publishers, 1986.

Brown, S. and Song, H. Finite element simulation of welding of large structures. *Journal of Engineering for Industry*, 114:441–451, 1992.

Champroux, E. and Lê, J.-L. *Livre Soudage coupage pour l'industrie*. Nathan-Air Liquide Welding, 1986.

Cherouat, A., Montay, G. and Lu, J. Study of residual stresses in complex parts by experimental and numerical methods. *Materials Science Forum*, 404-407:251–256, 2002.

Chiew, S.-P., Lie, S.-T., Lee, C.-K. and Huang, Z.-W. Fatigue performance of cracked tubular T joints under combined loads. I: Experimental. *Journal of Structural Engineering*, pp. 562–571, April 2004.

Coffin, L. A study of the effects of cyclic thermal stresses on a ductile metal. *Trans. ASME*, 76:931–950, 1954.

Dean, D. and Hidekazu, M. Prediction of welding residual stress in multi-pass butt-welded modified 9Cr–1Mo steel pipe considering phase transformation effects. *Computational Materils Science*, 37:209–219, 2006.

DebRoy, T. and David, S. Physical processes in fusion welding. *Reviews of Modern Physics*, 67(1):85–112, January 1995.

Dijkstra, O., Van Foeken, R., Romeijn, A., Karamanos, S. A., Van Wingerde, A., Puthli, R., Herion, S. and Wardenier, J. *Fatigue design guide for circular and rectangular hollow section multiplanar joints*. TNO-report, Delft University of Technology, 1996.

Dijkstra, O. and Van Straalen, I. Fracture mechanics and fatigue of welded structures. In *WRC Proceedings IIW*, pp. 225–239. IIW, 1997.

Dong, P. and Hong, J. *Recommendations for determining residual stresses in fitness-for-service assessment*. Welding Research Council Bulletin, WRC, November 2002.

Dover, W. and Holdbrook, S. Fatigue crack growth in tubular welded connections. *International Journal of Fatigue*, 2(1):37–43, January 1980.

Dover, W. D. and Monahan, C. C. The measurement of surface breaking cracks by the electrical systems acpd/acfm. *Fatigue & Fracture of Engineering Materials and Structures*, 17(12):1485–1492, December 1994.

Drezet, J.-M., Ayrault, D., Wisniewski, J., Pilvin, P., Carron, D. and Primaux, F. Experimental and numerical analysis of the hot tearing susceptibility of a CuCrZr alloy. *Mathematical Modelling of Weld Phenomena*, 9:997–1010, 2006.

Drezet, J.-M., Lima, M., Wagnière, J.-D., Rappaz, M. and Kurz, W. Crack-free aluminium alloy welds using a twin laser process. In *61st Inter. Conf. of the Inter. Institute of Welding, Graz, July 2008, invited lecture*, pp. 87–94. Safety and reliability of welded components in energy and processing industry, Eds. P. Mayr, G. Posch and H. Cerjak, 2008.

Drezet, J.-M. and Mokadem, S. Marangoni convection and fragmentation in laser treatment. *Material Science Forum*, 508:257–262, 2006.

Dubois, V. *Fatigue de détails soudés traités sous sollicitations d'amplitude variable.* Ph.D. thesis, Lausanne: EPFL Thesis 1260, 1994.

Easterling, K. *Introduction to the physical metallurgy of welding.* Butterworths and Co Publishers, 1983.

Elber, W. Fatigue crack closure under cyclic tension. *Engineering Fracture Mechanics*, 2(1):37–45, 1970.

EN 1993-1-1:2005. *Eurocode 3: Design of steel structures – Part 1-1: General rules and rules for buildings.* CEN, 2005.

EN 1993-1-9:2005. *Eurocode 3: Design of steel structures – Part 1-9: Fatigue.* CEN, 2005.

Fish, J. and Belytschko, T. *A first course in finite elements.* Wiley, 2007.

Fisher, J., Frank, K., Hirt, M. and McNamee, B. *Effect of Weldments on the Fatigue Strength of Steel Beams.* Technical Report, National Cooperative Highway Research Program, Report No.102, 1970.

Fitzpatrick, M. and Lodini, A. *Analysis of residual stress by diffraction using neutron and synchrotron radiation.* Taylor & Francis, 2003. ISBN 0-415-30397-4.

Forsyth, P. A two stage process of fatigue crack growth. In *Proc. Crack Prop. Symp., Cranfteld 1*, p. 76. 1962.

Francis, J., Bhadeshia, H. and Withers, P. Welding residual stresses in ferritic power plant steels, review. *Materials Science and Technology*, 23(9):1009–1020, 2007.

Frater, G. Strain concentration factors in rectangular hollow section truss gap K-connection – an experimental study. *Journal of Constructional Steel Research*, pp. 77–104, 1993.

FREY, F. and Jirousek, J. *Analyse des structures et milieux continus : méthode des éléments finis.* Traité de génie civil de l'Ecole Polytechnique Fédérale de Lausanne, Vol. 6. Presses Polytechniques et Universitaires Romandes, Lausanne, 2001.

Frickle, W. Effects of residual stresses on the fatigue behavior of welded steel structures. In *Proceedings of the first symposium on structural durability*, pp. 111–124. Ed. Sonsino, C. M., Darmstadt, 2005.

Geuzaine, C. and Remacle, J.-F. *version 2.5.0, http://www.geuz.org/gmsh/.* 2010.

Goldak, J., Chakravarti, A. and Bibby, M. A new finite-element model for welding heat-sources. *Metall. Trans. B*, 15B(2):299–305, 1984.

Griffith, A. The phenomena of rupture and flow in solids. *Philos. Trans. R. Soc. Lond. Ser. A Math. Phys. Eng. Sci.*, 221:163–198, 1920.

Gurney, T. Some recent work relating to the influence of residual stresses on fatigue strength. *Proc. Int. Conf. on Residual Stress in Welded Construction and Their Effects*, 1:151–163, 1977.

Gurney, T. *Fatigue of Welded Structures.* Cambridge University Press, Cambridge, 1979.

Gurney, T. R. The influence of thickness on the fatigue strength of welded joints. In *Proc. 2nd International Conference on the Behavior of Offshore Structures*, volume 1, pp. 523–534. 1981.

Gurney, T. R. The influence of thickness on fatigue of welded joints – 10 years on (a review of british work). In *Proc. 8th Intn. Conference, Offshore Mechanics & Arctic Engng.*, volume 3. 1989.

Hansbo, A. and Hansbo, P. A finite element method for the simulation of strong and weak discontinuities in solid mechanics. *Comput. Methods Appl. Mech. Engrg.*, 193(33-35):3523–3540, 2004.

Haze, T. and Aihara, S. *Metallurgical factors controlling HAZ toughness in HT50 steels, IIW document IX-1423-86.* International Institute of welding, 1986.

Hirt, M., Bez, R. and Nussbaumer, A. *TGC10, Construction métallique, notions fondamentales et méthodes de dimensionnement.* Presses Polytechniques et Universitaires Romandes, EPFL, 2006.

Hobbacher, A. *Discussion of the Thickness Effect at Welded Joints, IIW Doc JWG-XIII-XV-181-05.* International Institute of welding, 2005.

Hobbacher, A. *Recommendations for fatigue design of welded joints and components, IIW document XIII-1251-07 / XV-1254-07.* International Institute of welding, 2007.

Hughes, D., Bruno, G., Pirling, T. and Withers, P. First impressions of SALSA: the new engineering instrument at ILL. *Neutron News*, 17(3):28–32, 2006.

Husset, J., Lieurade, H., Maltrud, F. and Truchon, M. Fatigue crack growth monitoring using a crack front marking technique. *Welding in the World*, pp. 276–282, 1985.

Hutchings, M. T., Withers, P. J., Holden, T. M. and Lorentzen, T. *Introduction to the characterization of Residual Stress by Neutron Diffraction.* Taylor and Francis, 2005.

Irwin, G. Analysis of stresses and strains near the end of a crack traversing a plate. *Journal of applied mechanics*, 24, 1957.

ISF, W. and Joining Institute, A. *Ch.4. Classification of steels, welding of mild steels*, 2004.

Kaplan, D. and Lambert-Perlade, A. Influence des composés "martensite-austénite résiduelle" sur la ténacité des zones affectées par la chaleur lors du soudage des aciers C-Mn*. *La Revue de Métallurgie-CIT*, 153-154:889–898, 2001.

Kenney, K., Reuter, W., Reemsnyder, H. and Matlock, D. Fracture initiation by local brittle zones in weldments of quenched and tempered structural alloy steel plate. *Fatigue and Frature Mechanics, ASTM special technical publication*, 1321(9):427–449, 1997.

Kirsch, G. Theory of Elasticity and Application in Strength of Materials. *Zeitschrift des VDI*, 42(29):797–807, 1898.

Koppenhoefer, K. and Gordon, R. *IIW X-XV RSDP residual stress round robin results-phase 1, presentation at IIW 2000 annual assembly, Florence, Italy.* IIW document, IIW, 2000.

Kou, S. *Welding metallurgy.* John Willey and Sons, 2003.

Krebs, J. and Kassner, M. Influence of welding residual stresses on fatigue design of welded joints and components. *Welding in the world*, 51(7/8), 2007.

Lambert-Perlade, A. *Rupture par clivage de microstructures d'aciers bainitiques obtenues en conditions de soudage.* Ph.D. thesis, Ecole Nationale Supérieure des Mines de Paris, Mai 2001.

Lampman, S., Davidson, G. M., Reidenbach, F., Boring, R. L., Hammel, A., Henry, S. and W.W., S. *ASM Handbook: Fatigue and fracture*, volume 19. ASM International, 1996.

Laue-Langevin, I. *Annual report 2007.* Technical Report, Institute Laue-Langevin, 2007.

Lee, H. K., Nikbin, K. M. and O'Dowd, N. P. A generic approach for a linear elastic fracture mechanics analysisof components containing residual stress. *International Journal of Pressure Vessels and Piping*, 82:797–806, 2005.

Leggatt, R. Residual stresses in welded structures. *International Journal of Pressure Vessels and Piping*, 85:144–151, 2008.

Liedtke, M., Scheller, W. and Krampen, J. Welding recommendations for modern tubular steels. XII:507–513, 2009.

Lieurade, H. *Les contraintes résiduelles dans les constructions soudées*, chapter Les effets des contraintes résiduelles et du rapport R sur la résistance à la fatigue des éléments soudés. CETIM, 1987.

Lindgren, L.-E. Finite element modeling and simulation of welding Part 1: increased complexity. *Journal of Thermal Stresses*, 24:141–192, 2001a.

Lindgren, L.-E. Finite element modeling and simulation of welding Part 2:. *Journal of Thermal Stresses*, 24:195–231, 2001b.

Lindgren, L.-E. Finite element modeling and simulation of welding Part 3: efficiency and integration. *Journal of Thermal Stresses*, 24:305–334, 2001c.

Lu, J. *Handbook of Measurement of Residual Stresses.* CETIM, Society for Experimental Mechanics SEM, 1996.

Lu, J., Flavenot, J. F. and Lieurade, H. Intégration de la notion des contraintes résiduelles dans les bureaux dŠ études. 1991.

Lugg, M., Shang, H., Collins, R. and Michael, D. The measurement of surface crack inclination in metals using AC electric fields. *J. Phys. D: Appl. Phys.*, 21:1814–1821, 1988.

MacDonald, K. A. and Maddox, S. J. New guidance for fatigue design of pipeline girth welds. *Engineering failure analysis*, 10:177–197, 2003.

Macherauch, E., Wohlfahrt, H. and Wolfstieg, U. Zur zweckmässigen. Definition von Eigenspannungen. *Härterei-Technische Mitteilungen*, 28(3):201–211, 1973.

Macquet, P. Soudage MAG en construction métallique fil plein ou fil fourré. *Revue Construction Métallique*, pp. 63–69, 1999.

Maddox, S. J. *Fatigue strength of welded structures.* Abington publishing, 1991.

Maddox, S. J. Developments in fatigue design codes and fitness-for-service assessment methods. In *Proceedings IIW International Conference on Performance of Dynamically Loaded Welded Structures*. Welding Research Council, New York, 1997.

Maddox, S. J. Fatigue Design Rules For Welded Structures. *Prog. Struct. Engng Mater*, 2:102–109, 2000.

Manson, S. *Behaviour of materials under conditions of thermal stress*. Technical Report, National advisory committee for aeronautics, NACA-TN-2933, 1953.

Marshall, P. *Design of welded tubular connections, Basis and use of AWS provisions*. Elsevier Science Publishers, Amsterdam, 1992.

Masing, G. Eigenspannungen in kaltgereckten Metallen. *Tech. Physik*, 6:569–579, 1925.

Masubuchi, K. *Analysis of welded structures*. Pergamon Press, 1980.

Matelect, L. *Practical aspects of the ACPD technique*. Matelect LTD, 2006.

Mathar, J. Determination of Initial Stresses by Measuring the Deformation Around Drilled Holes. *ASME*, 56(4):249–254, 1934.

McClung, R. C. A literature survey on the stability and significance of residual stresses during fatigue. *Fatigue Fract. Engng. Mater. Struct.*, (30):173–205, 2007.

Michaleris, P. *Courses at the Pennsylvania State University*, 2011.

Miettinen, J. Calculation of Solidification-Related Thermophysical Properties for Steels. *Metallurgical and Materials Transactions B*, 28B:281–297, 1997.

Mochizuki, M., Hayashi, M. and Hattori, T. Numerical analysis of welding residual stress and its verification using neutron diffraction measurement. *Journal of Engineering Materials and Technology, Transactions of the ASME*, 122:98–103, January 2000.

Moës, N., Dolbow, J. and Belytschko, T. A finite element method for crack growth without remeshing. *International Journal for Numerical Methods in Engineering*, 46(1):131–150, 1999.

MORFEO. *v1.3 user manual*. Cenaero, 2009.

Newman, R. and Gurney, T. Fatigue test on plain plate specimens and transverse butt welds. *Br. Weld J.*, 6(12):569–594, 1959.

Niemi, F. W. M. S., E. *Fatigue analysis of welded components, Designer's guide to the structural hot-spot stress approach, IIW-1430-00*. International Institute of welding, 2006.

Nitschke-Pagel, T. *Eigenspannungen und Schwingfestigkeitsverhalten geschweisster Feinkorstähle (Residual stress and fatigue behaviour of welded fine grain steels)*. Diss. Tech. Univ. Braunsweig, 1994.

Nussbaumer, A., Herion, S., Veselcic, M. and Dietrich, R. New S-N curves for details in bridges with steel truss tubular. In *Tubular Structures XIII, Hong Kong, 15-17 December*. 2010. ISBN 978-0-415-58473-9.

Örjasäter, O. *Effect of plate thickness on fatigue of welded components, IIW-YWG XIII-XV-118-93*. International Institute of welding, 1995.

Pang, J. W. L., Holden, T. M. and Mason, T. E. The development of intergranular strains in a high-strength steel. *J. Strain Anal.*, 33:373–383, 1998.

Papazoglou, V. and Masubuchi, K. Numerical analysis of thermal stresses during welding including phase transformation effects. *Journal of Pressure Vessel Technology*, 104:198–203, 1982.

Paris, P. and Erdogan, F. A Critical Analysis of Crack Propagation Laws. *Trans. ASME, Series D, 85, 528-534.*, 1963.

Paris, P., Tada, H. and Donald, J. Service Load Fatigue Damage - A Historical Perspective. In *Proceedings of Fatigue Damage of Structural Materials*, volume 2. 1968.

Payne, J. and Porter Goff, R. Experimental determination of residual stresses in welded tubular T-joints. In *International Conference on Fatigue and Crack Growth in Offshore Structures, I. Mech. E., No C134/86*, pp. 10–116. 1986.

Peeker, E. *Extended numerical modeling of fatigue behaviour*. PhD Thesis EPFL 1617, Ecole Polytechnique Federale de Lausanne (EPFL), 1997.

Pirling, T., Bruno, G. and Withers, P. SALSA-A new instrument for strain imaging in engineering materials and components. *Materials Science and Engineering*, A(437):139–144, 2006.

Pommier, S., Gravouil, A., Moes, N. and Combescure, A. *La simulation numérique de la propagation des fissures*. Lavoisier, 2009.

Ponge, D. *Structural Materials - Steels*. Technical Report, Max-Planck-Insitut für Eisenforschung GmbH, Marie Curie Summer School, 2005.

Poutiainen, I. and Marquis, G. *A single-point structural stress assessment procedure for load-carrying fillet welds, IIW document XIII-2012-04/XV-1174-04*. International Institute of welding, 2004.

Radaj, D. *Welding Residual Stresses and Distortion : Calculation and Measurement*. Woodhead Publishing, 2003.

Raymond, L. and Chipman, J. Thermodynamic functions of iron. *Trans. Met. Soc. AIME*, 239:630–633, 1967.

Romeijn, A., Karamanos, S. and Wardenier, J. Effects of joint flexibility on the fatigue design of welded tubular lattice structures. In *Proceedings of the Seventh (1997) Offshore and Polar Engineering Conference*, pp. 90–97. International Society of Offshore and Polar Engineers, May 1997. ISBN 1-880635-32-X.

Saguy, H. and Rittel, D. Bridging thin and thick skin solutions for alternating currents in cracked conductors. *APPLIED PHYSICS LETTERS*, 87, 2005.

Saint-Germain, B. *Etude expérimentale et numérique des distorsions de structures mécano-soudées*. Ph.D. thesis, Ecole Centrale Paris, June 2006.

Sanders, W., Derecho, A. and Munse, W. Effect of external geometry on fatigue behaviour of welded joints. *Weld. Res. Suppl.*, 30(2), 1965.

Schijve, J. and Broek, D. The effect of frequency on the propagation of fatigue cracks. 1961.

Schumacher, A. *Fatigue behaviour of welded circular hollow section joints in bridges*. PhD thesis EPFL 2727, Swiss Federal Institute of Technology (EPFL), Lausanne, 2003.

Schumacher, A. and Nussbaumer, A. Experimental study on the fatigue behavior of welded tubular k-joints for bridges. *Engineering Structures*, 28:745–755, 2006.

Schumacher, A., Sturm, S., Walbridge, S., Nussbaumer, A. and Hirt, M. *Fatigue design of bridges with welded circular hollow sections*. Report ICOM 489E, Swiss Federal Institute of Technology (EPFL), Lausanne, 2003.

Shao, Y.-B., Lie, S. and Chiew, S. Effect of chord length ratio of tubular joints on stress concentration at welded region. In *12th International Symposium on Tubular Structures (ISTS 12), Shanghai, ISTS 12, 2008*. Balkema Publishers, 2008.

Shih, T. and Wei, R. Load and environment interactions in fatigue crack growth. pp. 237–250, 1974.

SINTAP. *Structural Integrity Assessment Proc. for Europ.Ind. (SINTAP)*. 1999.

Smith, I. and Smith, R. Defects and Crack Shape Development in Fillet Welded Joints. *Fatigue of Engineering Materials and Structures*, 5(2):151–165, 1982.

Spallation Neutron Source SINQ, P. S. I. website: http://sinq.web.psi.ch, 2009.

Stacey, A., Barthelemy, J.-Y., Leggatt, R. and Ainsworth, R. Incorporation of Residual Stresses into the SINTAP Defect Assessment Procedure. *Engineering Fracture Mechanics*, 67:573–611, 2000.

standard institute BSI, B. *BS 7910:1999. Guide on methods for accessing the acceptability of flaws in metallic structures*. British standard institute, 2000.

Steinhauer, E. *Cours de matériaux I et II, Métaux, Fascicule B*. polycopiés EPFL. Presses Polytechniques EPFL, 1998.

Stuhr, U., Grosse, M. and Wagner, W. The TOF-strain scanner POLDI with multiple frame overlap–concept and performance. *Materials Science and Engineering A*, 437:134–138, 2006.

Suresh, S. *Fatigue of materials*. Cambridge University Press, 1998.

Takahashi, K. and Ito, A. Effect of external geometry of reinforcement on the fatigue strength of a welded joint. *J. Jap. Wedl. Soc.*, 40(8):13, 1971.

Vallourec & Mannesmann Tubes, F. *The Aulnoye Tube Works*. V&M report, V & M FRANCE, 2003.

van Wingerde, A., van Delft, D. R. V., Wardenier, J. and Packer, J. Scale effects on the fatigue behaviour of tubular structures. In *IIW International Conference*. IIW, July 1997.

van Wingerde, A. M. *The fatigue behaviour of T- and X-joints made of square hollow sections*, volume 37. Heron, 1992.

Vishay Measurements, G. *Measurement of Residual Stresses by the Hole Drilling Strain Gage Method*. Tech Note TN-503-6, Measurements Group, 1996.

Walbridge, S. *A Probabilistic Fatigue Analysis of Post-Weld Treated Tubular Bridge Structures.* PhD thesis EPFL 3330, Ecole polytechnique federale de Lausanne (EPFL), 2005.

Wangh, G. and Blom, A. A strip model for fatigue crack growth predictions under general load conditions. *Engineering Fracture Mechanics*, 40:507–533, 1991.

Wardenier, J. *Hollow sections in structural applications.* CIDECT, 2001.

Webster, G. *Polycrystalline Materials: Determination of Residual Stresses by neutron Diffraction, ISO/TTA3 Technology Trends Assessment*, volume 3. International Organization for Standardization, 2001.

Welding Industries, B. *Filarc flux- and metal-cored welding wires.* Technical Report, Welding Industries B.V., Netherlands, 1999.

Westergaard, H. Bearing pressures and cracks. *J. Appl. Mech.*, 6:49–53, 1939.

Wimpory, R. C. and ohms, C. A step towards a complete uncertainty analysis of residual stress determination using neutron diffraction. *Materials Science Forum*, 638-642:2487–2492, 2010.

Withers, P., Turski, M., Edwards, L., Bouchard, P. and Buttle, D. Recent advances in residual stress measurement. *International Journal of Pressure Vessels and Piping*, 85(3):118–127, 2008.

Woods, R. and Milner, D. Motion in the Weld Pool in arc welding. *Weld. J.*, 50:163, 1971.

Yamaguchi, I., Terada, Y. and Nitta, A. On the fatigue strength of steels for ship structures, IIW Doc. XIII-425-1966. *IIW Doc.*, 1966.

Zacharia, T., Vitek, J., Goldak, J., DebRoy, T., Rappaz, M. and Bhadeshia, H. Modeling of fundamental phenomena in welds. *Modelling Simul. Mater. Sci. Eng.*, 3:265–288, 1995.

Zhao, X. L., Herion, S., Packer, J. A. and al. *Design guide for circular and rectangular hollow section joints under fatigue loading.* CIDECT, Comite International pour le developpement et l'etude de la construction tubulaire 8, TüV-Verlag Rheinland, Köln, 2000.

Zhao, X. L. and Packer, J. A. *Fatigue design procedure for welded hollow section joints.* Doc. XIII-1804-99, XV-1035-99, International Institute of Welding (IIW), Cambridge: Abington, 2000.

Zheng, X. A simple formula for fatigue crack propagation and a new method for the determination of DKth. *Engineering Fracture Mechanics*, 27(4):465–475, 1987.

Appendix A

Plans of tubular truss beams tested under fatigue

A.1 Execution plans

These execution plans were provided by the steel manufacturer Zwahlen and Mayr S.A.. Hereafter, plans are reproduced with a scale factor of 1:5 for the truss beam, 2:5 for the joint detail and 2:1 for the weld detail.

It has to be noted that the peculiar joints composed of non-continuous braces, called previously joints 5N-6, are missing in these plans. These joints were effectively welded to the upper chord of specimens S6 and S7 as shown in Fig. 6.1.

Figure A.1: Execution plan for the truss beam specimen S6 (dimensions in mm).

Figure A.2: Execution plan for the truss beam specimen S7 (dimensions in mm).

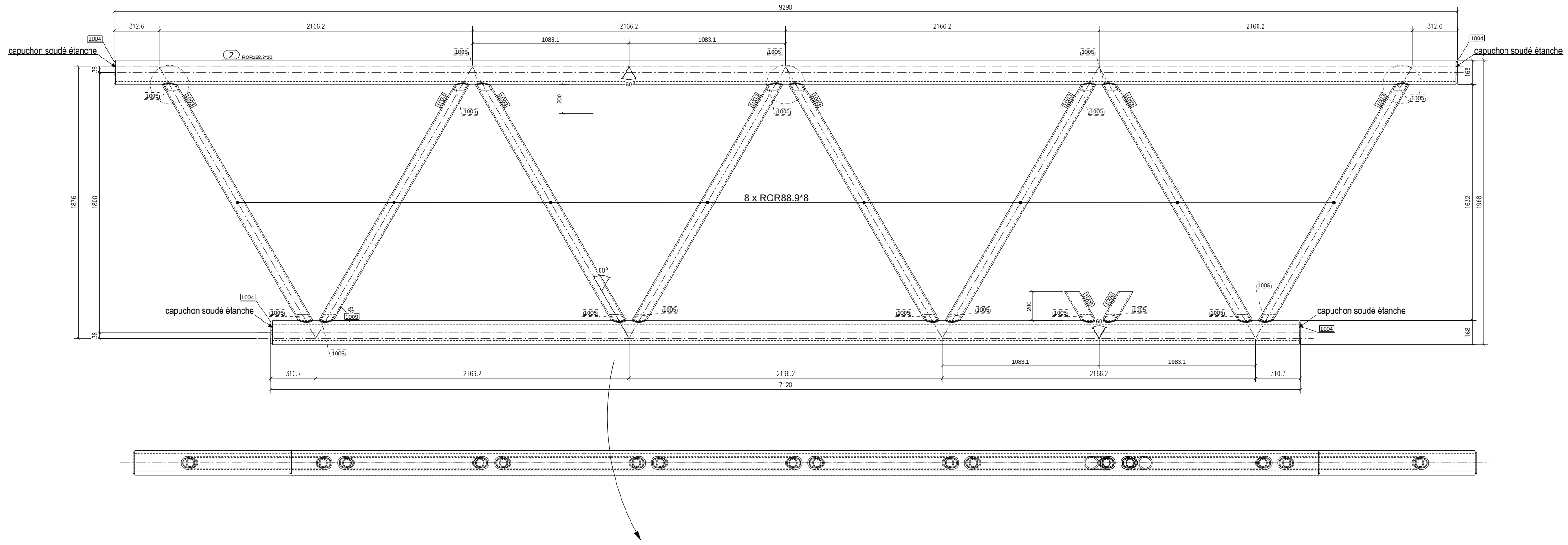
9290
312.6
2166.2
2166.2
2166.2
2166.2
312.6
1083.1
1083.1
1004
capuchon soudé étanche
2 ROR168.3*20
1004
capuchon soudé étanche
1003
200
60°
1876
1800
1632
1968
168
38
8 x ROR88.9*8
1004
capuchon soudé étanche
1009
60°
200
1004
capuchon soudé étanche
168
38
1083.1
1083.1
310.7
2166.2
2166.2
2166.2
310.7
7120

DETAIL SOUDURE

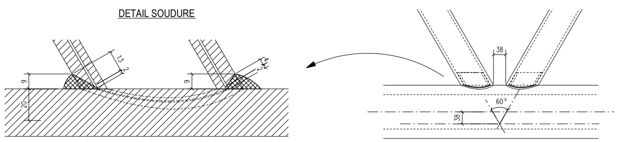
13.2
9
20
38
60°
38

◯ = Soudures parachevées
(martelage par aiguilles)

Remarques importantes:

-l'excentricité de 38 mm doit impérativement être respectée
-la poutre ne doit plus être sablée une fois que les soudures ont été effectuées

Phase	Nombre
2	1

** Liste pour le repère 2 à réaliser 1 x au total ** Aff. : 87880

Lot	Rep.	Désignation	Qte.	Profil	Qualité	Long.	Poids	Remarque
2	2	MEMBRURE	1	ROR168.3*20	S355J2H	9270	678.1	
2	1003	DIAGONALE	8	ROR88.9*8	S355J2H	1936	30.9	
2	1004	BOUCHON	4	PL10*150	S235JR	150	1.4	
2	1005	SUPPORT	18	ROR70*5	S355J2H	87	0.7	
2	1006	DIAGONALE	2	ROR88.9*8	S355J2H	282	4.5	
2	1009	MEMBRURE	1	ROR168.3*30	S355J2H	7100	726.2	
Poids total (kg)							1678.6	

Rep.	Désignation	Nb	Profil	Encombrement	Poids / pce
2	MEMBRURE	1	ROR168.3*20	168 X 1968 X 9290	1679

Qualité non spécifiées = S235JR
Soudures non spécifiées a = 4mm

CONSTRUCTIONS
METALLIQUES

ZWAHLEN & MAYR SA
Z.I. 2
CH-1860 AIGLE
T + 41 24 468 46 46
F + 41 24 468 46 00
www.zwahlen.ch

EPROUVETTE ESSAI

ASSEMBLAGE POUTRE2

noeuds tubulaires 2

Mandataire: EPFL ICOM

	Modification	dessiné le:	DES	RAF
		02.06.2008	PEH	NMO
A	SELON RETOUR APPROBATION DU 10.06.2008	13.06.2008	PEH	NMO

Echelle: 1:1 1:5 1:10
Position:
Liste: SP2

Traitement: Sans traitement
Finition: Sans traitement

PLAN n° 87880 - 002
A

DETAIL A Ech. 1/5

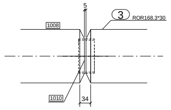
5
3 ROR168.3*30
1008
1010
34

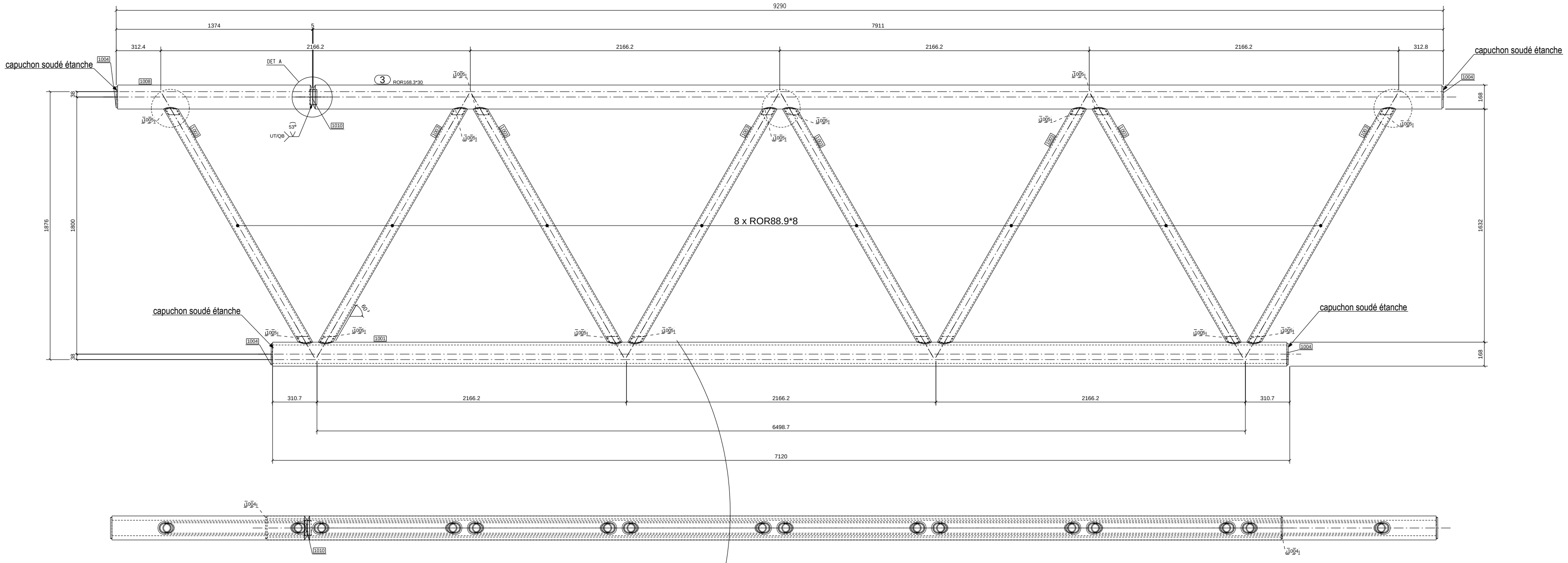
9290
1374
7911
312.4
2166.2
2166.2
2166.2
2166.2
312.8
capuchon soudé étanche
1004
1008
DET A
3 ROR168.3*30
1005
1010
UTIQB
1003
1876
1800
8 x ROR88.9*8
1632
168
38
capuchon soudé étanche
capuchon soudé étanche
1001
60°
310.7
2166.2
2166.2
2166.2
310.7
6498.7
7120

DETAIL SOUDURE

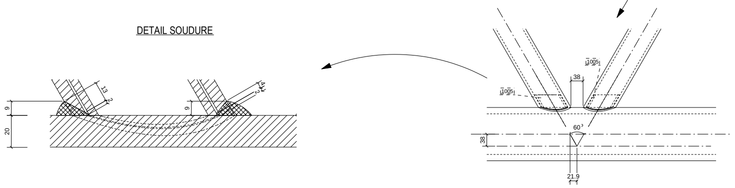
9
20
38
60°
38
21.9
1005

○ = Soudures parachevées (martelage par aiguilles)

Remarques importantes:

-l'excentricité de 38 mm doit impérativement être respectée
-la poutre ne doit plus être sablée une fois que les soudures ont été effectuées

Phase	Nombre
2	1

** Liste pour le repère 3 à réaliser 1 x au total ** Aff. : 87880

Lot	Rep.	Désignation	Qte.	Profil	Qualité	Long.	Poids	Remarque
2	3	MEMBRURE	1	ROR168.3*30	S355J2H	7901	808.2	
2	1001	MEMBRURE	1	ROR168.3*20	S355J2H	7100	519.3	
2	1003	DIAGONALE	8	ROR88.9*8	S355J2H	1936	30.9	
2	1004	BOUCHON	4	PL10*150	S235JR	150	1.4	
2	1005	SUPPORT	16	ROR70*5	S355J2H	87	0.7	
2	1008	MEMBRURE	1	ROR168.3*30	S355J2H	1364	139.5	
2	1010	TUBE	1	ROR108*4	S355J2H	50	0.5	
Poids total (kg)							1731.4	

Rep.	Désignation	Nb	Profil	Encombrement	Poids / pce
3	MEMBRURE	1	ROR168.3*30	168 X 1968 X 9290	1731

Qualité non spécifiées = S235JR
Soudures non spécifiées a = 4mm

CONSTRUCTIONS
METALLIQUES
ZWAHLEN & MAYR SA
Z.I. 2
CH-1860 AIGLE
T + 41 24 468 46 46
F + 41 24 468 46 00
www.zwahlen.ch

EPROUVETTE ESSAI

ASSEMBLAGE POUTRE 3

NOEUDS TUBULAIRES 3

Mandataire: EPFL ICOM

	Modification	dessiné le:	DES	RAF
		27.05.2008	PEH	NMO
A	SELON RETOUR APPROBATION DU 10.06.2008	13.06.2008	PEH	NMO

Echelle: 1:1 1:5 1:10
Position:
Liste: SP2

Traitement: Sans traitement
Finition: Sans traitement

PLAN n° 87880 - 003 A

A.2 Test setup plan

Figure A.3: Setup of the fatigue tests (scale 1:100).

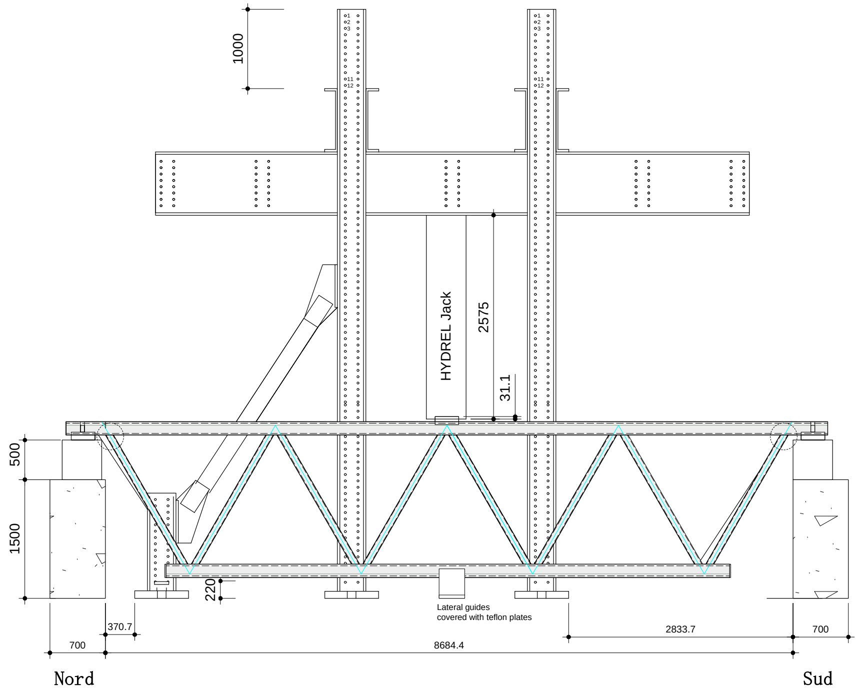
1000
HYDREL Jack
2575
31.1
500
1500
220
370.7
700
8684.4
2833.7
700
Lateral guides
covered with teflon plates
Nord
Sud

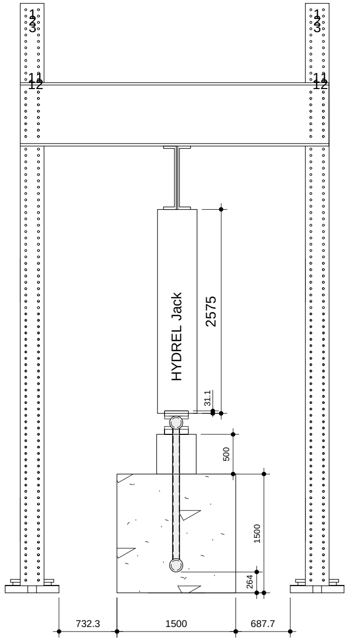
1
2
3
11
12
HYDREL Jack
2575
31.1
500
1500
264
732.3
1500
687.7

ÉCOLE POLYTECHNIQUE FÉDÉRALE DE LAUSANNE

FACULTE ENVIRONNEMENT NATUREL, ARCHITECTURAL ET CONSTRUIT ENAC
SECTION DE GENIE CIVIL
LABORATOIRE DE LA CONSTRUCTION METALLIQUE ICOM

Projet	IC 436 - Effets d'echelle			Date:	01.08.2008
Plan	436-05 Bati de charge				
Echelle.:	1:50	Unités:	mm	Auteur:	LB / CA

A.3 Strain measurements on truss beams

A.3.1 Plans of gauges positions

Figure A.4: Plan of gauges and ACPD positions on specimen S6 (scale 1:50).

Figure A.5: Plan of gauges and ACPD positions on specimen S7 (scale 1:50).

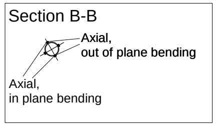
Section B-B

Axial,
out of plane bending
Axial,
in plane bending

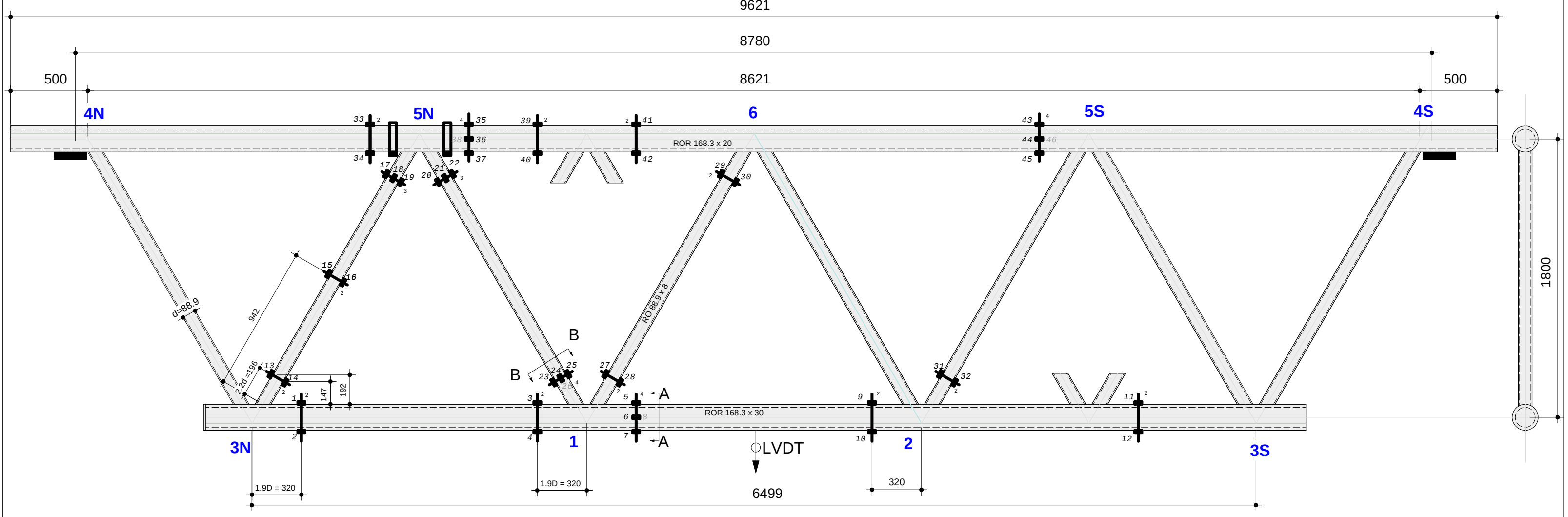
9621
8780
500
8621
500
4N
5N
6
5S
4S
33
34
35
36
37
38
39
40
41
42
43
44
45
46
ROR 168.3 x 20
17
18
19
20
21
22
29
30
15
16
942
d=88.9
RO 88.9 x 8
B
B
13
14
2.2d =196
147
192
23
24
25
26
27
28
31
32
1
2
3
4
5
6
7
8
A
A
9
10
11
12
ROR 168.3 x 30
3N
1
LVDT
2
3S
1.9D = 320
1.9D = 320
320
6499
1800

▬ Uniaxial strain gauges (46): HBM 1-LY11-10/120

▯ ACPD field probe

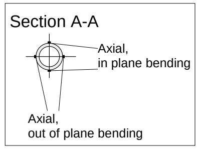
Section A-A

Axial,
in plane bending
Axial,
out of plane bending

ÉCOLE POLYTECHNIQUE FÉDÉRALE DE LAUSANNE

FACULTE ENVIRONNEMENT NATUREL, ARCHITECTURAL ET CONSTRUIT ENAC
SECTION DE GENIE CIVIL
LABORATOIRE DE LA CONSTRUCTION METALLIQUE ICOM

Projet	IC 436 - Effets d'echelle			Date:	23.07.2008
Plan	436-08 Plan de jauges POUTRE S6				
Echelle.:	1:25	Unités:	mm	Auteur:	LB /CA

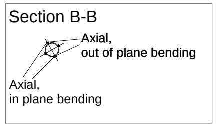
Section B-B
Axial,
out of plane bending
Axial,
in plane bending

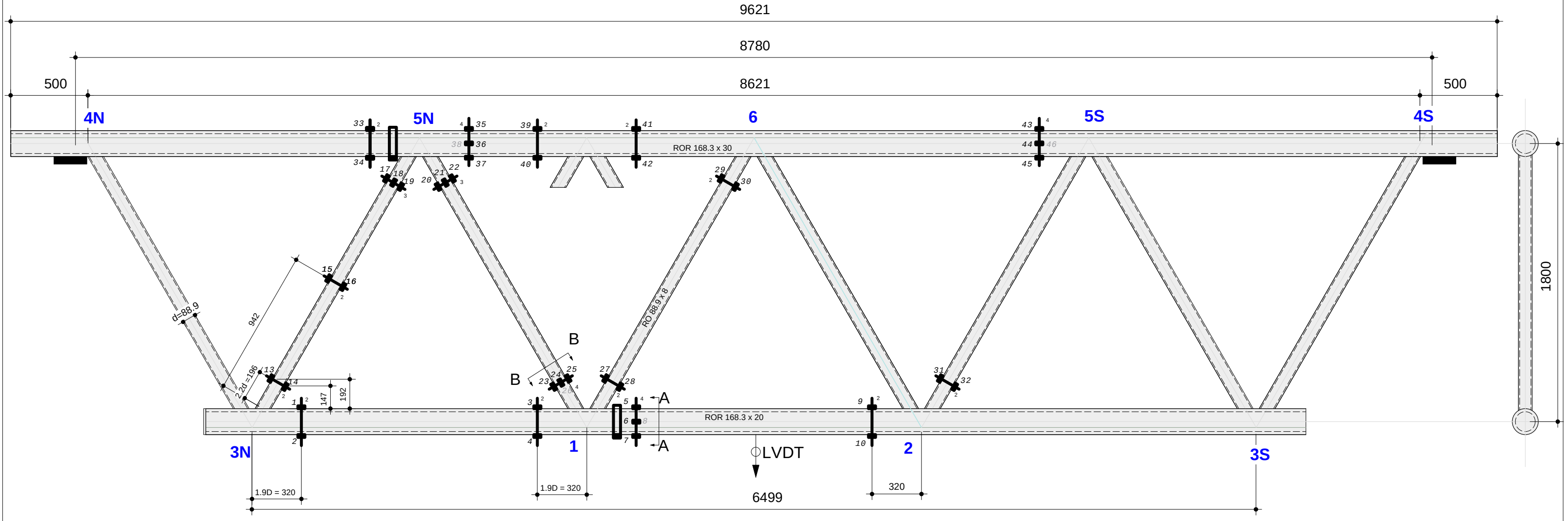
9621
8780
8621
500
500
4N
5N
6
5S
4S
ROR 168.3 x 30
ROR 168.3 x 20
RO 88.9 x 8
d=88.9
942
2d =196
147
192
1800
B
B
A
A
3N
1
2
3S
LVDT
1.9D = 320
1.9D = 320
320
6499
1
2
3
4
5
6
7
9
10
13
14
15
16
17
18
19
20
21
22
23
24
25
27
28
29
30
31
32
33
34
35
36
37
39
40
41
42
43
44
45

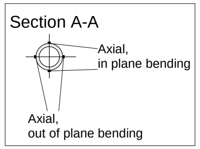
Section A-A
Axial,
in plane bending
Axial,
out of plane bending

▬ Uniaxial strain gauges (46): HBM 1-LY11-10/120

▯ ACPD field probe

FACULTE ENVIRONNEMENT NATUREL, ARCHITECTURAL ET CONSTRUIT ENAC
SECTION DE GENIE CIVIL
LABORATOIRE DE LA CONSTRUCTION METALLIQUE ICOM

Projet	IC 436 - Effets d'echelle			Date:	23.07.2008
Plan	436-08 Plan de jauges POUTRE S7				
Echelle.:	1:25	Unités:	mm	Auteur:	LB /CA

A.3.2 Strains measured from gauges

- **S6 specimen**
  - **Measurements under Q_{min}= 61 kN**
  - **Measurements under Q_{max}= 610 kN**
  - **Measurements under Q_{max} - Q_{min}= 550 kN** (subtraction of the second Table from the first one)

Number of cycles	Force [kN]	Displ. [mm]	Strain measurements [10^{-6}]																					
			1	**2**	**3**	**4**	**5**	**6**	**7**	**8**	**9**	**10**	**11**	**12**	**13**	**14**	**15**	**16**	**17**	**18**	**19**	**20**	**21**	**22**
initial test	61	1.1	6	25	12	17	14	24	42	29	13	42	8	22	-104	-60	-84	-82	-70	-97	-121	93	67	47
50000	61	1.1	5	25	11	15	13	26	42	25	13	41	7	20	-111	-63	-89	-83	-79	-115	-159	101	67	62
90000	60	1.1	5	24	11	15	13	25	40	25	12	40	6	20	-103	-60	-83	-81	-48	-85	-126	128	106	96
140000	61	0.8	3	19	8	12	10	19	32	20	10	32	5	16	-83	-49	-68	-66	-17	-70	-116	142	131	126
180000	59	1.0	4	21	9	13	11	20	35	22	10	35	5	18	-89	-53	-73	-70	-5	-78	-133	124	119	130
200000	59	0.8	3	19	8	12	10	18	32	21	10	32	5	17	-82	-50	-68	-65	8	-81	-147	114	115	138
230000	60	0.7	3	19	8	12	9	20	32	18	10	32	4	17	-80	-50	-67	-63	30	-84	-166	101	116	158

Number of cycles	Strain measurements [10^{-6}]																							
	23	**24**	**25**	**26**	**27**	**28**	**29**	**30**	**31**	**32**	**33**	**34**	**35**	**36**	**37**	**38**	**39**	**40**	**41**	**42**	**43**	**44**	**45**	**46**
initial test	60	67	88	72	-93	-89	-102	-81	80	57	-10	-32	-48	-43	-38	-36	-54	-31	-57	-26	-42	-42	-45	-34
50000	63	70	85	89	-96	-107	-124	-90	84	65	-6	-43	-53	-47	-46	-36	-64	-37	-69	-29	-45	-47	-53	-42
90000	102	97	113	124	-65	-71	-88	-58	111	105	28	-4	-19	-11	-10	-10	-26	-3	-30	5	-10	-10	-18	-10
140000	142	113	124	141	-49	-52	-69	-38	120	148	50	15	3	12	8	7	-5	17	-11	27	22	16	6	17
180000	154	103	103	127	-55	-51	-72	-46	102	165	46	6	0	4	-1	3	-9	8	-18	18	6	4	-5	5
200000	167	98	90	121	-58	-51	-73	-50	91	178	47	1	1	0	-6	2	-10	4	-20	16	4	0	-9	5
230000	189	95	72	119	-62	-49	-71	-49	72	203	52	-5	6	4	-10	-1	-8	1	-20	17	7	4	-11	1

Table A.1: Deflection and strain measurements (LVDT and uniaxial gauges) for S6 specimen under Q_{min}= 61 kN.

Numb. of cycles	**Force [kN]**	**Displ. [mm]**	**Strain measurements $[10^{-6}]$**																				
			1	**2**	**3**	**4**	**5**	**6**	**7**	**8**	**9**	**10**	**11**	**12**	**13**	**14**	**15**	**16**	**17**	**18**	**19**	**20**	**21**	**22**
initial test	611	10.3	47	241	101	153	128	234	415	275	123	417	64	209	-1072	-622	-865	-851	-608	-883	-1147	1051	784	573
50000	611	10.3	47	243	102	154	128	242	417	268	124	417	65	208	-1078	-625	-871	-852	-613	-876	-1163	1054	792	570
90000	610	10.6	47	242	102	154	128	241	415	267	123	416	64	209	-1068	-624	-865	-850	-584	-847	-1128	1079	825	606
140000	610	10.1	42	240	98	151	124	237	407	259	121	407	59	208	-1046	-615	-850	-832	-560	-820	-1115	1091	858	635
180000	610	10.5	40	246	100	152	125	241	413	261	122	413	56	214	-1055	-628	-862	-838	-563	-827	-1131	1077	850	646
200000	610	10.1	37	247	99	152	123	239	411	260	121	411	51	217	-1045	-629	-860	-829	-561	-833	-1138	1065	835	658
230000	610	10.0	33	249	97	152	120	239	411	256	121	407	41	225	-1035	-631	-859	-820	-552	-809	-1143	1043	860	681

Number of cycles	**Strain measurements $[10^{-6}]$**																						
	23	**24**	**25**	**26**	**27**	**28**	**29**	**30**	**31**	**32**	**33**	**34**	**35**	**36**	**37**	**38**	**39**	**40**	**41**	**42**	**43**	**44**	**45**	**46**
initial test	681	783	934	845	-811	-802	-915	-730	919	659	27	-209	-374	-305	-268	-255	-412	-190	-474	-114	-327	-282	-307	-271
50000	676	782	928	835	-809	-812	-931	-725	915	658	35	-218	-369	-299	-276	-252	-416	-187	-490	-101	-324	-268	-311	-284
90000	718	808	955	869	-779	-775	-893	-695	941	700	69	-178	-335	-263	-239	-225	-377	-153	-448	-68	-289	-232	-275	-252
140000	766	823	959	879	-758	-755	-876	-669	942	755	92	-160	-313	-239	-221	-209	-359	-130	-435	-40	-260	-202	-250	-229
180000	792	816	939	867	-769	-758	-883	-681	922	792	89	-168	-320	-246	-228	-214	-366	-138	-443	-49	-278	-215	-261	-240
200000	816	807	920	861	-774	-758	-883	-685	905	818	89	-173	-321	-250	-231	-215	-367	-141	-444	-52	-281	-218	-262	-242
230000	855	801	886	846	-774	-753	-880	-680	868	869	95	-177	-318	-246	-232	-215	-366	-141	-446	-48	-281	-213	-259	-242

Table A.2: Deflection and strain measurements (LVDT and uniaxial gauges) for S6 specimen under Q_{max}= 610 kN.

Number of cycles	**Force [kN]**	**Displ. [mm]**	**Strain measurements [10^{-6}]**																				
			1	**2**	**3**	**4**	**5**	**6**	**7**	**8**	**9**	**10**	**11**	**12**	**13**	**14**	**15**	**16**	**17**	**18**	**19**	**20**	**21**	**22**
initial test	550	9.2	41	216	89	137	114	211	373	246	110	375	56	187	-968	-562	-780	-768	-538	-786	-1026	958	717	526
50000	550	9.3	42	218	91	139	115	216	375	243	111	376	58	188	-967	-562	-781	-770	-534	-761	-1004	953	725	508
90000	550	9.5	42	218	91	139	115	216	375	242	111	376	57	189	-965	-564	-781	-768	-536	-762	-1002	951	719	510
140000	550	9.3	39	221	90	139	114	219	375	238	111	375	54	191	-963	-566	-782	-766	-542	-750	-999	948	727	509
180000	551	9.6	36	225	91	140	114	220	378	239	112	378	51	196	-966	-575	-789	-767	-558	-749	-998	953	731	516
200000	551	9.3	34	227	91	140	114	221	379	239	112	378	47	200	-963	-579	-792	-764	-569	-753	-991	951	721	520
230000	550	9.3	30	230	89	140	111	219	379	238	112	376	37	208	-955	-581	-792	-757	-582	-725	-977	942	744	524
Max. diff.[%]		4	40	7	2	2	4	5	2	3	2	1	59	11	-1	-3	-2	-2	-8	-8	-5	2	4	4
Aver.		9.3	38	222	90	139	114	217	376	241	111	376	51	194	-964	-570	-786	-766	-551	-755	-999	951	726	516
Std dev.		0.1	4.5	5.5	0.9	1.1	1.5	3.5	2.3	3.0	0.7	1.4	7.6	7.6	4.2	8.1	5.4	4.4	18.7	18.2	14.8	4.9	9.1	7.3

Number of cycles	**Strain measurements [10^{-6}]**																						
	23	**24**	**25**	**26**	**27**	**28**	**29**	**30**	**31**	**32**	**33**	**34**	**35**	**36**	**37**	**38**	**39**	**40**	**41**	**42**	**43**	**44**	**45**	**46**
initia test	620	717	847	773	-718	-713	-813	-649	840	602	37	-177	-326	-262	-231	-219	-359	-158	-418	-88	-284	-240	-262	-237
5000	613	712	843	746	-713	-705	-807	-635	831	593	41	-175	-315	-253	-230	-216	-352	-150	-421	-72	-279	-222	-257	-243
9000	616	712	841	745	-714	-704	-805	-636	830	595	41	-174	-315	-252	-229	-216	-351	-150	-418	-73	-279	-222	-257	-243
1400	623	710	835	738	-710	-703	-807	-631	822	608	42	-175	-316	-251	-228	-216	-354	-147	-424	-68	-282	-218	-256	-246
1800	638	713	835	740	-714	-707	-811	-634	820	627	43	-175	-320	-250	-227	-217	-356	-146	-425	-67	-283	-219	-255	-246
2000	649	709	830	740	-716	-707	-810	-636	814	640	42	-174	-322	-250	-225	-217	-357	-145	-425	-68	-285	-218	-253	-246
2300	666	706	814	727	-712	-704	-809	-631	797	665	43	-173	-324	-250	-222	-214	-359	-141	-426	-64	-288	-218	-249	-243
Max. diff. [%]	9	2	4	6	-1	-1	-1	-3	5	12	14	-2	-3	-5	-4	-2	-2	-11	-2	-27	-3	-9	-5	-4
Aver.	632	711	835	744	-714	-706	-809	-636	822	619	41	-175	-320	-253	-227	-217	-355	-148	-422	-72	-283	-222	-256	-243
Std dev.	19.5	3.4	10.9	14.0	2.7	3.3	2.7	6.2	13.9	26.9	1.9	1.3	4.4	4.4	3.1	1.7	3.1	5.3	3.4	7.9	3.2	8.0	4.1	3.3

Table A.3: Deflection and strains for S6 specimen under ΔQ= 550 kN.

- **S7 specimen**
  - **Measurements under** Q_{min}= **61 kN**
  - **Measurements under** Q_{max}= **610 kN**
  - **Measurements under** Q_{max} **-** Q_{min}= **550 kN** (subtraction of the second table from the first one)

Number of cycles	Force [kN]	Displ. [mm]	Strain measurements [10^{-6}]																					
			1	**2**	**3**	**4**	**5**	**6**	**7**	**8**	**9**	**10**	**11**	**12**	**13**	**14**	**15**	**16**	**17**	**18**	**19**	**20**	**21**	**22**
initial test	61	0.8	8	24	12	14	18	25	42	28	19	41	-	-	-87	-48	-68	-66	-488	-33	-408	108	-280	137
50000	60	0.8	8	24	12	14	18	25	41	27	18	41	-	-	-86	-48	-68	-66	-48	-58	-87	80	70	45
85000	60	0.3	4	13	6	7	9	13	22	15	10	22	-	-	-47	-26	-37	-35	-25	-31	-47	44	39	25

Number of cycles	Strain measurements [10^{-6}]																						
	23	**24**	**25**	**26**	**27**	**28**	**29**	**30**	**31**	**32**	**33**	**34**	**35**	**36**	**37**	**38**	**39**	**40**	**41**	**42**	**43**	**44**	**45**	**46**
initial test	417	-118	-373	-109	-499	-544	-121	-538	405	-245	71	-462	154	34	-640	-393	44	-464	64	-95	-478	-335	-3	-84
50000	50	59	75	65	-66	-57	-70	-56	74	51	-	-14	-21	-17	-14	-15	-25	-8	-31	-3	-18	-14	-16	-18
85000	28	31	41	36	-36	-31	-38	-30	41	28	-	-7	-12	-10	-7	-8	-14	-5	-17	-2	-11	-5	-8	-12

Table A.4: Deflection and strain measurements (LVDT and uniaxial gauges) for S7 specimen under Q_{min}= 61 kN.

Numb. of cycles	Force	Displ.	Strain measurements $[10^{-6}]$																					
	[kN]	[mm]	**1**	**2**	**3**	**4**	**5**	**6**	**7**	**8**	**9**	**10**	**11**	**12**	**13**	**14**	**15**	**16**	**17**	**18**	**19**	**20**	**21**	**22**
initial test	610	10.0	101	304	149	172	226	317	523	342	233	513	-	-	-1086	-592	-850	-815	-1020	-708	-1416	1045	516	665
50000	610	9.9	98	304	148	171	225	316	520	339	231	511	-	-	-1077	-590	-846	-811	-578	-730	-1088	1014	863	571
85000	610	9.5	89	299	143	164	217	304	501	327	222	494	-	-	-1042	-566	-817	-780	-555	-704	-1050	976	831	552

Nb of cycles	Strain measurements $[10^{-6}]$																							
	23	**24**	**25**	**26**	**27**	**28**	**29**	**30**	**31**	**32**	**33**	**34**	**35**	**36**	**37**	**38**	**39**	**40**	**41**	**42**	**43**	**44**	**45**	**46**
init	998	576	505	643	-1252	-1210	-918	-1181	1279	343	102	-616	-91	-159	-790	-563	-242	-555	-291	-117	-694	-507	-173	-273
50000	630	749	949	813	-816	-717	-865	-696	940	640	-	-168	-265	-209	-163	-185	-309	-98	-385	-23	-231	-184	-189	-207
85000	619	721	908	781	-785	-691	-832	-670	892	643	-	-162	-256	-201	-156	-179	-299	-95	-371	-22	-225	-176	-180	-201

Table A.5: Deflection and strain measurements (LVDT and uniaxial gauges) for S7 specimen under Q_{max}= 610 kN.

Number of cycles	Force [kN]	Displ. [mm]	Strain measurements [10^{-6}]																					
			1	**2**	**3**	**4**	**5**	**6**	**7**	**8**	**9**	**10**	**11**	**12**	**13**	**14**	**15**	**16**	**17**	**18**	**19**	**20**	**21**	**22**
initial test	550	9.1	92	280	136	159	208	291	481	315	214	472	-	-	-999	-545	-782	-749	-532	-675	-1008	938	796	528
50000	550	9.2	91	280	136	158	207	291	479	312	213	471	-	-	-991	-542	-778	-745	-531	-673	-1001	934	793	525
85000	550	9.2	86	286	136	157	207	291	479	312	212	472	-	-	-995	-540	-780	-744	-530	-673	-1003	932	793	528
Max. diff.[%]		1	8	2	0	1	0	0	0	1	1	0	-	-	-1	-1	0	-1	0	0	-1	1	0	0
Aver.		9	90	282	136	158	207	291	480	313	213	472	-	-	-995	-542	-780	-746	-531	-674	-1004	935	794	527
Std dev.		0.0	3.6	3.8	0.0	0.9	0.3	0.2	1.1	1.3	1.0	0.8	-	-	4.3	2.2	1.9	2.6	1.2	1.3	3.6	3.0	2.0	1.4

Number of cycles	Strain measurements [10^{-6}]																							
	23	**24**	**25**	**26**	**27**	**28**	**29**	**30**	**31**	**32**	**33**	**34**	**35**	**36**	**37**	**38**	**39**	**40**	**41**	**42**	**43**	**44**	**45**	**46**
initial test	581	694	878	752	-753	-666	-798	-643	874	588	32	-155	-245	-193	-150	-170	-285	-91	-355	-21	-216	-172	-171	-189
50000	580	690	874	747	-750	-660	-795	-640	866	589	0	-154	-244	-192	-149	-170	-284	-90	-354	-20	-213	-170	-173	-189
85000	591	690	867	745	-749	-660	-794	-639	852	614	0	-154	-245	-192	-149	-171	-285	-90	-354	-20	-214	-171	-172	-189
Max. diff. [%]	2	1	1	1	-1	-1	0	-1	3	4	-	0	0	-1	-1	0	0	-1	0	-7	-1	-1	-1	0
	584	691	873	748	-751	-662	-796	-641	864	597	11	-154	-244	-192	-149	-170	-285	-90	-354	-21	-214	-171	-172	-189
Std dev.	6.0	2.4	5.2	3.7	2.0	3.4	2.0	1.9	11.5	14.9	18.4	0.3	0.5	0.7	0.4	0.3	0.7	0.6	0.6	0.8	1.6	0.6	1.0	0.2

Table A.6: Deflection and strains for S7 specimen under ΔQ= 550 kN.

A.3.3 Stresses deduced from strains

- **S6 specimen**
  - **Stresses deduced from strains under** Q_{min}= **61 kN**
  - **Stresses deduced from strains under** Q_{max}= **610 kN**
  - **Stresses deduced from strains under** Q_{max} **-** Q_{min}= **550 kN** (subtraction of the second table from the first one)

Number of cycles	**Force [kN]**	**Stresses** [N/mm^2]																					
		1	**2**	**3**	**4**	**5**	**6**	**7**	**8**	**9**	**10**	**11**	**12**	**13**	**14**	**15**	**16**	**17**	**18**	**19**	**20**	**21**	**22**
initial test	61	1	6	3	4	3	6	10	7	3	10	2	5	-26	-15	-21	-20	-17	-24	-30	23	16	11
50000	61	1	6	3	4	3	6	10	6	3	10	2	5	-27	-15	-22	-20	-19	-28	-39	25	16	15
90000	60	1	6	3	4	3	6	10	6	3	10	2	5	-25	-15	-20	-20	-12	-21	-31	31	26	24
140000	61	1	5	2	3	2	5	8	5	2	8	1	4	-20	-12	-17	-16	-4	-17	-29	35	32	31
180000	59	1	5	2	3	3	5	9	5	3	9	1	4	-22	-13	-18	-17	-1	-19	-33	31	29	32
200000	59	1	5	2	3	2	4	8	5	2	8	1	4	-20	-12	-17	-16	2	-20	-36	28	28	34
230000	60	1	5	2	3	2	5	8	4	2	8	1	4	-20	-12	-16	-15	7	-21	-41	25	28	39

Number of cycles	**Stresses** [N/mm^2]																						
	23	**24**	**25**	**26**	**27**	**28**	**29**	**30**	**31**	**32**	**33**	**34**	**35**	**36**	**37**	**38**	**39**	**40**	**41**	**42**	**43**	**44**	**45**	**46**
initial test	15	16	22	18	-23	-22	-25	-20	20	14	-3	-8	-12	-11	-9	-9	-13	-8	-14	-6	-10	-10	-11	-8
50000	15	17	21	22	-24	-26	-30	-22	21	16	-1	-11	-13	-11	-11	-9	-16	-9	-17	-7	-11	-11	-13	-10
90000	25	24	28	30	-16	-17	-22	-14	27	26	7	-1	-5	-3	-2	-2	-6	-1	-7	1	-2	-2	-4	-2
140000	35	28	30	35	-12	-13	-17	-9	29	36	12	4	1	3	2	2	-1	4	-3	7	5	4	1	4
180000	38	25	25	31	-13	-13	-18	-11	25	41	11	2	0	1	0	1	-2	2	-4	5	1	1	-1	1
200000	41	24	22	30	-14	-13	-18	-12	22	44	12	0	0	0	-1	1	-2	1	-5	4	1	0	-2	1
230000	47	23	18	29	-15	-12	-17	-12	18	50	13	-1	2	1	-3	0	-2	0	-5	4	2	1	-3	0

Table A.7: Stresses calculated for S6 specimen under Q_{min}= 61 kN.

Number of cycles	**Force [kN]**	**Stresses** [N/mm^2]																					
		1	**2**	**3**	**4**	**5**	**6**	**7**	**8**	**9**	**10**	**11**	**12**	**13**	**14**	**15**	**16**	**17**	**18**	**19**	**20**	**21**	**22**
initial test	611	11	59	25	38	31	58	102	67	30	102	16	51	-263	-153	-212	-209	-149	-217	-282	258	193	141
50000	611	11	60	25	38	32	59	102	66	31	103	16	51	-265	-154	-214	-209	-151	-215	-286	259	195	140
90000	610	11	59	25	38	31	59	102	66	30	102	16	51	-262	-153	-212	-209	-143	-208	-277	265	203	149
140000	610	10	59	24	37	30	58	100	64	30	100	14	51	-257	-151	-209	-204	-137	-202	-274	268	211	156
180000	610	10	60	24	37	31	59	101	64	30	101	14	53	-259	-154	-212	-206	-138	-203	-278	265	209	159
200000	610	9	61	24	37	30	59	101	64	30	101	13	53	-257	-155	-211	-204	-138	-205	-280	262	205	162
230000	610	8	61	24	37	30	59	101	63	30	100	10	55	-254	-155	-211	-201	-136	-199	-281	256	211	167

Number of cycles	**Stresses** [N/mm^2]																						
	23	**24**	**25**	**26**	**27**	**28**	**29**	**30**	**31**	**32**	**33**	**34**	**35**	**36**	**37**	**38**	**39**	**40**	**41**	**42**	**43**	**44**	**45**	**46**
initial test	167	192	230	207	-199	-197	-225	-179	226	162	7	-51	-92	-75	-66	-63	-101	-47	-117	-28	-80	-69	-75	-67
50000	166	192	228	205	-199	-199	-229	-178	225	162	9	-54	-91	-74	-68	-62	-102	-46	-120	-25	-80	-66	-76	-70
90000	176	199	235	213	-191	-190	-219	-171	231	172	17	-44	-82	-65	-59	-55	-93	-38	-110	-17	-71	-57	-68	-62
140000	188	202	236	216	-186	-186	-215	-164	231	186	23	-39	-77	-59	-54	-51	-88	-32	-107	-10	-64	-50	-61	-56
180000	195	201	231	213	-189	-186	-217	-167	227	195	22	-41	-79	-60	-56	-53	-90	-34	-109	-12	-68	-53	-64	-59
200000	201	198	226	212	-190	-186	-217	-168	222	201	22	-42	-79	-61	-57	-53	-90	-35	-109	-13	-69	-53	-64	-59
230000	210	197	218	208	-190	-185	-216	-167	213	213	23	-44	-78	-61	-57	-53	-90	-35	-110	-12	-69	-52	-64	-60

Table A.8: Stresses calculated for S6 specimen under Q_{max}= 610 kN.

Number of cycles	Force [kN]	Stresses [N/mm^2]																					
		1	**2**	**3**	**4**	**5**	**6**	**7**	**8**	**9**	**10**	**11**	**12**	**13**	**14**	**15**	**16**	**17**	**18**	**19**	**20**	**21**	**22**
initial test	550	10	53	22	34	28	52	92	60	27	92	14	46	-238	-138	-192	-189	-132	-193	-252	235	176	129
50000	550	10	53	22	34	28	53	92	60	27	92	14	46	-238	-138	-192	-189	-131	-187	-247	234	178	125
90000	550	10	54	22	34	28	53	92	59	27	92	14	46	-237	-139	-192	-189	-132	-187	-246	234	177	125
140000	550	9	54	22	34	28	54	92	59	27	92	13	47	-237	-139	-192	-188	-133	-184	-245	233	179	125
180000	551	9	55	22	34	28	54	93	59	27	93	12	48	-237	-141	-194	-189	-137	-184	-245	234	180	127
200000	551	8	56	22	34	28	54	93	59	27	93	12	49	-237	-142	-195	-188	-140	-185	-243	234	177	128
230000	550	7	57	22	34	27	54	93	58	27	92	9	51	-235	-143	-195	-186	-143	-178	-240	232	183	129
Max. diff.[%]		40	7	2	2	4	5	2	3	2	1	59	11	-1	-3	-2	-2	-8	-8	-5	2	4	4
Aver.		**9**	**55**	**22**	**34**	**28**	**53**	**93**	**59**	**27**	**93**	**13**	**48**	**-237**	**-140**	**-193**	**-189**	**-135**	**-186**	**-246**	**234**	**178**	**127**
Std dev.		1.1	1.3	0.2	0.3	0.4	0.9	0.6	0.7	0.2	0.4	1.9	1.9	1.0	2.0	1.3	1.1	4.6	4.5	3.6	1.2	2.2	1.8

Number of cycles	Stresses [N/mm^2]																							
	23	**24**	**25**	**26**	**27**	**28**	**29**	**30**	**31**	**32**	**33**	**34**	**35**	**36**	**37**	**38**	**39**	**40**	**41**	**42**	**43**	**44**	**45**	**46**
initial test	152	176	208	190	-176	-175	-200	-160	206	148	9	-43	-80	-64	-57	-54	-88	-39	-103	-22	-70	-59	-64	-58
50000	151	175	207	183	-175	-173	-198	-156	204	146	10	-43	-77	-62	-56	-53	-87	-37	-103	-18	-69	-54	-63	-60
90000	151	175	207	183	-175	-173	-198	-156	204	146	10	-43	-77	-62	-56	-53	-86	-37	-103	-18	-69	-55	-63	-60
140000	153	174	205	181	-174	-173	-198	-155	202	149	10	-43	-78	-62	-56	-53	-87	-36	-104	-17	-69	-54	-63	-60
180000	157	175	205	182	-175	-174	-199	-156	202	154	11	-43	-79	-62	-56	-53	-88	-36	-105	-17	-70	-54	-63	-60
200000	160	174	204	182	-176	-174	-199	-156	200	157	10	-43	-79	-61	-55	-53	-88	-36	-104	-17	-70	-54	-62	-61
230000	164	173	200	179	-175	-173	-199	-155	196	163	10	-42	-80	-61	-54	-53	-88	-35	-105	-16	-71	-54	-61	-60
Max. diff. [%]	9	2	4	6	-1	-1	-1	-3	5	12	14	-2	-3	-5	-4	-2	-2	-11	-2	-27	-3	-9	-5	-4
Aver.	**155**	**175**	**205**	**183**	**-175**	**-174**	**-199**	**-156**	**202**	**152**	**10**	**-43**	**-79**	**-62**	**-56**	**-53**	**-87**	**-37**	**-104**	**-18**	**-70**	**-55**	**-63**	**-60**
Std dev.	4.8	0.8	2.7	3.5	0.7	0.8	0.7	1.5	3.4	6.6	0.5	0.3	1.1	1.1	0.8	0.4	0.8	1.3	0.8	1.9	0.8	2.0	1.0	0.8

Table A.9: Stresses calculated for S6 specimen under ΔQ= 550 kN.

- **S7 specimen**
  - **Stresses deduced from strains under** Q_{min}= **61 kN**
  - **Stresses deduced from strains under** Q_{max}= **610 kN**
  - **Stresses deduced from strains under** Q_{max} **-** Q_{min}= **550 kN** (subtraction of the second table from the first one)

Number of cycles	**Force [kN]**	**Stresses** [N/mm^2]																					
		1	**2**	**3**	**4**	**5**	**6**	**7**	**8**	**9**	**10**	**11**	**12**	**13**	**14**	**15**	**16**	**17**	**18**	**19**	**20**	**21**	**22**
initial test	61	2	6	3	3	4	6	10	7	5	10	-	-	-21	-12	-17	-16	-120	-8	-100	26	-69	34
50000	60	2	6	3	3	4	6	10	7	4	10	-	-	-21	-12	-17	-16	-12	-14	-21	20	17	11
85000	60	1	3	2	2	2	3	5	4	2	5	-	-	-12	-6	-9	-9	-6	-8	-12	11	10	6

Number of cycles	**Stresses** [N/mm^2]																						
	23	**24**	**25**	**26**	**27**	**28**	**29**	**30**	**31**	**32**	**33**	**34**	**35**	**36**	**37**	**38**	**39**	**40**	**41**	**42**	**43**	**44**	**45**	**46**
initial test	102	-29	-92	-27	-123	-134	-30	-132	100	-60	17	-113	38	8	-157	-96	11	-114	16	-23	-117	-82	-1	-21
50000	12	14	19	16	-16	-14	-17	-14	18	12	-	-3	-5	-4	-3	-4	-6	-2	-8	-1	-4	-3	-4	-4
85000	7	8	10	9	-9	-8	-9	-7	10	7	-	-2	-3	-2	-2	-2	-3	-1	-4	0	-3	-1	-2	-3

Table A.10: Stresses calculated for S7 specimen under Q_{min}= 61 kN.

Number of cycles	**Force [kN]**	**Stresses** [N/mm^2]																					
		1	**2**	**3**	**4**	**5**	**6**	**7**	**8**	**9**	**10**	**11**	**12**	**13**	**14**	**15**	**16**	**17**	**18**	**19**	**20**	**21**	**22**
initial test	610	25	75	36	42	55	78	128	84	57	126	-	-	-267	-146	-209	-200	-251	-174	-348	257	127	163
50000	610	24	75	36	42	55	78	128	83	57	126	-	-	-265	-145	-208	-199	-142	-179	-267	249	212	140
85000	610	22	74	35	40	53	75	123	80	55	121	-	-	-256	-139	-201	-192	-136	-173	-258	240	204	136

Number of cycles	**Stresses** [N/mm^2]																						
	23	**24**	**25**	**26**	**27**	**28**	**29**	**30**	**31**	**32**	**33**	**34**	**35**	**36**	**37**	**38**	**39**	**40**	**41**	**42**	**43**	**44**	**45**	**46**
initial test	245	141	124	158	-308	-297	-226	-290	314	84	25	-151	-22	-39	-194	-138	-59	-136	-72	-29	-171	-125	-43	-67
50000	155	184	233	200	-201	-176	-213	-171	231	157	-	-41	-65	-51	-40	-46	-76	-24	-95	-6	-57	-45	-46	-51
85000	152	177	223	192	-193	-170	-204	-165	219	158	-	-40	-63	-49	-38	-44	-73	-23	-91	-5	-55	-43	-44	-49

Table A.11: Stresses calculated for S7 specimen under Q_{max}= 610 kN.

Number of cycles	**Force [kN]**	**Stresses** [N/mm^2]																					
		1	**2**	**3**	**4**	**5**	**6**	**7**	**8**	**9**	**10**	**11**	**12**	**13**	**14**	**15**	**16**	**17**	**18**	**19**	**20**	**21**	**22**
initial test	550	23	69	33	39	51	72	118	77	53	116	-	-	-245	-134	-192	-184	-131	-166	-248	230	196	130
50000	550	22	69	34	39	51	71	118	77	52	116	-	-	-243	-133	-191	-183	-130	-165	-246	229	195	129
85000	550	21	70	34	39	51	71	118	77	52	116	-	-	-244	-133	-192	-183	-130	-165	-246	229	195	130
Max. diff.[%]		8	2	0	1	0	0	0	1	1	0	-	-	-1	-1	0	-1	0	0	-1	1	0	0
Aver.		**22**	**69**	**33**	**39**	**51**	**72**	**118**	**77**	**52**	**116**	-	-	**-244**	**-133**	**-192**	**-183**	**-131**	**-166**	**-247**	**230**	**195**	**129**
Std dev.		0.9	0.9	0.0	0.2	0.1	0.0	0.3	0.3	0.2	0.2	-	-	1.0	0.5	0.4	0.6	0.3	0.3	0.8	0.7	0.5	0.5

Number of cycles	**Stresses** [N/mm^2]																							
	23	**24**	**25**	**26**	**27**	**28**	**29**	**30**	**31**	**32**	**33**	**34**	**35**	**36**	**37**	**38**	**39**	**40**	**41**	**42**	**43**	**44**	**45**	**46**
initial test	143	171	216	185	-185	-164	-196	-158	215	144	8	-38	-60	-47	-37	-42	-70	-22	-87	-5	-53	-42	-42	-46
50000	143	170	215	184	-184	-162	-195	-157	213	145	0	-38	-60	-47	-37	-42	-70	-22	-87	-5	-52	-42	-42	-46
85000	145	169	213	183	-184	-162	-195	-157	209	151	0	-38	-60	-47	-37	-42	-70	-22	-87	-5	-53	-42	-42	-46
Max. diff. [%]	2	1	1	1	-1	-1	0	-1	3	4	-	0	0	-1	-1	0	0	-1	0	-7	-1	-1	-1	0
Aver.	**143**	**170**	**214**	**184**	**-184**	**-163**	**-196**	**-157**	**212**	**147**	**3**	**-38**	**-60**	**-47**	**-37**	**-42**	**-70**	**-22**	**-87**	**-5**	**-53**	**-42**	**-42**	**-46**
Std dev.	1.5	0.6	1.3	0.9	0.5	0.8	0.4	0.5	2.8	3.7	4.5	0.1	0.0	0.2	0.1	0.1	0.1	0.2	0.0	0.2	0.4	0.1	0.3	0.0

Table A.12: Stresses calculated for S7 specimen under ΔQ= 550 kN.

A.3.4 Structural truss model

S6 specimen

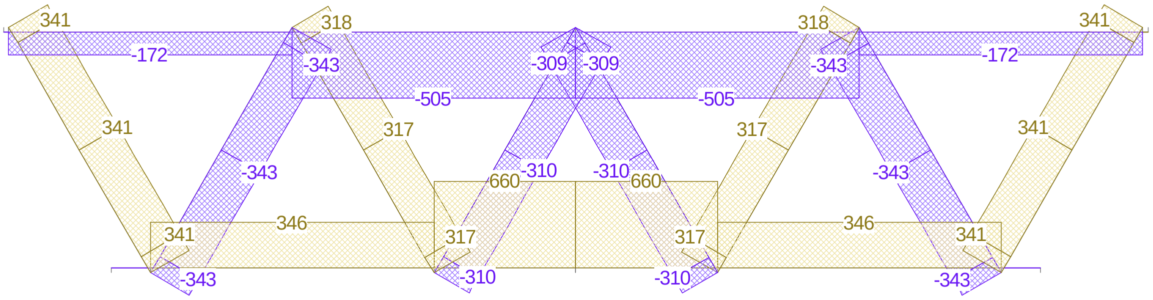
341
318
318
341
-172
-343
-309
-309
-343
-172
-505
-505
341
317
317
341
-343
660
-310
-310
660
-343
341
346
317
317
346
341
-343
-310
-310
-343

Figure A.6: Structural truss model for S6 specimen: axial force in kN given under dead weight and $\Delta Q = 550$ kN (scale 1:60).

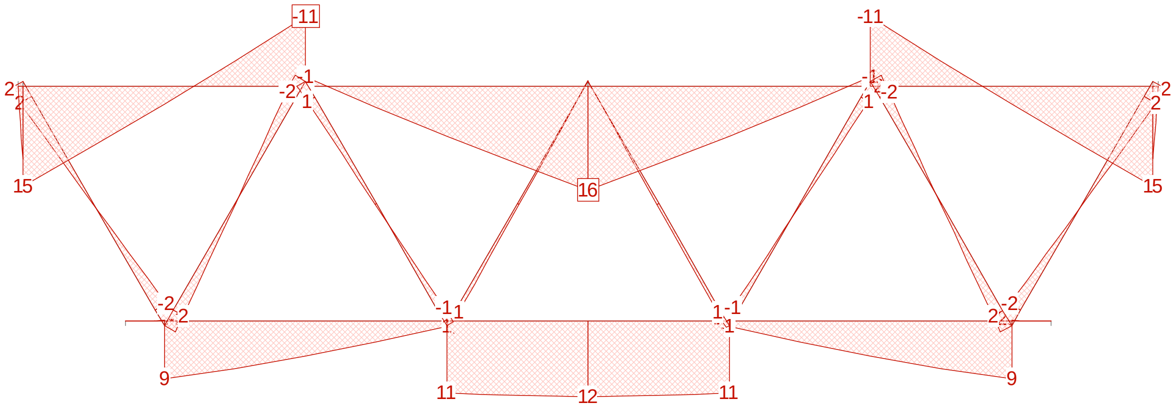
-11
-11
2
2
-2
1
1
-1
-2
1
2
2
15
16
15
-2
2
-1
1
1
-1
1
1
2
-2
9
11
12
11
9

Figure A.7: Structural truss model for S6 specimen: bending moment in kN.m given under dead weight and $\Delta Q = 550$ kN (scale 1:60).

- **S7 specimen**

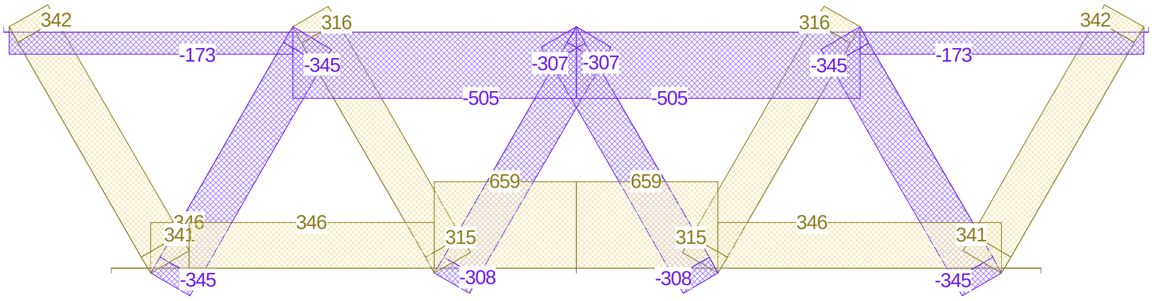
342
316
-173
-345
-307
-307
-505
-505
316
-345
-173
342
659
659
346
341
346
315
315
346
341
-345
-308
-308
-345

Figure A.8: Structural truss model for S7 specimen: axial force in kN given under dead weight and $\Delta Q = 550$ kN (scale 1:60).

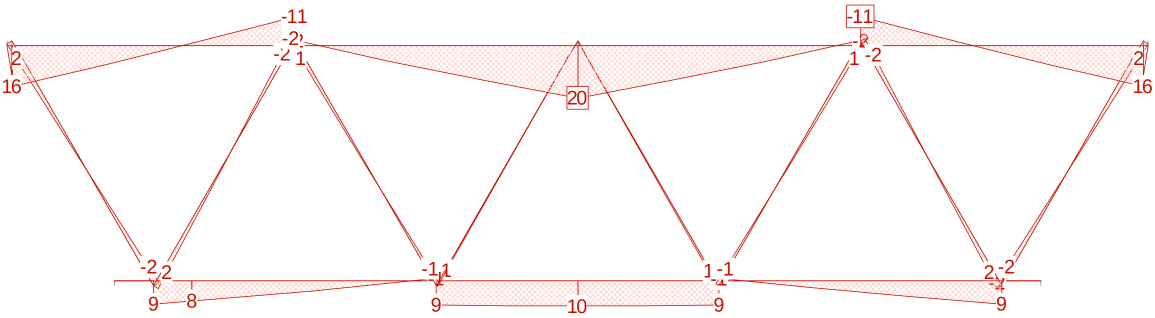
-11
-2
-2
1
2
16
20
-11
-2
1
-2
2
16
-2
2
-1
1
1
-1
2
-2
9
8
9
10
9
9

Figure A.9: Structural truss model for S7 specimen: bending moment in kN.m given under dead weight and $\Delta Q = 550$ kN (scale 1:60).

A.3.5 Nominal-to-axial stress ratio

Table A.13: Values of nominal-to-axial stress ratio for different geometries of joints 1 (at hs1), 3N (at hs1) and 5N (at hs1c).

									Nominal-to-axial stress ratio		
D	**T**	**d**	**t**	θ	α	β	γ	τ	**J1**	**J3N**	**J5N**
250	30	133	7	60	25	0.53	4.21	0.25	1.15	1.25	1.23
250	30	133	12.5	60	25	0.53	4.21	0.4	1.17	1.29	1.24
250	30	133	20	60	25	0.53	4.21	0.63	1.18	1.34	1.26
250	30	121	12.5	60	25	0.48	4.21	0.4	1.15	1.26	1.22
250	30	133	12.5	60	25	0.53	4.21	0.4	1.17	1.29	1.24
250	30	152.4	12.5	60	25	0.6	4.21	0.4	1.19	1.33	1.27
250	30	133	12.5	60	25	0.53	4.21	0.4	1.17	1.29	1.24
250	17.5	133	7.1	60	25	0.53	6.83	0.4	1.16	1.27	1.23
250	14.2	133	5.6	60	25	0.53	9	0.4	1.16	1.26	1.23
250	8.8	133	3.6	60	25	0.53	15	0.4	1.15	1.25	1.23
168	20	89	5	60	25	0.53	4.21	0.25	1.17	1.28	1.25
168	20	89	8	60	25	0.53	4.21	0.4	1.19	1.32	1.26
168	20	89	12.5	60	25	0.53	4.21	0.63	1.21	1.38	1.28
168	20	82.5	8	60	25	0.48	4.21	0.4	1.17	1.30	1.25
168	20	89	8	60	25	0.53	4.21	0.4	1.19	1.32	1.26
168	20	101.6	8	60	25	0.6	4.21	0.4	1.22	1.37	1.30
168	20	89	8	60	25	0.53	4.21	0.4	1.19	1.32	1.26
168	12.5	89	5	60	25	0.53	6.83	0.4	1.17	1.31	1.26
168	10	89	4	60	25	0.53	9	0.4	1.17	1.30	1.26
168	5.6	89	2.3	60	25	0.53	15	0.4	1.17	1.30	1.25
250	30	133	12.5	60	27.3	0.53	4.21	0.4	1.17	1.29	1.24
250	30	133	12.5	60	17.4	0.53	4.21	0.4	1.24	1.42	1.34
250	30	133	12.5	60	10	0.53	4.21	0.4	1.36	1.43	1.47
168	20	89	8	60	25.8	0.53	4.21	0.4	1.19	1.32	1.26
168	20	89	8	60	14.9	0.53	4.21	0.4	1.29	1.39	1.45
168	20	89	8	60	10	0.53	4.21	0.4	1.4	1.5	1.53

A.3.6 Hot-spot stresses

Table A.14: SCFs obtained for each joint from a linear interpolation of SCF table values (Schumacher et al., 2003) (at location hs1).

Joint	β	γ	τ	SCF_{ax-br}	SCF_{ipb-br}	SCF_{ax-ch}	SCF_{ipb-ch}
S6-3S	0.53	2.81	0.27	0.70	0.48	1.20	1.25
S6-3N	0.53	2.81	0.27	0.70	0.48	1.20	1.25
S6-1	0.53	2.81	0.27	0.70	0.48	1.20	1.25
S6-2	0.53	2.81	0.27	0.70	0.48	1.20	1.25
S6-5S	0.53	4.21	0.4	1.11	0.74	1.30	1.38
S6-5N	0.53	4.21	0.4	1.11	0.74	1.30	1.38
S7-3S	0.53	4.21	0.4	1.11	0.74	1.30	1.38
S7-3N	0.53	4.21	0.4	1.11	0.74	1.30	1.38
S7-1	0.53	4.21	0.4	1.11	0.74	1.30	1.38
S7-2	0.53	4.21	0.4	1.11	0.74	1.30	1.38
S7-5S	0.53	2.81	0.27	0.70	0.48	1.20	1.25
S7-5N	0.53	2.81	0.27	0.70	0.48	1.20	1.25

Table A.15: Total SCFs obtained for each joint at location hs1 for the crown toe on the tension side (tension brace and chord side tension brace).

Joint	**Stress partition of total**		**Stress partition in members**				SCF	SCF
	$\frac{\Delta\sigma_{nom-br}}{\Delta\sigma_{tot\ nom}}$	$\frac{\Delta\sigma_{nom-ch}}{\Delta\sigma_{tot\ nom}}$	$\frac{\Delta\sigma_{ax-br}}{\Delta\sigma_{nom-br}}$	$\frac{\Delta\sigma_{ipb-br}}{\Delta\sigma_{nom-br}}$	$\frac{\Delta\sigma_{ax-ch}}{\Delta\sigma_{nom-ch}}$	$\frac{\Delta\sigma_{ipb-ch}}{\Delta\sigma_{nom-ch}}$	$_{tot,1}$	$_{tot,1,cor}$
S6-3S	1.00	0.00	0.75	0.25	0.00	1.00	0.65	**0.55**
S6-3N	1.00	0.00	0.75	0.25	0.00	1.00	0.65	**0.55**
S6-1	0.90	0.10	0.83	0.17	1.14	-0.14	0.72	**0.61**
S6-2	0.89	0.11	0.83	0.17	1.13	-0.13	0.72	**0.62**
S6-5S	1.36	-0.36	0.73	0.27	1.04	-0.04	0.91	**0.78**
S6-5N	1.36	-0.36	0.74	0.26	1.04	-0.04	0.92	**0.78**
S7-3S	1.00	0.00	0.73	0.27	0.00	1.00	1.01	**0.87**
S7-3N	1.00	0.00	0.73	0.27	0.00	1.00	1.01	**0.87**
S7-1	0.86	0.14	0.79	0.21	1.01	0.00	1.07	**0.92**
S7-2	0.86	0.14	0.79	0.21	1.01	0.00	1.07	**0.92**
S7-5S	1.22	-0.22	0.74	0.26	1.08	-0.1	0.52	**0.45**
S7-5N	1.23	-0.23	0.74	0.26	1.08	-0.1	0.52	**0.44**

Table A.16: Total SCFs obtained for each joint at location hs1 for the crown toe on the compression side (compression brace and chord side compression brace).

Joint	**Stress partition of total**		**Stress partition in members**				SCF	SCF
	$\frac{\Delta\sigma_{nom-br}}{\Delta\sigma_{tot\ nom}}$	$\frac{\Delta\sigma_{nom-ch}}{\Delta\sigma_{tot\ nom}}$	$\frac{\Delta\sigma_{ax-br}}{\Delta\sigma_{nom-br}}$	$\frac{\Delta\sigma_{ipb-br}}{\Delta\sigma_{nom-br}}$	$\frac{\Delta\sigma_{ax-ch}}{\Delta\sigma_{nom-ch}}$	$\frac{\Delta\sigma_{ipb-ch}}{\Delta\sigma_{nom-ch}}$	$_{tot,1c}$	$_{tot,1c,cor}$
S6-3S	1.02	-0.02	0.75	0.25	6.62	-5.62	0.64	**0.55**
S6-3N	1.03	-0.03	0.75	0.25	5.00	-4.00	0.64	**0.54**
S6-1	1.19	-0.19	1.01	-0.01	2.15	-1.15	0.62	**0.53**
S6-2	1.19	-0.19	1.01	-0.01	2.20	-1.20	0.62	**0.53**
S6-5S	0.84	0.16	0.73	0.27	0.32	0.68	1.07	**0.91**
S6-5N	0.84	0.16	0.73	0.27	0.32	0.68	1.07	**0.91**
S7-3S	1.08	-0.08	0.73	0.27	2.37	-1.37	1.00	**0.85**
S7-3N	1.08	-0.08	0.73	0.27	2.37	-1.37	1.00	**0.85**
S7-1	1.38	-0.38	0.95	0.05	1.67	-0.67	1.03	**0.88**
S7-2	1.38	-0.38	0.95	0.05	1.67	-0.67	1.04	**0.89**
S7-5S	0.85	0.15	0.72	0.28	0.38	0.62	0.73	**0.62**
S7-5N	0.85	0.15	0.72	0.28	0.38	0.62	0.73	**0.62**

A.4 Dimensions and shape of the cracks

Table A.17: Crack shapes of specimen S6 in function of cycle numbers (N_3 is the number of cycles to through-thickness cracking). The gray line corresponds to the critical crack.

Joint n° (specimen S6)	Brace side	Ink marking at N = 90000 cycles			Beach marking at N = 140000 cycles			Joint open at N_3 [*]= 242000 cycles			
		a [mm]	2c [mm]	a/c	a [mm]	2c [mm]	a/c	a [mm]	2c [mm]	a/c	Φ [°]
S6-3S	tensile	8	52	0.31	16	80	0.4	25	240	0.21	48
(T=30 mm)	compressive	[†]			[‡]			5	40	0.25	50
S6-3N	tensile	7	46	0.3	15	75	0.4	25	125	0.4	40
(T=30 mm)	compressive	[†]			[‡]			11	60	0.37	40
S6-1	tensile	4	28	0.29	8	42	0.38	19	100	0.38	40
(T=30 mm)	compressive	[†]			[‡]			2	10	0.4	35
S6-2	tensile	3	48	0.13	9	60	0.3	20	110	0.36	40
(T=30 mm)	compressive	[†]			[‡]			4	27	0.3	35
S6-5S	tensile	[†]			[‡]			11	60	0.37	30
(T=20 mm)	compressive	[†]			[‡]			11	85	0.26	40
S6-5N	tensile	[†]			[‡]			12	70	0.34	40
(T=20 mm)	compressive	[†]			[‡]			16	100	0.32	30

[*] N_3 is the number of cycles to through-thickness cracking.

[†] not marked.

[‡] beach-mark not identifiable.

Table A.18: Crack shapes of specimen S7 in function of cycle numbers (N_3 is the number of cycles to through-thickness cracking). The gray line corresponds to the critical crack.

Joint n° (specimen S7)	**Brace side**	**Insp. at 50000 c.**	**Ink marking at N = 90000 cycles**			**Joint open at N_3 [*] = 111000 cycles**			
		2c [mm]	**a [mm]**	**2c [mm]**	**a/c**	**a [mm]**	**2c [mm]**	**a/c**	**Φ [°]**
S7-3S	tensile	45	20	100	0.4	35	225	0.31	48
(T=20 mm)	compressive		[†]			1	20	0.1	
S7-3N	tensile	35	18	115	0.31	27	150	0.36	38
(T=20 mm)	compressive		[†]			1	13	0.15	
S7-1	tensile		[†]			12	85	0.28	38
(T=20 mm)	compressive		[†]			2	22	0.18	35
S7-2	tensile	20	10	85	0.24	16	90	0.36	40
(T=20 mm)	compressive		[†]			3	24	0.25	45
S7-5S	tensile		[†]			0.5	13	0.1	
(T=30 mm)	compressive		[†]			1	18	0.1	
S7-5N	tensile		[†]			1	17	0.12	
(T=30 mm)	compressive		[†]			5.5	35	0.31	40

[*] N_3 is the number of cycles to through-thickness cracking.

[†] not marked.

Table A.19: Load cases and stresses applied on S6 joints with photos of final cracks obtained.

S6 Joint n° **/load case**	**Total idealized nominal stress range** $\Delta\sigma_{totnom}$ [N/mm^2] *	**Hot-Spot stress calculated** [N/mm^2]	**Crack photos**		**Cracks ordered from greater to smaller (depth a)**
Joint S6-3S 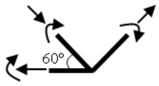	251	$\Delta\sigma_{hs,1}$= 139	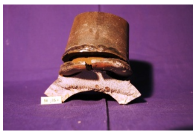	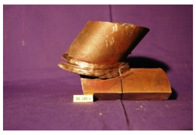	N°1
	-247	$\Delta\sigma_{hs,1c}$= -135	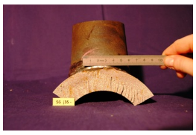		N°5 bis
Joint S6-3N 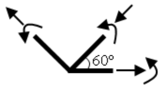	251 -245	$\Delta\sigma_{hs,1}$= 139 $\Delta\sigma_{hs,1c}$= -133	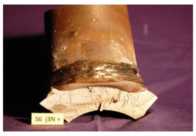	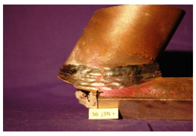	N°1 bis N°5
Joint S6-1 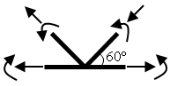	242 -144	$\Delta\sigma_{hs,1}$= 148 $\Delta\sigma_{hs,1c}$= -76	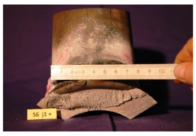	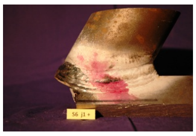	N°2 bis N°6 bis
Joint S6-2 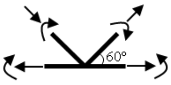	241 -145	$\Delta\sigma_{hs,1}$= 148 $\Delta\sigma_{hs,1c}$= -77	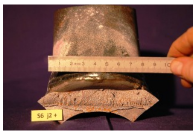		N°2 N°6
Joint S6-5S 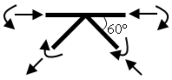	177	$\Delta\sigma_{hs,1}$= 139	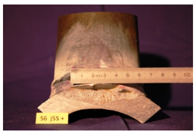	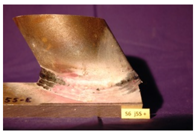	N°4 bis
	-310	$\Delta\sigma_{hs,1c}$= -284	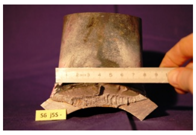	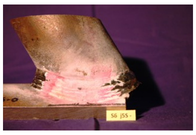	N°3 bis
Joint S6-5N 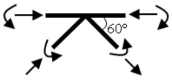	180	$\Delta\sigma_{hs,1}$= 141	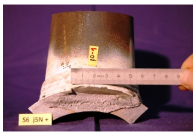	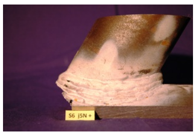	N°4
	-310	$\Delta\sigma_{hs,1c}$= -284	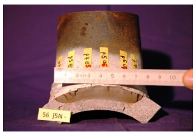	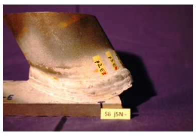	N°3

* stresses deducted from measured strains.

Table A.20: Load cases and stresses applied on S7 joints with photos of final cracks obtained.

S7 Joint n° /load case	**Total idealized nominal stress range** $\Delta\sigma_{totnom}$ [N/mm^2] *	**Hot-Spot stress calculated** [N/mm^2]	**Crack photos**	**Cracks ordered from greater to smaller (depth a)**
Joint S7-3S 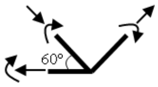	260 -241	$\Delta\sigma_{hs,1}$= 225 $\Delta\sigma_{hs,1c}$= -205	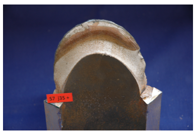 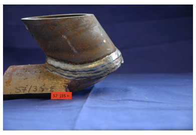	N°1 N°5
Joint S7-3N 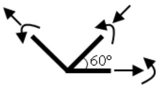	260 -241	$\Delta\sigma_{hs,1}$= 225 $\Delta\sigma_{hs,1c}$= -205	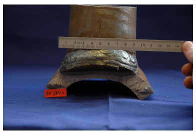	N°1 bis N°5 bis
Joint S7-1 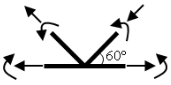	262	$\Delta\sigma_{hs,1}$= 240	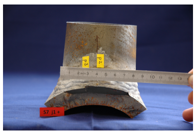 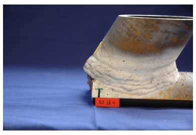	N°2 bis
	-133	$\Delta\sigma_{hs,1c}$= -117	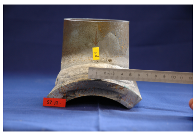	N°4 bis
Joint S7-2 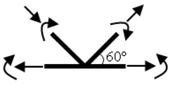	262	$\Delta\sigma_{hs,1}$= 240	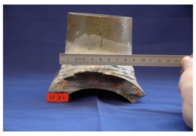 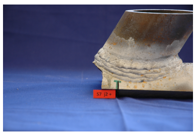	N°2
	-133	$\Delta\sigma_{hs,1c}$= -118	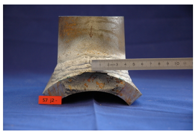	N°4
Joint S7-5S 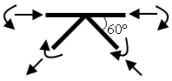	199	$\Delta\sigma_{hs,1}$= 89		N°6 bis
	-309	$\Delta\sigma_{hs,1c}$= -192	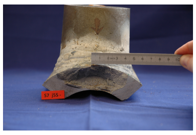	N°3 bis
Joint S7-5N 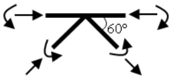	198	$\Delta\sigma_{hs,1}$= 88		N°6
	-309	$\Delta\sigma_{hs,1c}$= -192	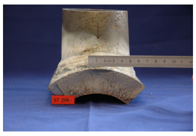	N°3

* stresses deducted from measured strains.

A.5 Crack depths recorded using the Alternating Current Potential Drop

Table A.21: Crack depths monitored using ACPD on specimen S6: probes 1 and 2 are situated in joint S6-J5N+, probes 3 to 8 are situated in joint S6-J5N-.

Number of cycles	**p1**	**p2**	**p3**	**p4**	**p5**	**p6**	**p7**	**p8**
10000	0	0	0	0	0	0.02	0.02	0
20000	0	0	0	0	0	0.03	0.02	0
30000	0.04	0	0	0	0	0.05	0.02	0.01
40000	0.07	0	0	0	0	0.07	0.06	0
50000	0.11	0	0.06	0	0.04	0.14	0.05	0.09
60000	0.15	0	0.1	0.03	0.07	0.27	0.08	0.19
70000	0.28	0	0.1	0.06	0.02	0.49	0.18	0.19
80000	0.45	0	0.1	0.05	0.05	0.82	0.3	0.19
90000	0.66	0	0.1	0.07	0.2	1.28	0.48	0.17
100000	0.95	0	0.1	0.07	0.53	1.8	0.68	0.18
110000	1.27	0.01	0.1	0.12	1.15	2.4	1.0	0.11
120000	1.59	0.03	0.1	0.17	2.0	3.0	1.4	0.1
130000	1.92	0.05	0.04	0.28	2.9	3.7	2.1	0.07
140000	2.24	0.08	0.02	0.39	3.8	4.5	3.1	0
150000	2.64	0.07	0.04	0.62	5.0	5.5	4.9	0.1
160000	3.05	0.11	0.11	1.07	6.2	6.6	6.6	0.25
170000	3.45	0.13	0.25	1.9	7.5	7.6	8.2	0.5
180000	3.85	0.18	0.48	3.5	8.8	8.7	9.8	0.9
190000	4.33	0.32	0.86	6.6	10.3	9.8	11.4	1.9
200000	4.9	0.62	1.62	9.0	11.5	10.9	12.8	3.7
210000	5.5	1.0	3.5	11.5	12.9	12.0	14.4	6.0
220000	6.2	1.5	6.2	13.2	14.1	13.1	15.9	7.9
230000	6.9	2.1	8.5	14.5	15.1	14.1	17.1	9.5
240000	7.7	2.8	10.7	15.7	16.2	15.0	18.3	10.8

Table A.22: Crack depths monitored using ACPD on specimen S7: probes 1 to 3 are situated in joint S7-J2, probes 4 to 8 are situated in joint S7-J5N.

Number of cycles	**p1**	**p2**	**p3**	**p4**	**p5**	**p6**	**p7**	**p8**
10000	0.03	0.02	0.01	0	0.02	0	0.02	0
20000	0.03	0.11	0.01	0	0.02	0	0.02	0.02
30000	0.04	0.29	0.01	0	0.02	0.02	0.02	0.02
40000	0.07	0.64	0.04	0	0	0.05	0.06	0.02
50000	0.13	1.3	0.15	0	0.55	0.07	0.05	0.03
60000	0.16	2.3	0.29	0.03	0.5	0.15	0.08	0.03
70000	0.17	3.3	0.64	0.06	0.5	0.2	0.18	0.04
80000	0.27	4.5	1.33	0.07	0.5	0.3	0.3	0.05
90000	0.31	6.1	2.63	0.1	0.5	0.55	0.48	0.07
100000	0.4	8.3	4.9	0.11	0.5	0.8	0.68	0.15
110000	1.52	10.9	7.7	0.18	0.52	2.4	1.2	0.17

Appendix B

Hole-Drilling Theory

B.1 Initial stress state (before drilling)

As shown in Fig. B.1 a **thin** plate with an infinite surface is subjected to a tensile **uniform stress**, representing uniaxial residual stress σ.

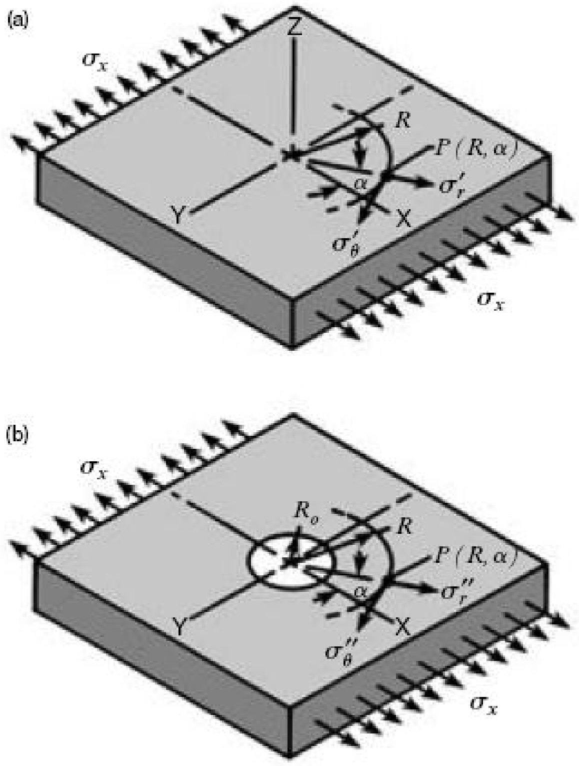
(a)
σ_x
Z
R
$P\,(R, \alpha)$
σ'_r
α
Y
X
σ'_θ
σ_x
(b)
σ_x
R_o
R
$P\,(R, \alpha)$
σ''_r
α
Y
X
σ''_θ
σ_x

Figure B.1: Stress states before and after the hole is drilled (Vishay Measurements, 1996).

This initial stress state can be expressed in polar coordinates (r, θ) after changing the coordinate system:

$$\begin{bmatrix} \sigma_r & \tau_{r\theta} \\ \sigma_{\theta r} & \sigma_\theta \end{bmatrix} = \begin{bmatrix} \cos\theta & \sin\theta \\ -\sin\theta & \cos\theta \end{bmatrix} \begin{bmatrix} \sigma & 0 \\ 0 & 0 \end{bmatrix} \begin{bmatrix} \cos\theta & -\sin\theta \\ \sin\theta & \cos\theta \end{bmatrix}$$

$$\Downarrow$$

$$\begin{cases} \sigma_r = & \sigma\cos^2\theta \\ \sigma_\theta = & \sigma\sin^2\theta \\ \tau_{r\theta} = & -\sigma\cos\theta\sin\theta \end{cases} \iff \begin{cases} \sigma_r = & \frac{\sigma}{2}(1+\cos 2\theta) \\ \sigma_\theta = & \frac{\sigma}{2}(1-\cos 2\theta) \\ \tau_{r\theta} = & -\frac{\sigma}{2}\sin 2\theta \end{cases} \tag{B.1}$$

B.2 Final stress state (after drilling)

After a 2a diameter hole has been drilled through the entire thickness of this plate, the stresses in the vicinity of the hole have changed because the stresses perpendicular to the free surface of the hole have been eliminated:

$$(\sigma_r)_{r=a} = 0 \qquad (\tau_{r\theta})_{r=a} = 0$$

In 1898, G. Kirsch (Kirsch, 1898) has presented the following solution for this case (thin wide plate under uniform plane stress):

$$\begin{cases} \sigma_r = & \frac{\sigma}{2}(1-\frac{a^2}{r^2}) + \frac{\sigma}{2}(1-\frac{a^2}{r^2})(1-\frac{3a^2}{r^2})\cos 2\theta \\ \sigma_\theta = & \frac{\sigma}{2}(1+\frac{a^2}{r^2}) - \frac{\sigma}{2}(1+\frac{3a^4}{r^4})\cos 2\theta \\ \tau_{r\theta} = & -\frac{\sigma}{2}(1-\frac{a^2}{r^2})(1+\frac{3a^2}{r^2})\sin 2\theta \end{cases} \tag{B.2}$$

We can note that, at the hole surface (r = a), $\sigma_\theta = \sigma(1 - 2\cos 2\theta)$ and its maximum value $\sigma_{\theta max} = 3\sigma$ is reached at $\theta = \pm\pi/2$

B.3 Stress and strain variation

Thus, by subtracting the initial from the final stresses in the plate, the stress variation at the distance r from the hole center can be obtained. This variation is also called stress relaxation induced by the drilling.

$$\begin{cases} \Delta\sigma_r = & -\frac{a^2}{r^2}\frac{\sigma}{2} + \frac{\sigma}{2}(\frac{3a^4}{r^4} - 4\frac{a^2}{r^2})\cos 2\theta \\ \Delta\sigma_\theta = & \frac{a^2}{r^2}\frac{\sigma}{2} - \frac{\sigma}{2}(\frac{3a^4}{r^4})\cos 2\theta \\ \Delta\tau_{r\theta} = & -\frac{\sigma}{2}(2\frac{a^2}{r^2} - \frac{3a^4}{r^4})\sin 2\theta \end{cases} \tag{B.3}$$

For an homogeneous and isotropic material with a linear-elastic behaviour, the strains inducing by the stresses variation can be obtained by means of the bidimensional Hooke's law:

$$\begin{cases} \varepsilon_r = & \frac{1}{E}(\sigma_r - \nu\sigma_\theta) = & -\frac{(1+\nu)}{E}\frac{a^2}{r^2}\frac{\sigma}{2} + \frac{\sigma}{2E}(\frac{3(1+\nu)a^4}{r^4} - 4\frac{a^2}{r^2})\cos 2\theta \\ \varepsilon_\theta = & \frac{1}{E}(\sigma_\theta - \nu\sigma_r) = & \frac{(1+\nu)}{E}\frac{a^2}{r^2}\frac{\sigma}{2} - \frac{\sigma}{2E}(\frac{3(1+\nu)a^4}{r^4} - 4\nu\frac{a^2}{r^2})\cos 2\theta \\ \gamma_{r\theta} = & \frac{1}{G}\tau_{r\theta} = & -\frac{1}{G}\frac{\sigma}{2}(2\frac{a^2}{r^2} - \frac{3a^4}{r^4})\sin 2\theta \end{cases} \tag{B.4}$$

where E and ν are the Young's modulus and the Poisson's ratio.

Since the strain gauge rosettes used for residual stress determination only measure the radial strain, the following equations will focus on the relaxed radial strains.

These strains can also be expressed as follows:

$$\varepsilon_r = \sigma(A + B\cos 2\theta) \qquad \begin{cases} A = & -\dfrac{(1+\nu)}{2E}\dfrac{a^2}{r^2} \\ B = & -\dfrac{(1+\nu)}{2E}\left(-\dfrac{3a^4}{r^4} + 4\dfrac{a^2}{(1+\nu)r^2}\right) \end{cases} \tag{B.5}$$

B.4 Strain variation under biaxial uniform stresses

The previous equations are available for uniaxial tensile residual stress. However, to represent the two principal residual stresses σ_{max} and σ_{min}, we superpose the radial strains induced by both of them. Obviously, the min-axis makes an angle of 90°with the max-axis.

$$\begin{aligned} \varepsilon_r = & \ \sigma_{max}(A + B\cos 2\theta) + \sigma_{min}(A + B\cos 2(\theta + \frac{\pi}{2})) \\ = & \ A(\sigma_{max} + \sigma_{min}) + B(\sigma_{max} - \sigma_{min})\cos 2\theta \end{aligned} \tag{B.6}$$

In the hole-drilling method, surface strains are measured by means of rosette composed of three electrical-resistance strain gauges placed around the drilling hole. As shown in Fig. B.2, one of the common rosette arrangement is the 45°rosette: direction of gauge 1 is the reference direction (the x-axis), gauge 2 is 45°or 135°clockwise of the reference and gauge 3 is 90°clockwise of the reference.

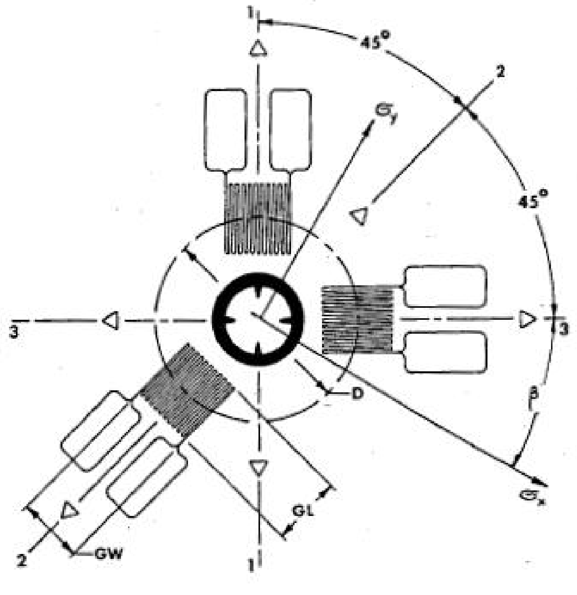

Figure B.2: Strain gauge rosette used for hole-drilling (ASTM, 2008).

As a consequence, if we introduce the radial measurements of gauges 1, 2 and 3 into equation (B.6), we can solve these three equations and find the magnitudes (σ_{max}, σ_{min}) and the directions (β) of the principal residual stresses.

$$\begin{cases} \varepsilon_{r,gauge1} = \varepsilon_1 & = A(\sigma_{max} + \sigma_{min}) + B(\sigma_{max} - \sigma_{min}) \cos 2\beta \\ \varepsilon_{r,gauge2} = \varepsilon_2 & = A(\sigma_{max} + \sigma_{min}) + B(\sigma_{max} - \sigma_{min}) \underbrace{\cos 2(-\frac{\pi}{4} + \beta)}_{= \sin 2\beta} \\ \varepsilon_{r,gauge3} = \varepsilon_3 & = A(\sigma_{max} + \sigma_{min}) + B(\sigma_{max} - \sigma_{min}) \underbrace{\cos 2(-\frac{\pi}{2} + \beta)}_{= -\cos 2\beta} \end{cases}$$

$$\Updownarrow$$

$$\begin{cases} A(\sigma_{max} + \sigma_{min}) = & & \dfrac{\varepsilon_1 + \varepsilon_3}{2} \\ -B(\sigma_{max} - \sigma_{min}) \cos 2\beta = & & \dfrac{\varepsilon_3 - \varepsilon_1}{2} \\ -B(\sigma_{max} - \sigma_{min}) \sin 2\beta = & A(\sigma_{max} + \sigma_{min}) - \varepsilon_2 = & \dfrac{\varepsilon_1 - 2\varepsilon_2 + \varepsilon_3}{2} \end{cases} \tag{B.7}$$

$$\Updownarrow$$

$$\begin{cases} \sigma_{max} = & \dfrac{(\sigma_{max} + \sigma_{min})}{2} + \dfrac{(\sigma_{max} - \sigma_{min})}{2} = \dfrac{\varepsilon_1 + \varepsilon_3}{4A} + \dfrac{1}{4B}\sqrt{(\varepsilon_3 - \varepsilon_1)^2 + (\varepsilon_1 - 2\varepsilon_2 + \varepsilon_3)^2} \\ \sigma_{min} = & \dfrac{(\sigma_{max} + \sigma_{min})}{2} - \dfrac{(\sigma_{max} - \sigma_{min})}{2} = \dfrac{\varepsilon_1 + \varepsilon_3}{4A} - \dfrac{1}{4B}\sqrt{(\varepsilon_3 - \varepsilon_1)^2 + (\varepsilon_1 - 2\varepsilon_2 + \varepsilon_3)^2} \\ \tan 2\beta = & \dfrac{\varepsilon_1 - 2\varepsilon_2 + \varepsilon_3}{\varepsilon_3 - \varepsilon_1} \end{cases}$$

$$\Updownarrow$$

$$\begin{cases} \sigma_{max} = & \dfrac{\varepsilon_1 + \varepsilon_3}{4A} + \dfrac{1}{4B}\sqrt{(\varepsilon_3 - \varepsilon_1)^2 + (\varepsilon_1 - 2\varepsilon_2 + \varepsilon_3)^2} \\ \sigma_{min} = & \dfrac{\varepsilon_1 + \varepsilon_3}{4A} - \dfrac{1}{4B}\sqrt{(\varepsilon_3 - \varepsilon_1)^2 + (\varepsilon_1 - 2\varepsilon_2 + \varepsilon_3)^2} \\ \tan 2\beta = & \dfrac{\varepsilon_1 - 2\varepsilon_2 + \varepsilon_3}{\varepsilon_3 - \varepsilon_1} \end{cases}$$

B.5 Coefficients taken into account the strain gauge area

In the previous equations, the coefficients A and B are defined at a point and do not take into account the average strain over the gauge area. Indeed, more satisfactory values of these coefficients, $\bar{A}$ and $\bar{B}$, can be calculated by integrating equations (B.4) over the gauges areas. It is also possible to obtain these values by experimental calibration.

Thus, the magnitudes (σ_{max}, σ_{min}) and the directions (β) of the principal residual stresses can be written as follows:

$$\begin{cases} \sigma_{max} = & \dfrac{\varepsilon_1 + \varepsilon_3}{4\bar{A}} + \dfrac{1}{4\bar{B}}\sqrt{(\varepsilon_3 - \varepsilon_1)^2 + (\varepsilon_1 - 2\varepsilon_2 + \varepsilon_3)^2} \\ \sigma_{min} = & \dfrac{\varepsilon_1 + \varepsilon_3}{4\bar{A}} - \dfrac{1}{4\bar{B}}\sqrt{(\varepsilon_3 - \varepsilon_1)^2 + (\varepsilon_1 - 2\varepsilon_2 + \varepsilon_3)^2} \\ \tan 2\beta = & \dfrac{\varepsilon_1 - 2\varepsilon_2 + \varepsilon_3}{\varepsilon_3 - \varepsilon_1} \end{cases} \tag{B.8}$$

Or by introducing new dimensionless and material-independent coefficients, $\bar{a}$ and $\bar{b}$:

$$\begin{aligned} \bar{a} &= -\frac{2E\bar{A}}{1+\nu} \\ \bar{b} &= -2E\bar{B} \end{aligned} \qquad \begin{cases} \sigma_{max} = & \dfrac{-E(\varepsilon_1+\varepsilon_3)}{2(1+\nu)\bar{a}} - \dfrac{E}{2\bar{b}}\sqrt{(\varepsilon_3-\varepsilon_1)^2+(\varepsilon_1-2\varepsilon_2+\varepsilon_3)^2} \\ \sigma_{min} = & \dfrac{-E(\varepsilon_1+\varepsilon_3)}{2(1+\nu)\bar{a}} + \dfrac{E}{2\bar{b}}\sqrt{(\varepsilon_3-\varepsilon_1)^2+(\varepsilon_1-2\varepsilon_2+\varepsilon_3)^2} \\ \tan 2\beta = & \dfrac{\varepsilon_1-2\varepsilon_2+\varepsilon_3}{\varepsilon_3-\varepsilon_1} \end{cases} \tag{B.9}$$

B.6 ASTM E837-8 formulations

In the ASTM E837-8, one can find the same equations expressed using others parameters, such as p, q, t and P, Q, T defined as follows :

$$\begin{aligned} p &= \frac{\varepsilon_1+\varepsilon_3}{2} \\ q &= \frac{\varepsilon_3-\varepsilon_1}{2} \\ t &= \frac{\varepsilon_1-2\varepsilon_2+\varepsilon_3}{2} \end{aligned} \qquad \begin{aligned} P &= \frac{(\sigma_y+\sigma_x)}{2} = \frac{-Ep}{\bar{a}(1+\nu)} \\ Q &= \frac{(\sigma_y-\sigma_x)}{2} = \frac{-Eq}{\bar{b}} \\ T &= \tau_{xy} = \frac{-Et}{\bar{b}} \\ \beta &= 1/2 \times \arctan\frac{-T}{-Q} \end{aligned} \tag{B.10}$$

B.7 Blind-hole drilling

The general theory, presented above, is developed for a through-thickness hole in the case of unifrom stresses. For the blind hole-drilling, the theory is quite similar apart from the calibration coefficients $\bar{a}$ and $\bar{b}$ which depend on the ratio depth over gauge circle diameter (z/D).

Therefore, in the case of incremental blind-hole drilling, the coefficients change at each incremental step.

The calibration constants indicate the relieved strains in a hole j steps deep, due to unit stresses within hole step k. Fig. 3 shows cross-sections of drilled holes for an example sequence where a hole is drilled in four depth steps. Within this sequence, calibration constant represents an intermediate stage where the hole has reached 3 steps deep, and has a unit stress acting within depth step 2. Numerical values of the calibration constants have been determined by finite element calculations (4) for standard rosette patterns, and are tabulated in this test method.

Appendix C

Strong and weak forms for transient non-linear heat conduction

Equations are developed steps by steps (strong formulation, weak formulation, finite element formulation) to obtain discrete equations that can be solved numerically (Fish and Belytschko, 2007; FREY and Jirousek, 2001).

C.1 The strong form (partial differential equations)

C.1.1 Energy balance (conservation of energy)

Considering the three-dimensional control volume in Fig. C.2, q is the surface heat flux flowing out through the boundaries of the control volume (rate of heat flow accross a surface in $W/mm^2 = J/(s.mm^2)$), s is defined as the heat generated or heat source (energy per unit volume and time in $W/mm^3 = J/(s.mm^3)$). The internal energy is denoted by U (energy in W = J/s).

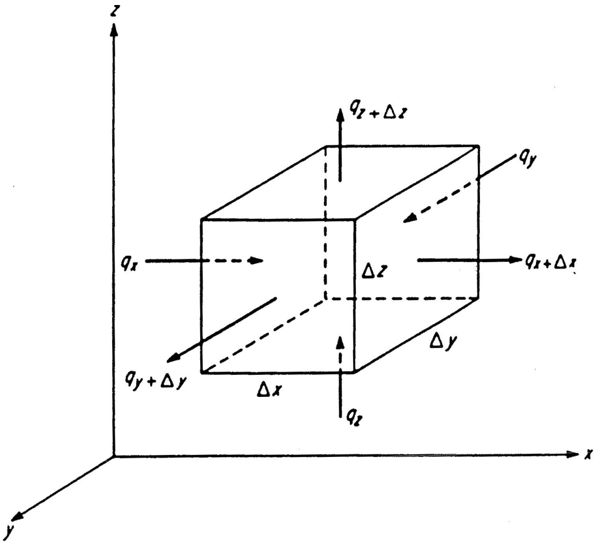

Figure C.1: 3D heat conduction in a control volume.

Energy balance in a control volume during an increment of time Δt implies that the change in internal energy must equal the heat energy generated and the difference between the heat flow entering and exiting through the surfaces of the control volume. Note that, for steady-state problem, the temperature is constant so that the internal energy do not change with time.

Thus, energy balance can be expressed as following:

$$U^{t+\Delta t} - U^t = \Delta t \; ((q_x - q_{x+\Delta x}) \; \Delta y \; \Delta z + (q_y - q_{y+\Delta y}) \; \Delta x \; \Delta z \\ + (q_z - q_{z+\Delta z}) \; \Delta x \Delta y + s \; \Delta x \; \Delta y \; \Delta z) \tag{C.1}$$

Internal energies U can be written as function of the specific internal energies u (in J/kg) multiplied by the density of the material ρ (in kg/mm^3): $U^t = \rho \; u^t \; \Delta x \; \Delta y \; \Delta z$.

Knowing that the partial derivative of $\mathrm{q_x}$ is defined as $\lim\limits_{\Delta x \to 0} \frac{q_x - q_{x+\Delta x}}{\Delta x} = \frac{\partial q_x}{\partial x}$, the equation (C.1) can be written:

$$\rho u^t + \frac{\partial \rho u^t}{\partial t} \Delta t - \rho u^t \quad = \quad \Delta t \; (\frac{q_x - q_{x+\Delta x}}{\Delta x} + \frac{q_y - q_{y+\Delta y}}{\Delta y} + \frac{q_z - q_{z+\Delta z}}{\Delta y} + s) \tag{C.2}$$

$$\Leftrightarrow \rho \frac{\partial u^t}{\partial t} \quad = \quad - \frac{\partial q_x}{\partial x} - \frac{\partial q_y}{\partial y} - \frac{\partial q_z}{\partial z} + s \tag{C.3}$$

or in the vector form ($\tilde{\nabla}$ the gradient operator):

$$\rho \frac{\partial u^t}{\partial t} \quad = \quad -\vec{\nabla}. \; \vec{q} + s \tag{C.4}$$

It is important to note that, in an **uncoupled transfer analysis** (thermal and mechanical problems are solved one after another), U, q and s depend only on the temperature difference and not on the strain and displacement fields.

C.1.2 Constitutive definition

The Fourier's law, constitutive equation for heat flow, expresses the heat flux as a function of temperature T:

$$\vec{q} \quad = \quad -k \vec{\nabla} T \tag{C.5}$$

where k is the temperature dependent thermal conductivity in W/(mm.°C) = J/(s.mm.°C).

Moreover, the rate of specific internal energies $\frac{\partial \mathrm{u^t}}{\partial \mathrm{t}}$ is related to the specific heat C (units in J/(kg.°C)) as shown in equ. (C.6). The specific heat C should only be function of the temperature in an uncoupled analysis. However, the latent heat L induced by the phase changes between solidus and liquidus is important. It is taken into consideration by including it as an equivalent specific heat value $\mathrm{C_{eq}} = \mathrm{C} + \mathrm{L}$ (see Fig. (C.1))

$$\frac{\partial u^t}{\partial t} \quad = \quad \frac{\partial u^t}{\partial T} \frac{\partial T}{\partial t} \tag{C.6}$$

$$= \quad C_{eq} \; \frac{\partial T}{\partial t} \tag{C.7}$$

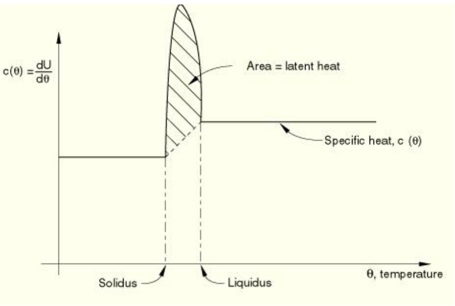

Figure C.2: Combination of specific heat and latent heat between solidus and liquidus temperatures (ABAQUS, 2009).

Thus, inserting equ. (C.5) and (C.7) into (C.4), we obtain (∇^2T the Laplacian operator):

$$\rho\, C_{eq}\, \frac{\partial T}{\partial t} = k\, (\frac{\partial^2 T}{\partial x^2} + \frac{\partial^2 T}{\partial y^2} + \frac{\partial^2 T}{\partial z^2}) + s \tag{C.8}$$

$$\Leftrightarrow \rho\, C_{eq}\, \frac{\partial T}{\partial t} = k\nabla^2 T + s \tag{C.9}$$

A second order equation is obtained (the order derivative is 2m=2). It implies that m=1, thus boundary conditions are needed at each point of the boundary. In our case, we have a heat flux boundary condition on a part of the boundary and on a temperature boundary condition on the other part.

C.1.3 Boundary conditions

In order to solve these partial differential equations, temperature boundary conditions or flux boundary conditions are requested.

Natural boundary condition (heat flux)

The flux normal to the boundary is prescribed to $\bar{\mathrm{q}}$:

$$q_n = \vec{q}.\vec{n} = \bar{q} \text{ on } \Gamma_{\mathrm{q}} \tag{C.10}$$

The prescribed flux $\bar{\mathrm{q}}$ results from natural convection and radiation to the environment.

Essential boundary condition (temperature)

Along the boundary, the temperature should equal the prescribed temperature $\bar{\mathrm{T}}$:

$$T = \bar{T} \text{ on } \Gamma_{\mathrm{T}} \tag{C.11}$$

Note that the boundary where the flux is prescribed Γ_{q} and where the temperature is prescribed Γ_{T} are complementary and do not intersect. They form together the entire boundary: $\Gamma = \Gamma_{\mathrm{q}} + \Gamma_{\mathrm{T}}$.

C.1.4 Summary

In summary, equations of the strong form problem are the following (vector notation):

$$\begin{cases} \text{Energy balance } \rho\, C_{eq}\, \dfrac{\partial T}{\partial t} = & -\vec{\nabla}.\, \vec{q} + s \\ \text{Fourier's law } \vec{q} = & -k\vec{\nabla}T \\ \text{Natural boundary condition } q_n = & \vec{q}.\vec{n} = \bar{q} \quad \text{on} \quad \Gamma_{\mathrm{q}} \\ \text{Essential boundary condition } T = & \bar{T} \quad \text{on} \quad \Gamma_{\mathrm{T}} \end{cases} \tag{C.12}$$

C.2 The weak form (integral form)

A weak form (integral form), equivalent to the strong form (differential equations), is developed. Indeed, the finite element equations are based on the weak form. The main advantages of the weak form is the lower derivative order of its equations and the fact that natural boundary conditions are already included in the form (FREY and Jirousek, 2001).

The weak form is obtained by multiplying the equations of the strong form (equ. (C.4)) (and the natural boundary condition (equ. (C.10)) by a weight function w and integrating over the domain Ω.

Beginning with the energy balance equation:

$$\int_\Omega w(\vec{\nabla}.\, \vec{q} - (s - \rho\, C_{eq}\, \frac{\partial T}{\partial t}))\; d\Omega \;=\; 0 \tag{C.13}$$

$$\Leftrightarrow \int_\Omega w\vec{\nabla}.\, \vec{q}\; d\Omega - \int_\Omega w(s - \rho\, C_{eq}\, \frac{\partial T}{\partial t}))\; d\Omega \;=\; 0 \tag{C.14}$$

Based on Green's formula, the first term of the previous equation is replaced:

$$\int_\Gamma w\vec{q}.\, \vec{n}\; d\Gamma - \int_\Omega \vec{\nabla}w.\, \vec{q}\; d\Omega - \int_\Omega w(s - \rho\, C_{eq}\, \frac{\partial T}{\partial t}))\; d\Omega \;=\; 0 \tag{C.15}$$

Since $\Gamma = \Gamma_{\mathrm{q}} + \Gamma_{\mathrm{T}}$, the first term can be written as followed. Moreover, substituting equ. (C.10), we obtain:

$$\int_\Gamma w\vec{q}.\, \vec{n}\; d\Gamma \;=\; \int_{\Gamma_q} w\vec{q}.\, \vec{n}\; d\Gamma + \int_{\Gamma_T} w\vec{q}.\, \vec{n}\; d\Gamma \tag{C.16}$$

$$= \int_{\Gamma_q} w\bar{q}\; d\Gamma + \int_{\Gamma_T} w\vec{q}.\, \vec{n}\; d\Gamma \tag{C.17}$$

$$= \int_{\Gamma_q} w\bar{q}\; d\Gamma \tag{C.18}$$

The weight function w stands for admissible temperature field $\hat{\mathrm{T}}$. It is required that $\mathrm{w} = 0$ when $\mathrm{T} = \bar{\mathrm{T}}$ on Γ_{T}, thus the last term of the equation (C.16) is eliminated.

Introducing it in equ. (C.15) and substituting $\tilde{\mathrm{q}}$ by equ. (C.5), the weak form (vector notation) is deducted:

$$\int_\Omega \vec{\nabla}w.\, \vec{q}\; d\Omega \;=\; \int_{\Gamma_q} w\bar{q}\; d\Gamma - \int_\Omega w(s - \rho\, C_{eq}\, \frac{\partial T}{\partial t}))\; d\Omega\ \forall \mathrm{w} \text{ with } \mathrm{w} = 0 \text{ on } \Gamma_{\mathrm{T}} \tag{C.19}$$

$$\Leftrightarrow \int_\Omega k\vec{\nabla}w.\, \vec{\nabla}T\; d\Omega \;=\; -\int_{\Gamma_q} w\bar{q}\; d\Gamma + \int_\Omega w(s - \rho\, C_{eq}\, \frac{\partial T}{\partial t}))\; d\Omega\ \forall \mathrm{w} \text{ with } \mathrm{w} = 0 \text{ on } \Gamma_{\mathrm{T}}$$

The weak form can also be written in the matrix notation (where **D** is the conductivity matrix):

$$\boxed{\int_{\Omega} (\boldsymbol{\nabla} w)^T \ \mathbf{D} \boldsymbol{\nabla} T \ d\Omega = - \int_{\Gamma_q} w \bar{q} \ d\Gamma + \int_{\Omega} w(s - \rho \ C_{eq} \ \frac{\partial T}{\partial t})) \ d\Omega}$$

$$\forall \mathrm{w} \text{ with } \mathrm{w} = 0 \text{ on } \Gamma_{\mathrm{T}} \tag{C.20}$$

The admissible field of temperature $\hat{\mathrm{T}}$ should be smooth enough, i.e. continuous enough (should have all derivatives of the required order) and satisfies the essential boundary condition.

The weak form is expressed with the first order derivative (m=1). Boundary conditions are needed at each point of the boundary.

C.3 The finite element formulation

From the weak form, the algebraic system of equations for element is developed. In the finite element method, the global equations are obtained by assembling the equations of all elements forming the domain. Then, global equations are solved.

The integrals of the weak form above should be summed over all the elements ($\mathrm{n_{el}}$ is the number of elements):

$$\sum_{e=1}^{n_{el}} (\int_{\Omega^e} (\boldsymbol{\nabla} w^e)^T \ \mathbf{D}^e \boldsymbol{\nabla} T^e \ d\Omega + \int_{\Gamma_q^e} w^{eT} \bar{q} \ d\Gamma - \int_{\Omega^e} w^{eT} (s - \rho \ C_{eq} \ \frac{\partial T}{\partial t})) \ d\Omega) = 0 \tag{C.21}$$

where the functions $\mathrm{T(x, y, z, t)}$ and $\mathrm{w^T(x, y, z, t)}$ are approximated as following on the element ($\mathrm{n_{en}}$ is the number of element nodes, $\mathbf{T}^{\mathrm{e}}$ is the matrix of element nodal temperatures, $\mathbf{w}^{\mathrm{e}}$ is the matrix of element nodal weight function values) (Fish and Belytschko, 2007):

$$T(x, y, z, t) \approx T^e(x, y, z, t) = \mathbf{N}^e(x, y, z)\mathbf{T}^e = \sum_{I=1}^{n_{en}} N_I^e(x, y, z) T_I^e \tag{C.22}$$

$$w(x, y, z, t) \approx w^e(x, y, z, t) = \mathbf{N}^e(x, y, z)\mathbf{w}^e = \sum_{I=1}^{n_{en}} N_I^e(x, y, z) w_I^e \tag{C.23}$$

Since we use hexahedral elements (3D) with 8 nodes (trilinear) in our case, $\mathrm{T(x, y, z, t)}$ and $\mathrm{w^T(x, y, z, t)}$ are linear functions. Therefore, $\mathrm{N_I^e(x, y, z)}$ are linear shape functions.

$$\begin{aligned} T^e(x, y, z, t) &= \sum_{I=1}^{8} N_I^e(x, y, z) T_I^e \\ w^e(x, y, z, t) &= \sum_{I=1}^{8} N_I^e(x, y, z) w_I^e \end{aligned} \tag{C.24}$$

The matrix of element nodal temperatures $\mathbf{T}^{\mathrm{e}}$ is related to the matrix of global temperature $\mathbf{T}$ by the gather matrix $\mathbf{L}^{\mathrm{e}}$ allowing the assembly of the element nodal values:

$$\mathbf{T}^e = \mathbf{L}^e \mathbf{T} \tag{C.25}$$

Therefore, inserting (C.25) in (C.24), we obtain:

$$
\begin{aligned}
T^e &= \mathbf{N}^e\mathbf{L}^e\mathbf{T} && \text{(C.26)}\\
w^{eT} &= (\mathbf{N}^e\mathbf{L}^e\mathbf{w})^T = \mathbf{w}^T\mathbf{L}^{eT}\mathbf{N}^{eT} && \text{(C.27)}
\end{aligned}
$$

And the gradient $\boldsymbol{\nabla}\mathrm{T}^{\mathrm{e}}$ and $\boldsymbol{\nabla}\mathrm{w}^{\mathrm{eT}}$ can be deducted:

$$
\begin{aligned}
\boldsymbol{\nabla}T^e &= \begin{bmatrix} \frac{\partial T}{\partial x} \\ \\ \frac{\partial T}{\partial y} \\ \\ \frac{\partial T}{\partial z} \end{bmatrix} = \begin{bmatrix} \frac{\partial N_1^e}{\partial x}T_1^e + \frac{\partial N_2^e}{\partial x}T_2^e + ... + \frac{\partial N_8^e}{\partial x}T_8^e \\ \\ \frac{\partial N_1^e}{\partial y}T_1^e + \frac{\partial N_2^e}{\partial y}T_2^e + ... + \frac{\partial N_8^e}{\partial y}T_8^e \\ \\ \frac{\partial N_1^e}{\partial z}T_1^e + \frac{\partial N_2^e}{\partial z}T_2^e + ... + \frac{\partial N_8^e}{\partial z}T_8^e \end{bmatrix}\\
&= \begin{bmatrix} \frac{\partial N_1^e}{\partial x} & \vdots & \frac{\partial N_2^e}{\partial x} & \vdots & ... & \vdots & \frac{\partial N_8^e}{\partial x} \\ \frac{\partial N_1^e}{\partial y} & \vdots & \frac{\partial N_2^e}{\partial y} & \vdots & ... & \vdots & \frac{\partial N_8^e}{\partial y} \\ \frac{\partial N_1^e}{\partial z} & \vdots & \frac{\partial N_2^e}{\partial z} & \vdots & ... & \vdots & \frac{\partial N_8^e}{\partial z} \end{bmatrix} \mathbf{T}^e = \boldsymbol{\nabla}\mathbf{N}^e\mathbf{T}^e = \mathbf{B}^e\mathbf{L}^e\mathbf{T} && \text{(C.28)}\\
\boldsymbol{\nabla}w^e &= \mathbf{B}^e\mathbf{L}^e\mathbf{w} && \text{(C.29)}
\end{aligned}
$$

The global matrices $\mathbf{T}$ and $\mathbf{w}$ are partitioned in order to take into account that, at nodes with essential boundary conditions, $\mathrm{T} = \bar{\mathrm{T}}$ and $\mathrm{w} = 0$. E stands for essential boundary conditions and F contains the rest of nodal values.

$$
\mathbf{d} = \begin{Bmatrix} \bar{\mathbf{T}}_E \\ \\ \mathbf{T}_F \end{Bmatrix}
$$

$$
\mathbf{w} = \begin{Bmatrix} 0 \\ \\ \mathbf{w}_F \end{Bmatrix}
$$

Thus, for all w_{F} ($w_I \neq 0$), equation (C.21) can be expressed as following:

$$
\begin{aligned}
&\mathbf{w}^T(\sum_{e=1}^{n_{el}}\mathbf{L}^{eT}(\underbrace{\int_{\Omega^e}\mathbf{B}^{eT}\mathbf{D}^e\mathbf{B}^e d\Omega}_{\mathbf{K}^e}\,\mathbf{L}^e\mathbf{T} + \underbrace{\int_{\Gamma_q^e}\mathbf{N}^{eT}\bar{q}\;d\Gamma}_{-\mathbf{f}_\Gamma^e} \underbrace{-\int_{\Omega^e}\mathbf{N}^{eT}s\;d\Omega}_{-\mathbf{f}_\Omega^e}\\
&\qquad + \underbrace{\int_{\Omega^e}\mathbf{N}^{eT}\rho\;C_{eq}\mathbf{N}^e d\Omega}_{\mathbf{C}^e}\,\mathbf{L}^e\frac{\partial\mathbf{T}}{\partial t}\;d\Omega)) = 0 && \text{(C.30)}\\
&\Leftrightarrow \mathbf{w}^T((\sum_{e=1}^{n_{el}}\mathbf{L}^{eT}\mathbf{K}^e\mathbf{L}^e)\mathbf{T} - (\sum_{e=1}^{n_{el}}\mathbf{L}^{eT}\mathbf{f}^e) + (\sum_{e=1}^{n_{el}}\mathbf{L}^{eT}\mathbf{C}^e\mathbf{L}^e)\frac{\partial\mathbf{T}}{\partial t}) = 0 && \text{(C.31)}\\
&\Leftrightarrow \mathbf{w}^T(\mathbf{K}\mathbf{T} - \mathbf{f} + \mathbf{C}\frac{\partial\mathbf{T}}{\partial t}) = 0 && \text{(C.32)}
\end{aligned}
$$

where $\mathbf{K}^{\mathrm{e}}$ is the element conductance matrix, $\mathbf{f}^{\mathrm{e}} = \mathbf{f}_\Gamma^{\mathrm{e}} + \mathbf{f}_\Omega^{\mathrm{e}}$ is the element flux matrix and $\mathbf{C}^{\mathrm{e}}$ is the element capacitance matrix. $\mathbf{K}$, $\mathbf{f}$ and $\mathbf{C}$ are the equivalent global matrices.

C.3.1 Time integration scheme used in ABAQUS

The system of first order differential equations (C.30) should be integrated with time. ABAQUS uses the backward difference algorithm and more precisely the backward Euler scheme given by:

$$\dot{T}_{t+\Delta t} = \left.\frac{\partial T}{\partial t}\right|_{t+\Delta t} = \frac{T_{t+\Delta t} - T_t}{\Delta t} \tag{C.33}$$

This non linear problem is solved using an iterative and incremental method, based on the Newton-Raphson method ($\mathrm{T_{n+1} = T_n - \frac{f(T_n)}{f'(T_n)}}$).

C.4 Problem solving options

All the parameters presented below were obtained iteratively by testing manually different combinations.

ABAQUS options

As explained in section C.3.1, non-linear problems are solved in ABAQUS using an incremental and iterative technique, based on the Newton-Raphson method. The time increment Δt used in ABAQUS is self-adaptive. It is based on the tolerances imposed by the user and by internal convergence criteria (residual heat flux $\leq 10^{-3}$ heat flux).

For the thermal analysis, the transient *HEAT TRANSFER is defined as follows:

```
*HEAT TRANSFER,DELTMX=50.
0.01,27.0,0.00001
```

where the DELTMX parameter limits the maximum change of temperature that may occur in an increment to 50°C, the initial time increment is set to 0.01 s, the total time period of the step is set to 27 s, it corresponds here to the time of the first welding step and the minimum time increment is imposed to 0.00001 s. There is no imposed values for the maximum time increment and the temperature change rate.

Therefore, there are two main criteria that limit the time increment value:

- the convergence criterion: if the convergence is not reached during the imposed time increment, the time increment is reduced a certain number of times until there is convergence.
- the maximum change of temperature $\Delta\mathrm{T_{max}}$ criterion: if $\Delta\mathrm{T_{max}}$ is exceeded during the imposed time increment, the time increment is reduced until there is convergence for a $\Delta\mathrm{T} < \Delta\mathrm{T_{max}}$.

Usually, as shown in Fig. C.3, the first criterion is the one that drives the welding steps and the beginning of the cooling steps, and the second criterion drives the end of the cooling step where the rate of temperature change decreases drastically.

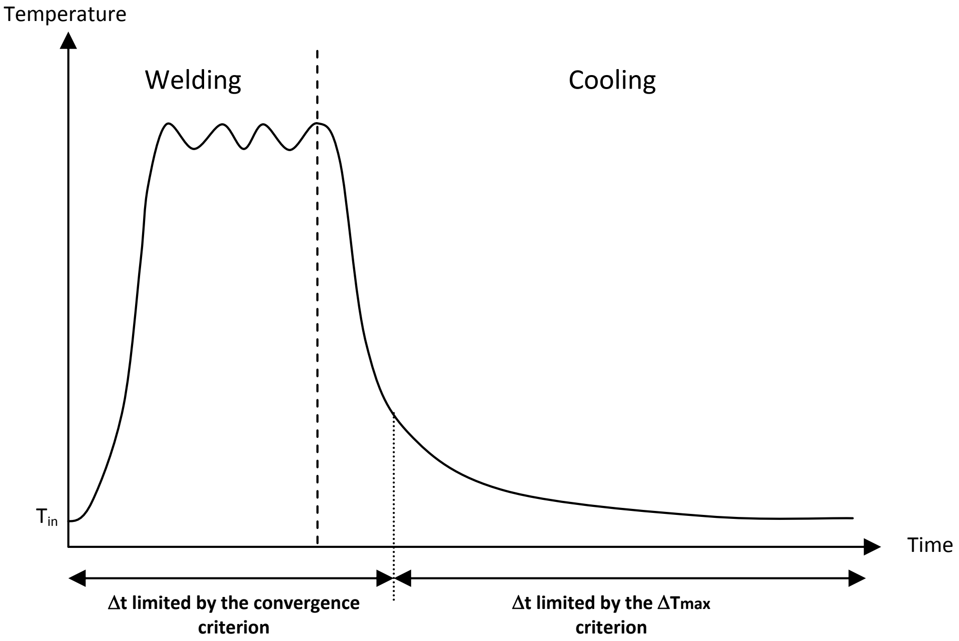
Temperature
Welding
Cooling
T_{in}
Time
Δt limited by the convergence criterion
Δt limited by the ΔTmax criterion

Figure C.3: Time increments driven by the convergence criterion or by the ΔT_{max} criterion.

For the mechanical analysis, the *STATIC option is defined as follows for the welding step:

```
*STATIC
0.001,27.0,1.e-12,0.1
```

And for the cooling step:

```
*STATIC
0.001,123.0,1.e-12
```

where the initial time increment is set to 0.001 s, the total time period of the step corresponds exactly to the one defined in the HEAT TRANSFER, the minimum time increment is imposed to $1.e^{-12}$ s and the maximum time increment is imposed to 0.1 s for the welding step in order to keep the increment small enough for a good accuracy.

MORFEO options

In MORFEO, the solving process is faster because it requires less iteration to converge.

The time incrementation is also adaptive but less flexible. The same 'AdaptiveStepper' is used for the thermal and mechanical analyses.

For the welding steps, the adaptive step of the transient computation is defined with the following parameters: DeltaInit, the initial time increment, is 0.1 s, DeltaMax, the maximum time increment, is 0.5 s, DeltaMin, the minimum time increment, 0.01s. If the previous time step converges successfully, the next one can be increased by an acceleration factor (FasterFactor = 1.5 in our case). Otherwise, if the convergence failed, the time increment can be decreased by a slowdown factor (SlowerFactor = 0.5).

For the cooling steps, DeltaInit, DeltaMax and DeltaMin are increased respectively to 0.5 s, 5.0 s and 0.05 s.

Appendix D

Residual stress field from ABAQUS parametric study

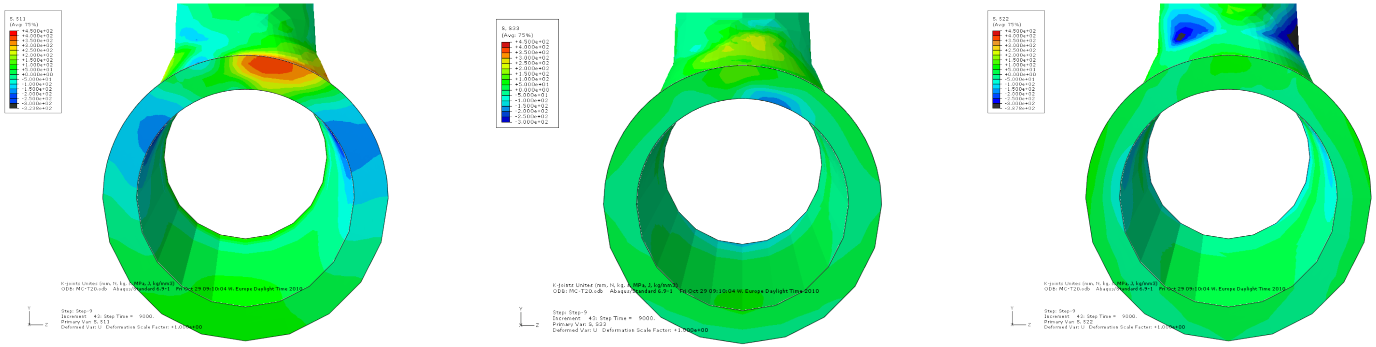

(a) Transverse stresses, right cross section **(b)** Longitudinal stresses, right cross section **(c)** Radial stresses, right cross section

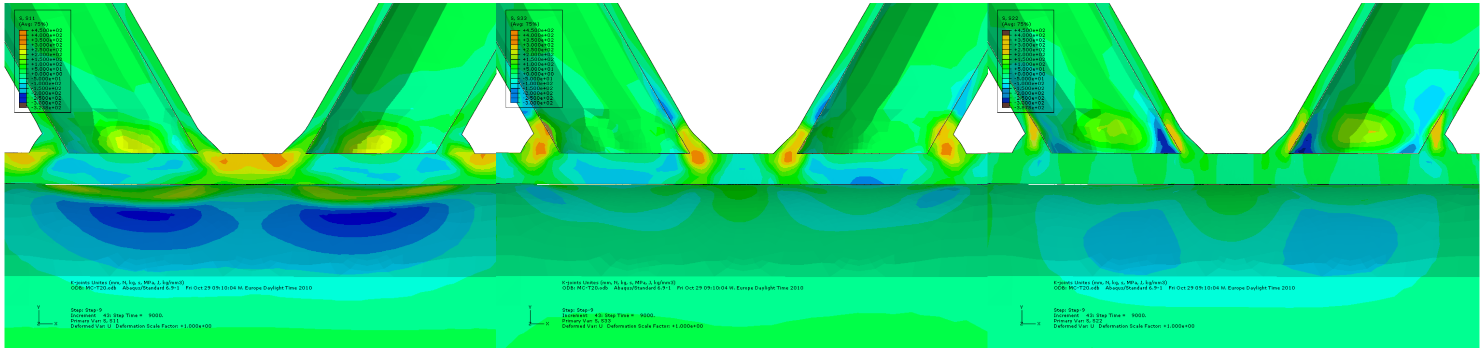

(d) Transverse stresses, axial cross section **(e)** Longitudinal stresses, axial cross section **(f)** Radial stresses, axial cross section

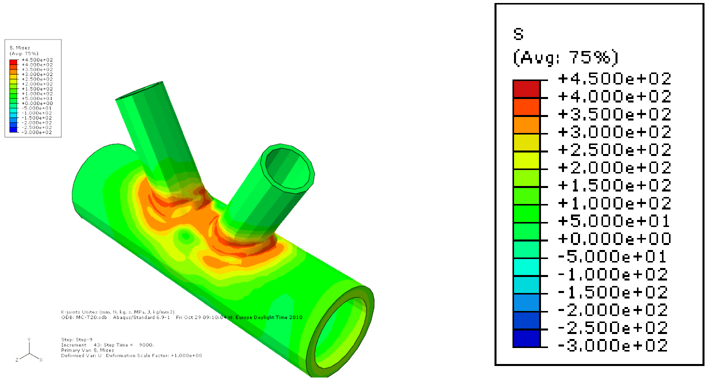
S
(Avg: 75%)
+4.500e+02
+4.000e+02
+3.500e+02
+3.000e+02
+2.500e+02
+2.000e+02
+1.500e+02
+1.000e+02
+5.000e+01
+0.000e+00
-5.000e+01
-1.000e+02
-1.500e+02
-2.000e+02
-2.500e+02
-3.000e+02

(g) Von Mises stresses

Figure D.1: Residual stresses for model Ref-T20 (model 1).

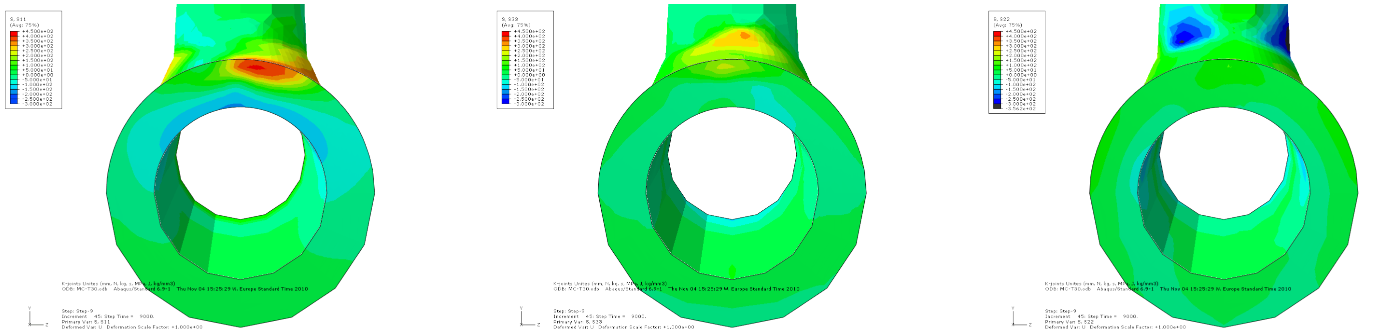

(a) Transverse stresses, right cross section **(b)** Longitudinal stresses, right cross section **(c)** Radial stresses, right cross section

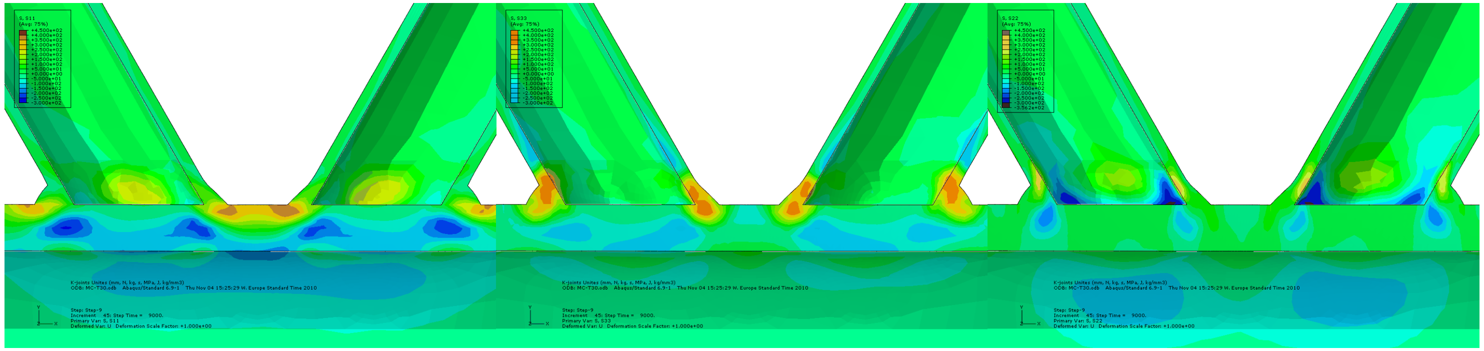

(d) Transverse stresses, axial cross section **(e)** Longitudinal stresses, axial cross section **(f)** Radial stresses, axial cross section

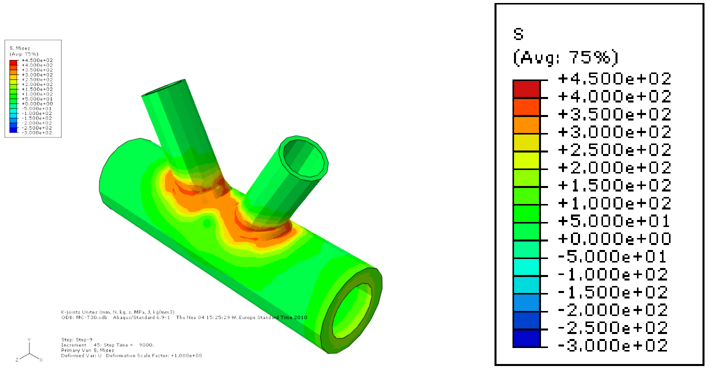
S
(Avg: 75%)
+4.500e+02
+4.000e+02
+3.500e+02
+3.000e+02
+2.500e+02
+2.000e+02
+1.500e+02
+1.000e+02
+5.000e+01
+0.000e+00
-5.000e+01
-1.000e+02
-1.500e+02
-2.000e+02
-2.500e+02
-3.000e+02

(g) Von Mises stresses

Figure D.2: Residual stresses for model Ref-T30 (model 1).

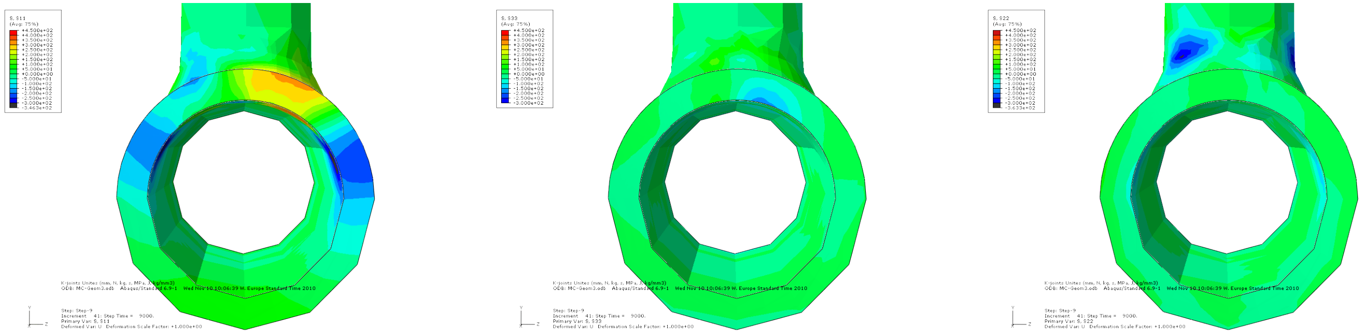

(a) Transverse stresses, right cross section **(b)** Longitudinal stresses, right cross section **(c)** Radial stresses, right cross section

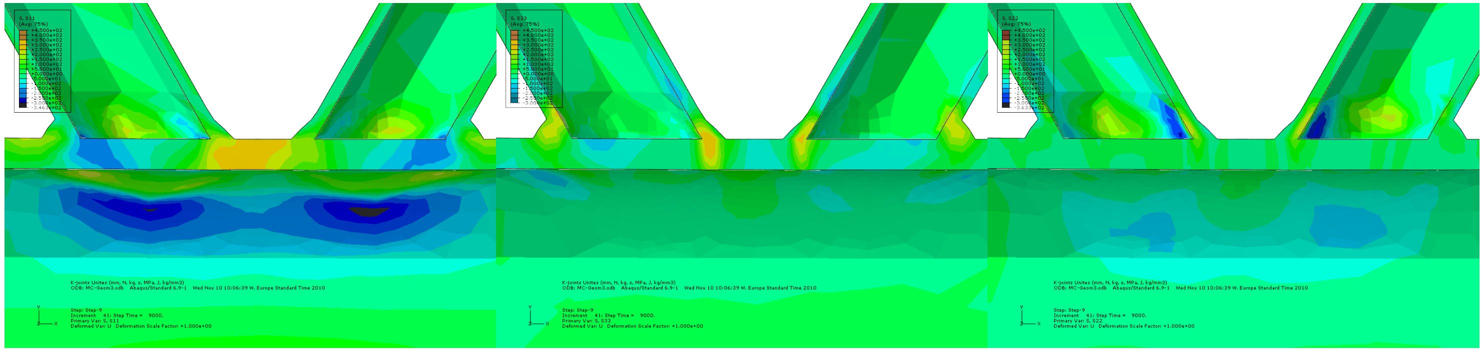

(d) Transverse stresses, axial cross section **(e)** Longitudinal stresses, axial cross section **(f)** Radial stresses, axial cross section

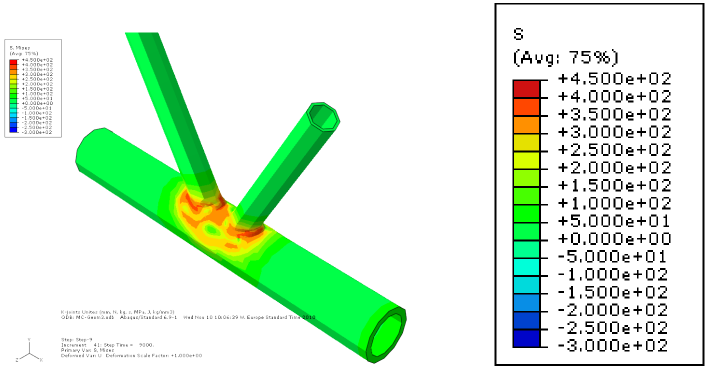

(g) Von Mises stresses

Figure D.3: Residual stresses for model 3.

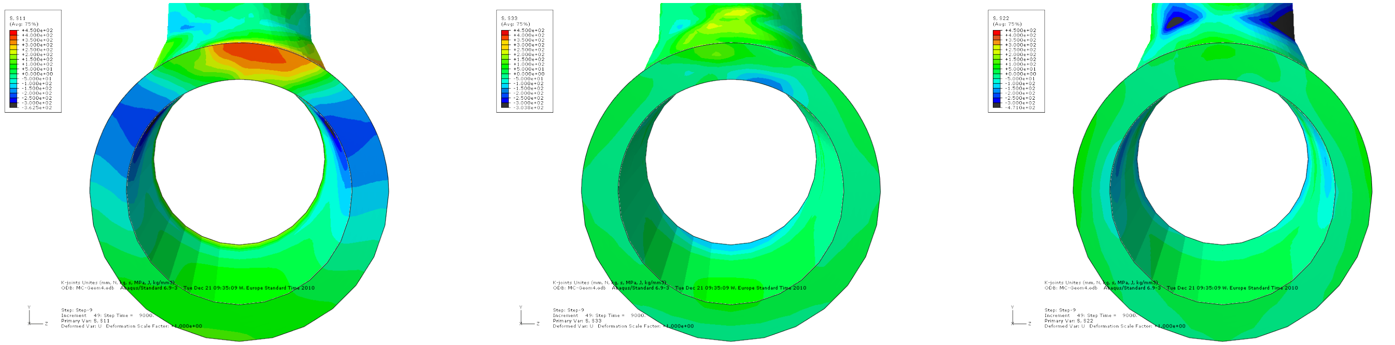

(a) Transverse stresses, right cross section **(b)** Longitudinal stresses, right cross section **(c)** Radial stresses, right cross section

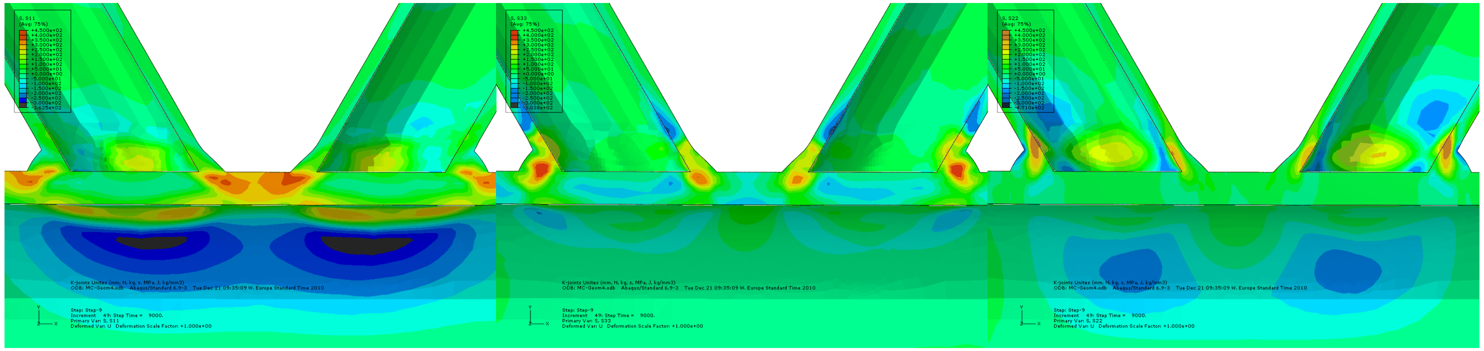

(d) Transverse stresses, axial cross section **(e)** Longitudinal stresses, axial cross section **(f)** Radial stresses, axial cross section

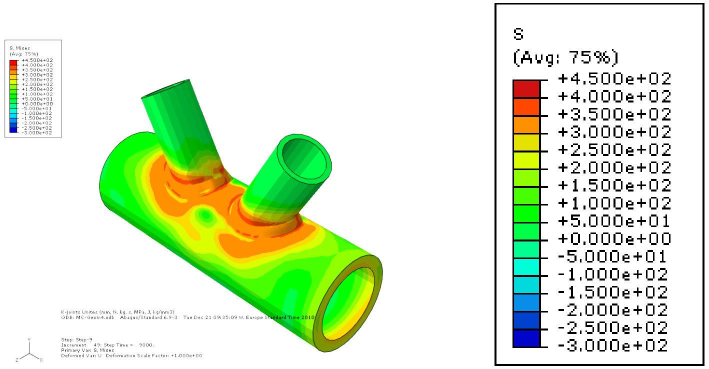
S
(Avg: 75%)
+4.500e+02
+4.000e+02
+3.500e+02
+3.000e+02
+2.500e+02
+2.000e+02
+1.500e+02
+1.000e+02
+5.000e+01
+0.000e+00
-5.000e+01
-1.000e+02
-1.500e+02
-2.000e+02
-2.500e+02
-3.000e+02

(g) Von Mises stresses

Figure D.4: Residual stresses for model 4.

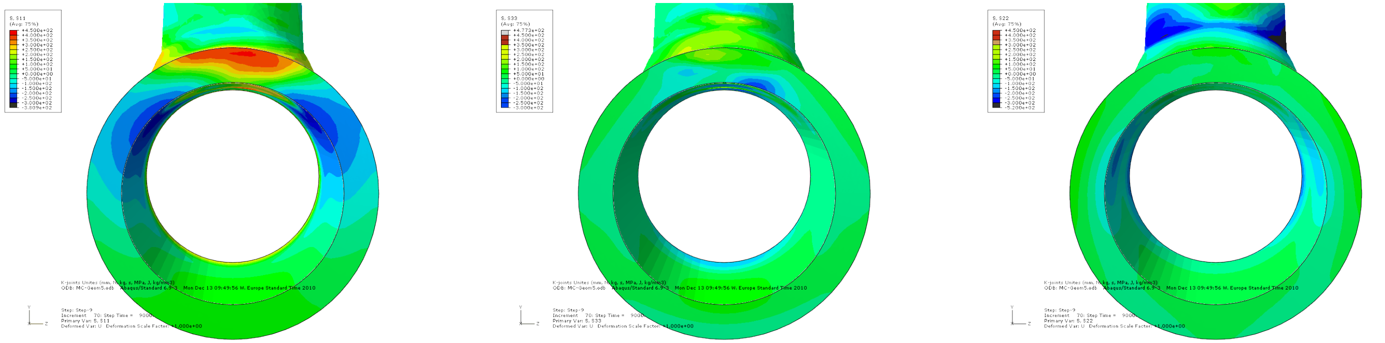

(a) Transverse stresses, right cross section **(b)** Longitudinal stresses, right cross section **(c)** Radial stresses, right cross section

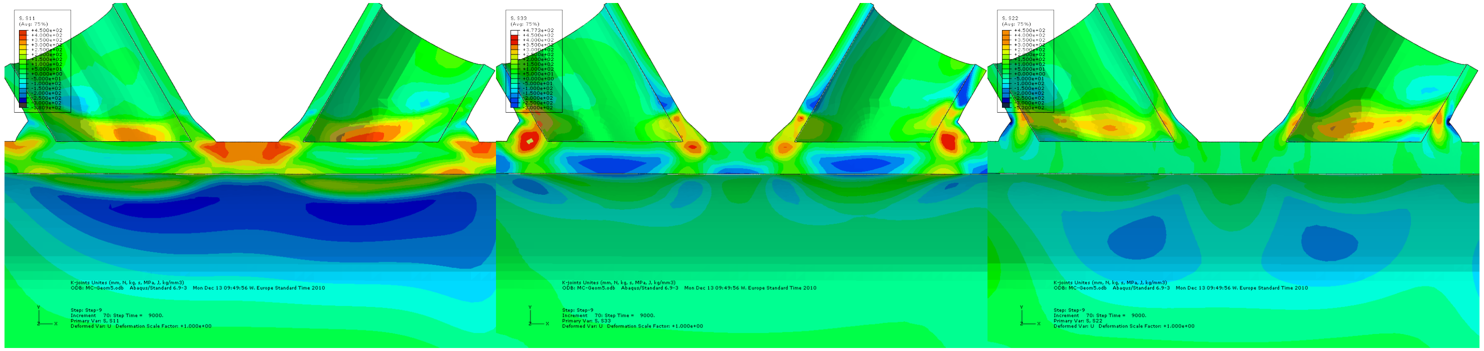

(d) Transverse stresses, axial cross section **(e)** Longitudinal stresses, axial cross section **(f)** Radial stresses, axial cross section

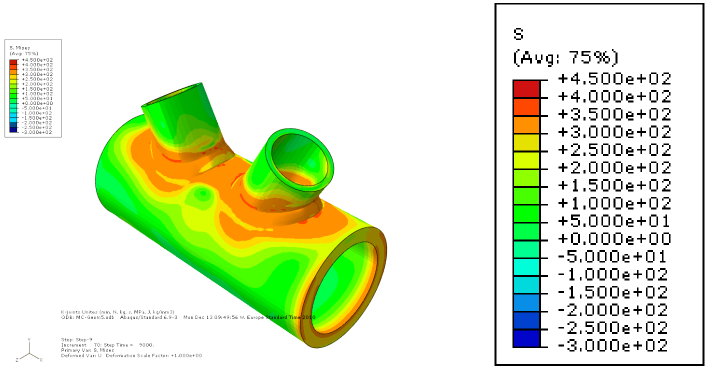
S
(Avg: 75%)
+4.500e+02
+4.000e+02
+3.500e+02
+3.000e+02
+2.500e+02
+2.000e+02
+1.500e+02
+1.000e+02
+5.000e+01
+0.000e+00
-5.000e+01
-1.000e+02
-1.500e+02
-2.000e+02
-2.500e+02
-3.000e+02

(g) Von Mises stresses

Figure D.5: Residual stresses for model 5.

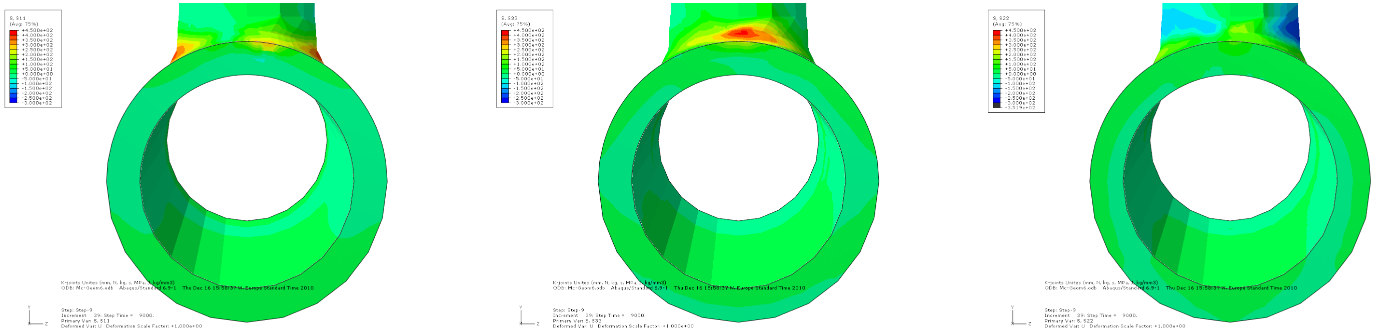

(a) Transverse stresses, right cross section **(b)** Longitudinal stresses, right cross section **(c)** Radial stresses, right cross section

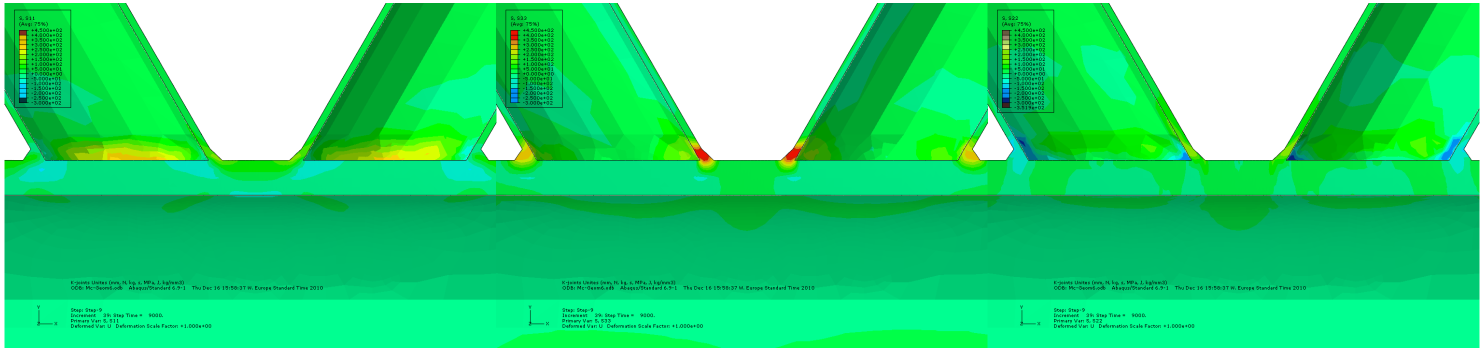

(d) Transverse stresses, axial cross section **(e)** Longitudinal stresses, axial cross section **(f)** Radial stresses, axial cross section

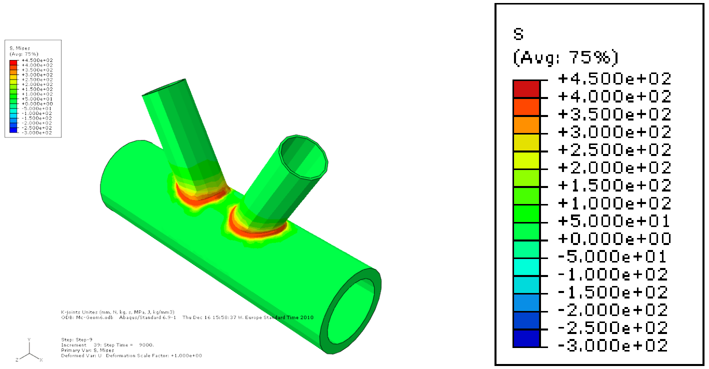
S
(Avg: 75%)
+4.500e+02
+4.000e+02
+3.500e+02
+3.000e+02
+2.500e+02
+2.000e+02
+1.500e+02
+1.000e+02
+5.000e+01
+0.000e+00
-5.000e+01
-1.000e+02
-1.500e+02
-2.000e+02
-2.500e+02
-3.000e+02

(g) Von Mises stresses

Figure D.6: Residual stresses for model 6.

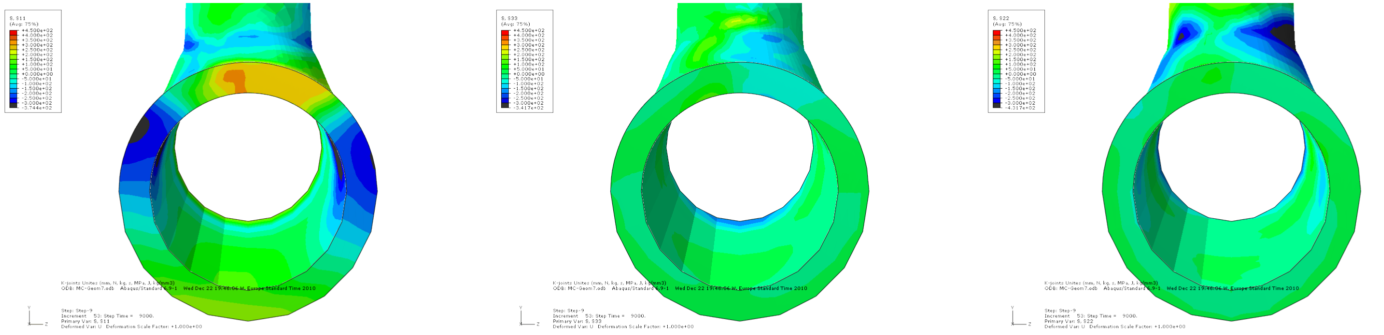

(a) Transverse stresses, right cross section **(b)** Longitudinal stresses, right cross section **(c)** Radial stresses, right cross section

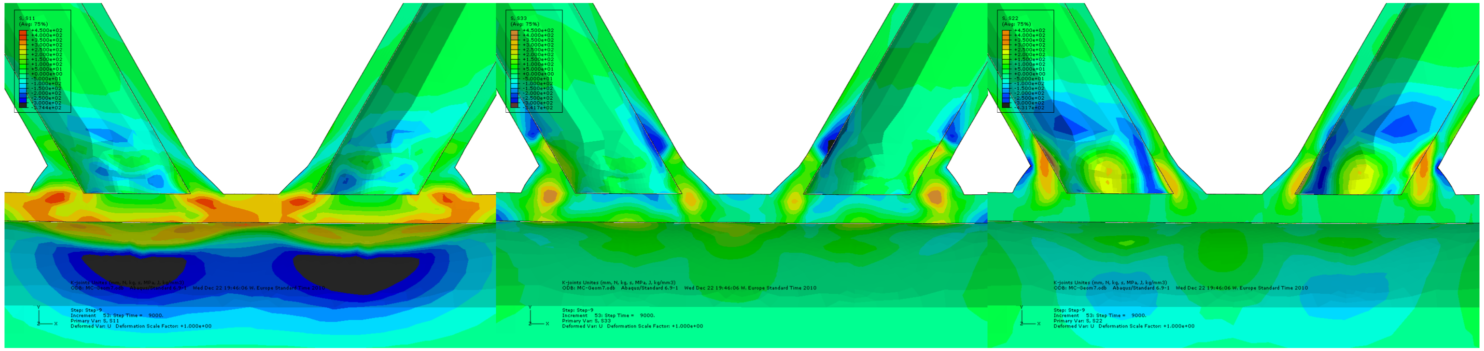

(d) Transverse stresses, axial cross section **(e)** Longitudinal stresses, axial cross section **(f)** Radial stresses, axial cross section

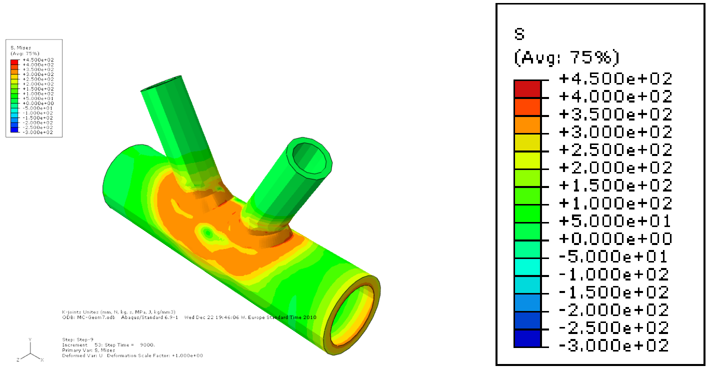
S
(Avg: 75%)
+4.500e+02
+4.000e+02
+3.500e+02
+3.000e+02
+2.500e+02
+2.000e+02
+1.500e+02
+1.000e+02
+5.000e+01
+0.000e+00
-5.000e+01
-1.000e+02
-1.500e+02
-2.000e+02
-2.500e+02
-3.000e+02

(g) Von Mises stresses

Figure D.7: Residual stresses for model 7.

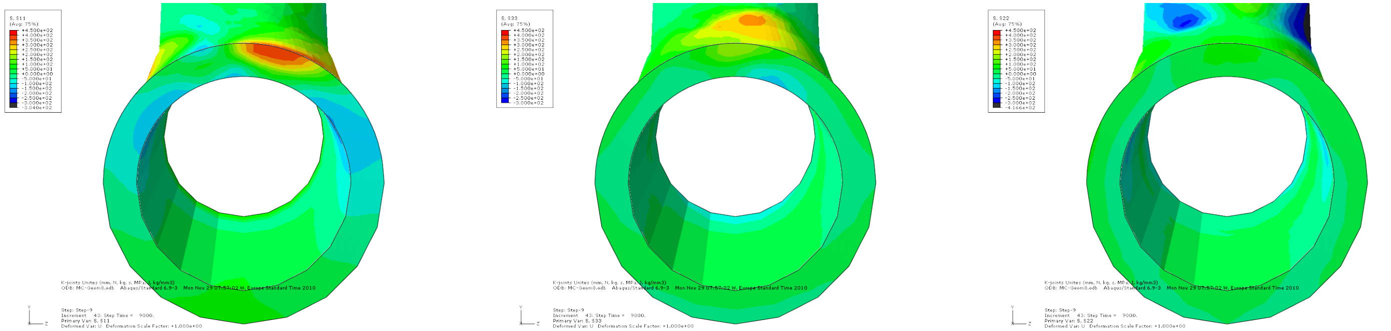

(a) Transverse stresses, right cross section **(b)** Longitudinal stresses, right cross section **(c)** Radial stresses, right cross section

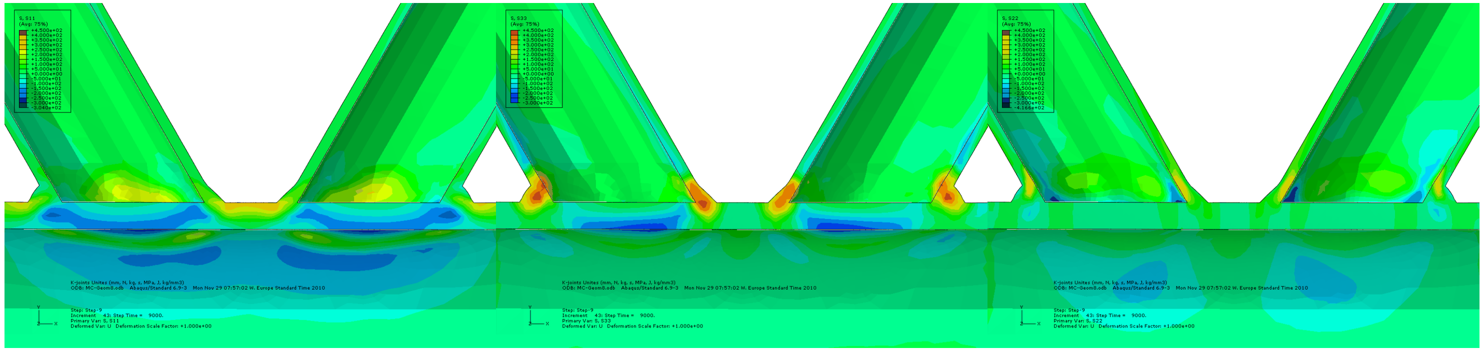

(d) Transverse stresses, axial cross section **(e)** Longitudinal stresses, axial cross section **(f)** Radial stresses, axial cross section

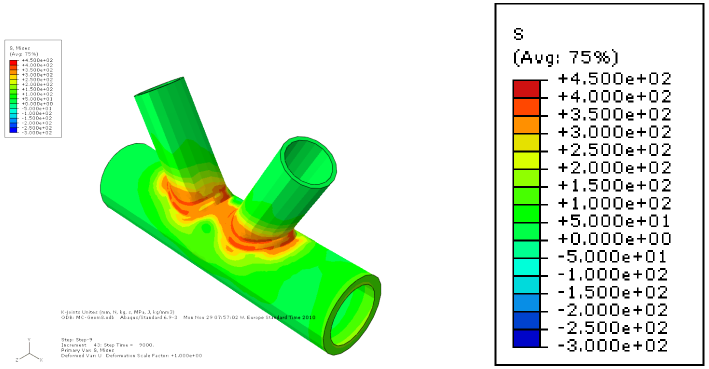

(g) Von Mises stresses

Figure D.8: Residual stresses for model 8.

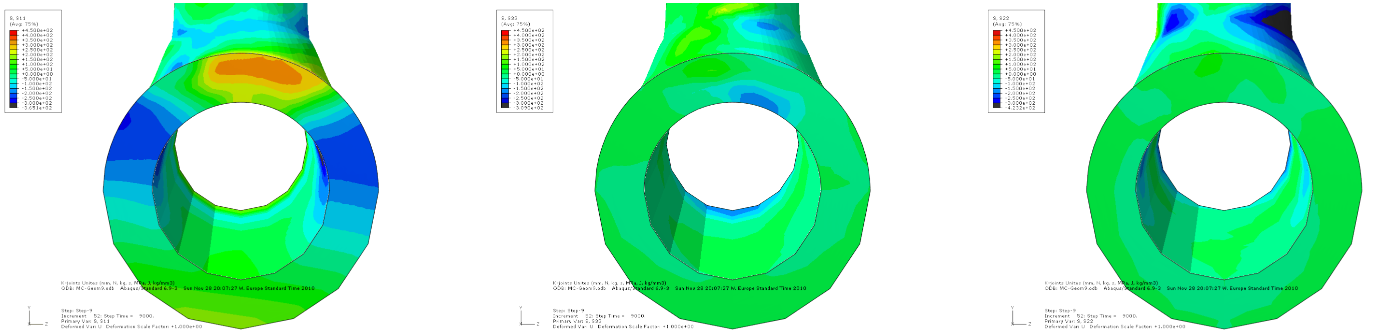

(a) Transverse stresses, right cross section **(b)** Longitudinal stresses, right cross section **(c)** Radial stresses, right cross section

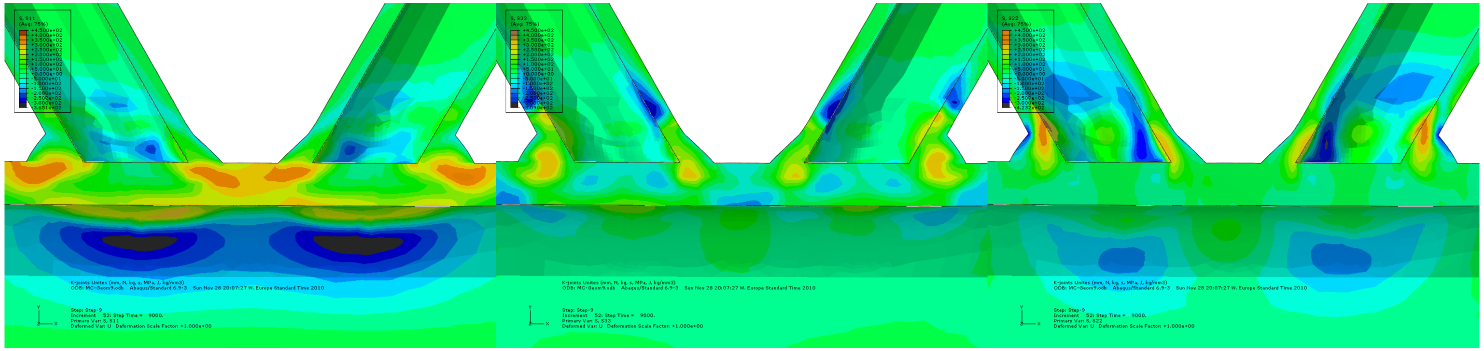

(d) Transverse stresses, axial cross section **(e)** Longitudinal stresses, axial cross section **(f)** Radial stresses, axial cross section

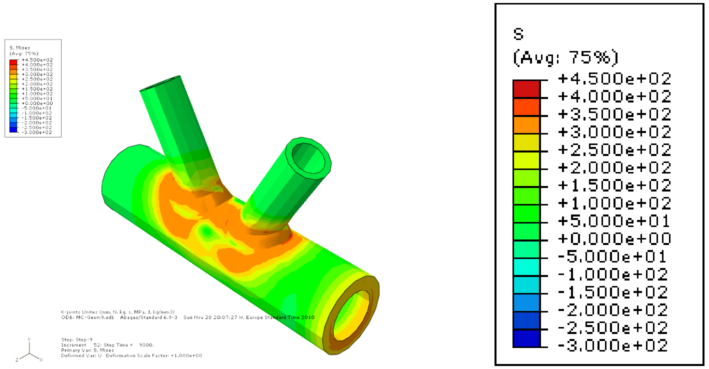
S
(Avg: 75%)
+4.500e+02
+4.000e+02
+3.500e+02
+3.000e+02
+2.500e+02
+2.000e+02
+1.500e+02
+1.000e+02
+5.000e+01
+0.000e+00
-5.000e+01
-1.000e+02
-1.500e+02
-2.000e+02
-2.500e+02
-3.000e+02

(g) Von Mises stresses

Figure D.9: Residual stresses for model 9.

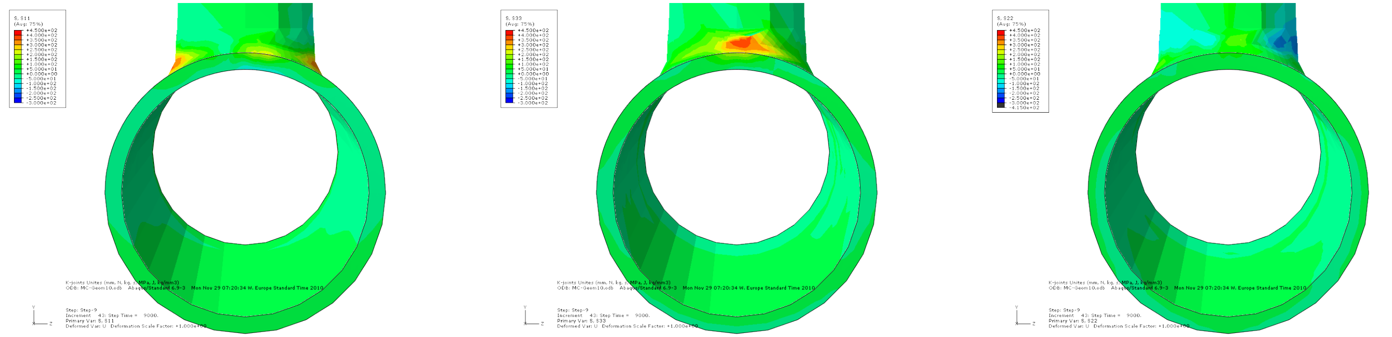

(a) Transverse stresses, right cross section **(b)** Longitudinal stresses, right cross section **(c)** Radial stresses, right cross section

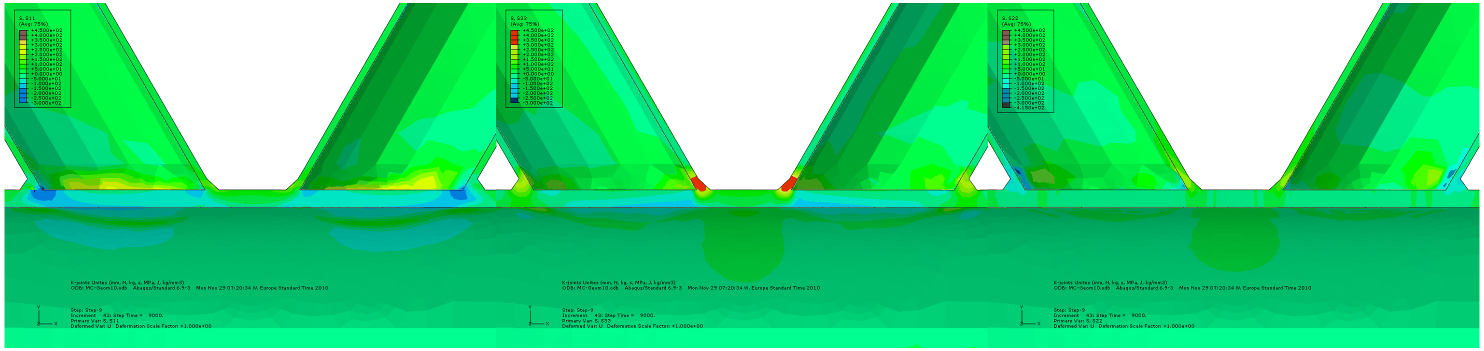

(d) Transverse stresses, axial cross section **(e)** Longitudinal stresses, axial cross section **(f)** Radial stresses, axial cross section

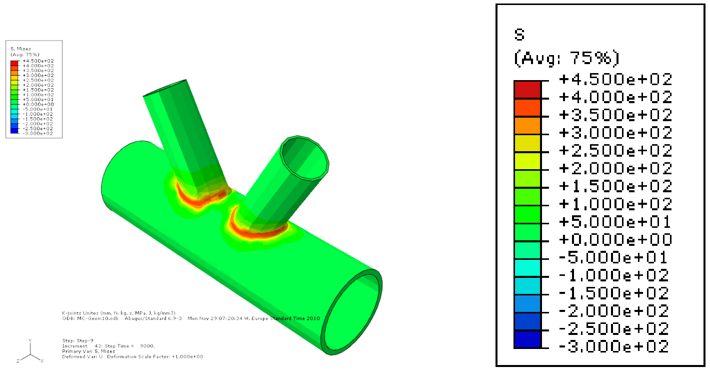
S
(Avg: 75%)
+4.500e+02
+4.000e+02
+3.500e+02
+3.000e+02
+2.500e+02
+2.000e+02
+1.500e+02
+1.000e+02
+5.000e+01
+0.000e+00
-5.000e+01
-1.000e+02
-1.500e+02
-2.000e+02
-2.500e+02
-3.000e+02

(g) Von Mises stresses

Figure D.10: Residual stresses for model 10.

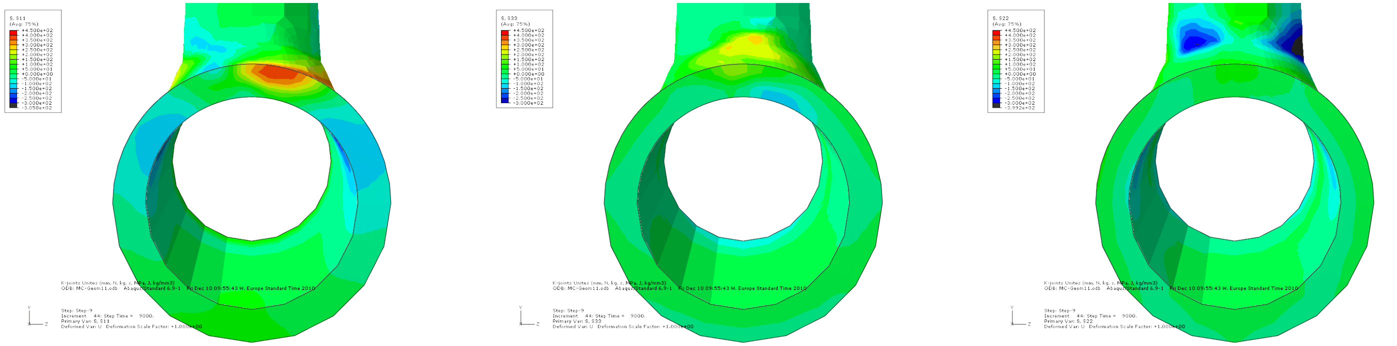

(a) Transverse stresses, right cross section **(b)** Longitudinal stresses, right cross section **(c)** Radial stresses, right cross section

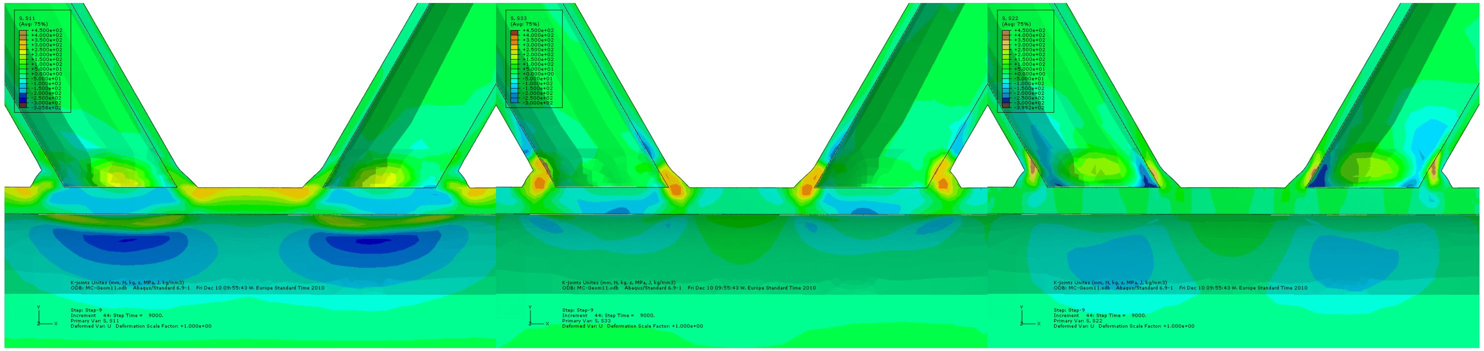

(d) Transverse stresses, axial cross section **(e)** Longitudinal stresses, axial cross section **(f)** Radial stresses, axial cross section

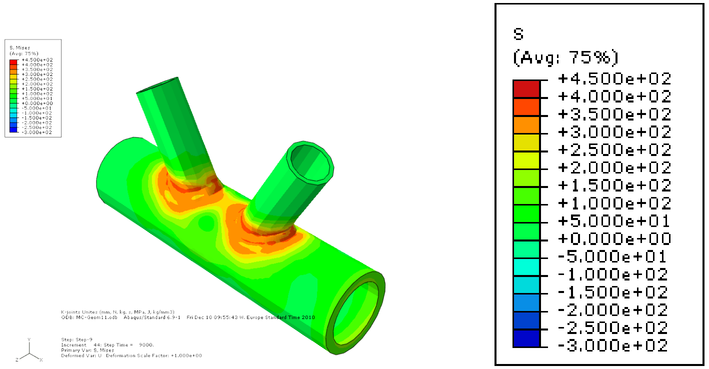

(g) Von Mises stresses

Figure D.11: Residual stresses for model 11.

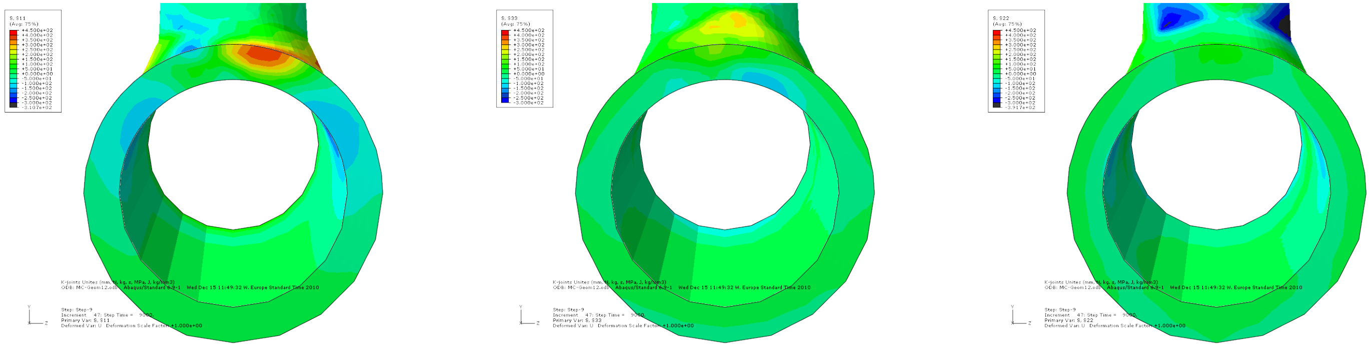

(a) Transverse stresses, right cross section **(b)** Longitudinal stresses, right cross section **(c)** Radial stresses, right cross section

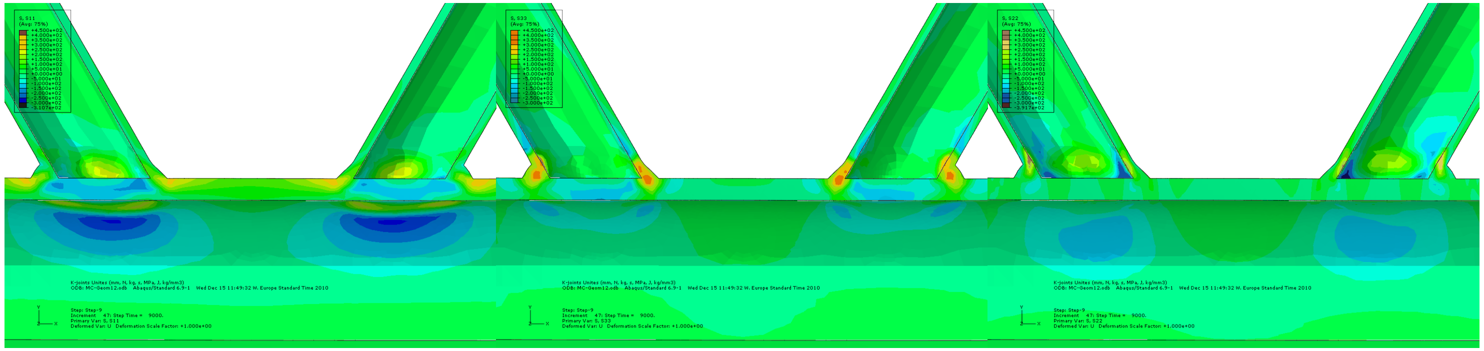

(d) Transverse stresses, axial cross section **(e)** Longitudinal stresses, axial cross section **(f)** Radial stresses, axial cross section

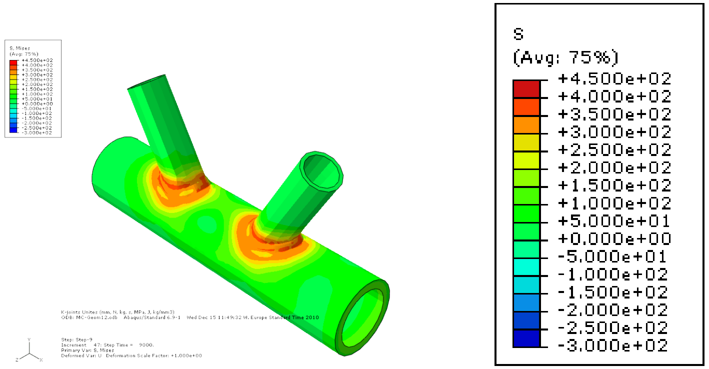
S
(Avg: 75%)
+4.500e+02
+4.000e+02
+3.500e+02
+3.000e+02
+2.500e+02
+2.000e+02
+1.500e+02
+1.000e+02
+5.000e+01
+0.000e+00
-5.000e+01
-1.000e+02
-1.500e+02
-2.000e+02
-2.500e+02
-3.000e+02

(g) Von Mises stresses

Figure D.12: Residual stresses for model 12.

CLAIRE ACEVEDO

Date of birth: April 23, 1978
claire.acevedo@a3.epfl.ch

EDUCATION

2007-2011	**Ph.D. expected in Mai 2011, Civil Engineering**, EPFL, Switzerland
2000-2002	**M.S., Civil Engineering**, Swiss Federal Institute of Technology (EPFL), Switzerland GPA 5.13/6.0
1999-2000	**Civil Engineering**, Ecole Polytechnique de Montreal, Montreal, Canada Year abroad, GPA 3.65/4.0
1997-1999	**B.S., Civil Engineering**, Swiss Federal Institute of Technology (EPFL), Switzerland GPA 4.73/6.0

EXPERIENCE

RESEARCH

2007-Present **Research and teaching Assistant**, Steel Structure Lab. ICOM, EPFL, Switz.
Thesis supervisors: Prof. A. Nussbaumer, Dr. J-M. Drezet

PhD thesis topic: Influence of residual stresses on fatigue response of welded tubular joints
Research objectives:

- Quantify the fatigue crack propagation in welded tubular joints through large-scale laboratory tests
- Quantify the residual stress distribution in welded tubular joints using neutron-diffraction, hole-drilling and X-ray methods
- Model and simulate (FEM) residual stresses induced by the welding process
- Combine the welding simulation with fatigue crack propagation analysis
- Examine the influence of residual stress distribution on the fatigue crack growth of welded tubular K-joints in order to optimize the fatigue-life of these joints

2006-2007 **Research Engineer**, Steel Structure Laboratory ICOM, EPFL, Switzerland
Supervisor: Prof. M. A. Hirt

Research Projects:

- Static and dynamic tests on the wing structure prototype for the challenging solar airplane from Bertrand Piccard called SOLAR IMPULSE (http://solar-impulse.epfl.ch/): a 10m long box made out of very light carbon-Kevlar sandwich panels
- Expertise report to verify security and stability of a group of existing buildings
- Participation in a Swiss federal roads project (OFROU) on 'New method for design of steel-concrete composite plate girder bridges', report 640
- Participation in a Swiss federal roads project (OFROU) on 'Evaluation of existing road bridges with an updated traffic load model', report 594
- MIKTI project on 'Evaluation and maintenance of composite bridges': fatigue tests and fatigue crack detection

Oct-Mar 2002 **Undergraduate Research Assistant**, LSC, EPFL, Switzerland
Supervisors: Prof. Frey, B. Rebora

Master thesis topic: Numerical solution for shells of revolution problems

Contribution to the Book chapter 'Coques de revolution. Theorie flexionnelle sous chargement de revolution' in *Analyse des structures et milieux continus: Coques*, F. Frey and M.-A. Studer, Presses polytechniques et universitaires romandes (2003)

Jun-Sep 2000 **Undergraduate Research Assistant**, IMAC, EPFL, Switzerland
Supervisors: Dr. B. Glisic, Prof. Pflug

Objective: Develop a fiber optic sensor for mortar material

INDUSTRY

2002-2006 **Design Engineer**, Guscetti-Tournier Civil Engineers, Geneva, Switzerland

Projects:

- Addition of three stories to the Rolex World Headquarters tower: steel structure and composite slabs
- Reinforcement of an existing building built at the beginning of the century by the famous engineer Robert Maillart
- Design of Sismondi high school: concrete structure with wood-concrete composite slab

PUBLICATIONS

JOURNAL PUBLICATIONS

- Acevedo, C. (2010). 'Constructions tubulaires, ruine des structures', Journal de la construction de la Suisse romande Batir focus, June 2010, pp.13.
- Acevedo, C., Evans A., Nussbaumer, A. 'Neutron diffraction investigations on residual stresses contributing to the fatigue crack growth in ferritic steel tubular bridges' (submitted to the International Journal of Pressure Vessels and Piping).
- Acevedo, C., Nussbaumer, A. 'Experimental proof of the effect of tensile residual stresses on fatigue crack growth in tubular joints loaded in compression' (submitted to the International Journal of Fatigue).
- Acevedo, C., Drezet, J.M., Lefebvre, J.-P., D'Alvise, L., Nussbaumer, A. 'Residual stresses in as-welded joints: finite element modeling and neutron diffraction stress measurements' (submitted to the Journal of Key Engineering Materials)
- Acevedo, C., Drezet, J.M., Nussbaumer, A. 'Numerical modeling and experimental investigation on welding residual stresses that influence the fatigue crack growth in tubular K-joints' (in submission process to the Fatigue & Fracture of Engineering Materials & Structures).
- Acevedo, C., Nussbaumer, A., Drezet, J.M. 'Schweisseigenspannungen Ermittlung und Ermdung Rissverhaltung an K-Rohrknoten unter druck' (in submission process to Stahlbau, August 2011).

REFEREED CONFERENCE PUBLICATIONS

- Acevedo, C., Nussbaumer, A. (2009). 'Residual Stress Estimation of welded tubular K-joints under fatigue loads'. Peer reviewed proceeding of the 12th International Conference on Fracture (ICF) 12 (T12.001), Ottawa, 12-17 July 2009.
- Acevedo, C., Nussbaumer, A. (2010). 'Influence of welding residual stresses on stable crack growth in tubular K-joints under compressive fatigue loadings', Peer reviewed proceeding of the 13th International Symposium on Tubular Structures (ISBN 978-0-415-58473-9), Hong Kong, 15-17 December 2010, pp.557-565.
- Acevedo, C., Drezet, J.M., Lefebvre, J.-P., D'Alvise, L., Nussbaumer, A. 'Residual stresses in as-welded joints: finite element modeling and neutron diffraction stress measurements', Proceedings of the 10th International Conference on Fracture and Damage Mechanics, Dubrovnik, 19-21 September 2011 (submitted).

- Acevedo, C., Drezet, J.M., Nussbaumer, A. 'Numerical modeling and experimental investigation on welding residual stresses that influence the fatigue crack growth in tubular K-joints', Proceedings of ICEAF II, 2nd International Conference on Engineering Against Fracture, Mykonos, 22-24 June 2011 (in submission process).

OTHER CONFERENCE PUBLICATIONS

- Acevedo, C., Nussbaumer, A. (2009). 'Study on crack propagation in tubular joints under compressive fatigue loadings', Proceedings of the International Conference on Fatigue Design 2009 (Cdrom ISBN 978-2-85400-908-8), Senlis, 25-26 November 2009.
- Acevedo, C., Nussbaumer, A. (2010). 'Residual stress effects in tubular K-joints crack growth', Proceedings of the 1st EPFL Doctoral Conference in Mechanics EDCM2010: Advances in Modern Aspects of Mechanics (ISBN 978-2-8399-0646-3), Lausanne, 19 February 2010.
- Zamiri, F., Acevedo, C., Nussbaumer, A. (2011). 'Investigation of technological size effects of welding on the fatigue life of tubular K-joints made of structural steel S355', Proceedings of the 4th International Conference on Fatigue Design 2011, Senlis, 23-24 November 2011 (in submission process).

PRESENTATIONS

- Acevedo, C., Nussbaumer, A. (2009). 'Influence of welding residual stresses on fatigue crack propagation under compression'. International Institute of Welding IIW, Commission XIII Fatigue of welded components and structures, Darmstadt, 5-6 March 2009.
- Acevedo, C., Nussbaumer, A. (2009). 'Residual Stress Estimation of welded tubular K-joints under fatigue loads'. Conference presentation to the 12th International Conference on Fracture (ICF) 12 (T12.001), Ottawa, 12-17 July 2009.
- Acevedo, C., Nussbaumer, A. (2009). 'Residual Stress Measurements of welded tubular K-joints'. MIT meetings, Boston, 3 and 5 August 2009.
- Acevedo, C., Nussbaumer, A. (2009). 'Study on crack propagation in tubular joints under compressive fatigue loadings', Conference presentation to the International Conference on the respective input of the numerical simulation and the experimental approach in Fatigue Design 2009 (Cdrom ISBN 978-2-85400-908-8), Senlis, 25-26 November 2009.
- Acevedo, C., Nussbaumer, A. (2010). 'Crack growth in K-joints driven by fatigue applied stresses and residuals stresses', Fatigue seminar with Prof. Sonsino and Prof. Marquis, Lausanne, 18 February 2010.
- Acevedo, C., Nussbaumer, A. (2010). 'Residual stress effects in tubular K-joints crack growth', Conference presentation to the 1st EPFL Doctoral Conference in Mechanics EDCM2010: Advances in Modern Aspects of Mechanics (ISBN 978-2-8399-0646-3), Lausanne, 19 February 2010.
- Acevedo, C., Nussbaumer, A. (2010). 'The MAG welding process used for tubular K-joint connections', Cenaero (Simulation technologies for Aeronautics) meetings, Lausanne, 23 April 2010.
- Acevedo, C., Nussbaumer, A. (2010). 'Influence des contraintes résiduelles sur la résistance à la fatigue des joints tubulaires soudés', Manifestation ICOM, Lausanne, 5 November 2010.
- Acevedo, C., Drezet, J.M., Nussbaumer, A. 'Numerical modeling and experimental investigation on welding residual stresses that influence the fatigue crack growth in tubular K-joints', Conference presentation to the ICEAF II, 2nd International Conference on Engineering Against Fracture, Mykonos, 22-24 June 2011 (will be attended).

TEACHING ACTIVITIES

2007-2008 **Lecturer (part time 40 %)**, University of Applied Sciences of Western Switzerland

- Teaching 'Structural Mechanics I', 'Structural Mechanics II' and 'Structural Mechanics III' for bachelor students in Architecture
- Responsible for semester and summer projects (BS)

2007-Present **Teaching Assistant**, Swiss Federal Institute of Technology (EPFL), Switzerland

Teaching assistant for several courses linked with steel construction:

- Courses: 'Steel Bridges' (MS), 'Steel Structures I and II' (BS), 'Steel Structures for architects' (BS')
- Supervision of three laboratory projects, two internship on residual stress measurements and several semester projects related to steel sheds and towers
- Co-supervision of master of science thesis related to welded tubular structures

EXTRACURRICULAR ACTIVITIES

In charge of the organisation of events and seminars at ICOM laboratory
Attended the workshop of the Institute for Value-based Enterprise, passed with great honor
Member of the International Association for Bridge and Structural Engineering IABSE
Vice president and treasurer of the EPFL association for exchange students (2000-2001)
Sports: climbing, contemporary dance, handball

LANGUAGE SKILLS

French: mother tongue; English: fluent; Spanish: basic; German: basic.